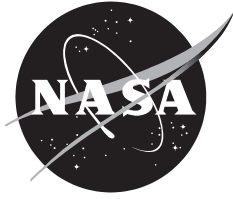


NASA/CR—2015–218871



# **Superboom Caustic Analysis and Measurement Program (SCAMP) Final Report**

*Juliet Page, Ken Plotkin, and Chris Hobbs  
Wyle Laboratories, El Segundo, California*

*Vic Sparrow and Joe Salamone  
The Pennsylvania State University, State College, Pennsylvania*

*Robbie Cowart and Joe Salamone  
Gulfstream Aerospace Corporation, Falls Church, Virginia*

*Kevin Elmer, H. Robert Welge, and John Ladd  
The Boeing Company, Chicago, Illinois*

*Domenic Maglieri  
Eagle Aeronautics, Inc., Newport News, Virginia*

*Andrew Piacsek  
Central Washington University, Ellensburg, Washington*

---

**August 2015**

## NASA STI Program ... in Profile

Since its founding, NASA has been dedicated to the advancement of aeronautics and space science. The NASA scientific and technical information (STI) program plays a key part in helping NASA maintain this important role.

The NASA STI program operates under the auspices of the Agency Chief Information Officer. It collects, organizes, provides for archiving, and disseminates NASA's STI. The NASA STI program provides access to the NTRS Registered and its public interface, the NASA Technical Reports Server, thus providing one of the largest collections of aeronautical and space science STI in the world. Results are published in both non-NASA channels and by NASA in the NASA STI Report Series, which includes the following report types:

- TECHNICAL PUBLICATION. Reports of completed research or a major significant phase of research that present the results of NASA Programs and include extensive data or theoretical analysis. Includes compilations of significant scientific and technical data and information deemed to be of continuing reference value. NASA counterpart of peer-reviewed formal professional papers but has less stringent limitations on manuscript length and extent of graphic presentations.
- TECHNICAL MEMORANDUM. Scientific and technical findings that are preliminary or of specialized interest, e.g., quick release reports, working papers, and bibliographies that contain minimal annotation. Does not contain extensive analysis.
- CONTRACTOR REPORT. Scientific and technical findings by NASA-sponsored contractors and grantees.
- CONFERENCE PUBLICATION. Collected papers from scientific and technical conferences, symposia, seminars, or other meetings sponsored or co-sponsored by NASA.
- SPECIAL PUBLICATION. Scientific, technical, or historical information from NASA programs, projects, and missions, often concerned with subjects having substantial public interest.
- TECHNICAL TRANSLATION. English-language translations of foreign scientific and technical material pertinent to NASA's mission.

Specialized services also include organizing and publishing research results, distributing specialized research announcements and feeds, providing information desk and personal search support, and enabling data exchange services.

For more information about the NASA STI program, see the following:

- Access the NASA STI program home page at <http://www.sti.nasa.gov>
- E-mail your question to [help@sti.nasa.gov](mailto:help@sti.nasa.gov)
- Phone the NASA STI Information Desk at 757-864-9658
- Write to:  
NASA STI Information Desk  
Mail Stop 148  
NASA Langley Research Center  
Hampton, VA 23681-2199

# Superboom Caustic Analysis and Measurement Program (SCAMP) Final Report

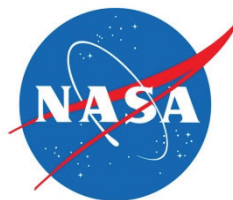
---

Wyle Report WR 12-21  
Contract Number NNL10AA08B  
Job No. T57777  
February 2013

---

## *Prepared for:*

NASA Langley Research Center  
9B Langley Blvd.  
Bldg. 1195B  
M/S 126  
Hampton, VA 23681-2199



## *Prepared by:*

Wyle  
Environmental and Energy  
Research & Consulting (EERC)



Headquarters: 200 12<sup>TH</sup> Street S, Suite 900  
Arlington, VA 22202  
703.413.4749

## **Project Team:**

---

*Authors:* Juliet Page, Ken Plotkin, Chris Hobbs, *Wyle*  
Vic Sparrow, Joe Salamone, *The Pennsylvania State University*  
Robbie Cowart, Joe Salamone, *Gulfstream*  
Kevin Elmer, H. Robert Welge, John Ladd, *Boeing*  
Domenic Maglieri, *Eagle Aeronautics*  
Andrew Piacsek, *Central Washington University*

Available from:

NASA STI Program  
Service Mail Stop 148  
NASA Langley Research Center  
Hampton, VA 23681-2199

National Technical Information  
5285 Port Royal Road  
Springfield, VA 22161  
703-605-6000

This report is also available in electronic form at <http://www.sti.gov/> and <http://ntrs.nasa.gov/>

# Table of Contents

Executive Summary ..... xiii

## Sections

---

1.0 Introduction ..... 1

    1.1 Background ..... 1

    1.2 Project Objectives ..... 2

    1.3 Tasks and Schedule ..... 3

2.0 Sonic Boom Focusing ..... 6

    2.1 Sonic Booms and Ray Tracing ..... 6

    2.2 Focusing Ray Geometry ..... 12

    2.3 Nonlinear Tricomi Equation and Focal Zone Scaling ..... 14

    2.4 Classic Focus Prediction: PCBoom and the Gill-Seebass Solution ..... 16

    2.5 Interfaces to Modern Focus Solutions ..... 19

    2.6 F-18 F-Function from CFD Analysis ..... 20

3.0 Flight Test ..... 23

    3.1 Objectives ..... 24

    3.2 Measurements Site and Microphone Array ..... 24

        3.2.1 Site ..... 24

        3.2.2 Ground Array ..... 25

        3.2.3 Elevated Measurements ..... 25

    3.3 Weather Data ..... 27

    3.4 Maneuver Design/Flight Test Matrix ..... 28

    3.5 Flight Planning: Where’s the Focus? ..... 32

3.6 Flight Test Execution ..... 33

    3.6.1 Preparation ..... 33

    3.6.2 Aircraft Waypoint Adjustment ..... 33

    3.6.3 Flights and Focus Data Acquired ..... 34

3.7 Sample Data and PCBoom Predictions ..... 38

3.8 SCAMP Collaborative Partners ..... 52

4.0	Selected Flight Conditions for Code Comparisons .....	53
4.1	Selection and Modeling of Flight Conditions.....	53
4.2	F-18 CFD Modeling for As-flown Flight Conditions .....	59
5.0	Gill-Seebass Method (PCBoom) .....	63
5.1	Methodology .....	63
5.2	Model Input Data .....	63
5.3	Comparisons with Measurement Data.....	63
5.4	Recommendations for Code Improvements .....	70
6.0	Pseudospectral Solution of Nonlinear Tricomi Equation (PSONTE).....	71
6.1	Formulation and Numeric Solutions.....	71
6.2	Preliminary Comparison with Flight Test .....	73
7.0	Nonlinear Progressive-wave Equation (NPE) .....	77
7.1	Description and Applicability.....	77
7.2	Modifications for Sonic Boom Modeling.....	78
7.3	Application of the NPE to Modeling Sonic Booms at Caustics .....	78
7.4	Using npe_scamp.....	79
7.5	Interface with PCBoom.....	80
7.5.1	Description and Usage.....	80
7.5.2	npe_scamp User Guide.....	80
7.5.3	pcboom2npe User Guide.....	81
7.5.4	Important NPE Considerations .....	82
7.6	Preliminary Results for npe_scamp.....	83
7.6.1	Demonstration Test: N-wave with Concave Ripple .....	83
7.6.2	SCAMP Flight 1264.....	86
8.0	Lossy Nonlinear Tricomi Equation (LNTE) .....	91
8.1	Methodology .....	91
8.2	Model Input Data - Alpha .....	94
8.3	Comparisons with Measurement Data - Alpha .....	97
8.4	Recommendations for Future Code Improvements.....	101
8.4.1	Beta improvements .....	101
8.4.2	Potential future improvements.....	102

9.0	Sonic Boom Focus Codes – Beta: Comparisons with Measured Data.....	103
9.1	Beta Overview .....	103
9.2	PCBoom and Gill-Seebass Method – Beta .....	103
9.3	PCBoom Input Data for LNTE and NPE .....	112
9.4	Lossy Nonlinear Tricomi Equations (LNTE) – Beta .....	122
9.4.1	LNTE Methodology .....	122
9.4.2	Model Input Data.....	122
9.4.3	Comparisons with measured data .....	123
9.5	Nonlinear Progress Wave Equation (NPE) – Beta.....	136
9.5.1	Background and Motivation .....	136
9.5.2	Scaled Ripple Approach .....	140
9.5.3	NPE Setup .....	144
9.5.4	NPE Results .....	144
9.5.5	Comparison with Flight Test .....	145
9.5.6	Conclusions and Potential Improvements.....	147
10.0	Low Boom Vehicle Analysis.....	150
10.1	Low-Boom Vehicle Descriptions.....	150
10.1.1	Gulfstream Configuration .....	150
10.1.2	Boeing Configuration .....	153
10.1.3	NASA Configurations .....	155
10.2	Focused Boom Analysis Process.....	156
10.3	PCBoom Gill-Seebass Low Boom Configuration Analysis.....	157
10.3.1	Gulfstream configuration .....	157
10.3.2	Boeing configuration .....	159
10.3.3	NASA configurations .....	162
10.3.4	Critical Analysis of Modeling Limitations – PCBoom Gill-Seebass.....	167
10.4	LNTE Low-Boom Configuration Analysis .....	167
10.4.1	Low Boom Configuration Analysis – LNTE .....	168
10.4.2	Critical Analysis of Modeling Limitations – LNTE.....	169
10.5	Low Boom Configuration Analysis – NPE .....	179
10.5.1	Low Boom Configuration Analysis – NPE.....	179
10.5.2	Critical Analysis – NPE.....	182
10.6	Low Boom Vehicle Analysis Summary and Conclusions.....	182
11.0	Profile Exploration and Focused Signatures .....	187
11.1	Profile Exploration Focused Signature Computational Process.....	188
11.2	Boeing Configuration / Profile / CFD Analysis.....	190
11.2.1	Transonic Acceleration Maneuver.....	190
11.2.2	Boeing Configuration .....	191
11.2.3	Boeing Profile Exploration Cases .....	192

11.2.4 Boeing CFD Analysis.....	196
11.3 Gulfstream Configuration / Profile / CFD Analysis.....	199
11.3.1 Gulfstream Profile Analysis.....	199
11.3.2 Gulfstream CFD Analysis.....	201
11.3.3 Gulfstream Performance Analysis .....	201
11.4 NASA Configuration / Profile / CFD Analysis.....	202
11.4.1 NASA Demonstrator Profile Analysis.....	203
11.4.2 NASA Demonstrator CFD Analysis .....	204
11.5 Lossy NTE Propagation and Low Boom Results .....	205
11.5.1 Methodology .....	205
11.5.2 Low Boom Configuration Analysis .....	206
11.5.3 Critical Analysis of Focus Boom Modeling.....	209
11.6 Analysis of Profile Exploration Results.....	256
11.6.1 Summary .....	256
11.6.2 Recommendations .....	259
12.0 Summary / Conclusions / Recommendations.....	262
12.1 Transition Focus Regime and Candidate Analytic/Numeric Focus Models.....	262
12.2 Flight Test Design and Execution.....	263
12.3 Model Validation and Development .....	264
12.4 Focusing of Low Boom Shaped Signatures.....	265
References.....	266

## Figures

1-1 Sonic Boom Ground Footprint Zones, from Maglieri (1980) .....	1
1-2 SCAMP Program Schedule – Year 1/Phase 1 .....	4
1-3 SCAMP Program Schedule – Year 2/Phase 2 .....	5
2-1 Mach Waves, Definition of Wave Coordinate $\chi$ , and Ray Normal to Waves .....	7
2-2 Ray Tube and Ray Tube Area .....	10
2-3 Ray Cone at Time $t$ and Initial Ray at Azimuth $\phi$ .....	10
2-4 Sonic Boom Generation, Propagation and Evolution .....	11
2-5 Variety of Sonic Boom Ray Paths .....	11
2-6 Sonic Boom Ray Paths and Footprint Regions, from Maglieri (1980).....	12
2-7 Focus - Acceleration to Supersonic Speed .....	12
2-8 Cutoff Caustic.....	13
2-9 Caustic from Pushover .....	13
2-10 Caustic in a Steady Turn – Top View .....	13
2-11 Caustic in a Steady Turn – 3D View, from Onyeonwu (1973) .....	14
2-12 Waveforms in the Vicinity of a Cutoff Caustic .....	15
2-13 Signature Shape Near Maximum Focus, Shock Not Fitted, from Gill and Seebass (1975) .....	17
2-14 Gill-Seebass Solution for Focused Shock Wave (Unit Step Function), Shock Inserted, from Gill and Seebass (1975) .....	17



2-15	Maximum Pressure Coefficient Ratio as a Function of $y$ for $u$ and $v$ based Shocks, from Gill and Seebass (1975) .....	18
2-16	PCBoom Caustic Tracing.....	19
2-17	CFD Predicted $\Delta P/P_o$ Cylinder Data at 3 Body Lengths, Boom7, $M=1.2$ .....	21
2-18	Computed Pressure Contours on the Vehicle Symmetry Plane and F-18 Surface, Boom7, $M=1.2$ .....	21
2-19	Close-Up of the Computed Pressure Contours, Boom7, $M=1.2$ .....	22
3-1	Notional SCAMP Measurement Site Layout Diagram .....	24
3-2	Example of Microphone on Ground Board .....	25
3-3	TG-14 used for Recording Sonic Booms in the Air .....	26
3-4	TG-14 Sonic Boom Recording, Flight 1264 Pass 4 .....	26
3-5	TG-14 Sonic Boom Recording, Flight 1264 Pass 5 .....	26
3-6	Cessna Operated Tethered Blimp for Elevated Microphones .....	27
3-7	NASA Ground Based Meteorological Station .....	28
3-8	NASA Mini-SODAR 4000.....	28
3-9	NASA GPS-sonde Prepared for Launch .....	28
3-10	Screen Shot of Focus Curvature Analysis Tool CUJO .....	29
3-11	Effect of Acceleration on Caustic Radius of Curvature .....	30
3-12	Effect of Pushover Rate on Caustic Radius of Curvature .....	30
3-13	Transition Focus and Audible Cues .....	34
3-14	Recordings at All Microphones, Flight 1264 Pass 4 .....	36
3-15	Recordings at All Microphones, Flight 1264 Pass 5 .....	37
3-16	Maximum focus booms and atmospheric profile, Maneuver A, Flight 1262 .....	39
3-17	Maximum focus booms and atmospheric profile, Maneuver A, Flight 1266 .....	40
3-18	Maximum focus booms and atmospheric profile, Maneuver B, Flight 1263 .....	41
3-19	Maximum focus booms and atmospheric profile, Maneuver B, Flight 1263 .....	42
3-20	Maximum focus booms and atmospheric profile, Maneuver C, Flight 1264.....	43
3-21	Maximum focus booms and atmospheric profile, Maneuver C, Flight 1269.....	44
3-22	Maximum focus booms and atmospheric profile, Maneuver C, Flight 1270.....	45
3-23	Maximum focus booms and atmospheric profile, Maneuver D, Flight 1265 .....	46
3-24	Maximum focus booms and atmospheric profile, Maneuver A offset, Flight 1272 .....	47
3-25	Maximum focus booms and atmospheric profile, Maneuver C offset, Flight 1273 .....	48
3-26	PCBoom Footprint, Flight 1264 Pass 5 .....	49
3-27	PCBoom Footprint, Near Array, Flight 1264 Pass 5 .....	49
3-28	Comparison between measured and as-flown PCBoom predicted focus locations.....	51
3-29	Comparison between measured and as-flown PCBoom predicted focus pressures.....	51
3-30	SCAMP Researchers, Partners and Collaborators.....	52
4-1	Velocity and Mach Number Profile for Pass 1264-4 (Pushover).....	54
4-2	Upper Air Profile for Flight 1264.....	55
4-3	Modeled Upper Air Profile for Flight 1264 .....	57
4-4	Caustic Line Under Track, Using Actual Trajectory and Atmosphere Data.....	58
4-5	Caustic Line Under Track, Using Modeled Trajectory and Atmosphere Data .....	59
4-6	CFD Predicted $\Delta P/P_o$ Cylinder Data at 3 Body Lengths Case C, $M=1.23$ .....	60
4-7	Computed Pressure Contours on the Vehicle Symmetry Plane and Surface from the Initial Solution (left) and the Final Grid-adapted Solution (right) Case C, $M=1.23$ .....	61
4-8	Computed Pressure Contours on the Vehicle Symmetry Plane and Surface from the Initial Solution (left)	

	and the Final Grid-adapted Solution (right) Case C, $M=1.23$ .....	61
5-1	Measured Maximum Focus, Maneuver A, 1266-4.....	64
5-2	Predicted Maximum Focus, Maneuver A, 1266-4.....	64
5-3	Measured Edge of Diffraction Zone, Maneuver A, 1266-4 .....	65
5-4	Predicted Edge of Diffraction Zone, Maneuver A, 1266-4. Carpet Boom is 1.49 psf.....	65
5-5	Measured Maximum Focus, Maneuver C, 1264-4.....	66
5-6	Predicted Maximum Focus, Maneuver C, 1264-4.....	66
5-7	Measured Edge of Diffraction Zone, Maneuver C, 1264-4 .....	67
5-8	Predicted Edge of Diffraction Zone, Maneuver C, 1264-4. Carpet Boom is 1.36 psf.....	67
5-9	Measured Maximum Focus, Maneuver D, 1265-2 .....	68
5-10	Predicted Maximum Focus, Maneuver D, 1265-2 .....	68
5-11	Measured Edge of Diffraction Zone, Maneuver D, 1265-2.....	69
5-12	Predicted Edge of Diffraction Zone, Maneuver D, 1265-2. Carpet Boom is 1.74 psf .....	69
6-1	Auger and Coulouvrat (2002) Solution for N-wave Focus .....	73
6-2	Auger and Coulouvrat (2002) Solution for Focal Zone with Non-N Incident Boom .....	73
6-3	Auger and Coulouvrat (2002) Solution for Focal Zone with Non-N Incident Boom .....	73
6-4	PCBoom Footprint for Flight 1264 Pass 1, in Vicinity of Array.....	74
6-5	PCBoom Focus Signature at Microphone 18, Flight 1264 Pass 1.....	74
6-6	Comparison of Focused Boom Predictions and Measurements PCBoom prediction (left), Flight 1264 Pass 1 measurement (center) and Auger-Coulouvrat method nonlinear Tricomi solution (right) .....	75
7-1	Illustration of Focusing Rays from an Accelerating Aircraft in a Homogeneous Atmosphere.....	78
7-2	Illustration of the NPE domain.....	79
7-3	Initial 2-D Wave Field used in the Focused N-wave Test .....	83
7-4	Initial Wave Profile used in the Focused N-wave Test.....	84
7-5	Focused N-wave Test, Solution at 20 Time Steps (.2 sec), Full Wave Field .....	84
7-6	Focused N-wave Test, Wave Profile, Focusing Axis Slice .....	84
7-7	Focused N-wave Test, Wave Profile, Wavefront Folding.....	85
7-8	Focused N-wave Test, Solution at 40 time steps (.4 sec), Full Wave Field .....	85
7-9	Focused N-wave Test, Solution at 40 time steps (.4 sec), Wave Profile, Focusing Axis.....	85
7-10	Focused N-wave Test, Solution at 40 time steps (.4 sec).....	86
7-11	Model of SCAMP flight 1264-4, Initial Wave Field from PCBoom.....	87
7-12	Flight 1264-4 computation, Initial Wave Profile at two locations: 1/2 (blue) and 1/4 (red) of the distance between the top and bottom boundaries .....	87
7-13	Model of SCAMP flight 1264-4, Solution at 8000 Time Steps (8 sec), Full Wave Field.....	88
7-14	Flight 1264-4 computation at timestep 8000 (8 sec).....	88
7-15	Level Acceleration Test, Solution at 40 Time Steps (.4 sec), Full Wave Field .....	89
7-16	Flight 1264-4 computation at timestep 12000 (12 sec).....	89
8-1	Depiction of the Focusing Condition Modeled by the Tricomi Equation.....	92
8-2	Near-field CFD Signatures for Case A and Case C .....	95
8-3	Far-field Propagated Signatures for Case A and C, Not Accounting for Maneuvering Aircraft Trajectory in the Ray Tube Area Calculation.....	96
8-4	Comparison of Carpet N-wave for Case C to the Scaled Far-field Signature .....	96
8-5	Pressure Field Solution of the Lossy Tricomi Code (Alpha) for Case A .....	97
8-6	Case A Comparison of Microphone #49 to Lossy Tricomi Code (Alpha) Output at $\bar{z} = 0.98$ .....	98
8-7	Case A Comparison of Microphone #17 to Lossy Tricomi Code (Alpha) Output at $\bar{z} = 0.18$ .....	98

8-8	Case A Comparison of Microphone #1 to Lossy Tricomi Code (Alpha) Output at $\bar{z} = 0.22$ .....	99
8-9	Pressure Field Solution of the Lossy Tricomi (Alpha) Code for Case C .....	100
8-10	Case C Comparison of Microphone #72 to Lossy Tricomi Code (Alpha) Output at $\bar{z} = 1.0$ .....	100
8-11	Case C Comparison of Microphone #60 to Lossy Tricomi Code (Alpha) Output at $\bar{z} = 0.15$ .....	101
8-12	Case C Comparison of Microphone #50 to Lossy Tricomi Code (Alpha) Output at $\bar{z} = 0.22$ .....	101
9-1	Measured Maximum Focus, Maneuver A, 1266-4.....	105
9-2	Predicted Maximum Focus, Maneuver A, 1266-4.....	105
9-3	Measured Edge of Diffraction Zone, Maneuver A, 1266-4.....	106
9-4	Predicted Edge of Diffraction Zone, Maneuver A, 1266-4. Carpet Boom is 1.49 psf.....	106
9-5	Measured Maximum Focus, Maneuver C, 1264-4.....	107
9-6	Predicted Maximum Focus, Maneuver C, 1264-4.....	107
9-7	Measured Edge of Diffraction Zone, Maneuver C, 1264-4 .....	108
9-8	Predicted Edge of Diffraction Zone, Maneuver C, 1264-4. Carpet Boom is 1.36 psf.....	108
9-9	Measured Maximum Focus, Maneuver D, 1265-2 .....	109
9-10	Predicted Maximum Focus, Maneuver D, 1265-2 .....	109
9-11	Measured Edge of Diffraction Zone, Maneuver D, 1265-2.....	110
9-12	Predicted Edge of Diffraction Zone, Maneuver D, 1265-2. Carpet Boom is 1.74 psf .....	110
9-13	Measured Focus at Sailplane, Maneuver C, 1264-4. $P_{max} = 2.06$ psf.....	111
9-14	Predicted Maximum Focus, Maneuver C, 1264-4, at Sailplane .....	111
9-15	Focal Zone as Defined by Tricomi Solution Region, with Tangent Ray Shown .....	113
9-16	Rays, Caustic and Focal Zone .....	114
9-17	Ray and Caustic Geometry for Maneuver A Ground Focus .....	115
9-18	Thin Shock Solution for $\delta$ Tangent Ray for Ground Focus A .....	116
9-19	Lossy Solution for $\delta$ Tangent Ray for Ground Focus A.....	116
9-20	Ray and Caustic Geometry for Maneuver C Ground Focus .....	117
9-21	Thin Shock Solution for $\delta$ Tangent Ray for Ground Focus C .....	117
9-22	Lossy Solution for $\delta$ Tangent Ray for Ground Focus C .....	118
9-23	Ray and Caustic Geometry for Maneuver D Ground Focus .....	118
9-24	Thin Shock Solution for $\delta$ Tangent Ray for Ground Focus D.....	119
9-25	Lossy Solution for $\delta$ Tangent Ray for Ground Focus D.....	119
9-26	Ray and Caustic Geometry for Maneuver C Sailplane Focus .....	120
9-27	Thin Shock Solution for $\delta$ Tangent Ray for Sailplane Focus C.....	120
9-28	Lossy Solution for $\delta$ Tangent Ray for Sailplane Focus C.....	121
9-29	Header for Tricomi Signature Input File (PCBurg output), Ground Focus C .....	121
9-30	Incoming Waveform Time History for Case A.....	126
9-31	Incoming Waveform Time History for Case C Sailplane.....	126
9-32	Incoming Waveform Time History for Case D.....	126
9-33	Incoming Waveform Time History for Case C Sailplane.....	126
9-34	Tricomi Pressure Field Solution for Case A .....	126
9-35	Case A Data Comparison Between 49 and the Tricomi Solution at $\bar{z} = 1.0$ .....	126
9-36	Case A data Comparison Between Microphone and the Tricomi Solution at $\bar{z} = 0.92$ .....	127
9-37	Case A Data Comparison Between Microphone 43 and the 46 Tricomi Solution at $\bar{z} = 0.85$ .....	127
9-38	Case A Data Comparison Between Microphone 40 and the Tricomi Solution at $\bar{z} = 0.78$ .....	127
9-39	Case A Data Comparison Between Microphone 37 and the Tricomi Solution at $\bar{z} = 0.70$ .....	127
9-40	Case A Data Comparison Between Microphone 34 and the Tricomi Solution at $\bar{z} = 0.62$ .....	127

9-41	Case A Data Comparison Between Microphone 30 and the Tricomi Solution at $\bar{z} = 0.51$ .....	127
9-42	Case A Data Comparison Between Microphone 28 and the Tricomi Solution at $\bar{z} = 0.45$ .....	128
9-43	Case A Data Comparison Between Microphone 30 and the Tricomi Solution at $\bar{z} = 0.51$ .....	128
9-44	Case A Data Comparison Between Microphone 22 and the Tricomi Solution at $\bar{z} = 0.31$ .....	128
9-45	Case A Data Comparison Between Microphone 19 and the Tricomi Solution at $\bar{z} = 0.245$ .....	128
9-46	Case A Data Comparison Between Microphone 17 and the Tricomi Solution at $\bar{z} = 0.19$ .....	128
9-47	Case A Data Comparison Between Microphone 15 and the Tricomi Solution at $\bar{z} = 0.125$ .....	128
9-48	Case A Data Comparison Between Microphone 12 and the Tricomi Solution at $\bar{z} = 0.07$ .....	129
9-49	Case A Data Comparison Between Microphone 9 and the Tricomi Solution at $\bar{z} = 0.00$ .....	129
9-50	Case A Data Comparison Between Microphone 6 and the Tricomi Solution at $\bar{z} = -0.07$ .....	129
9-51	Case A Data Comparison Between Microphone 3 and the Tricomi Solution at $\bar{z} = -0.14$ .....	129
9-52	Case A Data Comparison Between Microphone 21 and the Tricomi Solution at $\bar{z} = -0.21$ .....	129
9-53	Tricomi pressure field solution for Case C .....	129
9-54	Case C Data Comparison Between Microphone 72 and the Tricomi Solution at $\bar{z} = 1.0$ .....	130
9-55	Case C Data Comparison Between Microphone 70 and the Tricomi Solution at 0.87 .....	130
9-56	Case C Data Comparison Between Microphone 68 and the Tricomi Solution at 0.73 .....	130
9-57	Case C Data Comparison Between Microphone 66 and the Tricomi Solution at 0.60 .....	130
9-58	Case C Data Comparison Between Microphone 64 and the Tricomi Solution at 0.475 .....	130
9-59	Case C Data Comparison Between Microphone 62 and the Tricomi Solution at 0.335 .....	130
9-60	Case C Data Comparison Between Microphone 61 and the Tricomi Solution at 0.23 .....	131
9-61a	Case C Data Comparison Between Microphone 6- and the Tricomi Solution at 0.15 .....	131
9-61b	Close up View Comparison for the Front Shock from Figure 4-32a .....	131
9-61c	Close up View Comparison for the Rear Shock from Figure 4-32a.....	131
9-62	Case C Data Comparison Between Microphone 59 and the Tricomi Solution at 0.075 .....	131
9-63	Case C Data Comparison Between Microphone 58 and the Tricomi Solution at 0.03 .....	131
9-64	Case C data comparison between microphone 56 and the Tricomi solution at 0.12 .....	132
9-65	Case C data comparison between microphone 54 and the Tricomi solution at 0.27 .....	132
9-66	Case C data comparison between microphone 52 and the Tricomi solution at 0.42 .....	132
9-67	Case C data comparison between microphone 50 and the Tricomi solution at 0.60 .....	132
9-68	Case C data comparison between microphone 48 and the Tricomi solution at 0.72 .....	132
9-69	Case C data comparison between microphone 46 and the Tricomi solution at 0.87 .....	132
9-70	Tricomi pressure field solution for Case D .....	133
9-71	Case D data comparison between microphone 52 and the Tricomi solution at 0.915 .....	133
9-72	Case D data comparison between microphone 49 and the Tricomi solution at 0.73 .....	133
9-73	Case D data comparison between microphone 47 and the Tricomi solution at 0.54 .....	133
9-74	Case D data comparison between microphone 45 and the Tricomi solution at 0.40 .....	133
9-75	Case D data comparison between microphone 43 and the Tricomi solution at 0.26 .....	134
9-76	Case D data comparison between microphone 42 and the Tricomi solution at 0.20 .....	134
9-77	Case D data comparison between microphone 41 and the Tricomi solution at 0.13 .....	134
9-78	Case D data comparison between microphone 40 and the Tricomi solution at 0.03 .....	134
9-79	Case D data comparison between microphone 37 and the Tricomi solution at 0.15 .....	134
9-80	Case D data comparison between microphone 37 and the Tricomi solution at 0.15 .....	134
9-81	Case D data comparison between microphone 35 and the Tricomi solution at 0.29 .....	134
9-82	Case D data comparison between microphone 33 and the Tricomi solution at 0.43 .....	135
9-83	Case D data comparison between microphone 31 and the Tricomi solution at 0.57 .....	135

9-84	Tricomi pressure field solution for Case C sailplane .....	135
9-85a	Case C sailplane data comparison between microphone TG1 and the Tricomi solution at 0.125 .....	135
9-85b	Close up view comparison for the front shock .....	136
9-85c	Close up view comparison for the rear shock .....	136
9-86	Case C sailplane data comparison between microphone TG1 and the Tricomi solution at 0.063 .....	136
9-87	Acceleration caustic and computational domain for local solution of focus signature .....	137
9-88	Location and size of initial NPE grid.....	138
9-89	Dimensions associated with a curved wavefront in the initial NPE domain .....	139
9-90	Comparison of competing effects that constrain the size and location of the initial NPE grid.....	139
9-91	Upper and lower caustics associated with accelerating aircraft .....	140
9-92	Ray and wave pattern for single ripple NPE case .....	142
9-93	Close-up of focus region at 4000 meter wavefront, lower caustic .....	143
9-94	NPE solution in the vicinity of the caustic at x = 4000 meters .....	145
9-95	Comparison of NPE maximum focus prediction (red), propagated 4000 meters, with measured Maneuver C focus (black).....	146
9-96	Comparison of NPE maximum focus prediction (red), propagated 2500 meters, with measured Maneuver C focus (black).....	147
10-1	Isometric view of a potential Gulfstream Quiet Supersonic Jet .....	151
10-2	Comparison of predicted ground signatures for supersonic vehicles during cruise flight conditions with and without signature shaping .....	152
10-3	Equivalent Body for CFD Analysis of Gulfstream Configuration .....	152
10-4	QSJ Near Field Signatures at Mach 1.15 and Mach 1.20 .....	153
10-5	Boeing N+2 Low Boom Concept Aircraft.....	154
10-6	Pressure Field at Four Radii for Boeing Configuration .....	154
10-7	NASA Low Boom Demonstrator Concept Aircraft .....	155
10-8	765-076F Configuration from Reference 2-1 .....	156
10-9	Maximum Focus Solution for Gulfstream Configuration .....	157
10-10	Ray and Caustic Geometry for Gulfstream Focus Condition .....	158
10-11	Thin Shock Solution for $\delta$ Tangent Ray for focus of Gulfstream Low Boom Aircraft.....	159
10-12	Lossy Solution for $\delta$ Tangent Ray for focus of Gulfstream Low Boom Aircraft.....	159
10-13	Maximum Focus Solution for Boeing Configuration .....	161
10-14	Ray and Caustic Geometry for Boeing Focus Condition .....	161
10-15	Thin Shock Solution for $\delta$ Tangent Ray for Focus of Boeing Low Boom Aircraft .....	161
10-16	Lossy Solution for $\delta$ Tangent Ray for Focus of Boeing Low Boom Aircraft .....	162
10-17	Maximum Focus Solution for NASA Demonstrator Configuration .....	163
10-18	Ray and Caustic Geometry for NASA Demonstrator Focus Condition .....	163
10-19	Thin Shock Solution for $\delta$ Tangent Ray for Focus of NASA Demonstrator Aircraft.....	164
10-20	Lossy Solution for $\delta$ Tangent Ray for Focus of NASA Demonstrator Aircraft .....	164
10-21	Maximum Focus Solution for NASA N+2 Configuration.....	165
10-22	Ray and Caustic Geometry for NASA N+2 Focus Condition .....	165
10-23	Thin Shock Solution for $\delta$ Tangent Ray for Focus of NASA N+2 Aircraft.....	166
10-24	Lossy Solution for $\delta$ Tangent Ray for Focus of NASA N+2 Aircraft.....	166
10-25	Pressure Field Solution of the Lossy Tricomi Code for the Gulfstream Low Boom Signature and Focusing Conditions .....	170
10-26	Time History for the Gulfstream Low Boom Focusing Case at $\bar{z} = 1$ .....	171

10-27	Time History Comparison for the Gulfstream Low Boom Focusing Case between Maximum Overpressure $\bar{z} = 0.32$ and Maximum Underpressure $\bar{z} = 0.22$ .....	171
10-28	Time History for the Gulfstream Low Boom Focusing case at $\bar{z} = 0.5$ .....	172
10-29	Pressure Field Solution of the Lossy Tricomi Code for the Boeing N+2 Low Boom Signature and Focusing Conditions .....	173
10-30	Time History for the Boeing N+2 Low Boom Focusing Case at $\bar{z} = 1$ .....	173
10-31	Time History for the Boeing N+2 Low Boom Focusing Case at Maximum Overpressure $\bar{z} = 2$ .....	173
10-32	Time History for the Boeing N+2 Low Boom Focusing Case at $\bar{z} = 0.5$ .....	174
10-33	Pressure Field Solution of the Lossy Tricomi Code for the NASA Demonstrator Low Boom Signature and Focusing Conditions .....	174
10-34	Time History for the NASA Demonstrator Configuration Low Boom Focusing Case at $\bar{z} = 1$ .....	175
10-35	Time History for the NASA Demonstrator Low Boom Focusing Case at Maximum Overpressure ( $\bar{z} = 0.16$ ) .....	175
10-36	Time History for the NASA Demonstrator Configuration Low Boom Focusing Case at $\bar{z} = -0.5$ .....	176
10-37	Pressure Field Solution of the Lossy Tricomi Code for the NASA N+2 Configuration Low Boom Signature and Focusing Conditions .....	176
10-38	Time History for the NASA N+2 configuration low boom focusing case at $\bar{z} = 1$ .....	177
10-39	Time History for the NASA N+2 Configuration Low Boom Focusing Case at Maximum Overpressure ( $\bar{z} = 0.07$ ) .....	177
10-40	Time History for the NASA N+2 Configuration Low Boom Focusing Case at $\bar{z} = 1$ .....	178
10-41	Time History of the NASA N+2 Configuration Corresponding to $\bar{z} = 0.75$ Showing Small Amplitudes of Numerically Induced Oscillation .....	178
10-42	NPE Solution, Gulfstream QSJ .....	180
10-43	NPE solution, Boeing N+2 .....	180
10-44	NPE solution, NASA Demonstrator .....	181
10-45	Comparison at maximum focus between Gill-Seebass, NPE and Lossy NTE Solutions for Gulfstream QSJ .....	183
10-46	Comparison at maximum focus between Gill-Seebass and Lossy NTE Solutions for Boeing N+2 SST .....	184
10-47	Comparison at maximum focus between Gill-Seebass and Lossy NTE Solutions for NASA Demonstrator .....	184
10-48	Comparison at maximum focus between Gill-Seebass and Lossy NTE Solutions for NASA N+2 Configuration .....	185
11-1	Estimated effect of acceleration on sonic boom focusing from (Haglund, 2074) .....	188
11-2	Measured effect of acceleration and lateral displacement on focus overpressure, from (Wanner, 1972) .....	188
11-3	Ray diagram for focus and $\delta$ tangent ray .....	189
11-4	Sample raycau “.foc” output file .....	190
11-5	Lossy $\delta$ tangent boom: PCBoom output for input to Lossy NTE .....	190
11-6	System Level Experimental Validation BM#2 (QEVC3) General Arrangement .....	191
11-7	Transonic Acceleration Altitude Profiles .....	194
11-8	Transonic Acceleration dM/dt Profiles .....	195
11-9	Boeing CFD Using Overflow (Navier-Stokes) for the Boeing BM#2 Config. (Low Boom Design Point) H/L = 1 .....	196
11-10	Boeing CFD Using Overflow (Navier-Stokes) for the Boeing BM#2 Config. (Low Boom Design Point) H/L = 3 .....	196

11-11	Case 1 Cylinder Solutions provided at H/L = 1& 3 .....	197
11-12	Under-track signatures (dP/P vs Axial location) .....	197
11-13	Gulfstream Low Boom Passenger Aircraft Configuration .....	198
11-14	Notional Quiet Supersonic Jet Flight Envelope and Parametric Profiles .....	199
11-15	Gulfstream CFD pressure flowfield of the axisymmetric geometry .....	200
11-16	Optimal Profile leveraging the NASA UEET and the IIPSS projects .....	201
11-17	NASA Sonic Boom Demonstrator Vehicle artist rendering .....	202
11-18	NASA Demonstrator Vehicle CFD Analysis, undertrack pressure distribution .....	203
11-19	NASA Demonstrator Vehicle CFD Analysis, cylinders at one body length .....	204
11-20	Pressure field contour for NASA Case 1, 33479 ft., Mach 1.166, $\dot{m}=0.00134$ .....	209
11-21	Metrics plots for NASA Case 1, 33479 ft., Mach 1.166, $\dot{m}=0.00134$ .....	209
11-22	Time history corresponding to the peak overpressure ( $\bar{z} = 0.19$ ) for NASA Case 1, 33479 ft., Mach 1.166, $\dot{m}=0.00134$ .....	210
11-23	Time history corresponding to the highest PL ( $\bar{z} = 0.03$ ) for NASA Case 1, 33479 ft., Mach 1.166, $\dot{m}=0.00134$ .....	211
11-24	Time histories for NASA Case 1, 33479 ft., Mach 1.166, $\dot{m}=0.00134$ at four different $\bar{z}$ locations: a) $\bar{z} = 1.0$ , b) $\bar{z} = 0.6$ , c) $\bar{z} = 0.2$ and d) $\bar{z} = -0.2$ .....	211
11-25	Pressure field contour for NASA Case 2, 35821 ft., Mach 1.175, $\dot{m}=0.00138$ .....	212
11-26	Metrics plots for NASA Case 2, 35821 ft, Mach 1.175, $\dot{m}=0.00138$ .....	212
11-27	Time history corresponding to the peak overpressure ( $\bar{z} = 0.17$ ) for NASA Case 2, 35821 ft., Mach 1.175, $\dot{m}=0.00138$ .....	213
11-28	Time history corresponding to the highest PL ( $\bar{z} = 0.03$ ) for NASA Case 2, 35821 ft., Mach 1.175, $\dot{m}=0.00138$ .....	213
11-29	Time histories for NASA Case 2, 35821 ft., Mach 1.175, $\dot{m}=0.00138$ at four different $\bar{z}$ locations: a) $\bar{z} = 1.0$ , b) $\bar{z} = 0.6$ , c) $\bar{z} = 0.2$ and d) $\bar{z} = -0.2$ .....	214
11-30	Pressure field contour for NASA Case 3, 38154 ft., Mach 1.169, $\dot{m}=0.00103$ .....	215
11-31	Metrics plots for NASA Case 3, 38154 ft., Mach 1.169, $\dot{m}=0.00103$ .....	215
11-32	Time history corresponding to the peak overpressure ( $\bar{z} = 0.18$ ) for NASA Case 3, 38154 ft., Mach 1.169, $\dot{m}=0.00103$ .....	216
11-33	Time history corresponding to the highest PL ( $\bar{z} = 0.03$ ) for NASA Case 3, 38154 ft., Mach 1.169, $\dot{m}=0.00103$ .....	216
11-34	Time histories for NASA Case 3, 38154 ft., Mach 1.169, $\dot{m}=0.00103$ at four different $\bar{z}$ locations: a) $\bar{z} = 1.0$ , b) $\bar{z} = 0.06$ , c) $\bar{z} = 0.2$ and d) $\bar{z} = 0.2$ .....	217
11-35	Pressure field contour for NASA Case 4, 40525 ft., Mach 1.161, $\dot{m}=0.00066$ .....	218
11-36	Metrics plots for NASA Case 4, 40525 ft., Mach 1.161, $\dot{m}=0.00066$ .....	218
11-37	Time history corresponding to the peak overpressure ( $\bar{z} = 0.17$ ) for NASA Case 4, 40525 ft., Mach 1.161, $\dot{m}=0.00066$ .....	219
11-38	Time history corresponding to the highest PL ( $\bar{z} = 0.04$ ) for NASA Case 4, 40525 ft., Mach 1.161, $\dot{m}=0.00066$ .....	219
11-39	Time histories for NASA Case 4, 40525 ft., Mach 1.161, $\dot{m}=0.00066$ at four different $\bar{z}$ locations: a) $\bar{z} = 1.0$ , b) $\bar{z} = 0.6$ , c) $\bar{z} = 0.2$ and d) $\bar{z} = -0.02$ .....	220
11-40	Pressure field contour for Boeing Case 1, 40000 ft., Mach 1.156, $\dot{m}=0.00036$ .....	221
11-41	Metrics plots for Boeing Case 1, 40000 ft., Mach 1.156, $\dot{m}=0.00036$ .....	221
11-42	Time history corresponding to the peak overpressure ( $\bar{z} = 0.22$ ) for Boeing Case 1, 40000 ft., Mach 1.156, $\dot{m}=0.00036$ .....	222

11-43	Time history corresponding to the highest PL ( $\bar{z} = 0.04$ ) for Boeing Case 1, 40000 f.t, Mach 1.156, $\text{mdot}=0.00036$ .....	222
11-44	Time histories for Boeing Case 1, 40000 ft, Mach 1.156, $\text{mdot}=0.00036$ at four different $\bar{z}$ locations: a) $\bar{z} = 1.0$ , b) $\bar{z} = 0.6$ , c) $\bar{z} = 0.2$ and d) $\bar{z} = 0.2$ .....	223
11-45	Pressure field contour for Boeing Case 2, 38498 ft, Mach 1.23, $\text{mdot}=0.00316$ .....	224
11-46	Metrics plots for Boeing Case 2, 38498 ft, Mach 1.23, $\text{mdot}=0.00316$ .....	224
11-47	Time history corresponding to the peak overpressure ( $\bar{z} = 0.25$ ) for Boeing Case 2, 38498 ft., Mach 1.23, $\text{mdot}=0.00316$ .....	225
11-48	Time history corresponding to the highest PL ( $\bar{z} = 0.02$ ) for Boeing Case 2, 38498 ft., Mach 1.23, $\text{mdot}=0.00316$ .....	225
11-49	Time histories for Boeing Case 2, 38498 ft, Mach 1.23, $\text{mdot}=0.00316$ at four different $\bar{z}$ locations: a) $\bar{z} = 1.0$ , b) $\bar{z} = 0.2$ , c) $\bar{z} = 0.6$ and d) $\bar{z} = -0.02$ .....	226
11-50	Pressure field contour for Boeing Case 3, 45000 ft., Mach 1.153, $\text{mdot}=0.0001$ .....	227
11-51	Metrics plots for Boeing Case 3, 45000 ft., Mach 1.153, $\text{mdot}=0.0001$ .....	228
11-52	Time history corresponding to the peak overpressure ( $\bar{z} = 0.21$ ) for Boeing Case 3, 45000 ft., Mach 1.153, $\text{mdot}=0.0001$ .....	228
11-53	Time history corresponding to the highest PL ( $\bar{z} = 0.05$ ) for Boeing Case 3, 45000 ft., Mach 1.153, $\text{mdot}=0.0001$ .....	228
11-54	Time histories for Boeing Case 3, 45000 ft., Mach 1.153, $\text{mdot}=0.0001$ at four different $\bar{z}$ locations: a) $\bar{z} = 1.0$ , b) $\bar{z} = 0.6$ , c) $\bar{z} = 0.2$ and d) $\bar{z} = -0.02$ .....	229
11-55	Pressure field contour for Boeing Case 4, 45000 ft., Mach 1.17, $\text{mdot}=0.00111$ .....	230
11-56	Metrics plots for Boeing Case 4, 45000 ft., Mach 1.17, $\text{mdot}=0.00111$ .....	230
11-57	Time history corresponding to the peak overpressure ( $\bar{z} = 0.22$ ) for Boeing Case 4, 45000 f.t, Mach 1.17, $\text{mdot}=0.00111$ .....	231
11-58	Time history corresponding to the highest PL ( $\bar{z} = 0.06$ ) for Boeing Case 4, 45000 ft., Mach 1.17, $\text{mdot}=0.00111$ .....	231
11-59	Time histories for Boeing Case 4, 45000 ft, Mach 1.17, $\text{mdot}=0.00111$ at four different $\bar{z}$ locations: a) $\bar{z} = 1.0$ , b) $\bar{z} = 0.6$ , c) $\bar{z} = 0.2$ and d) $\bar{z} = -0.02$ .....	232
11-60	Pressure field contour for Boeing Case 5, 45000 ft., Mach 1.211, $\text{mdot}=0.00295$ .....	233
11-61	Metrics plots for Boeing Case 5, 45000 ft, Mach 1.211, $\text{mdot}=0.00295$ .....	233
11-62	Time history corresponding to the peak overpressure ( $\bar{z} = 0.23$ ) for Boeing Case 5, 45000 ft., Mach 1.211, $\text{mdot}=0.00295$ .....	234
11-63	Time history corresponding to the highest PL ( $\bar{z} = 0.06$ ) for Boeing Case 5, 45000 ft., Mach 1.211, $\text{mdot}=0.00295$ .....	234
11-64	Time histories for Boeing Case 5, 45000 ft., Mach 1.211, $\text{mdot}=0.00295$ at four different $\bar{z}$ locations: a) $\bar{z} = 1.0$ , b) $\bar{z} = 0.6$ , c) $\bar{z} = 0.2$ and d) $\bar{z} = -0.02$ .....	235
11-65	Pressure field contour for Gulfstream Case 1, 38000 ft., Mach 1.182, $\text{mdot}=0.0005$ .....	236
11-66	Metrics plots for Gulfstream Case 1, 38000 ft., Mach 1.182, $\text{mdot}=0.0005$ .....	236
11-67	Time history corresponding to the peak overpressure ( $\bar{z} = 0.05$ ) for Gulfstream Case 1, 38000 ft., Mach 1.182, $\text{mdot}=0.0005$ .....	237
11-68	Time histories for Gulfstream Case 1, 38000 ft, Mach 1.182, $\text{mdot}=0.0005$ at four different $\bar{z}$ locations: a) $\bar{z} = 1.0$ , b) $\bar{z} = 0.6$ , c) $\bar{z} = 0.2$ and d) $\bar{z} = -0.02$ .....	238
11-69	Pressure field contour for Gulfstream Case 2, 38000 ft., Mach 1.19, $\text{mdot}=0.001$ .....	239
11-70	Metrics plots for Gulfstream Case 2, 38000 f.t, Mach 1.19, $\text{mdot}=0.001$ .....	239
11-71	Time history corresponding to the peak overpressure ( $\bar{z} = 0.05$ ) for Gulfstream Case 2, 38000 ft., Mach 1.19, $\text{mdot}=0.001$ .....	240



11-72	Time histories for Gulfstream Case 2, 38000 ft, Mach 1.19, mdot=0.001 at four different $\bar{z}$ locations: a) $\bar{z} = 1.0$ , b) $\bar{z} = 0.6$ , c) $\bar{z} = 0.2$ and d) $\bar{z} = -0.02$ .....	241
11-73	Pressure field contour for Gulfstream Case 3, 38000 ft., Mach 1.208, mdot=0.002.....	242
11-74	Metrics plots for Gulfstream Case 3, 38000 ft., Mach 1.208, mdot=0.002 .....	242
11-75	Time history corresponding to the peak overpressure ( $\bar{z} = 0.05$ ) for Gulfstream Case 3, 38000 ft., Mach 1.208, mdot=0.002.....	243
11-76	Time histories for Gulfstream Case 3, 38000 ft., Mach 1.208, mdot=0.002 at four different $\bar{z}$ locations: a) $\bar{z} = 1.0$ , b) $\bar{z} = 0.6$ , c) $\bar{z} = 0.2$ and d) $\bar{z} = -0.02$ .....	244
11-77	Pressure field contour for Gulfstream Case 4, 40000 ft., Mach 1.182, mdot=0.0005.....	245
11-78	Metrics plots for Gulfstream Case 4, 40000 ft., Mach 1.182, mdot=0.0005 .....	245
11-79	Time history corresponding to the peak overpressure ( $\bar{z} = 0.04$ ) for Gulfstream Case 4, 40000 ft., Mach 1.182, mdot=0.0005.....	246
11-80	Time histories for Gulfstream Case 4, 40000 ft, Mach 1.182, mdot=0.0005 at four different $\bar{z}$ locations: a) $\bar{z} = 1.0$ , b) $\bar{z} = 0.6$ , c) $\bar{z} = 0.2$ and d) $\bar{z} = -0.02$ .....	247
11-81	Pressure field contour for Gulfstream Case 5, 38000 ft, Mach 1.19, mdot=0.001.....	248
11-82	Metrics plots for Gulfstream Case 5, 40000 ft, Mach 1.19, mdot=0.001 .....	248
11-83	Time history corresponding to the peak overpressure ( $\bar{z} = 0.28$ ) for Gulfstream Case 5, 40000 ft., Mach 1.19, mdot=0.001.....	249
11-84	Time histories for Gulfstream Case 5, 40000 ft, Mach 1.19, mdot=0.001 at four different $\bar{z}$ locations: a) $\bar{z} = 1.0$ , b) $\bar{z} = 0.6$ , c) $\bar{z} = 0.02$ and d) $\bar{z} = -0.02$ .....	250
11-85	Pressure field contour for Gulfstream Case 6, 40000 ft., Mach 1.208, mdot=0.002.....	251
11-86	Metrics plots for Gulfstream Case 6, 40000 ft., Mach 1.208, mdot=0.002 .....	251
11-87	Time history corresponding to the peak overpressure ( $\bar{z} = 0.27$ ) for Gulfstream Case 6, 40000 ft., Mach 1.208, mdot=0.002.....	253
11-88	Time histories for Gulfstream Case 6, 40000 ft., Mach 1.209, mdot=0.002 at four different $\bar{z}$ locations: a) $\bar{z} = 1.0$ , b) $\bar{z} = 0.6$ , c) $\bar{z} = 0.02$ and d) $\bar{z} = -0.02$ .....	253
11-89	Comparison of Power Spectral Density (PSD) spectra at different $\bar{z}$ locations for NASA Case 4.....	254
11-90	Comparison of Power Spectral Density (PSD) spectra at different $\bar{z}$ locations for Boeing Case 3 .....	254
11-91	Comparison of Power Spectral Density (PSD) spectra at different $\bar{z}$ locations for Gulfstream Case 4 .....	255
11-92	Summary of PL, rank ordered, for all configurations.....	257
11-93	Effect of grazing angle on focal zone ground footprint .....	258

## Tables

1-1	SCAMP Publications Summary .....	3
2-1	Steady State Flight Conditions for CFD Analysis .....	20
3-1	Selected SCAMP Focus Flight Maneuvers.....	31
3-2	Final Flight Test Matrix.....	32
3-3	Maneuvers Flown on Each Supersonic Pass .....	35
3-4	Maximum Focus Boom Signatures and Atmospheric Effects .....	50
3-5	PCBoom Prediction of Geometric Caustic Locations and Measured Maximum Focus Locations .....	50
4-1	As-Flown Flight Test Matrix.....	53
4-2	Selected Passes for Analysis - Primary and Alternates .....	56

4-3	Summary of Radii of Curvature along Caustic - Actual and Modeled Data .....	59
4-4	Steady-State Flight Conditions for CFD Runs .....	60
5-1	Summary of Comparison between Measured Foci and PCBoom Predictions .....	70
7-1	Input File Variables for npe_scamp .....	81
7-2	Input File Parameters for pcboom2npe .....	82
7-3	Standard Output from pcboom2npe .....	82
8-1	Input Conditions for the Two Comparison Cases.....	95
9-1	Summary of Comparison between Measured Foci and PCBoom Predictions .....	112
9-2	Focusing Parameters for the Beta Version Comparison Cases .....	122
9-3	Listing of Case A Comparison Figures .....	123
9-4	Listing of Case C Comparison Figures.....	124
9-5	Listing of Case D Comparison Figures .....	124
9-6	Listing of Case C Sailplane Comparison Figures .....	124
9-7	Tricomi Scaling Parameters for SCAMP Maneuvers .....	141
10-1	Input Conditions for the Low Boom Configurations .....	166
10-2	Computational Domain Dimensions for the Low Boom Configurations.....	167
10-3	Tricomi Scaling Parameters and Boundary Conditions for Low Boom Configurations.....	178
10-4	Summary of Peak Overpressures, psf for Focused Signatures .....	181
11-1	Desired Focused Boom Run Matrix.....	192
11-2	Mission Study Run Matrix .....	192
11-3	Afterburner Thrust Trade.....	193
11-4	Flight Conditions for CFD and PCBOOM6 Runs.....	194
11-5	Summary of Focus Conditions .....	199
11-6	NASA Sonic Boom Demonstrator Description .....	202
11-7	NASA Configuration Focus Conditions .....	203
11-8	Summary of Flight Conditions for the Profile Exploration Study .....	205
11-9	Summary of Focusing Parameters for the Tricomi Code .....	206
11-10	Summary of Metric Values for Each Case in the Profile Exploration Study.....	206
11-11	Summary of $\bar{z}$ Locations that Correspond to Each Metric Value in Table 11-15 .....	207
11-12	Comparison of Tricomi Domain Distances in Terms of the Physical Coordinates .....	208
11-13	Key Noise Metrics and Positions within Diffraction Layer .....	256
11-14	Summary of Maximum PL, SELA and Flight Conditions .....	256

## Executive Summary


The objectives of the Superboom Caustic Analysis and Measurement (SCAMP) Program were to develop and validate, via flight-test measurements, analytical models for sonic boom signatures in and around focal zones as they are expected to occur during commercial aircraft transition from subsonic to supersonic flight, and to apply these models to focus boom prediction of low-boom aircraft designs. The SCAMP program has successfully investigated sonic boom focusing both analytically and experimentally, while gathering a comprehensive empirical flight test and acoustic dataset, and developing a suite of focused sonic boom prediction tools.

An experimental flight and acoustic measurement test was designed during the initial year of the SCAMP program, with execution of the SCAMP flight test occurring in May 2011. The current SCAMP team, led by Wyle, includes partners from the Boeing Company, Pennsylvania State University, Gulfstream Aerospace, Eagle Aeronautics, and Central Washington University. Numerous collaborators have also participated by supporting the experiment with human and equipment resources at their own expense. The experiment involved precision flight of a McDonnell Douglas (now Boeing) F-18B executing different maneuvers that created focused sonic booms. The maneuvers were designed to center on the flight regime expected for commercial supersonic aircraft transonic transition, and also span a range of caustic curvatures in order to provide a variety of conditions for code validations.

The SCAMP experiment was designed to capture concurrent F-18B on-board flight instrumentation data, high-fidelity ground-based and airborne acoustic data, and surface and upper air meteorological data. Close coordination with NASA Dryden resulted in the development of new experimental instrumentation and techniques to facilitate the SCAMP flight-test execution, including the development of an F-18B Mach rate cockpit display, TG-14 powered glider in-flight sonic boom measurement instrumentation and “Where’s the Focus?” (WTF) software for near-real time way-point computation accounting for local atmospheric.

In May 2011, 13 F-18B flights were conducted during 5 flying days over a 2 week period. A densely populated 10,000 ft-long ground acoustic array with 125-ft microphone spacing was designed to capture pre-, focus, and post-focus regions. The ground-based acoustic array was placed in a nominally east-west orientation in the remote Cuddeback lakebed region, north of Edwards AFB. This area was carefully selected to avoid placing focused booms on populated areas or solar power facilities. For the SCAMP measurement campaign, approvals were obtained to temporarily extend the Black Mountain supersonic corridor northward by three miles. The SCAMP flight tests successfully captured 70 boom events, with 61 focus passes, and 9 calibration passes. Seventeen of the focus passes and three of the calibration passes were laterally offset; with the others being centerline flights. Airborne incoming sonic boom wave measurements were measured by the TG-14 for 10 of the F-18B flight passes including one maximum focus signature, several N-u combinations, several overlapped N-u signatures, and several evanescent waves.

During the 27-month program, the SCAMP team developed a suite of integrated computer codes with sonic boom focusing predictive capabilities: PCBoom, Lossy Nonlinear Tricomi Equation Method (LNTE) and the Nonlinear Progressive wave Equation (NPE) method. PCBoom propagates the rays through the atmosphere and, in addition to legacy focus signature prediction based on the Gill-Seebass method, provides input source characteristics and propagation parameters to LNTE and NPE. LNTE, a Tricomi solver that incorporates atmospheric losses, computes the focus signature at the focus, and computes the focus



signature in the vicinity of the focal zone, including the evanescent and post-focus zones. LNTE signature auralization from low-boom vehicle designs has been demonstrated in the NASA Langley Interior Effects Room (IER). The NPE has also been validated for use in prediction of focused ground boom signatures in sonic boom focal zones. The NPE formulation has the capability to incorporate atmospheric turbulence in the predictions. This has been applied to sonic boom propagation in the past. Prediction of turbulence effects on focal zone signatures was not, however, explored during the SCAMP program.

In summary, the SCAMP program was an extremely successful example of contractor team-NASA-partner collaboration, with such notable firsts as:

- Most densely packed ground microphone array of any sonic boom transition flight experiments in the United States or internationally.
- Con-current and synchronized ground and airborne measurements including capture of in-coming pressure waves above the planetary boundary layer.
- Largest focused boom data set ever gathered, spanning 70 flight passes with 37 focus signatures placed in the 81-microphone array.
- Development and validation of two new sonic boom focusing models that account for atmospheric loss mechanisms and have the ability to predict focused booms from shaped low-boom vehicle configurations.
- Demonstrated viability of auralizing analytical focus boom signatures indoors.

## 1.1 Background

Supersonic flight results in a sonic boom footprint with various zones as illustrated in Figure 1-1. Researchers have been investigating aircraft design techniques to minimize the primary carpet boom, and the SSBD program (Pawlowski et al., 2005) demonstrated in full scale the persistence of sonic boom shaping. Other footprint regions such as the secondary carpet boom and signatures in regions near lateral cutoff are expected to be significantly smaller than the primary carpet boom. This leaves the transition focus boom as the primary emphasis of the SCAMP program.

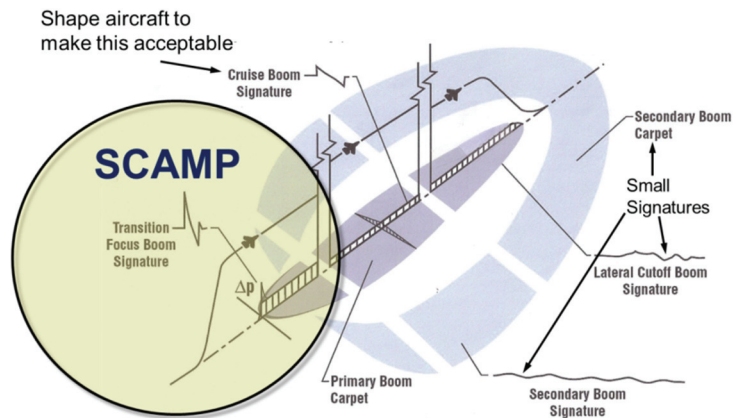


**Figure 1-1. Sonic boom ground footprint zones, from Maglieri (1980)**

Early measurements of booms from maneuvering flight<sup>1-1, 1-2</sup> demonstrated that there could be significant boom amplitude enhancements in focal zones, and also the potential for complex multi-signature patterns. Subsequently, there have been three major dedicated focus boom flight tests:

- Operation Jericho (Wanner et al., 1972), conducted by the French in the late 1960s and early 1970s, consisted of three phases. Jericho-Focalisation investigated focus due to acceleration at low altitude (2000 feet; 600 meters). Jericho-Virage investigated focus due to acceleration and turns at high altitude (36,000 feet; 11 km). Jericho-Carton addressed additional effects of acceleration and lateral spread on focusing, and also examined the "super focus" that occurs at a cusp such as the intersection of the caustic and "pseudo caustic".
- In 1970, NASA conducted flight tests at Jackass Flats, NV, with instrumentation on the ground and also on a 1529-foot (466 meter) BREN tower (Haglund and Kane, 1974). This research investigated Mach cutoff for on-track flights and for lateral cutoff. Most flights were at steady low Mach numbers. Quantitative results were variable because of the sensitivity of focusing at low Mach number to small changes in flight condition and also due to atmospheric turbulence.
- In 1994, Project Have BEARs (Downing et al., 1998), a concerted research program conducted by the Air Force Research Laboratory, the USAF Test Pilot School, Wyle, and Eagle Aeronautics,

commenced,, involving the use of F-16 aircraft, which were flown to generate focus booms at positions of the aircrews' choosing using level accelerations, dives, pushover and turn maneuvers.

A common factor of these tests was that they concentrated on the locations of foci, the conditions that generated them, and the peak pressure of focused N-wave booms. Signature shapes were qualitatively noted, but (other than peak pressures) no comparison to theory was made. During the Shaped Sonic Boom Experiment, two pushover focus maneuvers, from steady level flight at Mach 1.4, were performed (Plotkin et al., 2005).

There are currently four models for predicting sonic boom focal zones and signatures:

- PCBoom, which traces focal zones and their geometry, and applies single-shock numeric focus results independently to each shock in a focusing boom (Page et al., 2010).
- Auger and Coulouvrat's (2002) pseudospectral method, with improvements by Marchiano et al. (2003).
- ODU's reformulation/replication of Auger et al.'s pseudospectral method (Kandil and Zheng, 2005).
- Piacsek's (1995) implementation of NPE (McDonald, 2002).

Model 1 places focusing in the full context of aircraft maneuvers and the real atmosphere. The other three address signatures in the vicinity of a caustic. Models 2 and 3 are variations of solutions of the nonlinear Tricomi equation, applied to plane (or near plane) waves in a smooth gradient. Model 4 is an alternate formulation, which can address both smooth focusing gradients and the presence of turbulent irregularities. During the SCAMP program, PCBoom (Model 1) was further developed and interfaced with the LNTE (Model 3) and the NPE (Model 4) codes.

## 1.2 Project Objectives

Acceleration to supersonic speeds is a necessary maneuver for commercial supersonic flight. Proper understanding of the resultant focal zone is necessary for environmental assessment of this type of aircraft, and potential mitigation of the boom overpressures in this region. This is a key element for the ultimate manufacture and operation of this kind of aircraft. The physics governing sonic boom focusing are described in Chapter 2. The objective of the SCAMP research program is to validate the physical formulation of the sonic boom focusing algorithms via flight-test measurements, develop, improve, and validate computer models using flight-test data and to apply the tools to predict focus booms for low-boom aircraft designs. As will be described in subsequent sections of this report, the existing implementations of the algorithms each have been developed, critically examined, improved, and validated using SCAMP flight-test data and applied to a variety of low-boom aircraft designs.

The primary goal of the first year was to design, plan, and conduct flight tests to gather a comprehensive empirical dataset of focused sonic boom maneuvers suitable for validation of the aforementioned sonic boom focusing computer models. The measurement data collected includes time synchronized vehicle trajectory and operating state; meteorological data, and high-fidelity ground-based and elevated acoustic recordings. Chapter 3 describes the SCAMP measurement design, planning, and execution. During the first 15 months, the focus boom tools were developed and compared with a selection of SCAMP measured data

(Chapter 4). Computational Fluid Dynamics were used to model the as-flown F-18B flight conditions to define the incoming pressure signatures for PCBoom (Chapter 4). The four focus computational models (alpha codes) were compared with the SCAMP measurement data, critically assessed, and improvements were identified. Chapters 5, 6, 7, and 8 describe the formulation, numerical implementation, and comparison with SCAMP data for PCBoom, PSONTE 1, NPE, and LNTE alpha codes. Subsequent model improvements were made to the tools (beta codes), which showed improvements when compared with SCAMP measurement data (Chapter 9). An examination of focus boom signatures from low-boom flight vehicles was conducted and flight research findings were also used to improve the focus boom tools (Chapter 10). An additional Profile Exploration task was undertaken as a means to understand and bracket the effect of alternate flight profiles on shaped focus signatures (Chapter 11). A summary of findings and recommendations for the direction of future sonic boom focused signature research is presented in Chapter 12.

### 1.3 Tasks and Schedule

The SCAMP program lasted 27 months and is fully documented in this report. Additional documents created under the SCAMP project are itemized in Table 1-1. At the time of this writing, a SCAMP special session is scheduled to occur during the January 2013 American Institute of Aeronautics and Astronautics (AIAA) Aerospace Sciences Meeting for which eight SCAMP technical papers have been submitted and approved (Table 1-2). An additional article about the LNTE model development has been submitted to the AIAA Journal and is currently under review. An overall SCAMP project schedule may be found in Figures 1-2 and 1-3 for Phase 1 and Phase 2, respectively.

**Table 1-1. SCAMP Publications Summary**

Software Development Plan (TN 10-02)
Interface Control Document (TN 10-03)
Preliminary Flight Test Plan (TN 10-06)
Final Flight Test Plan (TN 10-07) (Draft Dec 2010, Final Feb 2011)
Acoustic Data Report (Jun 2011 TN 11-02)
Year 1 Report (Jul 2011 WR 11-16)
Measurement Comparison Report (Oct 2011 WR 11-23)
Low Boom Analysis Report (WR 11-26) (Dec 2011, Jan 2012, Final Apr 2012)
Beta Comparison (Mar 2012 WR 12-08)
Profile Exploration (Jul 2012 WR 12-18)
Final Report (This document) (Feb 2013 WR 12-21)

<sup>1</sup> During Year 1, a Tricomi code (PSONTE) - a direct replication of Auger and Coulouvrat's method - was developed, but was dropped in year 2 because it was a subset of the LNTE method and offered no particular advantage.

**Table 1-2. January 2013 AIAA Aerospace Sciences Meeting, SCAMP Special Session Technical Papers**

SCAMP: Superboom Caustic Analysis and Measurement Program

SCAMP: Experimental Design of a Sonic Boom Focus Flight Test

SCAMP: Rapid Focused Sonic Boom Waypoint Flight Planning Methods, Execution, and Results

SCAMP: Focused Sonic Boom Experimental Execution and Measurement Data Acquisition

SCAMP: Application of PCBoom to Measured Sonic Boom Focus Analysis

SCAMP: Solution of the Lossy Nonlinear Tricomi Equation for Sonic Boom Focusing

SCAMP: Application of Nonlinear Progressive Wave Equation to Sonic Boom Transition Focus

SCAMP: Supersonic Passenger Transport Transonic Acceleration Flight Profiles with Considerations of Focused Sonic Boom

SCAMP Program Schedule						Project and Calendar Years and Months													
	Wyle	PSU	Gulfstream	Eagle	CWU	Boeing	TASK DESCRIPTION	Project Year 1 - Phase 1											
								CY 2010						CY 2011					
								1	2	3	4	5	6	7	8	9	10	11	12
<b>Phase 1 - ARRA Funded Tasks</b>																			
<b>3.1 Development of 3 Sonic Boom Focus Research Codes</b>																			
3.1.4	X	o	o	o	o		Kick-off Prep / Project Planning	----											
D1	X	o	o	o	o		Kick-off Meeting @ LaRC		M										
3.1.1	X						PCB6+Focus Interface /Gill-Seebass Focus	-----+											
D2	X	o			o		Software Development Plan	--▲											
D2	X	o			o		Interface Control Document	--▲											
D3	X						PCB6 +Focus Interface Code - ALPHA										\$		
3.1.2	X						PCB6+Pseudosp.(Kandil's Auger/Coulvorat)	-----+											
D4	X						PCB6+Pseudospectral Focus - ALPHA										\$		
3.1.3					X		CWU Piacsek Nonlinear Progr. Wave Model	-----+											
D5					X		CWU Piacsek Code - ALPHA										\$		
<b>3.2 Flight Validation Planning</b>																			
3.2.1	X	o	o	o	o		Initial Flight Test Plan Development	-----+											
D2	X	o	o	o	o		Initial Flight Test Plan				▲								
D2	X	o	o	o	o		Flight Test Planning Meeting at DFRC				M								
	X						G.R.A.S. Mic Calibration Assessment / Algorithm				▲			▲					
3.2.2					X		F-18 F-functions / CAD / CFD Analysis	-----+											
D1					X		F-18 F-fcn, CAD, CFD Solutions Delivery										▲		
3.2.3	X		o				Final Flight Test Plan Development	-----+											
D3	X	o	o	o	o		Final Flight Test Plan										R		
D3	X						Briefing Materials (2 days in advance)										▲		
D3	X	o	o	o	o		Final Flight Test Planning Meeting @ DFRC										M		
<b>3.3 Execution of Sonic Boom Focus Flight Validation Experiment</b>																			
3.3.1	X	o	o	o	o		Flight Field Test Support												
D1	X	o	o	o	o		Flight Test - 2 week measurement period										↔		
3.3.2	X	o	o	o	o		Digital Database Development (Mic Data)										-----▲		
D2	X						Develop G.R.A.S. 40AQ process for low-F										-----▲		
D2	X	o	o	o	o		Database Delivery - Calibrated Mic Data										▲		
<b>3.4 Reporting</b>																			
D1	X	o	o	o	o		Monthly Technical Progress Reports - Due 5th		▲	▲	▲	▲	▲	▲	▲	▲	▲		
D1	X	o	o	o	o		Quarterly ARRA Reports (Business)		▲			▲			▲				
D1	X	o	o	o	o		Written Annual Report (Technical)												
D2	X	o	o	o	o		Briefing Slides (2 days in advance)												
D2	X	o	o	o	o		Annual Oral Year 1 Review @ LaRC												

Contract Issued 6/21/2010

Subcontract Technical Progress Report Inputs due by the 5th of the Calendar Month

Prime Technical progress reports due to NASA by the 10th of the Calendar Month

Year 2 - Quarterly Progress Reports

-- Task execution

+ Incremental Milestone

X Task lead

o Task Involvement

**Figure 1-2. SCAMP Program Schedule – Year 1/Phase 1**





## Sonic Boom Focusing

### 2.1 Sonic Booms and Ray Tracing

Sonic boom analysis generally begins with discussion of the linearized flow pressure field about a supersonic projectile, as given by Equation (2-1) (Whitham, 1952; Whitham, 1956; Hayes, Haefeli, Kulsrud, 1969; Maglieri, Plotkin, 1991).

$$\delta p(\chi, r) = \frac{\mathcal{P}_o M^2}{(2\beta r)^{1/2}} F(\chi) \quad (2-1)$$

where

$\delta p = p - p_o$  = pressure disturbance relative to ambient

$\chi = x - \beta r$  = phase variable parallel to vehicle

$p_o$  = ambient pressure

$M$  = Mach number

$\gamma$  = ratio of specific heats

$x$  = axial coordinate parallel to flight path

$r$  = radial coordinate

$$\beta = \sqrt{M^2 - 1}$$

$F$  = Source F-function

The F-function is usually stated as its relation to area rule linearized flow theory,

$$F(\chi) = \frac{1}{2\pi} \int_0^{\chi} \frac{A_e''(\tilde{x})}{(x - \tilde{x})^{1/2}} d\tilde{x} \quad (2-2)$$

where  $A_e(x)$  is the equivalent cross-sectional area of the projectile. Note that  $F$  and  $A_e$  are functions of body coordinate  $x$ , while the phase variable  $\chi$  appears in the propagation relation, Equation (2-1). The meaning of  $\chi = x - \beta r$  is sketched in Figure 2-1. Lines of constant  $\chi$  are simply the Mach waves originating at axial position  $x$  along the body.

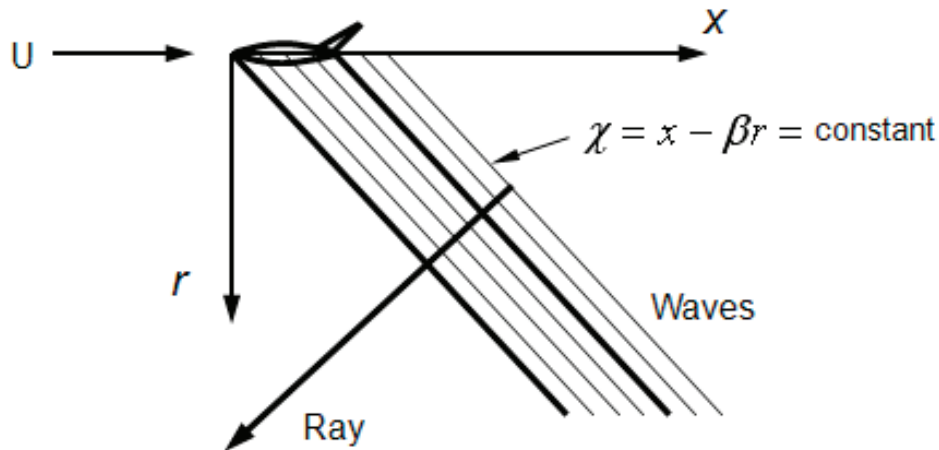


Figure 2-1. Mach Waves, Definition of Wave Coordinate  $\chi$ , and Ray Normal to Waves.

Equation (2-1) does not require that  $F$  be obtained from Equation (2-2). It is simply an acoustic source function. The only requirement is that the wave have locally plane wave behavior, such that  $\chi$  is the appropriate combination of  $x$  and  $r$  and there can be amplitude changes such as the  $1/\sqrt{r}$  term that have gradient scales large compared to the signal wavelength. Whitham (1952) wrote a general form of Equation (2-1) in simpler form as

$$\frac{\delta p}{p} = \frac{F(\tau)}{\sqrt{B}} \quad (2-3)$$

where  $B$  is a generalization of  $r$  to represent any slowly varying amplitude change and  $\tau$  is a time based equivalent of  $\chi$ . Whitham wrote  $S$  rather than  $B$ , specifying that  $S$  could be a constant (plane wave),  $s$  (propagation distance, cylindrical wave) or  $s^2$  (propagation distance squared, spherical wave). He also noted that  $S$  could represent a general ray tube area and could include acoustic impedance variations. We use  $B$  here to represent that general form. Ray tracing, ray tube area and acoustic impedance will be discussed shortly.

In Equation (2-3) the time-based variable

$$\tau = t - \frac{s}{a} \quad (2-4)$$

represents phase along a ray that is normal to the wavefronts sketched in Figure 2-1, where  $s$  is the propagation distance along the ray and  $a$  is the ambient sound speed.  $F(\tau)$  and  $F(\chi)$  are not the same function, since one is a function of time and the other of length, but both forms are used in the literature with length units generally applied to external scaling of both forms. The arrival time of wavefront of phase  $\tau$  is  $t = \tau + s/a$ . If the propagation medium has varying sound speed  $a_0$ , the arrival time generalizes to

$$t = \tau + \int_0^s \frac{ds}{a_0} \quad (2-5)$$

The appearance of N-waves at the ground, rather than waves that closely mimic the aircraft configuration, is a consequence of propagation not actually being linear. Whitham (1952, 1956) proposed that the linear solution gave the correct wave amplitude to first order, but that the wave shapes (or ray arrival times) were only correct to zeroth order. A uniformly valid first order solution could be obtained by adjusting propagation speed to first order.  $a_0$  in Equation (2-5) is replaced with  $a_0 + \delta_a + \delta_u$ , where  $\delta_a$  is the perturbation to sound speed and  $\delta_u$  is the local volume velocity associated with the acoustic wave. This adjustment can be quantified in terms of an age parameter  $\Lambda$  and the F-function, so that (Hayes, Haefeli, Kulsrud, 1959; Page, Plotkin, Wilmer, 2010).

$$\frac{\delta p}{p} = \frac{F(\tau - \Lambda(s))F(\tau)}{\sqrt{B}} \quad (2-6)$$

where

$$\Lambda(s) = \frac{\gamma+1}{2\gamma} \int_0^s \frac{ds}{a_0 \sqrt{B}} \quad (2-7)$$

The steepening embodied in Equation (2-6) leads to wave coalescence and formation of shocks. Those details are well documented in the literature, particularly the method of Middleton and Carlson (1965), which is implemented in PCBoom (Page, Plotkin, Wilmer, 2010). Note that the age parameter depends only on ray tracing parameters, as does the amplitude term in Equation (2-6).

Propagation of booms through a real atmosphere with gradients is addressed by the method of geometrical acoustics. The formulation employed is that of Blokhintzev (Blokhintzev, 1946), which addresses wind, sound speed, and density gradients. An equivalent simpler derivation for a windless atmosphere, following that of Officer (1958), is presented in detail by Plotkin (1971) and summarized below.

Consider propagation through an atmosphere with variable ambient sound speed and density, with no wind velocity and neglecting gravitational buoyancy. The wave equation is

$$\frac{\partial^2 p}{\partial t^2} - \rho_0 a_0^2 \bar{\nabla} \cdot \frac{1}{\rho_0} \bar{\nabla} p = 0 \quad (2-8)$$

where  $p$  now refers to the acoustic overpressure.  $a_0$  and  $\rho_0$  are the ambient sound speed and density.

A solution is sought of the form

$$p(x, y, z, t) = P(x, y, z) e^{i\omega \left[ t - \frac{W(x, y, z)}{a_\infty} \right]} \quad (2-9)$$

where

$\omega$  = frequency

$a_\infty$  = fixed reference sound speed

$P(x,y,z)$  = amplitude function

$W(x,y,z)$  = wavefront function

$t - W/a_\infty$  is a generalization of the earlier phase relation  $t - s/a$  relation, and  $P$  is a generalization of the  $1/\sqrt{B}$  amplitude relation.

Substituting Equation (2-9) into Equation (2-8) and separating the real and imaginary parts, the following two equations are obtained:

$$1 - \frac{a_0^2}{a_\infty^2} (\nabla W)^2 = \frac{a_0^2}{\omega^2} \left( \frac{\bar{\nabla} \rho_0}{\rho_0} \bullet \frac{\bar{\nabla} P}{P} - \frac{\nabla^2 P}{P} \right) \quad (2-10)$$

$$\nabla^2 W + \bar{\nabla} W \bullet \left( 2 \frac{\bar{\nabla} P}{P} - \frac{\bar{\nabla} \rho_0}{\rho_0} \right) = 0 \quad (2-11)$$

Note that the only terms dependent on  $\omega$  are on the right hand side of Equation (2-10). Those terms are of order  $(\lambda/L)^2$ , where  $\lambda$  is the wavelength of the signal and  $L$  is the scale length of atmospheric gradients and amplitude changes. If the short wavelength limit,  $\lambda \ll L$ , is taken, Equation (2-10) becomes

$$1 - \frac{a_0^2}{a_\infty^2} (\nabla W)^2 = 0 \quad (2-12)$$

so that there is no frequency dependence, and the system is non-dispersive. Equation (2-12) is the eikonal equation, familiar from geometrical optics, and states that the gradient of  $W$  is proportional to the local index of refraction. Propagation is along geometrical rays orthogonal to wavefronts  $W$ .

Once a ray field is computed by any suitable ray tracing algorithm,  $\bar{\nabla} W$  may be written  $\frac{a_\infty}{a_0} \hat{n}$ , where  $\hat{n}$  is the unit vector field representing ray direction. Equation (2-11) may then be written

$$\bar{\nabla} \bullet \left( \hat{n} \frac{P^2}{\rho_0 a_0} \right) = 0 \quad (2-13)$$

which has the obvious form of a continuity equation. Defining a ray tube as a bundle of rays, Equation (2-13) integrates to

$$P \left( \frac{S}{\rho_0 a_0} \right)^{1/2} = \text{constant} \quad (2-14)$$

where  $S$  is the ray tube area. Figure 2-2 is a sketch of a ray tube and its cross-sectional area. The quantity  $\rho_0 a_0$  is the acoustic impedance, and Equation (2-14) represents conservation of energy within a ray tube.

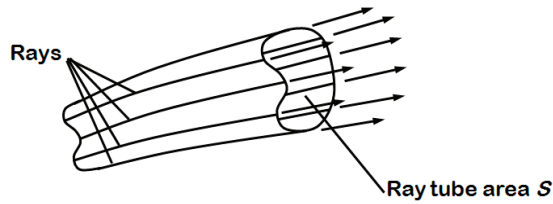


Figure 2-2. Ray Tube and Ray Tube Area.

When winds are present, the acoustic equations are more complex, but are given by Blokhintzev (Blokhintzev, 1946) and are implemented in all state of the art sonic boom programs.

Sonic boom rays can be traced by any of the familiar methods from optics, including Fermat's principle and Snell's law. Ray tracing begins with an initial ray on a ray cone generated at any given time at the aircraft. Figure 2-3 illustrates a ray cone and an initial ray at azimuth  $\phi$ . (Note that  $\phi$  is about the aircraft's roll axis, relative to earth referenced down.)

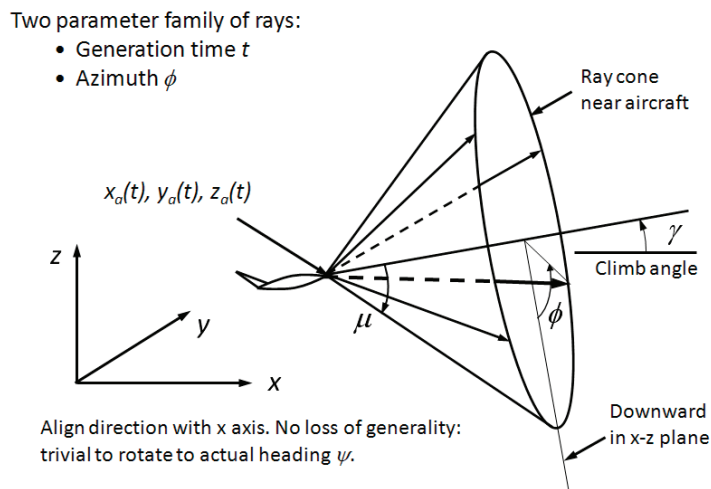


Figure 2-3. Ray Cone at Time  $t$  and initial ray at Azimuth  $\phi$ .

The independent variables for selecting a ray are aircraft time  $t$  and the azimuth  $\phi$ . In software implementations of boom theory, it is typical to use four rays, separated by small increments in  $t$  and  $\phi$ . There are two widespread styles in use. The first is that in the ARAP program (Hayes, Haefeli, Kulsrud, 1969), where differential relations are developed for the ray path and ray tube area. Those relations are in the form of quadratures, which then evaluated numerically. The second that used in the Thomas program (Thomas, 1972), where each ray is traced numerically and the ray tube areas obtained by differences between them.

Figure 2-4 is a sketch of sonic boom generation and propagation in a nutshell. The boom is generated at the aircraft, then propagates along rays that are traced by geometrical acoustics. The signature ages and evolves nonlinearly, per Whitham's rule. In the Earth's atmosphere, where temperature and sound speed decrease with altitude, the rays are generally concave upward, as sketched. Wind and/or temperature inversions can change that trend. Figure 2-5 is a sketch of potential propagation conditions. Propagation to the primary boom carpet is generally as shown in Figure 2-4, although wind conditions can sometimes

lead to downward propagation. If the boom propagates into the upper stratosphere or the mesosphere, where temperatures increase, it can propagate downward and even reach the ground as a secondary boom away from the primary carpet. Ray tube area - and amplitude - can change due to refraction (as drawn) and also due to maneuvers, which affect the initial convergence or divergence between rays forming a ray tube.

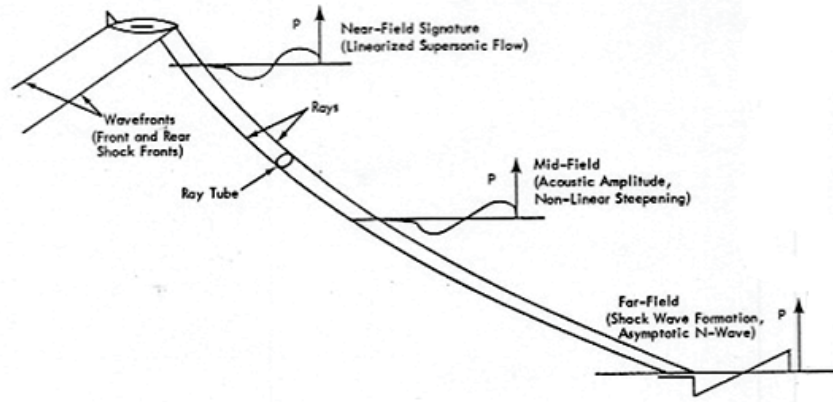


Figure 2-4. Sonic boom generation, propagation and evolution

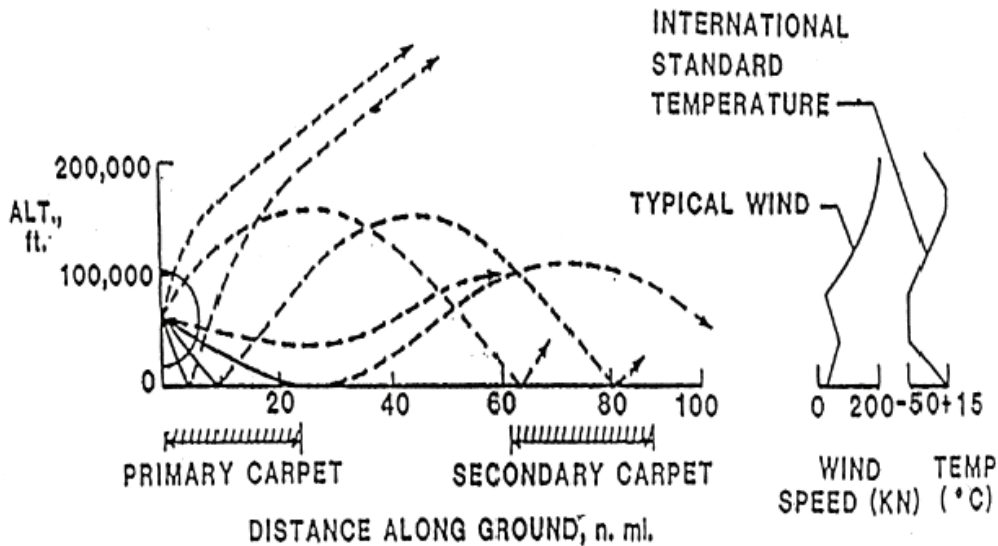


Figure 2-5. Variety of sonic boom ray paths.

Figure 2-6 is a schematic of ground booms that can occur during a supersonic flight. There is a primary carpet area that varies as fuel load and altitude changes through the flight. There may be a secondary boom area, displaced from the primary carpet, if some of the downward refraction situations shown in Figure 2-6 exist. At the beginning of the supersonic carpet there is a focused superboom region associated with transition from subsonic to supersonic speed. That focus region is the impetus for the SCAMP program. Focusing ray patterns are discussed in the next section.

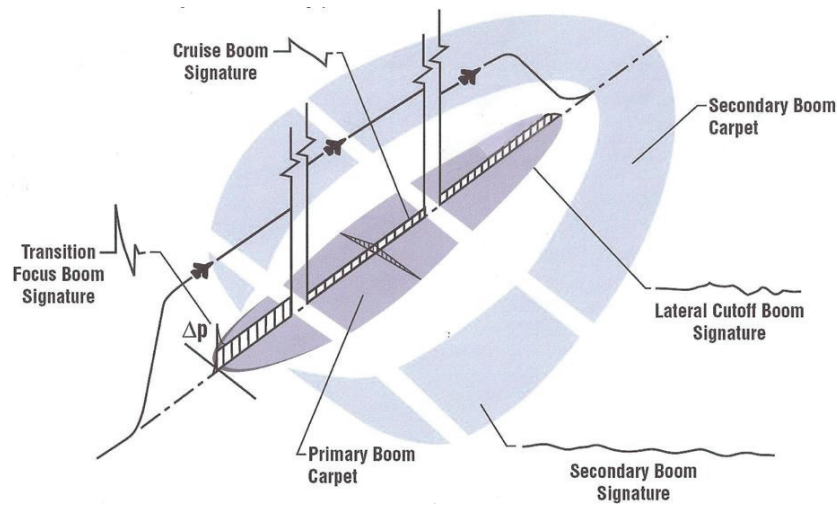


Figure 2-6. Sonic boom ray paths and footprint regions, from Maglieri (1980).

## 2.2 Focusing Ray Geometry

Because boom propagates along rays, and rays can converge, it is possible to have focusing situations where ray tube area vanishes and the linear acoustics solution discussed in Section 2.1 is singular. This does, indeed, occur, and focused booms are referred to as superboms. Figure 2-7 illustrates one type of focus associated with acceleration. As the aircraft accelerates, the Mach angle decreases and rays eventually cross. Crossing of rays is not in itself a focus, but rather a crossing of differentially separated rays. That occurs along a distributed line called a caustic. The caustic is also an envelope of rays. Note that rays are tangent to it, and do not penetrate onto the shadow side. It is not physically impossible for a finite portion of wavefront to converge to a single point, but it is very unlikely and a distributed caustic is the typical focusing situation.

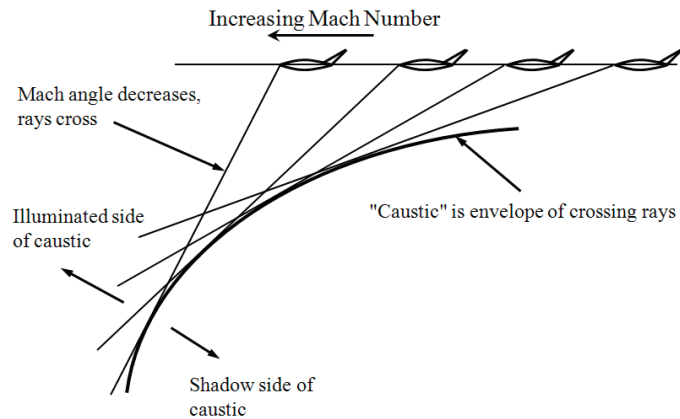
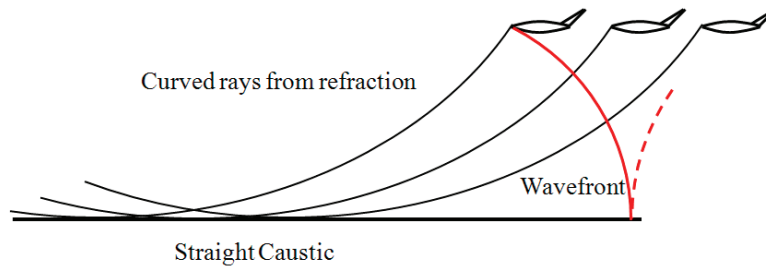


Figure 2-7. Focus - acceleration to supersonic speed.

Figure 2-8 shows another focusing situation, cutoff caused by refraction when steady flight is just below the cut-off Mach number. In this case the rays are curved and the caustic is straight. A wavefront is shown in Figure 2-8, showing how the wave appears to be reflected from the caustic.





**Figure 2-8. Cut-off caustic.**

Caustics can also be caused by curved flight paths. Figure 2-9 shows a caustic associated with a pushover, and Figure 2-10 shows a simple in-plane focus from a steady turn.

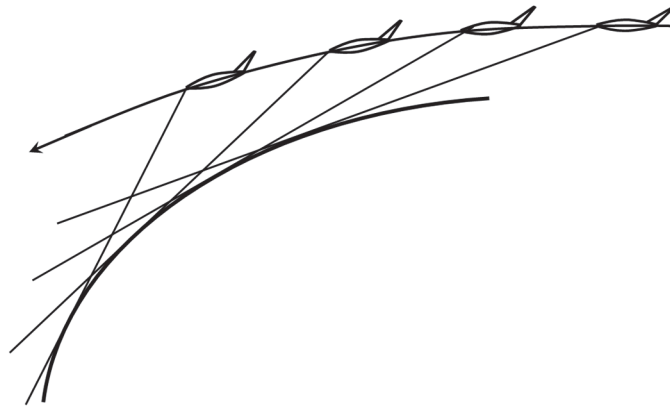


**Figure 2-9. Caustic from pushover.**

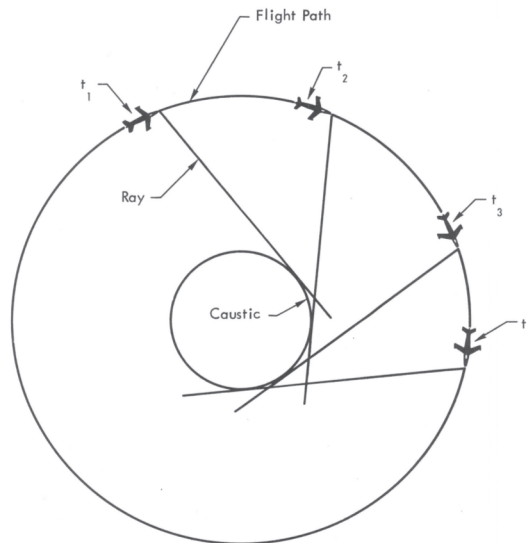


**Figure 2-10. Caustic in a steady turn – top view.**

Figures 2-7 through 2-10 are two dimensional geometries, essentially cuts through a full three-dimensional focus where the caustic is a surface, not just a line. Figure 2-11 shows the full three dimensional caustic for a steady turn (Onyeonwu, 1973). The shaded surface is the caustic, equivalent to the caustic line in Figure 2-8, while the folded surface on the left is the wavefront reflected from the caustic, equivalent to that shown in Figure 2-8.

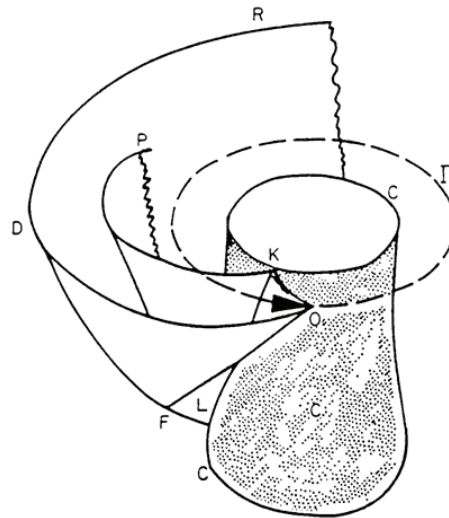


**Figure 2-11. Caustic in a steady turn – 3D View, from Onyeonwu (1973).**

While Figures 2-7 through 2-11 appear to be different situations, and more elaborate maneuvers can have more complex three-dimensional caustics, the behavior in the focal zone – where signatures are amplified – is similar for all. Geometrical acoustics remains valid until the rays reach the edge of a thin layer, the diffraction zone, surrounding the caustic. Behavior in the diffraction zone is described in Section 2.3..

If a cut is taken that contains a ray that is tangent to the caustic and is normal to the caustic, the local geometry will look like either Figure 2-7 or 2-8. Moreover, if the coordinates are defined along the caustic and normal to the caustic, all cases reduce to the geometry shown in Figure 2-7. It is analogous to a boundary layer, where the outer flow defines the environment. For caustics, the key geometry of the converging ray system is the relative curvature between the ray and the caustic. The governing equations and scaling laws are presented in the next section.

## 2.3 Nonlinear Tricomi Equation and Focal Zone Scaling

Figure 2-12 is a more detailed view of a focus in local caustic coordinates, from a wave perspective, showing the types of waveforms expected. The wave to the left has not yet reached the caustic, and far above it will be a conventional boom. Ray tube area at the caustic is zero, which implies a singular result if geometrical acoustics are applied. But the caustic is an edge, and violates the geometric acoustics condition that scales of  $P$  (see Equation 2-9) are large compared to wavelength, so diffraction serves to limit the signature amplitude at the caustic. Diffraction tends to limit low frequencies more than high, so the shocks amplify more than the expansion part of the boom, hence an incoming N-wave will have a U-wave shape at its maximum. The other waves have interacted with the caustic, with the post-focus U-wave reflected and a low-frequency wave passing below the caustic.

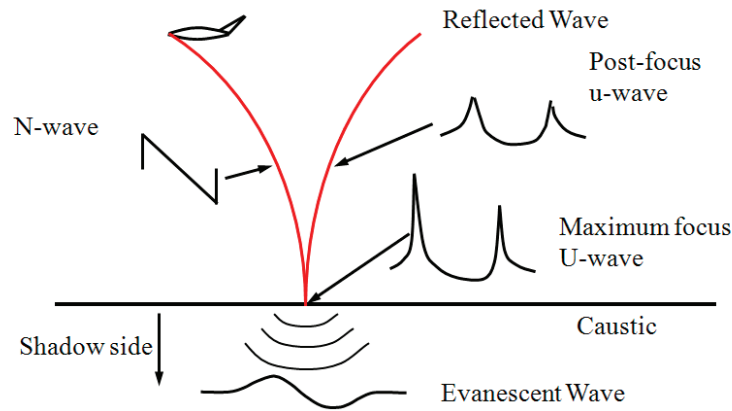


Figure 2-12. Waveforms in the vicinity of a cut-off caustic.

The equations describing behavior at a caustic were set down by Guiraud (1965). In formulating and writing the equations for a weak nonlinear wave (as is appropriate for sonic booms) and linearizing the sound speed gradient in the vicinity of the caustic, behavior in this region is governed by the nonlinear Tricomi equation

$$\phi_{yy} - (y/R + \phi_x)\phi_{xx} = 0 \quad (2-15)$$

where  $x$  is the coordinate along the caustic,  $y$  is the coordinate normal to the caustic,  $\phi$  is the perturbation velocity potential, and  $R$  is the curvature of the ray in the linear gradient region near the caustic. ( $R$  is the relative curvature between ray and caustic if this is transformed from a curved caustic.) Note that Equation (2-15) is hyperbolic for  $y > 0$ , so that the waves above the caustic are indeed waves and propagate along rays. It is elliptic below the caustic Equation (2-15), so that the disturbance below the caustic, labeled “evanescent wave”, is a non-propagating subsonic disturbance (much like a subsonic lift pulse) and decays with distance below the caustic. The second term in the parenthesis is nonlinear steepening, exactly the weak nonlinear term that corresponds to aging of boom signatures.

Guiraud (1965) examined the Tricomi equation’s similarity properties and derived a scaling law for the maximum focus. If the overpressure, cast as a pressure coefficient, at a reference location  $y_{ref}$  is  $C_{P_{ref}}$ , then the maximum overpressure at the focus is given by

$$\frac{C_{P_{max}}}{C_{P_{ref}}} \propto \left[ \frac{y_{ref}}{RC_{P_{ref}}} \right]^{1/5} \quad (2-16)$$

so that an amplification factor can be defined in terms of reference conditions and  $R$ . Note that as  $C_{P_{ref}}$  increases, the amplification decreases. so, scaling is nonlinear. There is thus a nonlinear scaling parameter in addition to  $R$ .

The constant of proportionality in Equation (2-16) can be obtained from theoretical solutions to the nonlinear Tricomi equation or from experimentation. During early studies of focus boom, when the

maximum peak was of primary interest, there was some controversy over the value of the constant. Plotkin and Cantril (1976) showed that some of this inconsistency was due to the difference between theoretical solutions with zero shock thickness and the finite thickness of measured shocks. They showed that, if shock thickness was applied consistently, a single constant applied to flight test (Wanner, Vallee, Vivier, They, 1972), laboratory (Sanai, Toong, Pierce, 1976) and theoretical (Gill, Seebass, 1975) foci.

Further analysis of scaling of the nonlinear Tricomi equation was performed by Hayes (1969) and by Seebass (1970) who also developed a numerical solution method.

## 2.4 Classic Focus Prediction: PCBoom and the Gill-Seebass Solution

The first successful solution of the nonlinear Tricomi equation for sonic boom focusing was by Gill and Seebass (1975) and Gill (1974). They obtained numeric solutions to the Tricomi Equation for a step function incident wave, representing a thin shock wave. They began with a dimensional form of the nonlinear Tricomi equation in wave-fixed coordinates

$$\left[ \frac{Y}{R} + \frac{\gamma+1}{U} \Phi_x \right] \Phi_{xx} + \Phi_{yy} = 0 \quad (2-17)$$

where U is the flow speed. Sound speed varies linearly, and equals U at Y=0. R in Equation (35) is twice the actual radius of curvature of the rays.

By applying Guiraud's similitude in the form

$$\begin{aligned} \Phi &= \frac{US^{5/3}}{(\gamma+1)R^{2/3}} \phi \\ X &= Sx \\ Y &= R^{1/3} S^{2/3} y \end{aligned} \quad (2-18)$$

they obtained the non-dimensional form

$$(y + \phi_x) \phi_{xx} - \phi_{yy} = 0 \quad (2-19)$$

The linear characteristics of this equation are  $p, q = x \pm y^{2/3}$ , and the initial condition is specified as a function of  $p$  on  $q = -1$ :

$$\phi_x(p) = -\mu y^{-1/4} F(p) \quad (2-20)$$

where  $\mu$  is an amplitude parameter. In view of the transformation, the solution should be independent of  $\mu$ , and Gill and Seebass found that this was the case for values of  $\mu$  from 0.00001 through 0.1. Retaining this parameter was useful to their numeric scheme, and a value of 0.1 was used.

Their computational approach was to introduce a coordinate strain transformation that reduced it to the linear Tricomi equation, for which solutions were known (Ludwig, 1966). Linear solutions, in terms of Airy functions, were constructed, then transformed back to  $x, y$  coordinates. The procedure is analogous to Whitham's rule, except that two dimensions are involved.

Figure 2-13 shows Gill and Seebass's solution for  $u = \phi_x$  obtained for a step function shock with  $\mu = -0.1$  at  $y = 0.45$ . Transformation from the strained coordinates to the  $x, y$  plane results in the signature folding over. If a thin shock wave is inserted, using the area balancing rule, the maximum value of  $-u$  is 0.39, as shown in Figure 2-14.

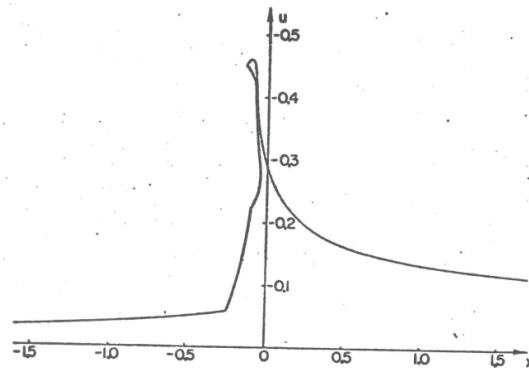


**Figure 2-13. Signature shape near maximum focus, shock not fitted, from Gill and Seebass (1975).**

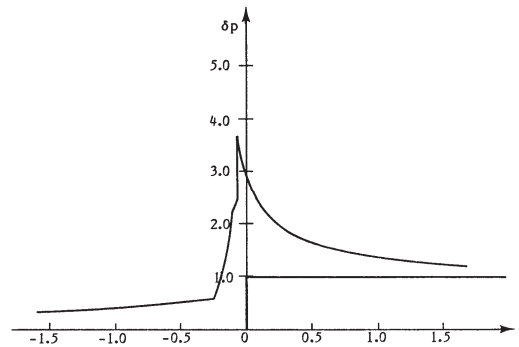


**Figure 2-14. Gill-Seebass solution for focused shock wave (unit step function), shock inserted, from Gill and Seebass (1975).**

The peak shock amplitude does not occur at the geometric caustic, but (as is consistent with diffraction) some distance above it in the illuminated zone. Figure 2-15 shows the amplitude as a function of non-dimensional distance  $y$  above the caustic. Note that there are two curves, depending on whether the two-dimensional shock fitting is performed to satisfy balance in the  $u$  or  $v$  direction. Hayes (Hayes, 1970) pointed out that the shock fitting part of this problem is not well posed, and that it would not be possible to satisfy shock jump conditions simultaneously for  $u$  and  $v$ . The two curves are, however, very close and in the context of the second order approximations involving Hayes's concern is not significant.

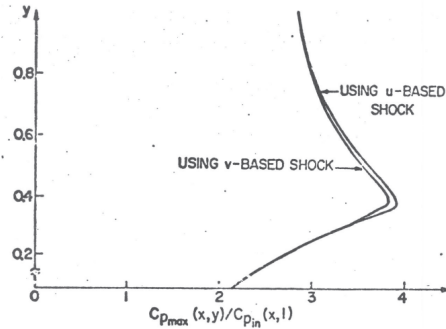


**Figure 2-15. Maximum pressure coefficient ratio as a function of  $y$  for  $u$  and  $v$  based shocks, from Gill and Seebass (1975).**

With Gill and Seebass’s numeric solution matching flight test and laboratory measurements, Plotkin and Cantril (1976) took the solution shown in Figure 2-14 as a universal result for a shock, and added it to a version of Thomas’s (1972; 1970) boom propagation code. That effort, conducted in the 1970s, was sponsored by the NASA Marshall Space Flight Center (MSFC) for use in environmental assessment of focus booms from Space Shuttle launches. The code was initially known as “The Wyle/MSFC focus boom program.” In the 1980s, when the code was hosted on terminal-based systems where programs required a file name (rather than physically handing in a card deck) it was named “Foboom”. In the 1990s, after two unsuccessful efforts by others to host a different full sonic boom code onto a PC, Foboom was updated to Fortran 77, successfully implemented on a PC, and denoted PCBoom3 (Plotkin, 1998). PCBoom has continued to evolve with further features, updated to Fortran 90/95, packaged with supporting utilities and user interfaces, and is denoted PCBoom6 (Page et al., 2010).

Focus implementation in PCBoom6 is essentially the same as developed for the original Wyle/MSFC code. The process is:

1. The program traces rays at a given  $t$ ,  $\phi$ , as for non-focusing booms
2. If a focus is detected, by virtue of the ray tube area vanishing, the focus coordinates are marked, the ray curvature at the focus computed, and the program goes into focus mode.
3. In focus mode, three additional ray tubes are traced at trajectory points ahead of and behind the original, as illustrated in Figure 2-16. The original is Point 1. If focus is not in a plane of symmetry,  $\phi$  is adjusted at each of the additional points such that caustic tracing is in the plane containing the ray and normal to the surface.
4. The caustic curvature is computed from Points 1, 2, and 3. Point 4 is used to test for anomalous conditions, such as cusp straddle.
5. Boom evolution and aging is implemented as for a non-focus boom, but at each ray step the caustic diffraction zone dimensions are computed from the scaling law. Geometric acoustic evolution ends just outside the focal zone, at a position corresponding to  $q = -1$  in Equation (2-20).
6. The maximum focus signature is obtained by applying the Gill-Seebass solution (Figure 2-14) to each shock in the incident boom, using Guiraud’s similitude for scaling. This is applied independently to each shock.
7. Post focus booms are approximated by acoustically propagating the diffraction part of the Gill-Seebass solution (the focus signature in Figure 2-14 minus the incident step) along a ray, assuming linear ray spreading beyond the focus.

The process has some issues, primarily the application of a step-function focus solution to every shock in the signature. It has, however, been very successful in predicting the peak amplitude of focus booms and the time between N-waves and u-waves in post-focus N-u combinations. With the 21<sup>st</sup> Century advent of modern solutions these issues will be addressed in the new focused boom models. This was, in fact, one of the goals of the SCAMP program.

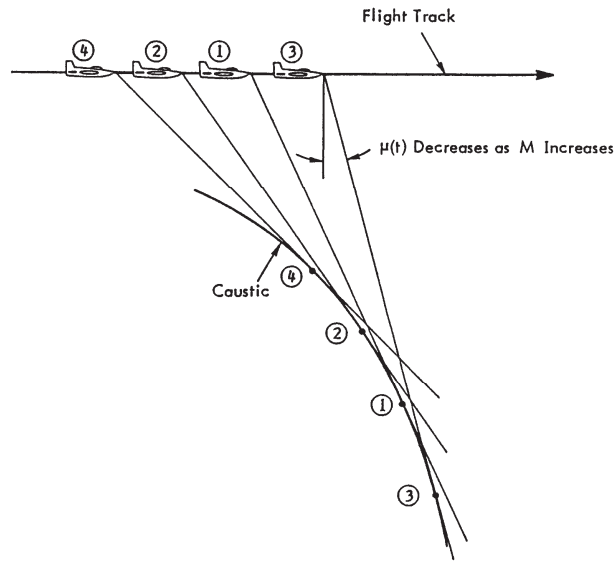


Figure 2-16. PCBoom caustic tracing.

## 2.5 Interfaces to Modern Solutions

Two types of modern focus solutions are being developed under the SCAMP effort:

- Solutions to the nonlinear Tricomi equations, described in 6.0 and 8.0.
- Nonlinear Progressive Wave Equation (NPE), described in 7.0.

The Gill-Seebass solution currently in PCBoom is a Tricomi solution, so the scaling quantities needed are already computed. Those quantities are the ray/caustic curvature, the scaled distance to the focus, and the signature at the edge of the diffraction zone. Those have always been computed internally. As part of PCBoom5/6's Over The Top mode, those quantities, together with ray coordinates, are written to an "OTT" file for selected rays. The interface to Tricomi solutions is thus already in place. Small interfaces, consisting of code-specific I/O matching may be needed for particular Tricomi codes.

NPE, as a wave equation solver, requires as input an in-coming wave field at some distance before the focal zone. This is in contrast to the Tricomi solvers, which need only the in-coming wave on a focusing ray. The OTT file contains ray paths and the accompanying OTS file defines the waveforms. PCBoom can, however, be run for multiple time steps at fine intervals, with output to the OTT file. The intended interface procedure for NPE was therefore to run PCBoom for a number of time steps at short intervals, along with fine integration time steps along the rays, and specify output to an OTT file. The OTT file output was also updated to simplify extraction of the caustic points, such that the final wave field solution could be interpolated onto coordinates parallel to and normal to the caustic, in the same form as Tricomi solutions. As will be discussed in 6.0, this procedure encountered difficulty with diffraction from the edges of the initial

wave, and also was in conflict with the need for the NPE process to generate the caustic. A scaled approach, similar to that used for Tricomi interfacing, was ultimately used.

## 2.6 F-18 F-Function from CFD Analysis

Boeing was tasked to provide PC-Boom input  $\Delta P/P_\infty$  cylinder data for flight-test planning purposes. This involved first generating detailed aircraft geometry grids representing the test aircraft (NASA’s F-18B with only the center auxiliary fuel tank attached) at certain supersonic flight conditions. Boeing’s BCFD code was then exercised on with these geometry data at several steady-state conditions. Simulated inlet and nozzle flow conditions were determined from an F/A-18C (essentially the same for current purposes as the F-18B) engine cycle deck. These conditions were selected to cover the range of conditions expected to be flown during the flight test.

Most SCAMP maneuvers were expected to involve focus with the aircraft at 35,000 feet and a Mach number between 1.2 and 1.3. Some maneuvers were expected to be conducted as pushovers, with unloading to as low as 0.25g. One candidate maneuver was to be slow acceleration at constant 40,000 feet, for which PCBoom analysis indicated that focus would occur at Mach 1.17. On September 7, 2010, several candidate maneuvers were flown in the simulator at NASA’s Dryden Flight Research Center (DFRC). Four CFD analyses were performed, using detailed conditions taken from the simulator as the aircraft passed through four conditions. Table 2-1 lists the four CFD flight conditions. CFD Case 1 was intended to apply directly to the 40,000-foot slow acceleration maneuver. The other three were intended to be interpolated between Mach 1.1 and 1.3, and to unloaded conditions. These were used as inputs to PCBoom for test planning. Following the flight test, CFD solutions were generated for “as-flown” conditions for each maneuver.

**Table 2-1. Steady State Flight Conditions for CFD Analysis**

CFD Case	Mach	Altitude	Simulator Run for flight conditions	g
1	1.17	40,500	Boom7	1.0
2	1.2	35,000	Boom13	1.0
3	1.3	35,000	Boom6	1.0
4	1.3	35,000	Boom6, modified*	0.25*

\* Angle of attack was reduced from Boom6 actual to accomplish this.

To obtain high resolution of the expected compression and expansion waves in the CFD, a “grid-adaption” process was utilized whereby flow gradients from an initial solution are used to cluster grid points where they are needed and used for a subsequent flow solution. Three of these grid-adaption iterations were used to obtain the final flow data that was interpolated to a solution cylinder (Figure 2-17) at a radius of three body lengths as input to the boom prediction program PCBoom.





**Figure 2-17. CFD predicted  $\Delta P/P_o$  cylinder data at three body lengths, Boom7,  $M = 1.2$ .**

The computational grid size ranged from 17 million for the initial solution to 40 million in the final adapted solution. Since the computed conditions had zero sideslip angle, the CFD analyses assumed a symmetric flow condition with the centerplane of the vehicle using a reflection boundary condition type. Because of the inviscid nature of pressure wave propagation, the flow was computed using the Euler equation solver of the BCFD program and does not include viscous contributions (like boundary layers) in the analyses.

A comparison of the computed pressure contours between the initial (no-adaption) case and the final (two adaption iterations) case is shown below in Figure 2-18.

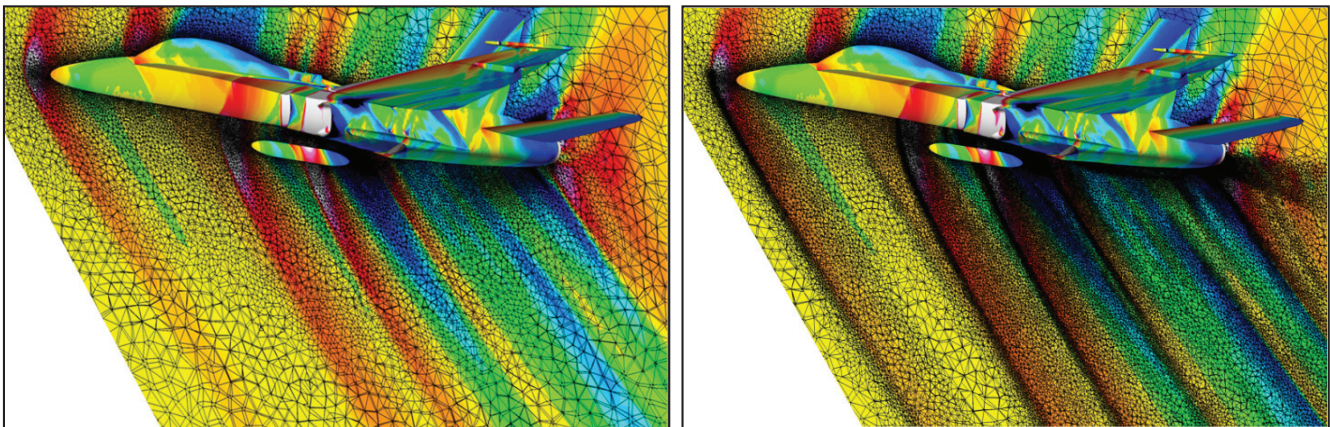


**Figure 2-18. Computed pressure contours on the vehicle symmetry plane and F-18 surface, Boom7,  $M = 1.2$ .**

Pressures shown from the initial solution (left) and the final grid-adapted solution (right).

The adaption used in these analyses simply divides the current cell in half if it meets a gradient sensitivity criterion. Boeing is currently developing a non-isotropic adaption that will allow a collapse of the grid cells to better resolve a directional gradient (across a shock for example) instead of the isotropic addition that is

done currently. An enlarged view of Figure 2-18 is shown below in Figure 2-19 and illustrates the manner in which the grid adaption adds cells to both surface and off-body grid regions.

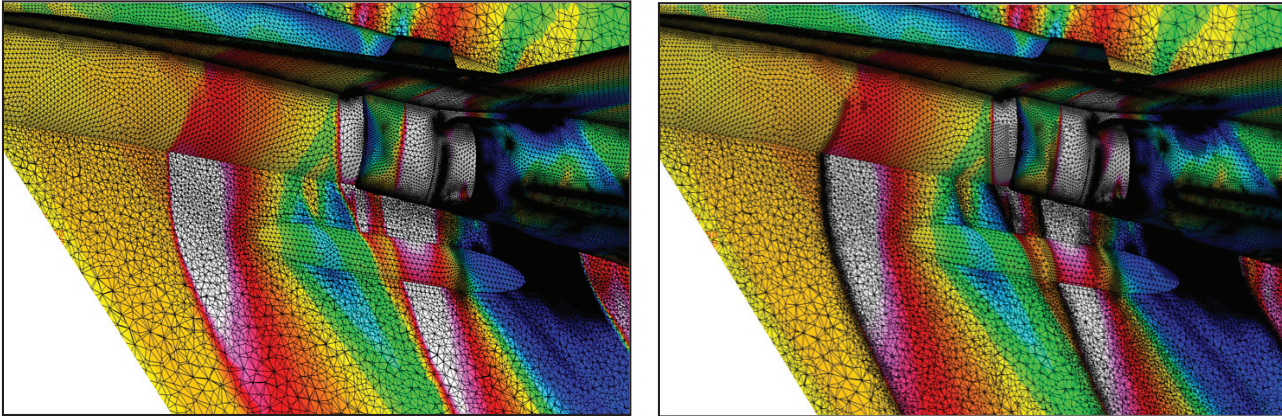


**Figure 2-19. Close-up of the computed pressure contours, Boom7,  $M = 1.2$ .**

Shown on the vehicle symmetry plane and surface from the initial solution (left) and the final grid-adapted solution (right).

The experiment involved precision flight of an F-18B executing various maneuvers that create focused sonic booms. The maneuvers have been designed to center on the flight regime expected for commercial supersonic aircraft transonic transition, and also span a range of caustic curvatures in order to provide a variety of conditions for code validations.

The maneuvers to be flight tested include the following:

- Two different level accelerations at 35,000 feet. These span conditions within the expected flight envelope of commercial supersonic aircraft.
- Pushovers at various angular rates from approximately 45,000 feet, with focus occurring at flight altitudes within the envelope of commercial supersonic aircraft. These are intended to provide a wider range of caustic curvatures.

The experiment is designed to capture concurrent F-18B on-board flight instrumentation data, high-fidelity ground-based acoustic data and surface and upper air meteorological measurements. The flight experiment was conducted in the Black Mountain Supersonic Corridor in the R-2508 Range Complex at Edwards Air Force Base (EAFB). The Corridor was expanded a few miles to the north of its usual boundary for this flight series. The aircraft flown was the NASA Dryden F-18B, Ship #852.

The acoustic instrumentation array consisted of a 10,000-foot line of microphones spaced at 125 feet. The flight track was aligned with the 10,000-foot long microphone array. The location for this ground-based acoustic measurement array was an area in the Cuddeback Air-to-Ground Gunnery Range north and east of EAFB, California.

Flight measurements were conducted on-track, in a plane of symmetry corresponding to the formal focusing theory. Focus footprints extend laterally, where the ray geometry is skew. Off-track measurements are thus also needed for complete understanding of focal zone footprints. Off-track measurements were achieved by flying the aircraft along a path laterally displaced from the linear measurement array.

Additional projects leveraged the SCAMP flight testing and performed concurrent measurements. These efforts were led by NASA and others and were not within the Wyle team scope of effort. Since data will ultimately be shared and are noted here for completeness.

- In-flight schlieren imagery of the F-18B flight maneuvers by MetroLaser;
- Sonic boom measurements above the planetary boundary layer to be captured by acoustic instrumentation aboard the US Air Force TG-14 Powered Sailplane, operated by NASA with oversight by the USAF;
- NASA SonicBREWS (Sonic Boom Resistant Earthquake Warning System) program consisting of several buried accelerometers near the focal zone (Wurman, Haering, Jr., and Price, 2011).

## 3.1 Objectives

The primary objective of the experiment was to gather a comprehensive dataset of focused sonic boom maneuvers suitable for validation of sonic boom-focusing computer models. The data collected included time synchronized vehicle trajectory and operating state, meteorological data, and high-fidelity ground-based acoustic recordings.

## 3.2 Measurements Site and Microphone Array

### 3.2.1 Site

The primary acoustic instrumentation array was located at the Cuddeback Air-to-Ground Gunnery Range, California. Primary acoustic measurements were on-track, in a plane of symmetry corresponding to the formal theory. Off-track measurements were achieved by flying the aircraft along a path laterally displaced from the linear measurement array. A notional graphic of the SCAMP measurement site layout is provided in Figure 3-1. Noted on the graphic in Figure 3-1 are the 81 ground microphone locations, the locations of the meteorological equipment (SONic Detection And Ranging (SODAR) wind profiler, GPSsonde launch site, Ground-based MET stations) as well as the location of a tethered blimp that lifted elevated microphones.

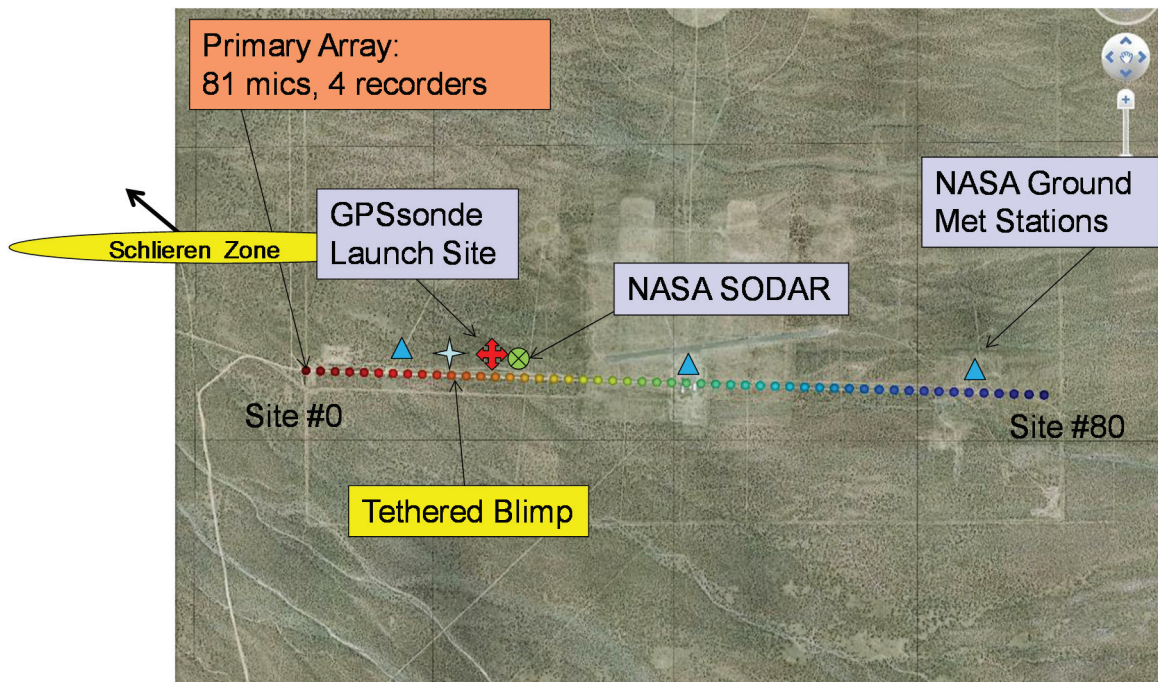
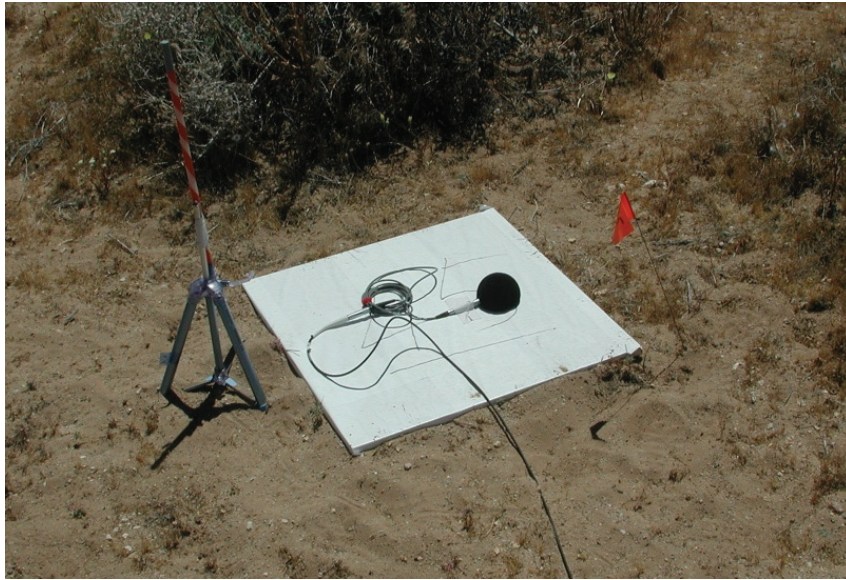


Figure 3-1. Notional SCAMP measurement site layout diagram.

### 3.2.2 Ground Array

Two arrays of microphones were deployed as well as a microphone on a powered sailplane. The first was the main array consisting of 81 microphones on ground boards spaced 125 feet apart. The microphone array was oriented in an East-West direction with the microphones all pointing West, the preamp taped to the ground board, and a half wind screen covering the microphone. Figure 3-2 shows the deployment of Microphone #45. All were set up in a consistent fashion. A detailed report (Hobbs, Page, Plotkin, 2011).was prepared containing microphone GPS survey coordinates, and documenting the microphone measurement data.



*Figure 3-2. Example of microphone on ground board.*

### 3.2.3 Elevated Measurements

NASA operated a TG-14 powered sailplane (Figure 3-3) with an on-board microphone in order to measure the focused sonic boom above the planetary boundary layer, before it became distorted by atmospheric turbulence. During daily flight planning, the location of the focal zone was determined at the flight altitude of the TG-14. These waypoints were provided to the TG-14 pilot who then proceeded to fly the TG-14 back and forth perpendicular to the ground measurement array. At the time when the pilot reached the maneuver initiation location, the TG-14 shut down the engines in order to reduce background noise and capture a clean sonic boom signal. Two examples of TG-14 recorded sonic booms are presented in Figures 3-4 and 3-5.



**Figure 3-3. TG-14 powered glider used for recording sonic booms in the air.**  
(Source: NASA)

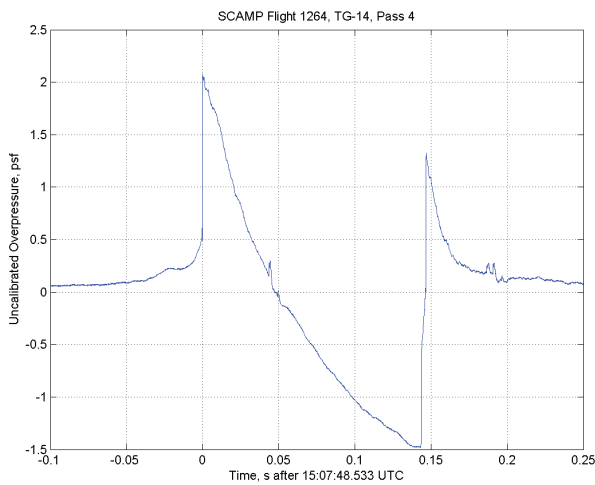


**Figure 3-4. TG-14 sonic boom recording, Flight 1264 Pass 4.**

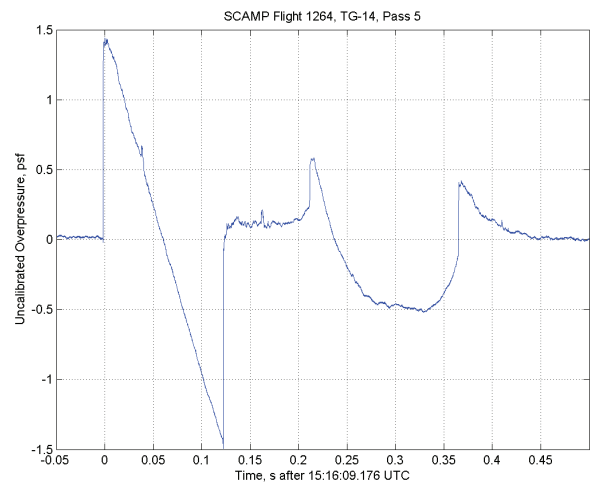


**Figure 3-5. TG-14 sonic boom recording, Flight 1264 Pass 5.**

Cessna, collaborators with the SCAMP program, provided a tethered balloon that carried microphones to altitudes of 1500Ft AGL (Figure 3-6). This was performed successfully during a portion of the SCAMP measurements when permitted by local wind and weather conditions.



*Figure 3-6. Cessna operated tethered blimp for elevated microphones.*

### 3.3 Weather Data

A significant number of weather data acquisition resources were utilized in making the SCAMP measurements. These were principally provided and operated by NASA. Three ground-based meteorological stations (Figure 3-7) were deployed along the measurement array at approximate locations indicated in Figure 3-1. The NASA Mini-SODAR 4000 was also deployed for the duration of the recording of SCAMP measurements (Figure 3-8). Every morning a GPS-sonde was launched in order to obtain upper atmospheric data and conduct flight planning. During each SCAMP flight, an additional GPS-sonde was launched so that accurate wind and temperature profile data would be available for the analysis and validation activities conducted during the second year of the SCAMP program.



**Figure 3-7. NASA ground-based meteorological station.**



**Figure 3-8. NASA Mini-SODAR 4000.**



**Figure 3-9. NASA GPS-sonde prepared for launch.**

### 3.4 Maneuver Design / Flight Test Matrix

The objective of the test was to obtain focus data under conditions relevant for a commercial supersonic aircraft and to exercise the focus models. As shown in Section 2, the primary scaling parameter in a focal zone is the relative radius of curvature between a caustic and its tangent ray. It was necessary to assess the curvature associated with expected operational transition maneuvers and to assess methods to obtain variations in that curvature.



Boeing and Gulfstream identified transition conditions that they expected to apply to small commercial supersonic aircraft. They were:

- Acceleration of about 2 knots/second at 35,000 feet Mean Sea Level (MSL).
- Acceleration of about 0.5 knots/second at 40,000 feet MSL.

These are likely to take place during a slight climb, but level flight is within the expected range. These two conditions were denoted SSBJ1 and SSBJ2. Acceleration of 2 knots/second is a Mach rate (Mdot) of about 0.0035/second. To reduce clutter when communicating, Mach rates within the project were presented as milli-Mdot (mMdot), so the SSBJ2 rate is 3.5 mMdot.

Parametric sensitivity studies of maneuvers and focusing were performed using a purpose-written program denoted Caustic Undertrack Jacobian Operator (CUJO), which used analytic relations for under-track focus developed by Plotkin and Cantril (1975). CUJO had a graphical interface, shown in Figure 3-10. It could be interactively steered to vary accelerations and pushover rates. During that steering, organized files were written that could be analyzed for optimum maneuver design. Figures 3-11 and 3-12 show two CUJO results – the effect of acceleration and pushover rate, respectively, on ray/caustic radius of curvature.

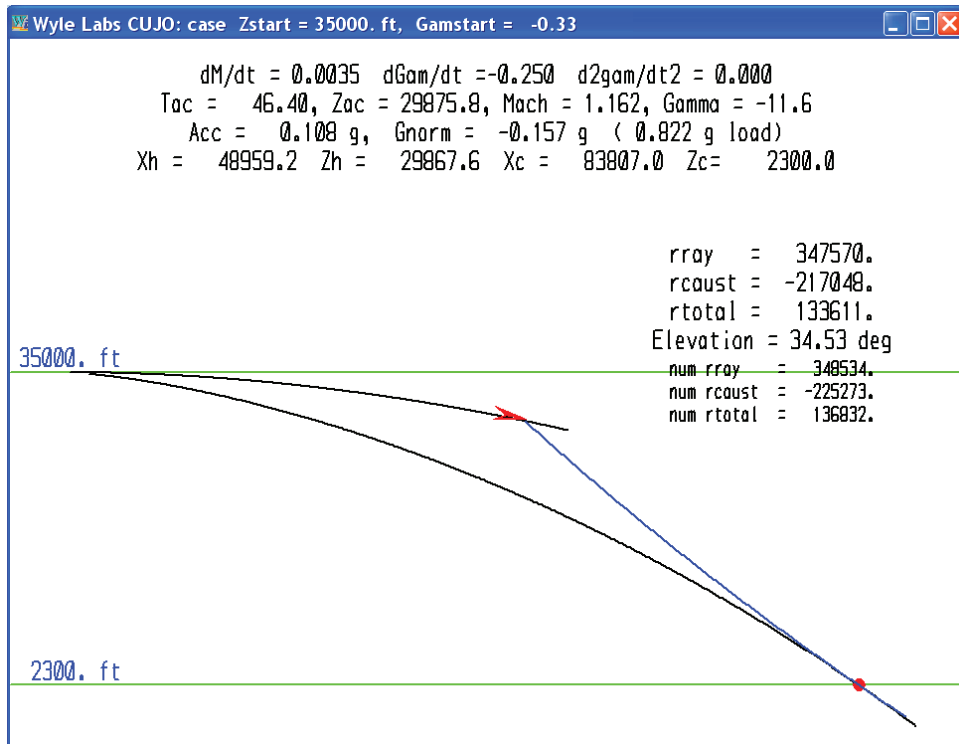
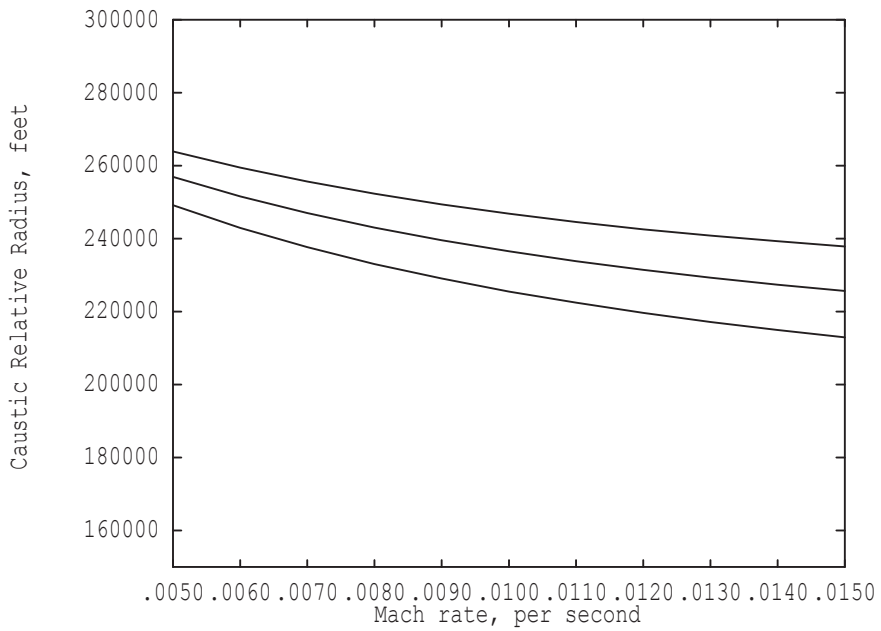
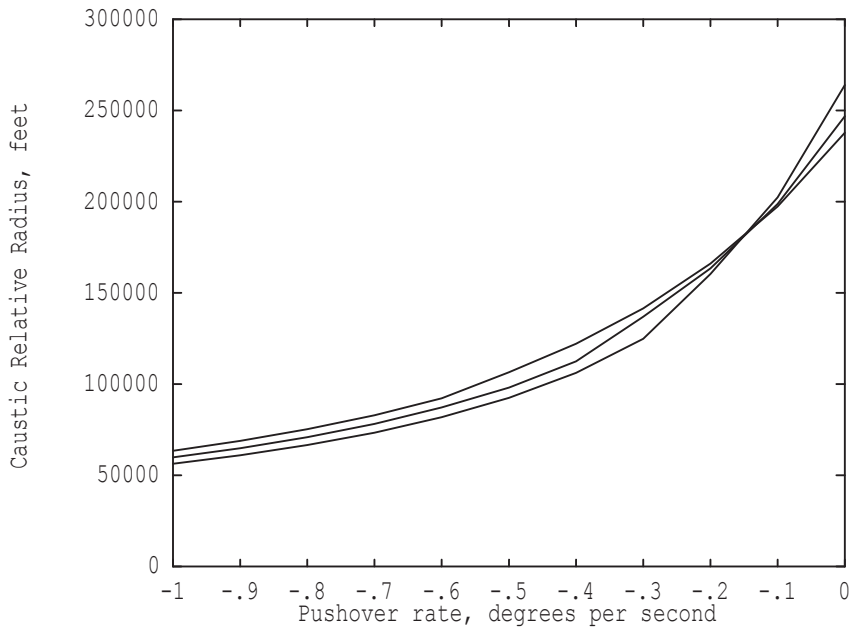


Figure 3-10. Screen shot of focus curvature analysis tool CUJO.



**Figure 3-11. Effect of acceleration on caustic radius of curvature.**



**Figure 3-12. Effect of pushover rate on caustic radius of curvature.**

Acceleration was found to have a relatively small effect on curvature, with radius of curvature in Figure 3-11 varying within the range 220,000 to 250,000 feet. Pushovers, shown in Figure 3-12, had a more direct effect on curvature, with radius of curvature as small as 50,000 feet possible at a rate of  $-1^\circ$  per second. That rate at a flight speed in the low supersonic range corresponded to unloading the aircraft to about zero g.

The initial candidate flight-test matrix consisted of the following:

- SSBJ1: 2 kt/sec level acceleration at 35,000 ft;
- SSBJ2: 0.5 kt/sec level acceleration at 40,000 ft;
- High power acceleration at 35,000 ft; and
- Pushover from 45,000 ft: high power, gamma-dot -0.5 deg/sec.

These maneuvers were tested on the simulator at NASA DFRC on 7 and 14 September 2010. Aided by Mdot and gamma-dot displays programmed into the simulator for this project, but not available on the actual aircraft, it was determined that these maneuvers were feasible and could be executed within the available airspace. A flight test on 15 November 2010 provided additional experience and confirmation. Mdot and gamma-dot displays were not available, so most tests were flown at either mil power or high power, and gamma-dot was approximated by holding constant g. It was found that constant g yielded a good approximation of gamma-dot, with 0.8 g corresponding to -0.25 degrees/second, 0.6 g to -0.5 degrees/second and 0.4 g to -0.75 degrees/second. PCBoom analysis of the maneuvers showed that constant power acceleration was not suitable, since Mdot would diminish with airspeed and cause excess variations in caustic curvature.

NASA DFRC developed an in-cockpit Mdot meter. As noted above, to reduce clutter in the display it was calibrated to show mMdot. The aircraft's existing display provided suitable g displays to the pilots.

The maneuvers were further developed by additional simulator testing and test flights. The final selection for maneuvers is itemized in Table 3-1:

**Table 3-1. Selected SCAMP Focus Flight Maneuvers**

A. SSBJ1: mMdot = 3.5, level at 35000 feet
B. High power, level at 35000 feet
C. Pushover from 45000 feet, mMdot = 3.5, g = 0.8 (gamma-dot = -0.25 degrees/second)
D. Pushover from 45000 feet, mMdot = 3.5, g = 0.6 (gamma-dot = -0.5 degrees/second)

Maneuver SSBJ2 was dropped because it used excessive fuel and airspace, and was also sensitive to atmospheric variations. Pushovers at higher rates were ruled out because of airspace floor limits.

Three additional conditions were added to the flight matrix – steady level passes at 35,000 feet, Mach 1.17, 1.20, and 1.30. These corresponded to the three CFD analysis conditions and were denoted E, F, and G.

The final proposed flight-test matrix is shown in Table 3-2. The letters listed with each maneuver correspond to those given above. The “Atmospheric Condition” column indicates a desire to collect some data under turbulent conditions, but with no control over the weather that aspect became a target of opportunity and a decision factor as the testing proceeded. The off-track conditions were based on the largest feasible offset without approaching the “distant thunder” zone near cutoff.

**Table 3-2. Final Flight-Test Matrix**

Maneuver	Atmospheric Condition	Track	Number of Passes <sup>1</sup>	Flight # <sup>2</sup>
E. Steady 1.17	Good	CL	2	1
F. Steady 1.2	Good	CL	2	1
G. Steady 1.3	Good	CL	2	1
A. SSBj1	Good	CL	5	2
B. Level	Good	CL	5	3
C. Pushover 1	Good	CL	5	4
D. Pushover 2	Good	CL	5	5
E. Steady 1.17	Good	10 deg, 12600 ft	1	6
F. Steady 1.2	Good	20 deg, 18700 ft	1	6
G. Steady 1.3	Good	30 deg, 27000 ft	1	6
A. SSBj1	Good	20 deg, 18000 ft	3	7
B. Level	Good	30 deg, 29000 ft	3	8
C. Pushover 1	Good	40 deg, 28000 ft	3	9
A. SSBj1	Turbulent	CL	4	10
B. Level	Turbulent	CL	4	11
C. Pushover 1	Turbulent	CL	4	12

1. Number of good passes; 2. Nominal, depending on test conditions

A final practice flight was flown on 24 March 2011. This provided a test of the in-flight instrumentation and displays, and reference flight data for the Where’s The Focus? day-of-flight planning procedure described in Section 3.5.

### 3.5 Flight Planning: Where’s the Focus?

The March 24, 2011 practice flight provided a reference trajectory for each of the maneuvers. If atmospheric conditions were identical to those for the practice flight, these would define the initial waypoint necessary to place the focus on the array. The atmosphere is not, of course, constant, so a procedure denoted “Where’s The Focus?” (WTF) was developed by NASA. The procedure consisted of the following steps:

1. The flight path for the practice flight was converted to air mass relative parameters, as required for a PCBoom trj file, using the inertial tracking data and the time-of-flight atmosphere. This provided a reference trajectory for each maneuver.
2. Weather was obtained from a pre-flight GPSsonde launched at the test site.
3. PCBoom was run for the reference trajectory, using the pre-flight atmosphere.
4. The inertial heading of the resultant trajectory and the coordinates of the focus were noted.
5. The heading and initial point of the reference trajectory were changed by the differences between those in Steps 3 and 5 above, with a target approximately 25 percent along the array.
6. PCBoom was run again to confirm the expected focus target.

The initial waypoint and heading were then communicated to the pilot.

On occasion changing atmospheric conditions caused the focus to not impact the expected position. The initial waypoint and heading were then refined by iterations between the passes on each flight. Those iterations were executed by audible identification of boom types, as described in Section 3.6.2.

## 3.6 Flight-Test Execution

### 3.6.1 Preparation

The flight test was executed from 10 May through 20 May 2011. Prior to execution, all equipment was shipped to NASA DFRC and most field team members who were not local to the area arrived 4 May. Setup took place from 4 May through 9 May. All personnel taking part at the test site received training in Desert Tortoise procedures, Hot Weather Safety, and Unexploded Ordnance Safety.

During conduct of the test, communications protocols as specified in the test plan (Plotkin et al., 2011) were followed. In general, operators of each instrumentation system was in radio or voice contact with the Test Director. Communication with the pilot in the aircraft was done by the Flight Director, who relayed any information provided by the Test Director. Recording systems were turned on according to a “Mark” call from the aircraft as it approached its waypoint, and left running for an appropriate length of time after the boom was heard.

### 3.6.2 Aircraft Waypoint Adjustment

As described in Section 3.5, the WTF procedure was used to compute aircraft Initial Point (IP) and heading. Changing atmospheric conditions could cause variations in the focus locations, necessitating adjustment of the IP.

Immediately following the completion of the first supersonic pass, the approximate location of the point of maximum focus within the array was determined audibly by observing the acoustic events associated with the focus flight at various locations along the array. After each aircraft pass, the four station recorder personnel, located along the 10,000-foot linear microphone array, were polled for what they heard, proceeding from up-track to down-track locations along the array. This information was then used to adjust, if required, the aircraft IP for the next pass.

Instrument personnel were briefed prior to the test-flight program as to the protocol to be used following each sonic boom pass that describes what acoustic events they might observe that are associated with the acceleration and pushover/acceleration flights. Figure 3-13, which was used for the briefings, presents a sketch showing the development of the on-track pre-focus, focus, post-focus and carpet boom regions associated with an accelerated flight of an aircraft transitioning from subsonic to supersonic speed. The aircraft is flying from left to right and the view is looking to the north across the west-to-east 10,000-foot microphone array. At the top portion of the figure is shown the development of the bow-shock wave and its intersection with the ground as the aircraft accelerates from  $M = 0.90$  to  $M = 1.3$ . Only the bow-shock is depicted. Also shown are the pressure signatures that would be observed at various positions on the ground A through H along the acceleration path.

In the pre-focus region, ahead of the focus “caustic” line, the nature of the pressure disturbances are low frequency noise signatures that increase in amplitude as the focus is approached. Thus, an observer at location A may not experience any sounds, whereas at locations B and C, they would experience a “whooshing” sound, then a heavier rumbling sound, or thud, respectively. At the focus, location D, which may be on the order of 100 m to 200 m in width, an observer would experience the intense “U-shaped” focus signature as a loud BANG BANG. In the post-focus region that follows the focus, anywhere from three to four shocks may be experienced. For example, at location E, the observer would hear a BANG-BANG-BANG, the intensity being somewhat less than that of the focus. At locations F and G, where the N-wave and U-wave become evident, the observer would hear a less intense BANG-BANG of the N-wave followed by the “pop-pop” of the refracted U signature. The pop-pop is usually, but not always, lower in

amplitude than the N-wave BANG-BANG. The cadence, i.e., the time between the bang-bang-pop-pop, increases between locations F and G. Once one enters the carpet boom region, the U-wave has disappeared due to atmospheric refraction and an observer experiences only the lower level BANG-BANG of the carpet N-wave.

While Figure 3-13 depicts a level acceleration flight, development and acoustic events associated with the focusing resulting from the pushover acceleration flights are equivalent to those discussed above, so the procedure was the same for all focus passes.

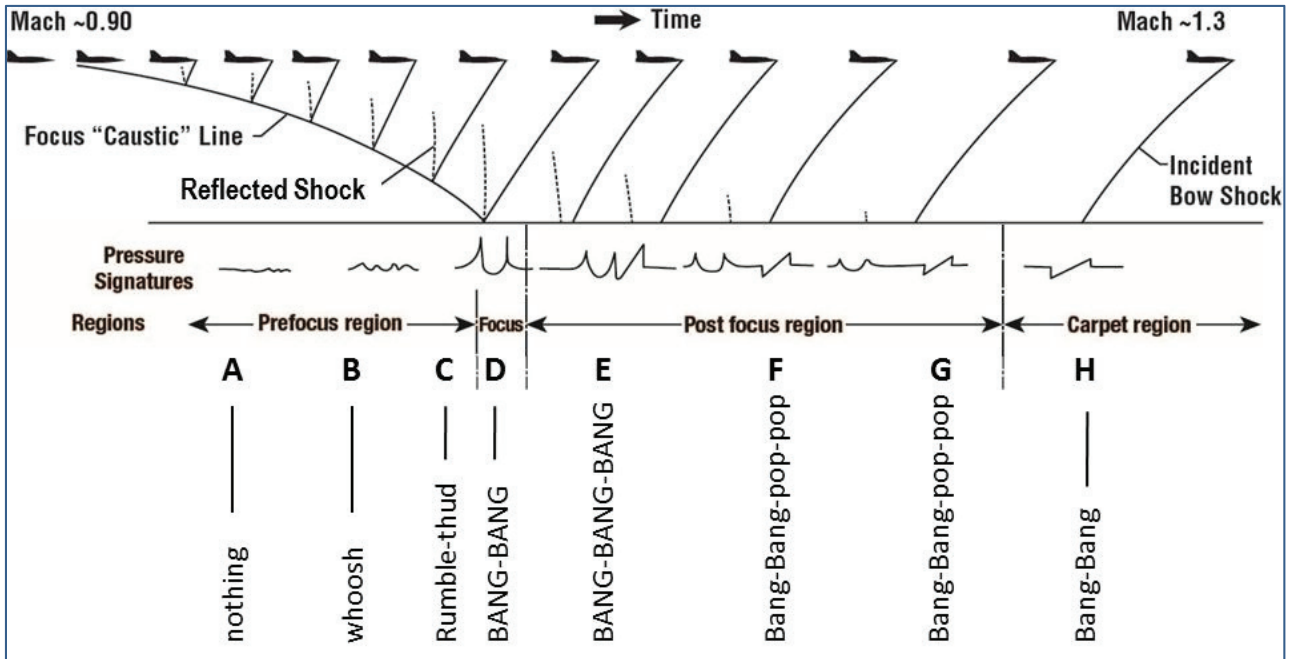


Figure 3-13. Transition focus and audible cues.

### 3.6.3 Flights and Focus Data Acquired

A total of 13 F-18B flights were made, with four to seven passes per flight. Table 3-3 lists the flights and the maneuver flown on each pass. There were 61 focus condition passes. Maximum focus booms were recorded within the array for 37 passes. Of those, 32 captured full events, recording all of the signature types depicted in Figure 3-2.

**Table 3-3. Maneuvers Flown on Each Supersonic Pass**

Date	Flight	Pass 1	Pass 2	Pass 3	Pass 4	Pass 5	Pass 6	Pass 7
10 May	1261	E	E	F	F	G	G	-
10 May	1262	A	A	A	A	A	-	-
10 May	1263	B	B	B	B	B	B	-
11 May	1264	C	C	C	C	C	-	-
11 May	1265	D	D	D	D	D	-	-
12 May	1266	A	A	A	A	A	A	-
12 May	1267	B	B	B	B	B	B	B
12 May	1268	Ao	Ao	Ao	Ao	Ao	-	-
16 May	1269	C	C	C	C	-	-	-
16 May	1270	C	C	C	C	C	-	-
20 May	1272	Ao	Ao	Ao	Ao	Ao	-	-
20 May	1273	Co	Co	Co	Co	Co	-	-
20 May	1274	Fo	Go	Eo	Ao	Ao	-	-

Note: Table 3-1 Describes the Focus Maneuvers A,B,C,and D and Table 3-2 the Steady Flight Conditions E,F, and G

Following the flight test, acoustic data were calibrated and processed. Key elements were the aircraft flight trajectory, the weather data, and the acoustic data. The acoustic data were processed such that the pressure time histories from all microphones on a given pass spanned the same time. This was implicit for microphones on a given recorder and the processing extended the synchronization across all recorders. The time span was selected to begin three seconds before the first event (or projected event) at Site 00 and ten seconds after the last event at Site 80.

Initial analysis included preparing waterfall plots of all the microphone data for each pass. Figures 3-14 and 3-15 show examples of these for two successful executions of Maneuver C. In these two examples, the complete focus, from before the evanescent wave until after the N and post-focus U have separated, was captured. Of the 61 focus passes executed, 32 recordings of this nature were obtained. An additional 5 passes yielded maximum focus on the array, but near one end such that the full event was not captured. The software that generated the waterfall plots also identified the maximum overpressure and its location. That is seen in the fifth line of the text block in the upper left corner of each plot.

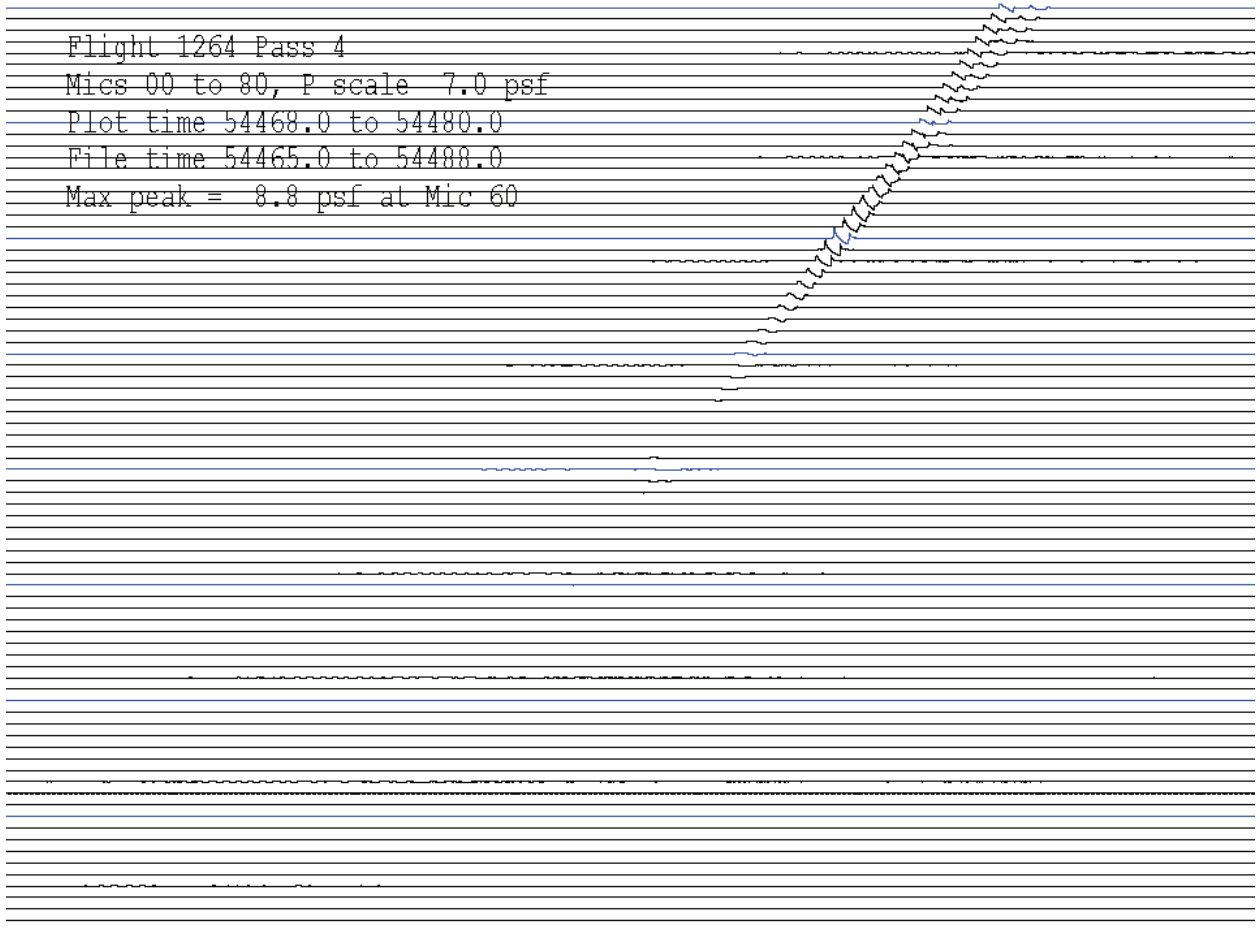


**Figure 3-14. Recordings at all microphones, Flight 1264 Pass 4.**  
Microphone 00 at bottom, 80 at top. Every tenth microphone in blue.



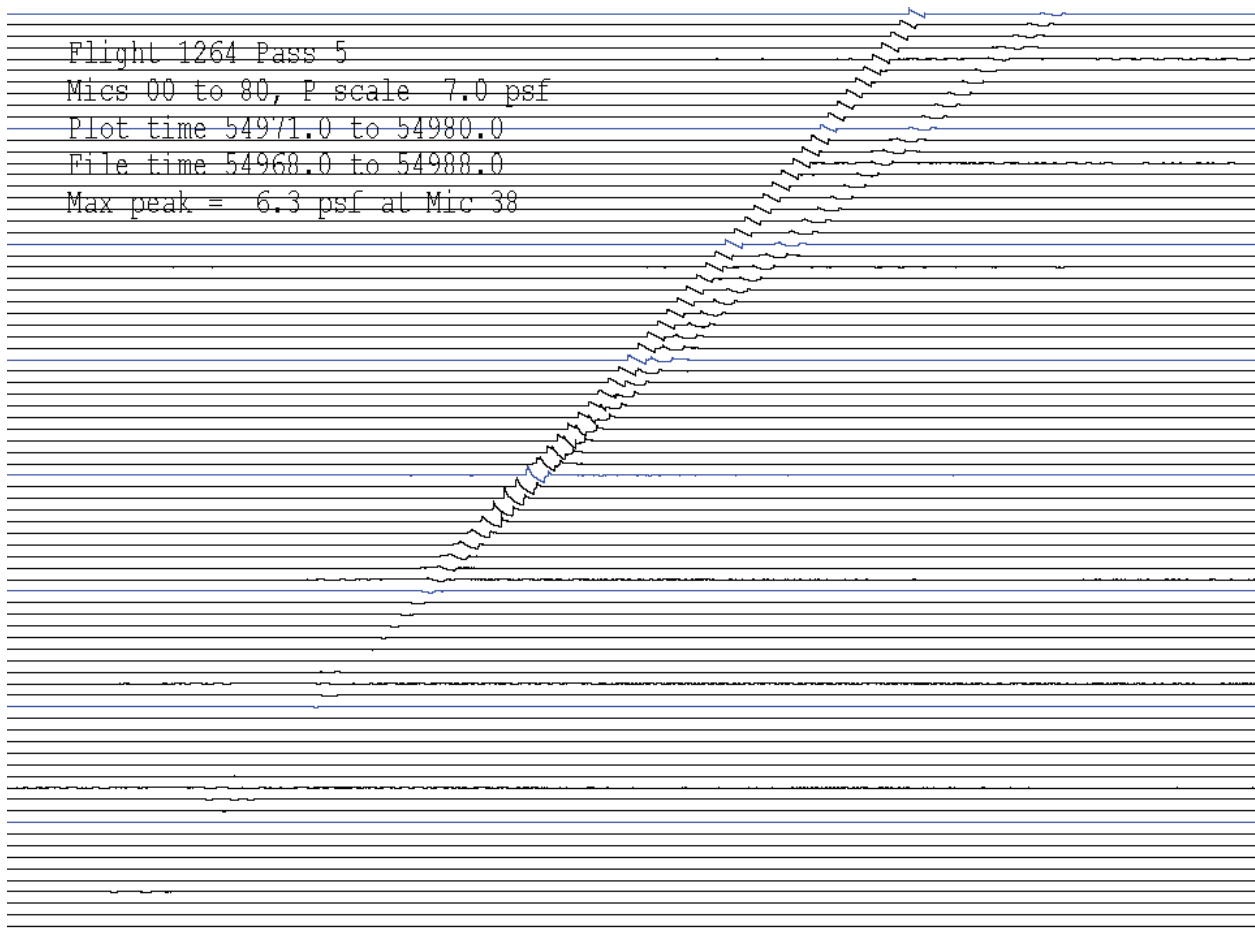


**Figure 3-15. Recordings at all microphones, Flight 1264 Pass 5.**

Microphone 00 at bottom, 80 at top. Every tenth microphone in blue.

Figures 3-16 through 3-25 show all of the maximum focus booms, as identified from the waterfall plots. The order of presentation is Maneuvers A, B, C, D, A offset, C offset, and by flight number where foci from a given maneuver were captured on more than one flight. Part a of each figure shows the boom signatures. The data file identification (flight and pass, sample rate, and channel (microphone position number) - see Hobbs, Page, Plotkin, (2011) for details of the data file naming convention), together with peak overpressures, for the signatures in each file are listed. Part b of each figure shows the atmospheric profile for the time of flight. Three horizontal gray lines in part b indicate the 2785-foot ground elevation at the Cuddeback site, 35,000 feet (the nominal focus generating altitude) and 45,000 feet (the altitude from which pushovers began). The profiles in Figures 3-17 through 3-25 are from GPSsondes launched at Cuddeback, and begin at 2785 feet. The profile in Figure 3-16 is from a GPSsonde launched at EAFB, and begins at 2370 feet.

Table 3-4 summarizes the atmospheric conditions and signature repeatability/cleanliness. Superadiabatic temperature profiles are interpreted to represent turbulent conditions. For the signatures recorded under

favorable conditions (modest wind and stable temperature profile) the signature shapes are remarkably consistent from pass to pass and also between maneuvers. The following specific observations are noted:

- For most flights the signatures show good repeatability.
- The signatures for Flights 1262, 1263, and 1270 (Figures 3-16, 3-18, and 3-22) show atmospheric effects on the expansion portion.
- The signatures for Flights 1263, 1267, 1270, and 1265 (Figures 3-18, 3-19, 3-22, and 3-23) have atmospheric spikes on one of the passes of the set. These appear on both the bow and tail shocks.
- The signatures for Flights 1266, 1264, 1269, 1272, and 1273 (Figures 3-17, 3-20, 3-21, 3-24, and 3-25) are associated with temperature inversions. All the signatures are normal focus types, with most clean of atmospheric effects – no spikes on bow or tail shocks.
- Winds below 10,000 feet were fairly uniform for most flights and had little influence on the signatures. Wind gradients for flights 1262 and 1269 were strong, and probably contributed to the distortion seen in those signatures.
- On the signatures with atmospheric spikes, the spikes appear to be equal for the bow and tail shocks.
- Distortion of the shocks appears to be primarily spiking, rather than rounding or rise time increase.

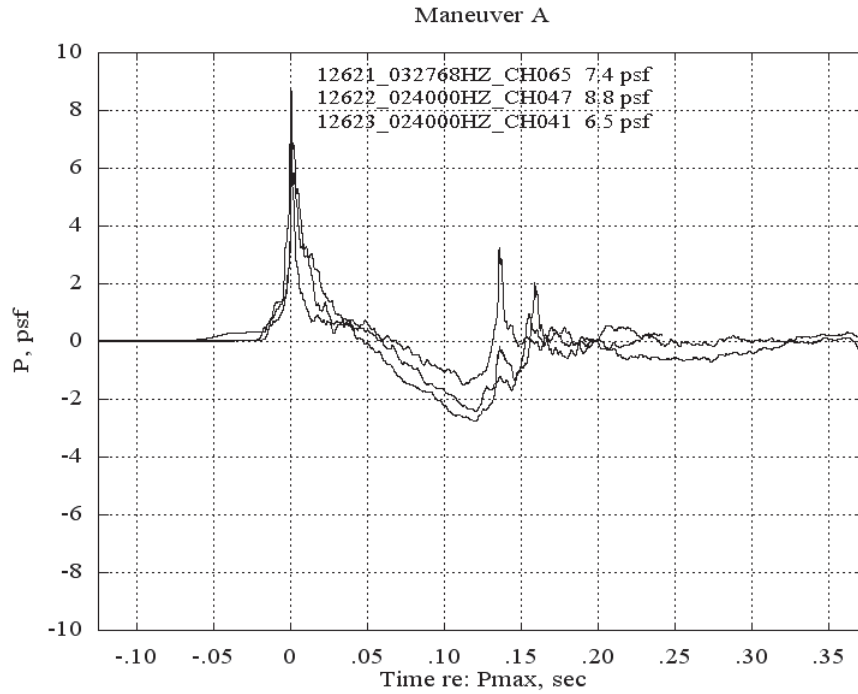
### 3.7 Sample Data and PCBoom Predictions

PCBoom runs were performed for several of the passes, using the GPS tracking data and the corrected GPSsonde atmospheric profiles. The air mass relative flight parameters required by PCBoom were obtained by subtracting wind at altitude from the inertial velocities. Mach number was obtained by dividing true airspeed by the sound speed at altitude. Figure 3-26 shows a typical PCBoom footprint, for Flight 1264 Pass 1. Figure 3-27 shows a closeup of the footprint near the array. Two things should be noted:

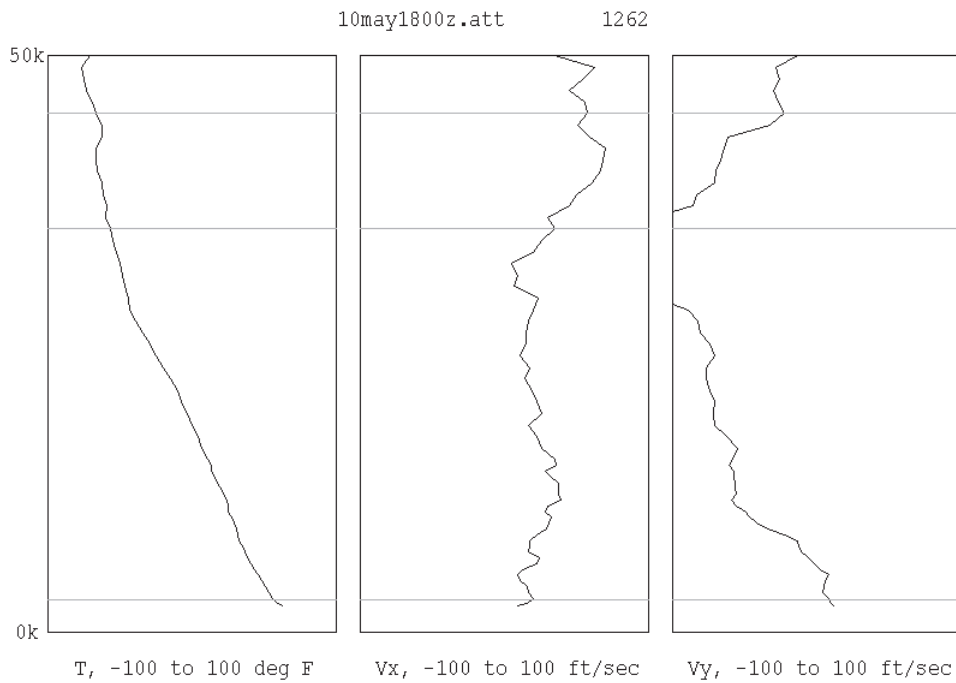
- The psf contours are not particularly smooth. This is a consequence of jitter in the trj and att files, associated with numeric differentiation of the GPS data. This was improved by modeling the trajectory and atmosphere, as will be discussed in Section 5.0.
- The focus is within the array.

Not only is the focus (as determined by the leading edge of the footprint) within the array, but the measured focus position agrees well with PCBoom prediction. Table 3-5 lists the PCBoom-calculated focus locations and the measured focus positions for Flight 1264. Noting that (per discussion in Section 2) the actual focus is expected to occur somewhat downtrack of the calculated geometric caustic, agreement is excellent.

The irregular focus footprint seen in Figure 3-27 is in stark contrast to the very well behaved smooth progression of the focal zone seen in Figures 3-14 and 3-15. Focus location, as determined by the leading edge of the footprint, depends on flight parameters of Mach number, heading, climb angle, and altitude. The signature amplitude depends in general on first derivatives of those quantities, and focus signatures depend on second derivatives.

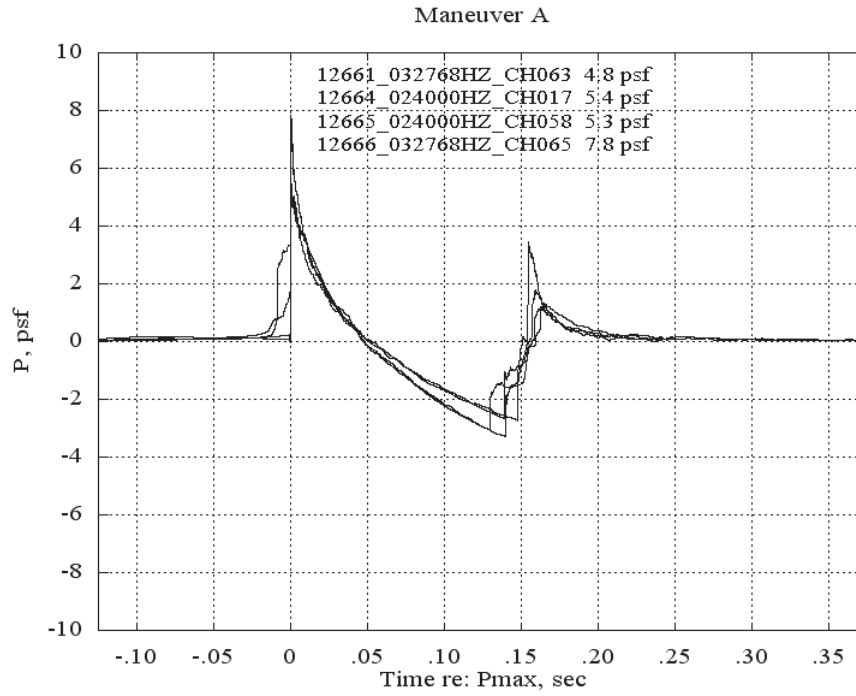


a. Maximum focus booms

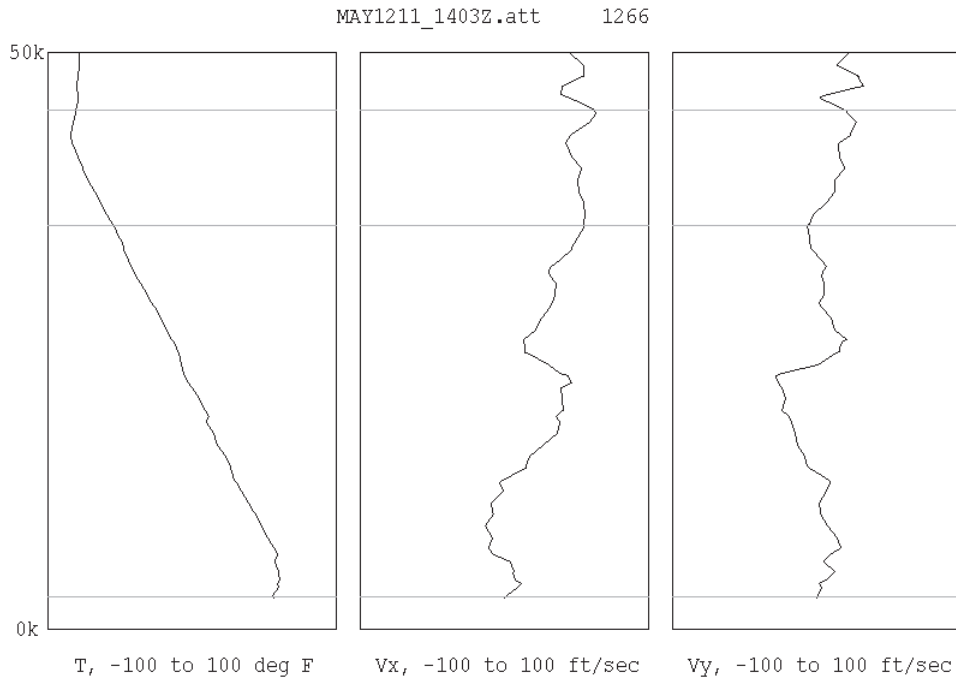


b. Time of flight atmosphere profile

Figure 3-16. Maximum focus booms and atmospheric profile, Maneuver A, Flight 1262.

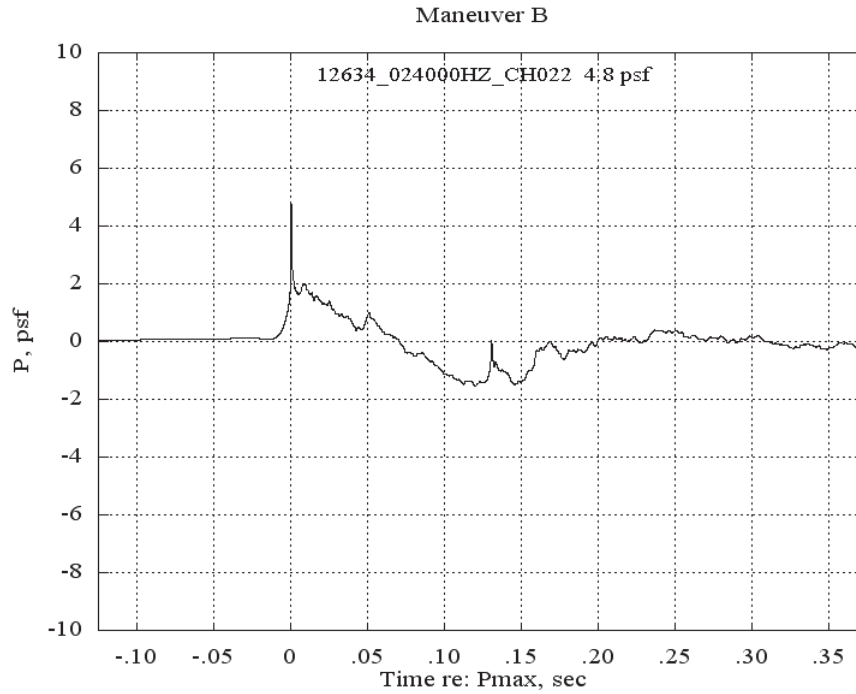


*a. Maximum focus booms*

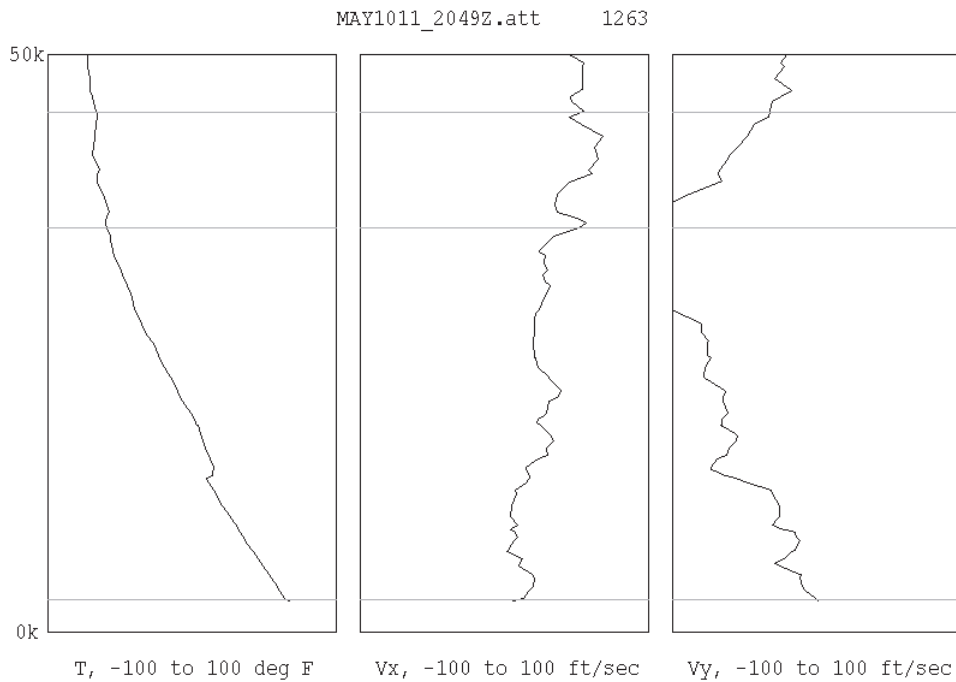


*b. Time of flight atmosphere profile*

**Figure 3-17. Maximum focus booms and atmospheric profile, Maneuver A, Flight 1266.**

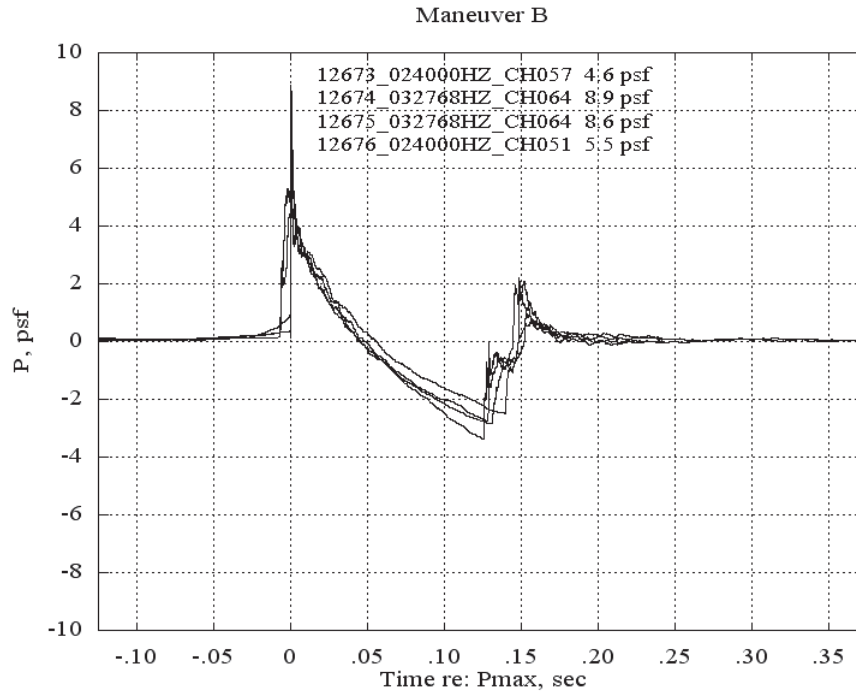


a. Maximum focus booms

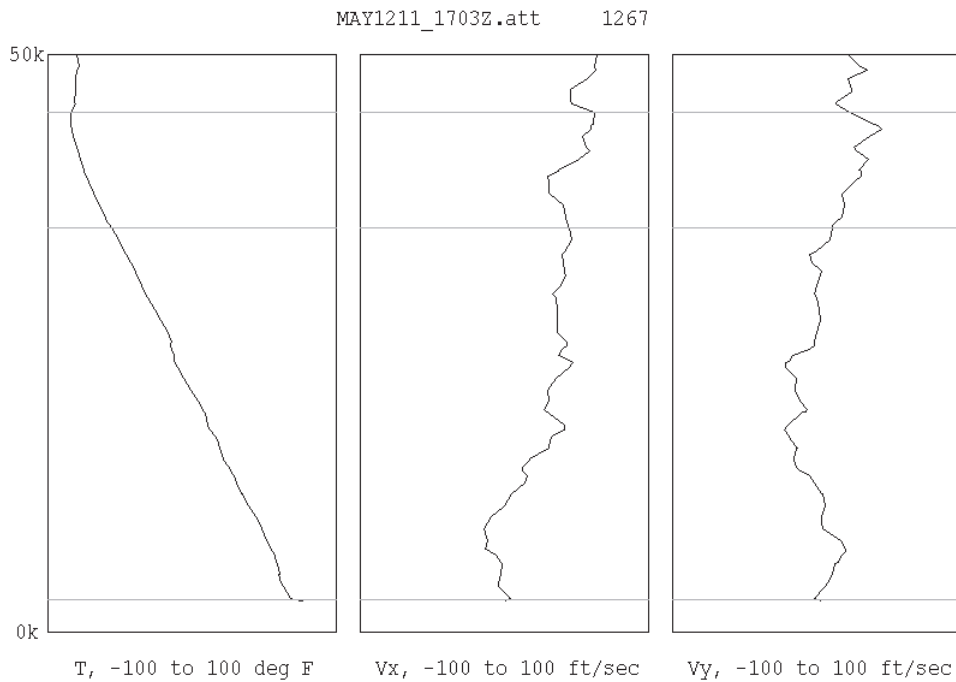


b. Time of flight atmosphere profile

Figure 3-18. Maximum focus booms and atmospheric profile, Maneuver B, Flight 1263.

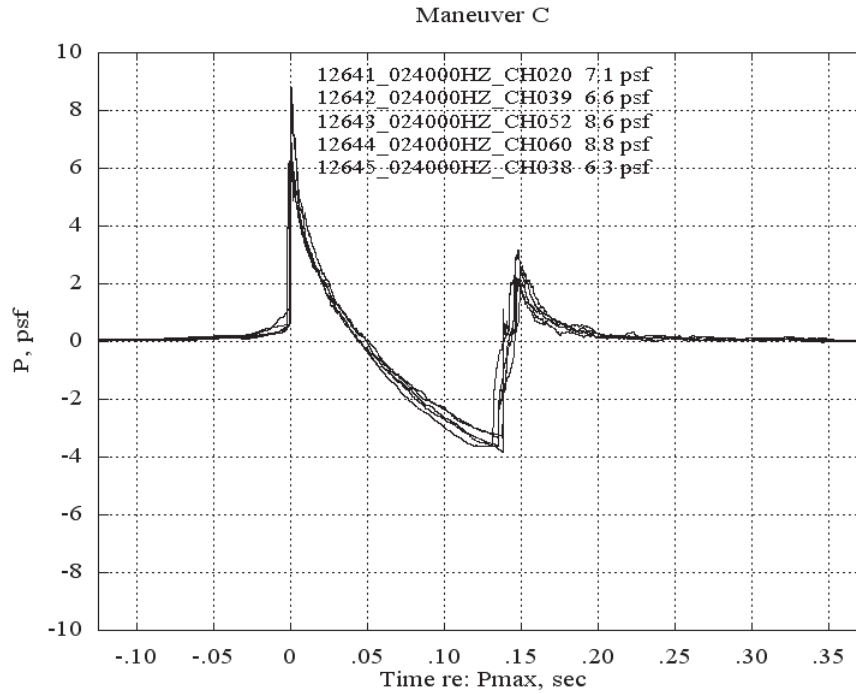


*a. Maximum focus booms*

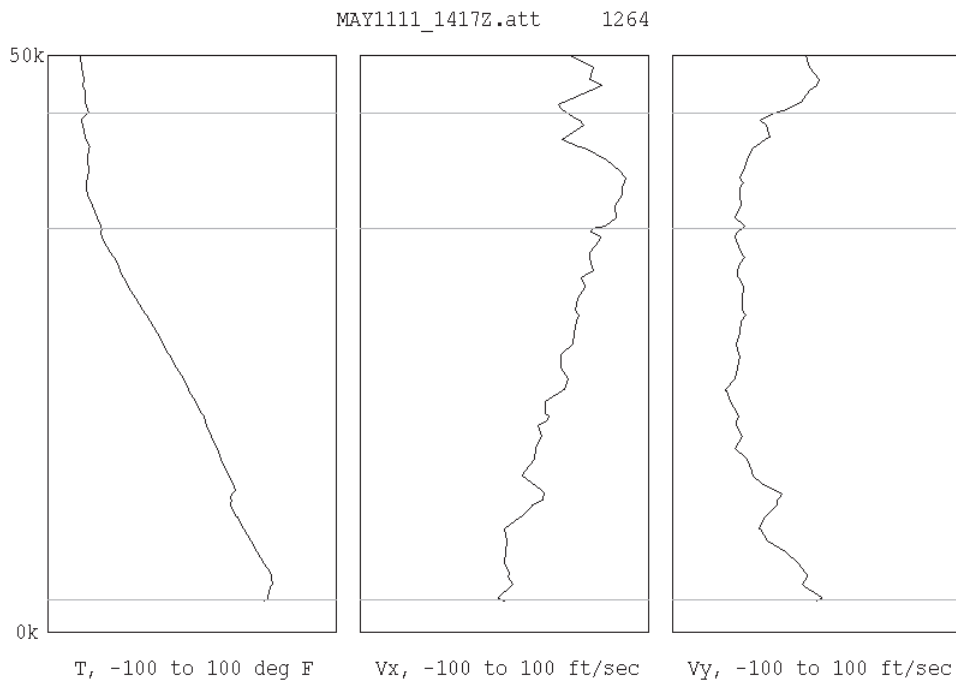


*b. Time of flight atmosphere profile*

**Figure 3-19. Maximum focus booms and atmospheric profile, Maneuver B, Flight 1267.**

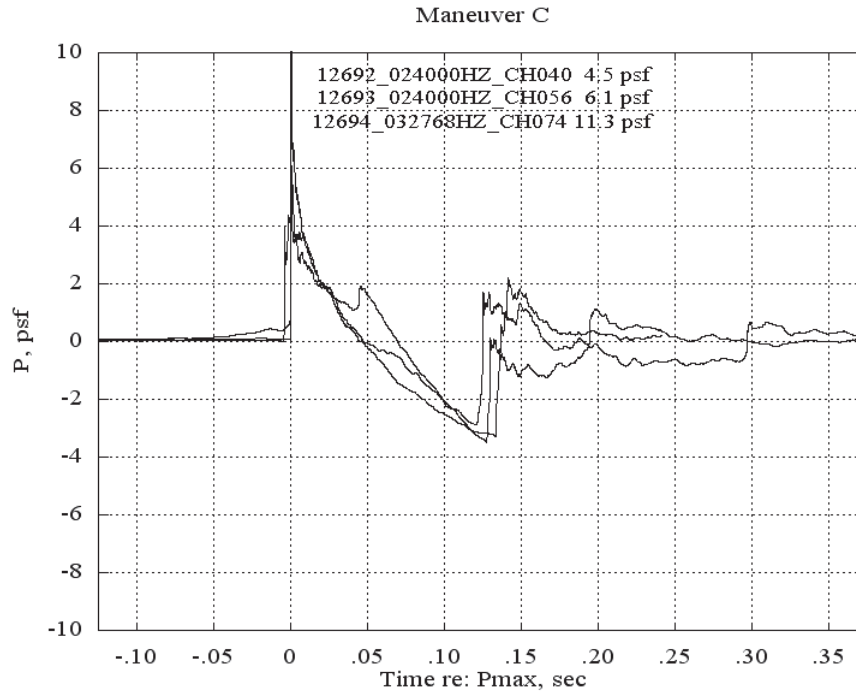


a. Maximum focus booms

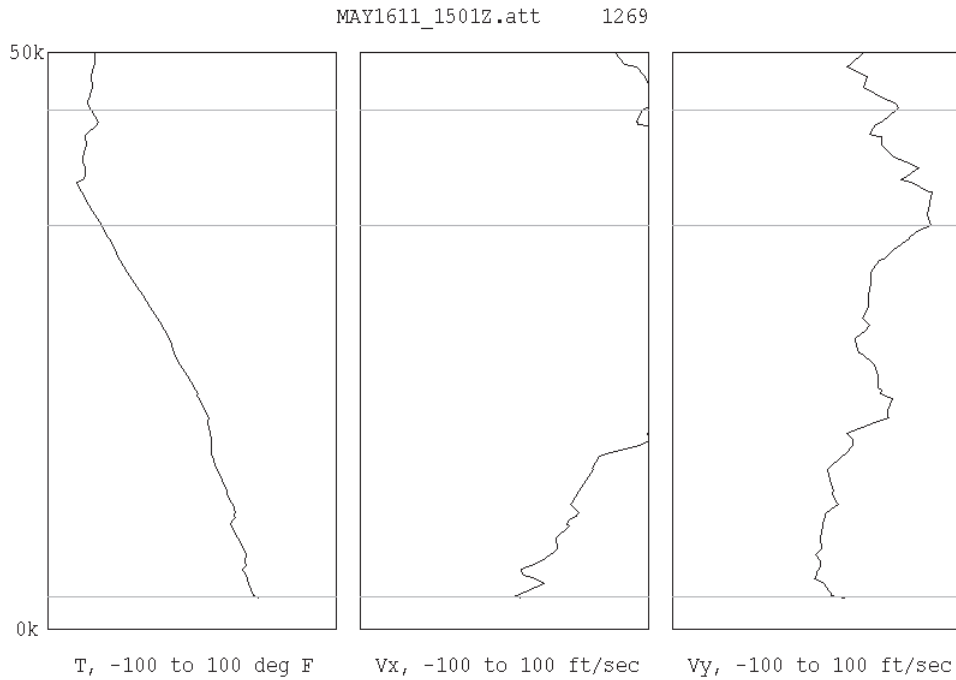


b. Time of flight atmosphere profile

Figure 3-20. Maximum focus booms and atmospheric profile, Maneuver C, Flight 1264.



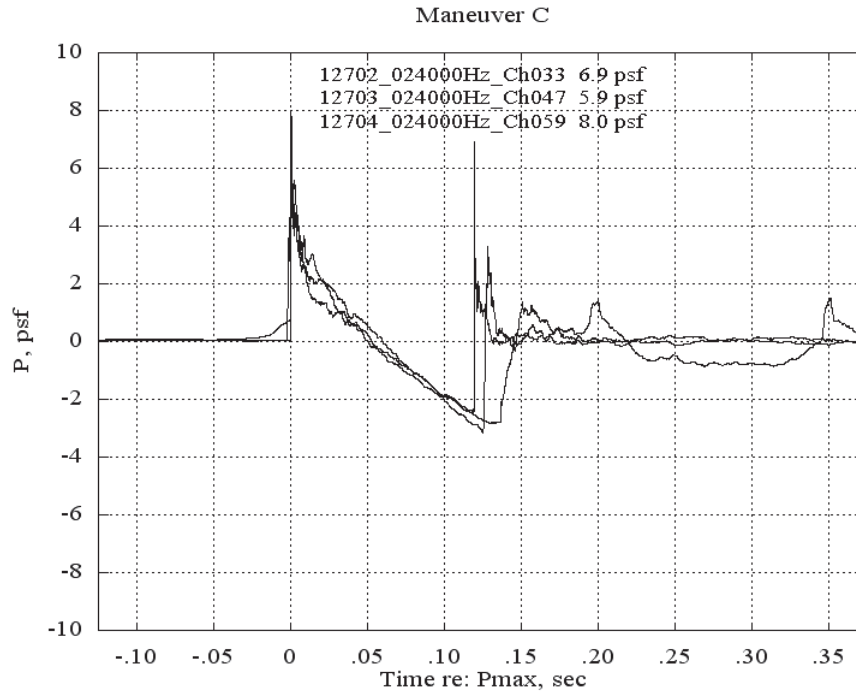
a. Maximum focus booms



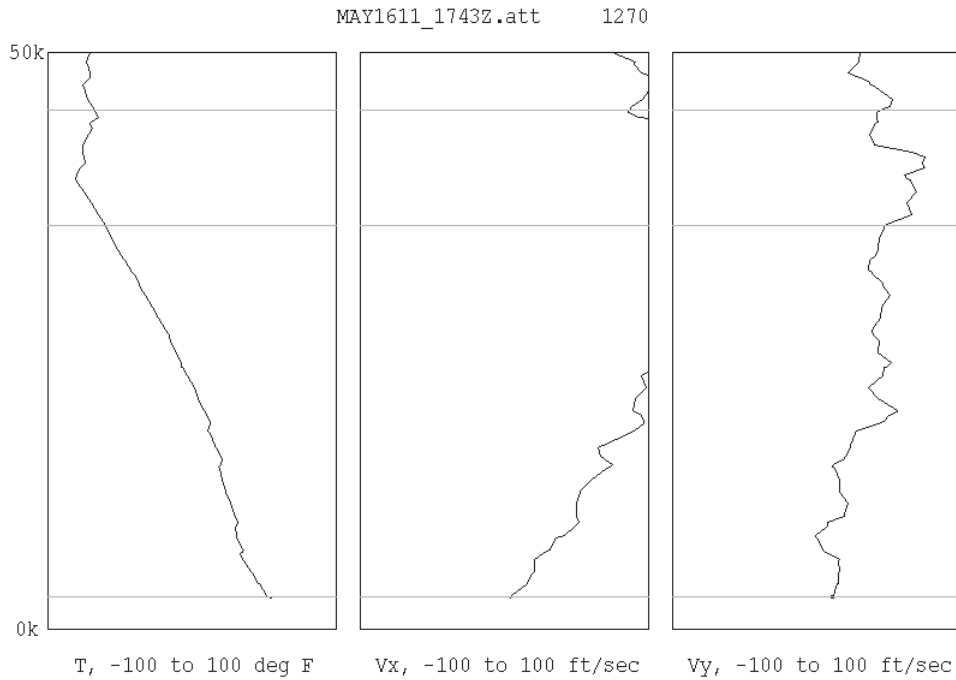
b. Time of flight atmosphere profile

Figure 3-21. Maximum focus booms and atmospheric profile, Maneuver C, Flight 1269.



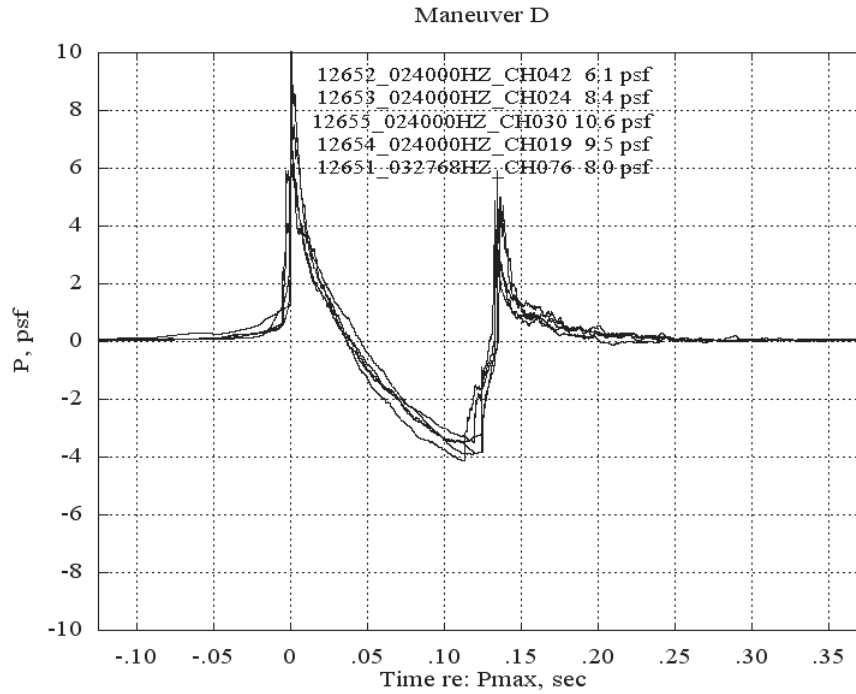


a. Maximum focus booms

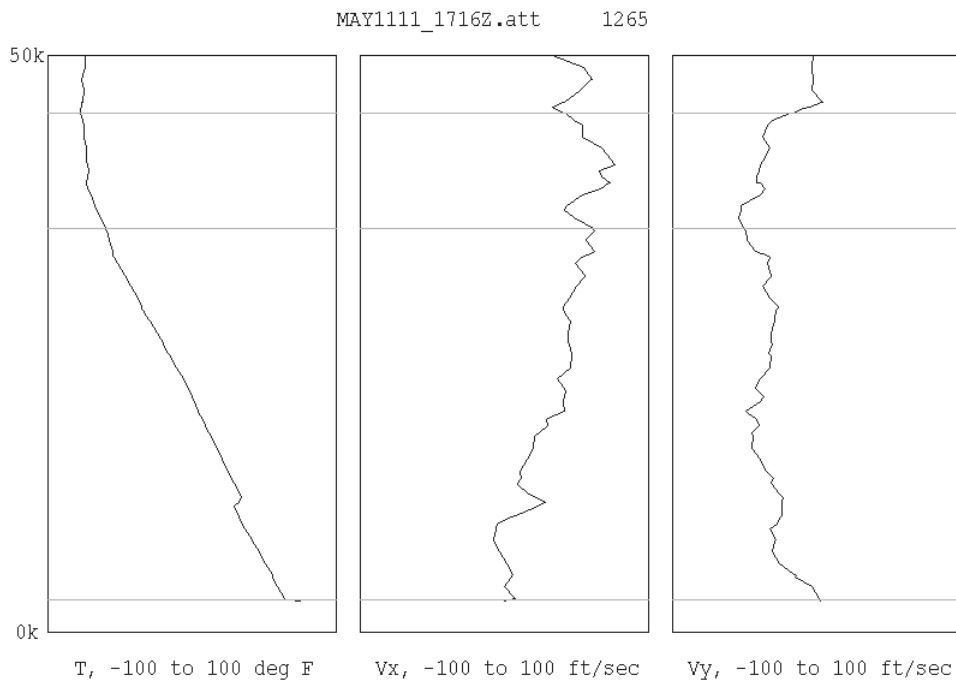


b. Time of flight atmosphere profile

Figure 3-22. Maximum focus booms and atmospheric profile, Maneuver C, Flight 1270.

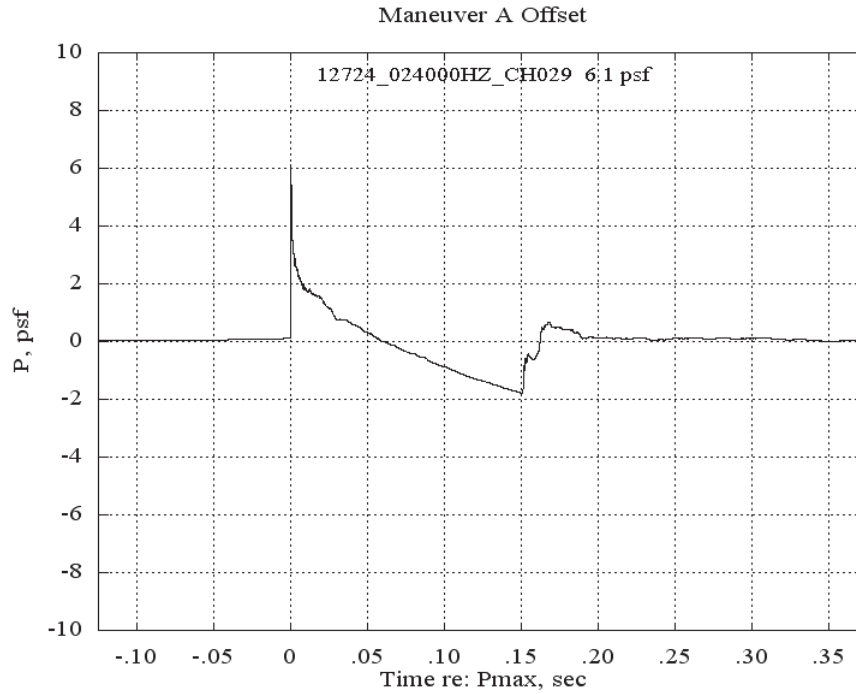


a. Maximum focus booms

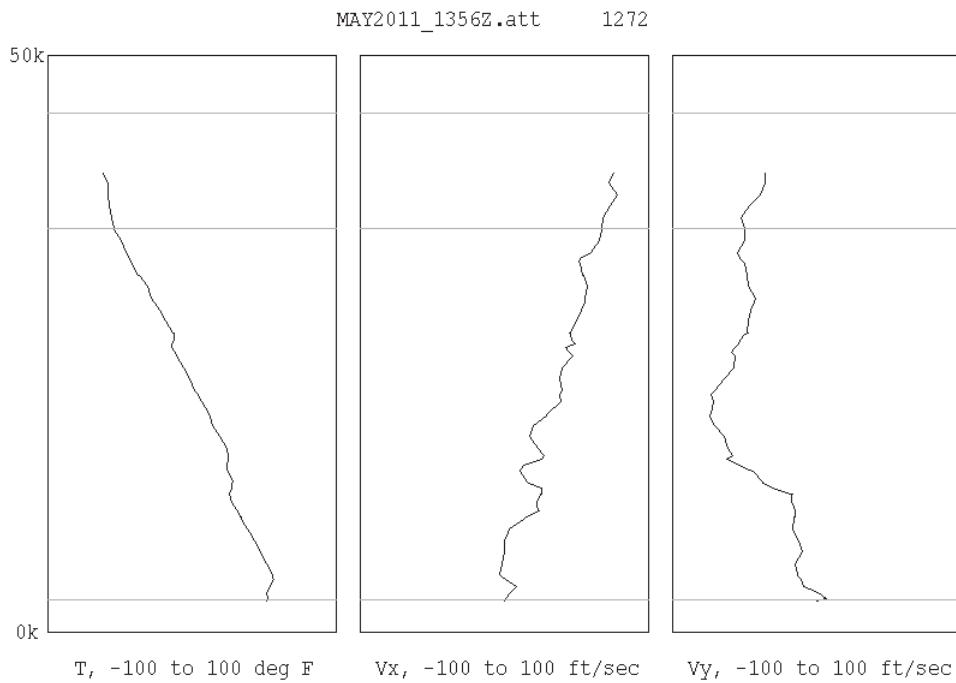


b. Time of flight atmosphere profile

Figure 3-23. Maximum focus booms and atmospheric profile, Maneuver D, Flight 1265.

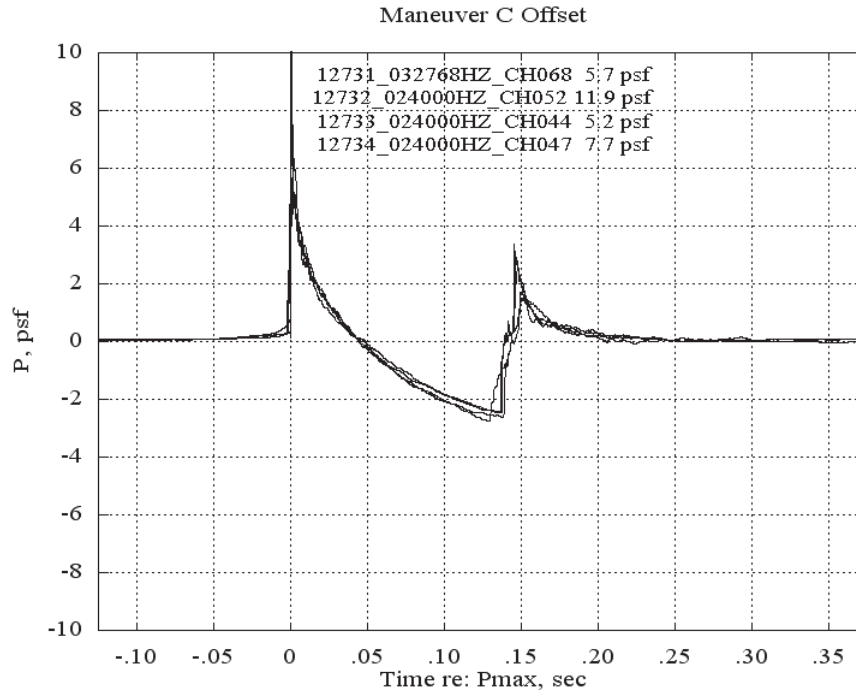


a. Maximum focus booms

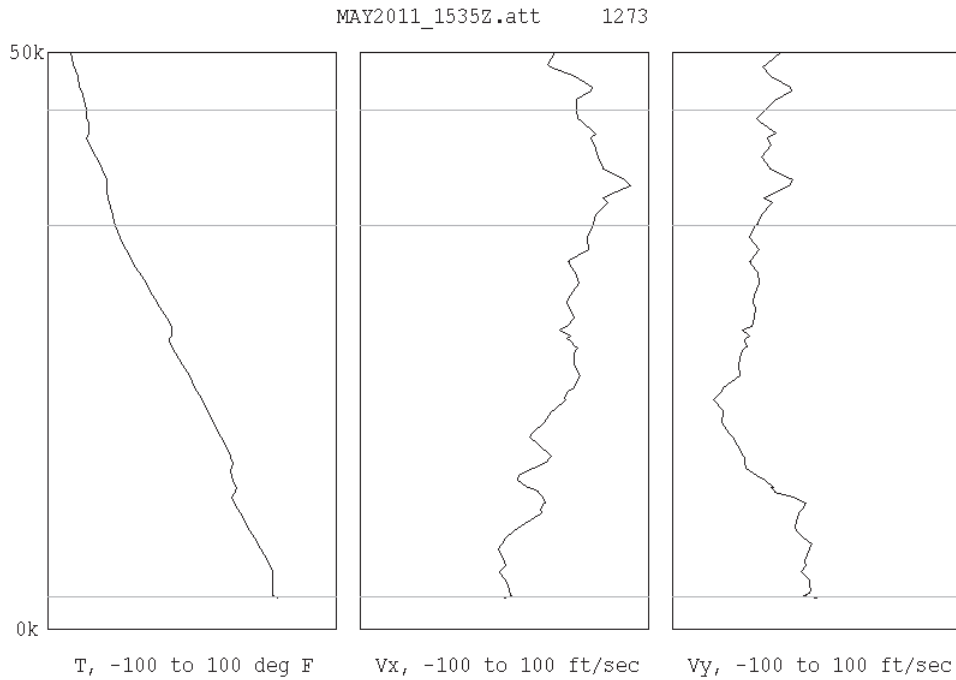


b. Time of flight atmosphere profile

Figure 3-24. Maximum focus booms and atmospheric profile, Maneuver A offset, Flight 1272.



*a. Maximum focus booms*



*b. Time of flight atmosphere profile*

**Figure 3-25. Maximum focus booms and atmospheric profile, Maneuver C offset, Flight 1273.**

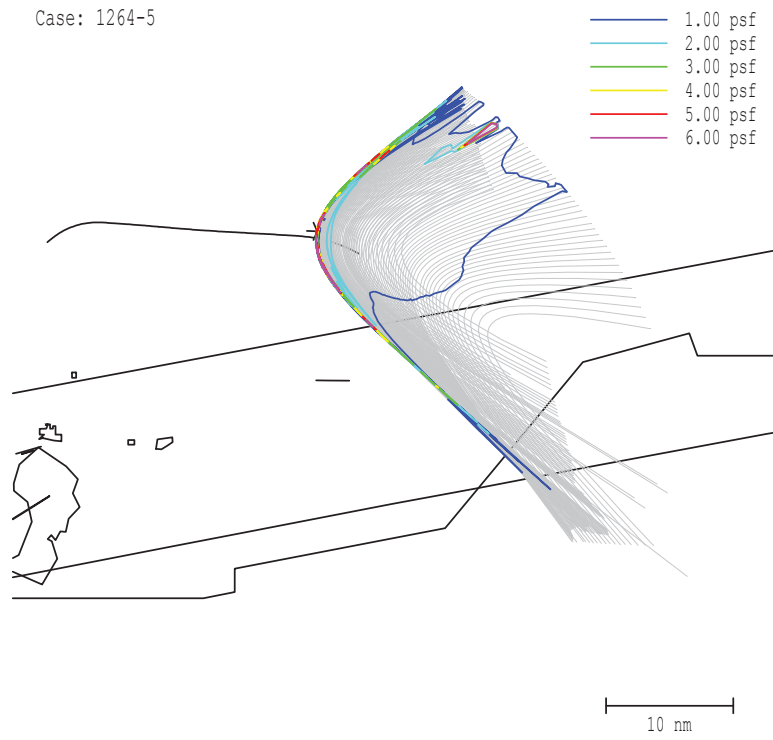


**Figure 3-26. PCBoom footprint, Flight 1264 Pass 5.**

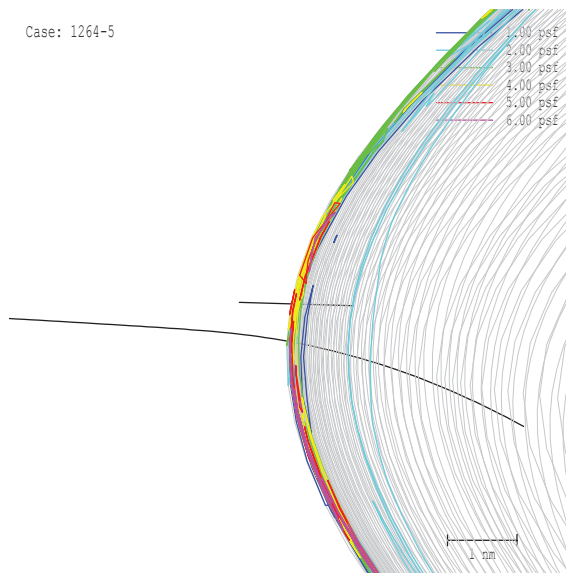


**Figure 3-27. PCBoom footprint, near array, Flight 1264 Pass 5.**

**Table 3-4. Maximum Focus Boom Signatures and Atmospheric Effects**

b	Flight	Temperature Profile	Wind Profile	Atmospheric Effects	Atm Influence on Expansion	Atm Influence on Bow/Tail Shock	Repeatability
A	12621	Superadiabatic	Lrge Grad	Yes	Yes	peaking	No
A	12661	Inversion	Uniform	No	No	No	Yes
B	1263	Adiabatic / superadiabatic	Uniform	Yes	Yes	Spikes on 1 Pass	No
B	12673	Adiabatic	Uniform	Yes	No	Spikes on 1 Pass	Yes
C	12641	Inversion	Uniform	No	No	No	Yes
C	1269	Inversion / Adiabatic	Lrge Grad	No	No	No	Yes
C	1270	Adiabatic / superadiabatic	Uniform	Yes	Yes	Spikes on 1 Pass	No
D	1265	Adiabatic	Uniform	Yes	No	Spikes on 1 Pass	Yes
A offset	1272	Inversion	Uniform	No	No	No	No
C offset	1273	Inversion / Adiabatic	Uniform	No	No	No	Yes

**Table 3-5. PCBoom Prediction of Geometric Caustic Locations and Measured Maximum Focus Locations**

Pass	Predicted Mic (Geometric Caustic)	Measured Mic (Max Focus)
1664-1	18	20
1664-2	34	37
1664-3	50	52
1664-4	56	60
1665-5	37	37

The PCBoom predicted focus locations and overpressures, together with the focus locations and overpressures identified in the waterfall plots, were collected in a text file, “summary.txt,” that is included in the digital data archive. Figure 3-28 is a plot comparing measured and predicted focus locations for the 32 full focus captures. Agreement is excellent, as for the samples shown in Table 3-5. (“Good (\*) only” in the legend refers to the 32 passes, which are flagged by “\*” in the summary file.)

Figure 3-29 shows a comparison between measured and predicted peak focus overpressures for the same 32 passes. Agreement is not particularly good, and is a consequence of artifacts associated with the numeric differentiation of actual flight data and artifacts in the atmospheric profiles. The atmospheric file in particular poses issues. In the GPSsonde profiles, shown as Part b of Figures 3-16 through 3-25, there is very often a fine structure in the wind. That structure occurs over gradient distances, which are not small compared to boom wavelength. This violates the smooth gradient assumption of geometrical acoustics. While the numerical algorithms in PCBoom follow that detail, the wave propagating through it will physically smooth the fine structure. That is why the measured focal zones (Figures 3-14 and 3-15) are smooth while the PCBoom footprint (Figure 3-27) from as-flown data is irregular. For quantitative analysis, smooth-modeled atmospheres and trajectories were used. That is discussed in Section 4.

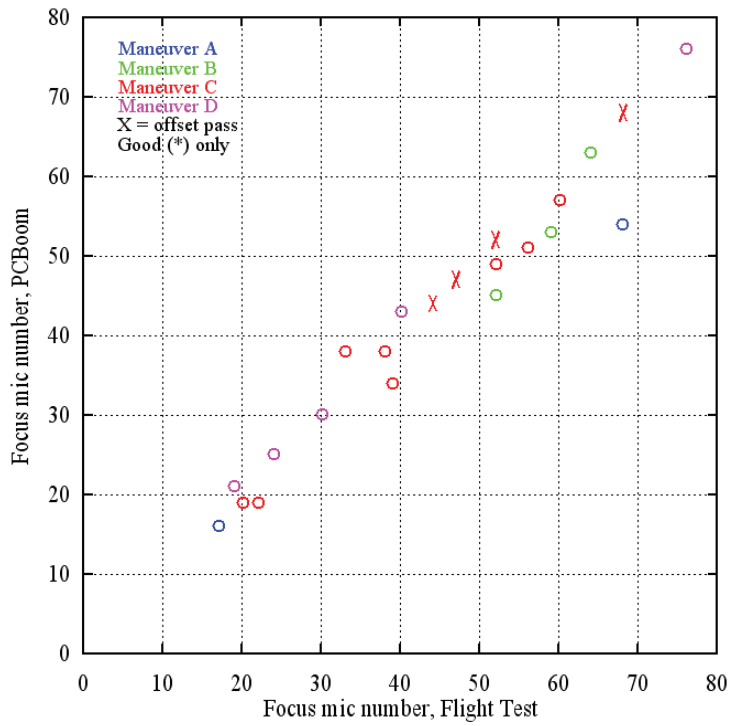


Figure 3-28. Comparison between measured and as-flown PCBoom predicted focus locations.

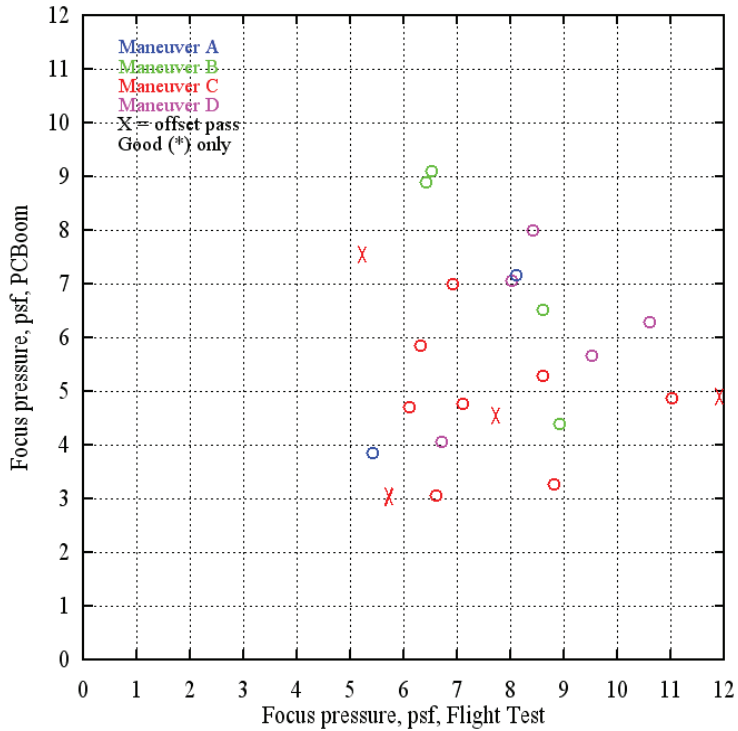


Figure 3-29. Comparison between measured and as-flown PCBoom predicted focus pressures.

### 3.8 SCAMP Collaborative Partners

The SCAMP team, led by Wyle and the National Aeronautics and Space Administration (NASA), includes partners from the Boeing Company, Pennsylvania State University, Gulfstream Aerospace, Eagle Aeronautics, and Central Washington University and collaborators from Northrop Grumman, Cessna, Nagoya University, and the United States Air Force (Figure 3-31). Both NASA Langley and NASA Dryden provided a considerable number of personnel and acoustic measurement equipment for the primary recording array. The Boeing Company provided a significant amount of resources for SCAMP beyond their contract, including several engineers and tens of miles of pre-amp cables for the primary instrumentation array. Boeing also outfitted and operated one of the four recording stations on the ground array. To assist with the setup, operation, and dismantling of NASA's measurement system, three graduate students from the Pennsylvania State University Graduate Program in Acoustics were provided invitational travel orders from NASA Langley Research Center to enable their participation in the field-test measurements. Northrop Grumman engineers were also on site to setup and operate one of the four recording stations comprised of Northrop Grumman equipment. The vertical element of the ground array consisted of a helium blimp provided and operated by Cessna to capture in-coming sonic booms above the ground. An additional two researchers from Nagoya University provided assistance with setup, operating, and dismantling of the ground array. The U.S. Department of the Interior, Bureau of Land Management, Ridgecrest office personnel were also SCAMP partners and granted permission to use the site. Seismic Warning Systems scientists were on site to record sonic booms at and below ground level with their seismic instrumentation. Metro Laser scientists were also on site to experiment with their in-flight schlieren equipment.



Figure 3-30. SCAMP researchers, partners, and collaborators.



## Selected Flight Conditions for Code Comparisons

### 4.1 Selection and Modeling of Flight Conditions

As discussed in Section 3.4, the flight test consisted of four focusing maneuvers:

- A. SSBJ1:  $m\dot{M} = 3.5$ , level at 35,000 feet;
- B. High power, level at 35,000 feet;
- C. Pushover from 45,000 feet,  $m\dot{M} = 3.5$ ,  $g = 0.8$  ( $\dot{\gamma} = -0.25$  degrees/second); and
- D. Pushover from 45,000 feet,  $m\dot{M} = 3.5$ ,  $g = 0.6$  ( $\dot{\gamma} = -0.5$  degrees/second).

These were supported by three steady level conditions, corresponding to pre-flight CFD flow analysis:

- E. Mach 1.17 at 35,000 feet;
- F. Mach 1.20 at 35,000 feet; and
- G. Mach 1.30 at 35,000 feet.

All maneuvers were flown along the centerline. All maneuvers except B included passes offset to the side. Table 4-1 lists them as-flown test matrix. “o” denotes an offset pass.

**Table 4-1. As-Flown Flight-Test Matrix**

Date	Flight	Pass 1	Pass 2	Pass 3	Pass 4	Pass 5	Pass 6	Pass 7
10 May	1261	E	E	F	F	G	G	-
10 May	1262	A	A	A	A	A	-	-
10 May	1263	B	B	B	B	B	B	-
11 May	1264	C	C	C	C	C	-	-
11 May	1265	D	D	D	D	D	-	-
12 May	1266	A	A	A	A	A	A	-
12 May	1267	B	B	B	B	B	B	B
12 May	1268	Ao	Ao	Ao	Ao	Ao	Ao	-
16 May	1269	C	C	C	C	-	-	-
16 May	1270	C	C	C	C	C	-	-
20 May	1272	Ao	Ao	Ao	Ao	Ao	-	-
20 May	1273	Co	Co	Co	Co	Co	-	-
20 May	1274	Fo	Go	Eo	Ao	Ao	-	-

As discussed in Section 3.7, initial data analysis consisted of reviewing waterfall plots of booms recorded on the main array. Examples of these were shown in Figures 3-14 and 3-15 for two successful executions of Maneuver C. Success in matching the focus location was shown in Figure 3-18. There was considerable scatter between predicted and measured peak focus pressures, as shown in Figure 3-19.

Smoothness of the aircraft trajectory and atmosphere is a major consideration for analysis. Figure 4-1 shows an example of airspeed and Mach number calculations for one pass of Maneuver C (-0.25 degree/second pushover – axis scales omitted). The inertial velocity from GPS data ( $V_{gps}$ ) looks reasonably smooth, but some small irregularities can be seen that are amplified in higher derivatives. The air mass velocity ( $V_{airmass}$ ) has some significant features, associated with the aircraft passing through layers of varying wind. Figure 4-2 (repeated from Figure 3-20) shows the upper air profile associated with Flight 1264. The scale ranges are shown for temperature,  $V_x$  (vector wind velocity to the east) and  $V_y$  (vector wind velocity to the north). Horizontal lines are indicated for 2785 feet (ground elevation at the test site), 35,000 feet (nominal altitude for level flights), and 45,000 feet (initial altitude for pushovers). Three features are apparent in the upper air profile:

- There is a tail wind, which is why  $V_{airmass}$  is generally smaller than  $V_{gps}$ ;
- There are large scale wind variations between 35,000 and 45,000 feet, which explains the larger features in  $V_{airmass}$  and Mach; and
- There is considerable small-scale wind structure throughout.

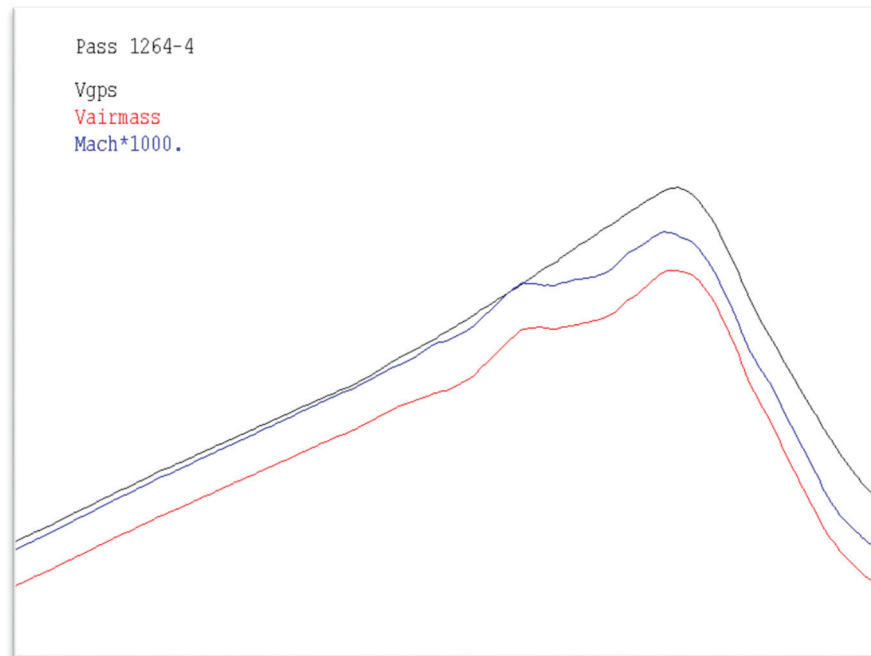


**Figure 4-1. Velocity and Mach number profile for Pass 1264-4 (Pushover).**

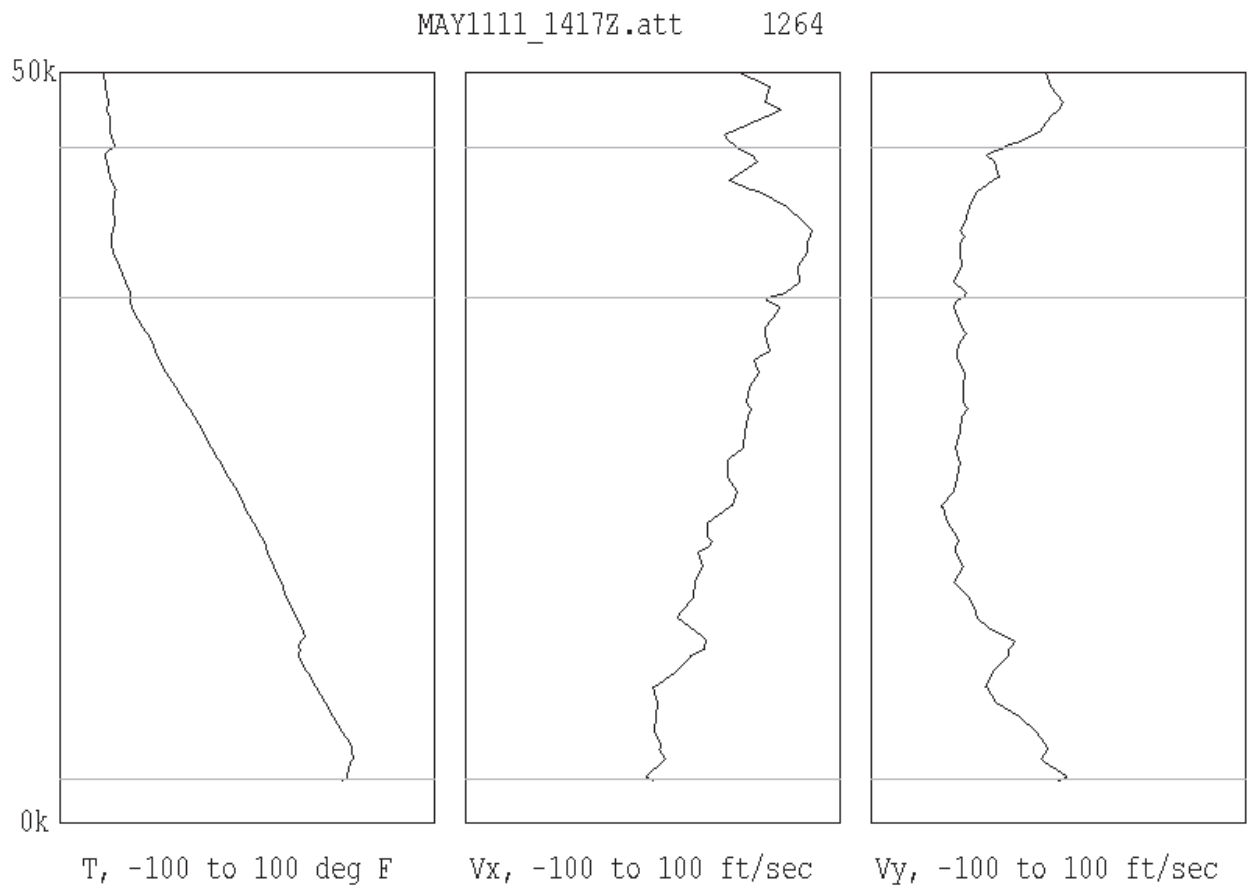


**Figure 4-2. Upper air profile for Flight 1264.**

High winds caused problems with the nominal test matrix, changing the refraction conditions from those intended. The lowest wind conditions for centerline passes of A, B, C, or D occurred on 11 May (Flights 1264, 1265 and 1266) and 12 May (Flight 1267). Profiles for those four passes are similar to that shown in Figure 4-6. Winds aloft on 16 May, when additional passes of Maneuver C were conducted, were well in excess of 100 ft/second (about 60 knots).

It was decided to concentrate code comparisons on Maneuvers A (Flight 1266), C (Flight 1264) and D (Flight 1265). These were all on 11 May, and had the lowest winds aloft of all the test days. B (Flight 1267) was also a candidate, but as a level acceleration did not offer significant curvature differences than A. A, C, and D all have the same acceleration (3.5 mMdots) and differ in pushover rate (0.00, -0.25, and -0.50 degrees/second), thus offering a good sequence through curvatures. Selection of passes to analyze was based on the ground array having captured the full diffraction zone, and the general appearance of the trajectories and footprints. There was more than one good run of each. Table 4-2 lists the selected passes. Shown are the maneuver type, flight/pass, aircraft time  $T_{ac}$  (seconds after midnight), altitude (feet), Mach number, Mach rate (per second), flight path angle  $\gamma$  (degrees) and  $\gamma$  rate (degrees/second). The quantities are shown for the time at which the focus at the ground was generated. These were determined from the PCBoom runs.

**Table 4-2. Selected Passes for Analysis - Primary and Alternates**

Maneuver	Flight	Tac	Altitude	Mach	gamma	gammadot
A	1266-4	53094.5	35740	1.16	-0.1	0.04
	1266-6	53949.5	35080	1.18	0.2	-0.01
C	1264-4	54414.5	43050	1.23	-8.1	-0.28
	1264-2	53200.0	43135	1.23	-8.8	-0.31
	1264-3	53817.0	42550	1.22	-10.3	-0.38
D	1265-2	62976.5	38500	1.30	-19.5	-0.42
	1265-4	63972.0	37200	1.29	-22.1	-0.49
	1265-3	63476.0	38500	1.30	-19.8	-0.43

When computing sonic boom, there is a hierarchy associated with trajectory quantities and their derivatives. To compute the location of a boom, the aircraft position, heading, flight path angle ( $\gamma$ ), and Mach number are needed. To obtain the boom amplitude, the first derivatives of Mach, heading, and  $\gamma$  are needed. To compute signature at a focus, second derivatives of those quantities are needed.

The small-scale structures seen in Figures 4-1 and 4-2 cause computational difficulties with trajectory quantities. The irregularities seen in Figures 3-14 and 3-15, and the poor peak pressure results, seen in Figure 4-19, are attributable to those structures. Ray tracing is also affected by the atmospheric structures. The higher detail is not directly relevant to the boom. Ray tracing is valid when gradient scales are large compared to wavelength, so the trajectory and atmosphere must be smoothed or modeled in a smooth way. Several smoothing methods were tried and not found to be satisfactory. The analysis was therefore modeled in the following way:

1. Conditions in Table 4-2 were taken as the reference point for a trajectory.
2. Those conditions were extrapolated back to an earlier time.
3. PCBoom’s “TADVANCE” mode, which models the trajectory as a sequence of quadratic segments, was used to model the trajectory.
4. The atmosphere was modeled by a few straight lines.

The trajectory modeled in Steps 1 through 3 was iterated such that the focus generated at the conditions in Table 4-2 intersected the array at the point where the maximum focus boom was measured.

Figure 4-3 shows the modeled atmosphere corresponding to that shown in Figure 4-2. The fine structure eliminated outside of the ray tracing approximation, and leads to very irregular ray and caustic calculations. When diffraction is considered, details associated with the fine structure would represent turbulent scattering about a nominal mean.

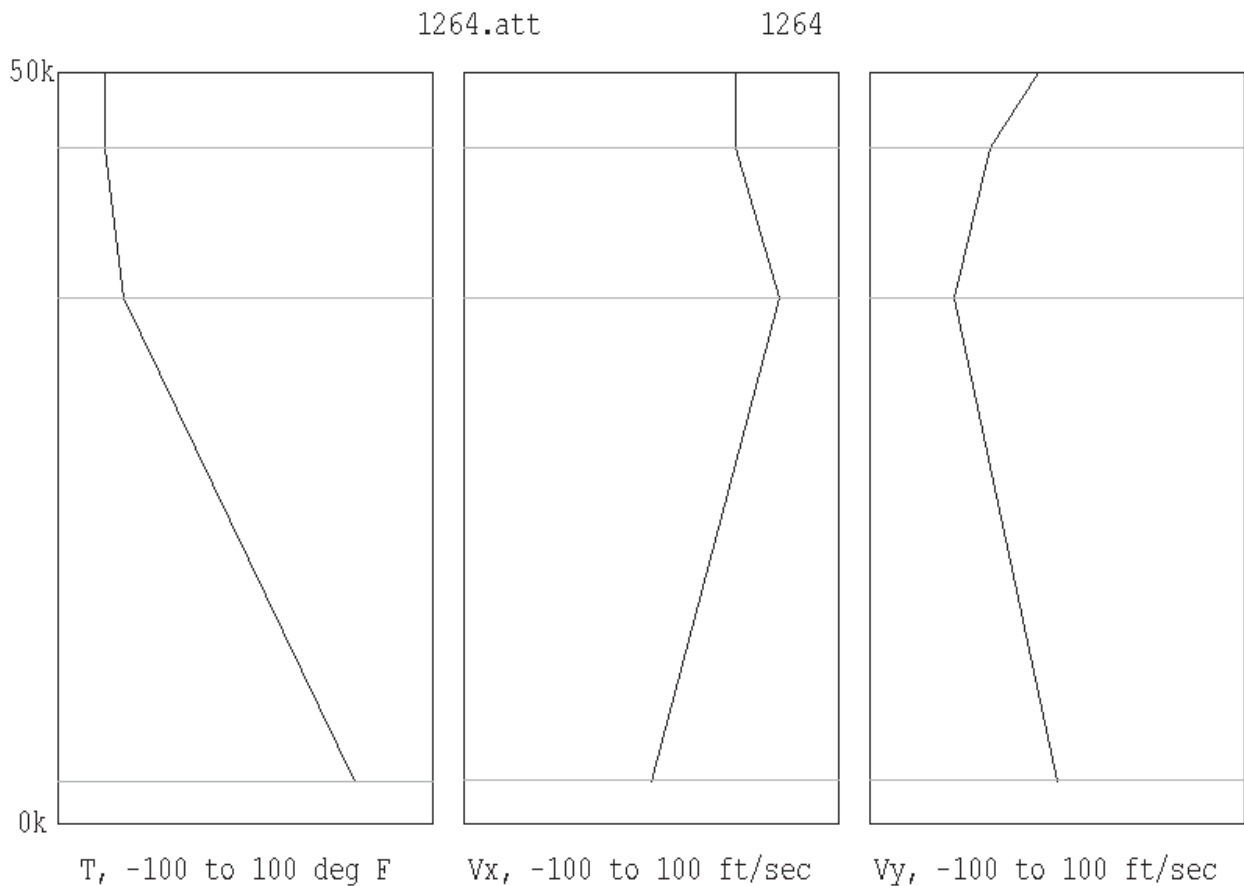


**Figure 4-3. Modeled upper air profile for Flight 1264.**

The effects handled by modeling the trajectory and atmosphere can be seen by examining the caustic and its properties as it approaches and intersects the ground. Figures 4-4 and 4-5 are plots of the caustic for pass 1264-4, before and after modeling. Features of each plot are:

- The trajectory (seen in the upper left).
- The caustic (seen as a diagonal line across the figure).
- Points on the caustic corresponding to specific times at the aircraft (red circles).
- Points where the rays intercept the ground (green circles).
- A black circle indicating a point selected for analysis (This is at the bottommost red point in each figure).
- Text giving pertinent data for the selected point. The fifth line (Zfoc, Radius) is of interest. It is the altitude at which the focus point occurs, together with the radius of curvature computed by PCBoom for that point. The curvature shown on that line is the relative curvature between the ray and caustic, as required by the focal zone models.

Note that the caustic points (red circles) are unevenly spaced in Figure 4-4 and the caustic even doubles back on itself in places, while the caustic and its points are smooth and evenly spaced in Figure 4-5. Table 4-3 summarizes the altitude and radii of curvature along the caustic, corresponding to the final seconds of flight generation time. A “-” for radius means the focus curvature calculation in PCBoom failed. The altitudes for the modeled case progress smoothly, and radius of curvature is stable and varies smoothly. Values for the actual data are very irregular. The caustic itself is reasonably smooth even for actual data, and it is possible to compute the radius of curvature of the caustic by fitting a circle to the red points. The quantity needed for the focal zone models is, however, the relative curvature between the ray and caustic. The fine scale variations seen in Figure 4-2 cause substantial variation in PCBoom’s ray curvature calculation, and are responsible for a significant part of the variability seen in the “actual” columns of Table 4-3.

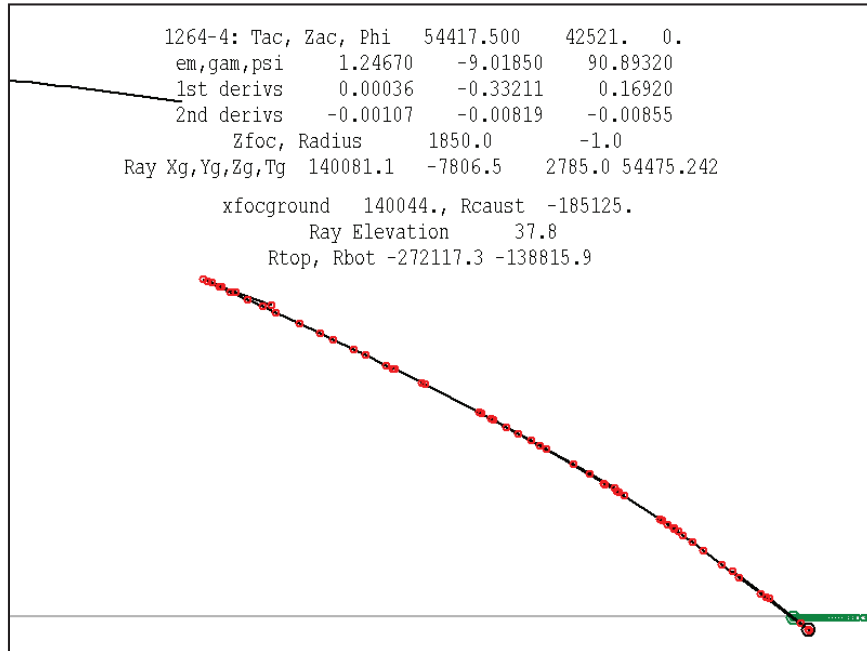


Figure 4-4. Caustic line under track, using actual trajectory and atmosphere data.

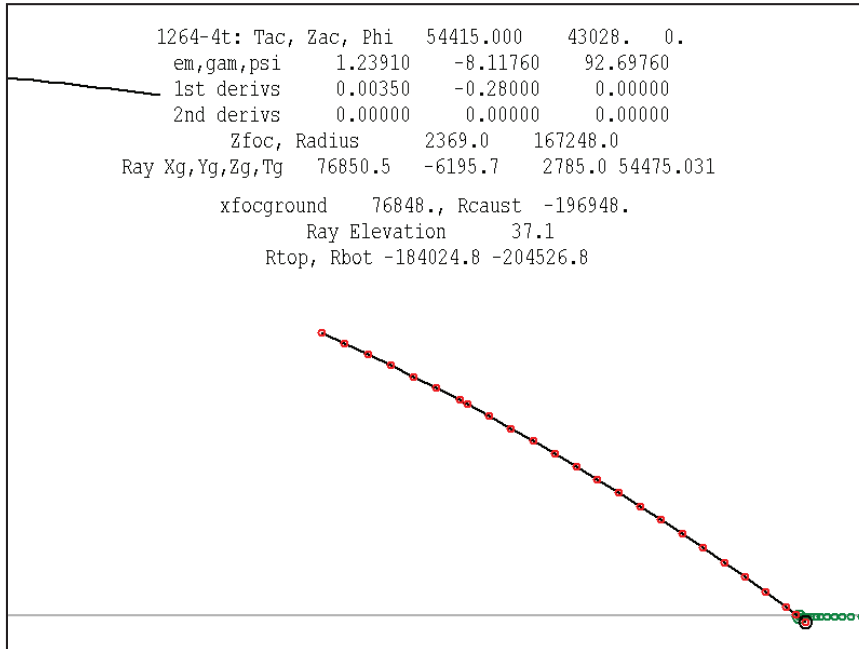


Figure 4-5. Caustic line under track, using modeled trajectory and atmosphere data.

Table 4-3. Summary of Radii of Curvature along Caustic - Actual and Modeled Data

Aircraft Time	Actual Trajectory and Atmosphere		Modeled Trajectory and Atmosphere	
	Zfoc	Radius	Zfoc	Radius
54409.5	9998	-	13381	161044
54410.0	10253	32067	12354	161514
54410.5	10356	118360	11319	161802
54411.0	9620	133422	10258	162921
54411.5	9134	82933	9180	163670
54412.0	8603	165550	8085	164302
54412.5	7946	264533	6973	164673
54413.0	6884	475320	5856	164817
54413.5	5912	585427	4710	165990
54414.0	4383	116016	3548	166699
54414.5	2342	-	2961	166970
54415.0	4662	-	2369	167248

## 4.2 F-18 CFD Modeling for As-flown Flight Conditions

Boeing was tasked to provide PC-Boom input delta ( $\Delta P/P_0$  cylinder data) in order to generate focused boom predictions for flight-test planning purposes and for validation and improvement of sonic boom focusing codes. This involved first generating detailed aircraft geometry grids representing the test aircraft (NASA's F-18C with only the center auxiliary fuel tank attached) at certain supersonic flight conditions. Boeing's BCFD code was then exercised on with these geometry data at several steady-state conditions (see Table 4-4). These conditions were selected to cover the range of conditions flown during the flight test. Simulated

inlet and nozzle flow conditions were determined from an F/A-18C engine cycle deck. CFD results were generated for three “as-flown” conditions and the corresponding  $\Delta P/P_o$  cylinder data at three body lengths from the vehicle has been provided for analysis.

**Table 4-4. Steady-State Flight Conditions for CFD Runs**

Condition	CFD Results
Condition C: 1264	4, M 1.227, 42,000', $\alpha = 2.29^\circ$
Condition D: 1265	2, M 1.302, 38,000', $\alpha = 1.27^\circ$
Condition A: 1265	2, M 1.159, 34,000', $\alpha = 2.05^\circ$

To obtain high resolution of the expected compression and expansion waves predicted from the CFD, a “grid-adaption” process was utilized whereby flow gradients from an initial solution are used to cluster grid points near high regions of flow gradients as shockwaves. The current data is then interpolated to this enhanced grid as a starting solution and the flow solver is run to obtain a converged solution on this grid and the process is repeated. Three of these grid-adaption iterations were used to obtain the final flow data that was interpolated to a solution cylinder (Figure 4-6) at a radius of three body lengths as input to the boom prediction program PC-Boom. Grid adaption was not made on the upper region of the vehicle since this would add computational time and is not of significance for boom propagation to the ground.

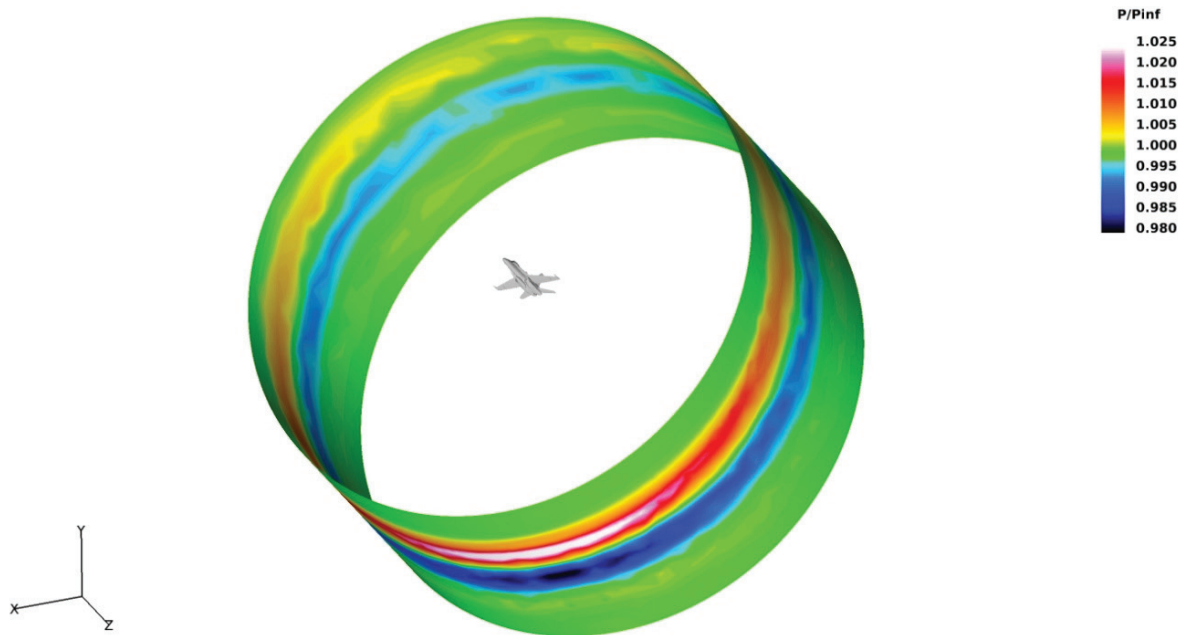


**Figure 4-6. CFD predicted  $\Delta P/P_o$  cylinder data at Three Body Lengths Case C,  $M = 1.23$ .**



The computational grid sizes ranged from 17 million for the initial solution to 40 million in the final adapted solution. Since the computed conditions had zero sideslip angle, the CFD analyses assumed a symmetric flow condition with the centerplane of the vehicle using a reflection boundary condition type. Because of the inviscid nature of pressure wave propagation, the flow was computed using the Euler equation solver of the BCFD program and does not include viscous contributions (like boundary layers) in the analyses.

A comparison of the computed pressure contours between the initial (no-adaptation) solution and the final (two adaptation iterations) solution for Case C is shown below in Figure 4-7.

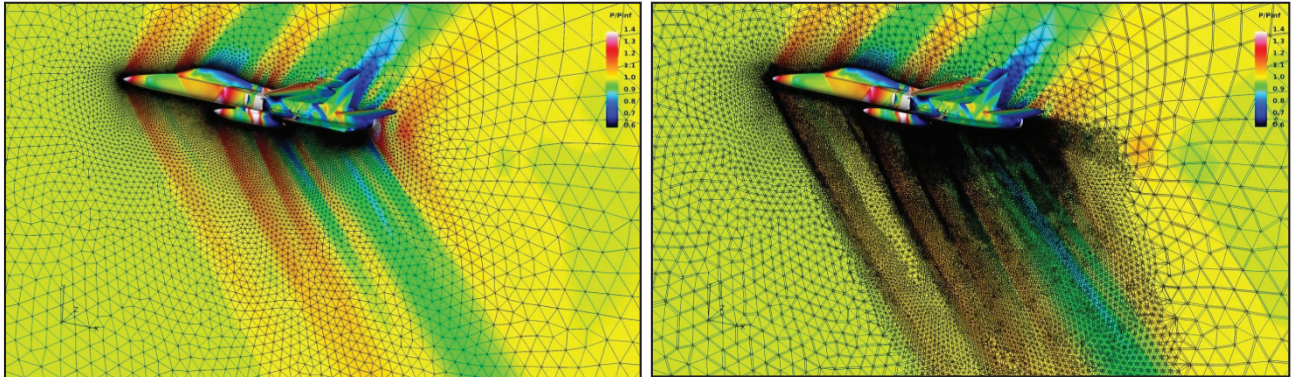


**Figure 4-7. Computed pressure contours on the vehicle symmetry plane and surface from the initial solution (left) and the final grid-adapted solution (right) Case C,  $M = 1.23$ .**

The adaption used in these analyses simply divides the current cell in half if it meets a gradient sensitivity criterion. Boeing is currently developing a non-isotropic adaption that will allow a collapse of the grid cells to better resolve a directional gradient (across a shock for example) instead of the isotropic addition, which is presently done. An enlarged view of Figure 4-7 is shown below in Figure 4-8 and illustrates the manner in which the grid adaption adds cells to both surface and off-body grid regions.

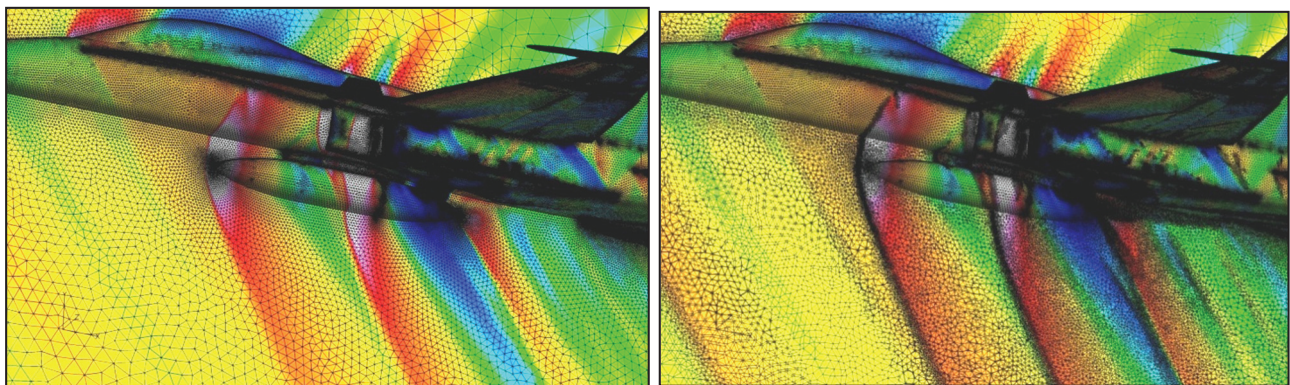


**Figure 4-8. Computed pressure contours on the vehicle symmetry plane and surface from the initial solution (left) and the final grid-adapted solution (right) Case C,  $M = 1.23$ .**

*Intentionally left blank*

## Gill-Seebass Method (PCBoom)

### 5.1 Methodology

The Gill-Seebass focused shock solution, Guiraud's similitude, and implementation in PCBoom were discussed in detail in Sections 2.3 and 2.4. Application of this method is implicit in running PCBoom.

### 5.2 Model Input Data

The input data for the Gill-Seebass focus solution is the input data to PCBoom, as discussed in depth in Section 2. Properties fundamental to sonic boom ray tracing, worth noting with regard to PCBoom, are:

- Sonic boom location requires only the flight Mach number, aircraft heading angle, aircraft flight path (climb/dive) angle, and the atmospheric profile.
- Prediction of the amplitude of the boom also requires the aircraft configuration plus first derivatives of Mach, heading, and flight path angle. This also provides focus location.
- Prediction of focus amplitude also requires the second derivatives of Mach, heading, and flight path angle.

In addition, it must be remembered that ray tracing applies in the short wave limit, with wavelength small compared to atmospheric gradient scales. The simplifying modeling discussed in Section 4.1 is necessary for the current analysis, and has formed the input data for PCBoom and Gill-Seebass focal zone modeling.

### 5.3 Comparisons with Measurement Data

Comparisons have been made between measured and predicted booms for the three flight conditions identified in Section 4. The particular comparisons made were:

- Peak pressure and signature shape at maximum focus. To coordinate the analysis, modeled PCBoom trajectories were synchronized to place the maximum focus at the measured maximum position.
- The location of the end of the diffraction zone (threshold of overlap of N and u) relative to the focus peak. The peak pressure and general shapes were also of interest.

For reference, the peak pressure for steady flight tangent to the focus condition has also been computed.

Comparisons are shown in the following sequence of figures. For each flight, four figures are shown:

- Measured maximum focus signature, generally surrounded by ones just before and just after.
- PCBoom maximum focus prediction.
- A sequence of measured signatures encompassing the end of the diffraction zone.
- PCBoom predicted signature that shows end-of-diffraction-zone threshold overlap.

In each case the peak pressure and the microphone position is noted. The equivalent carpet boom is noted on the predicted end-of-diffraction plot.

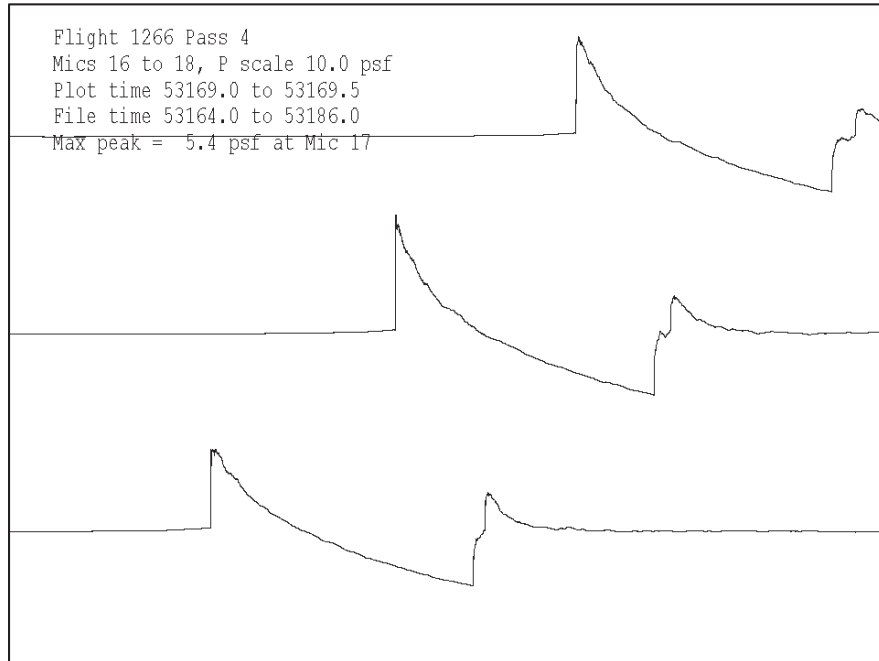


**Figure 5-1. Measured maximum focus, Maneuver A, 1266-4.**

Tac = 53094.000 sec, Phi = 0.00 deg, Xac = 14.13 -0.08 35.75 kft, M= 1.18  
 Pmax, Pmin = 6.19, -0.81 psf, Tg = 53166.656 sec, Xg, Yg = 85.14, -0.98 kft  
 Longitude = -117.408931 deg, Latitude = 35.279246 deg, Zgrnd = 2785.0 feet  
 Lpk = 143.4 dB, Lflt = 121.3 dB, CSEL = 114.0 dB, ASEL = 100.3 dB, Loud = 118.1 PldB  
 Ray coming from 271.3 degrees, elevation 19.2 degrees

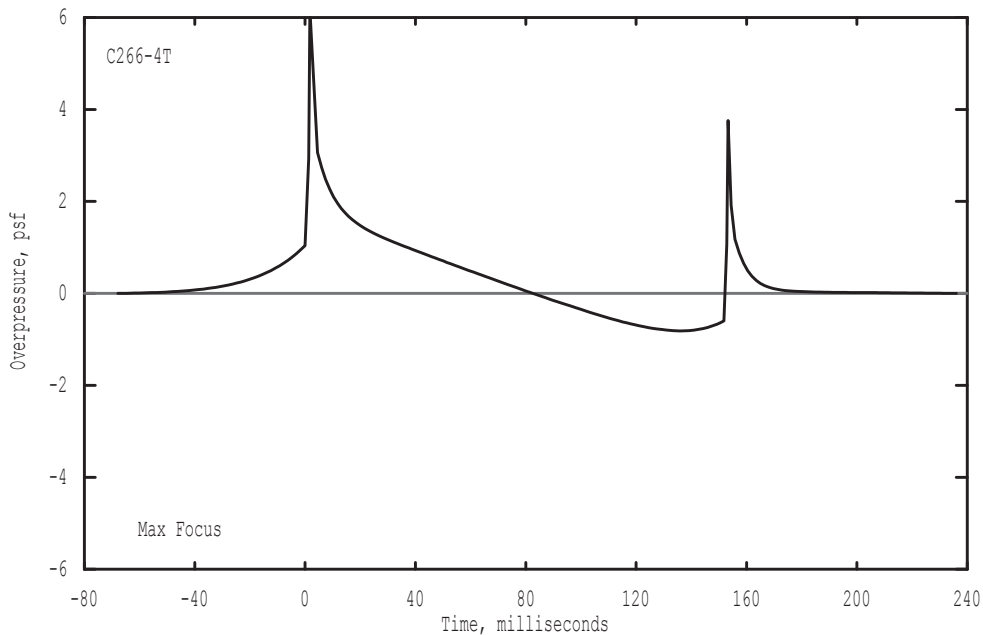


**Figure 5-2. Predicted maximum focus, Maneuver A, 1266-4.**

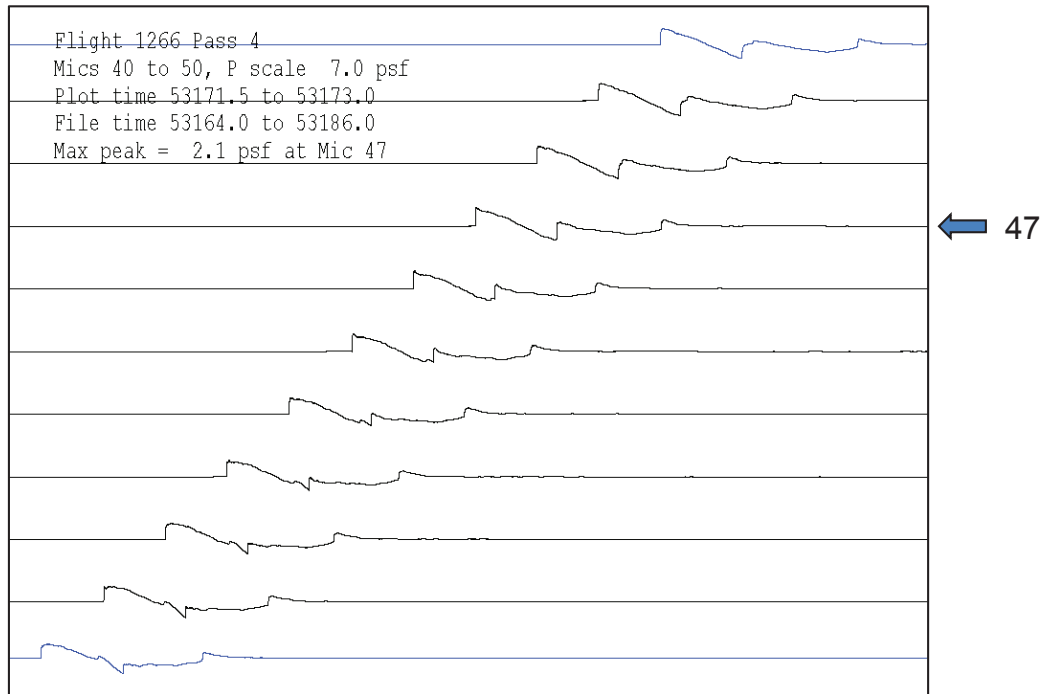


**Figure 5-3. Measured edge of diffraction zone, Maneuver A, 1266-4.**

Tac = 53104.738 sec, Phi = -0.23 deg, Xac = 27.16 -0.15 35.75 kft  
 Pmax, Pmin = 2.32, -1.93 psf, Tg = 53169.027 sec, Xg, Yg = 88.01, -1.07 kft  
 Longitude = -117.399292 deg, Latitude = 35.279023 deg, Zgrnd = 2785.0 feet  
 Lpk = 134.9 dB, Lflt = 121.2 dB, CSEL = 110.4 dB, ASEL = 93.7 dB, Loud = 111.3 PLdB  
 Ray coming from 271.5 degrees, elevation 23.6 degrees

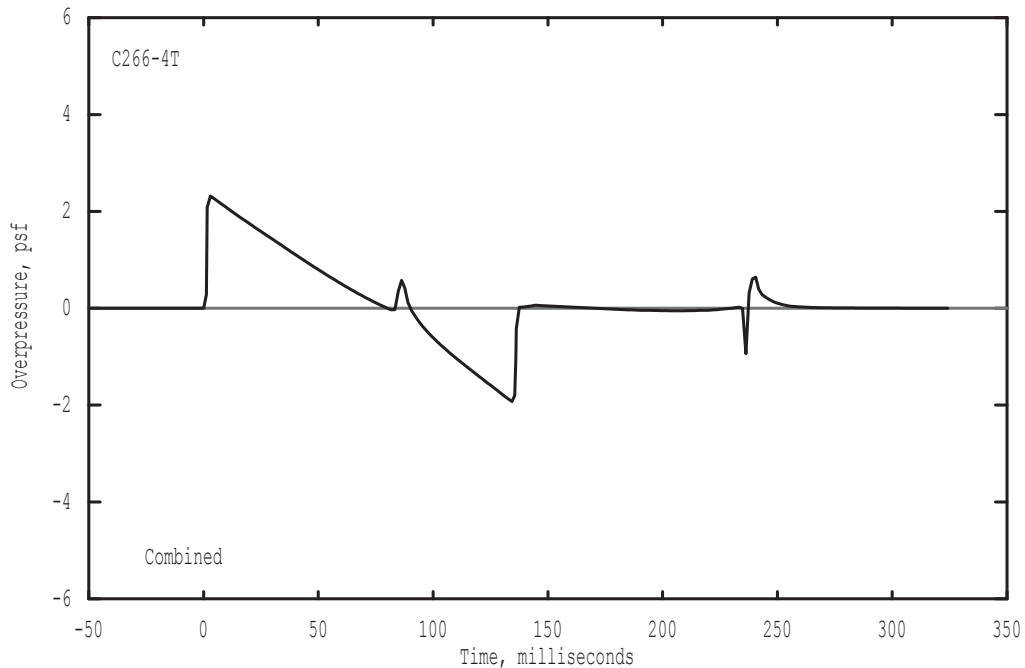


**Figure 5-4. Predicted edge of diffraction zone, Maneuver A, 1266-4. Carpet boom is 1.49 psf.**

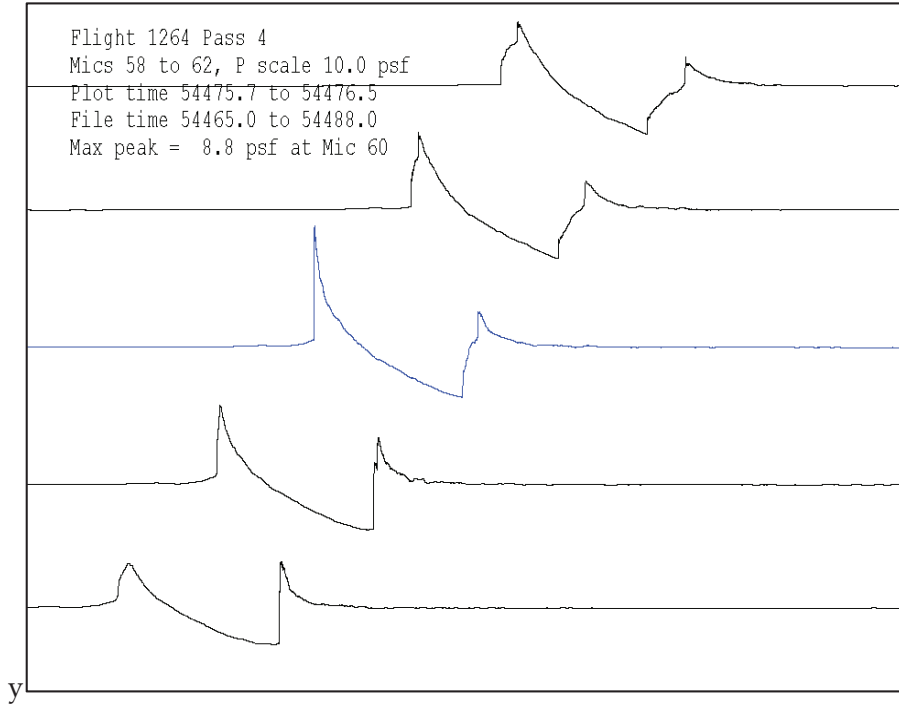


**Figure 5-5. Measured maximum focus, Maneuver C, 1264-4.**

Tac = 54415.000 sec, Phi = 5.00 deg, Xac = 27.49 -2.09 43.03 kft, M= 1.24  
 Pmax, Pmin = 7.67, -1.16 psf, Tg = 54475.324 sec, Xg, Yg = 77.30, -2.82 kft  
 Longitude = -117.390920 deg, Latitude = 35.278772 deg, Zgrnd = 2785.0 feet  
 Lpk = 145.3 dB, Lflt = 122.7 dB, CSEL = 115.4 dB, ASEL = 102.9 dB, Loud = 120.3 PLdB  
 Ray coming from 268.6 degrees, elevation 36.7 degrees

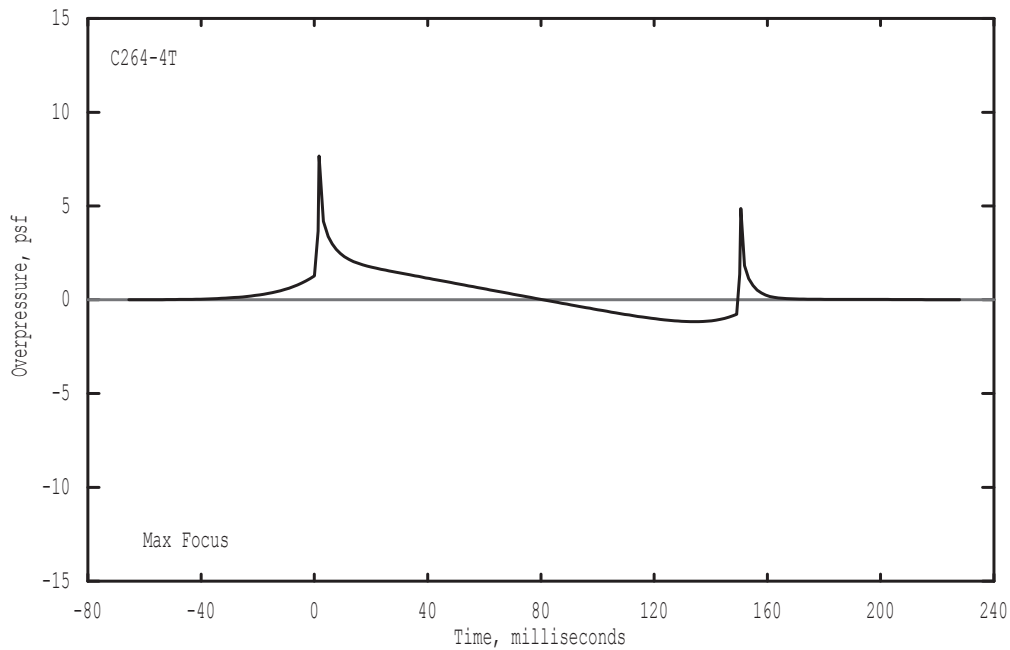


**Figure 5-6. Predicted maximum focus, Maneuver C, 1264-4.**

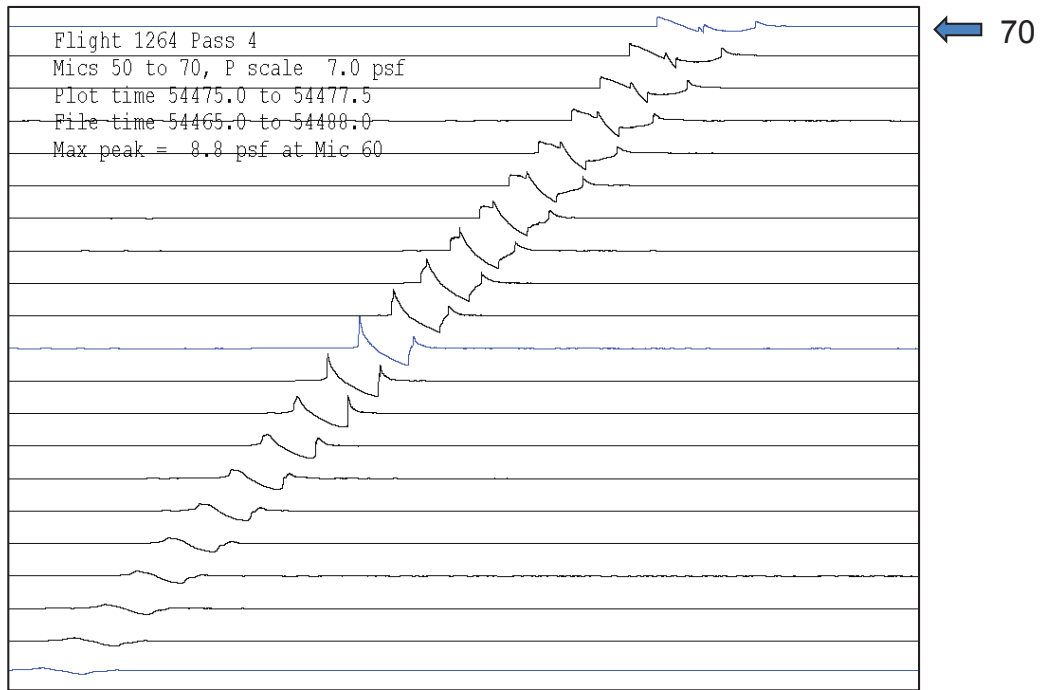


**Figure 5-7. Measured edge of diffraction zone, Maneuver C, 1264-4.**

Tac = 54425.379 sec, Phi = 5.86 deg, Xac = 40.44 -3.10 40.93 kft  
 Pmax, Pmin = 2.60, -2.15 psf, Tg = 54476.594 sec, Xg, Yg = 79.15, -2.86 kft  
 Longitude = -117.384702 deg, Latitude = 35.278653 deg, Zgrnd = 2785.0 feet  
 Lpk = 135.9 dB, Lflt = 122.1 dB, CSEL = 111.4 dB, ASEL = 95.4 dB, Loud = 113.1 PLdB  
 Ray coming from 267.1 degrees, elevation 43.1 degrees

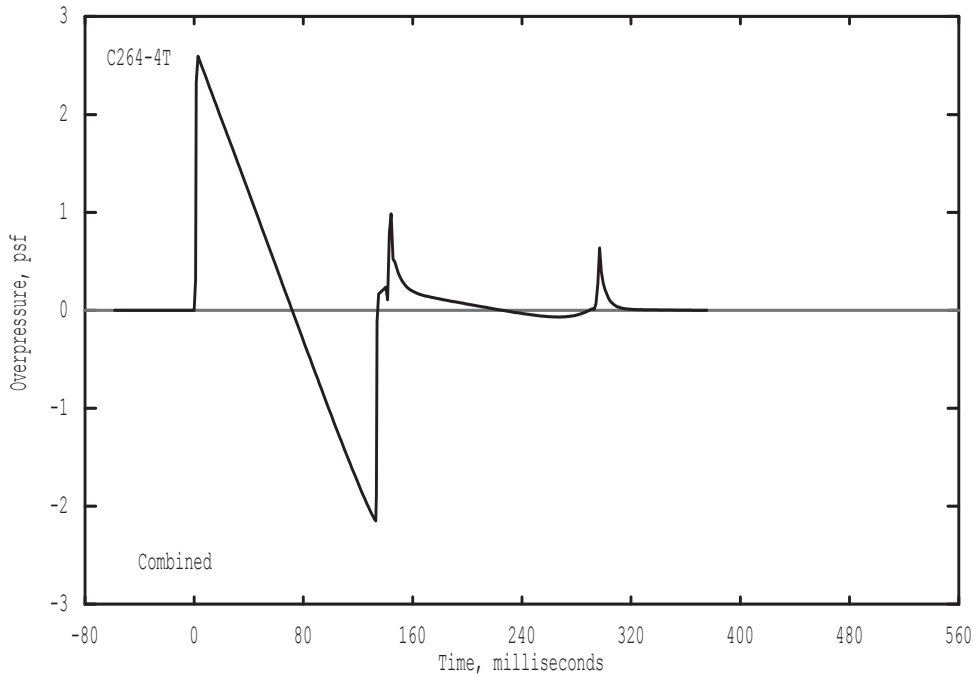


**Figure 5-8. Predicted edge of diffraction zone, Maneuver C, 1264-4. Carpet boom is 1.36 psf.**

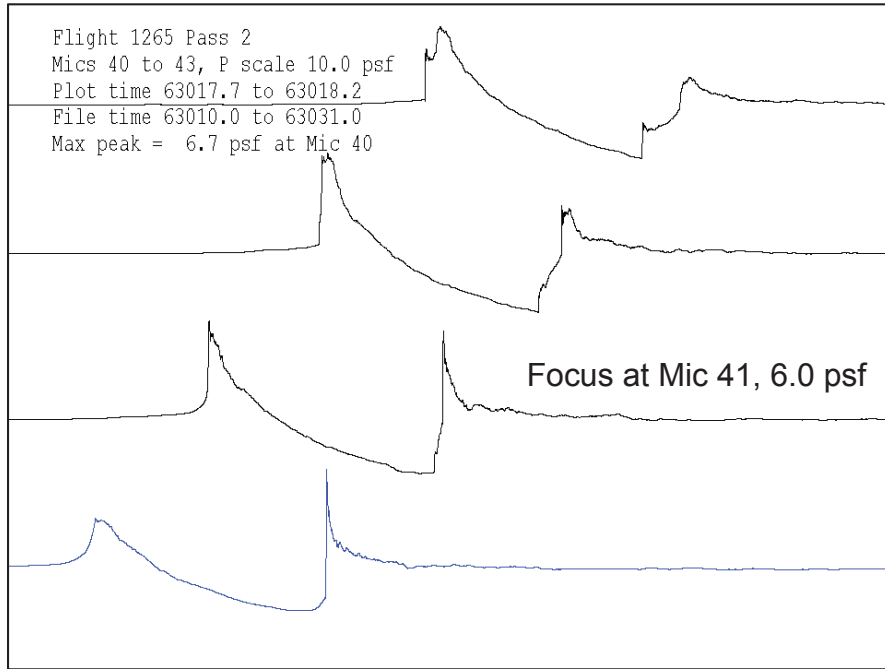


**Figure 5-9. Measured maximum focus, Maneuver D, 1265-2.**

Tac = 62972.000 sec, Phi = 5.00 deg, Xac = 27.53 -1.71 40.73 kft, M = 1.25  
 Pmax, Pmin = 8.29, -1.50 psf, Tg = 63021.207 sec, Xg, Yg = 63.77, -1.62 kft  
 Longitude = -117.398884 deg, Latitude = 35.278697 deg, Zgrnd = 2785.0 feet  
 Lpk = 146.0 dB, Lflt = 123.1 dB, CSEL = 116.2 dB, ASEL = 104.4 dB, Loud = 121.7 PLdB  
 Ray coming from 267.4 degrees, elevation 44.6 degrees

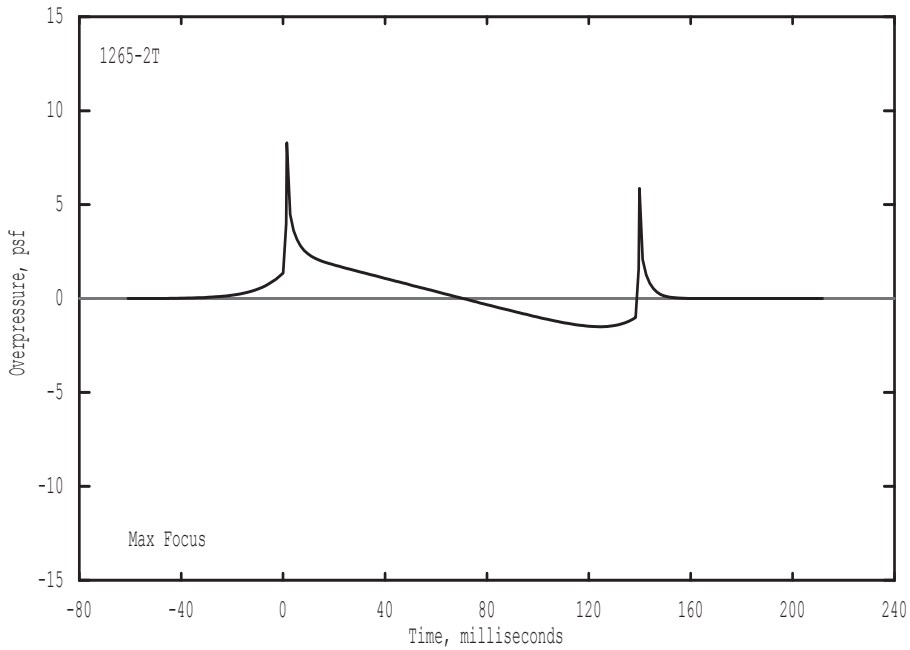


**Figure 5-10. Predicted maximum focus, Maneuver D, 1265-2.**



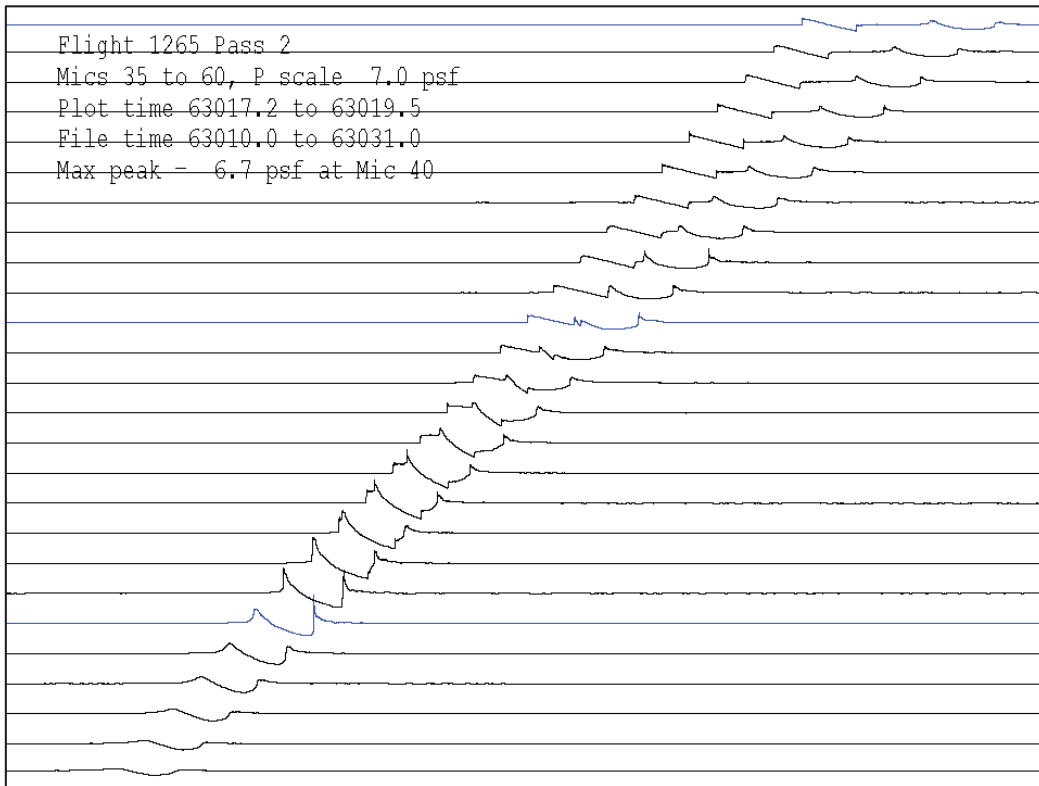


**Figure 5-11. Measured edge of diffraction zone, Maneuver D, 1265-2.**

Tac = 62981.020 sec, Phi = 6.15 deg, Xac = 38.65 -2.48 37.63 kft  
 Pmax, Pmin = 2.71, -2.29 psf, Tg = 63022.023 sec, Xg, Yg = 65.14, -1.54 kft  
 Longitude = -117.394302 deg, Latitude = 35.278910 deg, Zgrnd = 2785.0 feet  
 Lpk = 136.3 dB, Lflt = 122.6 dB, CSEL = 112.3 dB, ASEL = 96.5 dB, Loud = 114.3 PLdB  
 Ray coming from 265.2 degrees, elevation 51.7 degrees

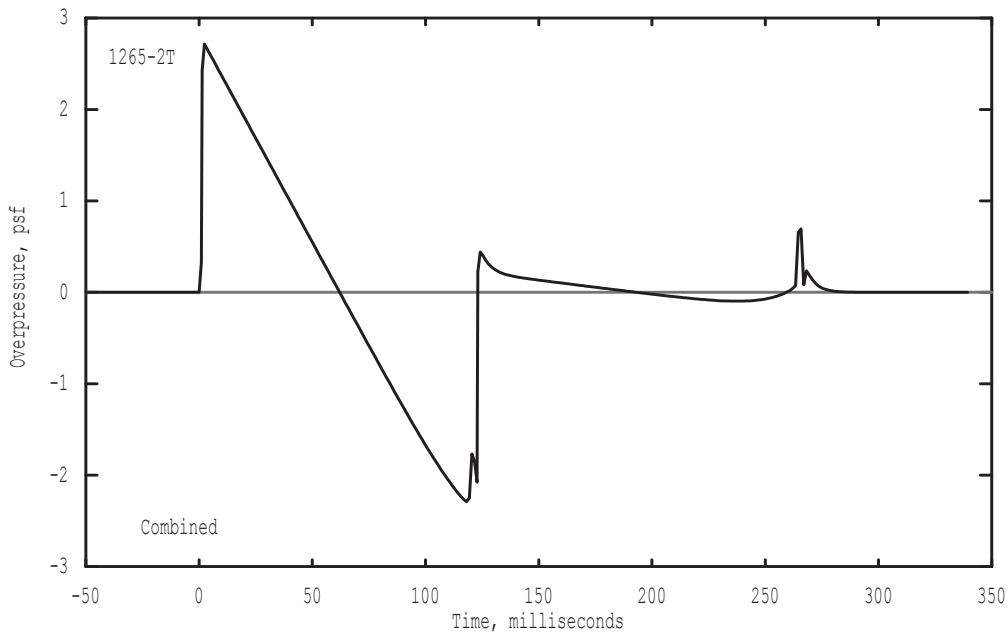


**Figure 5-12. Predicted edge of diffraction zone, Maneuver D, 1265-2. Carpet boom is 1.74 psf.**

The results are summarized in Table 5-1. There is reasonable agreement for Pmax and the diffraction zone size. The differences are probably due to the actual versus modeled atmosphere and maneuver. The predicted focus shape is reasonable near the bow shock. It is not correct near the rear shock, which is a reasonable outcome since the Gill-Seebass solution is for a single step, and does not account for the length associated with an N-wave.

**Table 5-1. Summary of Comparison between Measured Foci and PCBoom Predictions**

Maneuver	Pass	Pmax		Diffraction Zone	
		Prediction	Measurement	Prediction	Measurement
A	1266-4	5.4	6.2	3750	>2800
C	1264-4	8.8	7.7	1250	1875
D	1265-2	6.0	8.3	1250	1250

## 5.4 Recommendations for Code Improvements

The following recommendations were made for the Beta version:

1. Tools to assist in smoothing/modeling trajectories and atmospheres.
2. Replace the Gill-Seebass focused shock shape with one based on a modern Tricomi solver.
3. Expand the focal zone outputs (currently total curvature, sref and yref) to other parameters that are relevant to other solvers and scaling.

Recommendation 1 consisted of developing a utility “modatt” that enabled smoothing of the atmosphere and application of PCBoom’s TADVANCE mode to model the trajectory in the vicinity of the focus maneuver, as described earlier.

Recommendation 2 was found to be not feasible. The scaling in PCBoom is based on Guiraud’s similitude for a single shock and does not account for signature length. Without signature length scaling, it is not possible to apply a shape, only a peak amplitude.

Recommendation 3 was carried out with all necessary parameters written to the out file. Utility “raycau” reads those quantities as well as ray and caustic geometry, and provides an interface to PCBurg and LNTE.

## Pseudospectral Solution of Non-linear Tricomi Equation (PSONTE)

### 6.1 Formulation and Numeric Solution

While PCBoom's application of the Gill-Seebass shock solution was quite successful (Section 5), it carried the assumption that each shock was an independent entity and behaved as an isolated step. A major advance occurred 25 years later, when Auger and Coulouvrat (2002) obtained a new numeric solution for focus booms.

Auger and Coulouvrat began their solution with the nonlinear Tricomi equation written in dimensionless form for a wave with maximum overpressure  $P_{ac}$  characteristic duration  $T_{ac}$

$$\frac{\partial^2 \bar{p}_a}{\partial \bar{z}^2} - \bar{z} \frac{\partial^2 \bar{p}_a}{\partial \bar{\tau}^2} + \mu \frac{\partial^2}{\partial \bar{\tau}^2} \left( \frac{\bar{p}_a^2}{2} \right) = 0 \quad (6-1)$$

where

$$\begin{aligned} \bar{p}_a &= (p - p_0)/P_{ac} \\ \bar{\tau} &= [t - x(1 - z/R_{cau})/c_0]/T_{ac} \\ \bar{z} &= [2/(c_0^2 T_{ac}^2 R_{cau})]^{1/3} z = z/\delta \\ \mu &= 2\beta M_{ac} [R_{cau}/(2c_0 T_{ac})]^{2/3} \end{aligned}$$

$\delta$  is the characteristic thickness of the diffraction boundary layer around the caustic. Auger and Coulouvrat describe it as the distance at which the phases of in-coming and out-going signals differ by less than  $T_{ac}$ . The parameter  $\mu$  is a measure of nonlinear effects relative to diffraction. They note that for sonic booms this is generally small, of order 0.1.

Equation (6-1) was solved using an iterative algorithm based on an unsteady version:

$$\frac{\partial^2 \bar{p}_a}{\partial \bar{t} \partial \bar{\tau}} = \frac{\partial^2 \bar{p}_a}{\partial \bar{z}^2} - \bar{z} \frac{\partial^2 \bar{p}_a}{\partial \bar{\tau}^2} + \mu \frac{\partial^2}{\partial \bar{\tau}^2} \left( \frac{\bar{p}_a^2}{2} \right) \quad (6-2)$$

where  $\bar{t}$  is an artificial pseudotime variable. The solution method separated Equation (6-2) into a linear Tricomi equation (diffraction) and a nonlinear equation:

$$\frac{\partial^2 \bar{p}_a}{\partial \bar{t} \partial \bar{\tau}} = \frac{\partial^2 \bar{p}_a}{\partial \bar{z}^2} - \bar{z} \frac{\partial^2 \bar{p}_a}{\partial \bar{\tau}^2} \quad (6-3a)$$

$$\frac{\partial^2 \bar{p}_a}{\partial \bar{t} \partial \bar{\tau}} = \mu \frac{\partial^2}{\partial \bar{\tau}^2} \left( \frac{\bar{p}_a^2}{2} \right) \quad (6-3b)$$

These were rewritten in discretized form and solved by iteration. At each time step, they were advanced a  $\bar{t}$  step at a time, first (6-3a) in the frequency domain and (6-3b) in the time domain. At each step the boundary conditions – the incoming wave and a radiation condition – were applied at the top edge of the computational domain.

Figure 6-1 shows Auger and Coulouvat’s solution for an N-wave boom. Two solutions are shown: linear (dashed line) and nonlinear (solid line). The purpose of that calculation was to demonstrate that the method would agree with an analytic solution (linear case) and that including the nonlinear part did make a difference. Equally important is that the N-wave solution had the same properties as Plotkin and Cantril’s application of the Gill-Seebass solution separately to each shock. They also demonstrated that their solution matched Guiraud’s scaling law.

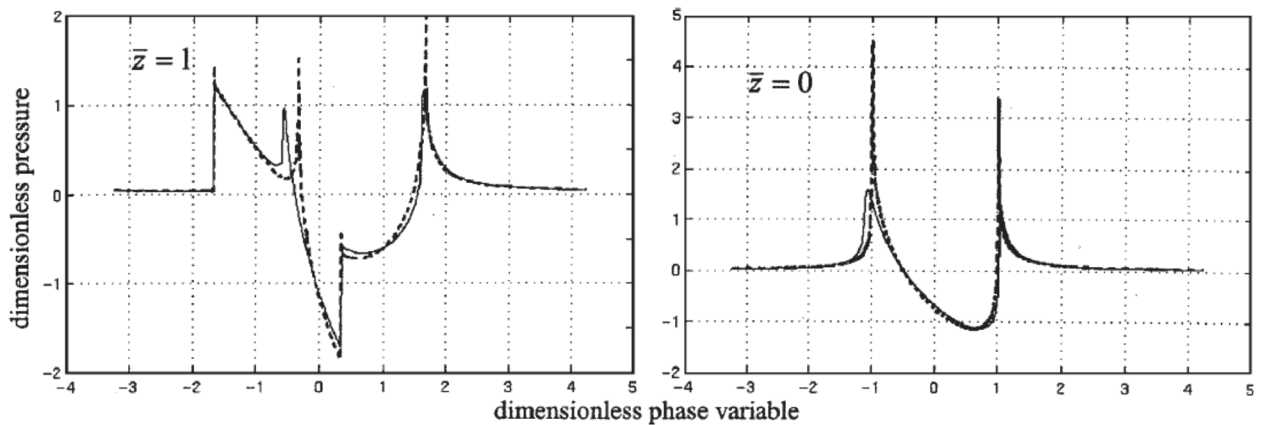


**Figure 6-1. Auger and Coulouvat (2002) solution for N-wave Focus.**

Figure 6-2 shows their solution for a Concorde boom. That boom differs from an N-wave in that there is a double shock at the front. The focus behavior for the rear shock is similar to the N-wave and the Plotkin-Cantril method. The focus behavior for the double shock at the front is quite different. The shocks interact, with the net focus factor considerably less than that of a single shock. This result shows that focusing of a boom with a complex shape will not be as loud as focusing of an N-wave boom.

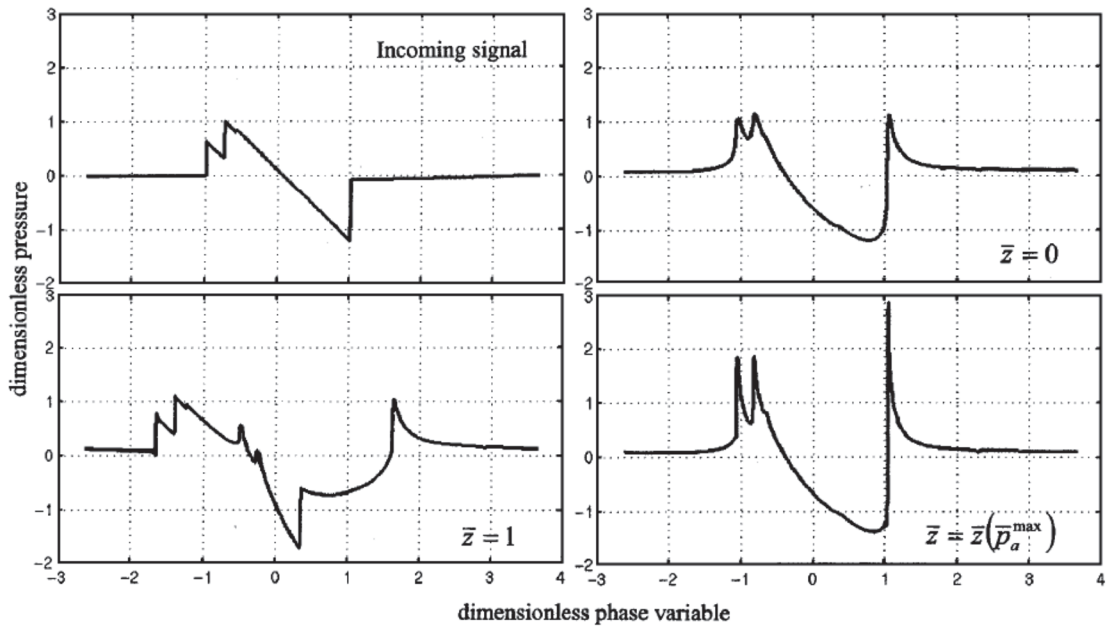


Figure 6-2. Auger and Coulouvrat (2002) solution for focal zone with non-N incident boom.

## 6.2 Preliminary Comparison with Flight Test

The flight tests were conducted in May 2011, and data reduced and qualified in June. All acoustic data were calibrated and processed. Some data, in particular calibrated aircraft performance data, are not yet available. GPS tracking data for the aircraft were available. Those data, together with weather data (Section 3), enabled preparation of preliminary PCBoom “trj” files.

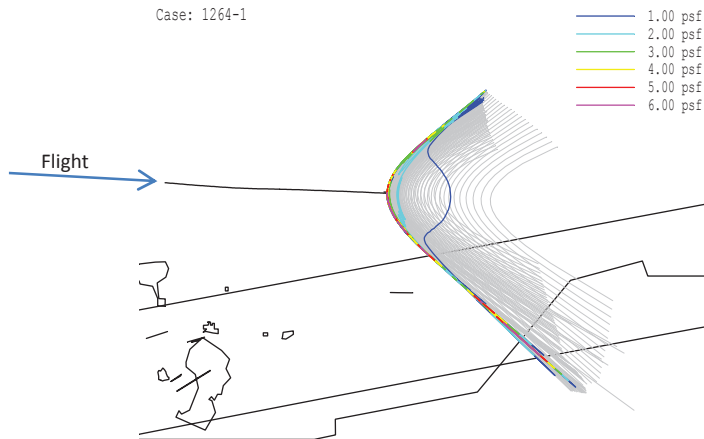


Figure 6-3. PCBoom footprint for Flight 1264 Pass 1.

Figure 6-3 is the PCBoom footprint for one of the pushover passes (Flight 1264 Pass 1, maneuver C,  $m\ddot{m}dot = 3.5/\text{second}$  and pushover  $-0.25 \text{ degrees/second}$ ). Figure 6-4 is a closer view of the footprint, in the vicinity of the array. Figure 6-5 is the predicted maximum focus signature along the centerline ( $\phi = 0$ ). The calculated location is Site 18, and the peak overpressure is 6.8 psf. The measured maximum focus boom for that flight was 7.1 psf at Site 20.

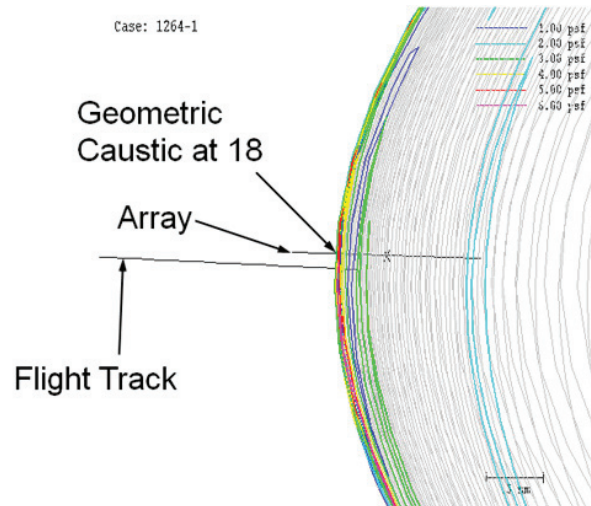


Figure 6-4. PCBoom footprint for Flight 1264 Pass 1, in vicinity of array.

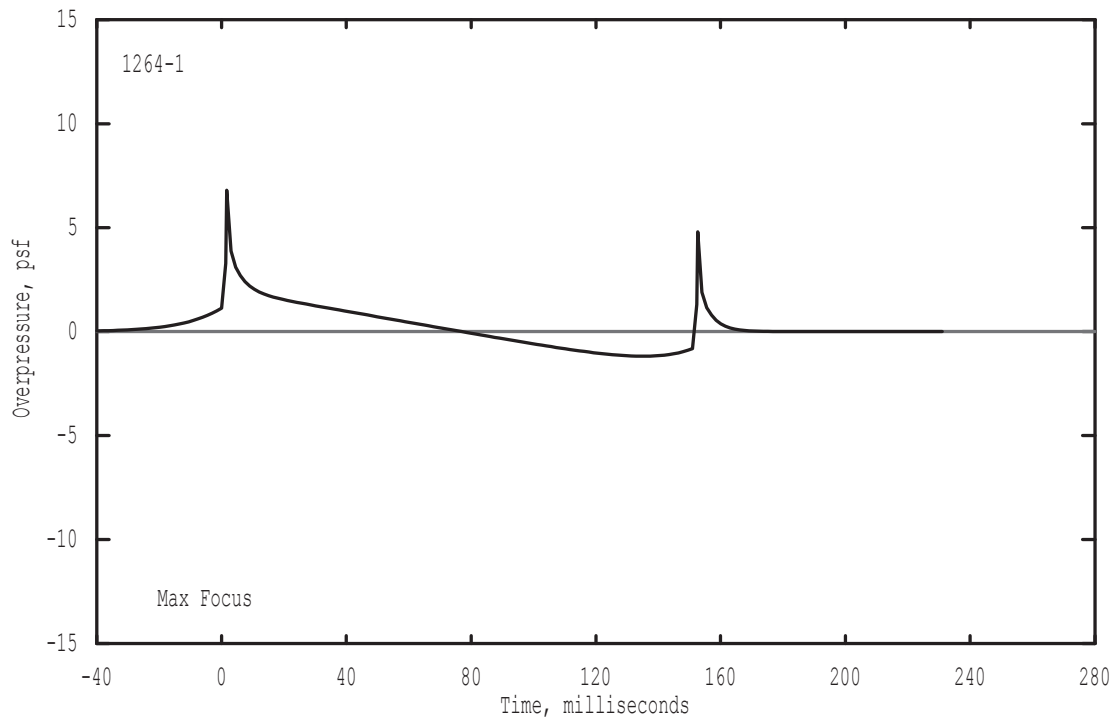
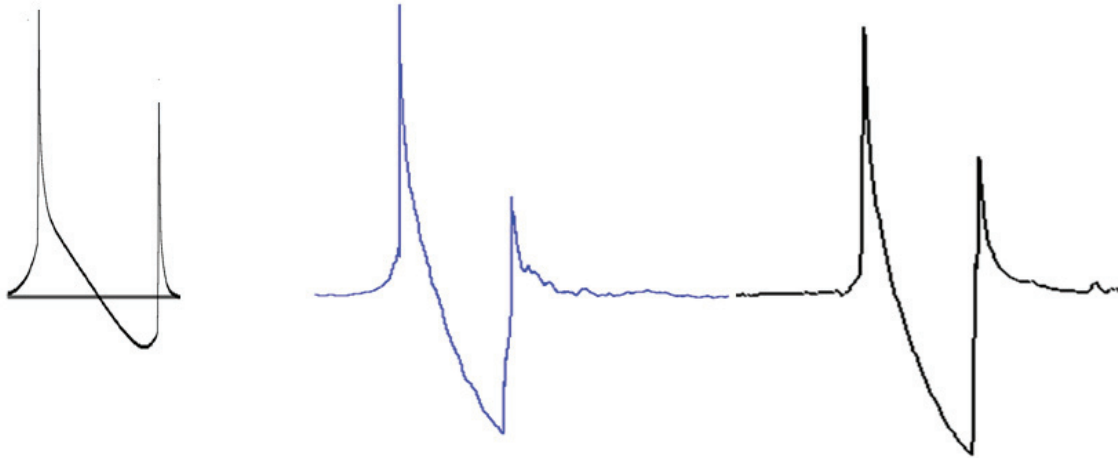


Figure 6-5. PCBoom focus signature at Microphone 18, Flight 1264 Pass 1.

Figure 6-6 shows the PCBoom predicted signature (rescaled from Figure 6-5), the measured boom, and the predicted boom from the Auger-Coulouvrat Tricomi solution method for an N-wave. The Tricomi solution boom is approximate, having been scaled from Kandil and Zheng's (2005; Maglieri et al., 2011) published results from their replication of Auger-Coulouvrat rather than computed for specific SCAMP conditions, but it looks very much like the measured boom. While the Gill-Seebass solution provides accurate prediction of the peak shock overpressure and "focus factor" the Auger-Coulouvrat method provides much closer agreement with the detailed shape of the focused waveform.

Kandil and Zheng replicated Auger and Coulouvrat's method as part of a NASA-funded focus boom study (Maglieri et al., 2011) and was intended to be one of the models evaluated as part of SCAMP. A working version of their code was, however, never delivered. Under SCAMP, an attempt was made to resurrect the code from a draft version of the program. The attempt was partially successful. It was, however, realized that this inviscid code would, at best, be a subset of the Lossy Nonlinear Tricomi Equation (LNTE) method discussed in Section 8, so effort was curtailed and resources redirected toward improving the interface between PCBoom and LNTE.



**Figure 6-6. Comparison of focused boom predictions and measurements. PCBoom prediction (left), Flight 1264 Pass 1 measurement (center), and Auger-Coulouvrat method nonlinear Tricomi solution (right).**

*Intentionally left blank*



## Nonlinear Progressive Wave Equation (NPE)

### 7.1 Description and Applicability

The NPE is a numerical approach to modeling the propagation of weak nonlinear pulses subject to refraction and diffraction. The original version was developed in 1986 by B. Edward McDonald and William Kuperman at the Naval Research Laboratory (NRL) with the goal of modeling underwater pulse propagation through caustics (McDonald and Kuperman, 1987). The NPE equation (Eq. 7-1) is formulated in the time domain, resembling the one-dimensional Burgers equation, but with additional terms that model diffraction in the transverse direction and refraction due to variations in the local sound speed.

$$\frac{\partial p}{\partial t} + c_0 \frac{\partial p}{\partial x} = -\frac{\partial}{\partial x} \left( c'p + \frac{\beta}{2} \frac{p^2}{\rho c_0} \right) - \frac{c_0}{2} \frac{\partial^2}{\partial z^2} \int_{-\infty}^x p dx' + \delta_{\text{eff}} \frac{\partial^2 p}{\partial x^2} \quad (7-1)$$

The left hand side represents linear plane wave propagation; the terms on the right hand side represent, respectively, refraction and nonlinearity, diffraction, and dissipation. The  $x$ -axis represents the primary direction of wave propagation, while the wave front is nominally parallel to the  $z$ -axis. The wave is assumed to be uniform along the third Cartesian coordinate. Cylindrical spreading can be applied if distance from the source is known.

The NPE, like its frequency domain equivalent – the Parabolic Equation (PE) – makes use of the paraxial approximation, which assumes that diffracted waves propagate within a relatively narrow angle with respect to the primary direction of propagation. The paraxial approximation is generally valid for waves with a slightly curved or rippled wavefront, or for propagation in a medium with small inhomogeneities. Thus, the NPE is well suited for the simulation of focused sonic booms propagating through turbulence (Piacsek, 1995). Recently, a "wide-angle" version of the NPE was developed by McDonald (McDonald, 2002) that extends the angular range of validity; this is implemented in the NPE2 code, which is the version used for the SCAMP project.

The NPE numerical implementation makes use of a robust shock capturing scheme while conserving energy and momentum (McDonald and Ambrosiano, 1984). A high degree of efficiency is achieved in the NPE code by having the computational domain move with the ambient sound speed, so that the wave evolution occurs over time scales associated with nonlinearity and diffraction, permitting large time steps.

It is important to note that the NPE solves for a non-dimensional acoustic quantity that is equivalent to acoustic pressure normalized by the ambient pressure. When plotting the results, the user should multiply the NPE output solution by an appropriate scaling quantity. In the results shown in Section 7-6 (McDonald, 2002), the scaling quantity is the atmospheric pressure (Pa) at the altitude of the calculation.

## 7.2 Modifications for Sonic Boom Modeling

The NPE (both narrow and wide-angle versions) has been adapted for atmospheric propagation by Piacsek (Piacsek, 1995, and Piacsek, 2002). Significant modifications include the addition of a dissipation term (see Eq. 7-1) that represents viscoelastic dissipation and steady-state molecular relaxation in air, a user-specified sound speed profile, customized grid initialization routines, and the incorporation of atmospheric turbulence (represented as random perturbations of the sound speed). It should be noted that when turbulence is included, time steps must be small and the efficiency of a wave-following computational domain no longer applies.

For the initial phase of the SCAMP project, we used the wide-angle version of the NPE adapted for atmospheric propagation, but without turbulence. The version of NPE2 modified for sonic boom propagation is called *npe\_scamp*. A new modification, specific to SCAMP, is the implementation of absorption at the top (and/or) bottom boundaries in order to suppress reflections.

## 7.3 Application of the NPE to Modeling Sonic Booms at Caustics

The original sequence of calculations for a SCAMP simulation run is generally as follows:

- (1) CFD codes produce F-functions based on an aircraft's specific design, speed, and altitude.
- (2) The PCBOOM code propagates these F-functions along rays, taking into account the aircraft's precise position vs. time and atmospheric conditions.
- (3) Shortly before rays reach the caustic, the PCBOOM solution is transferred to the NPE, which propagates the wave into the region of the caustic.

Figure 7-1 provides an illustration of focusing rays corresponding to level acceleration and no atmospheric refraction. The region encompassed by the initial NPE grid is superimposed. Detail of the NPE domain is shown in Figure 7-2.

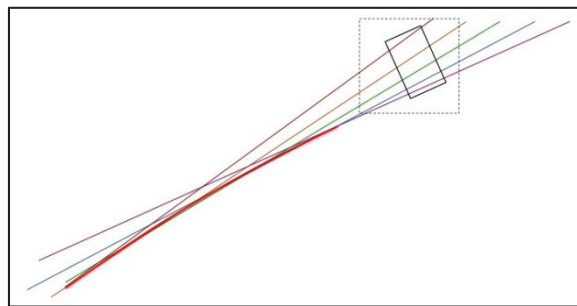


**Figure 7-1. Illustration of focusing rays from an accelerating aircraft in a homogeneous atmosphere. The caustic surface is shown with the bold red curve. The initial NPE domain is represented by the black rectangle. A close-up view of the dashed region is shown in Figure 7-2.**

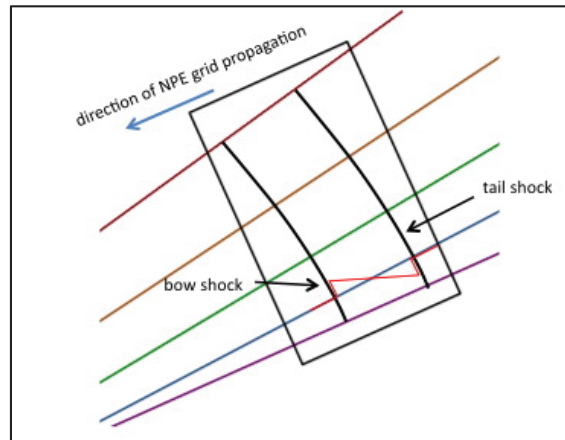


**Figure 7-2. Illustration of the NPE domain depicting the location where conversion from the PCBoom solution takes place. The NPE grid, represented by the area enclosed by the black rectangle, travels with the wave (to the left in this picture). The conversion program *pboom2npe* interpolates the acoustic pressure along rays to generate a rectangular array that encompasses the bow and tail shocks of the sonic boom.**

The NPE alpha version was initialized with a solution converted from PCBOOM output at a specified time relative to the time of first focus. The conversion is performed by the program *pboom2npe*,<sup>2</sup> which orients the rectangular NPE grid so that the "bottom ray" is parallel to the bottom grid boundary. The shock front is thus perpendicular to the bottom boundary and curves towards the front of the grid as it extends to the top of the grid, as illustrated in Figure 7-2. As the NPE grid moves in a straight line through the atmosphere in the direction of the bottom ray, the curved shock front will undergo focusing with nonlinearity, diffraction, and dissipation taken into account. Because the wavefront is not perpendicular to the top boundary, an absorbing region is imposed to suppress reflections from this boundary.

If the caustic surface curves away from the NPE domain, as shown in Figure 7-1, the region below the caustic will not be part of the NPE solution. However, atmospheric refraction generally produces an upward curving caustic, so the evanescent region below the caustic will be part of the NPE domain.

The NPE solution is expressed as a rectangular array of pressure values  $p_{ij}$ . An approximate sonic boom signature can be obtained simply by plotting a row of pressure values along the  $x$ -direction. This approach is reasonably accurate as long as the wavefront within the NPE domain is nominally perpendicular to the  $x$ -axis.

## 7.4 Using *npe\_scamp*

The *npe\_scamp* source code is written in FORTRAN77; the main program and all subroutines are contained within a single file: *npe\_scamp.f*.

All parameters that pertain to a particular run are specified in an ascii format input file (*npe\_scamp.inp*). Among these parameters is an indication of what type of initial pressure field to use. A typical SCAMP run will use a starter field generated by *pboom2npe*, as described in Section 7.5. The grid resolution (variables  $dx$  and  $dz$ ) specified in *npe\_scamp.inp* must match the resolution used in *pboom2npe* to generate the starter file.

Other important parameters include the orientation angle of the NPE grid (obtained from *pboom2npe*), the time step size, and the total number of time steps.

<sup>2</sup> *pboom2npe* was developed as part of the SCAMP project.

The NPE solution  $p(x_i, z_j)$  is written to disk in binary format at time intervals specified in *npe\_scamp.inp*. These output files also include information about the position of the grid and the local ambient sound speed. Plots of the full 2-D pressure field or slices  $p(x)$  can be generated using any commercial software with graphics capability, such as MATLAB or Mathematica.

A users guide for *npe\_scamp*, including full descriptions of each runtime parameter and the format for solution files, is provided in Appendix C.

## 7.5 Interface with PCBoom

### 7.5.1 Description and Usage

As described above, the NPE solution is a rectangular array of pressure values  $p_{ij}$  that constitute a discretized two-dimensional wave field. The starter field that is read in and the solution at later times that is written to disk all have the same rectangular format.

To obtain the NPE starter field, the pressure values that lie along adjacent rays at a particular moment in time, as computed by the PCBoom, must be interpolated at points corresponding to the rectangular NPE grid. This is accomplished by the program *pcboom2npe*, which was created for the SCAMP project.

The user specifies, via the input file *pcboom2npe.inp*, the propagation time along the first PCBoom ray (in seconds relative to the time of first focus) at which the conversion is to take place. The location of each point along a ray at the specified time, calculated by PCBoom and stored as latitude, longitude, and height, is read from a *\*.ott* file, where *\** indicates the run name. The ray positions are converted to npe grid coordinates.

The pressure signature along each ray is calculated using data in the corresponding *\*.ots* file (also produced by PCBoom) and the routine *agemch.f* (supplied by Wyle). An interpolation scheme is used to determine the pressure at each npe grid point. The resulting pressure array is written to a binary file *\*\_init.dat*.

As part of the conversion process, *pcboom2npe* calculates the angle (with respect to vertical) of the first PCBoom ray and orients the NPE grid so that the bottom boundary coincides with this ray. The grid propagation angle is written to standard output; the user must specify this angle in the *npe\_scamp* input file, as described above. A user's guide for *pcboom2npe*, including an example input file and output, is provided in Section 5.5.3.

### 7.5.2 npe\_scamp User Guide

The user must edit the **npe\_scamp.inp** file to specify the size and resolution of the npe grid and other details of the computation. The variables are labeled in the file and are described in Table 7-1. Note: only the first data line is used when *init\_type* = 0.

**Table 7-1. Input File Variables for npe\_scamp**

variable	data type	application
<b>runname</b>	string	The initial data file and all output files use this name
<b>init_type</b>	integer	Indicates how the initial data field is to be obtained. '0' corresponds to reading an existing npe format data file, such as is created by pboom2npe.
<b>nts</b>	integer	Desired number of time steps in the npe computation
<b>ngr</b>	integer	Number of time steps between data dumps
<b>nx</b>	integer	Dimension of the npe grid in the 'x' direction
<b>nz</b>	integer	Dimension of the npe grid in the 'y' direction
<b>dx</b>	real	mesh interval in the 'x' direction (meters)
<b>dz</b>	real	mesh interval in the 'y' direction (meters)
<b>dt</b>	real	Time step size (seconds)
<b>angle</b>	real	Angle that x-axis of npe grid makes with respect to the vertical (radians)
<b>range0</b>	real	Distance from source of the initial pressure field

### 7.5.3 pboom2npe User Guide

The pboom2npe program reads in \*.OTT and \*.OTS files created by PCBoom and writes an NPE format file containing the 2-D pressure field at a time specified by the user (see description of pboom2npe input file below). The basic algorithm is as follows:

1. User specifies a time interval before focus occurs. This is the variable Tback, which is read in from pboom2npe.inp. In the example provided, Tback = 5.0 s.
2. An absolute time for the conversion is calculated:  $T_{npe} = T_{ac1} + T_{focus1} - T_{back}$ , where Tac1 and Tfocus1 apply to the first ray in the .OTT file. Tnpe corresponds to when the "snapshot" of the sonic boom is taken and is converted to npe format.
3. Starting with the first ray, the last Pnt # on the ray that occurs prior to Tnpe is identified (inpe). Linear interpolation between adjacent ray points is used to find the precise latitude, longitude, and height of the ray at Tnpe.
4. The angle that the ray makes with the ground is calculated from the change in height and Sprop between adjacent ray points. The angle is used to convert latitude, longitude, and height to NPE coordinates (The origin of the npe grid coincides with the first ray at Tnpe and x is parallel to the first ray [at Tnpe]).
5. A call to agemch is made, using age(inpe), where the age variable is also interpolated between ray points.
6. The aged signature p(t) is converted to p(x) by simply scaling the output time points by c0(inpe). This is equivalent to assuming that the ray is straight within the npe grid (i.e., on the scale of the length of the N-wave, or ~30 m).
7. A two-dimensional linear interpolation scheme is used to calculate the pressure at each point on the NPE grid.

The user specifies, via the input file "pboom2npe.inp", the propagation time along the first PCBOOM ray, relative to the time of first focus, at which the conversion is to take place.

The pressure field is written to a binary file *\*\_init.dat*.

The user must specify the parameters listed in Table 7-2 in *pcboom2npe.inp*.

**Table 7-2. Input File Parameters for *pcboom2npe***

<b>dx</b>	<b>NPE grid spacing (meters) in the primary propagation direction</b>
dy	NPE grid spacing (meters) in the transverse direction
nx	Number of grid elements in the primary propagation direction
ny	Number of grid elements in the transverse direction
Tback	Time (seconds before first ray focus) at which conversion takes place
Runname	Character string that forms the basis of file names associated with a run

During execution of *pcboom2npe*, the information in Table 7-3 is written to standard output (the terminal screen):

**Table 7-3. Standard Output from *pcboom2npe***

<b>Lx and Ly</b>	<b>Physical dimensions of the npe grid (meters)</b>
*.ott	File name that is being read
<b>Angle</b>	Made by first ray with respect to vertical (degrees)
	NPE coordinates of each ray
	Total number of rays inside the npe grid
	The revised value of <b>ny</b> , which depends on the number and spacing of rays

*The values of **Angle** and **ny** must be used in preparing the corresponding *npe\_scamp* run.  
Note that the variable **ny** corresponds to **nz** in *npe\_scamp*.*

## 7.5.4 Important NPE Considerations

In order for the interpolation scheme in *pcboom2npe* to produce a smooth wavefront, the ray positions calculated by PCBoom must be precise to within a hundredth of an inch.

The user sets the dimension of the NPE grid along the x-axis (the propagation direction) and the maximum dimension along the z-axis. These values are specified in the input file for *pcboom2npe*. The actual dimension along the z-axis is determined by the position of the final ray in the \*.ott file. If the coordinates of a ray lie outside the maximum NPE domain, then the \*.ott file is closed. The number of rays included in the conversion are written to standard out, along with the final grid dimensions and the propagation angle.

The effective solution domain within the NPE grid diminishes as computation proceeds due to diffraction from the shock front edge that is absorbed at the top boundary. Thus, the desired size of the NPE solution domain and the duration of the NPE simulation should be established before running PCBoom, so that the appropriate number of rays are included.

## 7.6 Preliminary Results for npe\_scamp

### 7.6.1 Demonstration Test: N-wave with Concave Ripple

The NPE capabilities are demonstrated with a previously examined test case of an N-wave with a concave rippled wavefront (Piacsek, 1995, 2002).<sup>5-2,5-5</sup> This test case is useful for verifying that modifications to the NPE code for atmospheric propagation, including the recent implementation of absorption boundaries, are working satisfactorily. Here, the NPE grid contains 401 points in the x-direction and 101 points in the z-direction;  $\Delta x = 0.1$  m and  $\Delta z = 0.5$  m; the time step  $\Delta t$  is 0.01 sec. Absorption is applied to 15 percent of the computational domain along both the top and bottom boundaries.

As described in (Piacsek, 2002), the initial N-wave has a wavefront with concave curvature, such that focusing occurs at the center of the wavefront. Geometric acoustics, combined with weak shock theory, predicts a folded shock front within the boundaries of caustics that diverge from the point of first focus (Keller, 1954 and Witham, 1956). Along the center line, the wave profile shows only one shock (plus a tail shock), but at locations away from the center, but within the caustic region, the profile contains two shocks at both the front and tail of the sonic boom.

The full pressure field of the initial wave is shown in Figure 7-3 and the N-wave shock profile through the center line is shown in Figure 7-4. The full field solution after 20 time steps is shown in Figure 7-5 and pressure profiles along the center line and at two other locations are shown in Figures 7-6 and 7-7, respectively. The corresponding plots of the solution after 40 time steps are shown in Figures 7-8, 7-9, and 7-10. In the plots of the full wave field, pressure is represented by the vertical axis; the N-wave profile, and the curved wavefront. These variables are clearly seen. The propagation direction is to the right.

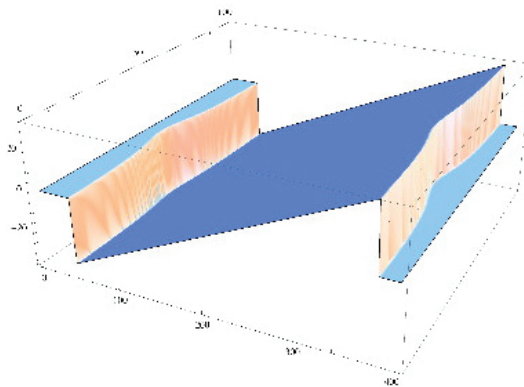


**Figure 7-3. Initial 2-D wave field used in the focused N-wave test.**

**The x-axis, pointing towards the lower right, is the primary direction of propagation. Pressure amplitude is represented on the vertical axis with the scale in Pa. The N-wave profile is seen along the x-axis and the curved shock front is seen along the transverse axis.**

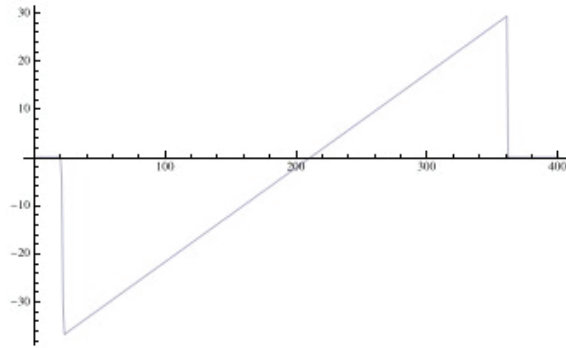


**Figure 7-4. Initial wave profile used in the focused N-wave test.**

*This plot is a slice along the x-axis of the 2-D field shown in Fig. 2a. Pressure scale is in Pa. The horizontal scale shows grid index numbers; conversion to meters (from the back of the grid) can be made by multiplying by the step size, 0.1 m.*

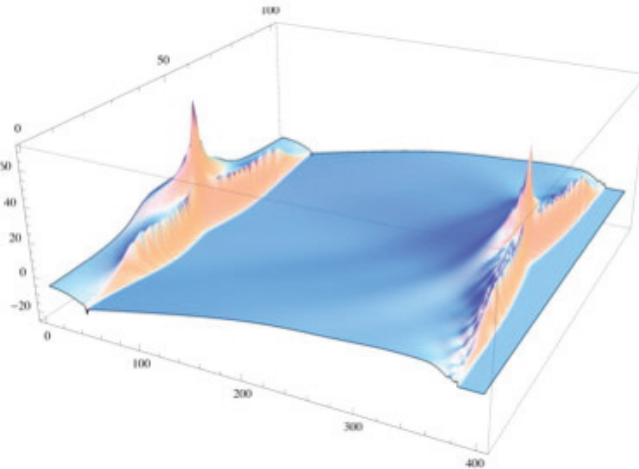


**Figure 7-5. Focused N-wave test, Solution at 20 time steps (0.2 sec), full wave field.**

*Propagation is towards the lower right of the picture. At the center of the wavefront curvature, focusing creates a localized increase in shock amplitude. Wavefront folding is exhibited by the double shock front on either side of the focusing axis. The effects of diffraction from the caustics are apparent behind the shocks. Absorption at the top and bottom boundaries suppresses reflections.*

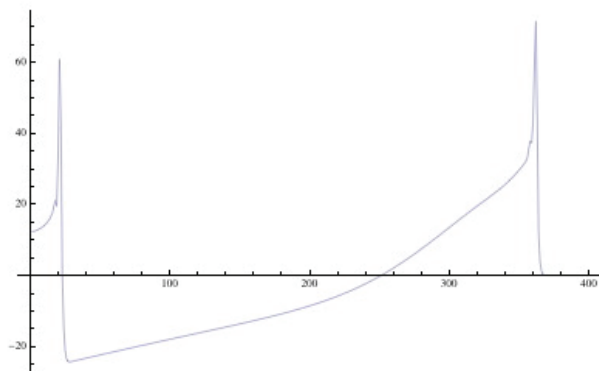


**Figure 7-6. Focused N-wave test, wave profile, focusing axis slice.**

*Focused N-wave test, solution at 20 time steps (.2 seconds), wave profile corresponding to slice along the focusing axis of the 2-D wave field. Note near U-shape of wave associated with propagation through a caustic.*



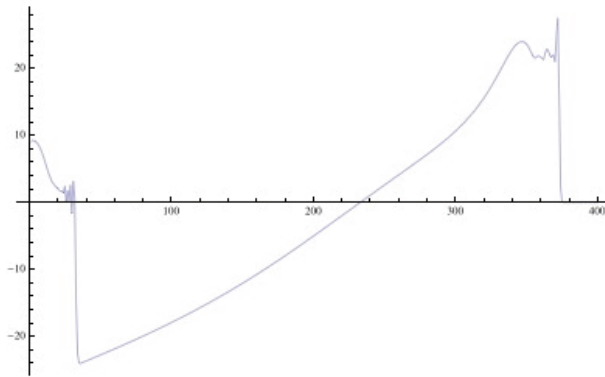


**Figure 7-7. Focused N-wave test, wave profile, wavefront folding.**

*Focused N-wave test, solution at 20 time steps (0.2 seconds), wave profile corresponding to slice along x-axis located about 1/3 of the way up from the bottom boundary. Note the double peak associated with wavefront folding.*

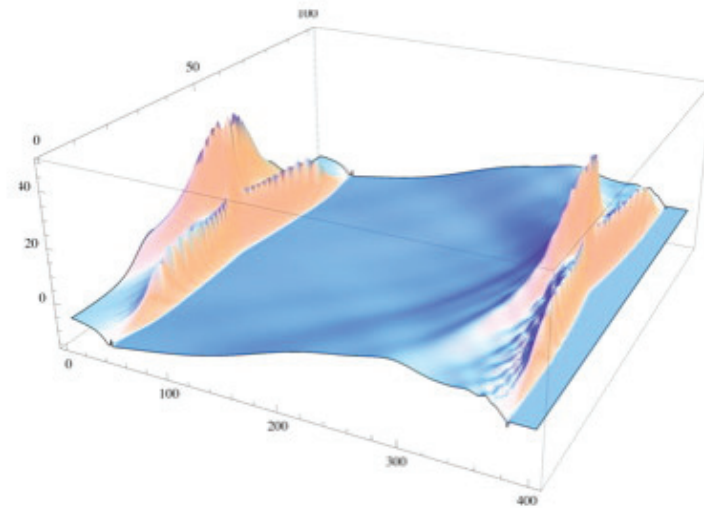


**Figure 7-8. Focused N-wave test, solution at 40 time steps (0.4 sec), full wave field.**

*Propagation is towards the lower right of the picture. The folded wavefront region has broadened as the caustics diverge, while the radius of curvature has decreased due to nonlinear self refraction.*

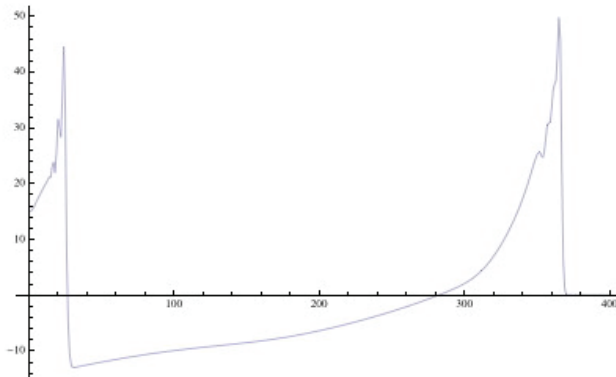


**Figure 7-9. Focused N-wave test, solution at 40 time steps (0.4 sec), wave profile, focusing axis.**

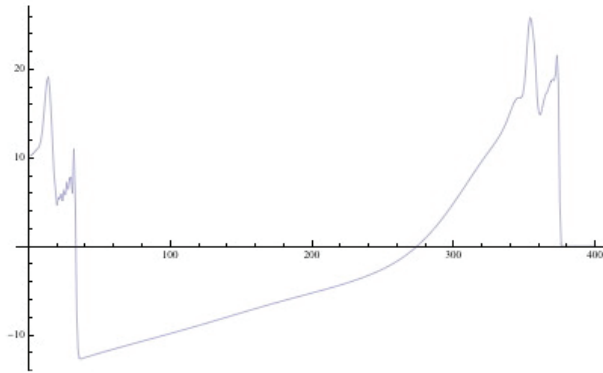


**Figure 7-10. Focused N-wave test, solution at 40 time steps (0.4 sec).**  
Wave profile corresponding to slice along x-axis located about 1/3 of the way up from the bottom boundary.

The solution at 20 time steps ( $t = 0.2$  sec) shows the folded wavefront structure and profiles away from the center line contain two shocks at both the front and back of the N-wave. The shock amplitude at the center of focusing is significantly increased from the initial value. The solution at 40 time steps ( $t = 0.4$  sec) shows the spreading of the caustics away from the center line, compared to the earlier solution. Damping of the solution along the top and bottom boundaries is also evident.

## 7.6.2 SCAMP Flight 1264

A preliminary application of *npe\_scamp* was made using an initial pressure field created by *pcboom2npe* from a PCBoom run corresponding to SCAMP flight 1264, pass 4. (Comparisons of NPE predictions using the updated version of the code for SCAMP flight 1264 pass 4 may be found in Section 9.) The pressure field was converted to NPE coordinates twenty-one seconds before the rays in the center of the grid reach the caustic (at the ground). The height of this initial grid is 6888 m (22,600 ft). The grid resolution is  $\Delta x = 0.02$  m and  $\Delta z = 0.1$  m, resulting in grid dimensions of 2800 by 4000 points. Twenty-eight rays are encompassed within this domain. The time step  $\Delta t$  is 0.001 sec.

The initial pressure field is shown in Figure 7-11. The pressure profile is an N-wave; examples at two locations along the wavefront are shown in Figure 7-12. Absorption is applied to 15 percent of the computational domain along both the top and bottom boundaries, where the concave wavefront is incoming.

The full solution at 8000 time steps (8 seconds of propagation) is shown in Figure 7-13. Attenuation at the top and bottom boundaries is due to artificial absorption, which makes wave truncation gradual. However diffraction from this truncation is unavoidable and is seen as a slowly advancing wavefront behind the front and tail shocks of the N-wave. The caustic advances into the computational domain from below. Although the caustic has not yet reached the domain at time step 8000, the pressure profiles (Figure 7-14) show that focusing is stronger closer to the bottom boundary.

At 12,000 time steps (12 seconds of propagation), diffraction from the truncated wave has propagated further into the domain, corrupting all but a narrow strip of the solution within the center, as shown in Figure 7-15. At this point, the NPE grid has propagated 4/7 of the way to the desired focus location. Clearly, the diffracted wave will corrupt the entire solution before the focal point is reached. The initial grid cannot be enlarged or located closer to the ground because doing so would require including the caustic within the domain, which is forbidden. This is explained in more detail in Section 9. Pressure profiles at time step

12,000 are shown in Figure 7-16. The profile located closer to the bottom boundary, thus closer to the caustic, exhibits the characteristic shape of an N-wave in the vicinity of a caustic.

This alpha calculation shows that the transition from pboom to npe\_scamp works as designed and that the npe algorithms is correctly capturing the physics of the focusing scamp sonic boom, but the signature has not fully evolved into the expected shape as seen in the data presented in Section 5. Full evolution was obtained in the improved beta version, presented in Section 9 along with comparison with flight-test data.

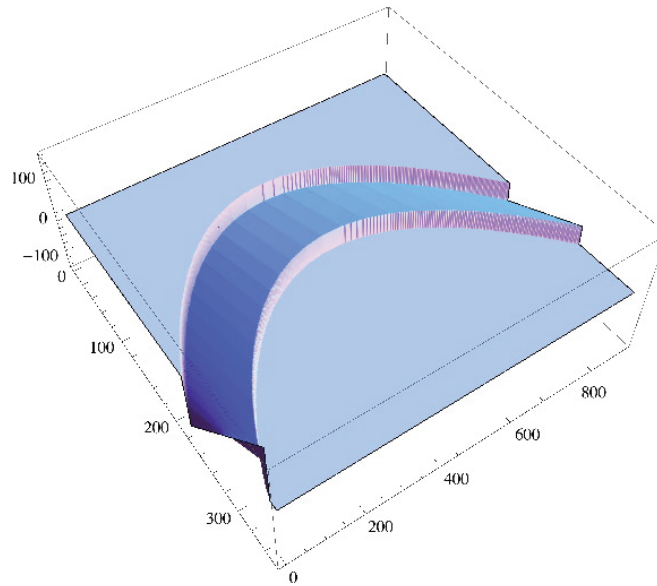


**Figure 7-11. Model of SCAMP Flight 1264-4, initial wave field from PCBoom.**

*Initial wave field 21 seconds before focusing occurs along the center ray.. Propagation is towards the lower right of the picture.*

*X and Y axes are labeled with grid index values; the Z axis is labeled with units of Pascals.*

*The concave wavefront created by focusing rays will generate diffracted waves at the boundaries.*

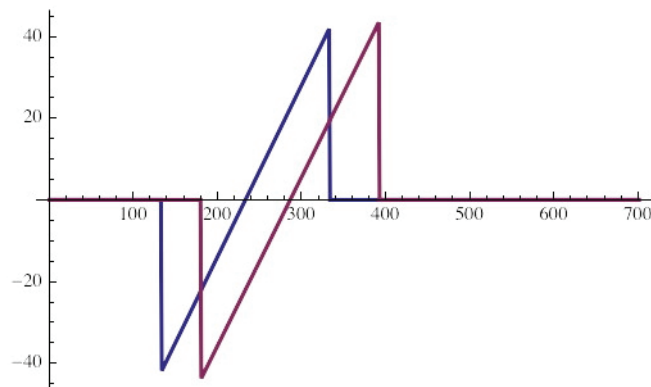


**Figure 7-12. Flight 1264-4 computation, initial wave profile at two locations: 1/2 (blue) and 1/4 (red) of the distance between the top and bottom boundaries. Numbers along X-axis indicate grid index values; numbers on the Y-axis indicate pressure in Pa.**

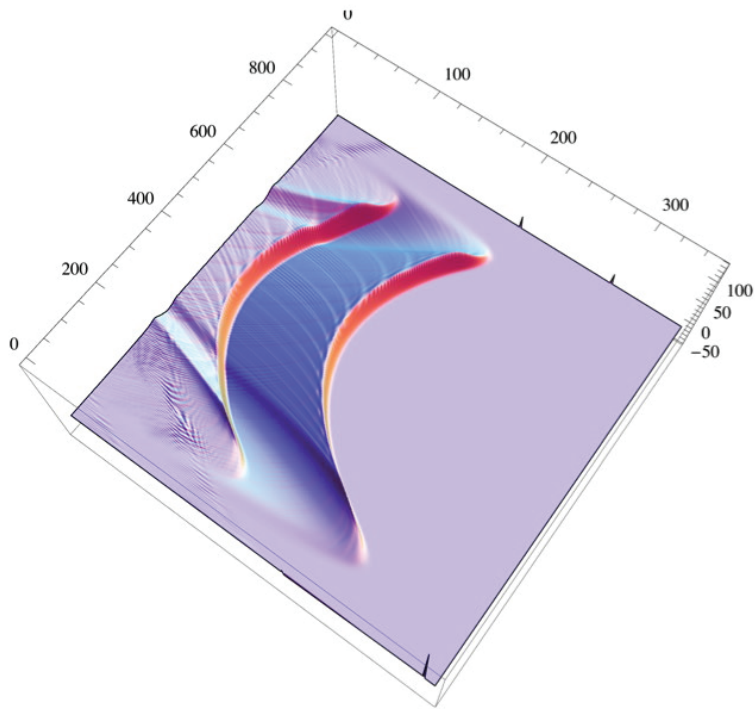


**Figure 7-13. Model of SCAMP Flight 1264-4, Solution at 8000 time steps (8 sec), full wave field.**

*Absorption applied to the top and bottom boundaries is evident. Diffraction resulting from wave truncation overlaps with the solution behind the wave fronts. Ripples along the shock fronts are numerical artifacts.*

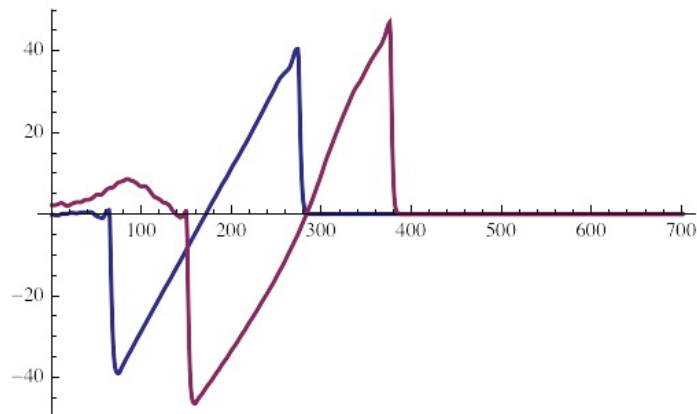


**Figure 7-14. Flight 1264-4 computation at time step 8000 (8 sec). Pressure profiles at two locations: 1/2 (blue) and 1/4 (red) of the distance between the top and bottom boundaries. Numbers along X-axis indicate grid index values; numbers on the Y-axis indicate pressure in Pa. The profile closer to the bottom boundary exhibits greater amplification due to proximity to the caustic.**

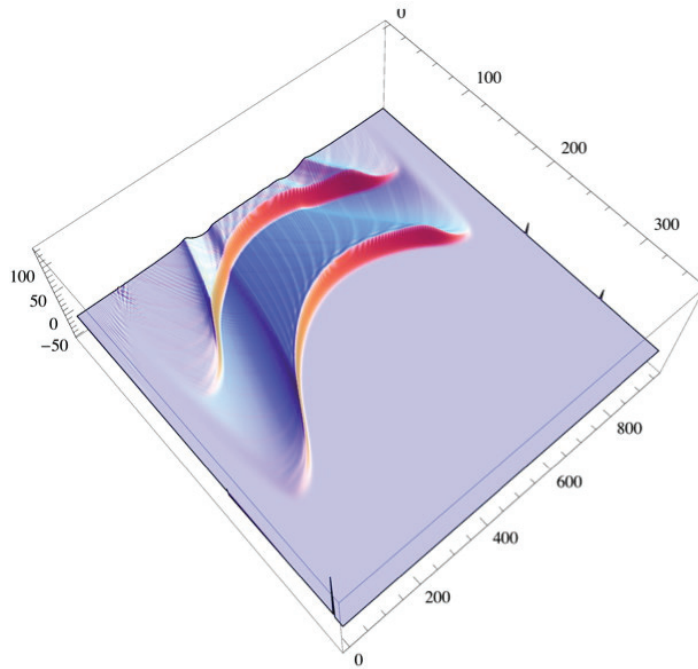


**Figure 7-15.** Level acceleration test, solution at 40 time steps (0.4 sec), full wave field.  
 Note the spreading zone of diffraction from the edge of the shock front where absorption is applied.

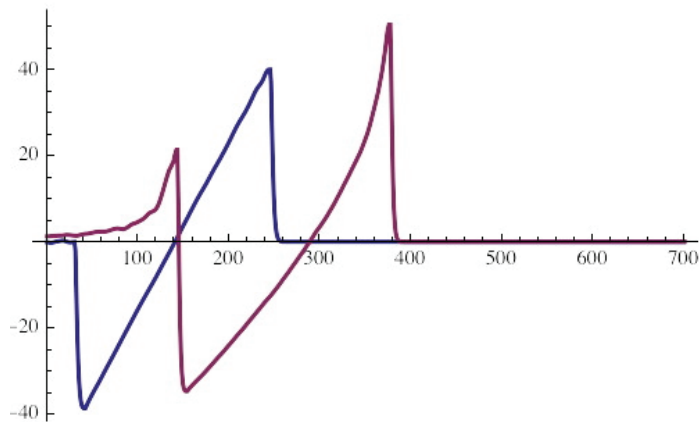


**Figure 7-16.** Flight 1264-4 computation at time step 12000 (12 sec).  
 Pressure profiles at two locations: 1/2 (blue) and 1/4 (red) of the distance between the top and bottom boundaries. Numbers along X-axis indicate grid index values; numbers on the Y-axis indicate pressure in Pa.  
 The caustic has nearly reached the location of the red profile.

*Intentionally left blank*

## Lossy Nonlinear Tricomi Equation (LNTE)

### 8.1 Methodology

Figure 8-1 shows an illustration of the focusing condition modeled by the Tricomi equation. The model equation and Tricomi code allow one to observe how an in-coming wave is modified in the vicinity of a caustic, undergoes amplitude changes and phase changes from going through the caustic, as well as the sound that penetrates into the shadow zone. The derivation and solution methodology follows the mathematical steps and computational algorithm developed by Auger and Coulouvrat (2002). Their derivation began with the equations of fluid motion and applied acoustic perturbation to the pressure, density, entropy, temperature and acoustic velocity. They arrived at the Tricomi equation using an eikonal function obtained from formulating the propagation through the caustic in terms of the ray and caustic geometry. The derivation of the LNTE for this research used their same formulation of the problem, except the contribution of the thermoviscous and molecular relaxation terms were retained throughout the derivation. The thermoviscous and molecular relaxation effects contribute to absorption and dispersion when sound propagates through the atmosphere. Inclusion of these effects in the Tricomi equation is important because atmospheric losses play a dominant role in the rise time and amplitude of shocks present in sonic booms. The rise time and amplitude of the shocks have an impact in the resulting acoustic metrics (such as the Perceived Level [Stevens, 1972] and the A-weighted sound exposure level) calculated for sonic boom waveforms (Shepherd and Sullivan, 1991).

The Tricomi code described in this section determines a solution to the lossy nonlinear Tricomi equation (eq. 8-1) when provided an in-coming waveform, acoustical parameters, and atmospheric conditions.

$$\frac{\partial^2 p}{\partial \bar{z}^2} - \bar{z} \frac{\partial^2 p}{\partial \bar{t}^2} + \frac{\beta}{\varepsilon^2 \rho_0 c_0^2} \frac{\partial^2 p^2}{\partial \bar{t}^2} + \left( \frac{\bar{\alpha}}{\varepsilon^2} + \sum_{v=1}^2 \frac{\bar{\theta}_v / \varepsilon^2}{1 + \bar{\tau}_v \frac{\partial}{\partial \bar{t}}} \right) \frac{\partial^3 p}{\partial \bar{t}^3} = 0 \quad (8-1)$$

The first two terms correspond to diffraction, the next term to nonlinearity, and the last term to the thermoviscous and relaxation effects. The code solves for the solution of equation (8-1) by adding an unsteady pressure term, introducing a pseudotime variable,  $\sigma$ , and iterating from an initial guess to arrive at a final solution (eq. 8-2).

$$\frac{\partial^2 p}{\partial \sigma \partial \bar{t}} = \frac{\partial^2 p}{\partial \bar{z}^2} - \bar{z} \frac{\partial^2 p}{\partial \bar{t}^2} + \frac{\beta}{\varepsilon^2 \rho_0 c_0^2} \frac{\partial^2 p^2}{\partial \bar{t}^2} + \left( \frac{\bar{\alpha}}{\varepsilon^2} + \sum_{v=1}^2 \frac{\bar{\theta}_v / \varepsilon^2}{1 + \bar{\tau}_v \frac{\partial}{\partial \bar{t}}} \right) \frac{\partial^3 p}{\partial \bar{t}^3} \quad (8-2)$$

The pseudotime variable,  $\sigma$ , is not related to the dimensionless time variable,  $\bar{t}$ . The dimensionless time is given by  $\bar{t} = f_{ac} t$ , which is the retarded time,  $t$ , scaled by the characteristic acoustic frequency,  $f_{ac}$ . As the code iterates in pseudotime, the left hand term in the above equation tends to zero and the solution to equation 6-1 is determined.

The variable  $\mathcal{E}$  is a smallness parameter that represents the ratio of the characteristic wavelength,  $\lambda_{ac}$ , to the diffraction boundary layer thickness,  $d$ .

$$\mathcal{E} = \frac{\lambda_{ac}}{d} = \lambda_{ac} \left[ \frac{R_{tot} c_0^2}{2 f_{ac}^2} \right]^{-\frac{1}{3}} = \left[ \frac{2 \lambda_{ac}}{R_{tot}} \right]^{\frac{1}{3}} \quad (8-3)$$

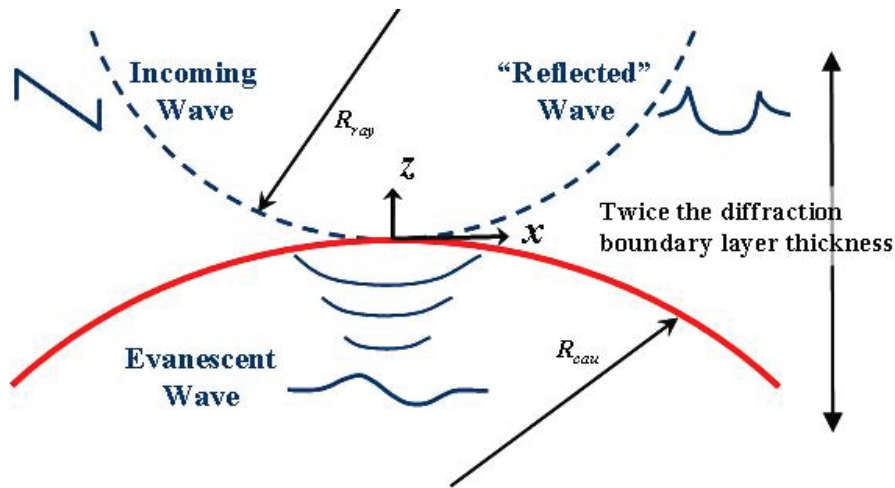


Figure 8-1. Depiction of the focusing condition modeled by the Tricomi Equation.

In equation 8-3,  $R_{tot}$  is the total radius of curvature for the caustic condition. The vertical distance,  $\bar{z}$ , in the above equations is a ratio of the physical distance,  $z$ , away from the caustic (in the direction normal to it) to the diffraction boundary layer thickness,  $d$ . The ratio is given by eq. 8-4:

$$\bar{z} = z \left[ \frac{R_{tot} c_0^2}{2 f_{ac}^2} \right]^{-\frac{1}{3}} \quad (8-4)$$

If the pressure variable in eq. 8-1 was normalized by a characteristic acoustic pressure,  $P_{ac}$ , the coefficient in front of the nonlinear term in eq. 8-1 would appear as presented in the literature:

$$\frac{\mu}{2} = \frac{\beta P_{ac}}{\varepsilon^2 \rho_0 c_0^2} = \frac{\beta P_{ac}}{\rho_0 c_0^2} \left[ \frac{R_{tot} f_{ac}}{2 c_0} \right]^{\frac{2}{3}} \quad (8-5)$$



where the variable  $\mu$  is a coefficient representing the strength of the nonlinear effects relative to diffraction effects. The value of  $P_{ac}$  is typically set to the peak amplitude of the in-coming waveform at  $\bar{z} = 1$ . Also, the variable  $\beta$  is the usual coefficient of nonlinearity.

The last term of both equations (eqs. 8-1 and 8-2) is a newly derived term to account for absorption and dispersion effects. The variable  $\bar{\alpha}$  represents thermoviscous absorption, given by:

$$\bar{\alpha} = \frac{\delta f_{ac}}{c_0^2} \quad (8-6)$$

where  $\delta$  is the diffusivity of sound. The variable  $\bar{\theta}_v$  is the dispersion/relaxation coefficient given by:

$$\bar{\theta}_v = f_{ac} \tau_v m_v = f_{ac} \tau_v \left( \frac{c_{\infty,v}^2 - c_0^2}{c_0^2} \right) \quad (8-7)$$

In equation 8-7 (and also in eqs. 8-1 and 8-2), the  $v$  is a summation index from 1 to 2 (for oxygen and nitrogen molecular relaxation, respectively). Also, the variable  $\tau_v$  is the relaxation time and  $c_{\infty,v}$  is the frozen speed of sound. Note that in equations 8-1 and 8-2, the dimensionless relaxation time,  $\bar{\tau}_v$ , is given by  $\bar{\tau}_v = f_{ac} \tau_v$ .

A Fortran program was developed to numerically implement equation 8-2 as applied to the depiction in Figure 8-1. The Tricomi code in this research uses a numerical algorithm similar to Auger and Coulouvrat, except the numerical implementation of the LNTE includes an extra step to solve for the newly derived atmospheric loss mechanisms. The code solves for the computational domain using a splitting method in both the frequency and time domain. The diffraction and absorption/dispersion effects are solved in the frequency domain for each angular (dimensionless) frequency,  $\omega_n$ . The nonlinear effects are solved in the time domain. Prior to beginning the splitting method, the Fourier transform is applied to the computational domain. The first step then solves the absorption and dispersion effects:

$$i\omega_n \frac{\partial \hat{p}_n}{\partial t} = -i\omega_n^3 \left( \frac{\bar{\alpha}}{\varepsilon^2} + \sum_v \frac{\bar{\theta}_v / \varepsilon^2}{1 + i\omega_n \bar{\tau}_v} \right) \hat{p}_n \quad (8-8)$$

The next step solves for the diffraction effects:

$$i\omega_n \frac{\partial \hat{p}_n}{\partial t} = \omega_n^2 \bar{z} \hat{p} + \frac{\partial^2 \hat{p}_n}{\partial \bar{z}^2} \quad (8-9)$$

The code applies the inverse Fourier transform to the computational domain. The third step solves for the nonlinear effects:

$$\frac{\partial p}{\partial \sigma} = \frac{\beta}{\varepsilon^2 \rho_0 c_0^2} \frac{\partial p^2}{\partial \bar{t}} \quad (8-10)$$

Code execution to obtain a solution can be on the order of hundreds to thousands of iterations depending on the in-coming waveform and the contribution of the nonlinear effects. More details on code execution and convergence are found in the user notes/documentation for the Tricomi code.

## 8.2 Model Input Data – Alpha

Input data for the code consists of the in-coming acoustic waveform and its characteristic frequency, the total radius of curvature for the caustic geometry, and the atmospheric conditions at the caustic. Two passes from the SCAMP F-18 flight test were used to compare the lossy Tricomi code output to measured acoustic ground data – flight 1266, pass 4 (case A) and flight 1264, pass 4 (case C). Case A was a steady level flight at 35,740 feet, with an acceleration rate of 0.0035 mach/second. Case C was a pushover and acceleration from 45,000 feet. Details for the cases are in Section 2.2.

The total radius of curvature is not calculated by the code and must be computed prior to executing the Tricomi code. Table 8-1 contains the temperature, humidity, ambient pressure, and total radius of curvature for the two comparison cases presented in this section.

**Table 8-1. Input Conditions for the Two Comparison Cases**

Case	$f_{ac}$ (Hz)	$R_{tot}$ (meters)	Temperature (K)	Pressure (kPa)	Humidity (%)
A	7.87	70,105	287	91.8	45
C	7.95	48,769	284	91.3	40

Typically, the in-coming waveform is provided at a distance of  $\bar{z} = 1$  and the characteristic frequency is chosen as the reciprocal of the period of the sonic boom. The input acoustic data for each case began with near-field CFD (Section 4) computed for the flight conditions corresponding to the ray that intercepts the caustic at the ground (Figure 8-2). The near-field CFD was used as an input to a far-field propagation code that computed the free-field propagated signature in the vicinity of the caustic. The far-field propagation included the effects of nonlinearity, wind, atmospheric stratification and spreading, and absorption and dispersion due to thermoviscous effects and molecular relaxation effects. The resulting propagated signatures were multiplied by a ground reflection factor of 1.9 (Figure 8-3). Additionally, the free-field signature was scaled to account for the effects of a maneuvering aircraft on the ray-tube area (see Section 3) in order to match the carpet N-wave amplitude from the measured data (see for example Figure 8-4). The resulting output served as the input acoustic waveform to the Tricomi code. The ground reflection factor was not included in the input waveform of the Tricomi code. That scale factor will be applied to the output of the Tricomi solution.

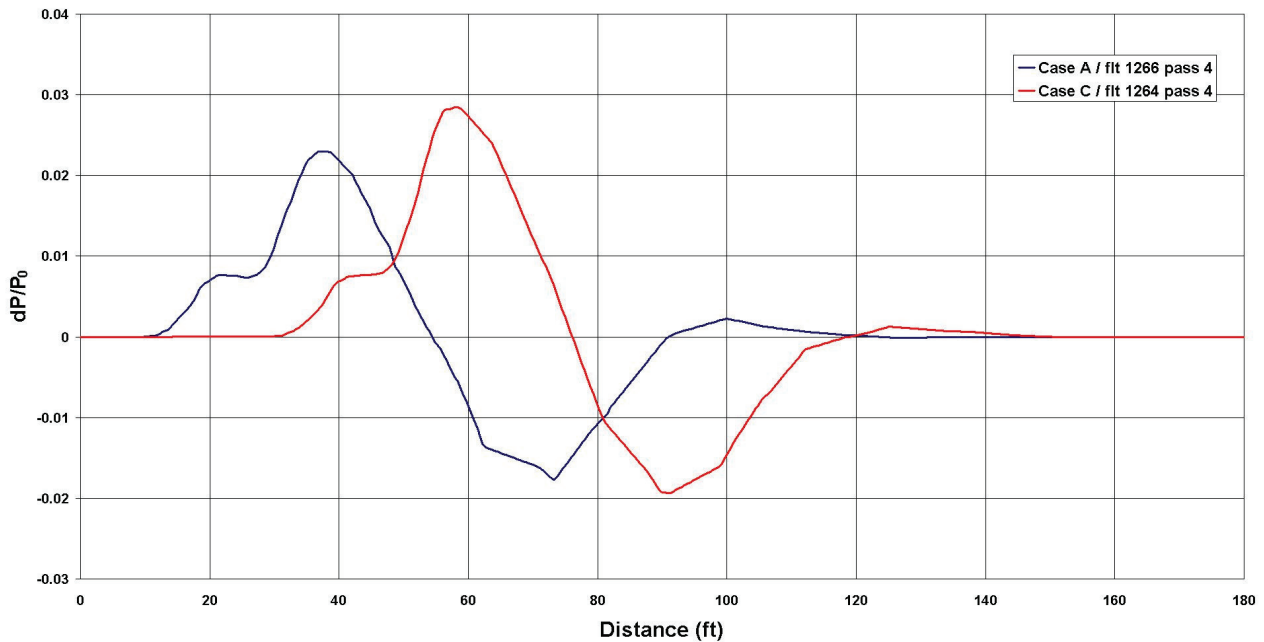


**Figure 8-2. Near-field CFD signatures for Case A and Case C.**

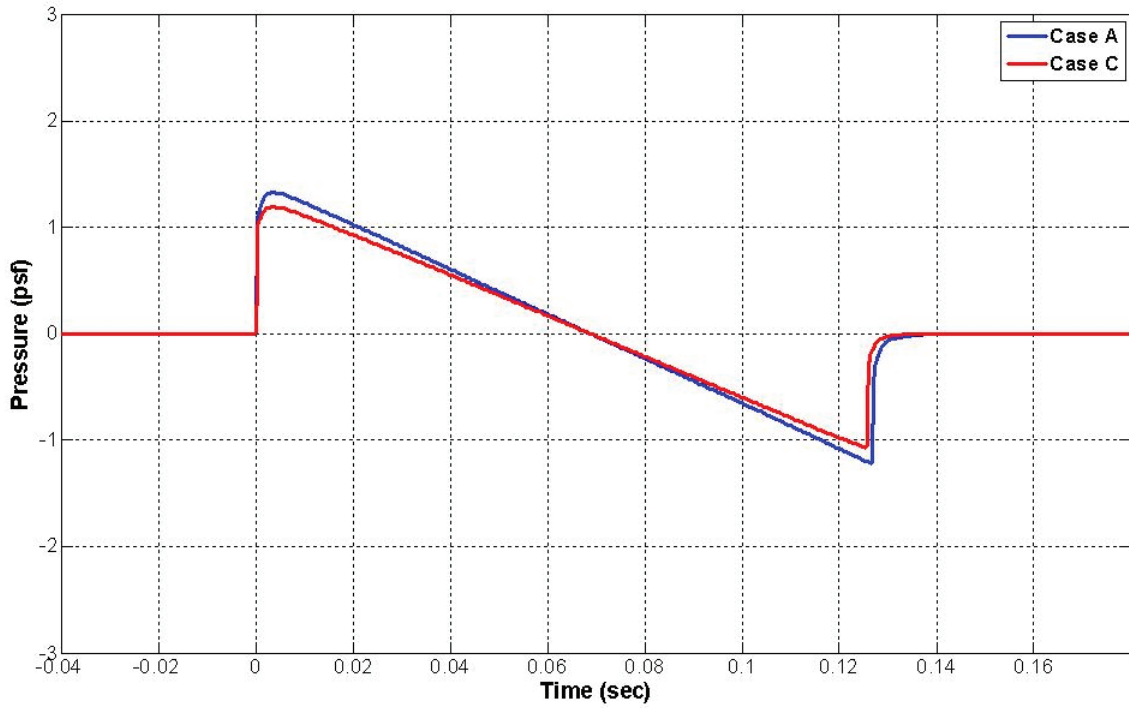


Figure 8-3. Far-field propagated signatures for Case A and C, not accounting for maneuvering aircraft trajectory in the ray tube area calculation

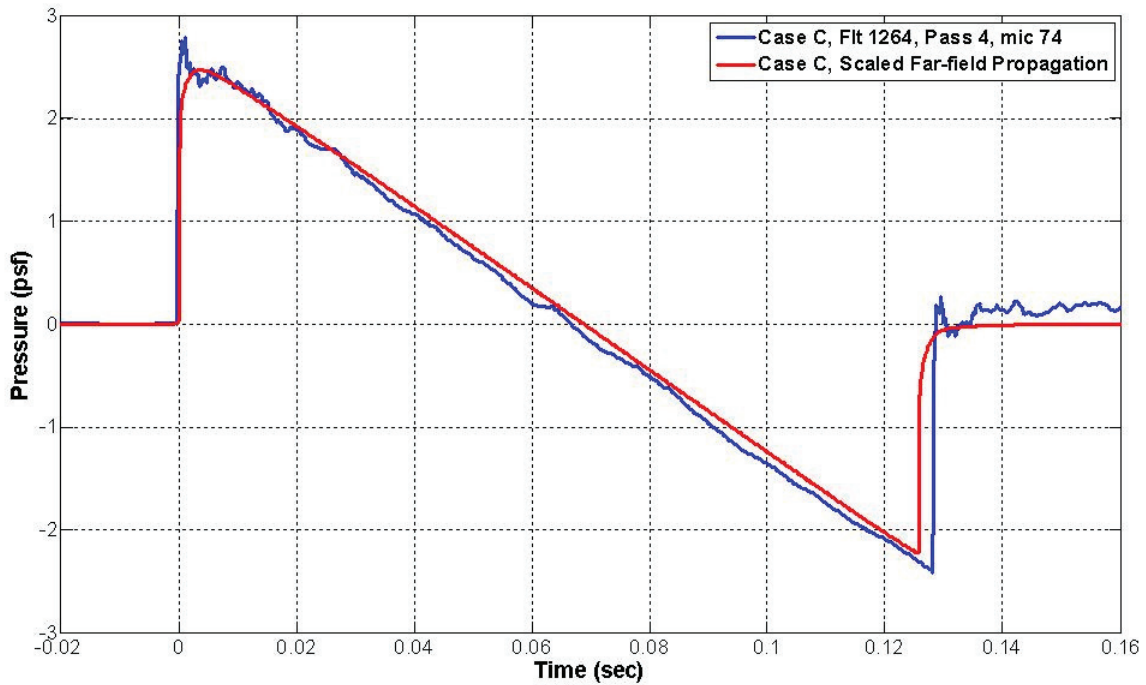


Figure 8-4. Comparison of carpet N-wave for Case C to the scaled far-field signature.

### 8.3 Comparisons with Measurement Data – Alpha

The pressure field in the vicinity of the caustic for case A is shown in Figure 6-5. The x-axis is the dimensionless time,  $\bar{t}$ , the y-axis is the dimensionless distance from the caustic,  $\bar{z}$ , and the solution is color shaded by amplitude of pressure in psf. The size of the domain is 16,384 points in the time-wise direction and 4,000 points in the z-direction. One can see the in-coming N-wave entering at upper left of the domain and reflecting off of the caustic near  $\bar{z} = 0$ . The U-wave exits the domain from the upper right of the domain and the evanescent wave amplitude decays rapidly in the shadow zone. Figure 6-6 is a comparison of microphone #49 from the SCAMP array compared to the lossy Tricomi equation prediction corresponding to  $\bar{z} = 0.98$ . The in-coming N-wave amplitude matches closely to the N-wave from the measured data. However, the period for the measured N-wave is slightly longer, resulting in a U-wave prediction that is also shorter than observed in the measured data. The predicted amplitude of the U-wave is higher than measured at that microphone location. Figure 6-7 is a comparison of microphone #17 compared to the lossy Tricomi equation prediction at  $\bar{z} = 0.18$ . The shape of the focused waveforms is similar, especially for the aft part of the signature. The peak overpressure is slightly overpredicted and the period of the predicted signature is slightly less than the measured period. Figure 6-8 shows a comparison between microphone #1 and  $\bar{z} = -0.22$ . There is good agreement between measured and predicted waveforms in this part of the shadow zone.

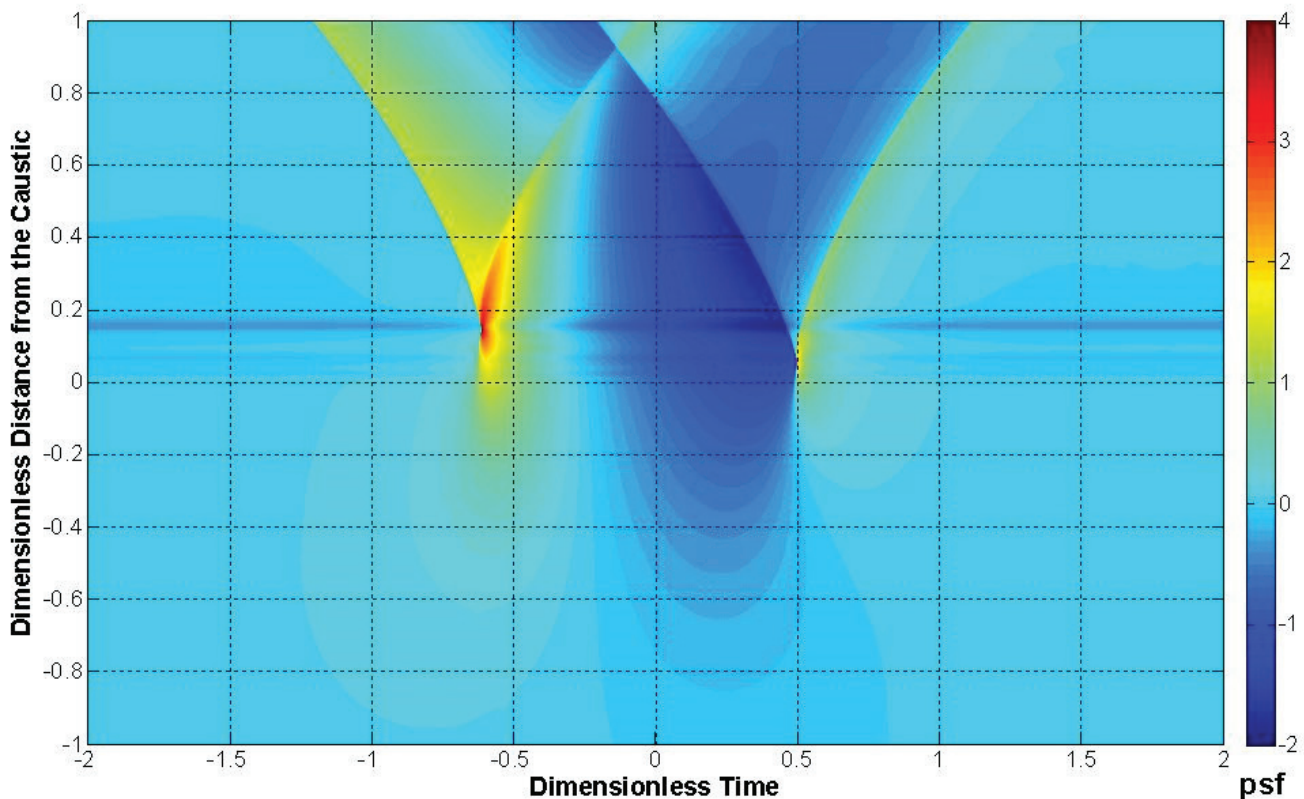


Figure 8-5. Pressure field solution of the Lossy Tricomi Code (Alpha) for Case A.

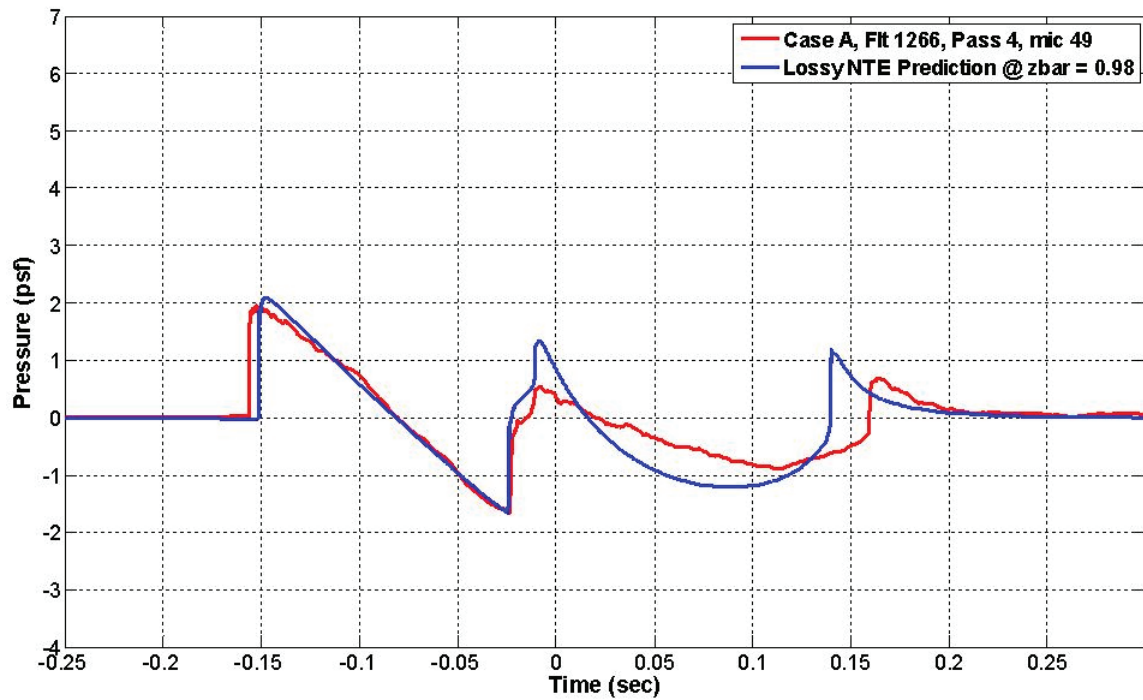


Figure 8-6. Case A comparison of microphone #49 to Lossy Tricomi Code (Alpha) output at  $\bar{z} = 0.98$ .

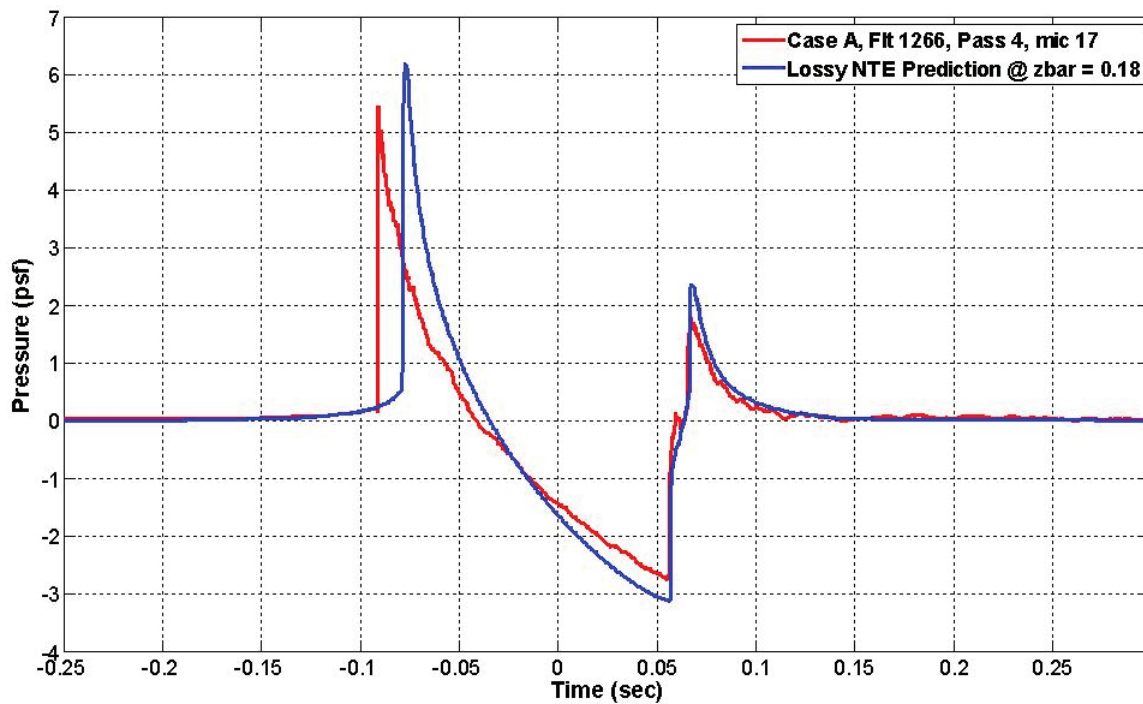
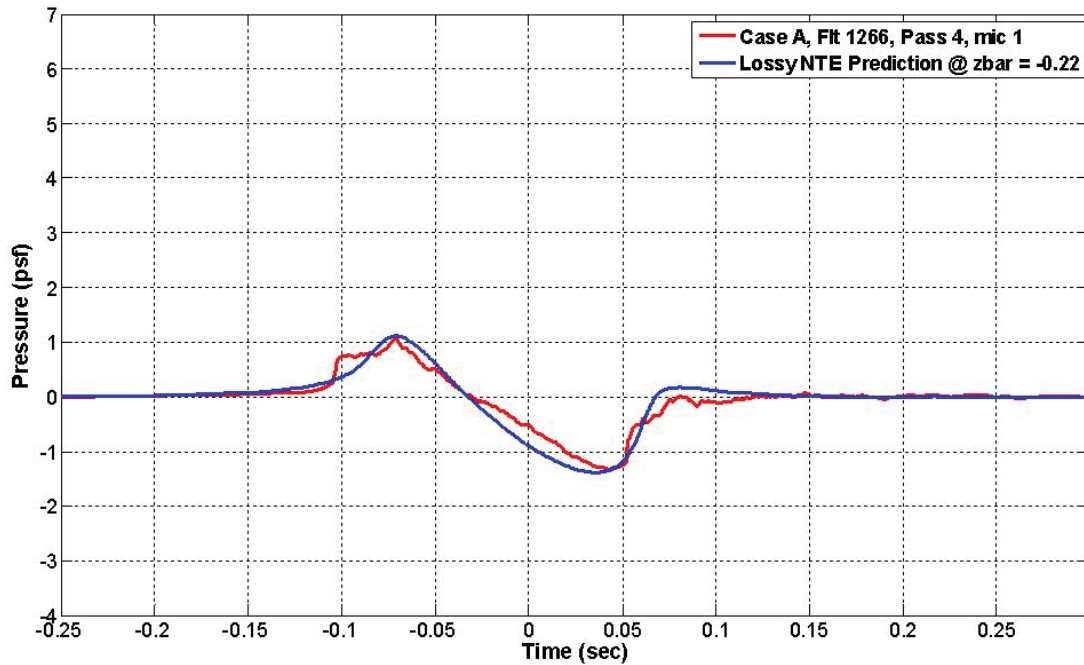


Figure 8-7. Case A comparison of microphone #17 to Lossy Tricomi Code (Alpha) output at  $\bar{z} = 0.18$ .



**Figure 8-8. Case A comparison of microphone #1 to Lossy Tricomi Code (Alpha) output at  $\bar{z} = -0.22$ .**

The pressure field in the vicinity of the caustic for case C is shown in Figure 8-9. The size of the domain is 16,384 points in the time-wise direction and 4,000 points in the  $z$ -direction. Again, one can see the incoming N-wave entering at upper left of the domain and reflecting off of the caustic near  $\bar{z} = 0$ . The U-wave exits the domain from the upper right of the domain and the evanescent wave amplitude decays rapidly in the shadow zone. Figure 6-10 is a comparison of microphone #72 from the SCAMP array compared to the lossy Tricomi equation prediction corresponding to  $\bar{z} = 1.0$ . The in-coming N-wave amplitude and period match well to the N-wave from the measured data. The U-wave amplitude is similar but the predicted period of the U-wave is slightly less than the measured data. Figure 6-11 is a comparison of microphone #60 compared to the lossy Tricomi equation prediction at  $\bar{z} = 0.15$ . The overall shape of the focused waveforms is similar but the first peak for the predicted waveform is much higher than that of the measured waveform. Figure 8-12 shows a comparison in the shadow zone between microphone #50 and  $\bar{z} = -0.55$ . The shape of the predicted and measured waveforms is similar, but the predicted amplitude of the evanescent wave is slightly less than the measured data. Figures 8-10 through 8-12 include a ground reflection factor of 1.9 for the predicted waveforms.

Assessment of the lossy Tricomi code prediction performance is somewhat challenging for several reasons. Atmospheric turbulence effects are not included in the prediction but are clearly visible in the measured data. Additionally, the input to the Tricomi code is contingent on the outputs and results from several predictions and conditions far upstream of the focusing region. The Tricomi code is dependent on the accuracy of the aircraft flight conditions and trajectory, the upper-air and ground weather measurements, and the fidelity of the near-field and far-field acoustic predictions of the in-coming waveform.

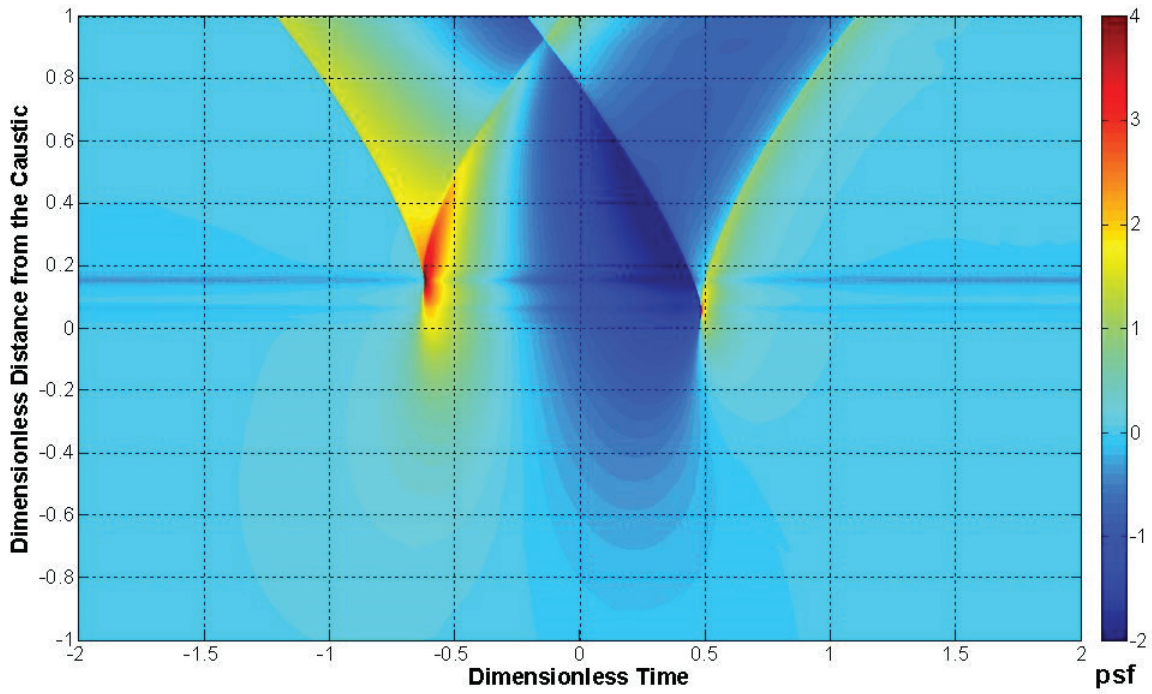


Figure 8-9. Pressure field solution of the Lossy Tricomi (Alpha) Code for Case C.

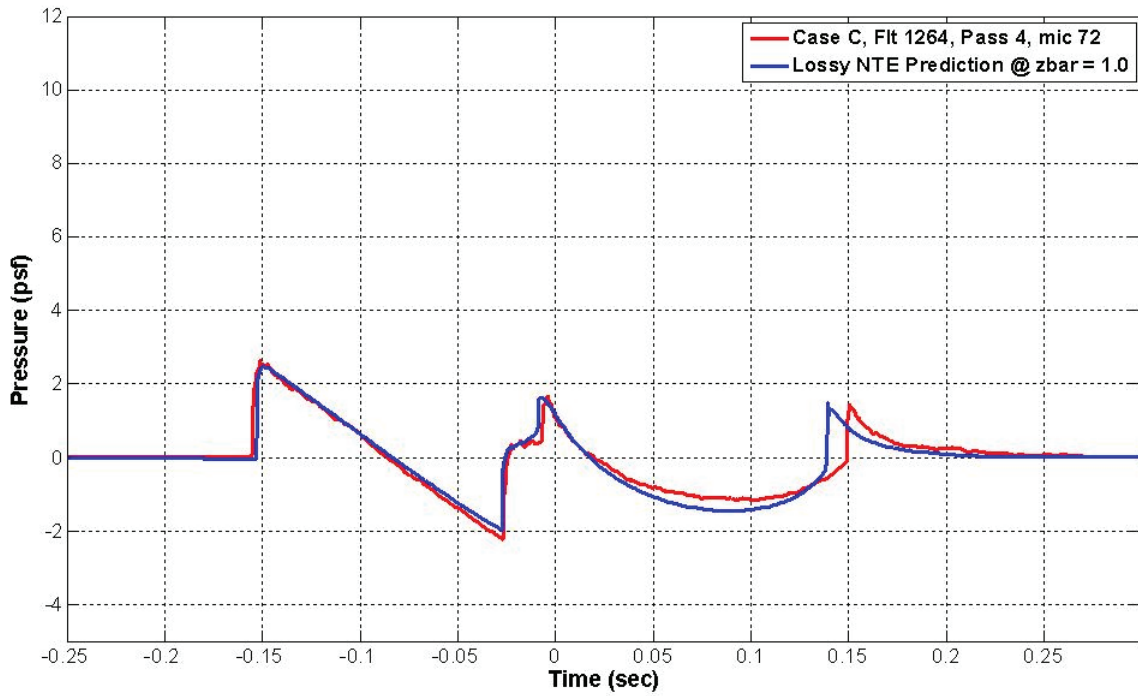


Figure 8-10. Case C comparison of microphone #72 to Lossy Tricomi Code (Alpha) output at  $\bar{z} = 1.0$ .



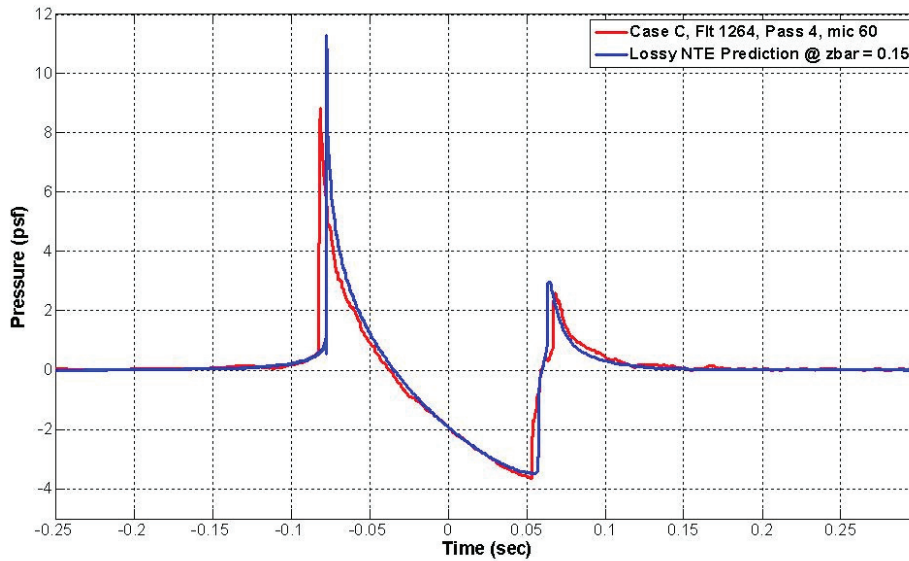


Figure 8-11. Case C comparison of microphone #60 to Lossy Tricomi Code (Alpha) output at  $\bar{z} = 0.15$ .

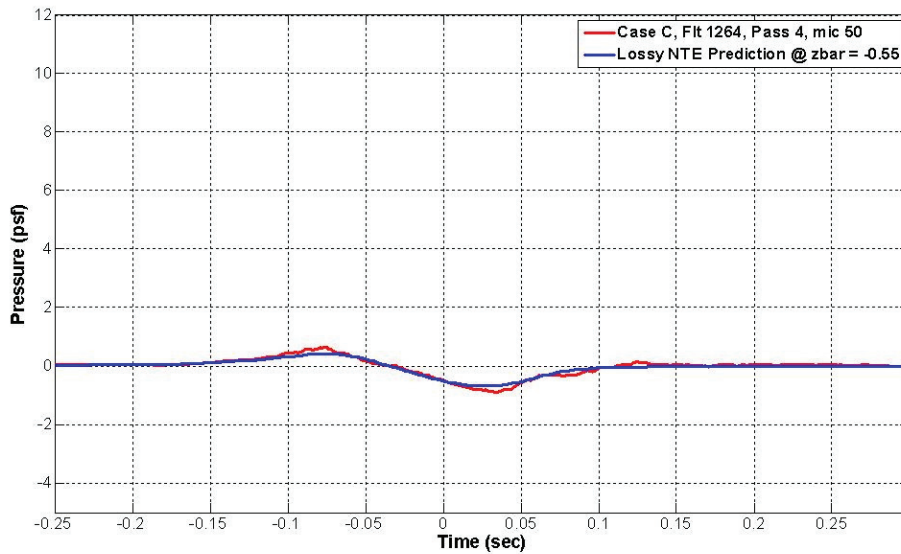


Figure 8-12. Case C comparison of microphone #50 to Lossy Tricomi Code (Alpha) output at  $\bar{z} = -0.22$ .

## 8.4 Recommendations for Future Code Improvements

### 8.4.1 Beta Improvements

The alpha version of the code did not include the effects of wind, and it was recommended that the beta version of the code account for the effects of wind in the vicinity of the caustic. This was incorporated in the beta version.

The computational resources required to run the code can be quite substantial due to the recommended grid density in the z-direction. The time required by the alpha version to compute a solution could take several

days. It was noted that there are many portions of the code that could be parallelized to take advantage of multi-processor platforms. Parallelization was included in the delta version of the code, and led to a substantial improvement in the run time of the code. This improvement was significant enough that other speed improvements considered for beta implementations were not pursued within the scope of SCAMP.

## 8.4.2 Potential Future Improvements

A possible code enhancement includes beginning the iterations at a larger time discretization to allow a rough estimate for the nonlinear solution to be determined. Then, after the lower sampling rate solution converges, the domain can be upsampled in time and the iterations can continue for the higher fidelity solution.

The evanescent part of the solution domain does not require a grid density as high as the hyperbolic region. The z-discretization scheme could possibly be modified to incorporate a dual density grid or some type of non-uniform grid to possibly improve the fidelity of the solution in the illuminated zone. Including this may not, however, necessarily result in a higher fidelity solution for the entire domain due to the numerical challenges associated with such a discretization scheme.

There are still some subtle numerical excursions in locations of the solution where very strong pressure rises exist, specifically in the region of the peak focusing location. Alternative numerical methods and analytical approaches could be attempted to mitigate the numerical artifacts and help better distinguish between the numerical and physical components of the Tricomi solution. Sescu and Abjeh (2010) presented the Tricomi equation in conservative law form and approached the solution of the sonic boom focusing using different mathematical methods than Auger and Coulouvrat. This method warrants consideration for application to the lossy nonlinear Tricomi equation. Sescu's formulation does not include loss mechanisms and the derivation of the conservative form. Therefore, the Tricomi equation would need to include those effects.

Coulouvrat (2011) presents a one-way wave equation that is not limited to a particular propagation angle range (unlike the parabolic method, which is limited to  $\pm 15^\circ$ ). This provides a formulation that is valid  $\pm 90^\circ$  from the main propagation axis and only neglects the backscattered component. This can account for the effects of nonlinearity, diffraction, and heterogeneities making it possible to have a model equation that can include the effects of both sonic boom focusing and atmospheric turbulence. Additionally, this model equation can potentially be used to predict the focusing effects at the lateral edge of the caustic line that intercepts the ground. The capability to predict the sonic boom at that location of the caustic is a capability that none of the Tricomi codes in this report will have. The HOWARD formulation does not include the atmospheric loss mechanisms and should be rederived to include those effects. The work required to augment the HOWARD formulation and develop a propagation code that implements the formulation is well beyond the scope of the current SCAMP effort but should strongly be considered for a future NRA topic.

## Sonic Boom Focus Code – Beta: Comparisons with Measured Data

### 9.1 Beta Overview

As described in sections 5, 7, and 8, recommended improvements were made to three of the sonic boom focus models. These improved beta codes were exercised for as-flown SCAMP conditions and compared with measurement data. Beta comparison for PCBoom is presented in Section 9.2, PCBoom also performs the atmospheric ray tracing and provides inputs to LNTE and NPE, and is described in Section 9.3. The Lossy Nonlinear Tricomi equation (LNTE) is described in Section 9.3, while the Nonlinear Progressive Wave Equation (NPE) is described in Section 9.4.

### 9.2 PCBoom and Gill-Seebass Method – Beta

The input data for the Gill-Seebass focus solution is the input data to PCBoom, as discussed in depth in Section 2. Properties fundamental to sonic boom ray tracing, worth noting with regard to PCBoom, are:

- Sonic boom location requires only the flight Mach number, aircraft heading angle, aircraft flight path (climb/dive) angle, and the atmospheric profile.
- Prediction of the amplitude of the boom also requires the aircraft configuration plus first derivatives of Mach, heading, and flight path angle. This also gives focus location.
- Prediction of focus amplitude also requires the second derivatives of Mach, heading, and flight path angle.

In addition, it must be remembered that ray tracing applies in the short wave limit, with a small wavelength compared to atmospheric gradient scales. The simplifying modeling discussed in Section 2 is necessary for the current analysis and has formed the input data for PCBoom and Gill-Seebass focal zone modeling. The tools used to model the trajectory and atmosphere (modtrj and modatt, respectively) are included in a utility package that is part of PCBoom.

One detail suggested in (Page, 2011) was to replace the Gill-Seebass focused shock shape with one from a modern Tricomi solver. This was not found to be feasible within PCBoom's Guiraud  $R_{cau}$ -based scaling structure. The modern Tricomi solution scaling is based on both  $R_{cau}$  and signature length,  $c_0 T_{ac}$ , which is not compatible with PCBoom's internal algorithms. PCBoom output does, however, contain the necessary boundary condition quantities for input to a Tricomi solver. These quantities are the ground caustic location and a signature along the delta-tangent ray as provided for low-boom configuration analysis in (Plotkin, 2012).

Another key input to PCBoom is the aircraft source F-function or equivalent. The CFD solutions at  $R/L = 3.0$ , as prepared by Boeing and presented in Section 2.4, were used for all PCBoom runs presented in this report. Starting radius is always an issue for application of CFD, so Boeing also provided data at  $R/L = 0.5$ , 1.0, and 2.0. PCBoom runs for the additional radii were performed for Maneuver A. The results for peak pressures and durations were:

$R/L = 3.0$ :  $P = 6.15$  psf,  $T = 151$  msec

- $R/L = 2.0$ :  $P = 6.04$  psf,  $T = 148$  msec

- $R/L = 1.0$ :  $P = 6.10$  psf,  $T = 143$  msec
- $R/L = 0.5$ :  $P = 5.96$  psf,  $T = 138$  msec

There is variation in both peak overpressure and duration, with a consistent reduction in duration at smaller starting radius.  $R/L = 0.5$  is, in general, too small a radius for credible propagation coupling, and  $R/L = 1.0$  (where the duration is about 5 percent shorter than for  $R/L = 3.0$ ) is generally marginal.  $R/L = 3.0$ . CFD data were used for all runs.

Section 9.4 presents a comparison of PCBoom predictions with measured SCAMP foci. Locations are predicted using as-flown trajectories and atmospheres. Focus signatures are predicted using the modeled quantities.

Section 9.5 presents the Tricomi “delta tangent” predictions that form the input boundary conditions to the Lossy Nonlinear Tricomi Equation, whose results are presented in Section 4.

Section 9.6 presents a critical analysis of the PCBoom process.

Comparisons have been made between measured and predicted booms for the flight conditions identified in Section 4. Comparisons made included:

- Peak pressure and signature shape at maximum focus. To coordinate the analysis, modeled PCBoom trajectories were synchronized to place the maximum focus at the measured maximum position.
- The location of the end of the diffraction zone (threshold of overlap of  $N$  and  $u$ ) relative to the focus peak. The peak pressure and general shapes were also of interest.

For reference, the peak pressure for steady flight tangent to the focus condition has also been computed.

Comparisons are shown in the following sequence of figures. For each ground boom measurement, four figures are shown:

- Measured maximum focus signature, generally surrounded by ones just before and just after.
- PCBoom maximum focus prediction.
- A sequence of measured signatures encompassing the end of the diffraction zone.
- PCBoom predicted signature that shows end-of-diffraction-zone threshold overlap.

In each case the peak pressure and the microphone position is noted. The equivalent carpet boom is noted on the predicted end-of-diffraction plot. For the focus boom captured on the sailplane, only the focus signatures are shown.

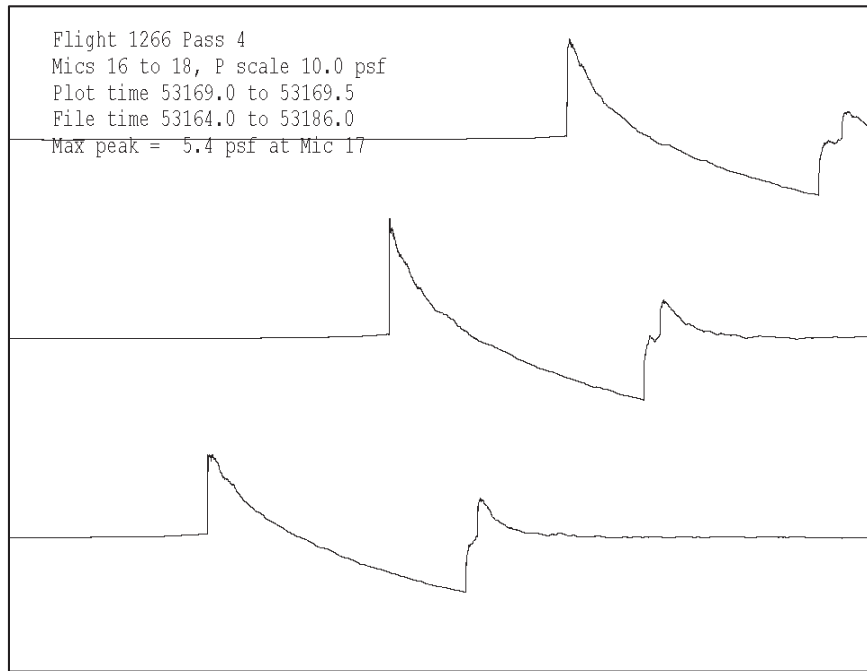


**Figure 9-1. Measured maximum focus, Maneuver A, 1266-4.**

Tac = 53094.000 sec, Phi = 0.00 deg, Xac = 14.13 -0.08 35.75 kft, M= 1.18  
 Pmax, Pmin = 6.19, -0.81 psf, Tg = 53166.656 sec, Xg, Yg = 85.14, -0.98 kft  
 Longitude = -117.408931 deg, Latitude = 35.279246 deg, Zgrnd = 2785.0 feet  
 Lpk = 143.4 dB, Lflt = 121.3 dB, CSEL = 114.0 dB, ASEL = 100.3 dB, Loud = 118.1 PLdB  
 Ray coming from 271.3 degrees, elevation 19.2 degrees

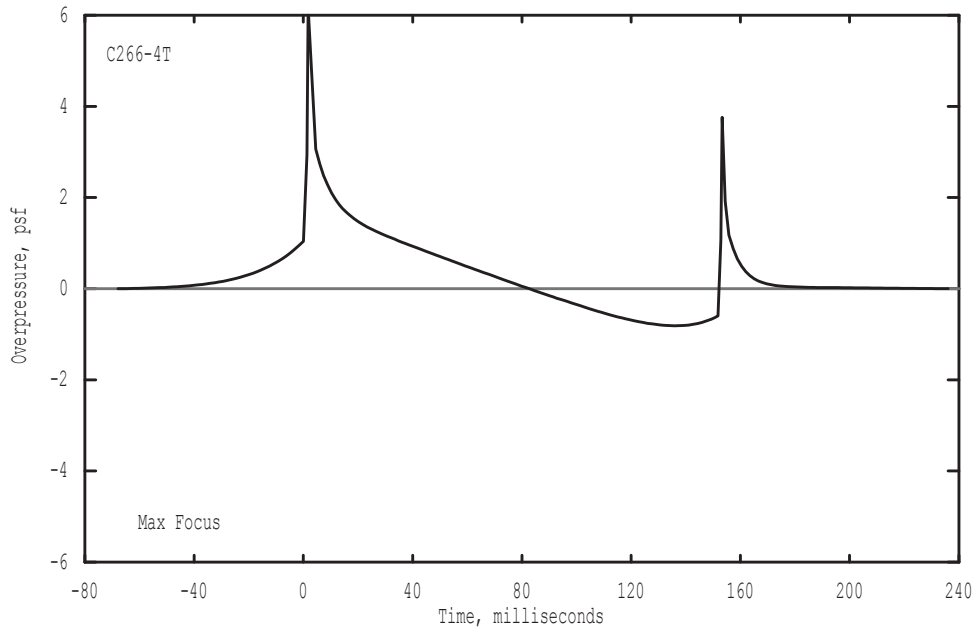


**Figure 9-2. Predicted maximum focus, Maneuver A, 1266-4.**

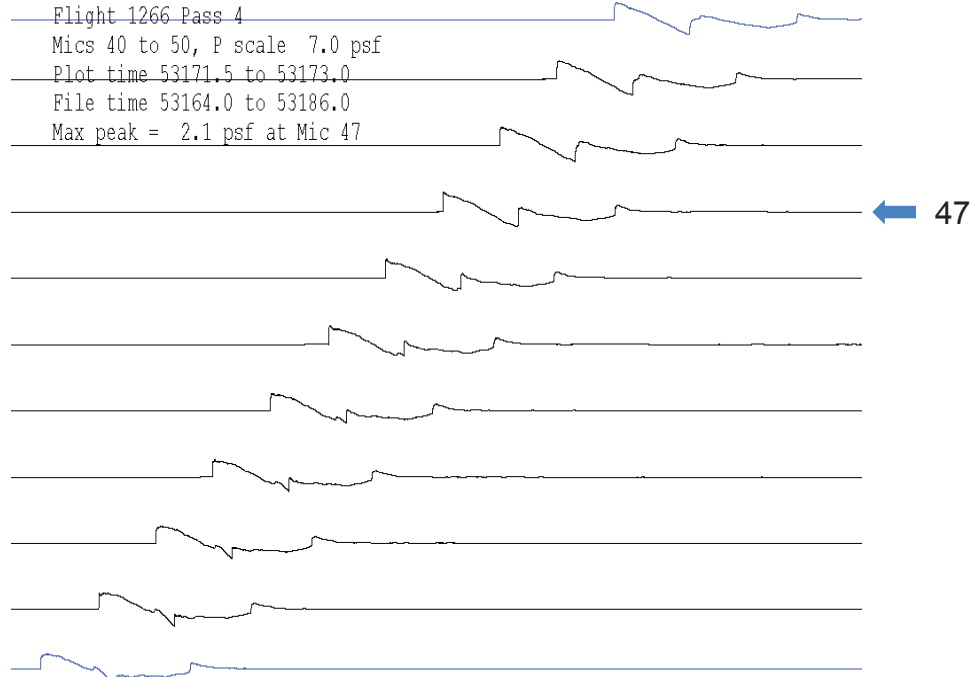


**Figure 9-3. Measured edge of diffraction zone, Maneuver A, 1266-4.**

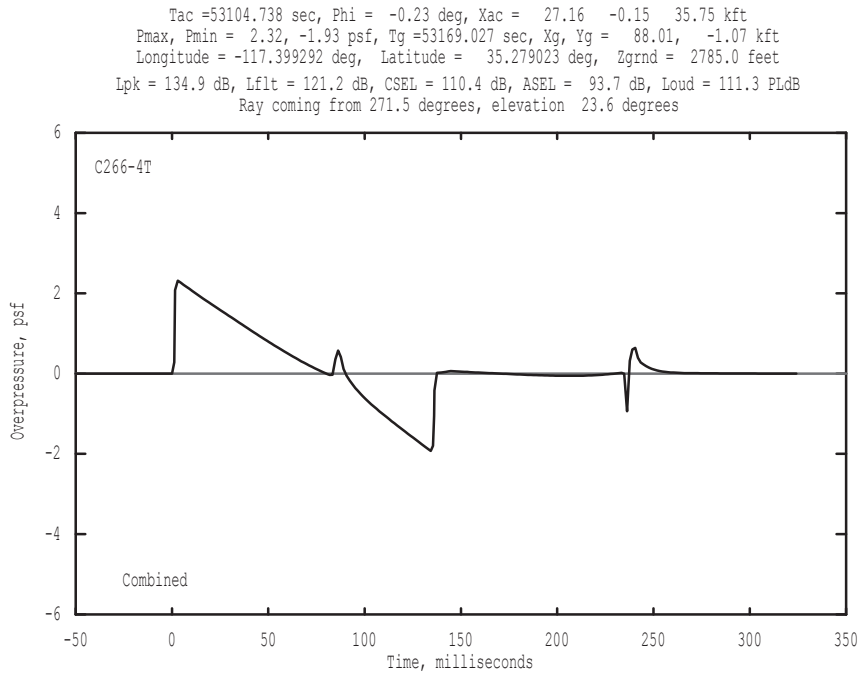


**Figure 9-4. Predicted edge of diffraction zone, Maneuver A, 1266-4. Carpet boom is 1.49 psf.**

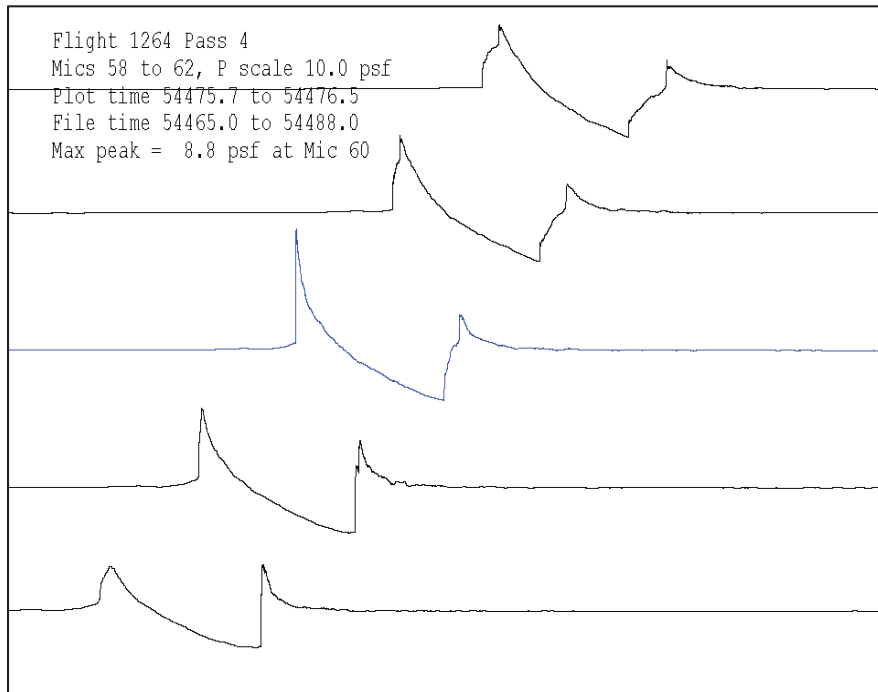


**Figure 9-5. Measured maximum focus, Maneuver C, 1264-4.**

Tac =54415.000 sec, Phi = 5.00 deg, Xac = 27.49 -2.09 43.03 kft, M= 1.24  
 Pmax, Pmin = 7.67, -1.16 psf, Tg =54475.324 sec, Xg, Yg = 77.30, -2.82 kft  
 Longitude = -117.390920 deg, Latitude = 35.278772 deg, Zgrnd = 2785.0 feet  
 Lpk = 145.3 dB, Lflt = 122.7 dB, CSEL = 115.4 dB, ASEL = 102.9 dB, Loud = 120.3 PLdB  
 Ray coming from 268.6 degrees, elevation 36.7 degrees

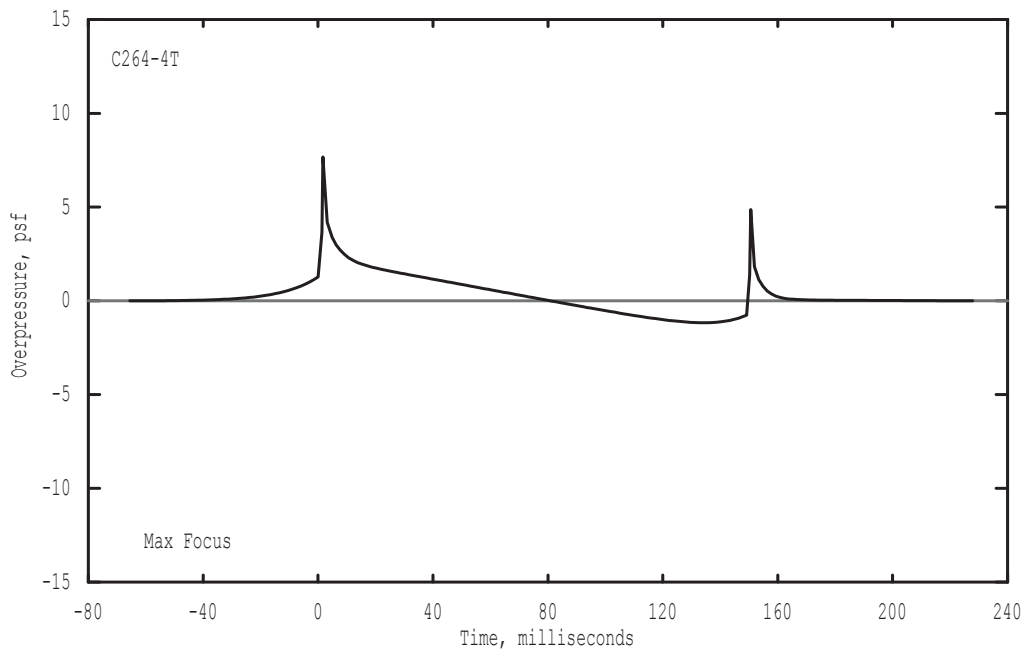


**Figure 9-6. Predicted maximum focus, Maneuver C, 1264-4.**

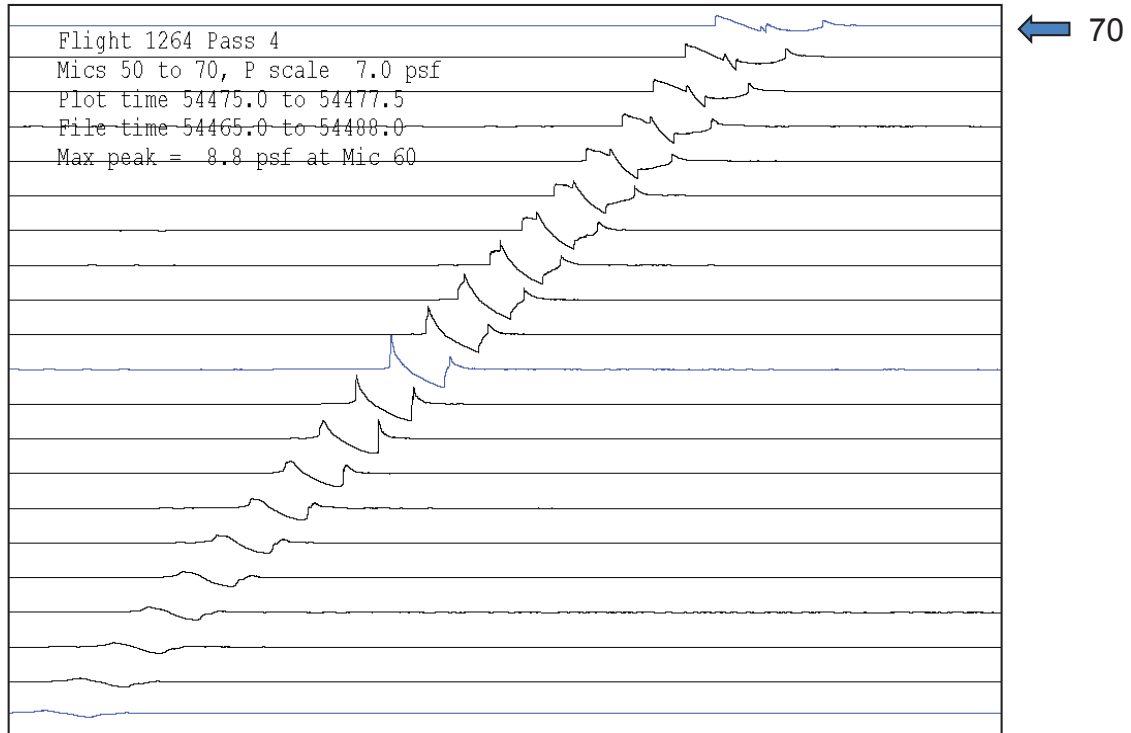


Figure 9-7. Measured edge of diffraction zone, Maneuver C, 1264-4.

Tac = 54425.379 sec, Phi = 5.86 deg, Xac = 40.44 -3.10 40.93 kft  
 Pmax, Pmin = 2.60, -2.15 psf, Tg = 54476.594 sec, Xg, Yg = 79.15, -2.86 kft  
 Longitude = -117.384702 deg, Latitude = 35.278653 deg, Zgrnd = 2785.0 feet  
 Lpk = 135.9 dB, Lflt = 122.1 dB, CSEL = 111.4 dB, ASEL = 95.4 dB, Loud = 113.1 PLdB  
 Ray coming from 267.1 degrees, elevation 43.1 degrees

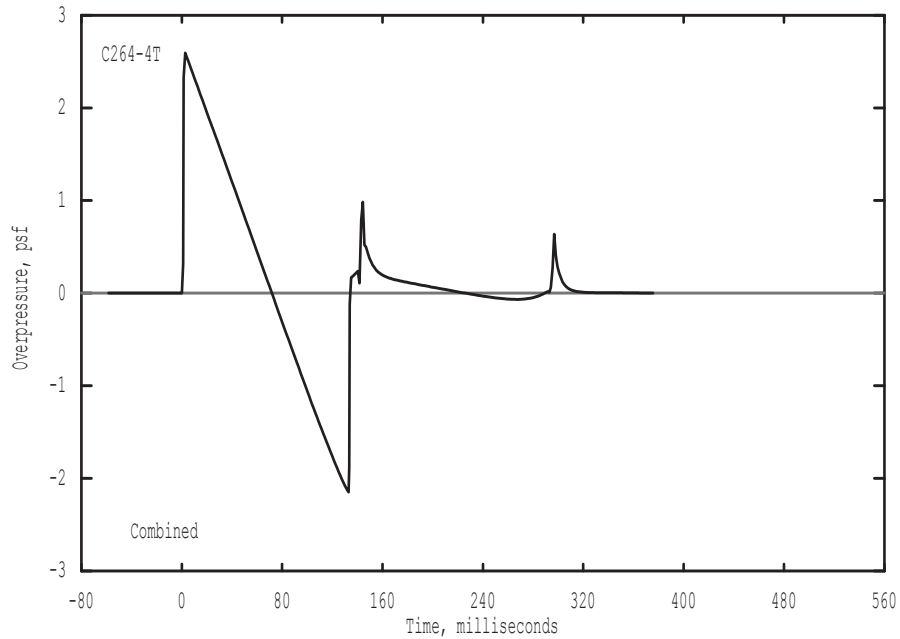
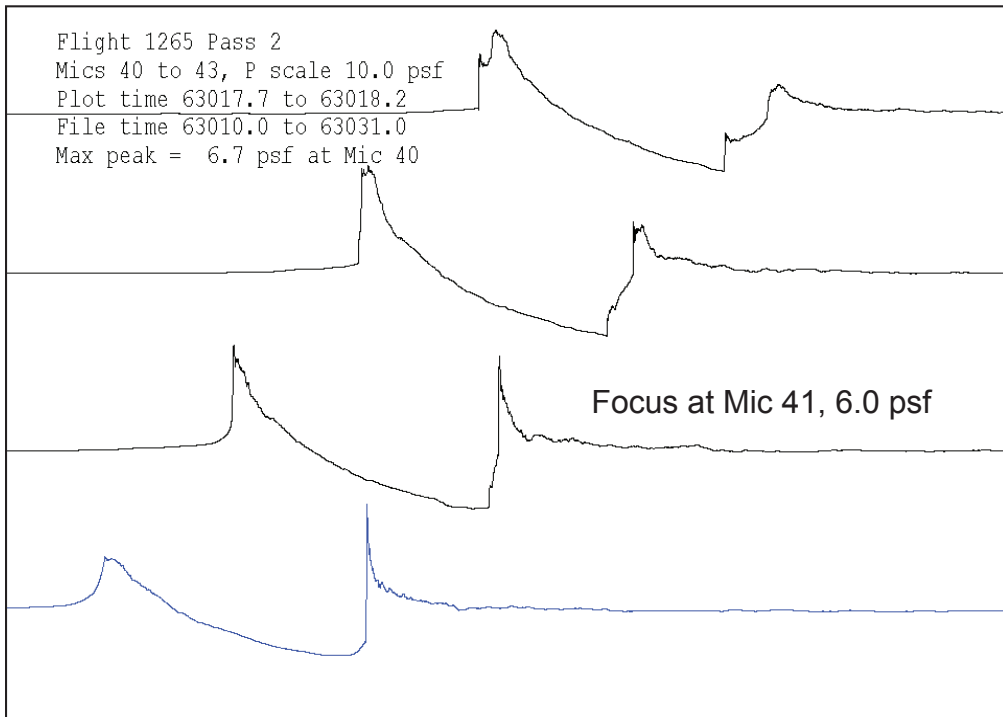


Figure 9-8. Predicted edge of diffraction zone, Maneuver C, 1264-4. Carpet boom is 1.36 psf.





**Figure 9-9. Measured maximum focus, Maneuver D, 1265-2.**

Tac = 62972.000 sec, Phi = 5.00 deg, Xac = 27.53 -1.71 40.73 kft, M= 1.25  
 Pmax, Pmin = 8.29, -1.50 psf, Tg = 63021.207 sec, Xg, Yg = 63.77, -1.62 kft  
 Longitude = -117.398884 deg, Latitude = 35.278697 deg, Zgrnd = 2785.0 feet  
 Lpk = 146.0 dB, Lflt = 123.1 dB, CSEL = 116.2 dB, ASEL = 104.4 dB, Loud = 121.7 PLdB  
 Ray coming from 267.4 degrees, elevation 44.6 degrees

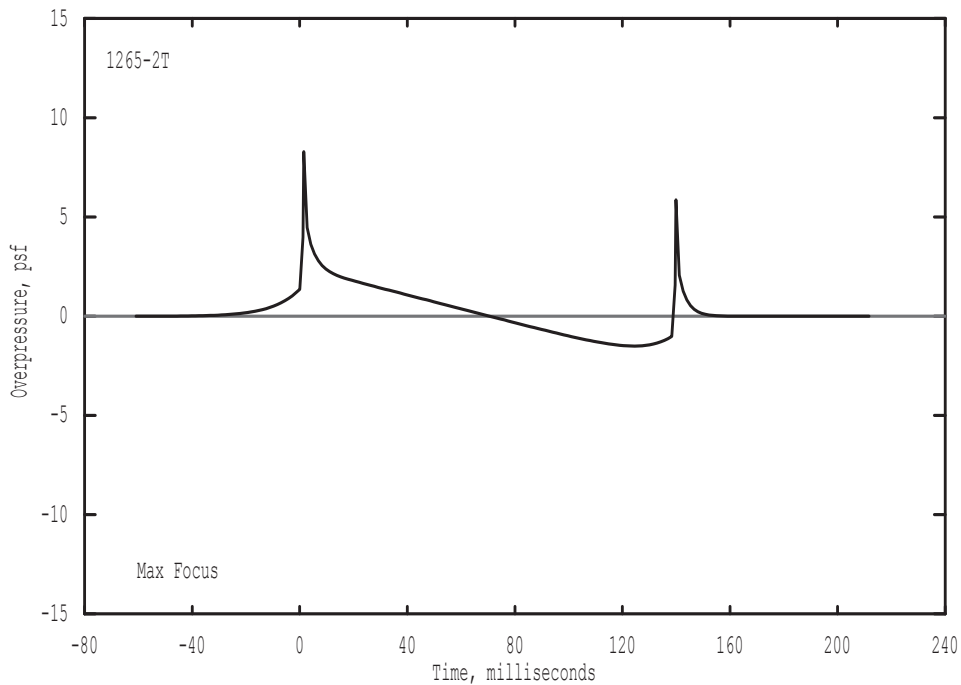


**Figure 9-10. Predicted maximum focus, Maneuver D, 1265-2.**

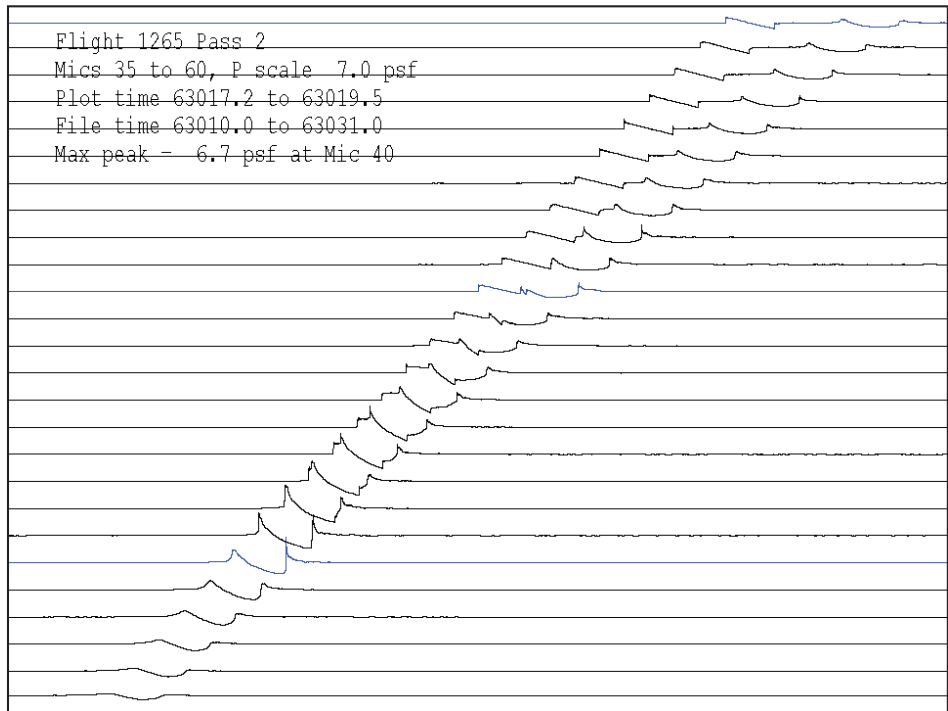


Figure 9-11. Measured edge of diffraction zone, Maneuver D, 1265-2.

Tac = 62981.020 sec, Phi = 6.15 deg, Xac = 38.65 -2.48 37.63 kft  
 Pmax, Pmin = 2.71, -2.29 psf, Tg = 63022.023 sec, Xg, Yg = 65.14, -1.54 kft  
 Longitude = -117.394302 deg, Latitude = 35.278910 deg, Zgrnd = 2785.0 feet  
 Lpk = 136.3 dB, Lflt = 122.6 dB, CSEL = 112.3 dB, ASEL = 96.5 dB, Loud = 114.3 PLdB  
 Ray coming from 265.2 degrees, elevation 51.7 degrees

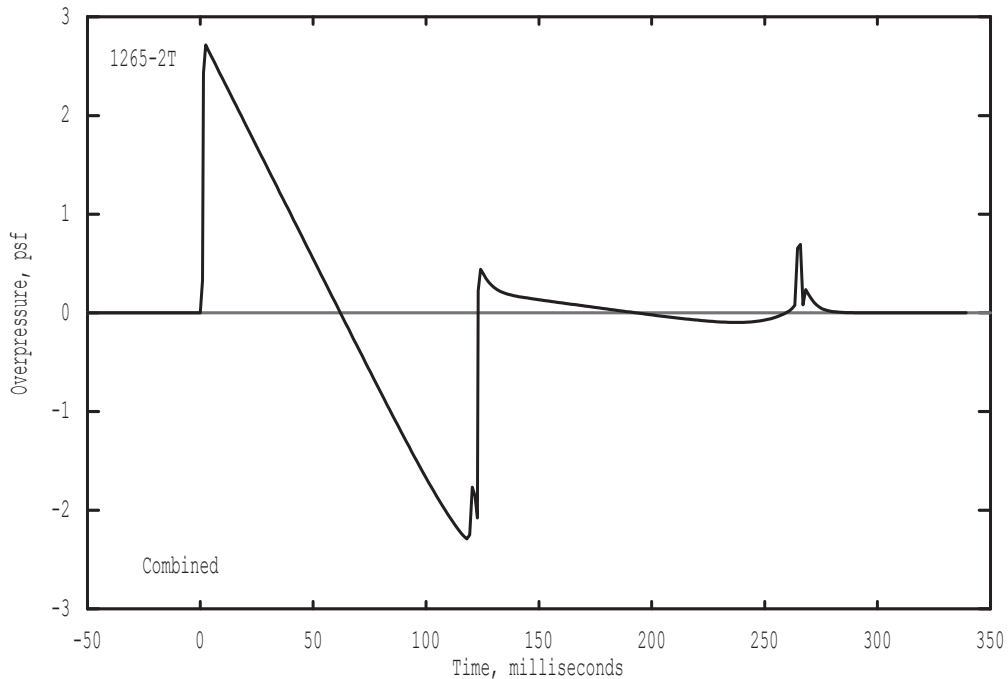
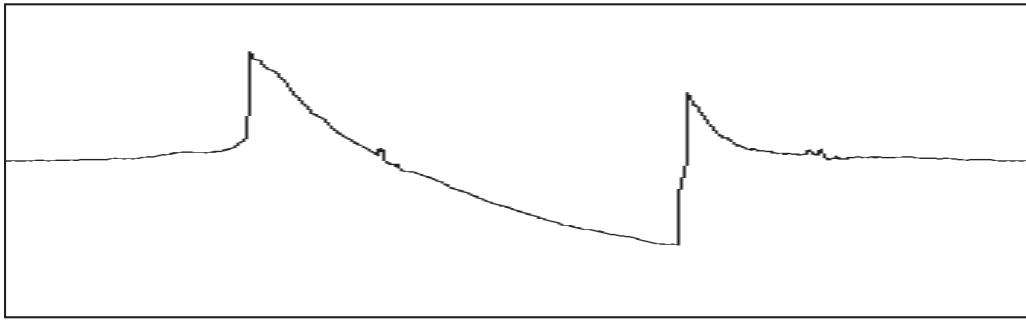
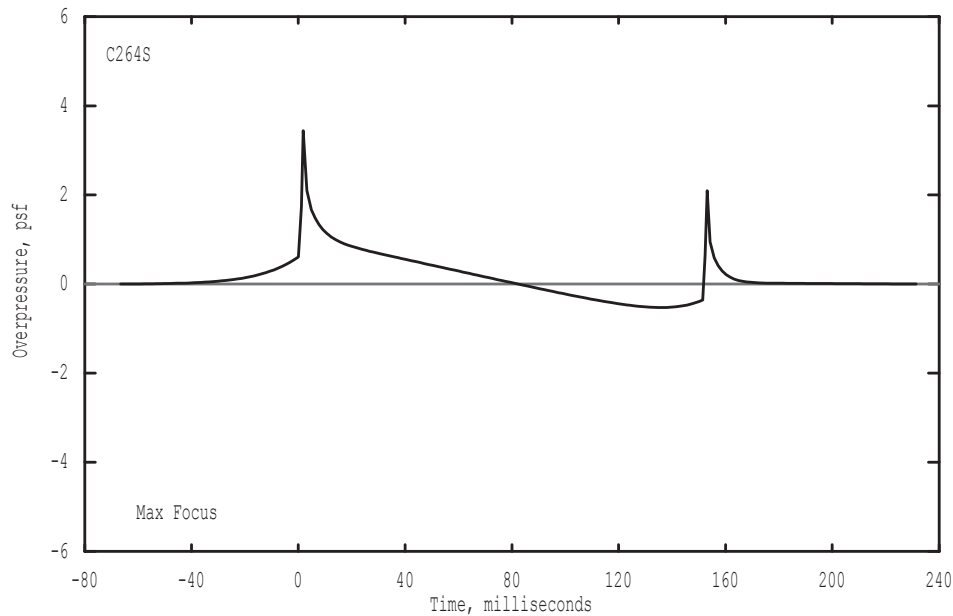


Figure 9-12. Predicted edge of diffraction zone, Maneuver D, 1265-2. Carpet boom is 1.74 psf.



**Figure 9-13. Measured focus at sailplane, Maneuver C, 1264-4.  $P_{max} = 2.06$  psf.**

Tac = 54410.398 sec, Phi = 5.00 deg, Xac = 21.86 -1.66 43.74 kft, M= 1.22  
 Pmax, Pmin = 3.44, -0.53 psf, Tg = 54467.746 sec, Xg, Yg = 70.45, -2.74 kft  
 Longitude = -117.413934 deg, Latitude = 35.278978 deg, Zgrnd = 7680.0 feet  
 Lpk = 138.3 dB, Lflt = 116.4 dB, CSEL = 108.8 dB, ASEL = 94.4 dB, Loud = 111.8 PLdB  
 Ray coming from 268.8 degrees, elevation 34.5 degrees



**Figure 9-14. Predicted maximum focus, Maneuver C, 1264-4, at sailplane.**

The results are summarized in Table 9-1. For the ground booms, where the measurement is known to include the maximum focus, there is reasonable agreement for  $P_{max}$  and the diffraction zone size. The differences are probably due to the actual versus modeled atmosphere and maneuver. The predicted focus shape is reasonable near the bow shock. It is not correct near the rear shock, which is a reasonable outcome since the Gill-Seebass solution is for a single step, and does not account for the length associated with an N-wave. The predicted  $P_{max}$  for the sailplane is larger than the measured value. It is likely that the captured signature was slightly on the shadow side of maximum, rather than the actual maximum. This is borne out by the Tricomi analysis in Section 4.

**Table 9-1. Summary of Comparison between Measured Foci and PCBoom Predictions**

Maneuver	Pass	Pmax		Diffraction Zone	
		Prediction	Measurement	Prediction	Measurement
A	1266-4	5.4	6.2	3750	>2800
C (ground)	1264-4	8.8	7.7	1250	1875
C (sailplane)	1266-4	3.4	2.1	1250	N/A
D	1265-2	6.0	8.3	1250	1250

### 9.3 PCBoom Input Data for LNTE and NPE

The wave field in the vicinity of a caustic is described by the nonlinear Tricomi equation, Equation (9-1). Auger and Coulouvrat (2002) wrote a non-dimensional form of the Tricomi equation for a wave with maximum overpressure  $P_{ac}$  and characteristic duration  $T_{ac}^*$ :

$$\frac{\partial^2 \bar{p}_a}{\partial \bar{z}^2} - \bar{z} \frac{\partial^2 \bar{p}_a}{\partial \bar{\tau}^2} + \mu \frac{\partial^2}{\partial \bar{\tau}^2} \left( \frac{\bar{p}_a^2}{2} \right) = 0 \quad (9-1)$$

where

$$\bar{p}_a = (p - p_0) / P_{ac} \quad (9-1a)$$

$$\bar{\tau} = [t - x(1 - z/R_{cau}) / c_0] / T_{ac} \quad (9-1b)$$

$$\bar{z} = [2 / (c_0^2 T_{ac}^2 R_{cau})]^{1/3} z = z / \delta \quad (9-1c)$$

$$\mu = 2\beta M_{ac} [R_{cau} / (2c_0 T_{ac})]^{2/3} \quad (9-1d)$$

$\delta$  is the characteristic thickness of the diffraction boundary layer around the caustic. The presence of a second length scale,  $c_0 T_{ac}$ , is a significant difference from the Guiraud and Gill-Seebass formulations.

Writing (9-1d) in more conventional aerodynamic notation (but still using  $c$  rather than  $a$  for sound speed),

$$\mu = (\gamma + 1) \frac{P_{ac}}{\rho_0 c_0^2} [R_{cau} / (2c_0 T_{ac})]^{2/3} \quad (9-2)$$

\* Care should be taken to not confuse signature duration  $T_{ac}$  with the notation  $T_{ac}$  used in PCBoom to denote aircraft time. The use of similar (or identical) symbols for different purposes is an unavoidable consequence of remaining consistent with the source literature, but the meaning is generally clear from the context.

Auger and Coulouvrat’s formulation is not part of PCBoom, but is relevant because PCBoom provides the inputs to the focus model described in Sections 6 and 8. A discussion of the boundary conditions and interface is therefore relevant.

Figure 9-15 shows the region associated with the Tricomi equation. The main part of the figure is taken from Auger and Coulouvrat (2002), and has a wave-fixed perspective. A ray, tangent to the caustic at the maximum focus, has been added in red. Notation to the right indicates (notionally) the edge of the diffraction zone at  $\bar{z} = 1$ . This is also the point where PCBoom defines the “Last Geometric Signature,” as described by Plotkin (1976) and Page (2010), representing its ray-oriented boundary condition. In PCBoom the Gill-Seebass solution for a step shock is applied to each shock in the last geometric signature, scaling the amplitude and shape according to Guiraud’s similitude. For modern Tricomi solvers, the boundary condition is the full incident signature at the top edge of the region, indicated by the N-wave in Figure 9-15.

Figure 9-16 shows the focal zone and its relation to the overall boom ray field. The Tricomi solution region is shown in the lower left, along with a “Caustic tangent ray” that is equivalent to the ray shown in Figure 9-15. A second ray, denoted “ $\delta$  tangent ray,” tangent to the top of the Tricomi region, is shown in Figure 9-16. The boundary condition for the Tricomi method presented in Section 9.4 is the “Incoming signature” shown along that ray at the top of the Tricomi region. This is different from the “Last Geometric Signature” boundary condition that PCBoom uses internally for the Gill-Seebass solution.

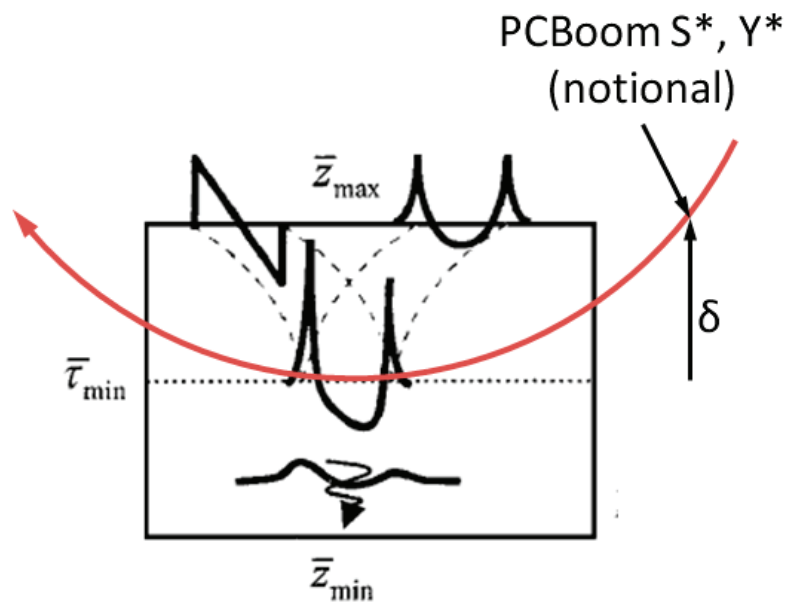


Figure 9-15. Focal zone as defined by the Tricomi Solution region, with tangent ray shown.

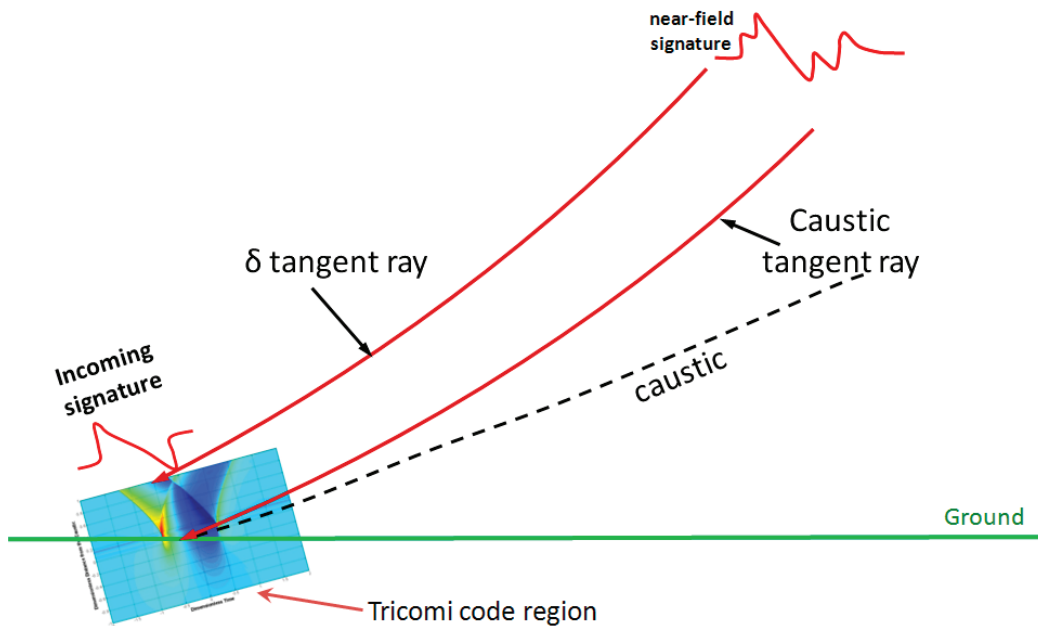


Figure 9-16. Rays, caustic, and focal zone.

The NPE method presented in Section 7 is different from the Tricomi methods, in that it does not trace rays, define a caustic, then apply a local diffraction solution. Rather, it propagates an initial wavefront and lets the physics evolve. It is also different in that the initial wavefront cannot contain the caustic, so propagation must begin at a location before formation of the caustic. Since PCBoom wavefronts are generated for supersonic flight, and the caustic for a transition focus begins at Mach 1, NPE requires a virtual initial wave that will evolve into an equivalent of the actual caustic.

There are thus three types of interfaces that PCBoom must provide for focus solution:

1. For Gill-Seebass, a last geometric signature at distance  $S^*$ , as described in (Witham, 1952) and (Plotkin, 1976). This is built in, and does not need any further attention.
2. For the Tricomi solution (presented in Section 9-4), in a solution along the  $\delta$  tangent ray (sketched in Figure 9-16),  $\delta$  is computed from the relations associated with Equation 3-6, and requires the ray/caustic curvature  $R$  and the wave duration  $T_{ac}$ .  $R$  is available from PCBoom's focus solution, and (because nonlinear steepening is very weak near the ground)  $T_{ac}$  can be taken from either the Gill-Seebass solution or the Last Geometric Signature. The FOBoom module of PCBoom was modified to compute and output those parameters. Once  $\delta$  is established, an interactive tool, raycau, was prepared to identify the correct ray. Because the Tricomi solver, presented in Section 8, includes molecular absorption losses, the signature must include losses. This is obtained by using the Burgers solver, PCBurg that is part of the PCBoom package (Page, 2010).
3. The NPE method requires a virtual wavefront uptrack of the caustic. PCBoom's role is to establish the dimensional quantities  $R_{can}$ ,  $c_0 T_{ac}$  and  $M_{ac}$  such that the NPE can be run for the correct nonlinear/diffraction ratio  $\mu$  and results scaled to match.

The PCBoom runs described above establish the basic ray tracing, and the signatures (Figures 9-2, 9-6, 9-10, and 9-14) are the Gill-Seebass maximum focus solutions for ground foci A, C, and D and sailplane focus C.

They define the geometric caustic. NTE requires as input a lossy signature on the delta-tangent ray, as defined by Figures 9-15 and 9-16. The information necessary for the NTE interface, 2 above, is contained in the updated (beta version) FOBoom .out and .age files.

Program raycau reads the .out and .age files and generates a ray diagram showing the caustic and the delta-tangent ray. Figure 9-17 is the ray diagram for Maneuver A ground focus. Figure 9-18 shows, for reference, the thin shock waveform at the edge of the Tricomi region, and Figure 9-19 shows the lossy waveform at the edge of the Tricomi region. The lossy waveform, generated by the PCBurg component of PCBoom, is the input to the lossy NTE. Figures 9-20 through 9-28 show the corresponding ray diagrams for Maneuvers C and D ground foci and Maneuver C sailplane focus. The user can adjust the focus point along the caustic and the tangent ray, but the program is set up to by default select the focus point closest to the ground and the tangent ray that passes closest to  $\delta$  from the ground focus. In the case of the sailplane, the “ground” was defined to be the sailplane’s altitude at the time of the boom, and a ground reflection factor of 1.0 (rather than the usual 1.9) was specified.

Figure 9-29 shows the header and first few data lines of the PCBurg output file that forms the input to Lossy NTE. The text at the top provides all necessary parameters, including the ground intercepts of the focus ray and the delta-tangent ray. Those points correspond to  $zbar = 0$  and 1, respectively, so that the NTE solution can be mapped to physical ground positions.

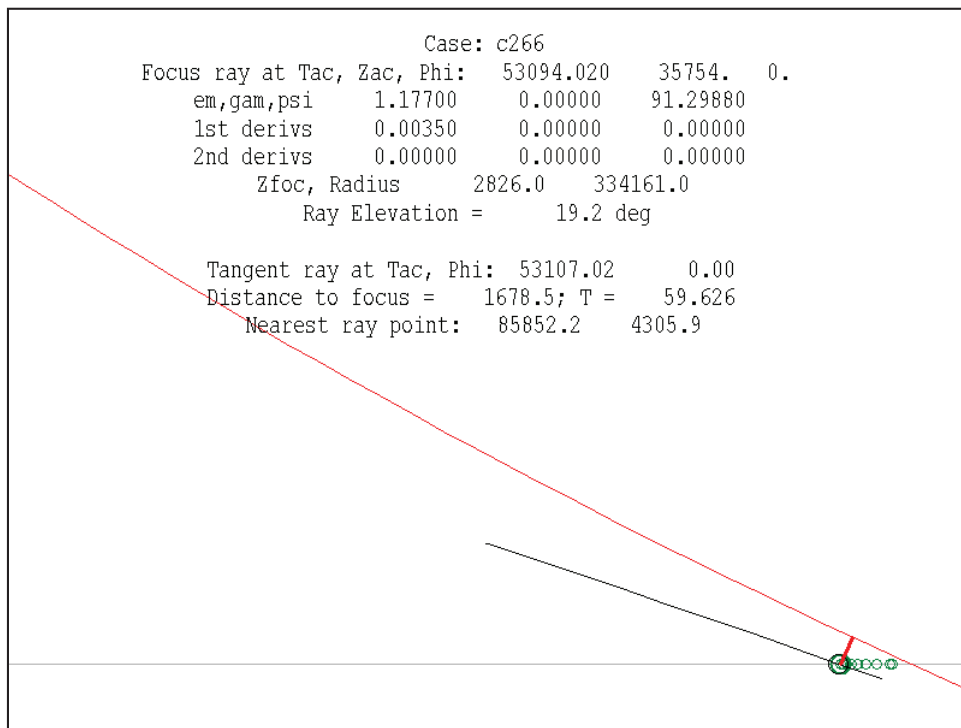
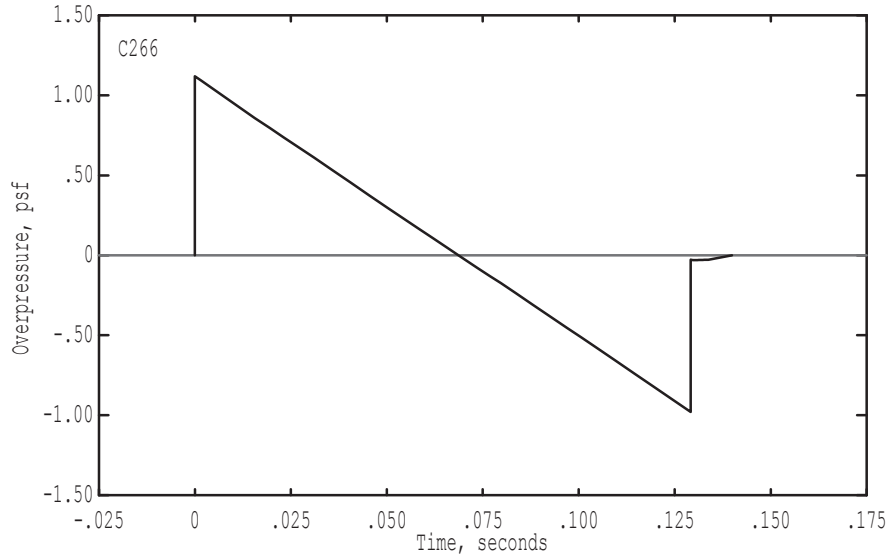


Figure 9-17. Ray and caustic geometry for Maneuver A ground focus.

Tac = 53107.02, Phi = 0.0: Thin Shock Solution, Free Field  
 T = 60.27; Z = 4000. feet, Pmax = 1.119 psf; Zac = 35754. feet  
 Press Enter to move down; Backspace to move up  
 Press B or b to begin Burgers evolution from this point



**Figure 9-18. Thin shock solution for  $\delta$  tangent ray for Ground Focus A.**

T = 60.27, Z = 4000.; Tac = 53107.02, Phi = 0.0, C266.ssg  
 Refl = 1.0, SampRate = 102400, Rise = 0.00009, Thick = 0.00062; Filtered  
 RH = 44.%, Temperature = 292.2 deg K, C266.age  
 Pmax = 0.98, ESEL = 113.83, CSEL = 102.77, ASEL = 88.65, PLdB = 106.17

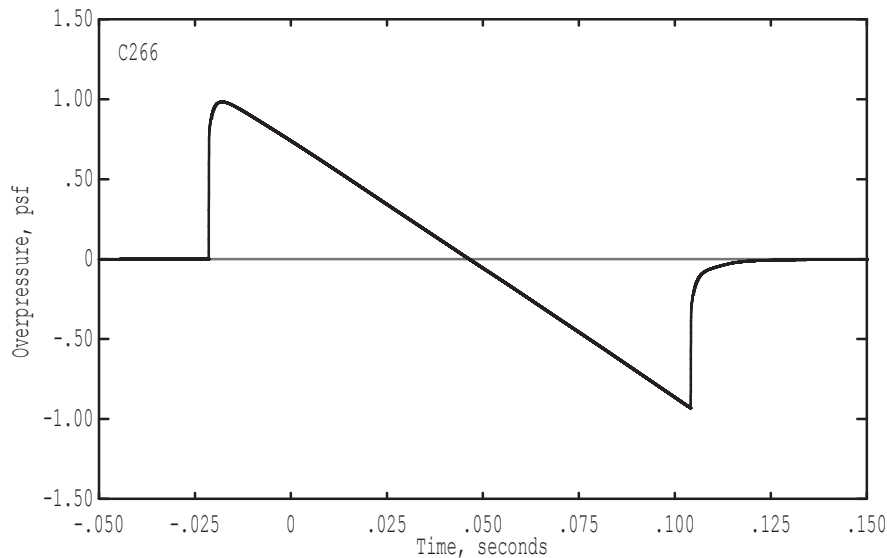


**Figure 9-19. Lossy solution for  $\delta$  tangent ray for Ground Focus A.**



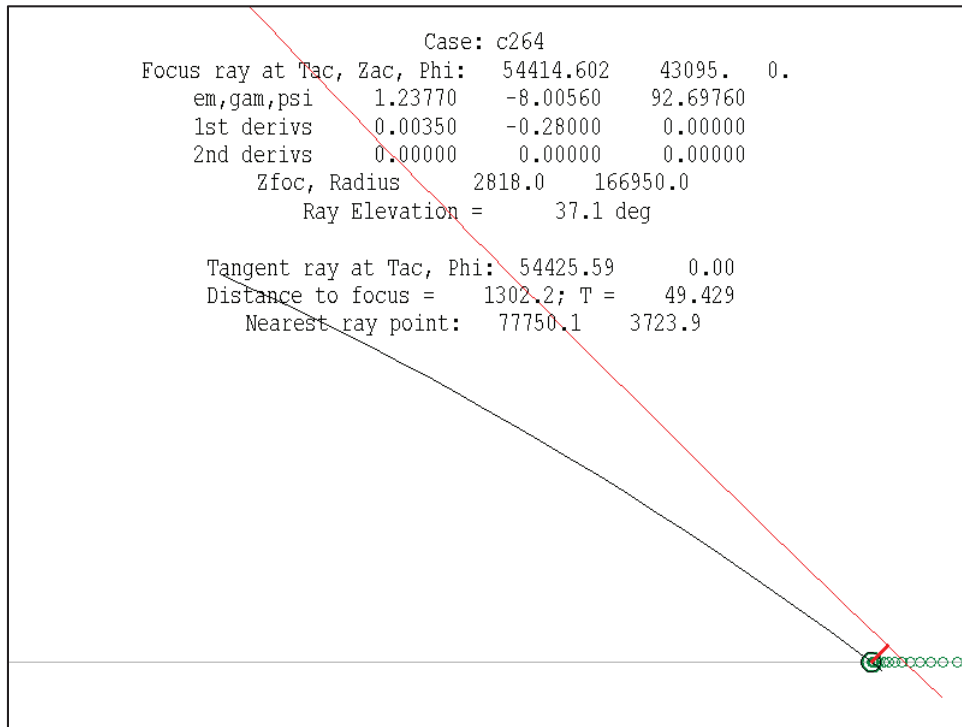


**Figure 9-20. Ray and caustic geometry for Maneuver C ground focus.**

Tac = 54425.59, Phi = 0.0: Thin Shock Solution, Free Field  
 T = 49.07; Z = 4000. feet, Pmax = 1.344 psf; Zac = 40878. feet  
 Press Enter to move down; Backspace to move up  
 Press B or b to begin Burgers evolution from this point

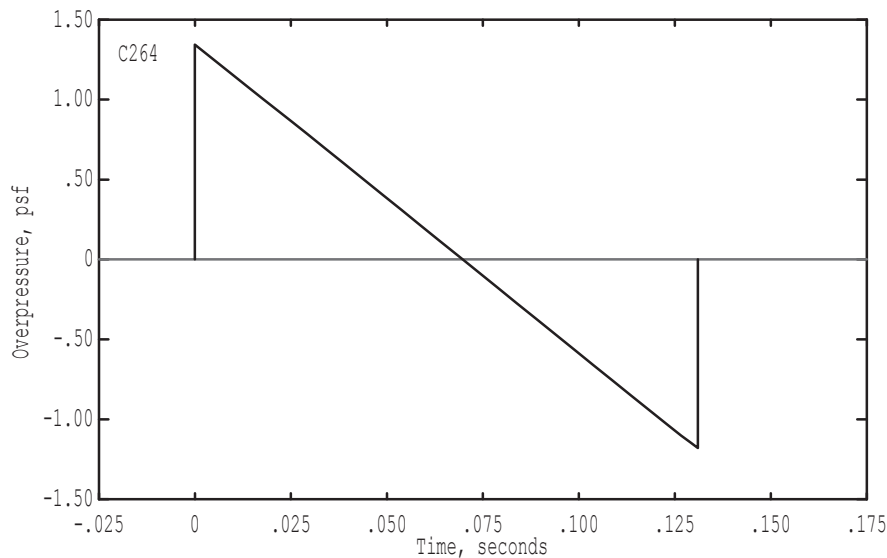


**Figure 9-21. Thin shock solution for  $\delta$  tangent ray for Ground Focus C.**

T = 49.07, Z = 4000.; Tac = 54425.59, Phi = 0.0, C264.ssg  
 Refl = 1.0, SampRate = 102400, Rise = 0.00009, Thick = 0.00015; Filtered  
 RH = 36.%, Temperature = 285.0 deg K, C264.age  
 Pmax = 1.19, ESEL = 115.59, CSEL = 104.68, ASEL = 91.32, PLdB = 108.86

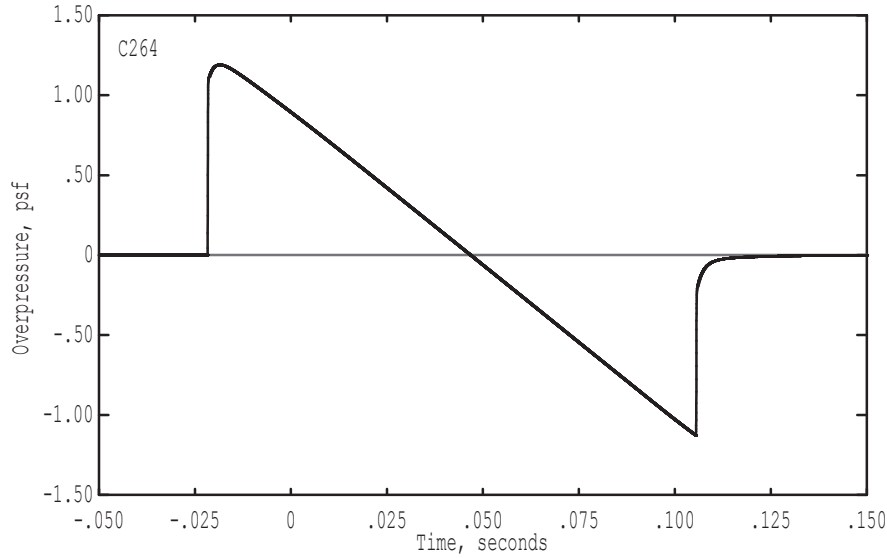


Figure 9-22. Lossy Solution for  $\delta$  tangent ray for Ground Focus C.

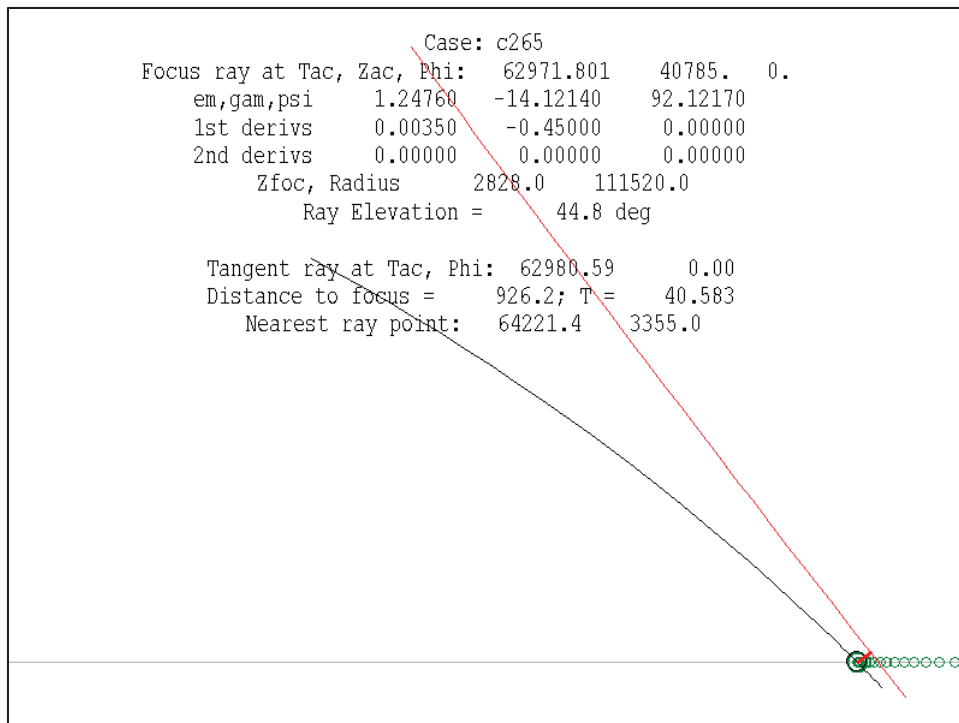
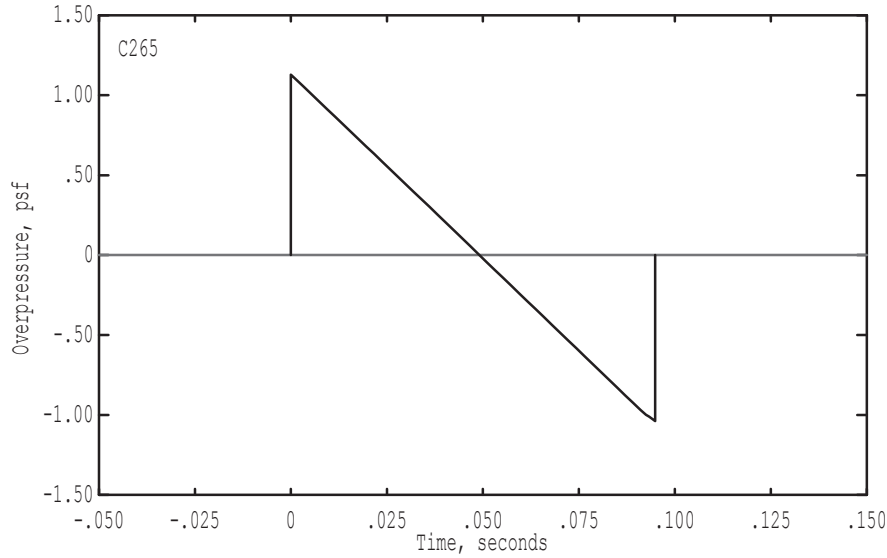


Figure 9-23. Ray and caustic geometry for Maneuver D ground focus.

Tac = 62980.59, Phi = 5.0: Thin Shock Solution, Free Field  
 T = 41.14; Z = 3000. feet, Pmax = 1.129 psf; Zac = 37788. feet  
 Press Enter to move down; Backspace to move up  
 Press B or b to begin Burgers evolution from this point



**Figure 9-24. Thin shock solution for  $\delta$  tangent ray for Ground Focus D.**

T = 41.14, Z = 3000.; Tac = 62980.59, Phi = 5.0, C265.ssg  
 Refl = 1.0, SampRate = 102400, Rise = 0.00011, Thick = 0.00038; Filtered  
 RH = 26.%, Temperature = 293.2 deg K, C265.age  
 Pmax = 1.00, ESEL = 113.03, CSEL = 103.55, ASEL = 89.49, PLdB = 106.87

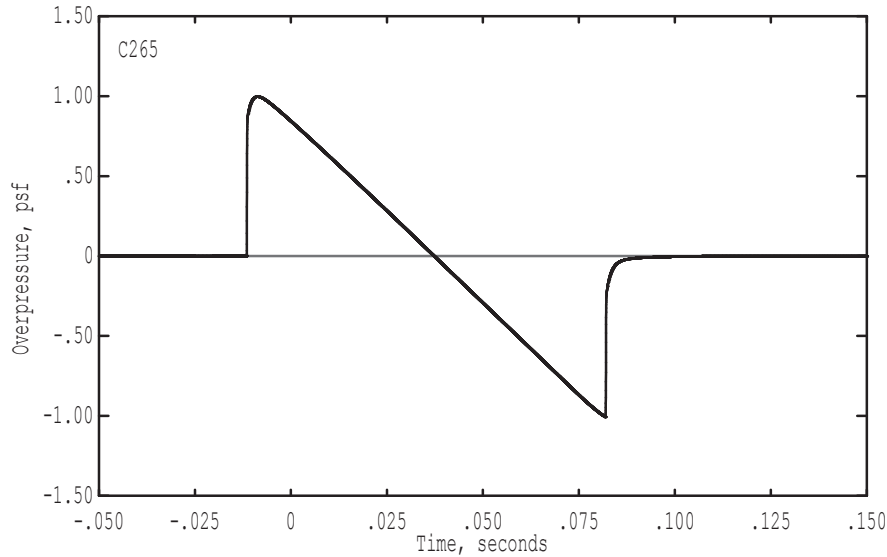


**Figure 9-25. Lossy Solution for  $\delta$  tangent ray for Ground Focus D.**

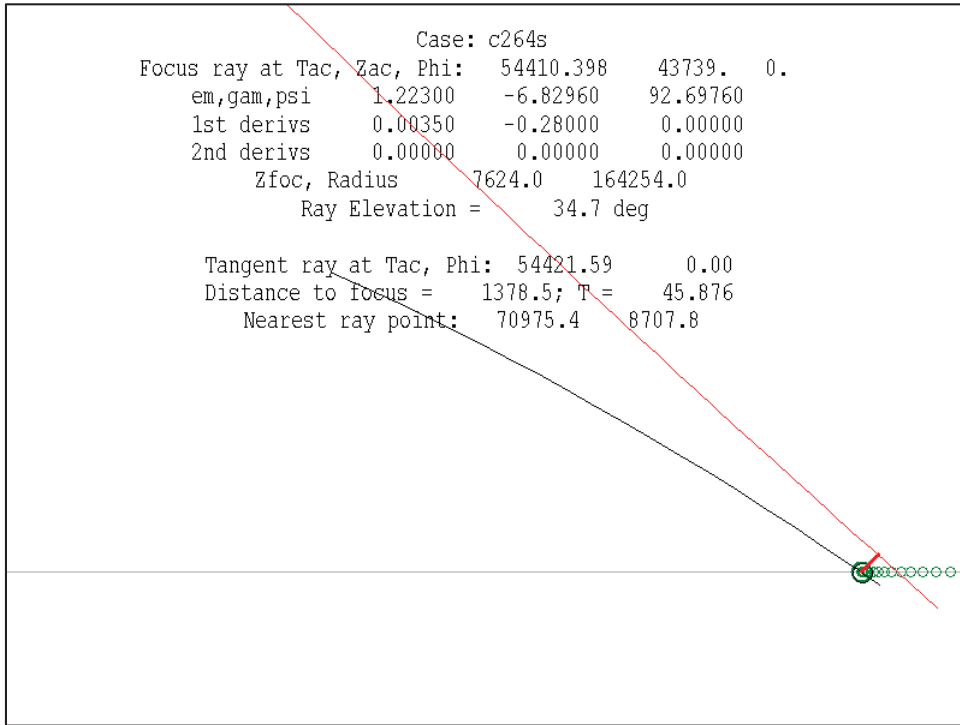


Figure 9-26. Ray and caustic geometry for Maneuver C sailplane focus.

Tac = 54421.59, Phi = 0.0: Thin Shock Solution, Free Field  
T = 45.48; Z = 9000. feet, Pmax = 1.242 psf; Zac = 41775. feet  
Press Enter to move down; Backspace to move up  
Press B or b to begin Burgers evolution from this point

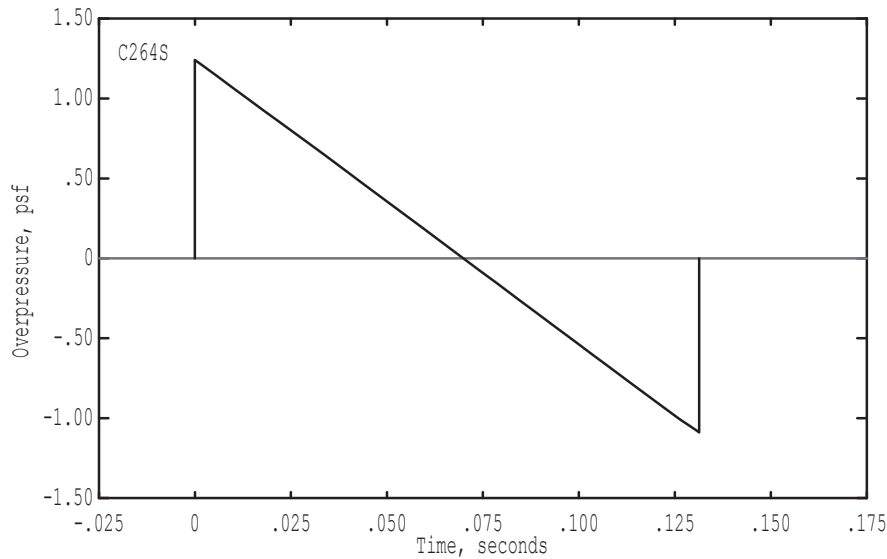
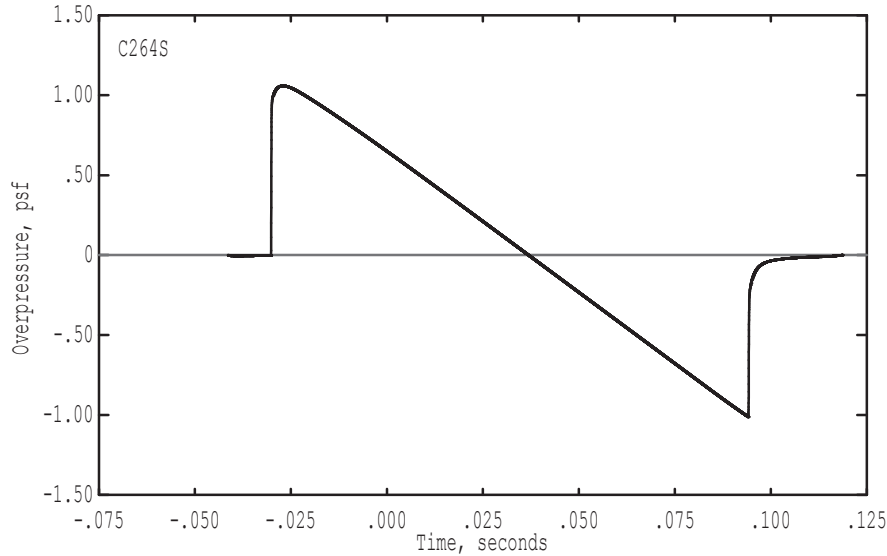


Figure 9-27. Thin shock solution for  $\delta$  tangent ray for Sailplane Focus C.

T = 45.48, Z = 9000.; Tac = 54421.59, Phi = 0.0, C264S.ssg  
 Refl = 1.0, SampRate = 102400, Rise = 0.00011, Thick = 0.00021; Filtered  
 RH = 49.%, Temperature = 274.4 deg K, C264S.age  
 Pmax = 1.06, ESEL = 114.53, CSEL = 103.52, ASEL = 89.85, PLdB = 107.27



**Figure 9-28. Lossy Solution for  $\delta$  tangent ray for Sailplane Focus C.**

T = 49.07, Z = 4000.; Tac = 54425.59, Phi = 0.0, C264.ssg  
 Refl = 1.0, SampRate = 102400, Rise = 0.00009, Thick = 0.00015; Filtered  
 RH = 36.%, Temperature = 285.0 deg K, C264.age  
 Pmax = 1.19, ESEL = 115.59, CSEL = 104.68, ASEL = 91.32, PLdB = 108.86  
 NPTS = 32768  
 Rcav = 166600

Tsig = 149  
 Delta = 1308  
 p0 = 1995.4  
 wind x,y,z = 0. 0. 0.  
 zbar = 0  
 x,y,z,tg = 76848.6 -6192.8 2785.0 54475.027  
 long,lat = -117.392463 35.269510  
 zbar = 1  
 x,y,z,tg = 78727.4 -6400.7 2785.0 54476.297  
 long,lat = -117.386153 35.268940

Time, sec	P, psf	pimag
-0.115826	0.000000	0.000000
-0.115816	-0.000006	0.000000
-0.115806	-0.000009	0.000000

**Figure 9-29. Header for Tricomi Signature Input File (PCBurg output), Ground Focus C.**

## 9.4 Lossy Nonlinear Tricomi Equations (LNTE) – Beta

### 9.4.1 LNTE Methodology

The beta version of the Tricomi code utilizes modifications to the PCBoom outputs. The PCBoom enhancements allow the beta version of the Tricomi code to execute without any manual preprocessing. The Tricomi code directly reads in the PCBoom Burgers output text file using the ‘-pb’ option from the command line and obtains the required focusing input parameters and in-coming pressure waveform.

The Tricomi code also automatically resamples the in-coming waveform from PCBoom if the sample rate is higher than 32,000 Hz to reduce the possible effects of numerically induced oscillations and also to reduce the computational memory and CPU time required to execute the code. The characteristic acoustic frequency is calculated automatically from the in-coming waveform. This is accomplished by computing the time that transpires between 5 percent and 95 percent of the energy in the in-coming waveform and taking the reciprocal of that value.

By default, the in-coming waveform is provided by PCBoom at  $\bar{z} = 1$  (one diffraction boundary layer thickness distance from the caustic) and the number of discretization points in the  $\bar{z}$ -axis is set to 4000. The Tricomi domain dimensions are also set by default to  $\bar{z}_{\max} = 1$  and  $\bar{z}_{\min} = -1$ .

According to Auger and Coulouvrat (2002), the effect of the wind is to translate the location of the caustic. The beta version of the Tricomi code can now account for the translation of the caustic location due to wind by using the information provided by the PCBoom output enhancements. These enhancements include the ground intercept coordinates (PCBoom x, y, z and lat/long) for the  $\bar{z} = 0$  and  $\bar{z} = 1$  locations. The Tricomi code interpolates/extrapolates these coordinates to the Tricomi domain between  $\bar{z}_{\min} = -1$  and  $\bar{z}_{\max} = 1$ . The beta version of the Tricomi code, when using the ‘-pb’ option, provides an ascii text output file that maps the Tricomi domain  $\bar{z}$  locations to the corresponding PCBoom coordinates.

### 9.4.2 Model Input Data

Figures 9-30 through 9-33 show the plots for the in-coming waveforms for Case A, Case C, Case D, and Case C sailplane, respectively. The focusing conditions for the four cases are listed in Table 9-2 below.

**Table 9-2. Focusing Parameters for the Beta Version Comparison Cases**

Case	$f_{ac}$ , Hz	$R_{tot}$ , m	$T_0$ , deg K	$P_0$ , kPa	RH, %	$Z_{min}$	$Z_{max}$	$Z_{pts}$
Case A	8.285	101804	287.0	91.8	45	-1	1	4000
Case C	8.174	48769	284.0	91.3	40	-1	1	4000
Case D	11.134	33637	293.2	95.2	26	-1	1	4000
Case C sailplane	8.13	50049	274.4	79.7	49	-1	1	4000

### 9.4.3 Comparisons with Measured Data

Tables 9-3 through 9-6 contain the lists for all of the figures for the Case A, Case C, Case D, and Case C sailplane, respectively. Figures 9-5, 9-24, 9-41, and 9-55 are the Tricomi pressure field solutions for the Case A, Case C, Case D, and Case C sailplane, respectively. Units for the pressure field are psf and the ground reflection factor was not included in those plots. The ground reflection factor of 1.9 is included in all other comparison plots with the exception of the sailplane comparisons. Figures 9-61b and 9-61c (not listed) are just close-in views of the front and rear shocks, respectively, for figure 9-61a (Case C, microphone 60). Figures 9-85b and 9-85c (also not listed) are just close-in views of the front and rear shocks, respectively, for figure 9-85a (Case C sailplane, microphone TG1). The Tricomi coordinate location chosen to compare to a microphone location was determined by looking at the best agreement in the data in between two microphone locations in the shadow zone. The nominal proportion of microphone spacing corresponding to the  $\bar{z}$  spacing was then approximately maintained for the rest of the microphones used in the data comparison for that case.

**Table 9-3. Listing of Case A Comparison Figures**

figure #	Microphone #	zbar
9-34	Tricomi solution pressure field	
9-35	49	1.00
9-36	46	0.92
9-37	43	0.85
9-38	40	0.78
9-39	37	0.70
9-40	34	0.62
9-41	30	0.51
9-42	28	0.45
9-43	25	0.36
9-44	22	0.31
9-45	19	0.245
9-46	17	0.19
9-47	15	0.125
9-48	12	0.07
9-49	9	0.00
9-50	6	-0.07
9-52	3	-0.14

**Table 9-4. Listing of Case C Comparison Figures**

figure #	Microphone #	zbar
9-53	Tricomi solution pressure field	
9-54	72	1.00
9-55	70	0.87
9-56	68	0.73
9-57	66	0.60
9-58	64	0.475
9-59	62	0.335
9-60	61	0.23
9-61a	60	0.15
9-62	59	0.075
9-63	58	0.03
9-64	56	-0.12
9-65	54	-0.27
9-66	52	-0.42
9-67	50	-0.60
9-68	48	-0.72
9-69	46	-0.87

**Table 9-5. Listing of Case D Comparison Figures**

figure #	Microphone #	zbar
9-70	Tricomi solution pressure field	
9-71	52	0.915
9-72	49	0.73
9-73	47	0.54
9-74	45	0.40
9-75	43	0.26
9-76	42	0.20
9-77	41	0.13
9-78	40	0.03
9-79	39	-0.01
9-80	37	-0.15
9-81	35	-0.29
9-82	33	-0.43
9-83	31	-0.57

**Table 9-6. Listing of Case C Sailplane Comparison Figures**

figure #	Microphone #	zbar
9-84	Tricomi solution pressure field	
9-85a	TG1	0.125
9-86	TG1	0.063



Case A comparisons show fairly good agreement between the measured data and the Tricomi predictions. Figure 9-35 shows the data comparison at the microphone closest to the upper edge of the Tricomi domain. The amplitude of the in-coming N-wave to the Tricomi solution is very close to the amplitude for the N-wave in microphone 49. The period of the in-coming waveform is a little short and as a result, the Tricomi solution predictions are all slightly shorter than the measured data in the Case A comparisons. However, the amplitude and overall waveform shape of the Tricomi solutions agrees well with most of the microphone measurements in both the illuminated and shadow zones. Attention should be given to the comparison in Figure 9-48. In the SCAMP review meeting held in October 2011, there were discussions held in regard to observed rear shock amplification in the measured data similar to what was measured in Figure 9-48. The rear shock amplification predicted by the Tricomi code closely resembles the measured data at microphone 12.

Case C comparisons show excellent agreement between the Tricomi predictions and the measured data. The amplitude and shape of the Tricomi predictions for both the illuminated and shadow zones show excellent agreement. Even though the in-coming waveform length and amplitude closely match the microphone measurement in Figure 9-54, the predicted U-wave period still is slightly less than the measured data. The waveform amplitude and shape agreement holds well for the evanescent waves, as observed in Figures 9-64 through 9-69.

Case D in Figure 9-71 shows the data comparison at the microphone closest to the upper edge of the Tricomi domain. The in-coming N-wave was much shorter than the measured N-wave and as a result, the periods of the predictions in the Tricomi solution are noticeably shorter than what was observed in the measured data. The waveform amplitude and shape agreements are fair, but not as good as Case A or Case C.

The dotted line in Figure 9-84 points to the  $\bar{z}$  location in the Tricomi solution that showed the best agreement to the TG1 microphone (occurred at  $\bar{z} = 0.125$ ). The rays output from PCBoom come close to the sailplane but the line between the ray coordinates for  $\bar{z} = 0$  and  $\bar{z} = 1$  do not exactly intersect the sailplane location. The Case C sailplane comparison in Figure 9-85a shows good agreement to the measured data for the waveform period and shape. The front shock amplitude prediction in Figure 9-85b appears to be over-predicted. However, the measured data shows the front shock amplitude may be influenced by atmospheric turbulence that the Tricomi code does not account for. The rear shock amplitude and shape shows good agreement between the measured data and the Tricomi code prediction. The  $\bar{z}$  location that corresponds the closest to the position of the powered glider during the measurement for this case is  $\bar{z} = 0.063$ . Figure 9-86 shows a comparison between the TG1 microphone and the Tricomi solution at  $\bar{z} = 0.063$ . There is good agreement between the front shock and the expansion. However, the rear shock in the Tricomi solution overpredicts the amplitude and the TG1 microphone measurement still shows two separate rear shocks that have not merged.

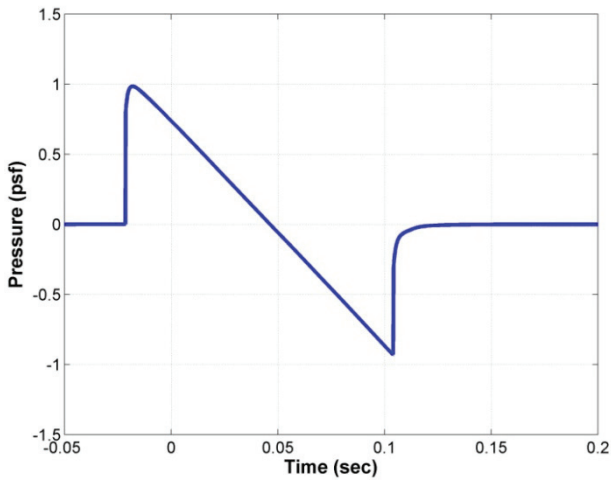


Figure 9-30. In-coming waveform time history for Case A.

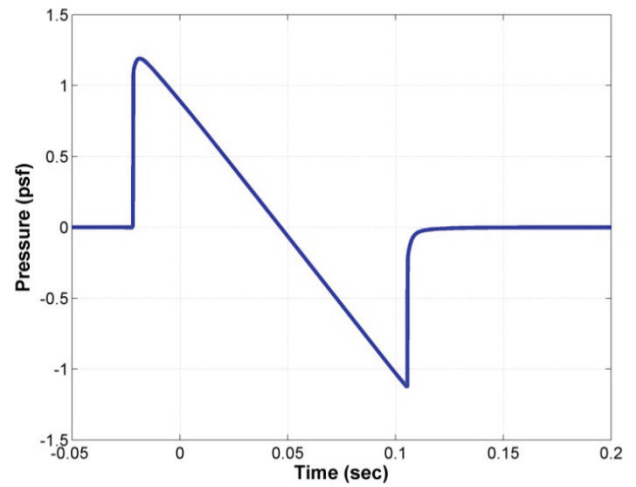


Figure 9-31. In-coming waveform time history for Case C.

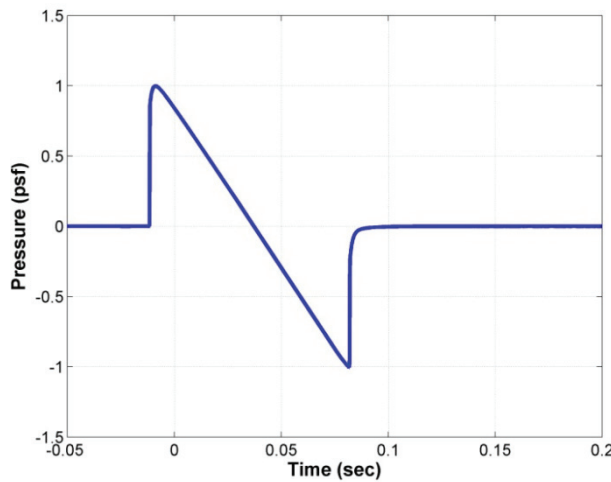


Figure 9-32. In-coming waveform time history for Case D.

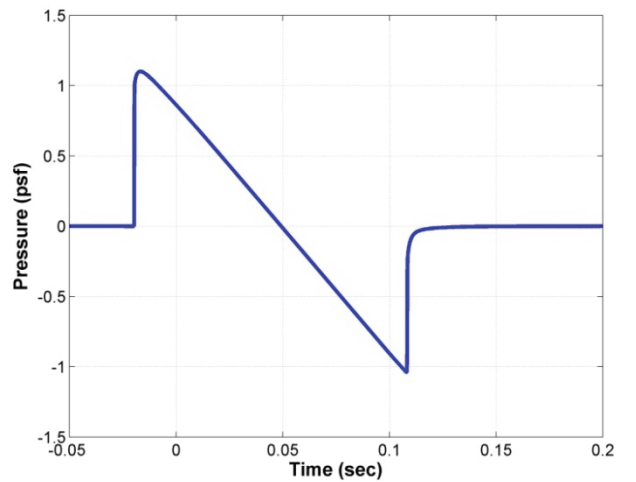


Figure 9-33. In-coming waveform time history for Case C sailplane.

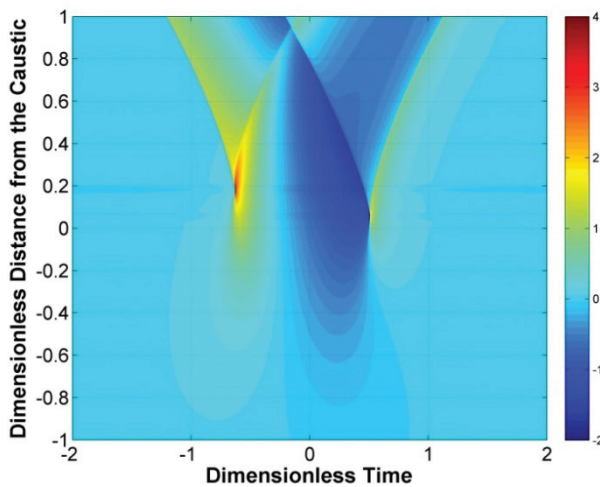


Figure 9-34. Tricomi Pressure Field Solution for Case A. Pressure units microphone are psf. The ground reflection factor is included in this plot.

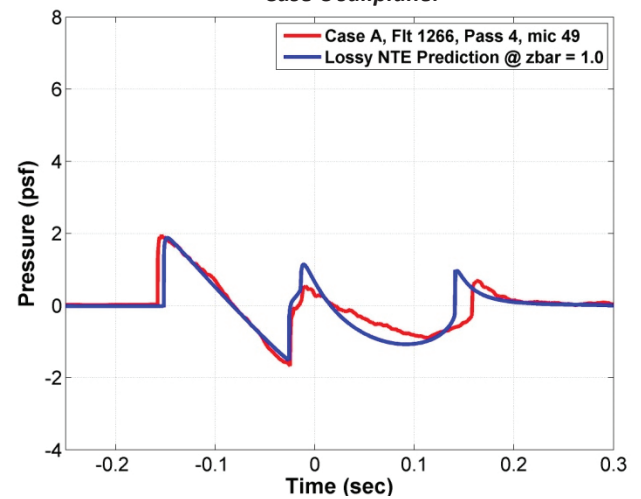


Figure 9-35. Case A data comparison between Case A data and the Tricomi Solution at  $\bar{z} = 1$ .

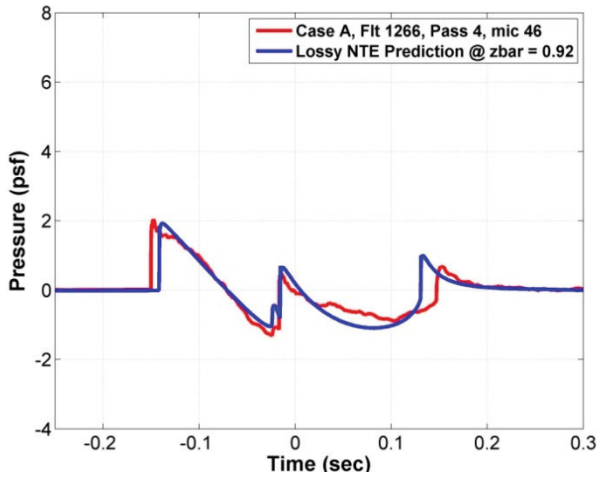


Figure 9-36. Case A data comparison between microphone 46 and the Tricomi Solution at  $\bar{z} = 0.92$ .

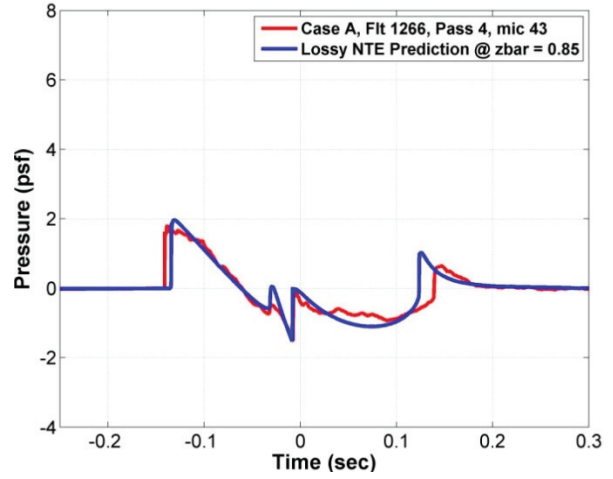


Figure 9-37. Case A data comparison between Microphone 43 and the 46 Tricomi Solution at  $\bar{z} = 0.85$ .

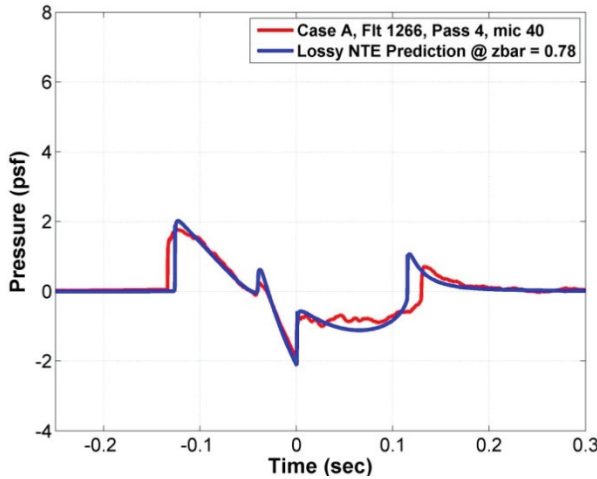


Figure 9-38. Case A data comparison between microphone 40 and the Tricomi Solution at  $\bar{z} = 0.78$ .

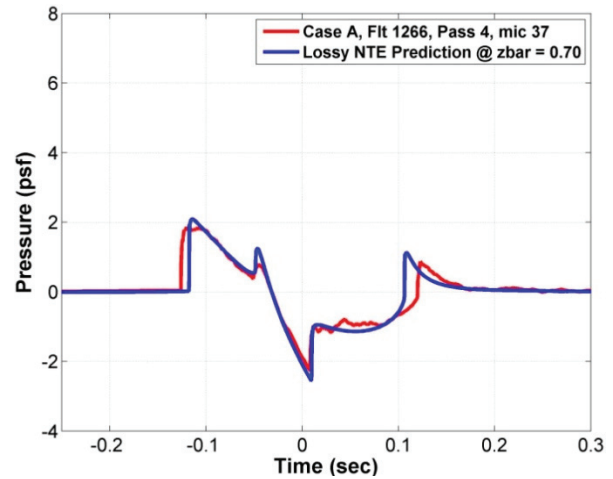


Figure 9-39. Case A Data Comparison between Microphone 37 and the Tricomi Solution at  $\bar{z} = 0.70$ .

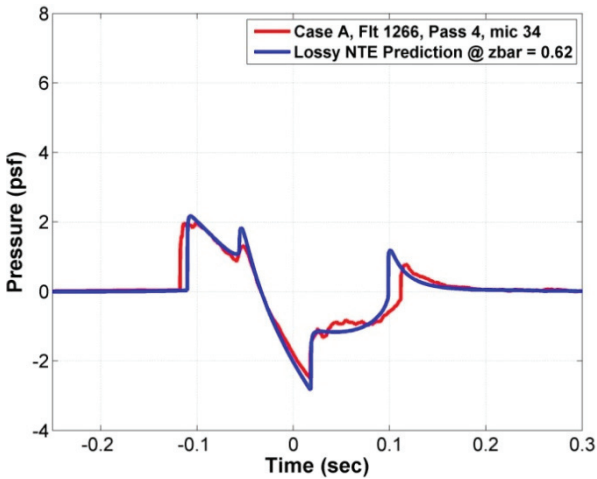


Figure 9-40. Case A data comparison between Microphone 34 and the Tricomi Solution at  $\bar{z} = 0.62$ .

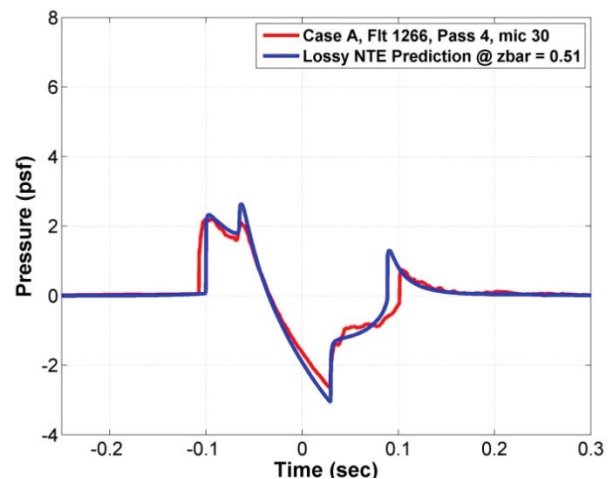


Figure 9-41. Case A data comparison between Microphone 30 and the Tricomi Solution at  $\bar{z} = 0.51$ .

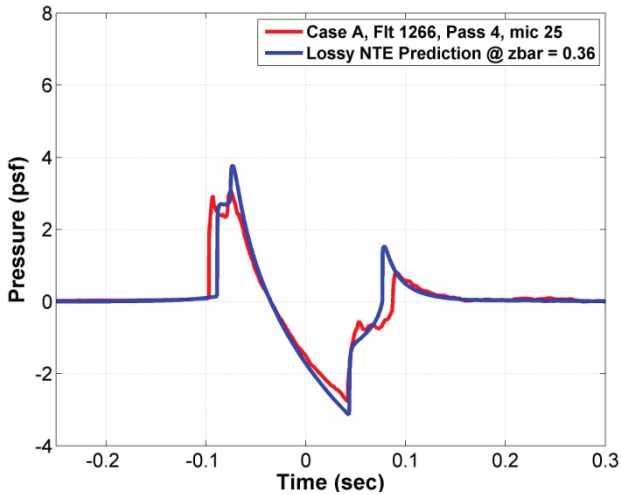


Figure 9-42. Case A data comparison between Microphone 28 and the Tricomi Solution at  $\bar{z} = 0.45$ .

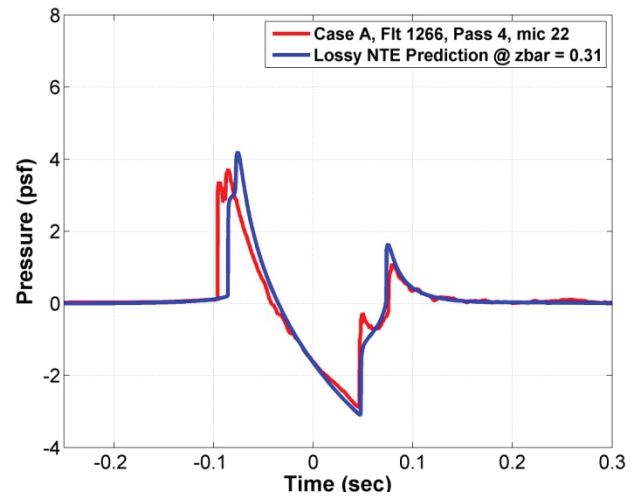


Figure 9-43. Case A data comparison between Microphone 25 and the Tricomi Solution at  $\bar{z} = 0.36$ .

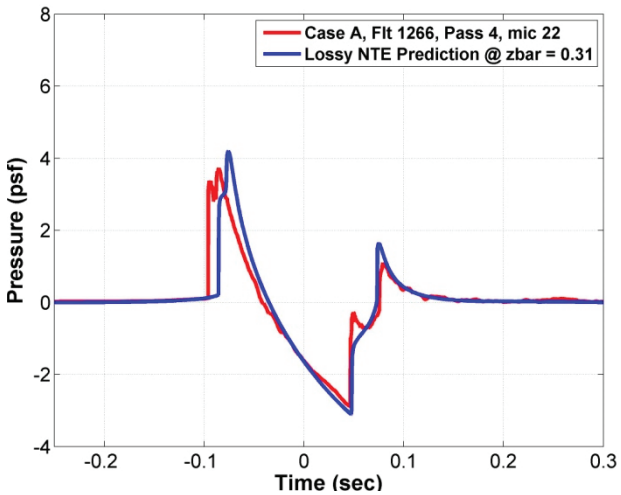


Figure 9-44. Case A data comparison between Microphone 22 and the Tricomi Solution at  $\bar{z} = 0.31$ .

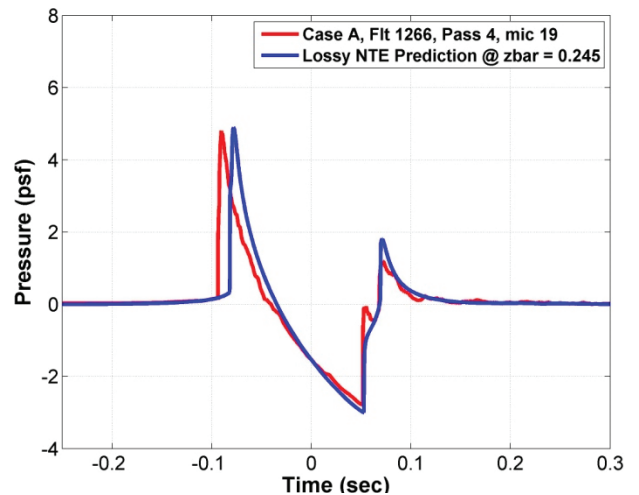


Figure 9-45. Case A data comparison between Microphone 19 and the Tricomi Solution at  $\bar{z} = 0.245$ .

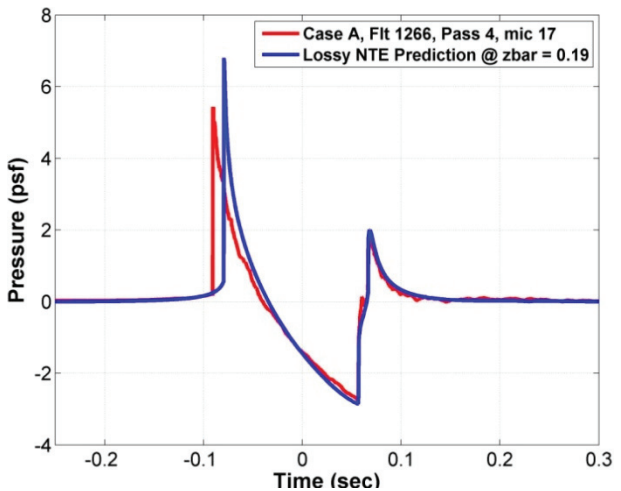


Figure 9-46. Case A data comparison between Microphone 17 and the Tricomi Solution at  $\bar{z} = 0.19$ .

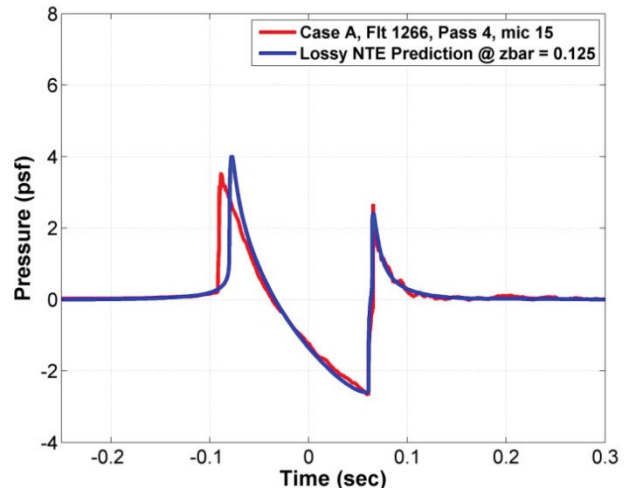


Figure 9-47. Case A data comparison between Microphone 15 and the Tricomi Solution at  $\bar{z} = 0.125$ .

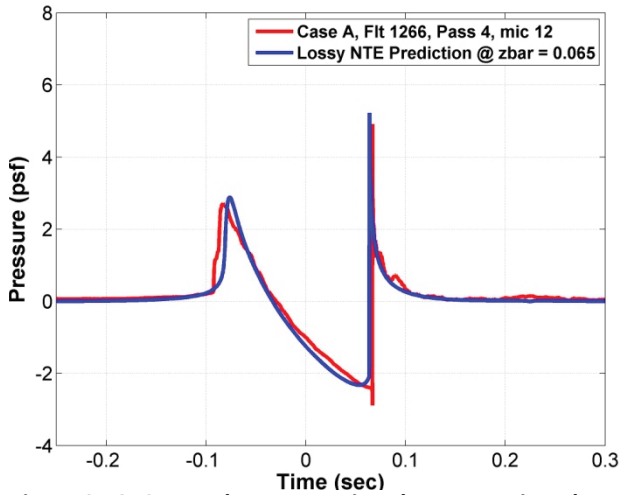


Figure 9-48. Case A data comparison between Microphone 12 and the Tricomi Solution at  $\bar{z} = 0.07$ .

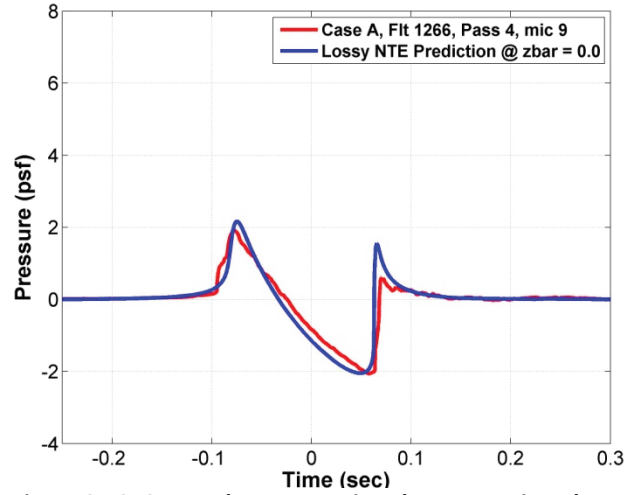


Figure 9-49. Case A data comparison between Microphone 9 and the Tricomi Solution at  $\bar{z} = 0.00$ .

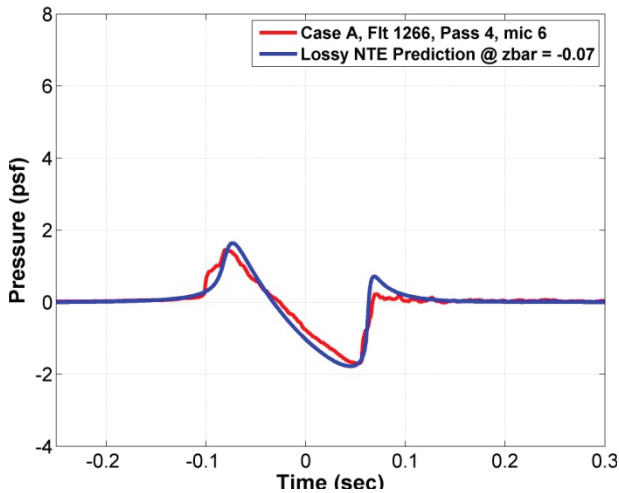


Figure 9-50. Case A data comparison between Microphone 6 and the Tricomi Solution at  $\bar{z} = -0.07$ .

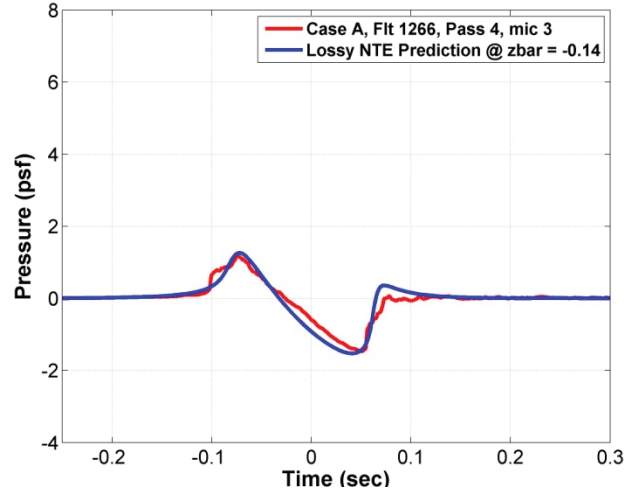


Figure 9-51. Case A data comparison between Microphone 3 and the Tricomi Solution at  $\bar{z} = -0.14$ .

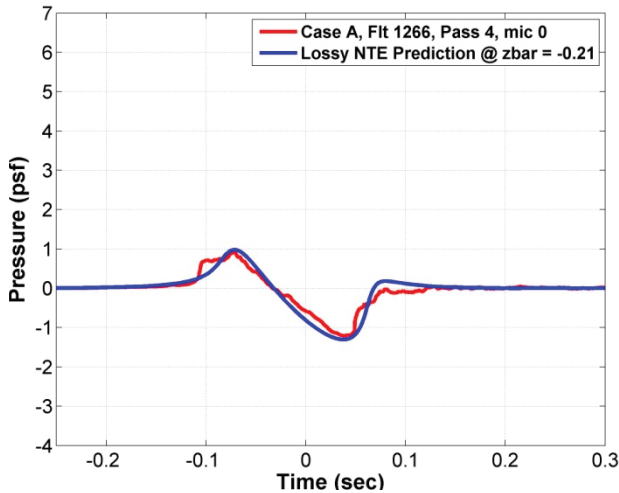


Figure 9-52. Case A data comparison between Microphone 0 and the Tricomi Solution at  $\bar{z} = -0.21$ .

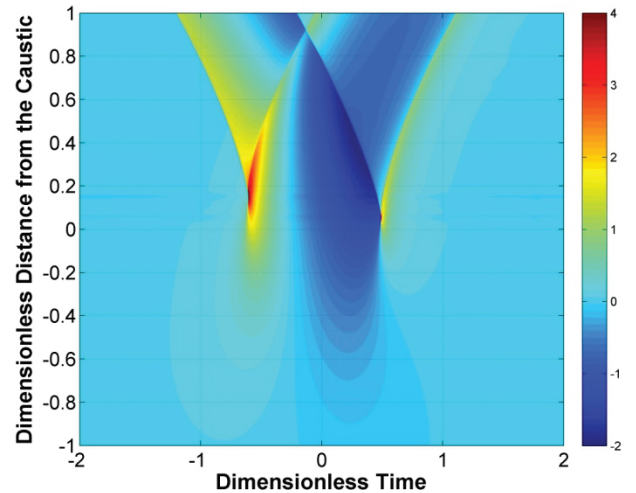


Figure 9-53. Tricomi pressure field solution for Case C. Pressure units are psf. The ground reflection factor is not included in this plot.

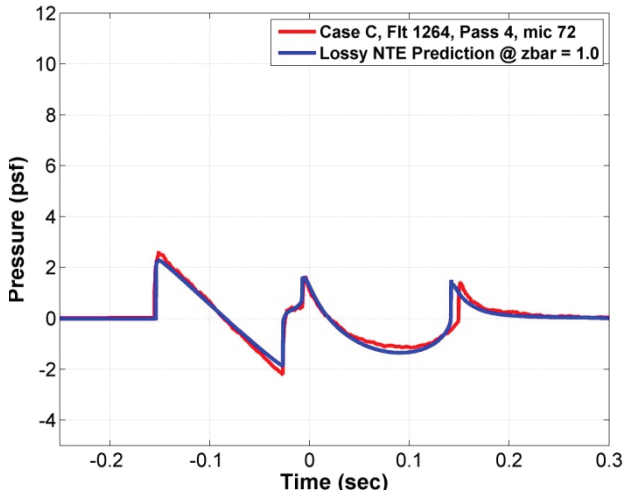


Figure 9-54. Case C data comparison between Microphone 72 and the Tricomi Solution at  $\bar{z} = 1.0$ .

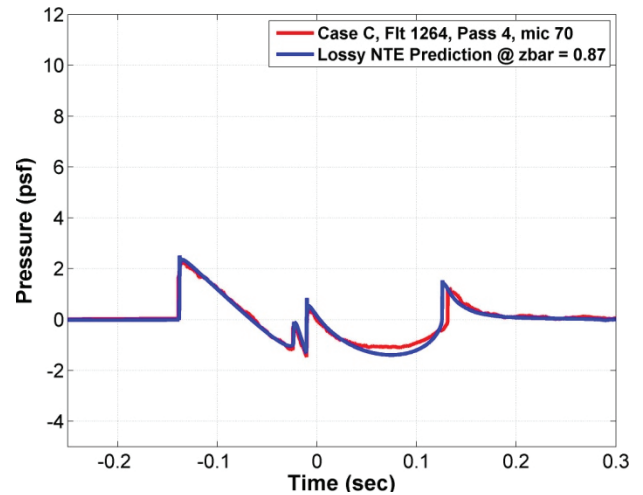


Figure 9-55. Case C data comparison between Microphone 70 and the Tricomi Solution at  $\bar{z} = 0.87$ .

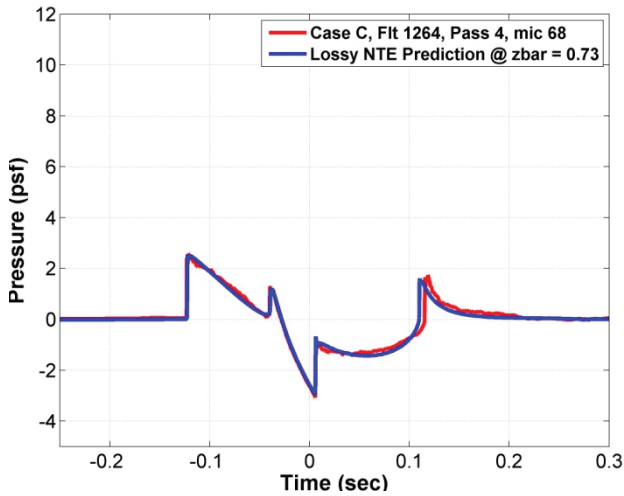


Figure 9-56. Case C data comparison between Microphone 68 and the Tricomi Solution at  $\bar{z} = 0.73$ .

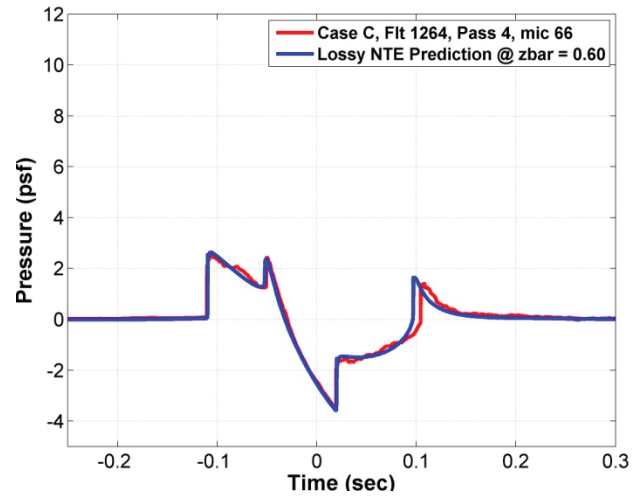


Figure 9-57. Case C data comparison between Microphone 66 and the Tricomi Solution at  $\bar{z} = 0.60$ .

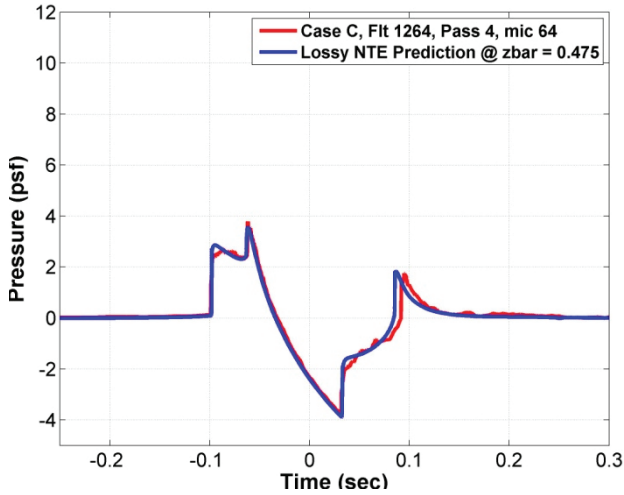


Figure 9-58. Case C data comparison between Microphone 64 and the Tricomi Solution at  $\bar{z} = 0.475$ .

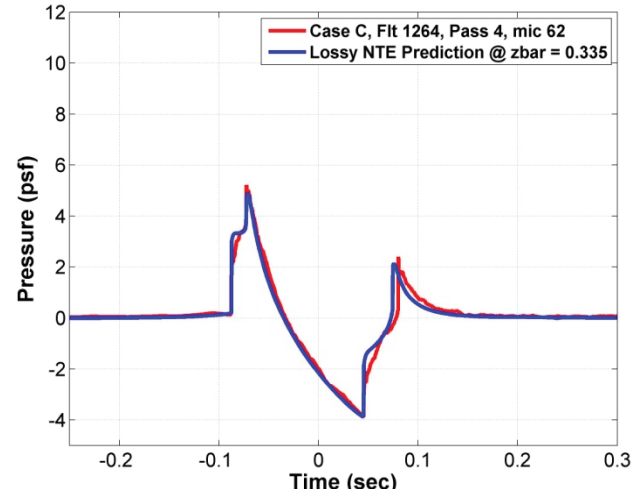


Figure 9-59. Case C data comparison between Microphone 62 and the Tricomi Solution at  $\bar{z} = 0.335$ .

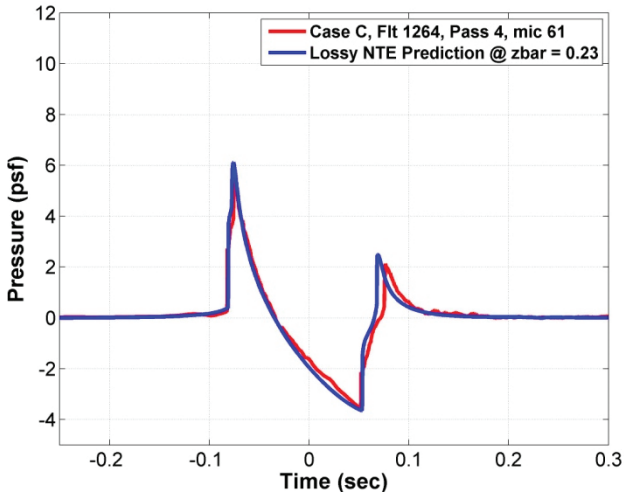


Figure 9-60. Case C data comparison between Microphone 61 and the Tricomi Solution at  $\bar{z} = 0.23$ .

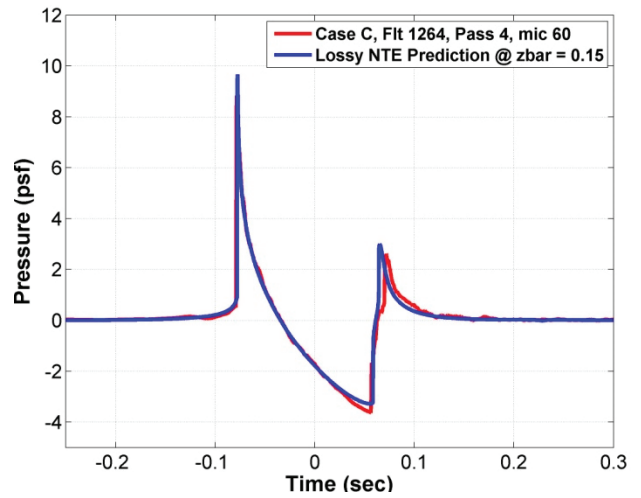


Figure 9-61a. Case C data comparison between Microphone 60 and the Tricomi Solution at  $\bar{z} = 0.15$ .

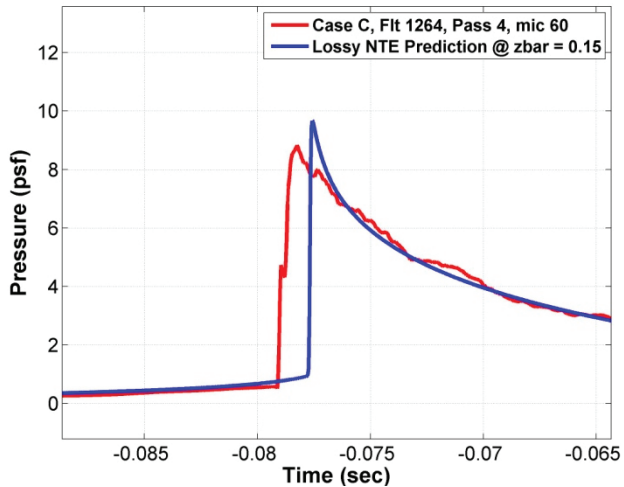


Figure 9-61b. Close-up comparison for the front shock from Figure 4-32a.

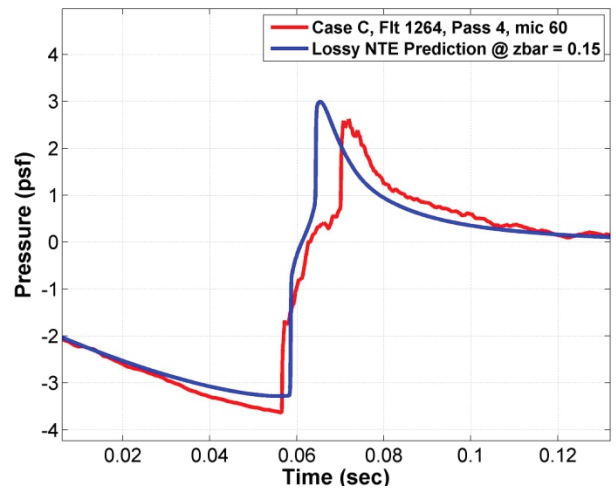


Figure 9-61c. Close-up view comparison for the rear shock from Figure 4-32a.

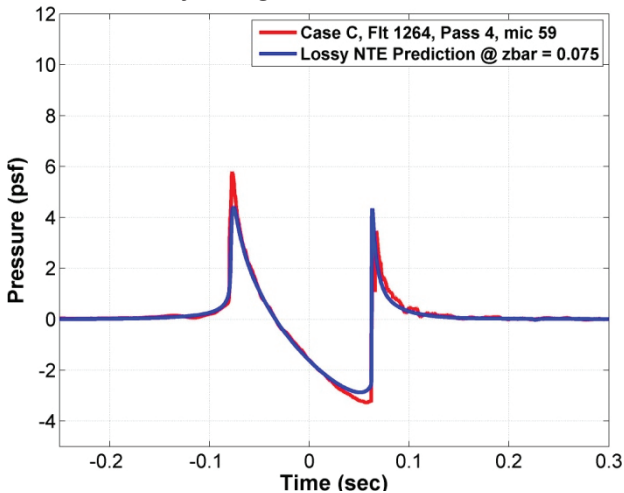


Figure 9-62. Case C data comparison between Microphone 59 and the Tricomi Solution at  $\bar{z} = 0.075$ .

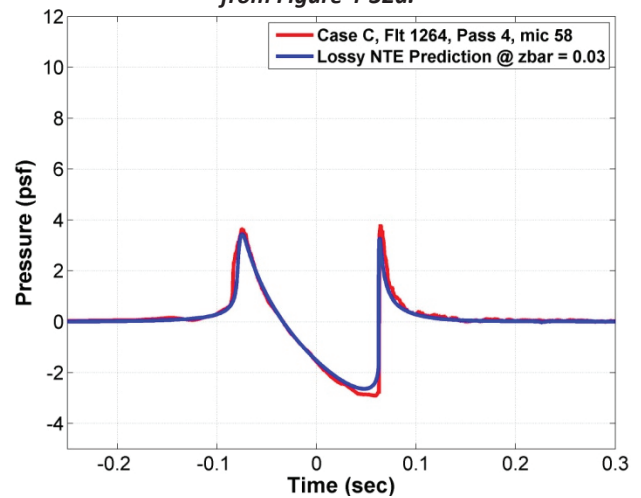


Figure 9-63. Case C data comparison between Microphone 58 and the Tricomi Solution at  $\bar{z} = 0.03$ .

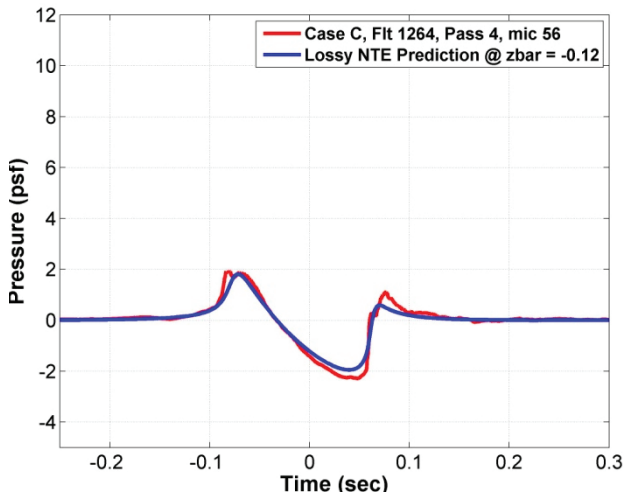


Figure 9-64. Case C data comparison between microphone 56 and the Tricomi solution at  $\bar{z} = -0.12$ .

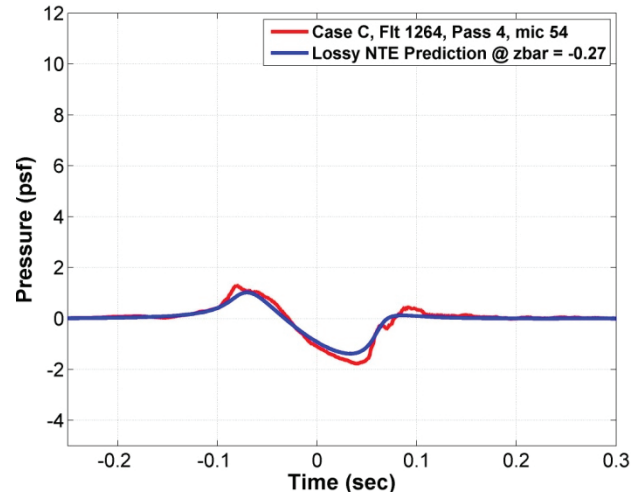


Figure 9-65. Case C data comparison between microphone 54 and the Tricomi solution at  $\bar{z} = -0.27$ .

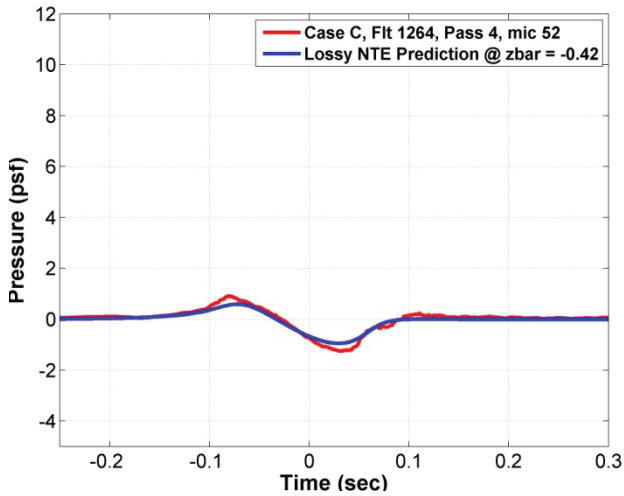


Figure 9-66. Case C data comparison between microphone 52 and the Tricomi solution at  $\bar{z} = -0.42$ .

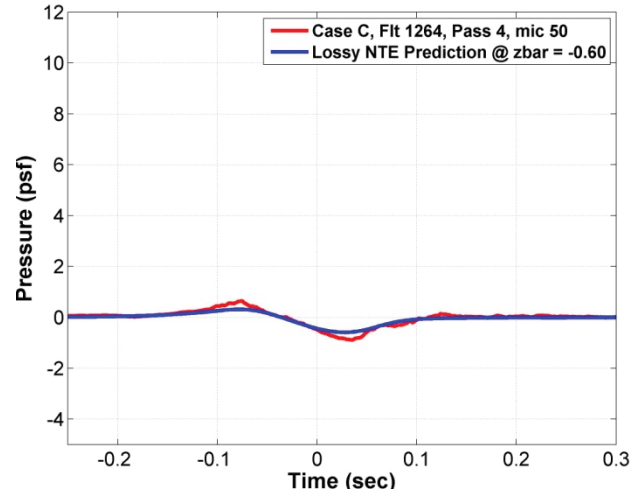


Figure 9-67. Case C data comparison between microphone 50 and the Tricomi solution at  $\bar{z} = -0.60$ .

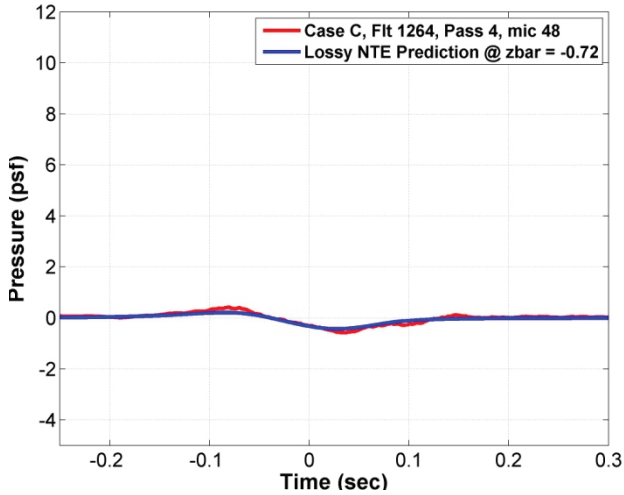


Figure 9-68. Case C data comparison between microphone 48 and the Tricomi solution at  $\bar{z} = -0.72$ .

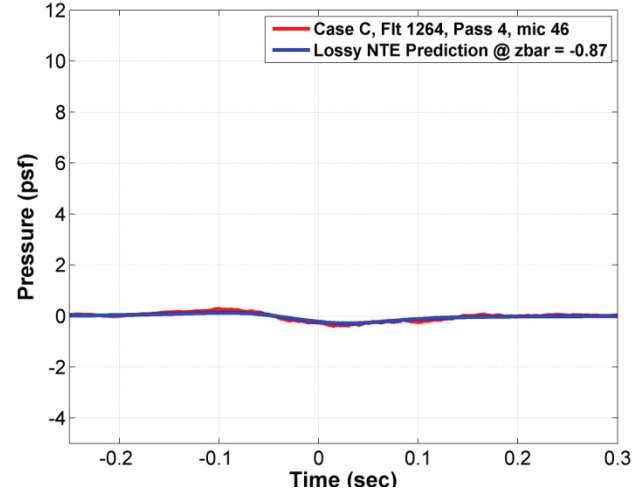


Figure 9-69. Case C data comparison between microphone 46 and the Tricomi solution at  $\bar{z} = -0.87$ .



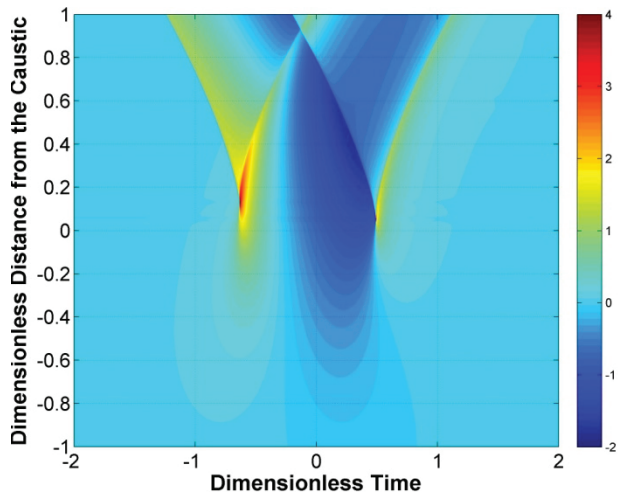


Figure 9-70. Tricomi pressure field solution for Case D. Pressure units are psf. The ground reflection factor is not included in this plot.

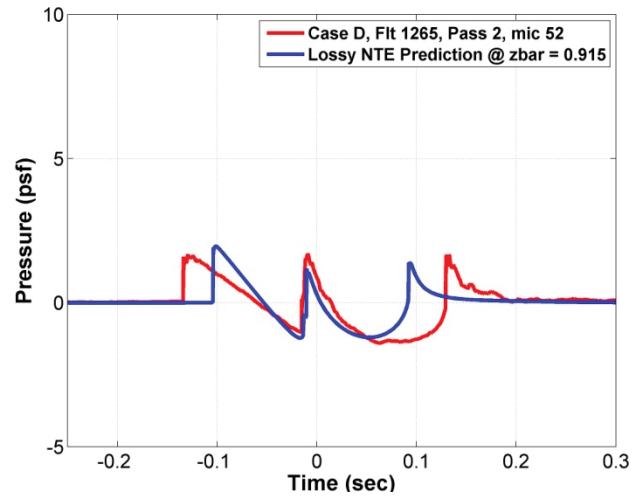


Figure 9-71. Case D data comparison between microphone 52 and the Tricomi solution at  $\bar{z} = 0.915$ .

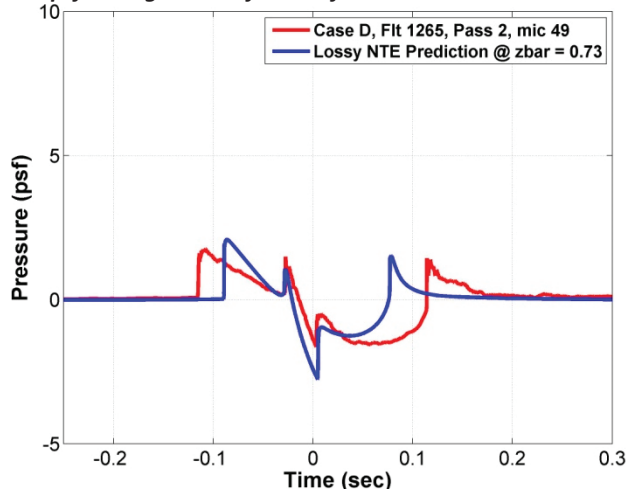


Figure 9-72. Case D data comparison between microphone 49 and the Tricomi solution at  $\bar{z} = 0.73$ .

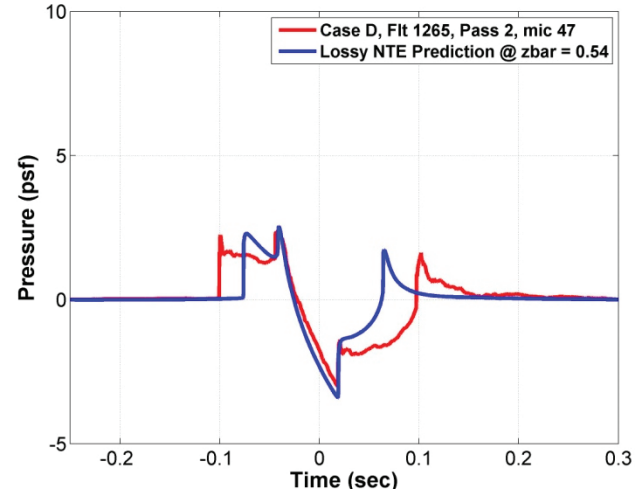


Figure 9-73. Case D data comparison between microphone 47 and the Tricomi solution at  $\bar{z} = 0.54$ .

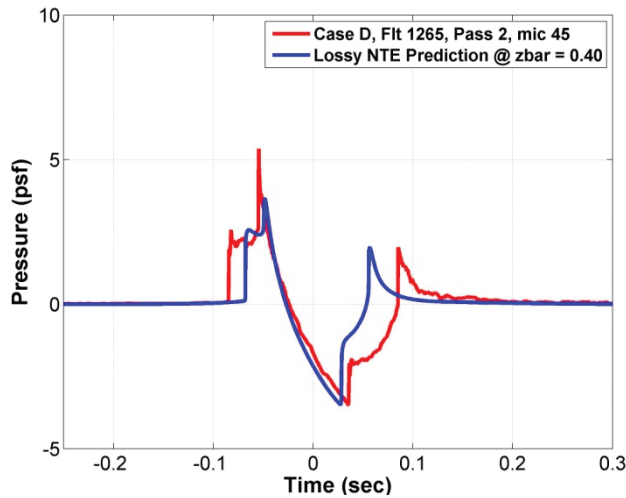


Figure 9-74. Case D data comparison between microphone 45 and the Tricomi solution at  $\bar{z} = 0.40$ .

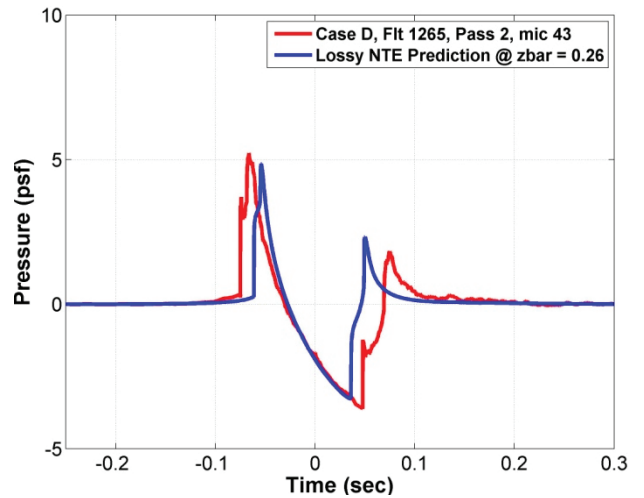


Figure 9-75. Case D data comparison between microphone 43 and the Tricomi solution at  $\bar{z} = 0.26$ .

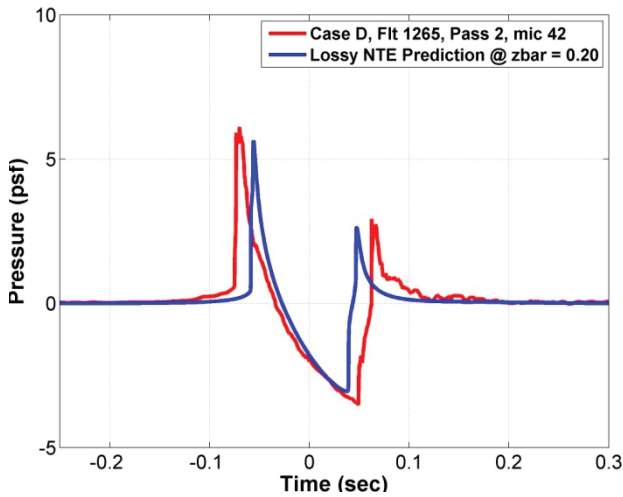


Figure 9-76. Case D data comparison between microphone 42 and the Tricomi solution at  $\bar{z} = 0.20$ .

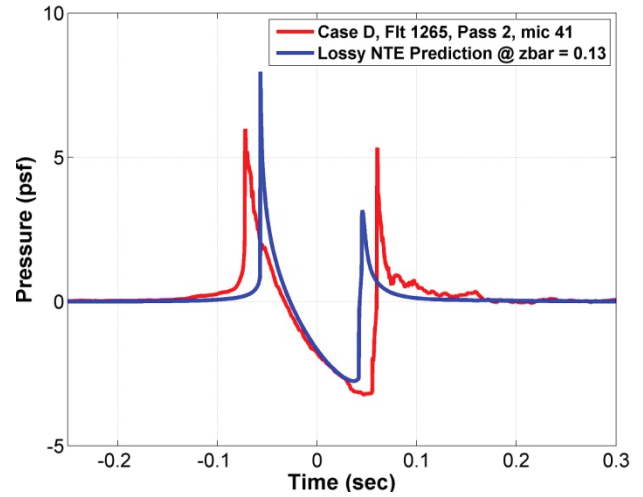


Figure 9-77. Case D data comparison between microphone 41 and the Tricomi solution at  $\bar{z} = 0.13$ .

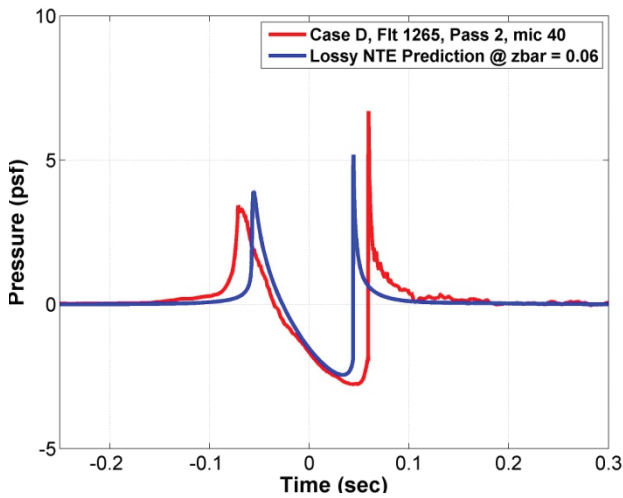


Figure 9-78. Case D data comparison between microphone 40 and the Tricomi solution at  $\bar{z} = 0.03$ .

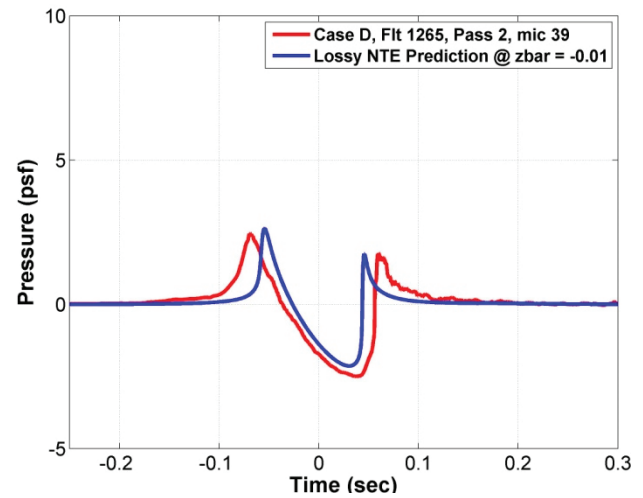


Figure 9-78. Case D data comparison between microphone 39 and the Tricomi solution at  $\bar{z} = -0.01$ .

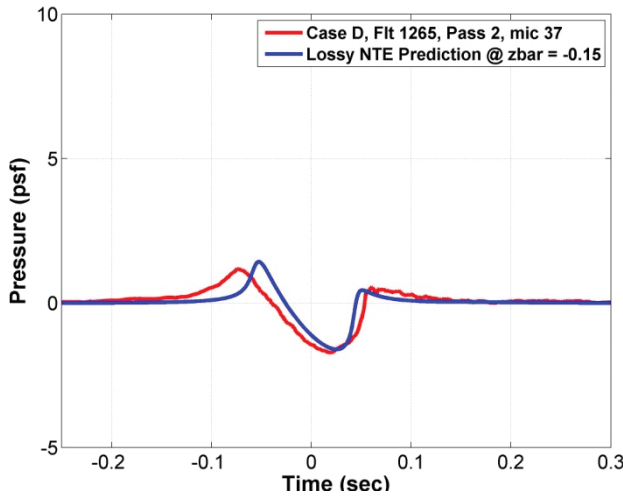


Figure 9-80. Case D data comparison between microphone 37 and the Tricomi solution at  $\bar{z} = -0.15$ .

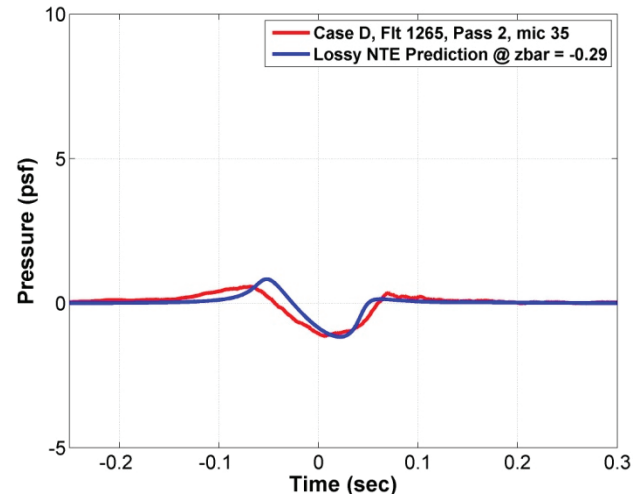


Figure 9-81. Case D data comparison between microphone 35 and the Tricomi solution at  $\bar{z} = -0.29$ .

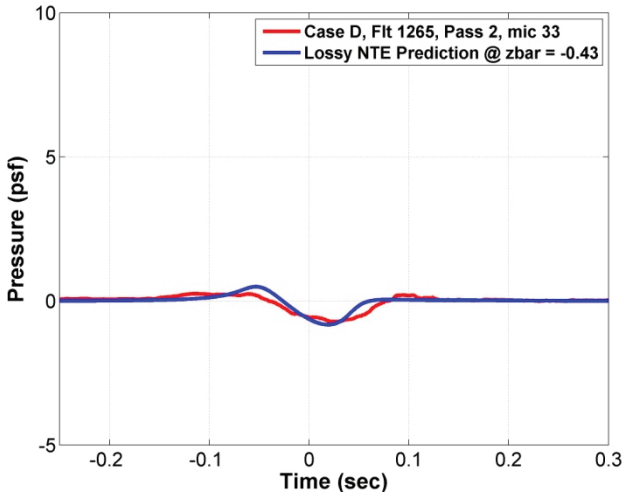


Figure 9-82. Case D data comparison between microphone 33 and the Tricomi solution at  $\bar{z} = -0.43$ .

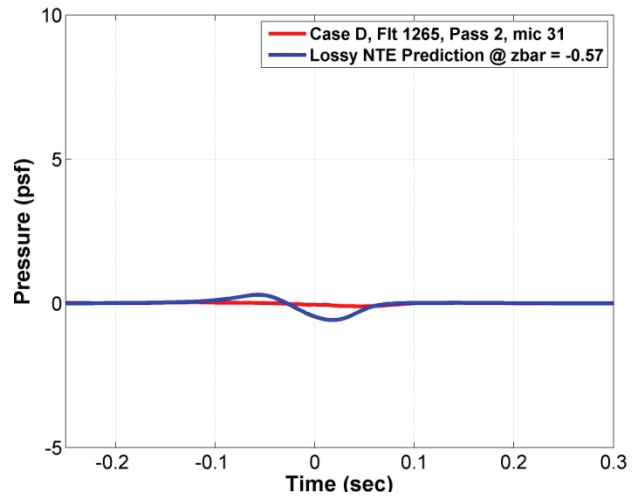


Figure 9-83. Case D data comparison between microphone 31 and the Tricomi solution at  $\bar{z} = -0.57$ .

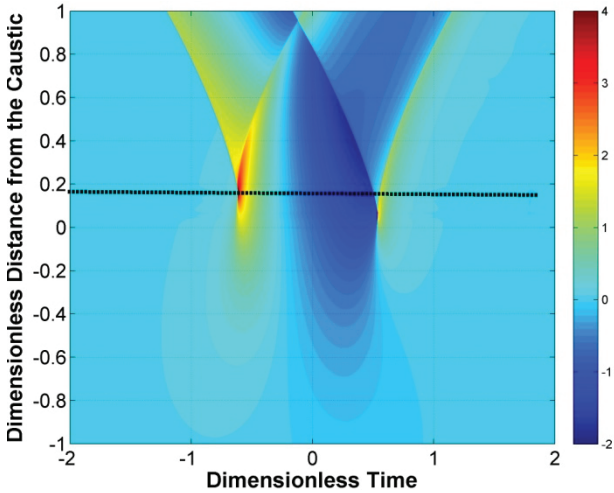


Figure 9-84. Tricomi pressure field solution for Case C sailplane. Pressure units are psf. The ground reflection factor is not included in this plot. The dashed line indicates the  $\bar{z}$  location for the comparison in Figure 4-56a.

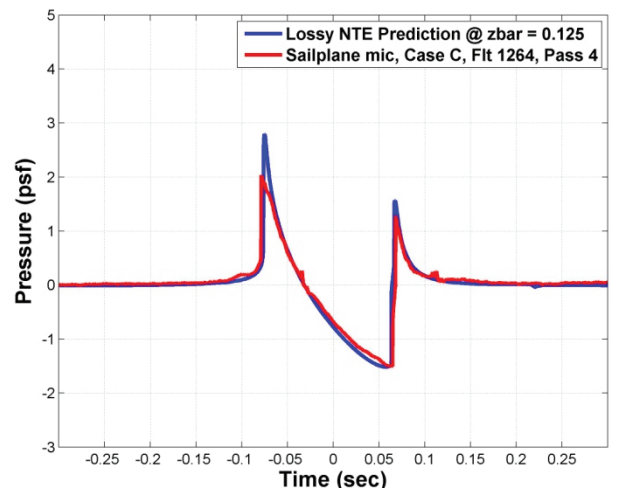


Figure 9-85a. Case C sailplane data comparison between microphone TG1 and the Tricomi solution at  $\bar{z} = 0.125$ .

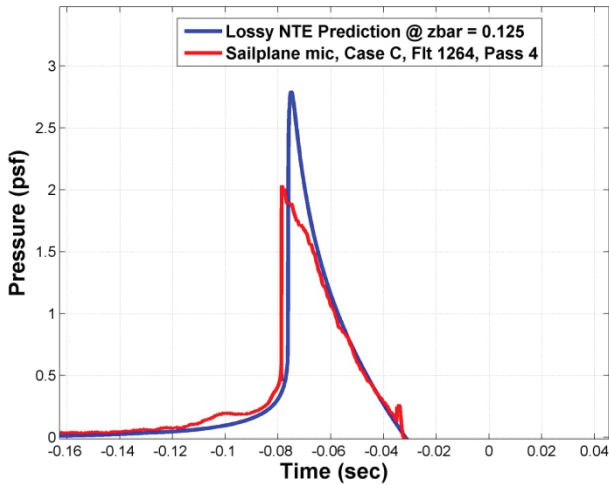


Figure 9-85b. Close-up view comparison for the front shock from figure 4-56.

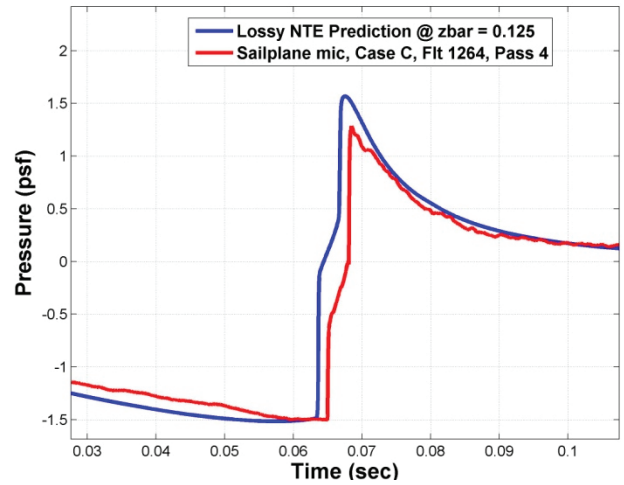


Figure 9-85c. Close-up view comparison for the rear shock from figure 4-56a.

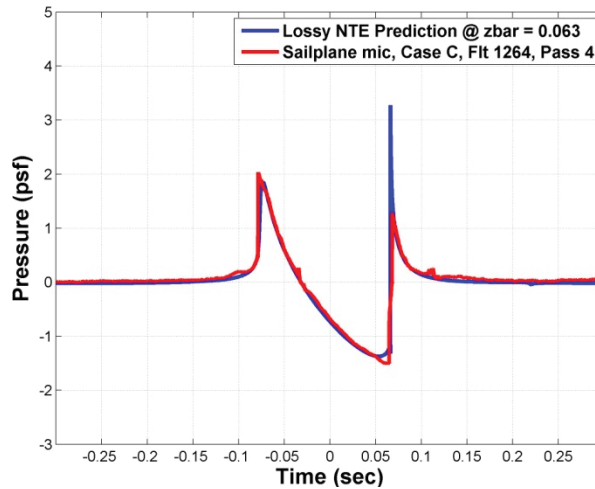


Figure 9-86. Case C sailplane data comparison between microphone TG1 and the Tricomi solution at  $\bar{z} = 0.063$ .

## 9.5 Nonlinear Progressive-wave Equation (NPE) – Beta

### 9.5.1 Background and Motivation

In Section 7 comparisons were presented between SCAMP flight-test data and several focus boom models. Application of the Nonlinear Progressive-wave Equation (NPE), using the original interface concept, was not as successful as some of the other models. This section describes the cause of the difficulties and a revised NPE application method that yields focus boom predictions.

Figure 9-87 shows the customary perspective of the caustic due to an acceleration focus, with the signature computed in the vicinity of the caustic by solution of the nonlinear Tricomi equation.

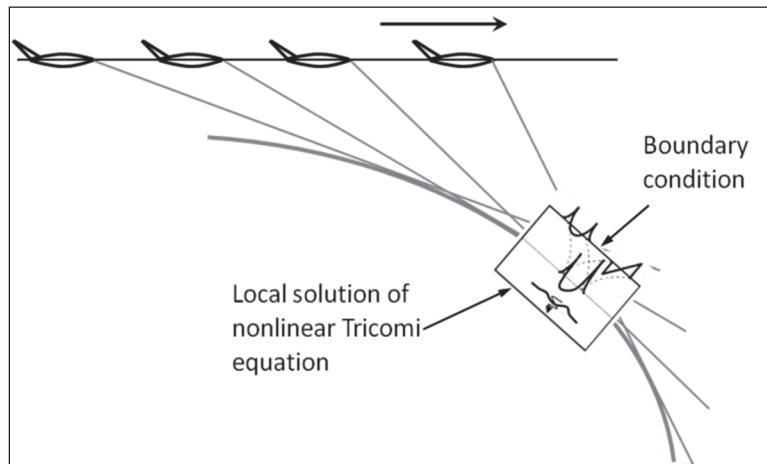


**Figure 9-87. Acceleration caustic and computational domain for local solution of focus signature.**

The NPE solution is a finite-difference calculation in the time domain, starting from an initial two-dimensional pressure field. It has been successfully used to compute caustic formation for propagation of shock waves through turbulence. It has benefit of not employing the kind of local linearization implicit in the Tricomi method. It can propagate waves from a starter field.

For the NPE alpha version, starter fields were prepared by using wavefronts generated by PCBoom for SCAMP focus cases, interpolated onto suitable rectangular grids. The initial wavefront was below the aircraft and above the ground focus. Figure 9-88 shows an initial NPE domain and its relation to the caustic. The NPE starter solution cannot contain the caustic, since it is based on the geometric solution. The location and size of the initial NPE grid are constrained by the geometry of the curved caustic associated with a given aircraft maneuver, as seen in Figure 9-88.

An additional constraint comes from the diffracted waves that emanate from the wavefront where it is truncated at (or near) the boundaries. As propagation time increases, there is a diminishing region within NPE solution domain that is unaffected by diffraction from the boundaries. This necessitates a large computational domain.

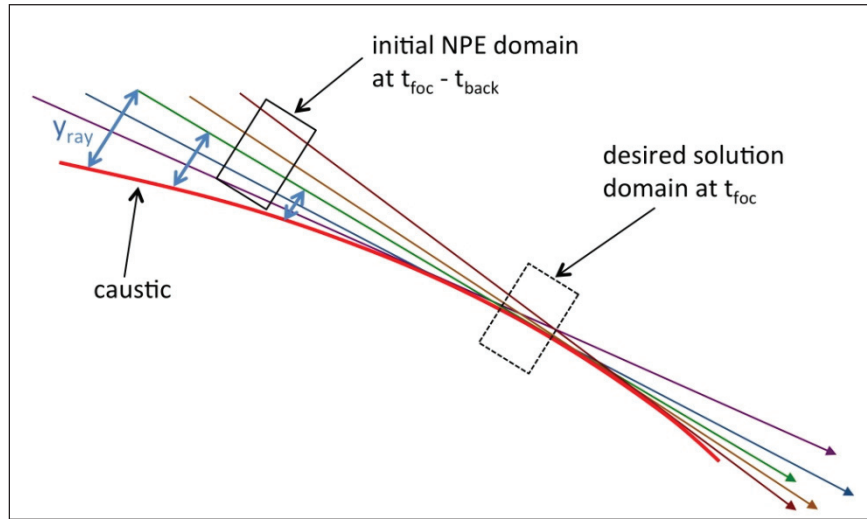


**Figure 9-88. Location and size of initial NPE grid.**

The geometric and diffraction constraints on domain size are specified by Equations 9-3a and 9-3b, respectively, which give the domain width as a function of time before focus, where  $R$  is the caustic radius,  $L_0$  is the wavefront curvature depth (described in Figure 9-89), and  $c_0$  is the ambient wave speed. These equations are plotted in Figure 9-90.

$$y_{geom} = R \left[ 1 - \cos \left( \frac{c_0 t}{R} \right) \right] \quad (9-3a)$$

$$y_{diff} = L_0 \sqrt{\frac{2c_0 t}{L_0} - 1} \quad (9-3b)$$

The interpretation of Figure 9-90 is that the NPE grid must be initialized at a time  $t > T_c$  before focus, where  $T_c$  is found by simultaneously setting  $y_{geom} = y_{diff}$ . This corresponds to when the grid can be made large enough to accommodate diffraction, but not include the caustic. Note that domain size is proportional to both  $R$  and  $L_0$ . The SCAMP flight conditions are such that  $R$  and  $L_0$  are sufficiently large to make  $T_c$  larger than the propagation time from aircraft to ground focus. These constraints prevented successful calculation of the focused signature by this approach.

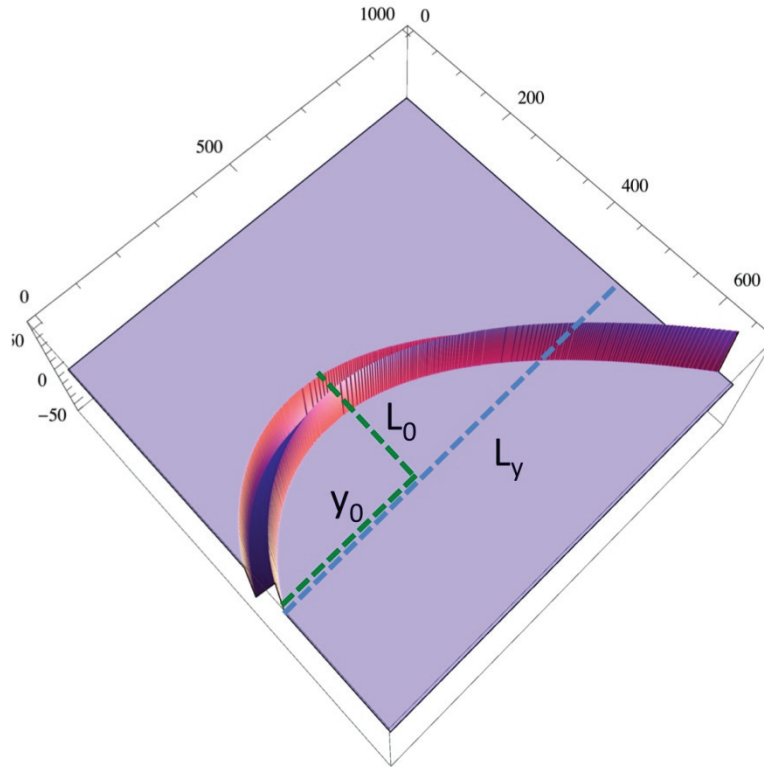


Figure 9-89. Dimensions associated with a curved wavefront in the initial NPE domain.

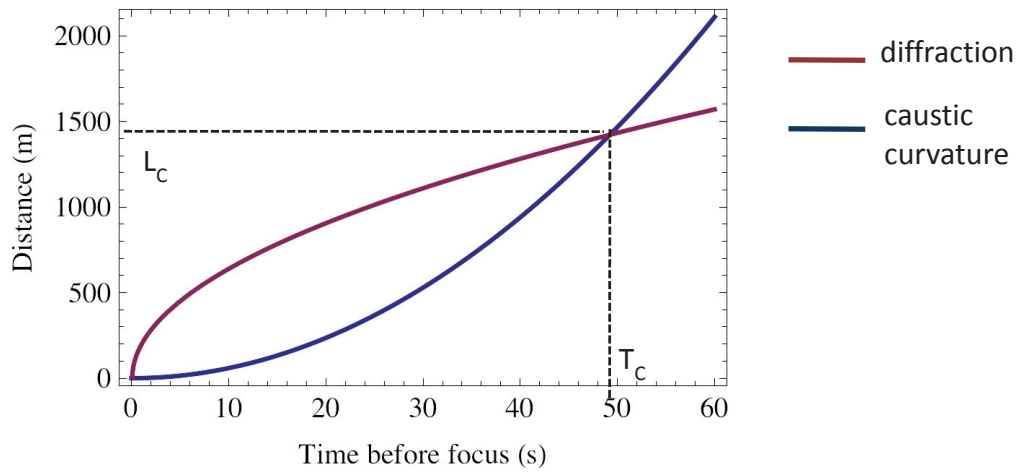
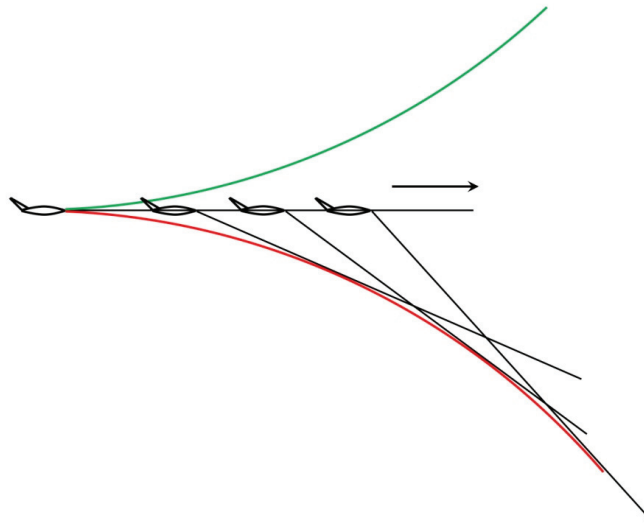


Figure 9-90. Comparison of competing effects that constrain the size and location of the initial NPE grid. Chosen parameters are the radius of relative caustic curvature,  $R=100000\text{m}$ , and the sonic boom wavelength,  $L_N=60\text{m}$ . At times earlier than  $T_c$ , the grid must be small enough to avoid overlapping the caustic, which means that diffracted waves will reach all parts of the solution.

### *Edges and Caustic Beginning*

The sketch in Figure 9-87 does not fully describe the caustic. For an aircraft accelerating through Mach 1, the caustic begins at the transonic point, and is not limited to below the aircraft. Figure 9-91 shows a more complete sketch, showing the caustic beginning at Mach 1 and the presence of an upper branch, the two branches originating at a cusp. (This is a two-dimensional sketch. The full caustic is a three-dimensional surface.) Ignoring the start of the caustic is one of the sources of the edge diffraction issue described above. To avoid this, it is necessary to use an initial wavefront prior to the cusp, so that the caustic is within the wave field and does not form an edge to the computational domain.



**Figure 9-91. Upper and lower caustics associated with accelerating aircraft.  
The cusp occurs where the aircraft first goes supersonic.**

## **9.5.2 Scaled Ripple Approach**

Piacsek (2002) used NPE to propagate a shock with a curved wavefront that is normal to the top and bottom domain boundaries, with results that are consistent with nonlinear geometric predictions of wave profiles and caustic locations. With such a “single ripple” wavefront, the caustic first forms at a cusp that is downstream of the initial wave. This type of initial condition eliminates both the diffraction constraints and the geometric constraints imposed by the SCAMP booms. Beginning the solution before the formation of the caustic cusp is analogous to initializing a SCAMP wave while the aircraft is still subsonic, as illustrated in Figure 9-91. This wavefront has been successfully applied to propagation of an N-wave.

Figure 9-92 shows the rippled wavefront at several propagation distances, along with associated rays and caustics (green and red curves). The black dot indicates the region of interest. Since the shock evolution in the vicinity of the caustic is determined by the local curvature in the center of the ripple, together with the shock amplitude and N-wave length, a scaled NPE solution can produce the focusing conditions of SCAMP sonic booms.



The appropriate scaling is found from the non-dimensional form of the nonlinear Tricomi Equation, or NTE, (from Auger and Coulouvrat):

$$\frac{\partial^2 \bar{p}_a}{\partial \bar{z}^2} - \bar{z} \frac{\partial^2 \bar{p}_a}{\partial \bar{\tau}^2} + \mu \frac{\partial^2}{\partial \bar{\tau}^2} \left( \frac{\bar{p}_a^2}{2} \right) = 0 \quad (9-4)$$

where

$$\bar{p}_a = (p - p_0) / P_{ac} \quad (9-5a)$$

$$\bar{\tau} = [t - x(1 - z/R_{cau}) / c_0] / T_{ac} \quad (9-5b)$$

$$\bar{z} = [2 / (c_0^2 T_{ac}^2 R_{cau})]^{1/3} z = z / \delta \quad (9-5c)$$

$$\mu = 2\beta M_{ac} [R_{cau} / (2c_0 T_{ac})]^{2/3} \quad (9-5d)$$

and

$P_{ac}$  = magnitude order of in-coming boom

$T_{ac}$  = characteristic duration of in-coming boom

$R_{cau}$  = relative radius of curvature between the ray and the caustic

$c_0$  = ambient sound speed

$\delta$  = diffraction layer thickness =  $(c_0^2 T_{ac}^2 R_{cau} / 2)^{1/3}$

Overbar quantities are non-dimensional forms of the physical quantities.

Writing (9-5d) in more conventional aerodynamic notation (but still using  $c$  rather than  $a$  for sound speed),

$$\mu = (\gamma + 1) \frac{P_{ac}}{\rho_0 c_0^2} [R_{cau} / (2c_0 T_{ac})]^{2/3} \quad (9-5e)$$

The SCAMP flight tests had  $T_{ac} = 127$  msec,  $P_{ac}$  about 2.5 psf (with doubling; 1.3 psf free field), and  $R_{cau} = 339,000$  ft, 167,000 ft, and 112,000 ft for Maneuvers A, C, and D, respectively. Parameters are listed in Table 9-7.

**Table 9-7. Tricomi Scaling Parameters for SCAMP Maneuvers**

Maneuver	$\mu$	$\delta$ (ft)
A	.1158	1513.
C	.0722	1195.
D	.0553	1046.

Equation (9-4) is usually solved for a  $\bar{z}$  domain from -1 to +1. For a given shape boom, the solution can apply to other durations ( $T_{ac}$ ) and caustic curvatures ( $R_{can}$ ) as long as  $\mu$  matches and  $T_{ac}$ ,  $P_{ac}$  are taken at  $\bar{z} = 1$ , i.e.,  $\bar{z} = \delta$ .

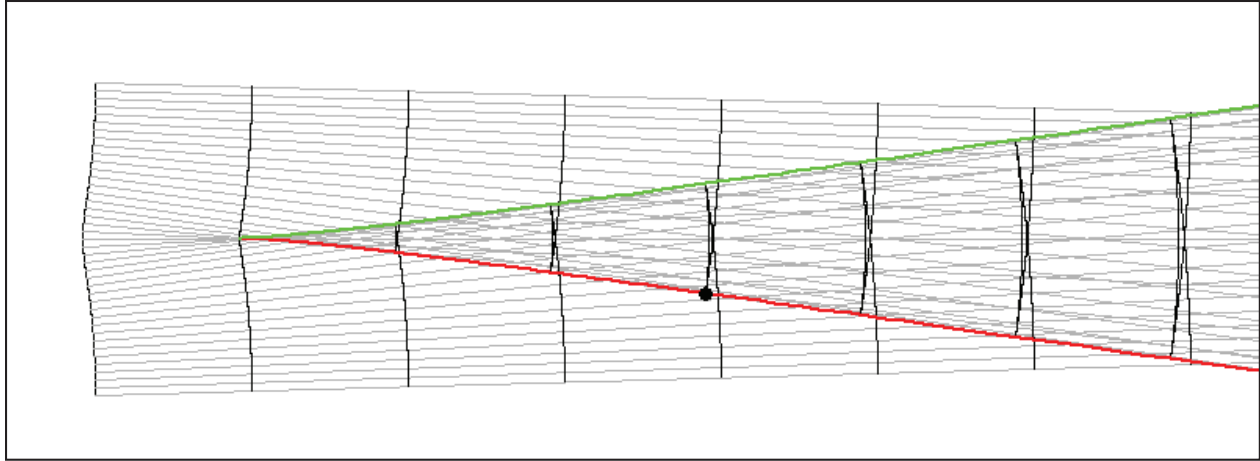


**Figure 9-92. Ray and wave pattern for single ripple NPE case.**

**Marker in bottom caustic is at  $x=3879$  meters,  $y=-354.9$  meters, and the local radius of curvature is 313,300 meters.**

The rays and wavefronts shown in Figure 9-92 stem from an initial wavefront given by Equation (5) in Piacsek (2002):

$$\tau_0(y) = \frac{L_0}{c_0} \left[ 1 + \frac{L_0}{2R_0} \left( \frac{y}{L_0} \right)^2 \right]^{-1} \quad (9-7)$$

where

$\tau_0$  = arrival time of the initial wave at  $x = 0$

$L_0$  = maximum depth of the ripple

$R_0$  = radius of curvature of the wavefront at  $y = 0$

For the current analysis,  $R_0 = 1000$  meters and  $L_0 = 100$  meters.

Because of the symmetry, there are upper and lower caustics, beginning at a cusp at  $R_0$ . The caustic curvature was obtained by numerically fitting a circle to caustic points. While Figure 9-92 shows 41 rays, the caustics were constructed from 2001 rays. Only the central 487 rays (initial wavefront  $y$  within  $\pm 230$  meters) generate caustics – the wavefront is convex beyond that.

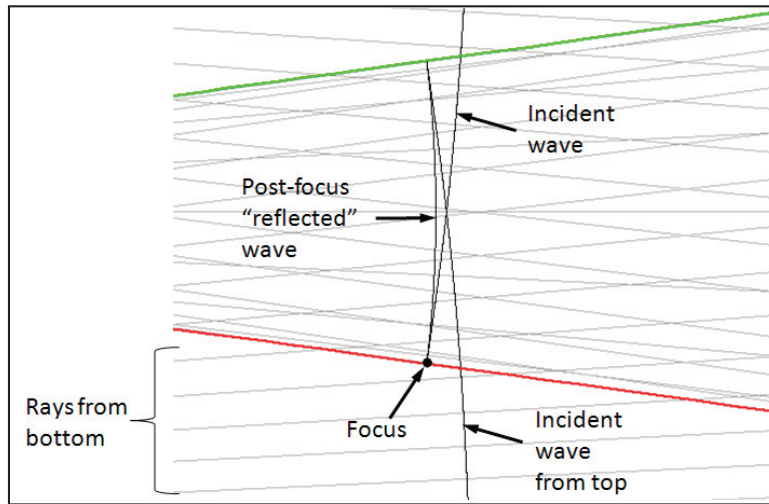


**Figure 9-93. Close-up view of focus region at 4000 meter wavefront, lower caustic.**

There is a marker in Figure 9-92 at the point where the 4000 meter wavefront intersects and is reflected from the lower (red) caustic. The coordinates and radius of curvature of the caustic at that point are shown. Figure 9-93 shows a close-up view of the area around the marked point. The point on the caustic corresponds to a focus, much as usually drawn for NTE. There is an overlap of waves associated with rays from the bottom half of the initial wavefront. The lower-half wave just to the right of the marked focus point is 77 meters ahead of it. If a suitable waveform can be assigned to the initial wave, with length such that the lower half wave does not overlap the top half and the lower caustic, then the result can be scaled to the flight test.

A suitable waveform must be such that the following conditions are met for the NPE case:

1.  $T_{ac}$  short compared to the distance between the focus and incident wave from the top: 77 meters (= 253 feet) for the Figure 9-92 and 9-93 cases.
2.  $T_{ac}$  and  $R_{cau}$  such that  $\delta$  lies within the converging region. In general, this should be less than the distance to the centerline.
3.  $P_{ac}$  such that  $\mu$  matches the full scale value in Table 9-7.

Re-arranging Equation (9-5c), the requirement for condition 2 may be written.

$$c_0 T_{ac} = \left( \frac{2\delta^3}{R_{cau}} \right)^{1/2} \quad (9-8)$$

Condition 1 may force a shorter duration.

Condition 3 follows from solving Equation (9-5d) for  $P_{ac}$ :

$$P_{ac} = \mu \frac{\rho_0 c_0^2}{(\gamma + 1)} \left[ (2c_0 T_{ac}) / R_{cau} \right]^2 \quad (9-9)$$

where  $\mu$  is the full-scale value (Table 9-7) that needs to be matched, and the remaining quantities are NPE scale.

For an initial run,  $c_0 T_{ac}$  was taken to be 18 m (slightly less than  $1/4$  of the 77 meter limit), so that for  $R_{cau} = 313300$  m,  $\delta = 370$  m, about the distance to the center. While a smaller  $\delta$  would be desirable, it would force a smaller  $c_0 T_{ac}$ , which would require a smaller step size and longer computational time.  $P_{ac}$  was taken to be 10 Pa, for which  $\mu = 0.0737$ , very close to the value for Maneuver C.

### 9.5.3 NPE Setup

The NPE is initialized with a wavefront that is the bottom half of the leftmost wavefront depicted in Figure 9-93. This rippled wavefront shape ensures that the wavefront will be normal to both the top and bottom boundaries, eliminating diffracted or reflected waves emanating from the boundaries. Truncated in the middle, the center of the ripple intersects the reflecting top boundary of the NPE domain. The top boundary is then the axis along which focusing occurs. As illustrated in Figures 9-92 and 9-93, the caustic cusp is located on this axis. As the solution propagates beyond the cusp, a caustic surface will grow into the NPE domain below the top boundary.

The spatial resolution of the NPE grid is  $\Delta x = .05$ m in the direction of propagation and  $\Delta y = .25$ m in the transverse direction. For the initial run, the N-wave has a length  $c_0 T_{ac}$  of 17.7m and is resolved with 354 grid points. The length of the NPE domain along the propagation axis is determined by the depth of the wavefront ripple ( $L_0$  from Equation (9-34)), the N-wave length, and the distance behind the initial N-wave needed to accommodate the lengthening N-wave and the reflected U-wave behind the caustic. The width of the NPE domain (along the transverse direction) is determined by the wavefront ripple parameters: a width of approximately  $2L_0$  provides a wavefront that is almost normal to the bottom boundary (a quadratic curve that is exactly normal to the boundary is spliced to the rippled wavefront). The spatial resolution and domain size described above result in a computational grid with 4200x4200 elements.

It was determined that the time step  $\Delta t$  must be smaller than  $1/20 \Delta x$  in order to avoid unstable ripple formation behind shocks. For the initial run,  $\Delta t = .002$  s. The solution was propagated to a distance of  $4 R_0 = 4000$ m, where the shock at the caustic has the scaled properties of SCAMP maneuver C, described in Table 9.7. The number of time steps needed to reach this propagation distance is

$$nts = \frac{2(4000\text{m})}{(340\text{m/s})(.002\text{s})} = 11765. \text{ The factor of two represents the need for two steps in the wide-angle}$$

NPE to propagate a distance  $c_0 \Delta t$ .

### 9.5.4 NPE Results

Figure 9-94 shows the results,  $p$  versus  $x$ , at five  $y$  positions for the above calculations. The caustic is at  $-370$  meters, so parts a, b, and c are on the illuminated side of the caustic while d and e are on the shadow side. Note the difference in amplitude scale for the five parts. The peak pressures for a through e are noted

in the caption. The peak pressure of 6.97 Pa for the leading Nwave in Figure 9-94a can be taken as  $P_{av}$ , although  $\zeta$  is short of being at  $\delta$ . The maximum focus wave is at Figure 9-94, with a peak of 12.79 Pa. The evanescent wave is seen to decay at lower values of  $z$ . This figure strongly resembles similar plots from nonlinear Tricomi calculations (e.g., Auger and Coulouvrat), although the coordinates of  $p$  versus  $x$  is reversed from the usual  $p$  versus  $t$ .

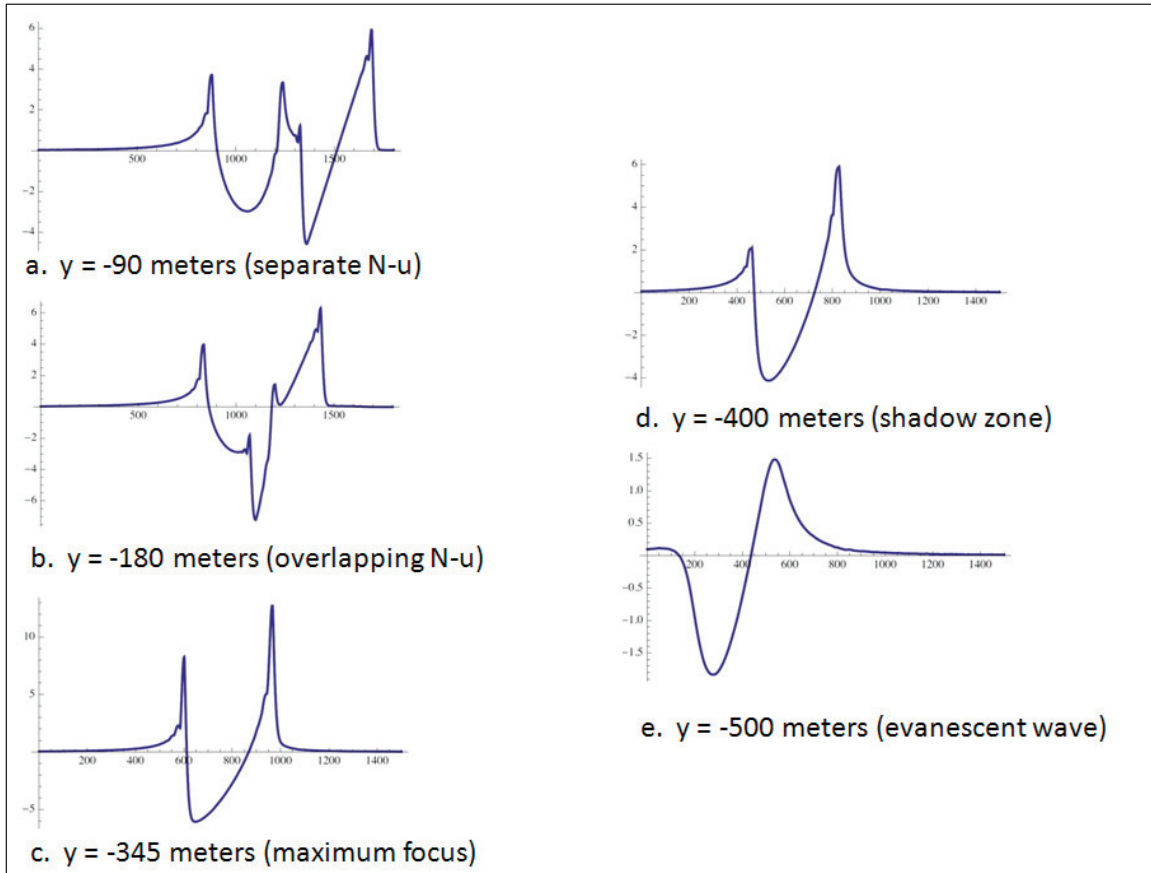


**Figure 9-94. NPE solution in the vicinity of the caustic at  $x = 4000$  meters.**  
**Peak pressures are a: 5.97 Pa, b: 6.30 Pa, c: 12.79 Pa, d: 5.90 Pa, e: 1.48 Pa.**

## 9.5.5 Comparison with Flight Test

Figure 9-95 shows the maximum focus NPE boom from Figure 9-94 scaled to Maneuver C, compared to the measured maximum focus for five Maneuver C foci, flight 1264. The calculated boom is scaled to full scale via Equations (9-4), and the coordinates have been transformed to  $p$  versus  $t$ . The signature duration matches well and the shape is in general agreement. The predicted peak overpressure of 5.27 psf is somewhat lower than the measured peak pressures of 7.1, 6.6, 8.6, 8.8, and 6.3 psf.

While  $\mu$  corresponds to full scale, the choice of  $\delta$  (to the centerline of the ripple wave field) was not appropriate, as this places the Tricomi boundary edge in a region that is converging differently from that closer to the caustic. An improvement to this method would be to propagate the signal a shorter distance,

taking the solution at a location where  $R_{cau}$  is smaller so that  $\delta$  would be smaller. The signature length,  $c_0 T_{ac}$ , used in the NPE calculation can also be shortened.

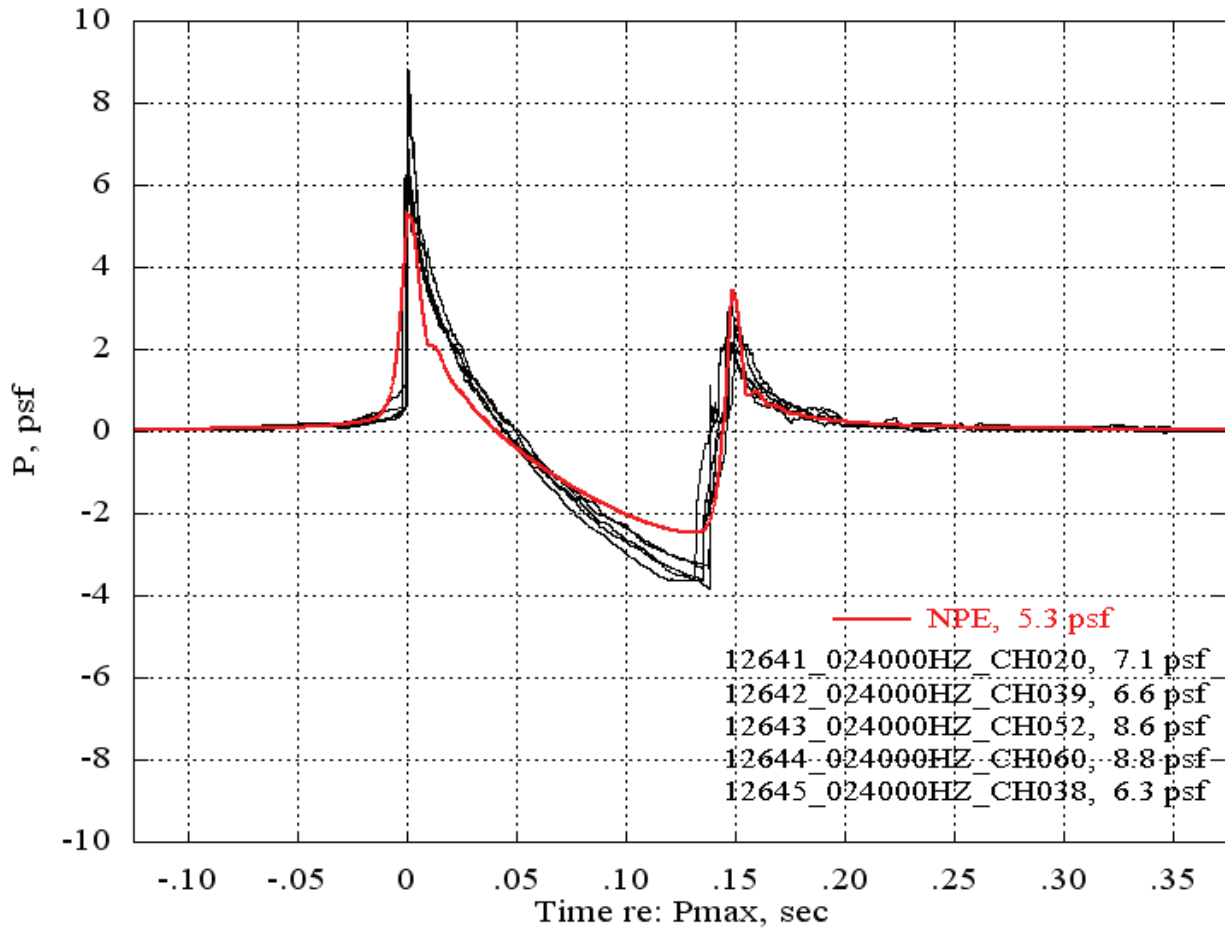


**Figure 9-95. Comparison of NPE maximum focus prediction (red), propagated 4000 meters, with measured Maneuver C focus (black).**

Figure 9-96 shows a similar comparison for this signature propagated to 2500 meters, rather than 4000 meters.  $R_{cau}$  at that distance is 53,000 meters, rather than 313,300 meters as for the case presented above. That radius is comparable to that for Maneuver C, but  $\mu = 0.0408$ , which is not in the range of any of the SCAMP foci.  $\delta$  is also smaller, but places the top of the diffraction layer around the middle of the wave field. A signature comparable to Figure 9-94a was not obtained, but (based on propagation distance) the N-wave peak is estimated to be 8 Pa rather than 6 Pa as in Figure 9-94. The fit is much better, but cannot be taken as reliable because of the estimated N-wave peak and the difference in  $\mu$ .

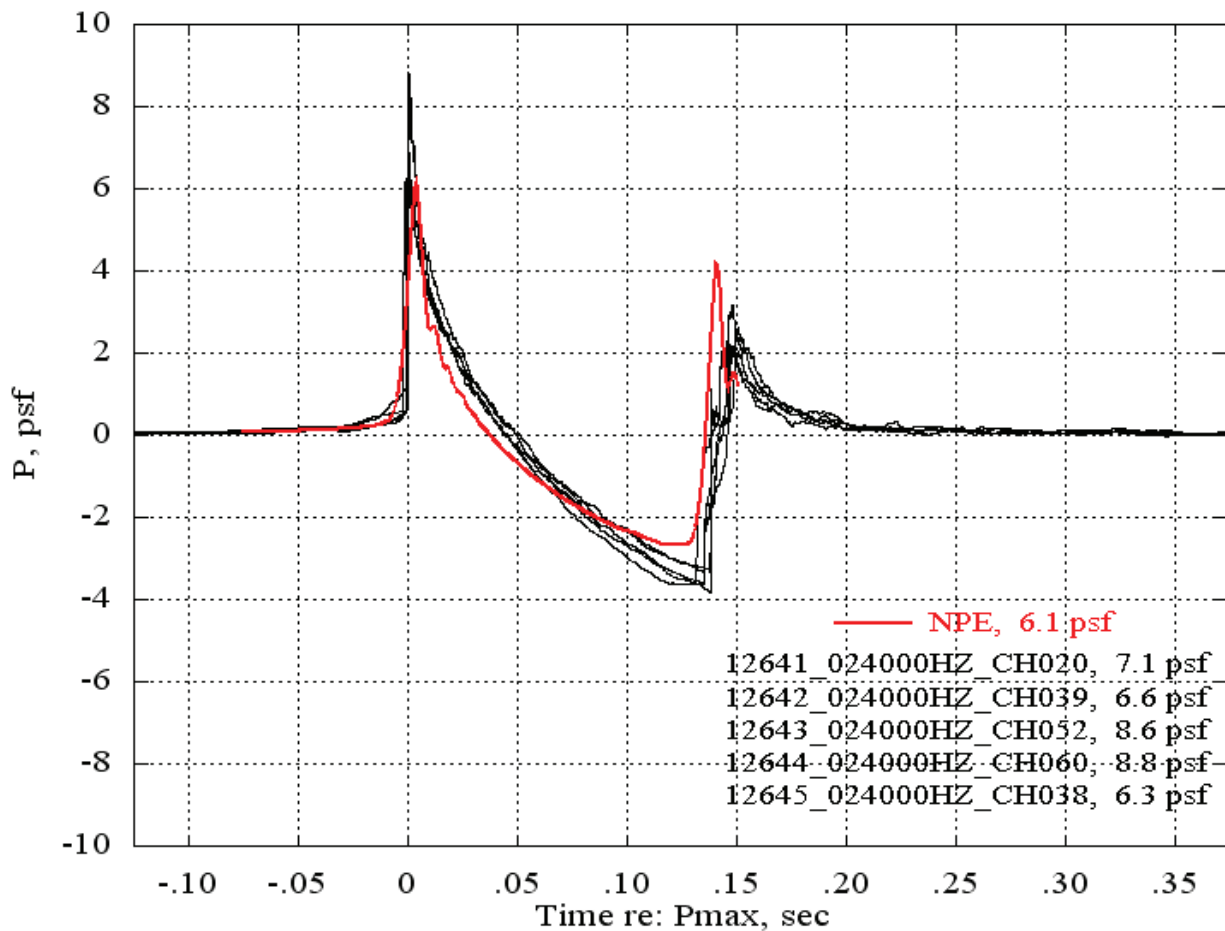


Figure 9-96. Comparison of NPE maximum focus prediction (red), propagated 2500 meters, with measured Maneuver C focus (black).

## 9.5.6 Conclusions and Potential Improvements

The original difficulties in applying NPE to SCAMP have been identified and are due to edge diffraction effects resulting from the truncation of a concave wavefront. Those effects can be avoided by recognizing the initial cusp and “mirror” caustic and defining the initial wave such that it is normal to the boundaries of the computational domain. The single ripple analyzed here satisfies those conditions. The resultant caustics have variable curvature, which is beneficial for domain exploration since one can examine the effect of curvature without changing the ray geometry. It is a potential issue for rigor because the SCAMP caustics were very close to constant curvature.

This analysis, and the results shown in Figures 9-95 and 9-96, represents the beta version of NPE-SCAMP. The following could be considered for future versions:

- Definition of a wavefront similar to the single ripple employed here, but designed such that the caustic curvature will have less variation. This can be achieved by employing `pcboom2npe` to generate a wavefront segment from the `pcboom` solution at a specified time (as in the original approach for initializing the NPE), aligning this wavefront so that it is normal to the domain boundary at the end closest to the caustic, and extending the other end of the wavefront artificially so that it is convex and becomes normal to the other boundary. With reflecting boundaries, this hybrid wavefront will have a ripple shape that generates a caustic with the correct curvature.
- Further development of Tricomi-based scaling to better represent SCAMP conditions. In particular, wavelength must be adjusted such that  $\delta$  lies within the converging ray region near the caustic
- Integrate initialization and running of code with plotting of output.





## Low Boom Vehicle Analysis

### 10.1 Low-Boom Vehicle Descriptions

Transition focus booms were examined for four low-boom configurations. Gulfstream provided data for a small (business jet) aircraft, Boeing provided data for medium-sized N+2 supersonic aircraft, and NASA provided data for two aircraft: a small low-boom demonstrator and a large N+2 aircraft. The transonic acceleration profile was provided for each.

This section contains a description of the low-boom configurations and focusing conditions.

#### 10.1.1 Gulfstream Configuration

##### *Configuration Overview*

The Gulfstream low-boom configuration for a Quiet Supersonic Jet (QSJ) achieves its signature shaping primarily from the Gulfstream Quiet Spike™. Figure 10-1 is an isometric view of a potential design configuration for a purpose-built QSJ that incorporates the use of the Gulfstream Quiet Spike™. It consists of telescoping segments of decreasing diameter that extend outward from the nose of the QSJ. The signature shaping avoids the classic “N-wave” shock in the front part of the signature by creating a confluence of smaller shocks that do not coalesce. Figure 10-2 is an example of the predicted effects of signature shaping during cruise conditions for a QSJ compared to a QSJ without shaping.

The additional main characteristics for a potential Gulfstream QSJ are:

- Capable of accommodating 8 to 14 passengers;
- Capable of Operating from General Aviation airports with airfield lengths of ~6,500 feet; ;
- Have a Mach 1.8 cruise;
- Have a range of ~4,000 nm;
- Produces a signature quiet enough for un-restricted flight over populated areas;
- Have a Maximum weight of ~100,000 pounds;
- Have a variable sweep wing;
- Possess a 50 percent fuel fraction; and
- Possess Stage 4 (or latest) noise certification levels.

The vehicle used by Gulfstream for this study is a result of on-going conceptual design studies for aircraft designed with a cruising speed of Mach 1.8. In lieu of having a completed 3-D aircraft configuration, the near-field analysis provided utilizes an equivalent configuration consisting of body of revolution with the Quiet Spike™ attached to its nose (see Figure 10-3). The resulting area distribution exhibits the same near-field pressure distribution at the zero-degree azimuth as the near-field design target for a potential full-scale QSJ. The body of revolution portion includes equivalent lift and thus ends with a finite area. Shaped sonic boom signature generation is associated with the second derivative of area. Therefore, details of the near-field signature are not necessarily visibly apparent in the figure.

### ***Operational Trajectory Leading to Focusing Conditions***

The potential QSJ aircraft would perform an acceleration/climb upon takeoff. The vehicle would become supersonic during the acceleration/climb segment prior to reaching the cruise segment of the mission. Ray tracing was conducted in PCBoom to determine the flight condition that leads to the ground intercept of the caustic at the undertrack location. The resulting aircraft flight conditions are:

- Mach 1.18;
- Mach rate of 0.001 mach/second;
- Altitude of 35,000 feet; and
- 2° climb angle.

The CFD analysis of the configuration from Figure 10-3 had been conducted at Mach 1.15 and Mach 1.20 (see Figure 10-4). The Mach 1.20 near-field data were the closer of the two cases to the Mach number of the focusing condition and were chosen for far-field propagation. The near-field signature Mach 1.20 at one body length away from the vehicle was propagated in PCBoom6 through the standard atmosphere down to an elevation corresponding to one diffraction boundary layer thickness from the caustic.

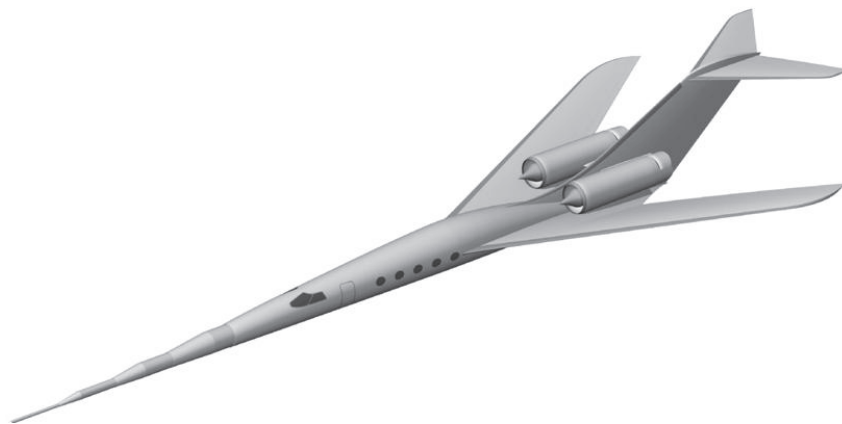


***Figure 10-1. Isometric view of a potential Gulfstream Quiet Supersonic Jet.***

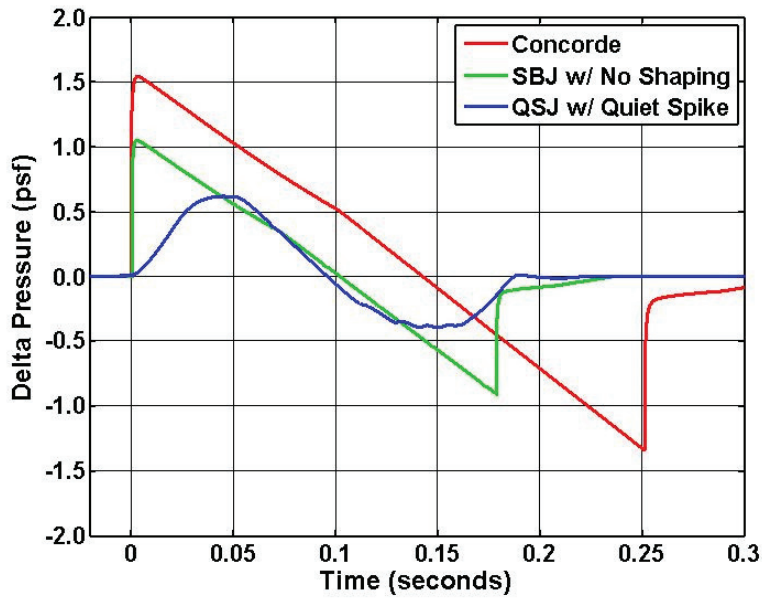


Figure 10-2. Comparison of predicted ground signatures for supersonic vehicles during cruise flight conditions with and without signature shaping.

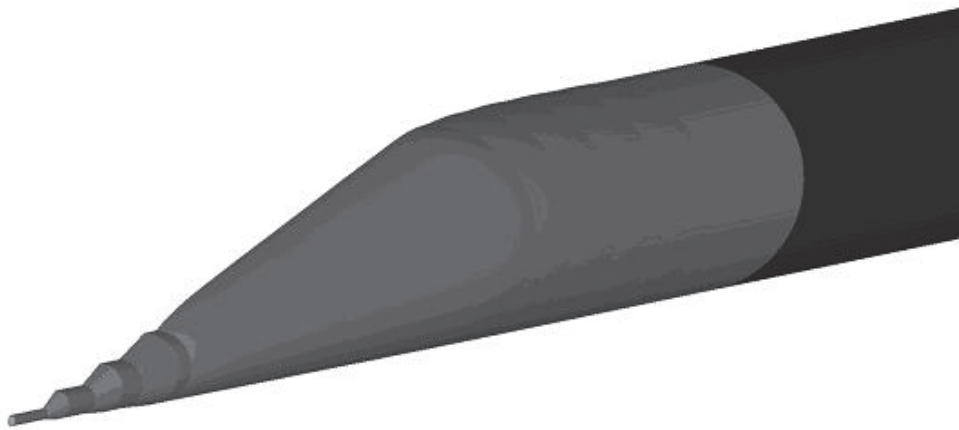


Figure 10-3. Equivalent body for CFD analysis of Gulfstream Configuration.

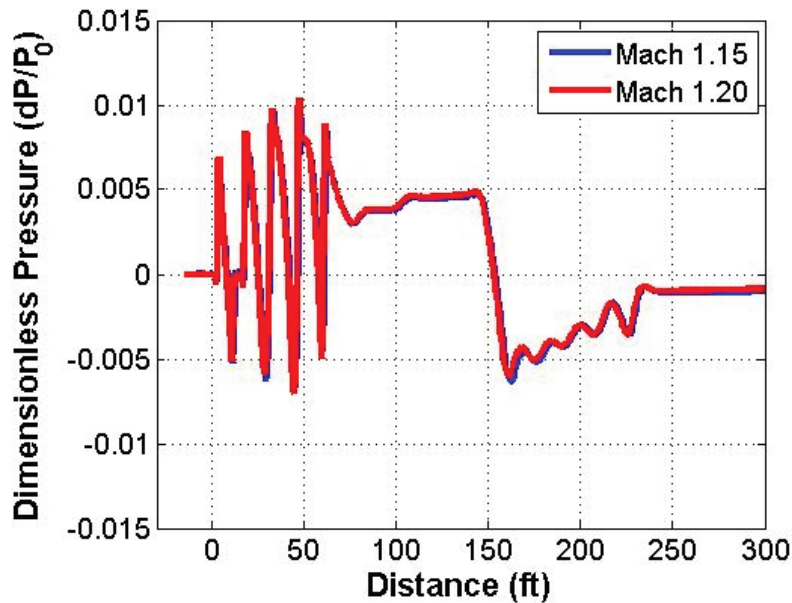
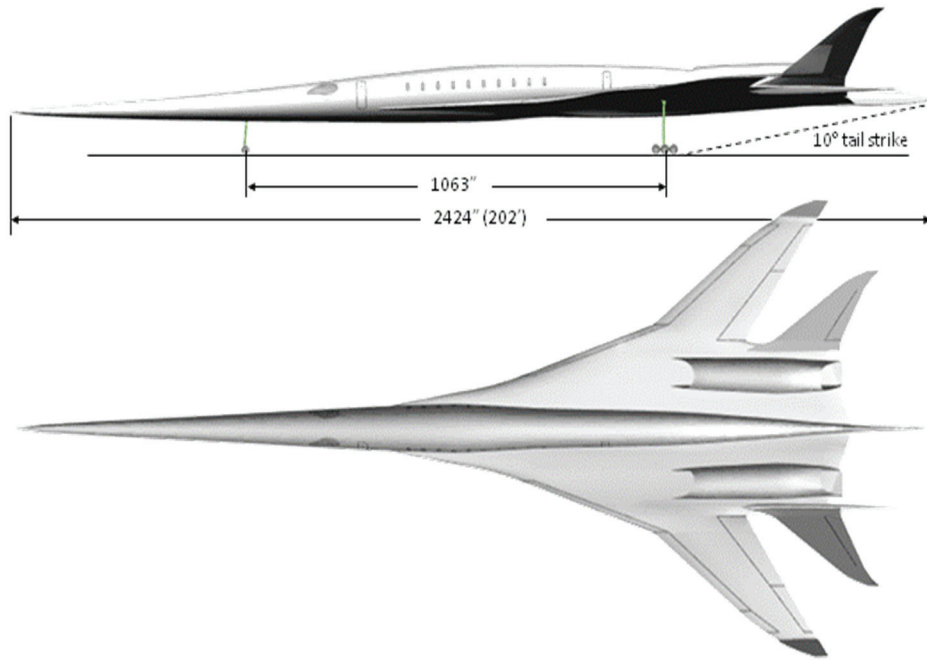


Figure 10-4. QSJ near-field signatures at Mach 1.15 and Mach 1.20.

### 10.1.2 Boeing Configuration

Boeing provided data for an “N+2” type aircraft concept developed during a system study (Welge, 2010). Variations of configurations range in capacity from 30 to 100 passengers. Cruise is Mach 1.6 to 1.8 at 45,000 to 50,000 feet. Transonic acceleration is expected to be at a Mach rate of 0.000875/second (0.5 kt/second, similar to Concorde) in level flight at 40,000 feet. Boeing provided data for a modified 30+ passenger concept from these System Studies – the 076E.

In a follow-on effort (Welge, 2010), modifications to the 076E configuration from the above System Study necessary to achieve low-boom signatures less than 85 PLdB were done under contract to NASA (*N+2 Supersonic System-Level Experimental Validation – NNL10AA00T*). Figure 10-5 shows the resulting configuration from the Experimental Validation contract.



**Figure 10-5. Boeing N+2 Low-Boom Concept Aircraft.**

The focus for the aircraft shown in Figure 10-5 is generated as it passes through Mach 1.165. Boeing provided cylinders of CFD data for Mach 1.15 at 40,000 feet, at radii of one, two, three and four body lengths. Figure 10-6 shows  $\delta p/p$  for the four cylinders. Body length for the configuration analyzed was 202 feet, and the cylinder at one body length was used for analysis. The one body length cylinder was selected for consistency with the other configurations, for which data at one body length were provided.

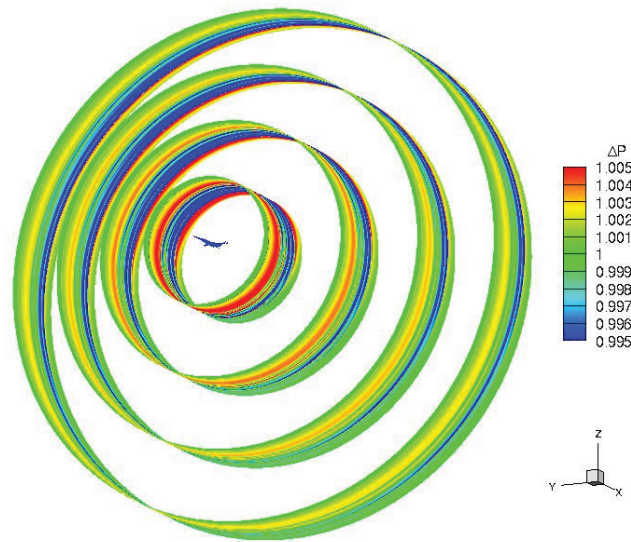


**Figure 10-6. Pressure field at four radii for Boeing Configuration.**

### 10.1.3 NASA Configurations

NASA provided two configurations – a small (36,000 pound, 127-foot long) low-boom demonstrator concept (Shields and Li, 2011) and a large (190,000 pound, 241-foot long) N+2 vehicle based on concepts in (Welge, 2010). Figure 10-7 shows the low-boom demonstrator aircraft, while Figure 10-8 shows Configuration 765-076F (Welge, 2010).

NASA provided detailed mission trajectories for both aircraft. Those were processed through PCBoom to determine the focus condition. The low-boom demonstrator generates its focus condition at Mach 1.19, accelerating at a Mach rate of 0.002/second as it passes through 34,000 feet at a climb angle of 1.8°. The N+2 aircraft generates its focus condition at Mach 1.158, accelerating at a Mach rate of 0.00044/second (0.25 kts/second) at an altitude of 46,400 feet at a slight climb of .005°. NASA provided CFD cylinders at those conditions, at a radius of one body length, for each aircraft.

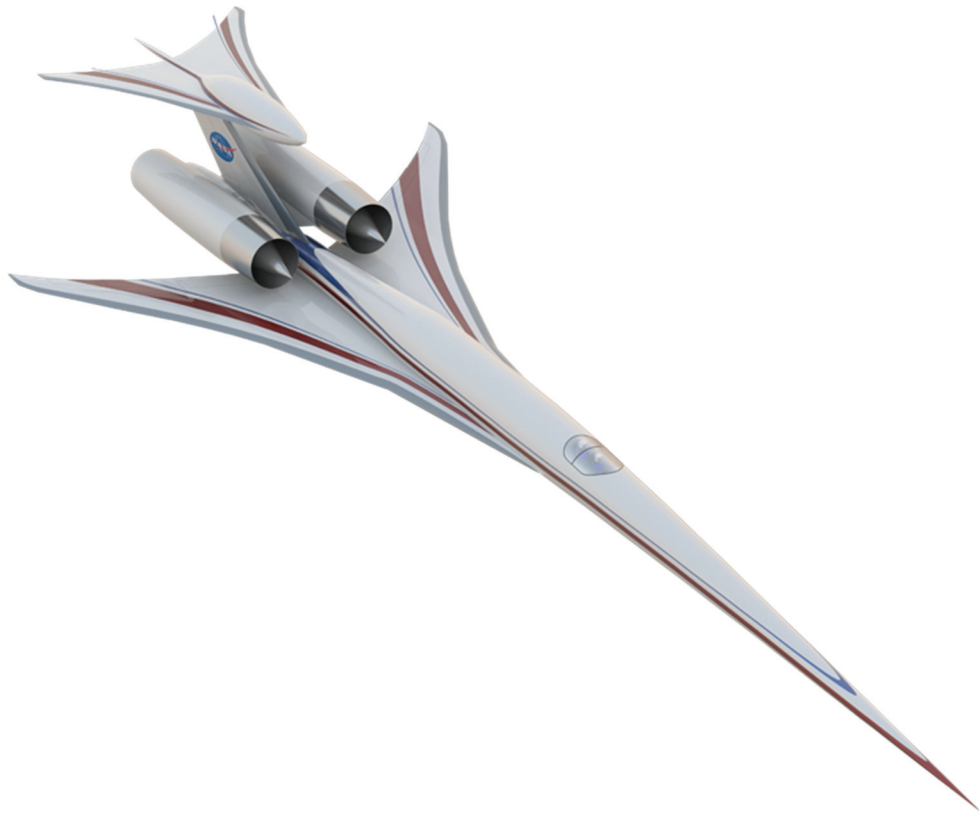


*Figure 10-7. NASA Low-Boom Demonstrator Concept Aircraft.*

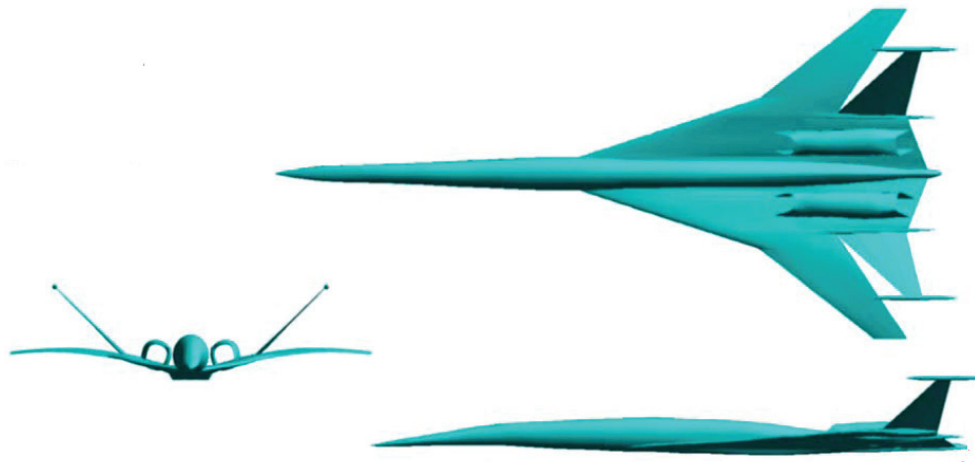


**Figure 10-8. 765-076F Configuration from Reference 2-1.**

## 10.2 Focused Boom Analysis Process

PCBoom provides the framework for focused boom analysis. In addition to providing the ray tracing, it also provides the input signatures to the LNTE and NPE Codes.

The data preparation process consisted of the following steps for each configuration:

1. PCBoom was run for the transonic profile. This determined the flight conditions (Mach number and altitude) at which focus was generated.
2. Gulfstream, Boeing, and NASA then prepared signatures under the aircraft for the focus-generating conditions. Gulfstream provided a line of  $\delta p/p$ , while Boeing and NASA provided cylindrical cuts through CFD solutions.
3. PCBoom was then run using the starting signatures. This directly provided the Gill-Seebass solution, and also provided inputs necessary for the other two focus solvers.

The interface to each of the three focus solvers is described in Sections 10-3, 10-4, and 10-5.

The NPE method presented in Section 7 is different from the Tricomi methods, in that it does not trace rays, define a caustic, then apply a local diffraction solution. Rather, it propagates an initial wavefront and enables the evolution of physics. The initial wavefront is readily constructed from a set of rays, at suitable intervals, covering the region between the two rays shown in Figure 9-16, with a suitable margin to encompass the edges above and below the diffraction region.

For the Tricomi solution, as presented in Section 8, a solution along the  $\delta$  tangent ray as sketched in Figure 9-16,  $\delta$  is computed from the relations associated with Equation 10-6, and requires the ray/caustic curvature  $R$  and the wave duration  $T_{ac}$ .  $R$  is available from PCBoom's focus solution, and (because nonlinear steepening is very weak near the ground)  $T_{ac}$  can be taken from either the Gill-Seebass solution or the Last Geometric Signature.

Once  $\delta$  is established, an interactive tool (described in the next section) has been prepared to identify the correct ray. Because the Tricomi solver presented in Section 8 includes molecular absorption losses, the signature must include losses. This is obtained by using the Burgers solver, PCBurg, that is part of the PCBoom package (Page, 2010).



The NPE method requires a series of rays in the plane of the focus. This is straightforward to obtain by running PCBoom in Over The Top (OTT) mode, ensuring that the trajectory begins before and after the two rays. This mode, usually used for over the top booms, generates an “.ott” file that contains the complete solutions (shape, age parameter, amplitude factor, atmospheric properties) at every mesh point on each ray. An accompanying “ots” file contains the starting signature for each ray, so that the waveform at an appropriate starting wavefront can be generated.

## 10.3 PCBoom Gill-Seebass Low-Boom Configuration Analysis

### 10.3.1 Gulfstream Configuration

A PCBoom run was set up for the vehicle described in Section 10.1.1. With the trajectory defined by the altitude, acceleration and climb angle at focus-generating condition, a TADVANCE format trajectory file was prepared, with the initial point adjusted such that the focus occurred as the vehicle passed through 35,000 feet. A standard atmosphere, and ground at sea level, was assumed. Figure 10-9 shows the maximum focus solution.<sup>3</sup> This includes final thickening of shocks with a  $1/p$  Taylor shock structure, and a ground reflection factor of 1.9.

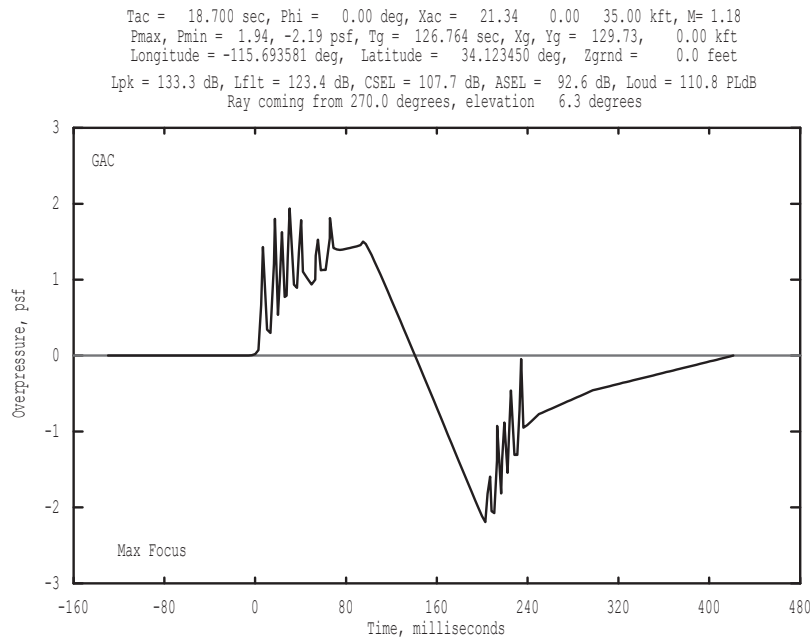


**Figure 10-9. Maximum focus solution for Gulfstream Configuration.**

<sup>3</sup>The starting signatures for the Gulfstream configuration presented here were based on computations at the time of the Alpha focused boom analysis. They have since been updated and are provided in Elmer (2013). These solutions were retained so that direct comparisons between PCBoom, Lossy NTE, and NPE predictions could be provided for a variety of low-boom signatures that retained their shaping.

For input to the Tricomi solver, the wave on the upper tangent ray is required. Figure 10-10 shows the ray geometry. The ray is propagating from the upper left to the lower right, the opposite convention. The following details are shown:

- The ground elevation, as a horizontal gray line.
- The caustic, in black.
- Green circles indicating where rays intersect the ground. The ground focus location is at the minimum time and position of these intersections.
- The  $\delta$  tangent ray, in red, together with a red line connecting its closest point to the focus.
- A data block at the top identifying the case and giving the trajectory data for the focus-generating point, the elevation of the focus (within a few feet of the ground) and the ray/caustic radius of the curvature (294,971 feet).
- The elevation angle and degrees of the intersection of the caustic and ray with the ground.
- A data block giving the generation time and azimuth of the  $\delta$  tangent ray, the distance to the focus, and related parameters.

For this case,  $\delta$  was calculated to be 2100 feet. Figure 10-10 is a screen image of interactive program “raycau”, which is the initial version of the PCBoom-to-TRICOMI utility tool noted in Section 10-2. It reads the PCBoom “out” file for a case. The  $\delta$  tangent ray is then found by stepping through all rays and observing the nearest ray point distance, stopping when that distance matches  $\delta$ . The tangent ray in this case was generated at aircraft time 41 seconds, which is slightly more than 22 seconds after the focus generation ray at aircraft time 18.5 seconds.

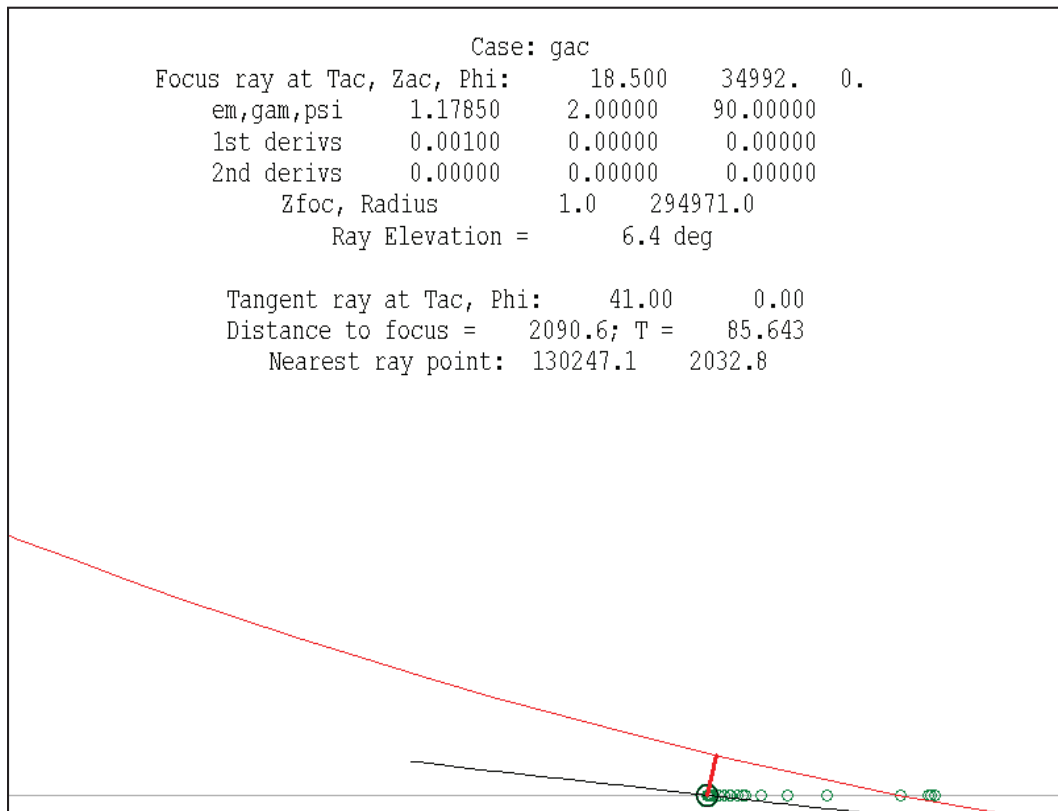


**Figure 10-10. Ray and caustic geometry for Gulfstream focus condition.**

The Tricomi boundary condition for this case is the signature along the  $T = 41$ ,  $\phi = 0$  ray as it passes the point of closest approach indicated in Figure 10-10. This was obtained by running PCBurg. Figure 10-11 shows the thin shock (lossless) signature. Figure 10-12 shows the signature including losses. The PCBoom and PCBurg run used the US Standard Atmosphere and the humidity profile presented in Annex C of ANSI Standard S1.26 (R2004). A sampling rate of 102.4 kHz was used for the Burgers solution.

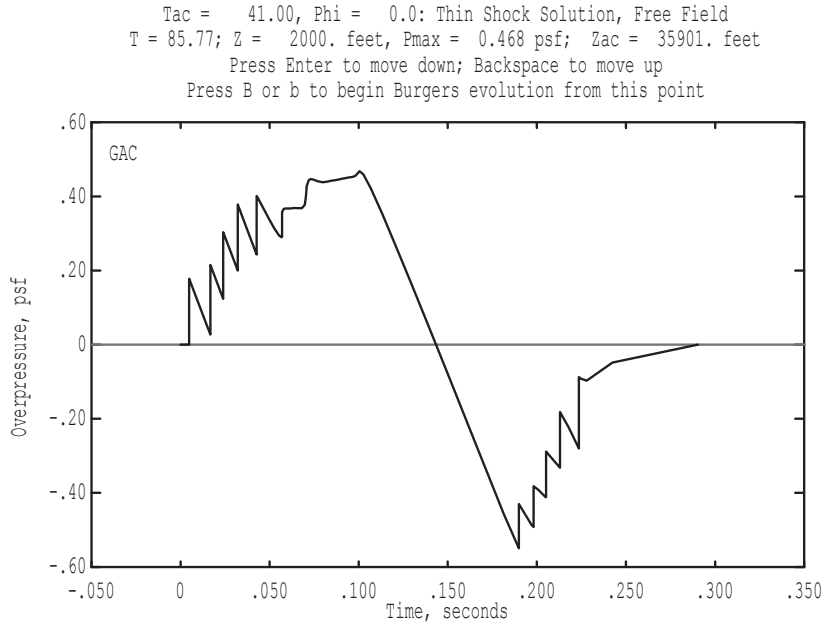


**Figure 10-11. Thin shock solution for  $\delta$  Tangent Ray for focus of Gulfstream Low-Boom Aircraft.**

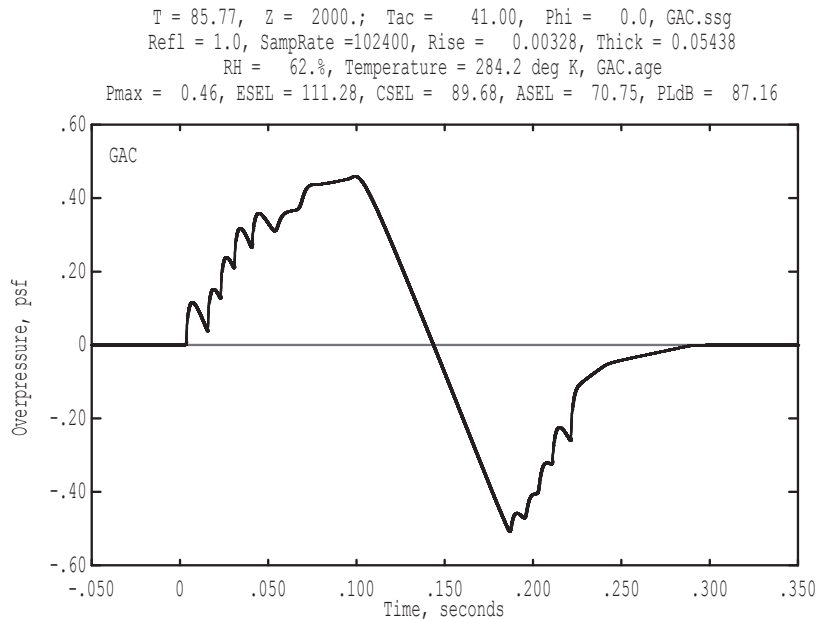


**Figure 10-12. Lossy Solution for  $\delta$  Tangent Ray for focus of Gulfstream Low-Boom Aircraft.**

### 10.3.2 Boeing Configuration

A PCBoom run was set up for the vehicle described in Section 10.1.2. With the trajectory defined by constant acceleration at 40,000 feet, a TADVANCE format trajectory file was prepared with the initial Mach number below cut-off condition. A standard atmosphere, and ground at sea level, was assumed. Figure 10-13 shows the maximum focus solution. This includes final thickening of shocks with a 1/p Taylor shock structure, and a ground reflection factor of 1.9.

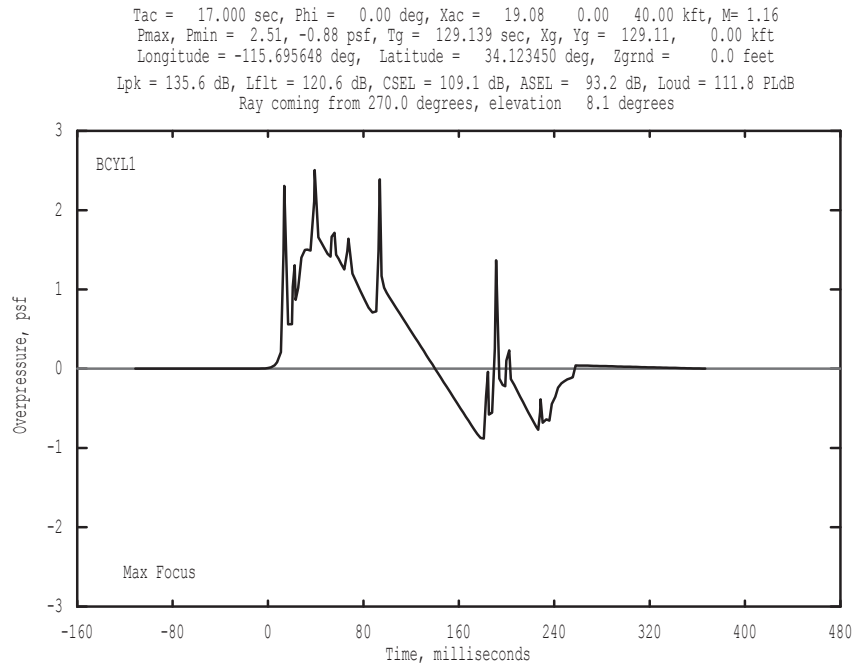


**Figure 10--13. Maximum focus solution for Boeing Configuration.**

Figure 10-14 is the ray diagram for this case, similar to that shown in Figure 10-12 in the previous section. The diffraction thickness  $\delta$  is approximately 2000 feet. Figures 10-15 and 10-16 show the thin shock and lossy solutions, respectively, at the boundary condition point on the  $\delta$  tangent ray. The standard atmosphere, with ANSI S1.26 humidity and a sampling rate of 102.4 kHz, was used for the lossy solution.

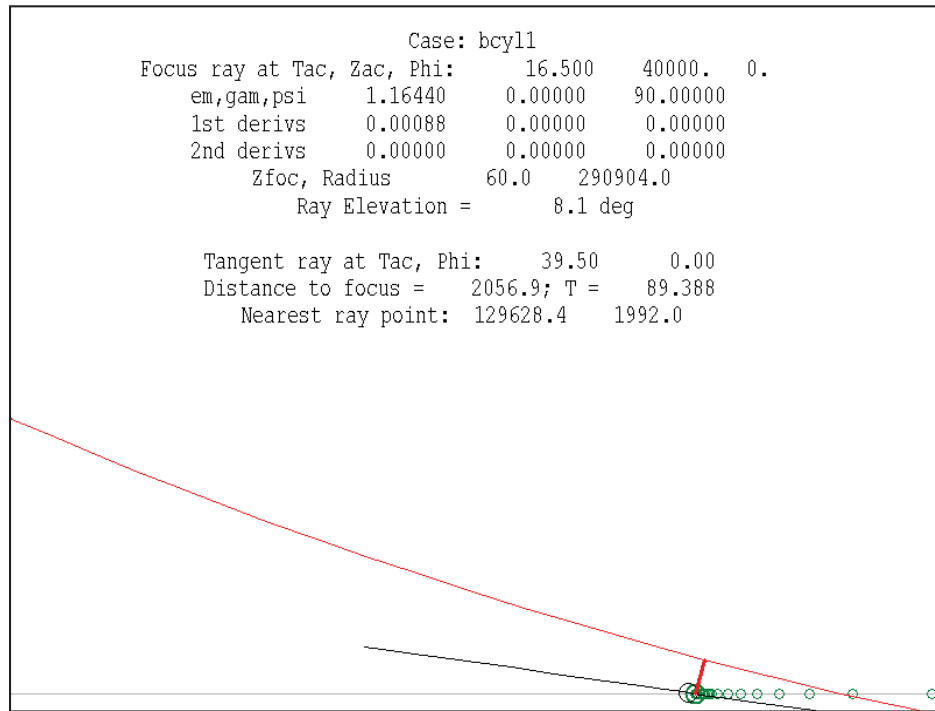


**Figure 10-14. Ray and caustic geometry for Boeing focus condition.**

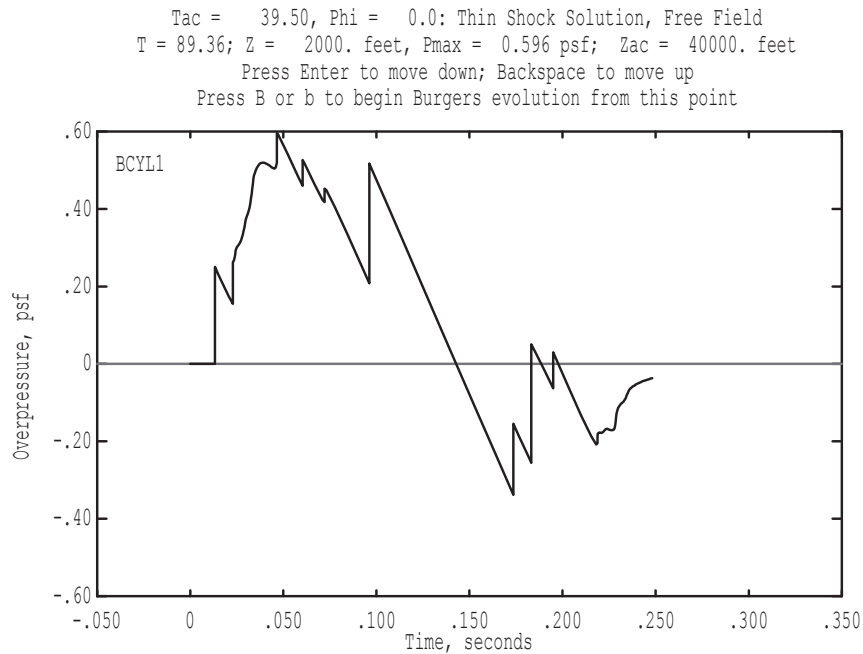


**Figure 10-15. Thin shock solution for  $\delta$  Tangent Ray for focus of Boeing Low- Boom Aircraft.**

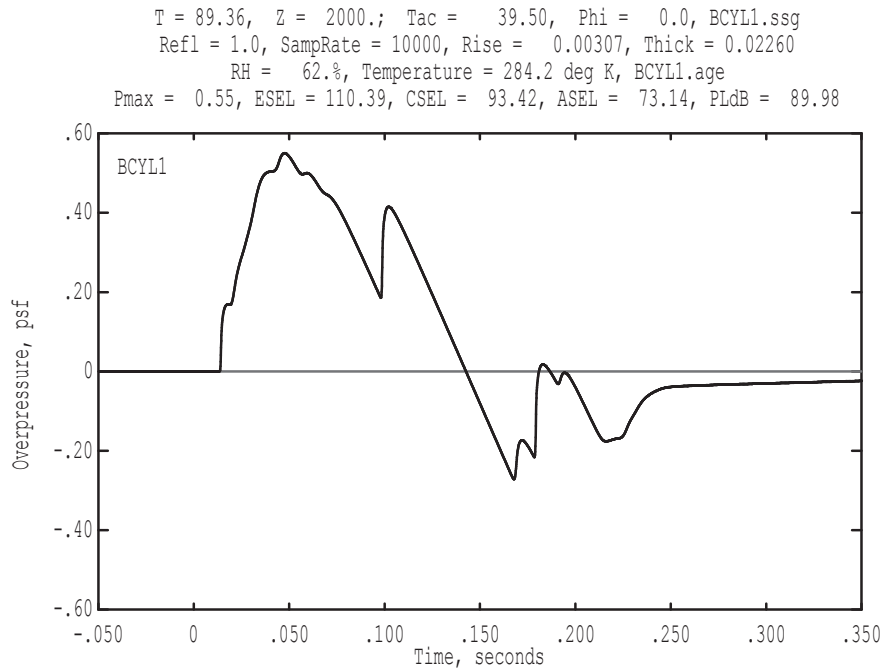


**Figure 10-16. Lossy Solution for  $\delta$  Tangent Ray for focus of Boeing Low-Boom Aircraft.**

### 10.3.3 NASA Configurations

PCBoom runs were set up for the two NASA configurations described in Section 10.1.3. NASA provided trajectories in the form of spreadsheets with the data required for PCBoom, although at time intervals of 10 to 30 seconds. These were interpolated to 1 second intervals for the transition acceleration region. The initial signatures were defined by the CFD cylinders.

Figures 10-17 through 10-20 show the PCBoom focus solution, the ray diagram, and thin shock and lossy solutions at the  $\delta$  tangent ray for the small demonstrator aircraft. Figures 10-21 through 10-24 show the same information for the N+2 aircraft. The diffraction thickness  $\delta$  for the demonstrator is 1400 feet, while that for the N+2 aircraft is 2100 feet.  $\delta$  for the demonstrator aircraft is smaller than for the others because of its shorter length. The ray/caustic radius of curvature is similar for all four cases.

Tac = 1016.350 sec, Phi = 0.00 deg, Xac = 303.72 0.00 33.93 kft, M= 1.19  
 Pmax, Pmin = 1.68, -0.75 psf, Tg = 1105.067 sec, Xg, Yg = 390.84, 0.00 kft  
 Lpk = 132.1 dB, Lflt = 114.6 dB, CSEL = 105.7 dB, ASEL = 92.5 dB, Loud = 109.9 PLdB  
 Ray coming from 270.0 degrees, elevation 11.9 degrees

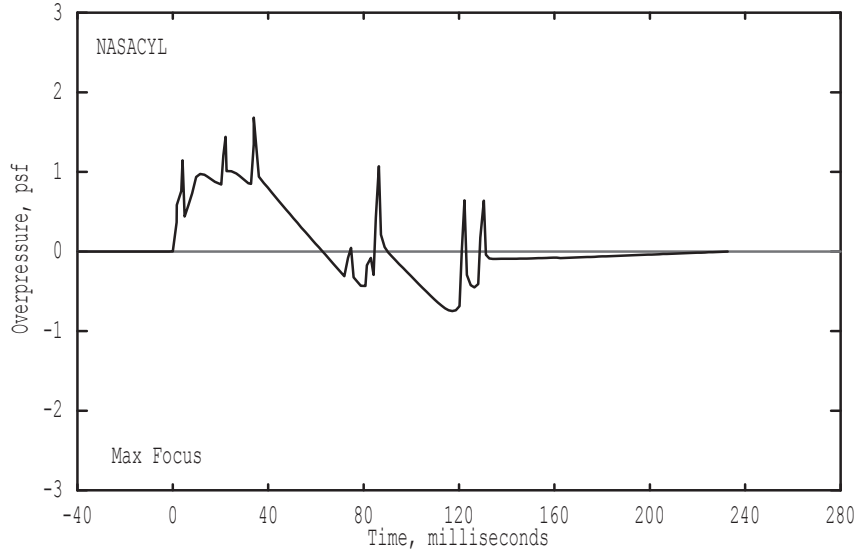


Figure 10-17. Maximum focus solution for NASA Demonstrator Configuration.

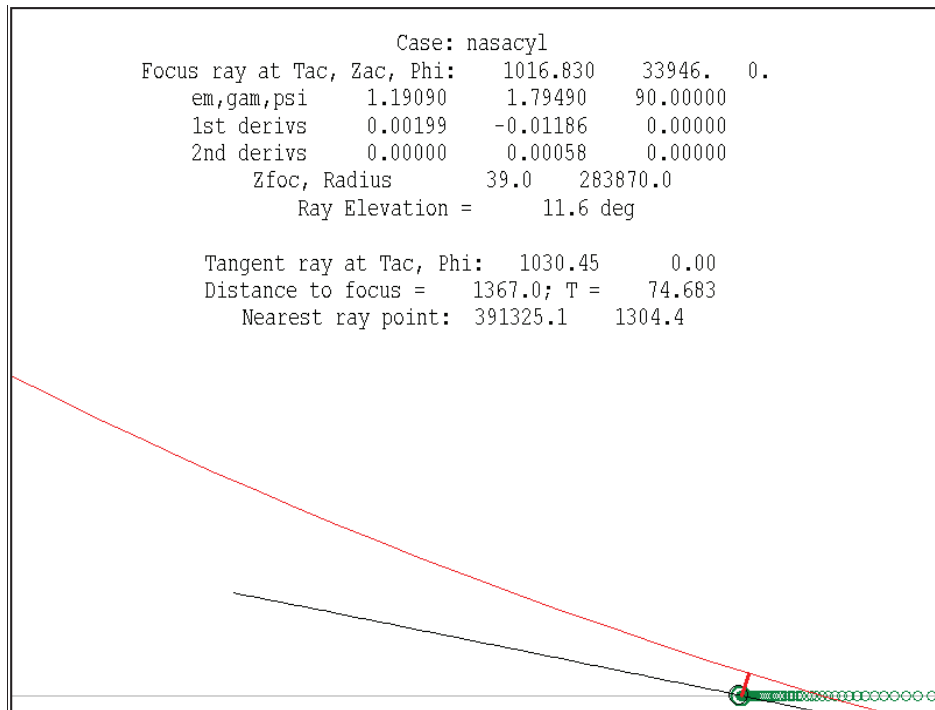
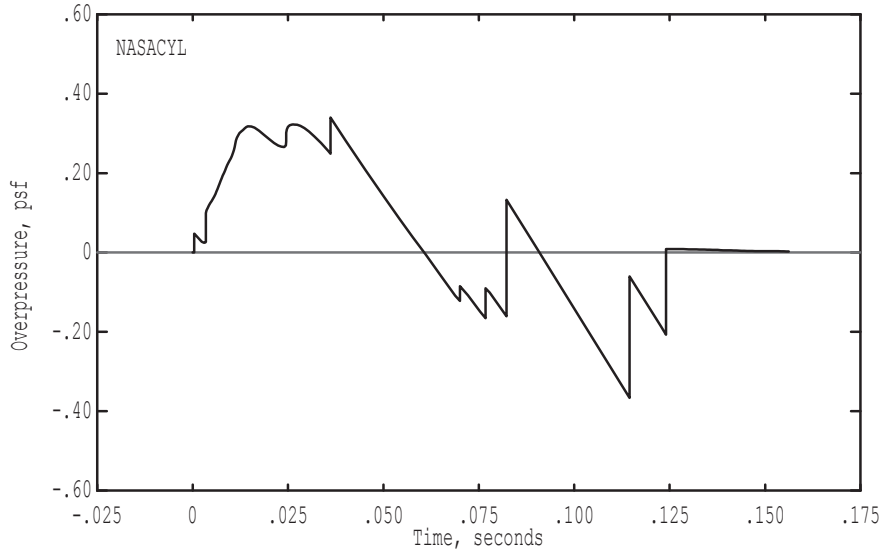


Figure 10-18. Ray and caustic geometry for NASA Demonstrator focus condition.

Tac = 1030.45, Phi = 0.0: Thin Shock Solution, Free Field  
 T = 72.59; Z = 2000. feet, Pmax = 0.340 psf; Zac = 34444. feet  
 Press Enter to move down; Backspace to move up  
 Press B or b to begin Burgers evolution from this point



**Figure 10-19. Thin shock solution for  $\delta$  Tangent Ray for focus of NASA Demonstrator Aircraft.**

T = 72.59, Z = 2000.; Tac = 1030.45, Phi = 0.0, NASACYL.ssg  
 Refl = 1.0, SampRate = 102400, Rise = 0.01039, Thick = 0.02078  
 RH = 62.%, Temperature = 284.2 deg K, NASACYL.age  
 Pmax = 0.31, ESEL = 103.87, CSEL = 92.79, ASEL = 74.67, PLdB = 91.23

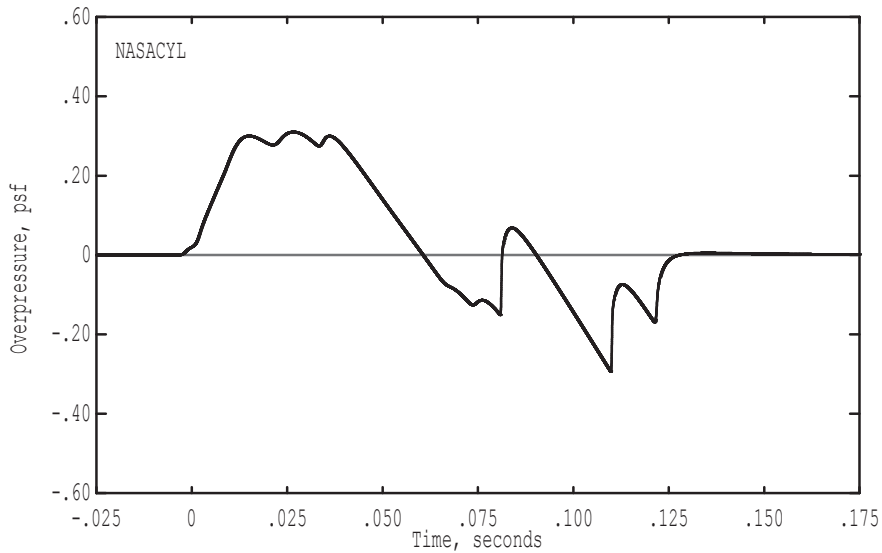


**Figure 10-20. Lossy Solution for  $\delta$  Tangent Ray for focus of NASA Demonstrator Aircraft.**



Tac = 1499.530 sec, Phi = 0.00 deg, Xac = 793.74 0.00 46.47 kft, M= 1.16  
Pmax, Pmin = 3.65, -1.39 psf, Tg = 1635.912 sec, Xg, Yg = 927.25, 0.00 kft  
Lpk = 138.8 dB, Lflt = 122.7 dB, CSEL = 109.8 dB, ASEL = 93.3 dB, Loud = 111.7 PLdB  
Ray coming from 270.0 degrees, elevation 5.0 degrees

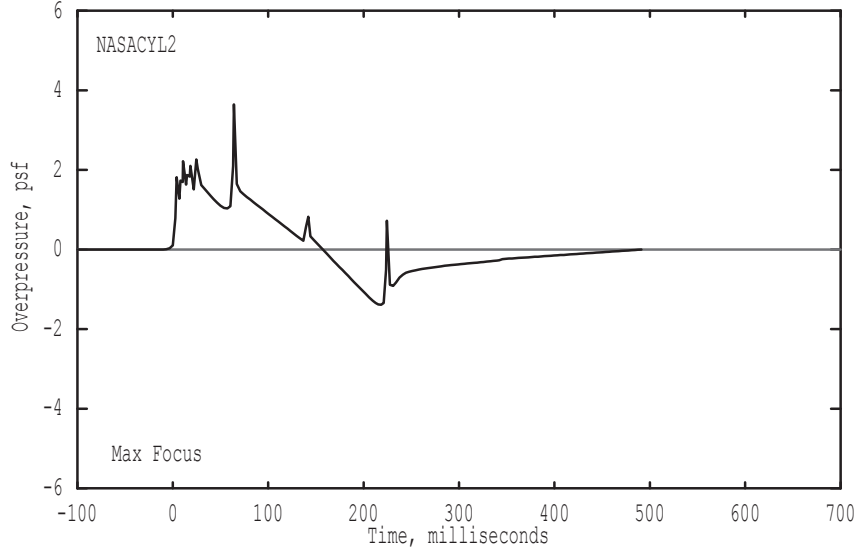


**Figure 10-21. Maximum focus solution for NASA N+2 Configuration.**

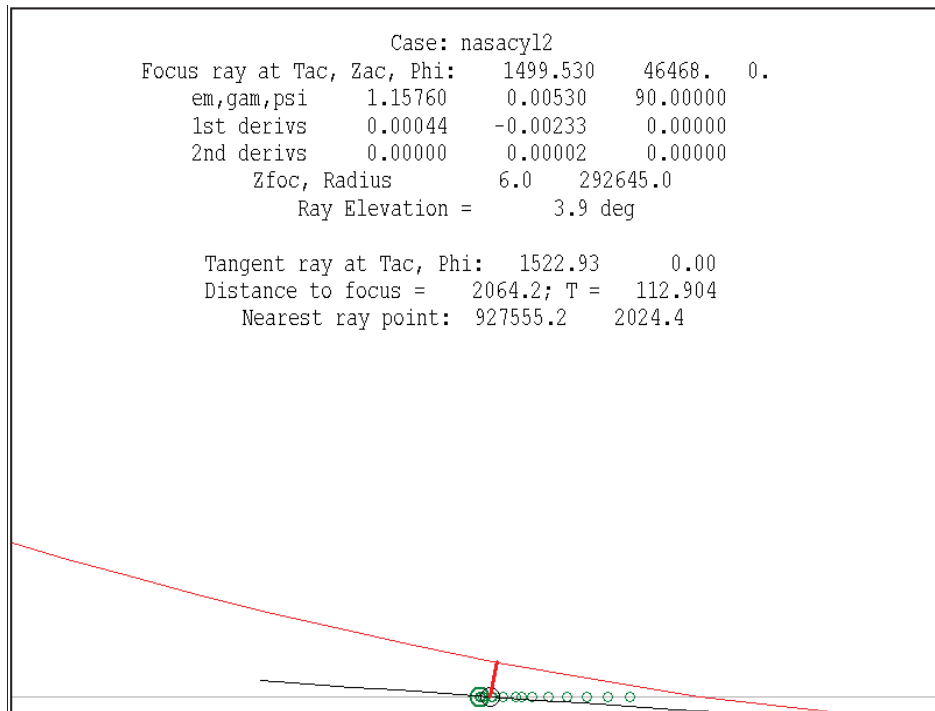


**Figure 10-22. Ray and caustic geometry for NASA N+2 focus condition.**

Tac = 1522.93, Phi = 0.0: Thin Shock Solution, Free Field  
 T =123.77; Z = 0. feet, Pmax = 0.925 psf; Zac = 46470. feet  
 Press Enter to move down; Backspace to move up  
 Press B or b to begin Burgers evolution from this point

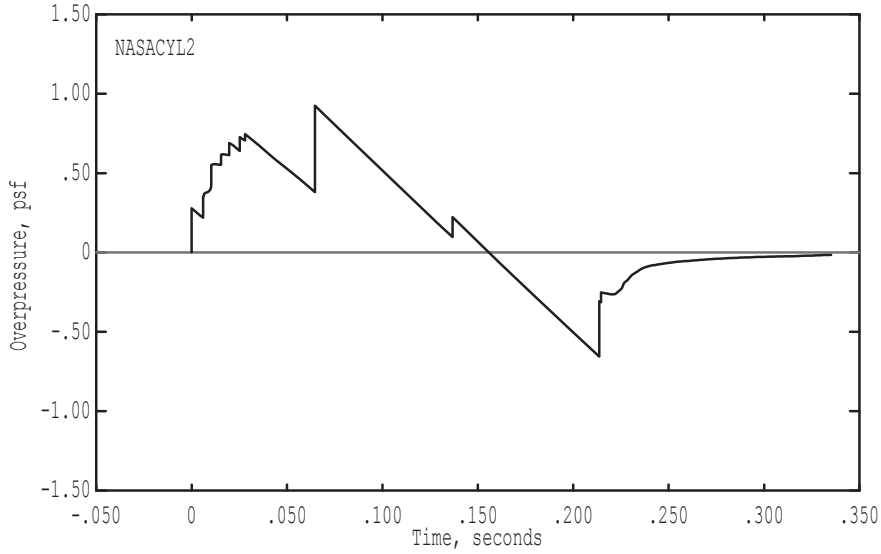


**Figure 10-23. Thin shock solution for  $\delta$  Tangent Ray for focus of NASA N+2 Aircraft.**

T =113.02, Z = 2000.; Tac = 1522.93, Phi = 0.0, NASACYL2.ssg  
 Refl = 1.0, SampRate =102400, Rise = 0.00061, Thick = 0.06713  
 RH = 62.%, Temperature = 284.2 deg K, NASACYL2.age  
 Pmax = 0.67, ESEL = 112.54, CSEL = 94.71, ASEL = 76.03, PLdB = 92.89

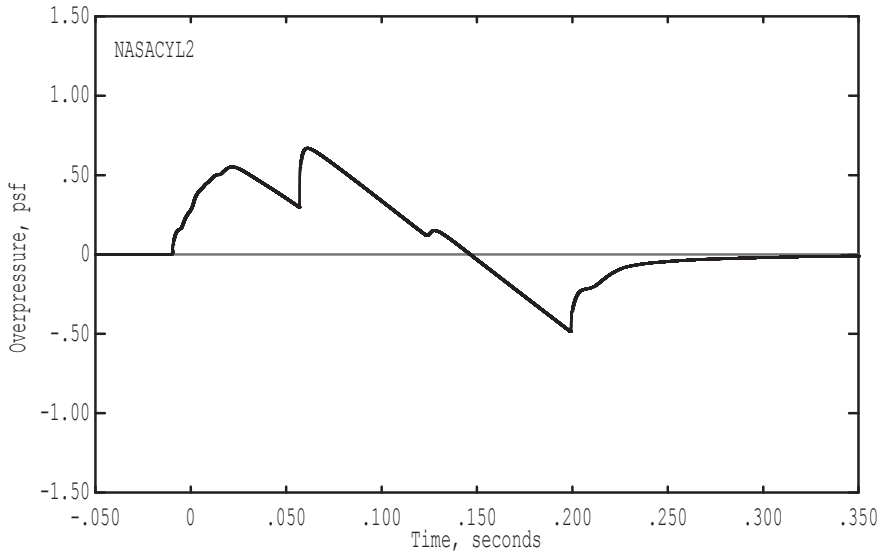


**Figure 10-24. Lossy Solution for  $\delta$  Tangent Ray for focus of NASA N+2 Aircraft.**

### 10.3.4 Critical Analysis of Modeling Limitations – PCBoom Gill-Seebass

The Gill-Seebass focus solution, as implemented in PCBoom, has proven to reliably predict peak overpressures for focused N-waves. Modern focus solutions (Auger and Coulouvrat, 2002) have shown that it does not predict the correct peak when shocks are in close proximity. SCAMP flight-test results (Chapters 5-8) showed good agreement with N-wave shock peaks, but that the signature shape further behind the bow shock and in front of the rear shock did not agree with measured focus signature.

These issues are directly attributable to the Gill-Seebass solution being for a single step shock, accounting for caustic radius of curvature  $R$  but not accounting for signature duration  $T_{ac}$ . The assumption that shocks can be locally considered to be steps is not appropriate for complex multi-shock shaped booms.

PCBoom’s ray tracing does, however, provide the appropriate inputs for the modern Tricomi solver presented in Section 8 and the NPE method presented in Section 7. The FOBoom module of PCBoom has been updated to improve the interface to those codes. The PCBurg module has been updated to include an anti-Gibbs filter and high sampling rate necessary for generating a Tricomi input boundary condition. A new utility, “raycau” (see Figures 10-10, 10-14, 10-18, and 10-22), has been written to assist in identifying the  $\delta$  tangent ray and signature for input to the Tricomi solver.

## 10.4 LNTE Low-Boom Configuration Analysis

The methodology for the Tricomi calculations of the low-boom signatures was the same as described in Section 8, however, the in-coming pressure signatures provided for this section were solely calculated from outputs obtained by PCBoom6 lossy propagations. This is an improvement over the method described in Section 8. The ray-tube area effects of a maneuvering aircraft were properly accounted for in the propagation of the low-boom signatures in this report. The in-coming low-boom signatures were all propagated with PCBoom6 at a sample rate of 102.4 kHz and then downsampled to 25.6 kHz for the Tricomi calculations.

The low-boom signatures were propagated through standard atmospheric conditions. The atmospheric conditions at the ground for the Tricomi calculations were also at standard atmospheric conditions (no winds). The focusing conditions for the low-boom configurations are listed in Table 10-1.

**Table 10-1. Input Conditions for the Low-Boom Configurations**

Low Boom Case	$f_{ac}$ (Hz)	$R_{tot}$ (meters)	Temperature (K)	Pressure (kPa)	Humidity (%)
Gulfstream	4.0	89922.	288.15	101.33	59.62
Boeing	4.0	88669.	288.15	101.33	59.62
NASA Demonstrator	7.7	86525.	288.15	101.33	59.62
NASA N+2	4.4	89199.	288.15	101.33	59.62

All of the in-coming waveforms were propagated in PCBoom6 to the location corresponding to one boundary layer thickness away from the caustic ( $\bar{z} = 1$ ). The number of points in the  $\bar{z}$  and time-wise dimensions in the computational domain were specified as in Table 10-2.

**Table 10-2. Computational Domain Dimensions for the Low-Boom Configurations**

Low Boom Case	$\bar{z}_{\min}$	$\bar{z}_{\max}$	Time dimension points	Z dimension points
Gulfstream	-1.	1.	32768	2000
Boeing	-1.	1.	32768	2000
NASA Demonstrator	-1.	1.	16384	4000
NASA N+2	-1.	1.	16384	4000

Note that the total number of points in the computational domain (~65.5 million) is the same for all cases. This number was to ensure that the computer used to plot and graph the Tricomi results had sufficient memory for the required post processing. The difference for the number of points in the time dimension was due to the zero padding required to ensure that the in-coming and out-going waveforms do not encroach on the time-wise domain boundaries at the  $\bar{z} = 1$  location.

### 10.4.1 Low-Boom Configuration Analysis – LNTE

#### *Gulfstream Configuration*

An overview of the Gulfstream low-boom configuration is provided in Section 10.1.2. The PCBoom6 lossy  $\delta$  tangent ray output shown in Figure 10-12 was used as the in-coming waveform to the lossy NTE code. That waveform was input to the lossy NTE code with its corresponding parameters from Table 10-1. The pressure contour from the resulting computations is shown in Figure 10-25. The ground reflection factor is not included in this plot. Figures 10-26 through 10-28 include a ground reflection factor of 1.9. Figure 10-26 is the slice of time corresponding to  $\bar{z} = 1$  at the top of the computational domain. The in-coming waveform (corresponding to Figure 10-12 multiplied by ground reflection) and out-going waveform are visible. However, the confluences of shocks at the front and aft of the in-coming waveform are not visible in the out-going waveform. Figure 10-27 shows a comparison of the time slices at the pressure maximum and pressure minimum in the vicinity of the caustic ( $\bar{z} = 0.32$  and  $\bar{z} = 0.22$  respectively). It is interesting to note that the pressure minimum value of -2.3 psf is greater (in absolute amplitude) than the pressure maximum of 1.8 psf. Figure 10-28 shows a time history at  $\bar{z} = -0.5$ , in the evanescent region. The pressure amplitude has already been reduced to a low level, down to pressure levels of approximately 0.2 psf and -0.3 psf for the pressure maximum and minimum, respectively.

#### *Boeing Configuration*

An overview of the Boeing low-boom configuration is provided in Section 10.1.2 of this report. The PCBoom6 lossy  $\delta$  tangent ray output shown in Figure 10-16 was used as the in-coming waveform to the lossy NTE code. That waveform was input to the lossy NTE code with its corresponding parameters from Table 10-1. The pressure contour from the resulting computations is shown in Figure 10-29. The ground reflection factor is not included in this plot. Figures 10-30 through 10-32 include a ground reflection factor of 1.9. Figure 10-32 is the slice of time corresponding to  $\bar{z} = 1$  at the top of the computational domain. The separation of the in-coming waveform and out-going waveform is visible. Figure 10-31 shows the time history at the peak pressure maximum, which occurs at  $\bar{z} = 0.2$ . The predicted peak pressure at the maximum focus is 2.7 psf. Figure 10-32 shows a time history at  $\bar{z} = -0.5$ . The pressure amplitude at that location in the evanescent region has decayed down to a peak pressure level of approximately 0.27 psf.

## NASA Demonstrator Configuration

An overview of NASA low-boom demonstrator configuration is provided in Section 10.1.3 of this report. The PCBoom6 lossy  $\delta$  tangent ray output shown in Figure 10-20 was used as the in-coming waveform to the lossy NTE code. That waveform was input to the lossy NTE code with its corresponding parameters from Table 10-1. The pressure contour from the resulting computations is shown in Figure 10-33. The ground reflection factor is not included in this plot. Figures 10-34 through 10-36 include a ground reflection factor of 1.9. Figure 10-34 is the slice of time corresponding to  $\bar{z} = 1$  at the top of the computational domain. The separation of the in-coming waveform and out-going waveform is visible. The flat top type of feature from the in-coming waveform is not present in the out-going wave from the caustic. Figure 10-35 shows the time history at the peak pressure maximum, which occurs at  $\bar{z} = 0.16$ . The predicted peak pressure at the maximum focus is 1.6 psf. Figure 10-36 shows a time history at  $\bar{z} = -0.5$ . The pressure amplitude at that location in the evanescent region has rapidly decayed down to a peak pressure level of approximately 0.15 psf.

## NASA N+2 Configuration

An overview of NASA N+2 low-boom configuration is provided in Section 10.1.3 of this report. The PCBoom6 lossy  $\delta$  tangent ray output shown in Figure 10-24 was used as the in-coming waveform to the lossy NTE code. That waveform was input to the lossy NTE code with its corresponding parameters from Table 10-1. The pressure contour from the resulting computations is shown in Figure 10-37. The ground reflection factor is not included in this plot. Figures 10-38 through 10-40 include a ground reflection factor of 1.9. Figure 10-38 is the slice of time corresponding to  $\bar{z} = 1$  at the top of the computational domain. The separation of the in-coming and outgoing waveforms is visible. The rounded front shock part of the incoming waveform is not visible in the outgoing waveform. Figure 10-39 shows the time history at the peak pressure maximum which occurs at  $\bar{z} = 0.07$ . The predicted peak pressure at the maximum focus is 3.07 psf. Figure 10-40 shows a time history at  $\bar{z} = -0.5$ . The pressure amplitude at that location in the evanescent region has very rapidly decayed down to a peak pressure level of approximately 0.34 psf.

### 10.4.2 Critical Analysis of Modeling Limitations – LNTE

Close examination of the computational solutions reveals that there are small numerically induced oscillations in regions of higher shock amplitudes. For example, Figure 10-41 is a time history of the NASA N+2 configuration corresponding to  $\bar{z} = 0.75$ . These oscillations are known to occur when the  $d\bar{z}$  is not small enough relative to the time-wise discretization spacing. It is recommended in future versions of the code that the number of points in the  $\bar{z}$ -direction is increased. This, however, would pose a challenge because the number of total points is already extremely high. It is also recommended to examine a  $\bar{z}$  discretization scheme in which  $d\bar{z}$  varies between the illuminated zone and the shadow zone.

In this analysis, there was enough separation between the in-coming and out-going waveforms to see the two individual waveforms at the  $\bar{z} = 1$  location. However, that separation is likely insufficient if one were to attempt to compute a focusing solution and subsequently propagate the out-going waveform. Depending on the goal of executing the Tricomi code, one may need to apply the in-coming waveform at  $\bar{z}$  higher than 1. This may also enlarge the computational domain due to the potential gridding that may be required in the time-wise dimension.

Convergence for these cases was determined manually by periodically stopping the calculation and observing the changes in the solution. The process of manually inspecting the Tricomi solutions is very time

consuming. As discussed in Section 8, an automated means of determining convergence would be beneficial.

Future analysis of the low-boom signatures will likely extend to non-standard atmospheres, including winds. The capability to include the influence of winds was also suggested in Section 8.

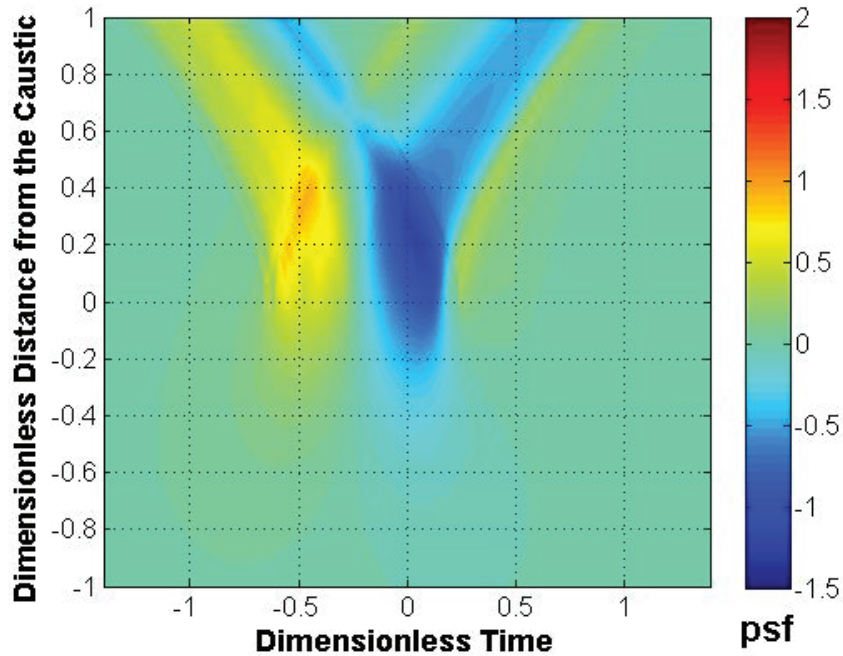


Figure 10-25. Pressure field solution of the Lossy Tricomi Code for the Gulfstream Low-Boom Signature and focusing conditions.

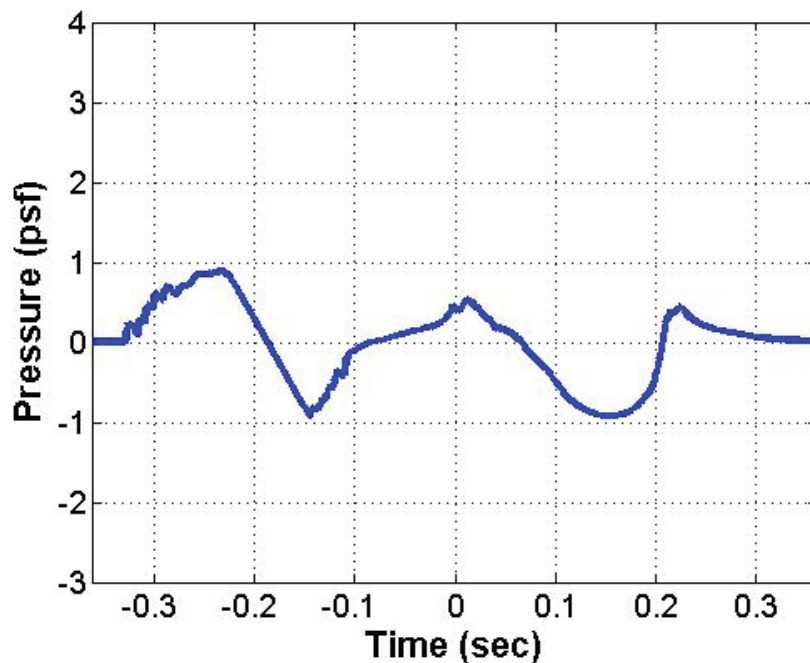


Figure 10-26. Time history for the Gulfstream low-boom focusing case at  $\bar{z} = 1$ .

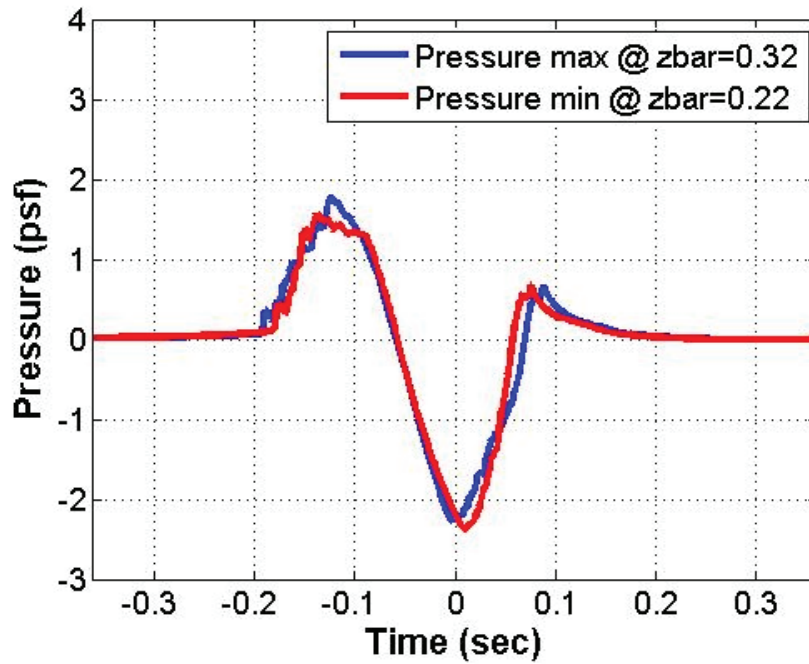


Figure 10-27. Time history comparison for the Gulfstream low-boom focusing case between Maximum Overpressure ( $\bar{z} = 0.32$ ) and Maximum Underpressure ( $\bar{z} = 0.22$ ).

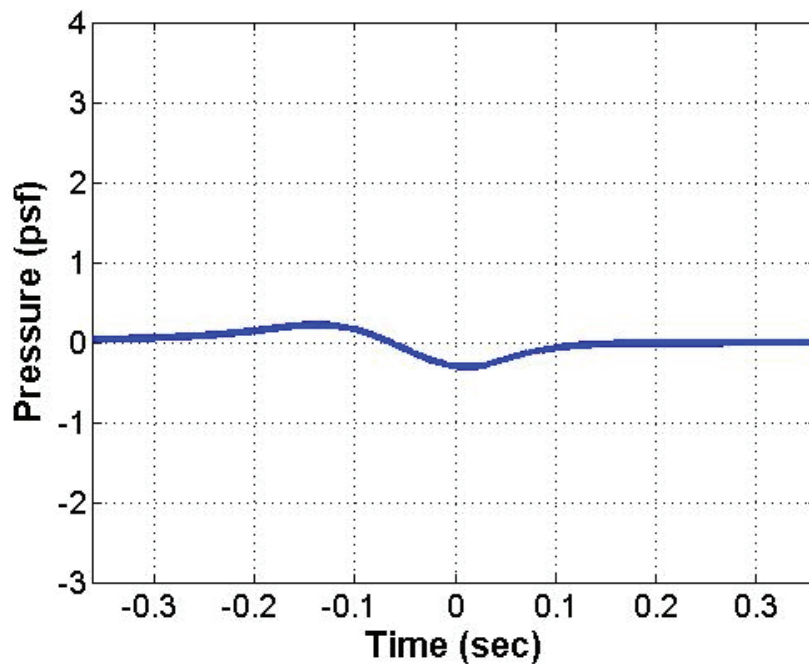


Figure 10-28. Time history for the Gulfstream low-boom focusing case at  $\bar{z} = -0.5$ .

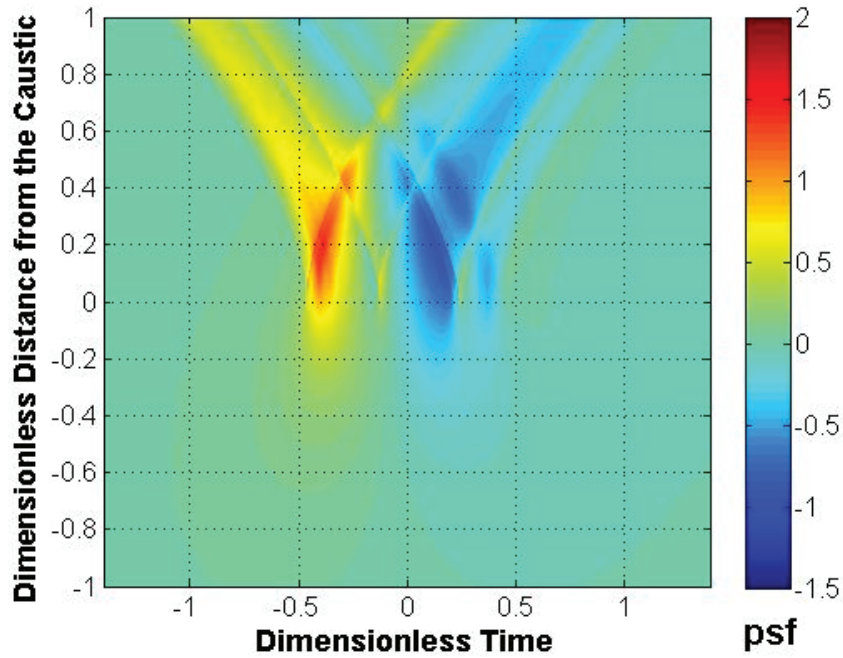


Figure 10-29. Pressure field solution of the Lossy Tricomi Code for the Boeing N+2 Low-Boom Signature and focusing conditions.

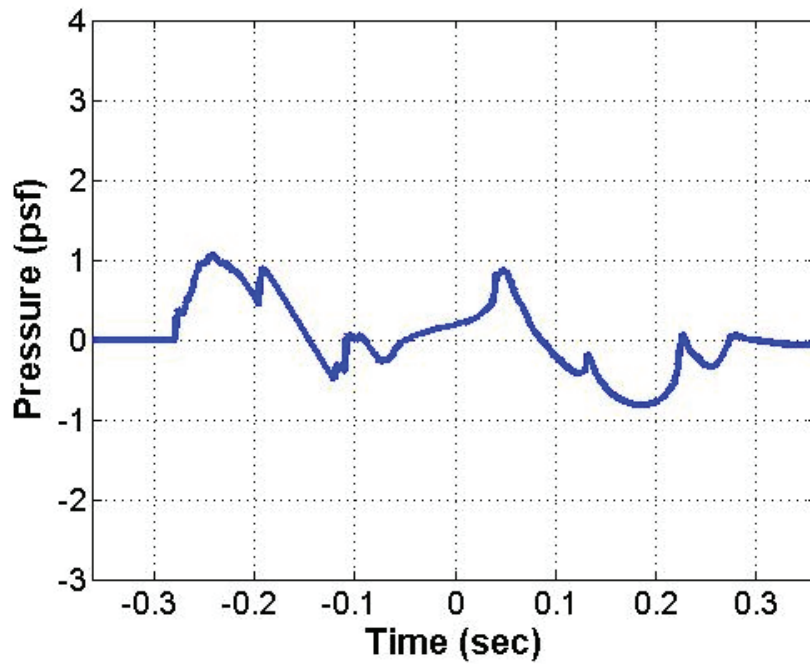


Figure 10-30. Time history for the Boeing N+2 Low-Boom Focusing Case at  $\bar{z} = 1$ .



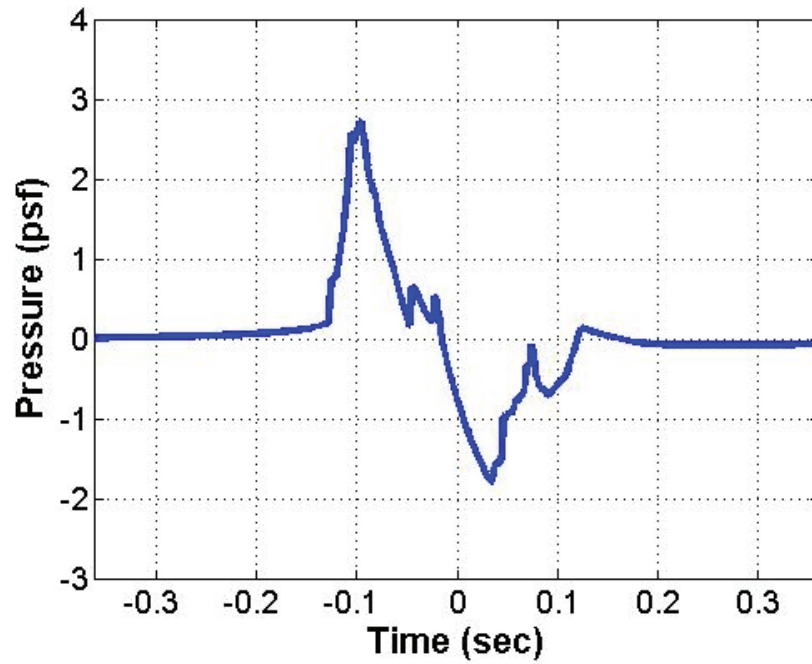


Figure 10-31. Time history for the Boeing N+2 Low-Boom Focusing Case at Maximum Overpressure ( $\bar{z} = 0.2$ ).

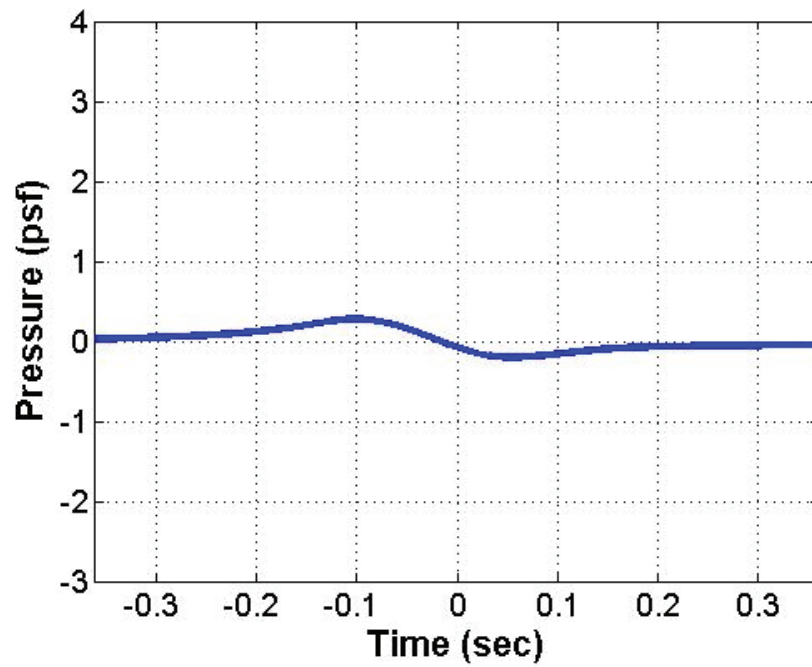


Figure 10-32. Time history for the Boeing N+2 Low-Boom Focusing Case at  $\bar{z} = -0.5$ .

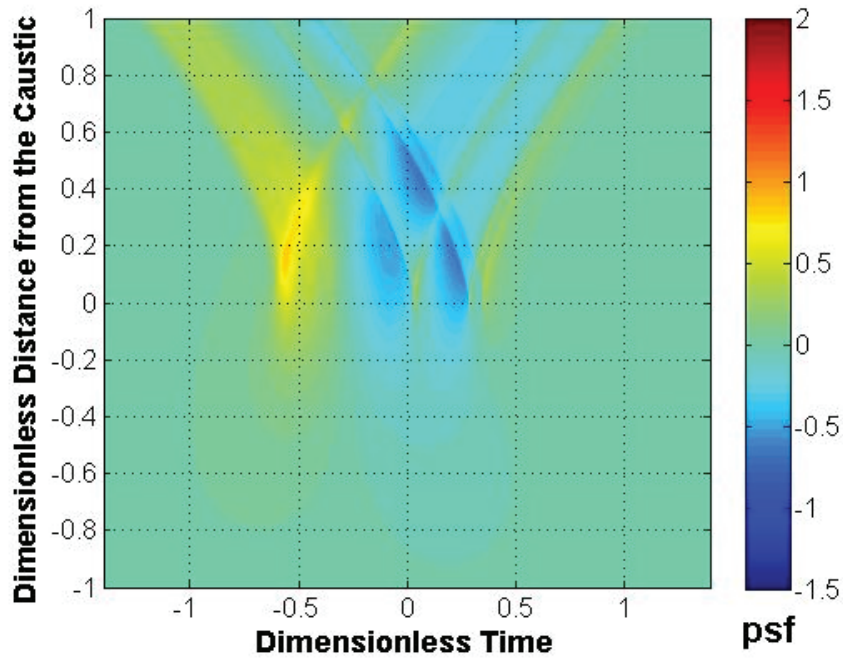


Figure 10-33. Pressure field solution of the Lossy Tricomi Code for the NASA Demonstrator low-boom signature and focusing conditions.

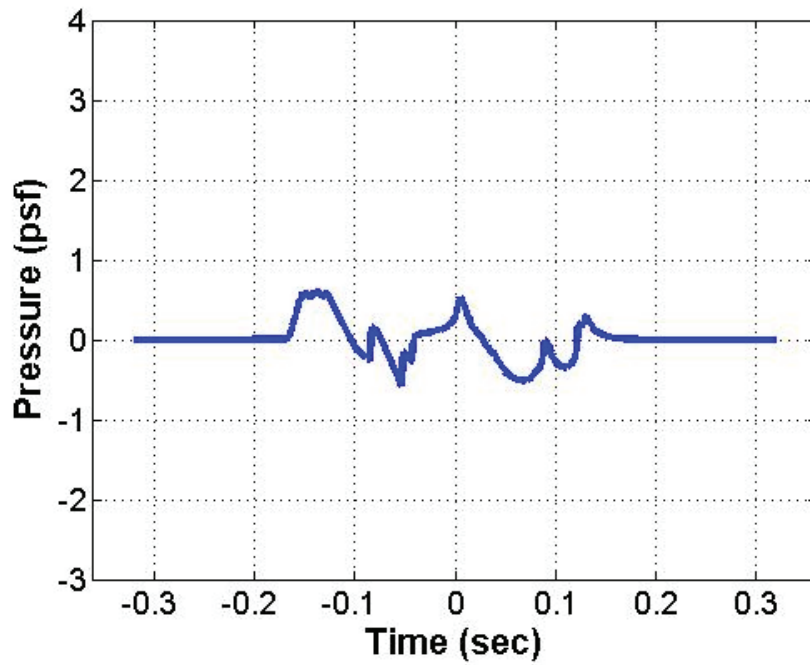


Figure 10-34. Time history for the NASA Demonstrator Configuration low-boom focusing case at  $\bar{z} = 1$ .

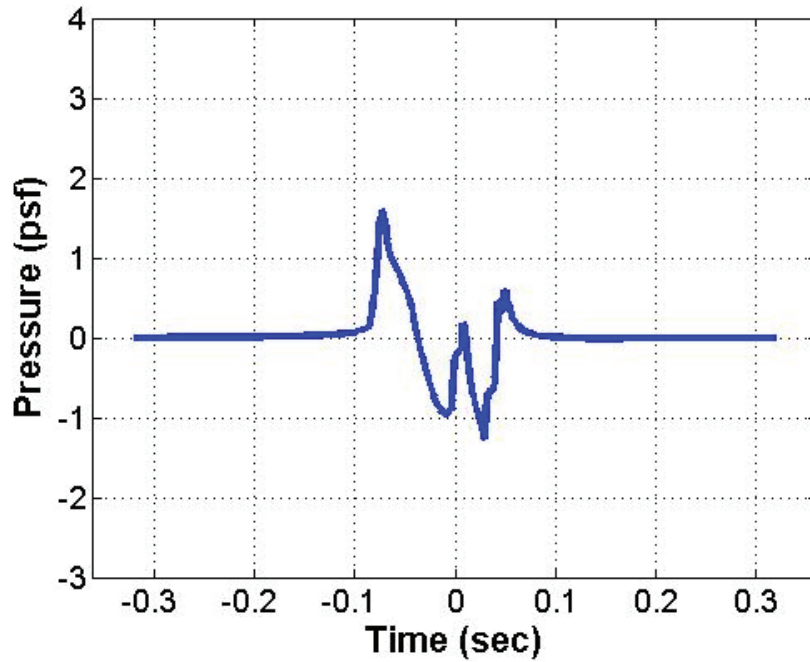


Figure 10-35. Time history for the NASA Demonstrator low-boom focusing case at Maximum Overpressure ( $\bar{z} = 0.16$ ).

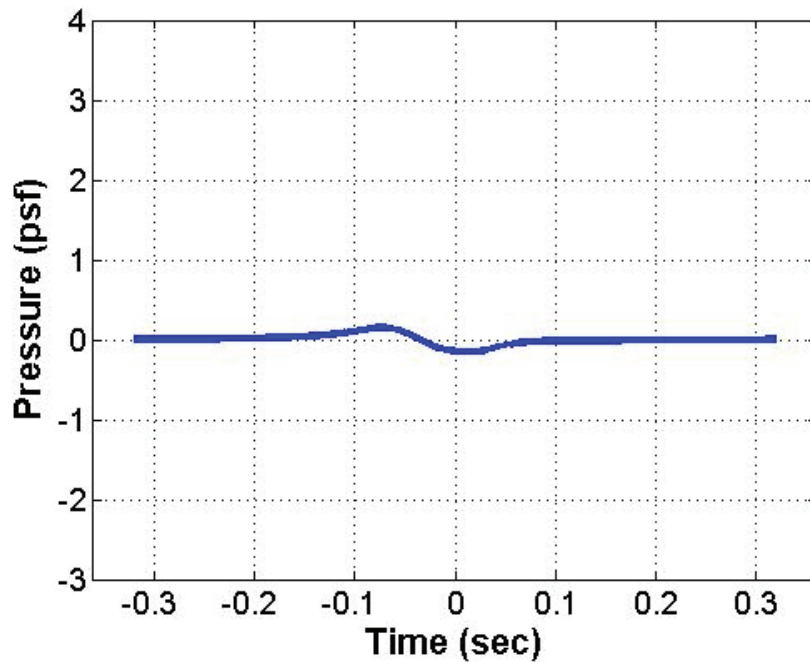


Figure 10-36. Time history for the NASA Demonstrator Configuration low-boom focusing case at  $\bar{z} = -0.5$ .

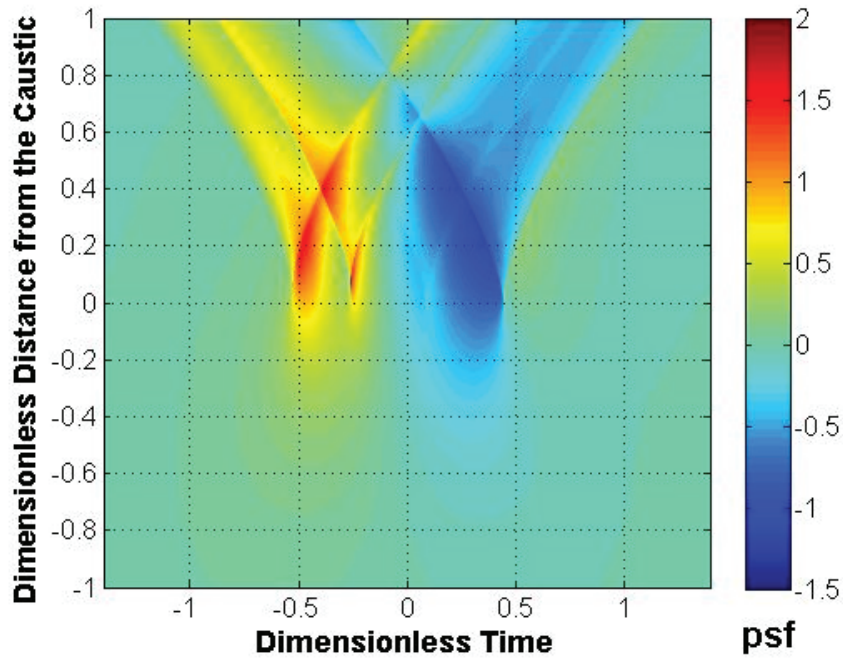


Figure 10-37. Pressure field solution of the Lossy Tricomi Code for the NASA N+2 Configuration low-boom signature and focusing conditions.

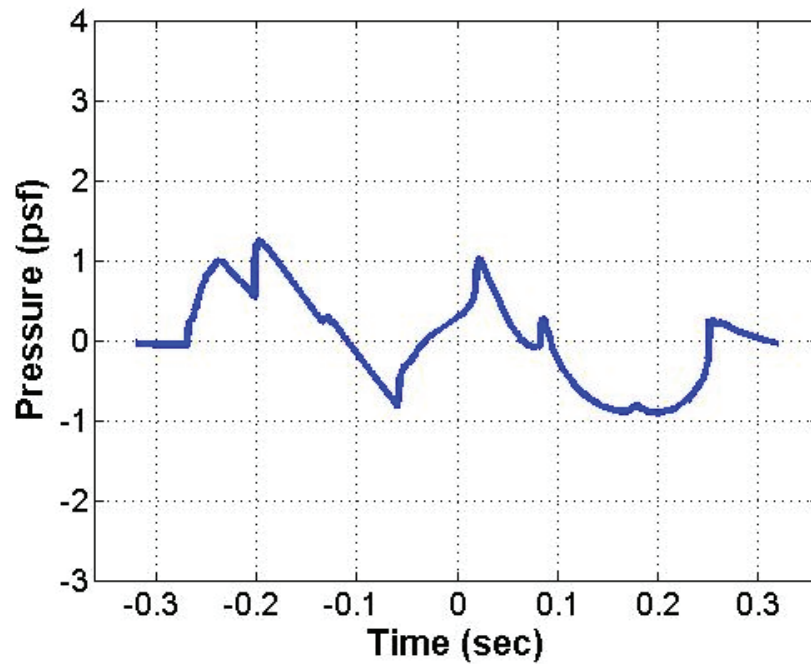


Figure 10-38. Time history for the NASA N+2 configuration low-boom focusing case at  $\bar{z} = 1$ .

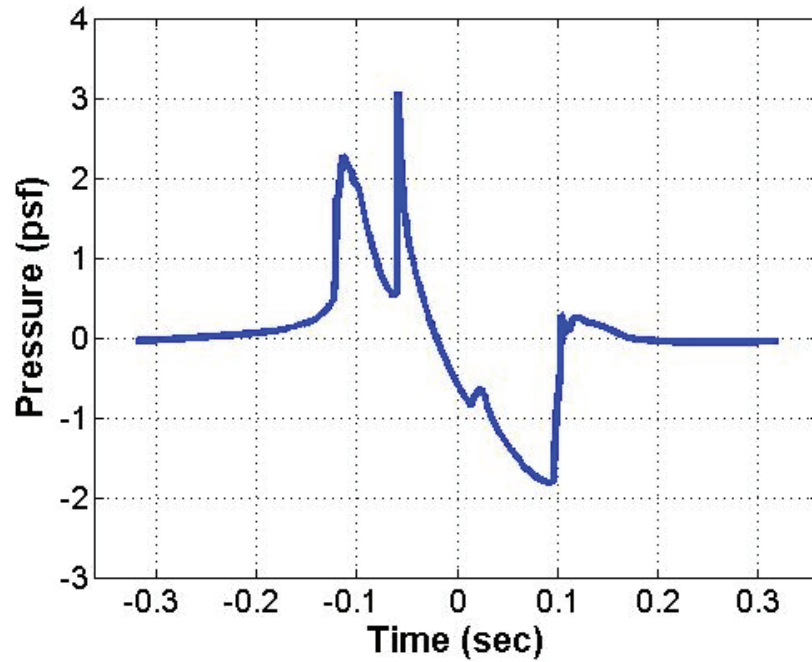


Figure 10-39. Time history for the NASA N+2 Configuration low-boom focusing case at Maximum Overpressure ( $\bar{z} = 0.07$ ).

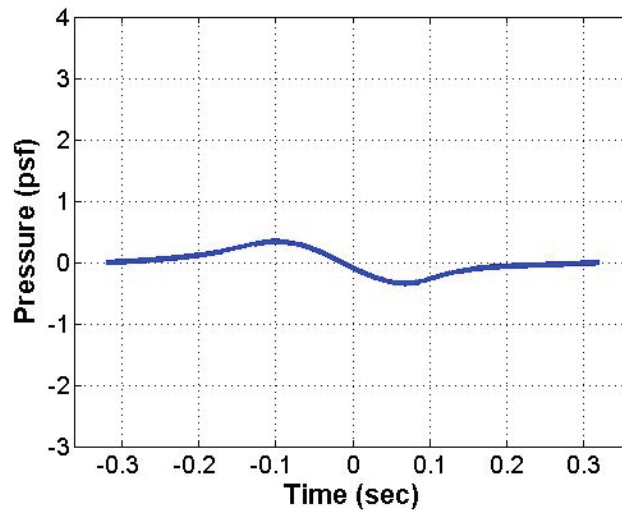


Figure 10-40. Time history for the NASA N+2 Configuration low-boom focusing case at  $\bar{z} = -0.5$ .

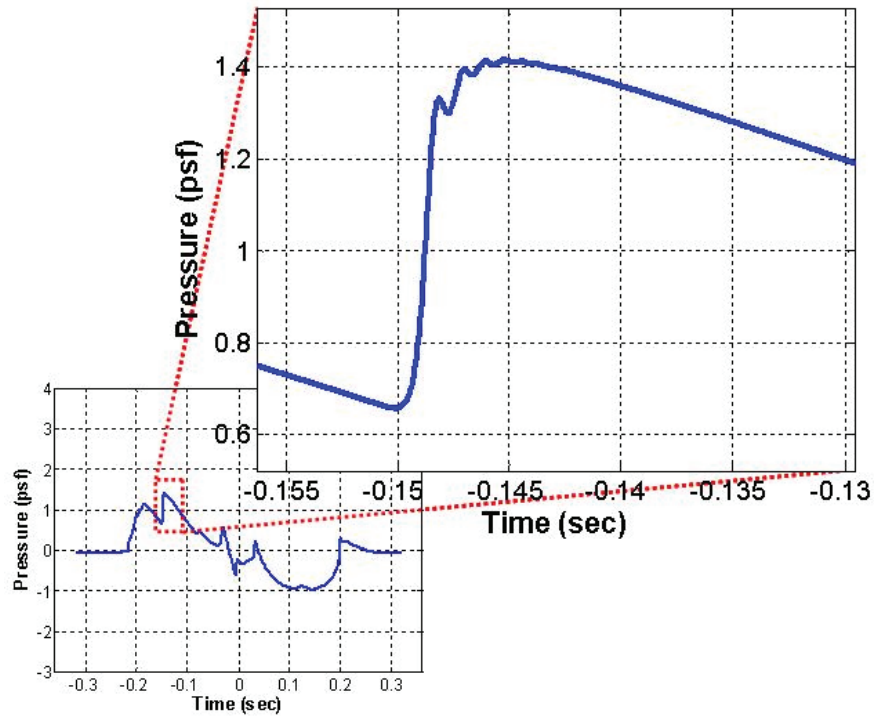


Figure 10-41. Time history of the NASA N+2 Configuration corresponding to  $\bar{z}=0.75$  showing small amplitudes of numerically induced oscillation.

## 10.5 NPE Low-Boom Configuration Analysis

The NPE solution is a finite-difference calculation in the time domain, starting from an initial two-dimensional pressure field, as discussed in Section 7.

### 10.5.1 Low-Boom Configuration Analysis – NPE

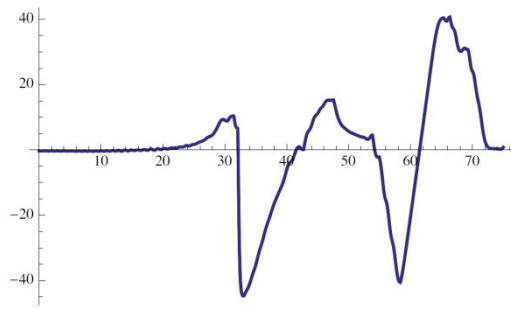
Table 10-3 lists pertinent scaling parameters for the four low-boom configurations. These are the caustic geometry and the boundary conditions at the delta tangent matching point. Focus analysis was done for the first three configurations in Table 10-3. That addresses three key types – a business jet, an N+2 airliner, and a small demonstrator.

**Table 10-3. Tricomi Scaling Parameters and Boundary Conditions for Low-Boom Configurations**

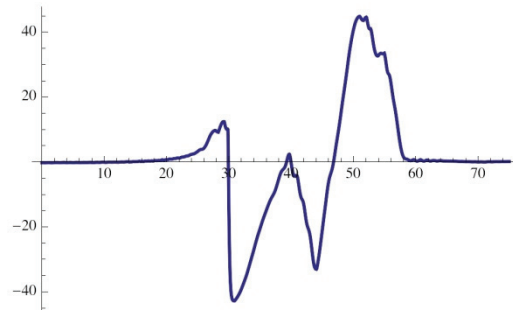
Vehicle	$R_c$ (ft)	$T_{ac}$	$\delta$	$P_{ac}$
Gulfstream QSJ	295000	240	2100	0.46
Boeing N+2	291000	240	2000	0.55
NASA Demonstrator	285000	125	1390	0.31
NASA N+2	292000	225	2073	0.67

The scaled ripple process, as described in Section 9.5.2, was used to interface PCBoom to NPE. Table 10-3 defines conditions at the delta-tangent point for Tricomi scaling. NPE requires input signatures at the initial wavefront. The input signature is nominally the near-field starting signature, for each vehicle. That signature ages as it propagates, with aging in the atmosphere depending on the age parameter as computed from PCBoom's ray tracing. NPE propagation is two dimensional through a uniform atmosphere. Aging can be adjusted by either introducing a density gradient or adjusting the amplitude of the starting signature. For the current analysis, the initial amplitude was adjusted. A length of 17.7 meters ( $T_{ac} = 53$  msec) was necessary to avoid overlap, and was used for all. The initial amplitude was chosen such that, when the NPE signature at the edge of the focal zone was scaled back to  $T_{ac}$  and  $P_{ac}$  in Table 10-3, the aging matched that of the PCBoom delta-tangent signatures shown in Figures 10-11 and 10-12 (Gulfstream QSJ), 10-15 and 10-16 (Boeing N+2), and 10-9 and 10-20 (NASA Demonstrator).

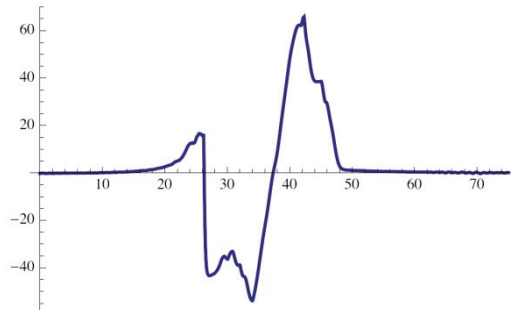
Figures 10-42 through 10-44 show the results,  $p$  versus  $x$ , at four  $y$  positions for the above calculations. The caustic is at -370 meters for all three cases, so parts a, b, and c of each are on the illuminated side of the caustic while d is on the shadow side. Note that the difference in amplitude scale for the five parts and that the leading shock is to the right in these coordinates.



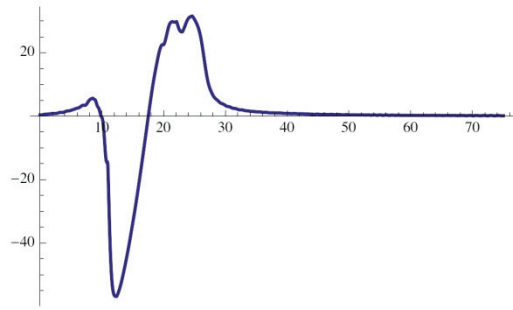
a.  $y = -75$  m, focal zone edge (reference)



b.  $y = -175$  m, overlapping

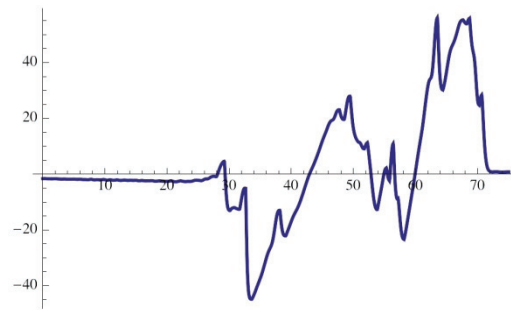


c.  $y = -245$  m, maximum focus

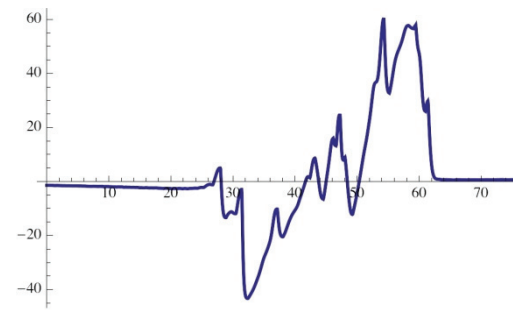


d.  $y = -400$  m, evanescent

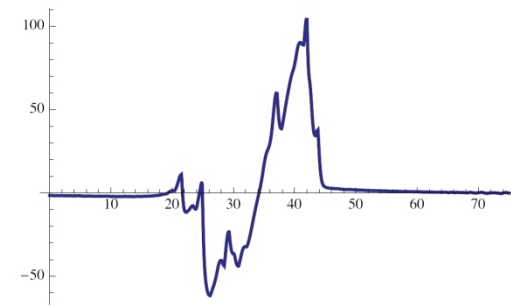
**Figure 10-42. NPE Solution, Gulfstream QSJ.**



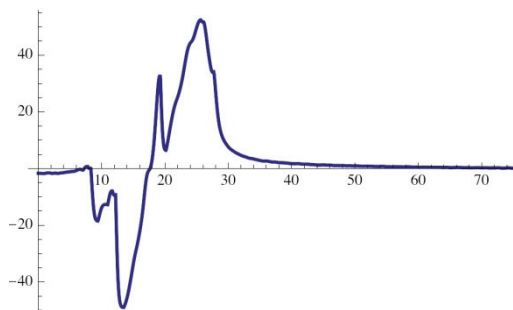
a.  $y = -85$  m, focal zone edge (reference)



b.  $y = -150$  m, overlapping



c.  $y = -245$  m, maximum focus



d.  $y = -400$  m, evanescent

**Figure 10-43. NPE solution, Boeing N+2.**



The signature in Part a of each figure is at the edge of the focus, just clear of overlap from the wave originating from the lower half of the initial wavefront, and corresponds to  $z\text{-bar} = 1$ . Part c is the maximum focus. Part b shows an intermediate overlapping wave, while part d shows a wave in the shadow zone. The sequence of waveforms is similar to that obtained from LNTE solutions, although the coordinates of  $p$  versus  $x$  are reversed from the usual  $p$  versus  $t$ .

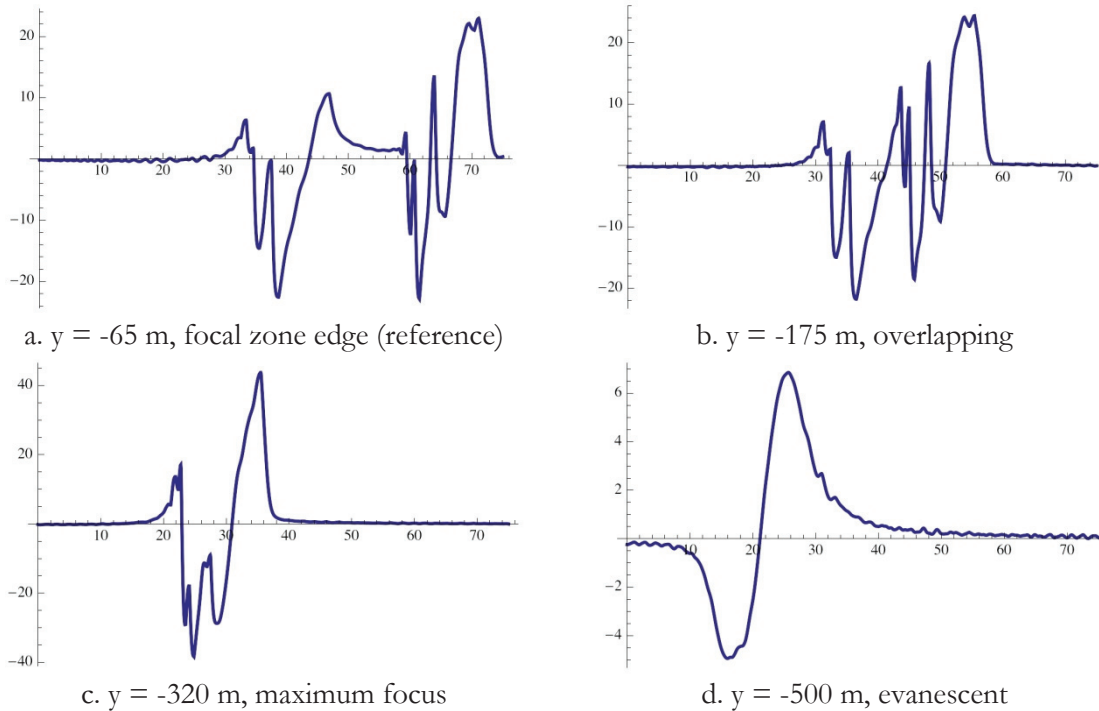


**Figure 10-44. NPE solution, NASA Demonstrator.**

The solutions in Figures 10-42 through 10-44 are at NPE calculation scale, not full physical scale. Scaling to the final result uses amplitude and time factors based on matching the reference wave (Part a of each figure) to Tac and Pac listed in Table 10-3. Matching factors were obtained in the following way:

- A viewing program “readpro” was written that displays the signatures in a manner similar to Figures 10-42 through 10-44, but is interactive in selecting the  $y$  value. The program allows saving of part of a signature.
- Using readpro, two signatures were saved in txt format – one at a reference position at the edge of the focal zone, and one at the maximum focus. These correspond to the signatures shown in Parts a and c of Figures 10-42 through 10-44.
- A second program “plottxt” was written that displayed the reference and focus NPE signatures, and overlaid the PCBoom delta-tangent signature (Figures 10-11/10-12, 10-15/10-16, or 10-19/10-20 as noted earlier) and the reference signature. The amplitude factor was automatically computed by the ratio between the reference and delta-tangent signatures. The time scale factor was obtained by interactively scaling the duration of the NPE reference signature.

plottxt includes a command to write the scaled focus signature to a file, together with the scaling factors.

The maximum focus signatures, converted to p versus t, are shown in Section 10.6 on common plots with NTE and PCBoom focus predictions. The comparison is discussed in Section 10.6. In general, the NPE solutions are somewhat lower in amplitude than LNTE, and tend to exhibit differences toward the rear. This is consistent with differences found between NPE predictions for N-waves and SCAMP measurements.

## 10.5.2 Critical Analysis – NPE

The prior difficulties in applying NPE to sonic boom focusing have been identified as due to edge diffraction effects. Those effects can be avoided by recognizing the initial cusp and “mirror” caustic, and defining the initial wave front as convex away from center. The single ripple analyzed here satisfies those conditions. The resultant caustics have variable curvature, which is beneficial for domain exploration since one can examine the effect of curvature without changing the ray geometry. It is a potential issue for rigor because the SCAMP flight test (Page, 2011) showed that caustics from transition focus maneuvers were very close to constant curvature. Variable caustic curvature is the most likely reason why the NPE solutions differ from the NTE solutions.

The current analysis demonstrates the viability of NPE for focus analysis. The following improvements would, however, be desirable to improve performance:

- Definition of a wavefront similar to the single ripple employed here, but designed such that the caustic curvature will have less variation.
- Further development of Tricomi-based scaling to better represent SCAMP conditions. In particular, wavelength must be adjusted such that  $\delta$  lies within the converging ray region near the caustic.
- Automation of the coupling to PCBoom and scaling. This is similar to the scaling tools developed to couple Tricomi solutions.

## 10.6 Low-Boom Vehicle Analysis Summary and Conclusions

Focus boom has been computed for four low-boom configurations. Focus occurs at flight conditions that do not correspond to the cruise design low-boom condition, so in addition to focus amplification the signatures are not low-boom shapes. All of the initial signatures had multi-shock character.<sup>4</sup> Figures 10-45 through 10-48 show the maximum focus signatures predicted by the Gill-Seebass method in PCBoom, the lossy NTE method, and Nonlinear Progressive Equation.

The peak overpressures for these signatures are presented in Table 10-4. Lossy NTE and Gill-Seebass results are of comparable magnitude, with some variation, while NPE results are about 30 percent lower.

**Table 10-4. Summary of Peak Overpressures, psf for Focused Signatures**

Vehicle	Lossy NTE	PCBoom	NPE
Gulfstream QSJ	1.8	1.94	1.36
Boeing N+2	2.7	2.51	1.97
NASA Demonstrator	1.6	1.68	1.16
NASA N+2	3.1	3.65	--

Early analysis by Auger and Coulouvrat of a simple double-shock signature yielded a result that a modern Tricomi solution had lower peak values than Gill-Seebass. This was correctly attributed to interaction

<sup>4</sup>The starting signatures for the Gulfstream configuration presented here were based on computations at the time of the Alpha focused boom analysis. They have since been updated and are provided in Elmer (2013). These solutions were retained so that direct comparisons between PCBoom, Lossy NTE, and NPE predictions could be provided for a variety of low-boom signatures, which retained their shaping.

between the shocks, and a consequence of Gill-Seebass being developed for a single shock. In the current results, there is no clear trend in the peak pressures between the two models, but the shapes vary significantly. The PCBoom predictions, which do not have proper molecular relaxation effects, have considerable spiky structure that is not seen in the lossy Tricomi solution. Given the limitations of the Gill-Seebass solution as implemented in PCBoom (step shock result applied to each shock, losses treated only by a simple Taylor structure), it is not expected that PCBoom's loudness predictions are credible. Because of the use of proper molecular absorption and favorable consistency with other Burgers solvers, it is expected that the lossy Tricomi solutions using PCBoom lossy  $\delta$  tangent ray input would yield credible loudness. The Gill-Seebass solution applies to individual shocks, while lossy NTE applies holistically to the full signature. Therefore it is also expected that the NTE solutions would be appropriate for structural response and indoor perception of booms.

The NPE method yielded results that were qualitatively similar to NTE, but lower in amplitude and with a tendency to differ towards the rear of the signature. The discrepancies are felt to be primarily because of the variable radius curvature of the ripple wave geometry. This can be addressed in the future by using a different ripple geometry, as discussed in Section 10.5.2. A secondary factor is not matching full scale  $\mu$ , which was due to adjusting the signature amplitude to obtain correct aging. This can be addressed by pre-aging the starting signature, or by introducing a density gradient.

The interface between PCBoom and the Tricomi solver has been improved via a utility that interactively displays the caustic rays and the focal zone diffraction region. The PCBurg module of PCBoom has been updated with an anti-Gibbs filter and higher sampling rate to provide the input signature needed at the boundary of the lossy Tricomi solver.

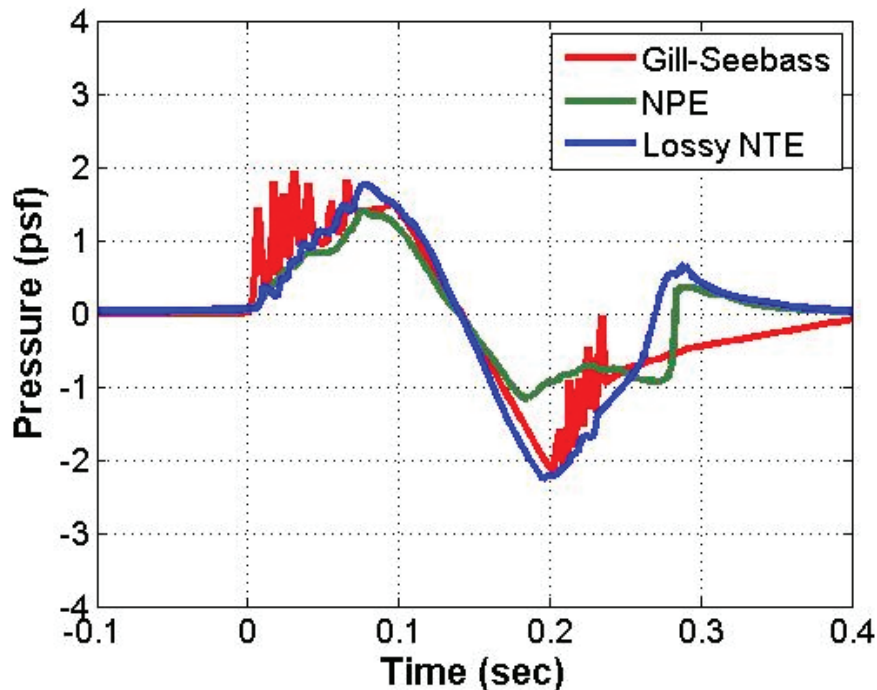


Figure 10-45. Comparison at maximum focus between Gill-Seebass, NPE, and Lossy NTE Solutions for Gulfstream QSJ.

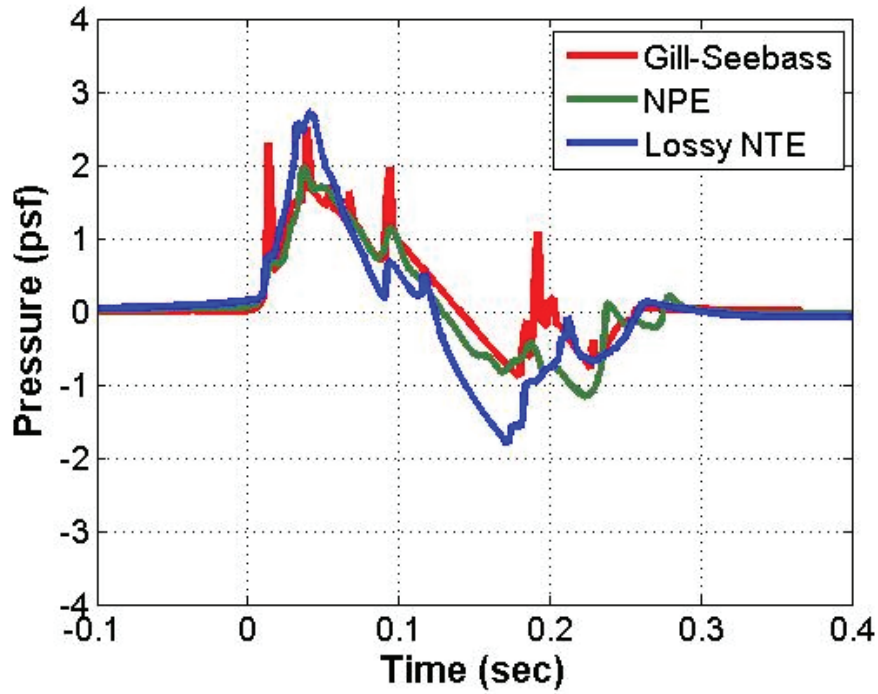


Figure 10-46. Comparison at maximum focus between Gill-Seebass and Lossy NTE Solutions for Boeing N+2 SST.

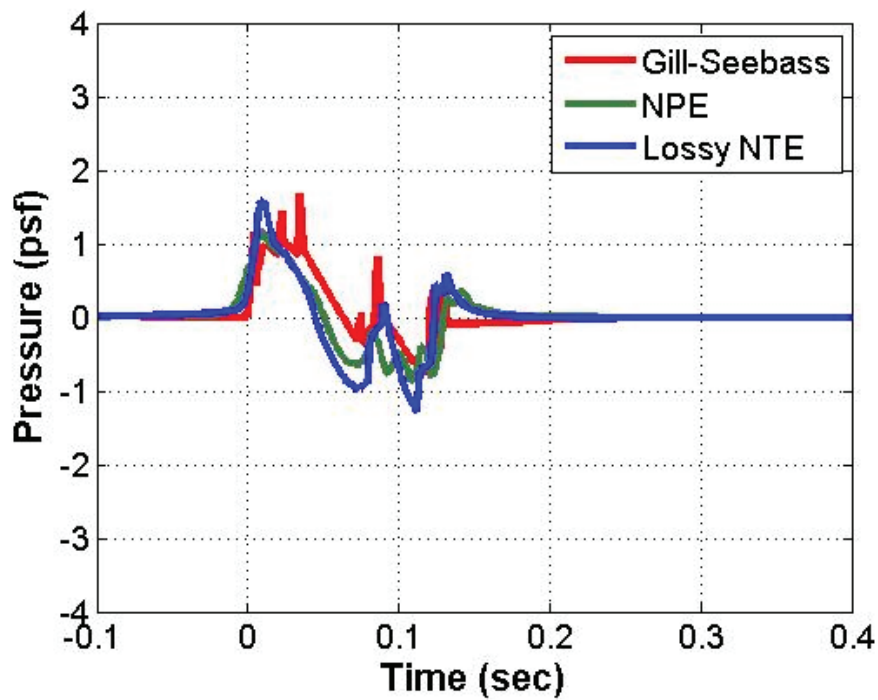


Figure 10-47. Comparison at maximum focus between Gill-Seebass and Lossy NTE Solutions for NASA Demonstrator

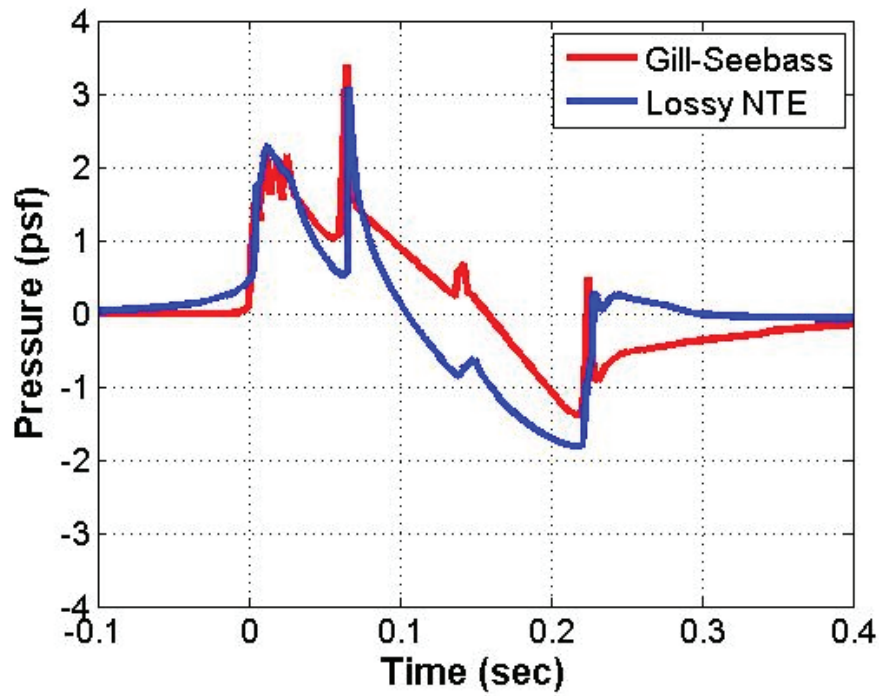


Figure 10-48. Comparison at maximum focus between Gill-Seebass and Lossy NTE Solutions for NASA N+2 Configuration.



*Intentionally left blank*

## Profile Exploration and Focused Signatures

The analysis presented in Section 10 considered only a single flight profile for each low-boom configuration. It is expected that the climb and acceleration profile would have some effect on loudness. Figure 11-1 shows some early estimates of the effect of aircraft acceleration on focusing, based in part on flight-test measurements near cut-off Mach number (Haglund, 1974). Figure 11-2 shows measured focus overpressures from the French Operation Jericho focus boom flight test, as a function of acceleration and lateral offset (Wanner, 1972). Figure 11-2 does not indicate a coherent trend consistent with Figure 1-1. More recently, Maglieri et al. (2011) conducted parametric analysis of the effect of flight profile on focusing of shaped sonic booms. That analysis found that focus amplitudes decreased with increasing altitude and increasing climb angle. Acceleration was found to have little or no effect.

The studies cited above considered either N-wave signatures or optimized simple flat-top or minimum shock signatures. They were also conducted, to a degree, without consideration of the interaction between configuration and performance. A study has therefore been conducted to explore the effect of flight profile on focusing of modern complex low-boom configurations, recognizing that the focus flight conditions would not correspond to optimized low-boom ground signature conditions. Three configurations studied in Chapter 10 were examined, each for four to six transition profiles. The aircraft configurations studied included a supersonic passenger transport, a supersonic business jet, and a small supersonic demonstrator. Flight profiles were varied by adjusting performance, either through re-sizing engines or applying an equivalent adjustment to drag. The analysis consisted of computing focus signatures for each case, then comparing the maximum loudness over the various flight conditions.

Sections 11.2, 11.4, and 11.5 present specifics concerning the aircraft configurations examined and the various flight profiles studied. Section 11.5 presents the focal zone results, including signatures and loudness metrics throughout the diffraction zone. Section 11.6 summarizes the results and presents recommendations.

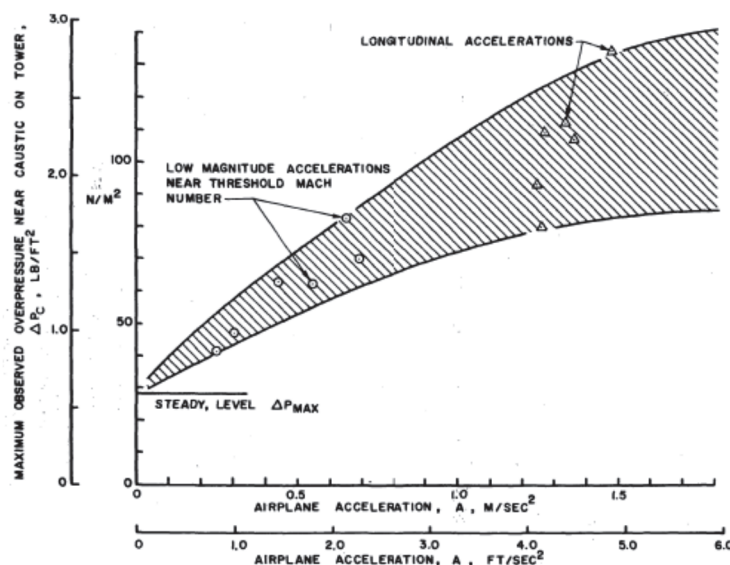


Figure 11-1. Estimated effect of acceleration on sonic boom focusing from (Haglund, 2074).

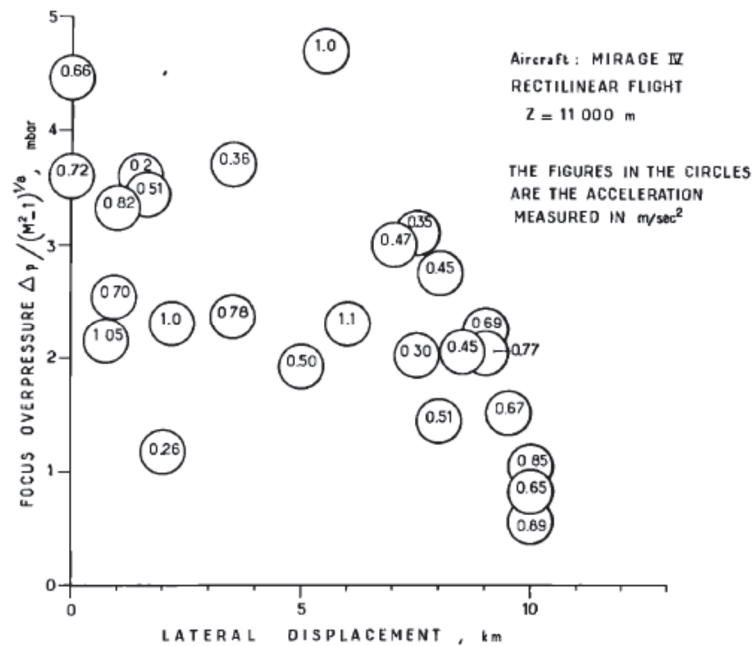


Figure 11-2. Measured effect of acceleration and lateral displacement on focus overpressure, from (Wanner, 1972).

## 11.1 Profile Exploration Focused Signature Computational Process

Sonic boom ray tracing and focusing has been described in Chapter 2. The interfaces between PCBoom, NPE, and LNTE have been described in Chapters 5-9 and are utilized for this analysis as well.

The analysis process for the profile exploration consisted of the following steps:

1. Aircraft designers (Boeing, Gulfstream, and NASA) configured each aircraft configuration as a low-boom aircraft, with four to six alternate transition climb trajectories.
2. PCBoom was run for each trajectory, with a placeholder F-function. This identified the focusing condition on the trajectory.
3. The aircraft designers prepared CFD near-field solutions for the focus condition.
4. PCBoom was run for the same trajectories as Step 1, but with the CFD near-field solutions. PCBoom utility “raycau” was run to confirm the focus condition and identify the  $\delta$  tangent ray.

Figure 11-3 is a typical raycau ray diagram. Its features, from top to bottom, are:

- The aircraft flight parameters at the focus condition;
- The aircraft flight time corresponding to the  $\delta$  tangent ray;
- The  $\delta$  tangent ray, shown in red;
- The caustic, shown in black; and
- Circles marking the focus point and (in green) ray intercepts with the ground.



Raycau computes diffraction thickness  $\delta$  and selects the correct  $\delta$  tangent ray, matching the distance from the focus point to the ray with  $\delta$ . The user can adjust this as necessary. Raycau writes a data block with file type “.foc” that contains the key information. Figure 11-4 is the .foc file corresponding to the ray diagram in Figure 11-3. It contains the ray information from the ray diagram. It also contains information in the last six lines, that relates the nondimensional Tricomi region coordinate to physical locations on the ground. That information is the coordinates (both local Cartesian and geographic) where the focus ray ( $zbar = 0$ ) and the  $\delta$  tangent ray ( $zbar = 1$ ) each intercept the ground. This provides a simple interpolation from the Lossy NTE output file (organized by  $zbar$ ) to ground locations.

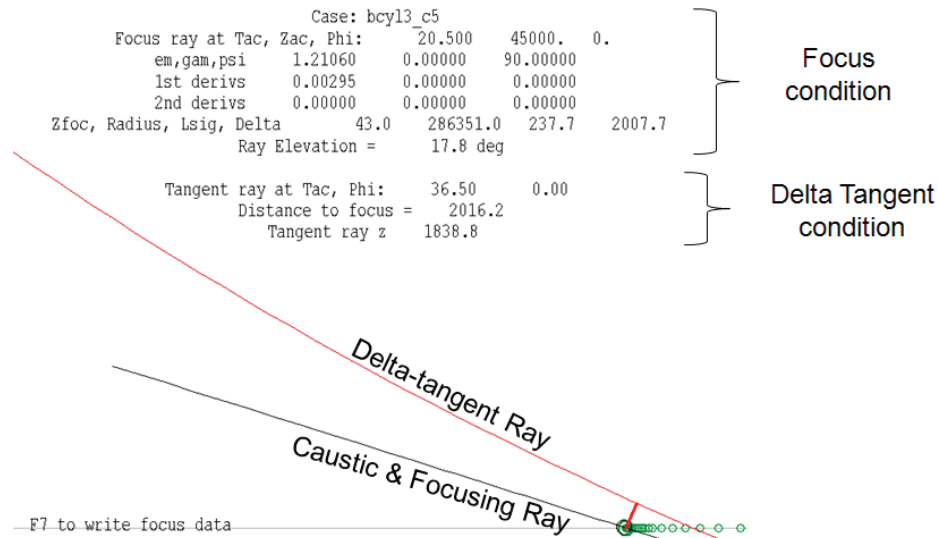


Figure 11-3. Ray diagram for focus and  $\delta$  tangent ray.

```

Case: bcyl3_c5
Focus ray at Tac, Zac, Phi: 20.500 45000. 0.00
Zfoc = 43.
Ray Elevation = 17.8 deg
Tangent ray at Tac, Phi = 36.50 0.00
Distance to focus = 2016.2
Tangent ray z = 1838.8

Rcau = 286351.
Tsig = 237.7
Delta = 2007.7
p0 = 2115.71
wind x,y,z = 0.00 0.00 0.00
zbar = 0
x,y,z,tg = 111130.8 0.0 0.0 115.910
long,lat = -115.755223 34.123450 0.0
zbar = 1
x,y,z,tg = 116097.2 0.0 0.0 120.039
long,lat = -115.738767 34.123450 0.0
  
```

Figure 11-4. Sample raycau “.foc” output file.

- Run PCBoom’s PCBurg module to obtain the lossy signature at the  $\delta$  tangent position. The “ft” (focus tangent) switch is used so that the selected ray corresponds to the  $\delta$  tangent ray in the foc file. PCBurg is run to the altitude (“Tangent ray z”) specified in the foc file; this is displayed on the PCBurg screen when run in feet mode.

Figure 11-3 shows the lossy  $\delta$  tangent solution from PCBurg for this example case. A txt file with the data is also written for input to the lossy NTE program.

- The Lossy NTE was then run for each case.

The Lossy NTE results are presented in Section 11.5, after the aircraft and profile descriptions in Sections 11.2, 11.3, and 11.4. The results are summarized and recommendations provided in Section 11.6.

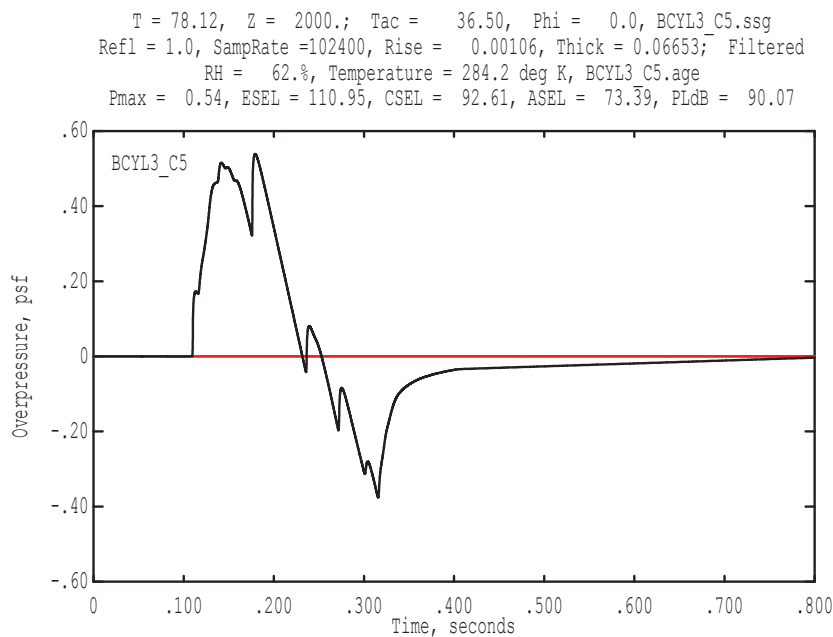


**Figure 11-5. Lossy  $\delta$  tangent boom – PCBoom output for input to Lossy NTE.**

## 11.2 Boeing Configuration/Profile/CFD Analysis

### 11.2.1 Transonic Acceleration Maneuver

The “Sound Barrier” in a simple way describes increased wave drag in the transonic flight regime. It is for that reason that supersonic aircraft are not usually designed to operate there and that transonic flight can often be a design constraint. The aircraft must have sufficient thrust to overcome the increased drag when accelerating to the design cruise condition. That being said, current engine technology and other design criteria for supersonic transports ensure that there is sufficient thrust to accelerate while maintaining or increasing flight level during this transition. Time spent in transition is, however, minimized. Older fighter jets performed a diving acceleration maneuver in order to help overcome the wave drag rise while minimizing the time to climb, whereas transports, such as the Concorde, were confined to level or climbing accelerations. Previous trajectory optimization studies (Berton, 2003 and Norris, 2012) have investigated minimum time,

fuel, and community noise. This study investigates what effects varying the transonic acceleration maneuver have on the focused boom.

### 11.2.2 Boeing Configuration

Boeing used the configuration of the N+2 Experimental Validation Study–Boom Model #2 (BM #2) developed for low boom at cruise for this study (Welge, 2010). Sonic boom and CFD results were generated at several focused boom conditions that were determined by analysis using the Boeing performance and sizing models in Boeing’s Computer Aided Sizing and Evaluation System (CASES) to provide a representative data set for the BM #2 configuration. The CASES models were used to conduct the following Supersonic Mission Study performance trades:

- Transonic Altitude Trade;
- Flight Path angle ( $\gamma$ ) Trade;
- Transonic Altitude +  $\gamma$ ; and
- Acceleration (Afterburner) Trade.

Figure 11-6 shows a 3-view of the Boeing BM#2 configuration, designed to carry 30 passengers 3,500 nm cruising at 55,000 feet at Mach 1.6.

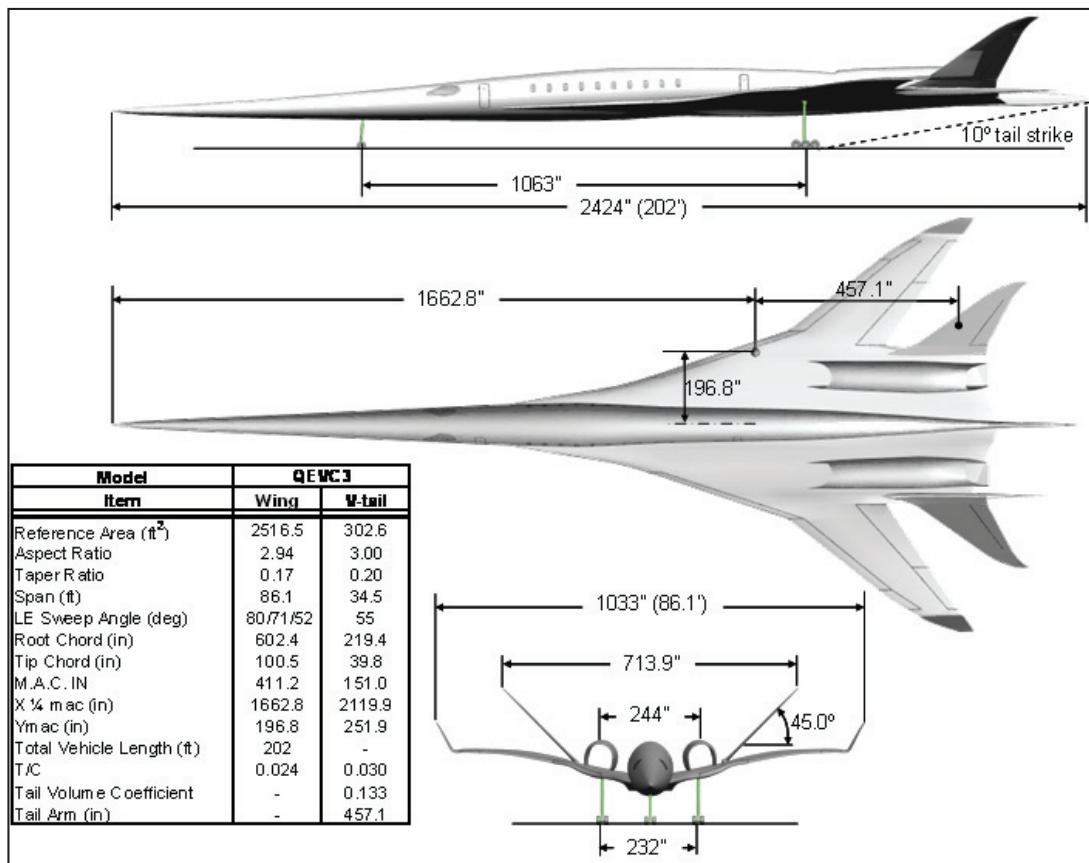


Figure 11-6. System Level Experimental Validation BM#2 (QEV3) general arrangement.

### 11.2.3 Boeing Profile Exploration Cases

In the test planning stage of the SCAMP F-18 experiment it was noted that the Boeing criteria for transonic acceleration was a modest 0.5 knots/second in level flight at 40,000 feet. This corresponds to a passenger comfort limit that was imposed in all of Boeing’s sizing studies. For this task, that requirement was relaxed in order to achieve higher acceleration rates. Table 11-1 shows the desired flight conditions covering a range of altitudes, climb angles, and, in particular, acceleration rates.

**Table 11-1. Desired Focused Boom Run Matrix**

Fn	accel_4 gamma input (deg)	max crz altitude (ft) X173	accel_4 Start Altitude (ft)	accel_4 End Altitude(ft)	Goal Accel (kts / sec)
scale as needed	0	55000	40550	40550	4
scale as needed	0	55000	40550	40550	2
scale as needed	0	55000	40550	40550	1
scale as needed	0		35000		0.51
scale as needed	0		45000		0.51
scale as needed	0		50000		0.51
scale as needed	1		35000		0.51
scale as needed	2		35000		0.51
scale as needed	3		35000		0.51
scale as needed	1		40000		0.51
scale as needed	2		40000		0.51
scale as needed	3		40000		0.51
scale as needed	1		40000		2.00
scale as needed	2		40000		2.00
scale as needed	3		40000		2.00

The CASES program was initially run with the performance model representative of the BM#2 configurations “as is”. The results for this study are shown in Table 11-2.

**Table 11-2. Mission Study Run Matrix**

	Fn (lbs)	accel_4 gamma input (deg)	max crz altitude (ft) x1.73	TOGW (lbs)	Range (NM)	Payload (lbs)	accel_4 Start Altitude (ft)
Baseline 765-076l	49531	0	55000	180068	3437	7351	40550
Cruise Altitude Trade	49531	0	60000	180015	3452	7350	40550
Gamma Trade	49531	-1	55000	180010	3447	7350	40550
	49531	-2	55000	180005	3452	7350	40550
	49531	-3	55000	180018	3461	7350	40550
	49531	1	55000	fails			40550
	49531	2	55000	fails			40550
	49531	3	55000	fails			40550
Transonic Altitude Trade	49531	0	55000	180025	3437	7350	40000
	49531	0	55000	180016	3440	7350	35000
	49531	0	55000	need to revise mission			30000
Transonic Alt+gamma	49531	0.5	55000	180001	3436	7350	35000
	49531	0.75		fails			35000

In addition to the “as is” performance model in CASES, the thrust model was modified to account for additional thrust that could be provided by an afterburner system during transonic acceleration. Although the vehicle was not resized to account for the weight of an afterburner system, the approach taken is sufficient to assess the effects on transonic acceleration and the subsequent sonic boom results. The results for this afterburner trade study are shown in Table 11-3.

Table 11-3. Afterburner Thrust Trade

	Fn	AB Factor	accel_4 gamma input	TOGW	accel_4 Start Altitude	accel_4 End Altitude	Cruise Start Altitude	Cruise End Altitude
Case 5	49531	2	0	180006	40550	40550	49158	55000
	49531	2	0	Fails	50000	50000		55000
	49531	2	0	180005	45000	45000	49185	55000
	49531	2	0	180004	40000	40000	49156	55000
	49531	2	0	180006	35000	35000	49137	55000
	49531	2	1	180017	35000	37039	49131	55000
	49531	2	2	180018	35000	39776	49119	55000
	49531	2	3	180002	35000	43993	49090	55000
	49531	1.8	0	Fails	50000	50000	50000	55000
	49531	1.8	0	180019	45000	45000	49201	55000
	49531	1.8	0	180021	40000	40000	49165	55000
	49531	1.8	0	180022	35000	35000	49143	55000
	49531	1.8	1	180023	35000	37456	49136	55000
	49531	1.8	2	180019	35000	41049	49121	55000
	49531	1.8	3	180003	35000	48242	49015	55000
	49531	1.7	0	Fails	50000	50000	50000	55000
	49531	1.7	0		45000	45000		55000
	49531	1.7	0		40000	40000		55000
49531	1.7	0		35000			55000	
49531	1.7	1		35000			55000	
49531	1.7	2		35000			55000	
49531	1.7	3	fails	35000			55000	
49531	1.6	0	Fails	50000	50000	50000	55000	
49531	1.6	0	180019	45000	45000	49231	55000	
49531	1.6	0	180004	40000	40000	49181	55000	
49531	1.6	0	180011	35000	35000	49155	55000	
49531	1.6	1	180007	35000	38098	49148	55000	
49531	1.6	2	180019	35000	43454	49123	55000	
49531	1.6	3	fails	35000			55000	
Case 4	49531	1.5	0	Fails	50000	50000	50000	55000
	49531	1.5	0	180011	45000	45000	49256	55000
49531	1.5	0	180003	40000	40000	49192	55000	
49531	1.5	0	180023	35000	35000	49161	55000	
49531	1.5	1	180014	35000	38575	49155	55000	
49531	1.5	2	180018	35000	45927	49111	55000	
49531	1.5	3	fails	35000			55000	
Case 3 Case 1	49531	1.4	0	Fails	50000	50000	50000	55000
	49531	1.4	0	180014	45000	45000	49294	55000
	49531	1.4	0	180022	40000	40000	49204	55000
	49531	1.4	0	180009	35000	35000	49172	55000
	49531	1.4	1	180010	35000	39242	49166	55000
	49531	1.4	2	Fails	35000			55000
	49531	1.4	3	Fails	35000			55000
	49531	1.3	0	fails	50000	50000	50000	55000
	49531	1.3	0	180017	45000	45000	49371	55000
	49531	1.3	0	180013	40000	40000	49225	55000
	49531	1.3	0	180024	35000	35000	49183	55000
	49531	1.3	1	180002	35000	40257	49182	55000
	49531	1.3	2	Fails	35000			55000
	49531	1.3	3	Fails	35000			55000
	49531	1.2	0	fails	50000	50000	50000	55000
	49531	1.2	0	180021	45000	45000	49723	55000
	49531	1.2	0	180004	40000	40000	49255	55000
	49531	1.2	0	180003	35000	35000	49202	55000
49531	1.2	1	180004	35000	42078	49207	55000	
49531	1.2	2	Fails	35000			55000	
49531	1.2	3	Fails	35000			55000	
49531	1.1	0	fails	50000	50000	50000	55000	
49531	1.1	0	180031	45000	45000	49974	55000	
49531	1.1	0	180009	40000	40000	49307	55000	
49531	1.1	0	180018	35000	35000	49225	55000	
49531	1.1	1	Fails	35000			55000	
49531	1.1	2	Fails	35000			55000	
49531	1.1	3	Fails	35000			55000	
49531	1	0	fails	50000	50000	50000	55000	
49531	1	0	180006	45000	45000	51438	55000	
49531	1	0	180025	40000	40000	49424	55000	
49531	1	0	180016	35000	35000	49265	55000	
49531	1	1	Fails	35000			55000	
49531	1	2	Fails	35000			55000	
49531	1	3	Fails	35000			55000	

Table 11-3 also highlights five cases for which CFD solutions were generated. These cases were selected to give the widest performance range possible for this Boeing configuration. The corresponding flight conditions used to propagate from the focused boom condition are shown in Table 11-4 for these five cases. A sixth case for a 3° dive is also listed.

**Table 11-4. Flight Conditions for CFD and PCBOOM6 Runs**

**Overflow solution files provided by Boeing at H/L = 1, and H/L = 3:**

C1 z = 40000 ft, M = 1.16  
 C2 z = 38500 ft, M = 1.23  
 C3 z = 45000 ft, M = 1.16  
 C4 z = 45000 ft, M = 1.17  
 C5 z = 45000 ft, M = 1.21  
 C6 z = 36500 ft, M = 1.18

**Final Conditions from PCBOOM6**

Case	Description	Z	M	Mdot	Gamma
bcyl3_c1	M1.16 AB=1.0 level @40 kft	40000	1.156	0.00036	0.000
bcyl3_c2	M1.23 AB=1.5 2 deg climb @38.5	38498	1.230	0.00316	2.000
bcyl3_c3	M1.16 AB=1.0 level @45 kft	45000	1.153	0.00010	0.000
bcyl3_c4	M1.17 AB=1.5 level @45 kft	45000	1.170	0.00111	0.000
bcyl3_c5	M1.21 AB=2.0 level @45 kft	45000	1.211	0.00295	0.000

Flight trajectories were generated for each case. The transonic acceleration portions of these trajectories are shown in Figures 11-7 and 11-8 for altitude vs Mach Number and Acceleration Rate (dM/dt) vs Mach Number, respectively. The interpolated focused boom conditions are highlighted with enlarged symbols.

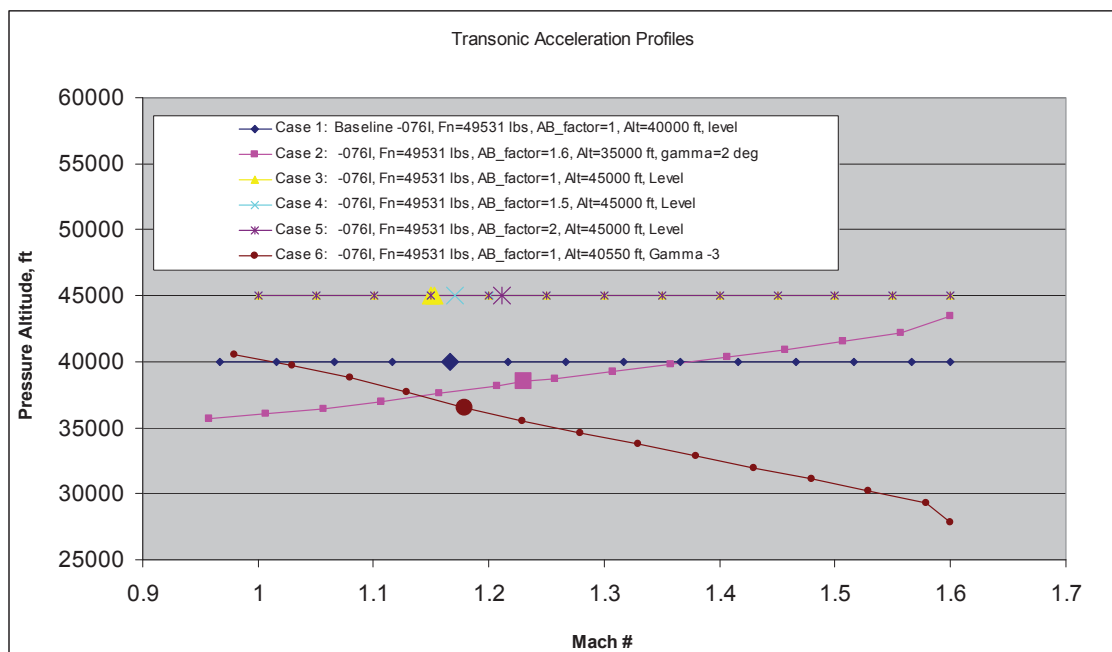


**Figure 11-7. Transonic acceleration altitude profiles.**

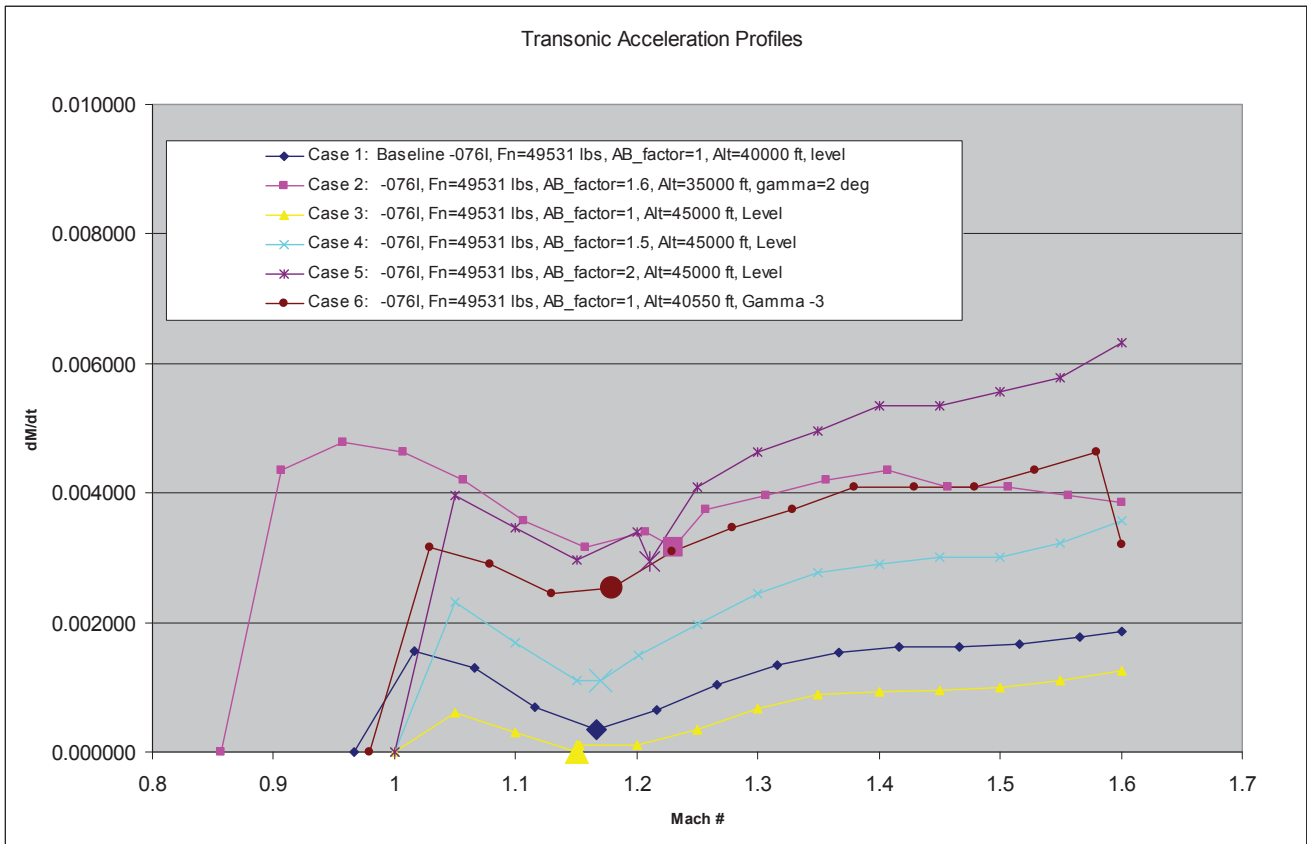
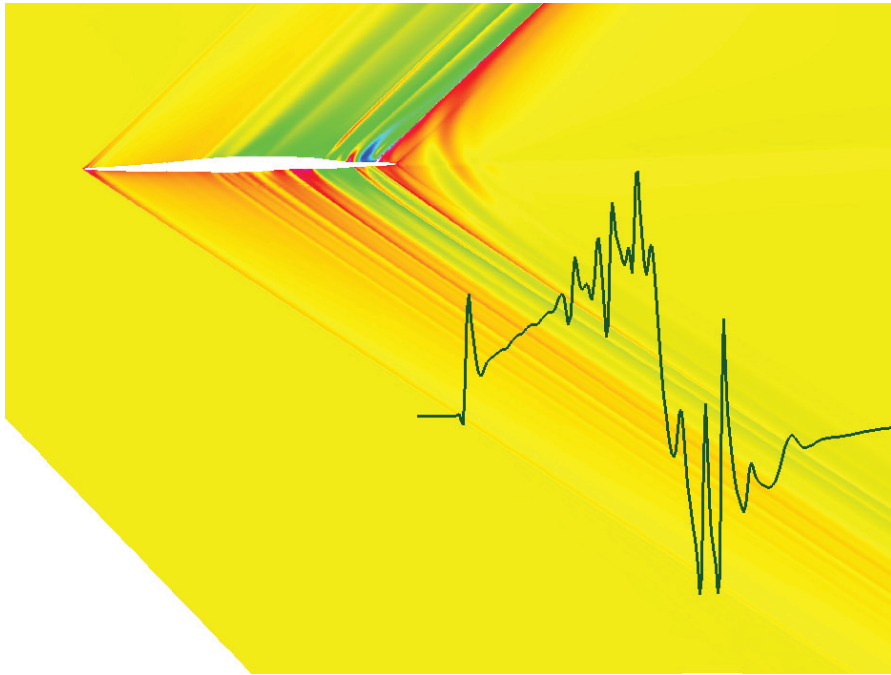


Figure 11-8. Transonic acceleration  $dM/dt$  profiles.

### 11.2.4 Boeing CFD Analysis

CFD analysis was conducted for the five flight conditions highlighted in Table 11-3. To provide a visual perspective, the under-track flow-field solution is shown in Figure 11-9 and Figure 11-10 for  $H/L = 1$  and  $H/L = 3$ , respectively.





*Figure 11-9. Boeing CFD using overflow (Navier-Stokes) for the Boeing BM#2 Configuration (low-boom design point)  $H/L = 1$ .*

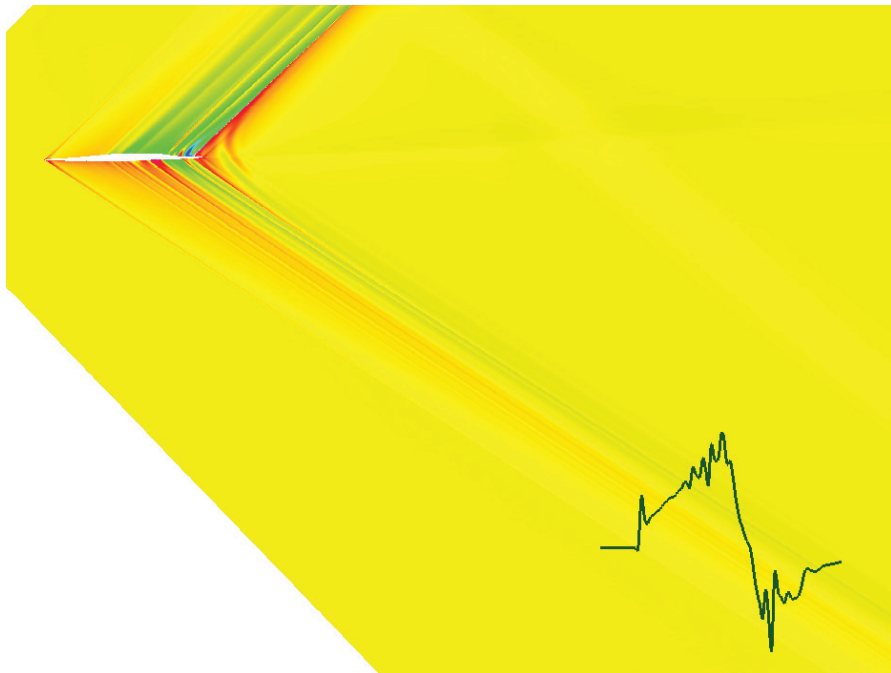


*Figure 11-10. Boeing CFD using overflow (Navier-Stokes) for the Boeing BM#2 Configuration (low-boom design point)  $H/L = 3$ .*

Although the under-track condition is of the utmost interest, a full cylinder solution was created to facilitate additional off-track analysis in a subsequent study. This is illustrated in Figure 11-11 at the Case 1 focusing condition.



Figure 11-11. Case 1 Cylinder Solutions provided at  $H/L = 1 \& 3$ .

The under-track  $dP/P$  was used as the starting signature for propagation in PCBoom. Under-track signatures for each of the six focusing flight conditions are shown in Figure 11-12.

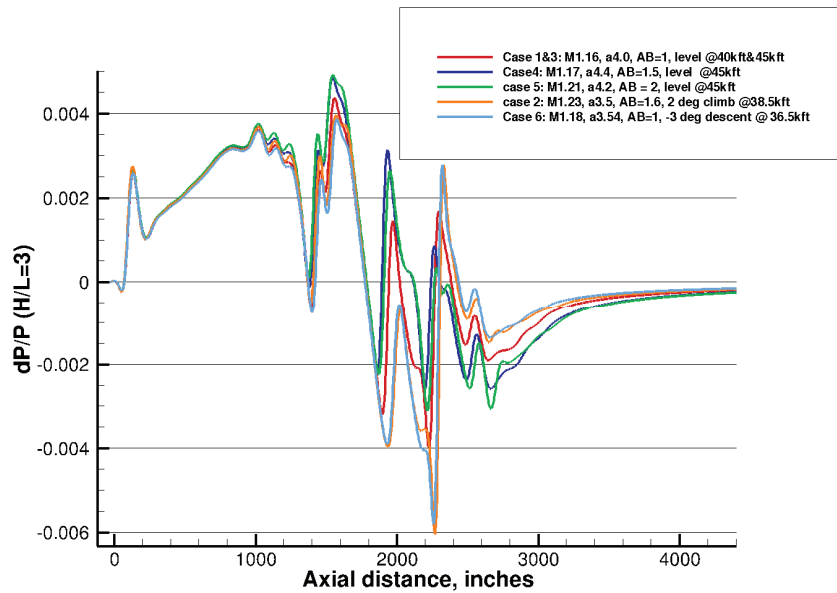
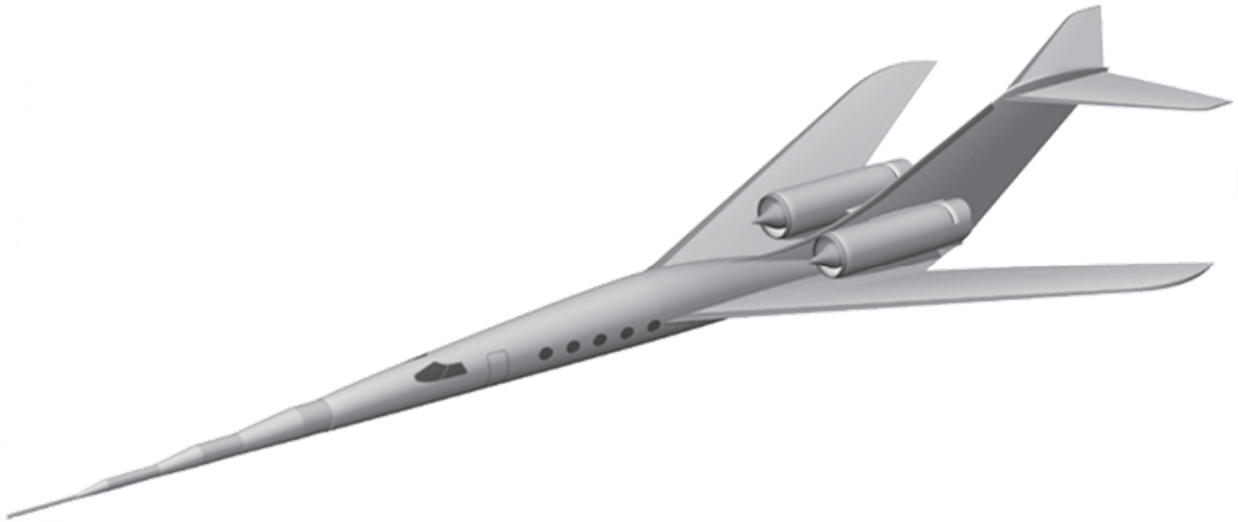


Figure 11-12. Under-track signatures ( $dP/P$  vs axial location).

Propagation results from the focus boom analysis are provided in Section 11.5.

## 11.3 Gulfstream Configuration/Profile/CFD Analysis

The Gulfstream configuration (Figure 11-13, Table 11-5) is an 8 to 14-passenger aircraft designed to operate from general aviation airports. The aircraft range is greater than 4000 nmi with a cruising speed of Mach 1.8 at 51,000 feet. It features a variable sweep wing and has a maximum take-off gross weight of less than 100,000 pounds.



*Figure 11-13. Gulfstream Low-Boom Passenger Aircraft Configuration.*

### 11.3.1 Gulfstream Profile Analysis

The baseline performance profile for this configuration involves a level acceleration at 35,000 feet through the transonic range at an acceleration rate of .001 Mach/second as indicated by the bold black line in Figure 11-14. The target design point for this configuration is Mach 1.8 with a 51,000-foot initial cruise altitude and 55,000-foot maximum top of climb cruise altitude. A parametric profile analysis considered altitudes of 38,000 feet and 40,000 feet and variations in  $\dot{M}$  from .0005 to .002 (Mach/sec). A total of six profiles were considered for the SCAMP Profile Exploration Task and were analyzed in PCBoom, with a determination of the focal point being made (Table 11-5).

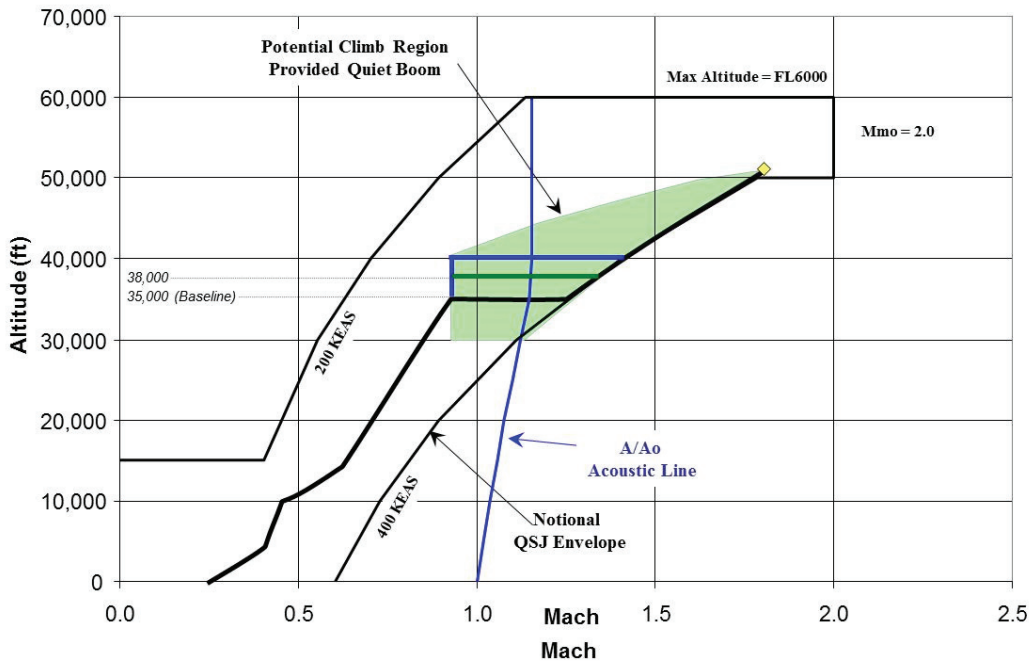


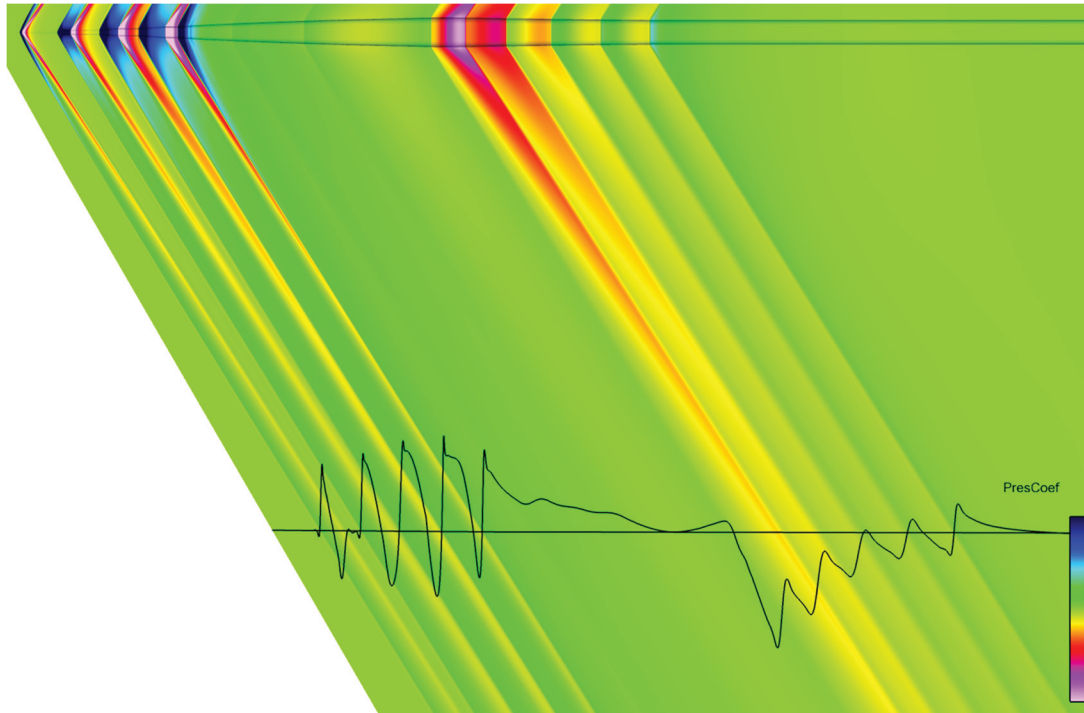
Figure 11-14. Notional quiet supersonic jet flight envelope and parametric profiles.

Table 11-5. Summary of Focus Conditions

Case #	Accel Rate (Mach/sec)	Climb	Z (Alt)	Mach # (at Focus)
gac_fl380_m118	0.0005	2 deg	38000	1.182
gac_fl380_m119	0.0010	2 deg	38000	1.190
gac_fl380_m121	0.0020	2 deg	38000	1.208
gac_fl400_m118	0.0005	2 deg	40000	1.182
gac_fl400_m119	0.0010	2 deg	40000	1.190
gac_fl400_m121	0.0020	2 deg	40000	1.209

### 11.3.2 Gulfstream CFD Analysis

An axisymmetric geometry was considered in the CFD analysis using the technique reported by Howe (2005). The six focus conditions were analyzed using the Overflow code, with an inviscid Euler analysis and 18 million grid points with the grid extending out to approximately two body lengths. The near-field pressure signatures were extracted at one body length (Figure 11-15).



*Figure 11-15. Gulfstream CFD pressure flowfield of the axisymmetric geometry.*

### 11.3.3 Gulfstream Performance Analysis

When developing the alternative profiles, the overall integrated airframe and engine performance was considered. Based on the NASA UEET Program (2005) and the Integrated Inlet-Propulsion Systems Study (IIPSS), the transonic acceleration regime was identified as critical due to the thrust/drag pinch. The baseline acceleration from 350-kt knots calibrated air speed (KCAS) to 400-kt knots equivalent air speed (KEAS) at 30,000 feet is indicated in Figure 11-16. During this profile exploration study it was found that alternate conditions for boom reduction further aggravated the thrust shortfall. Furthermore, the higher altitude transitions with lower acceleration rates are more difficult to achieve, and will require more fuel and time to reach the desired climb at constant  $W/\delta$ .

Propagation results from the focus boom analysis are provided in Section 11.5. A strong aft shock is present in both the far-field propagation and the focus boom results. This is a byproduct of the vehicle operating under flight conditions well away from the cruise flight conditions (FL510, Mach 1.8). The deviation from the design flight conditions adversely impacted the near-field pressure distribution in the aft part of the vehicle and contributed to the strong aft shock. The strong shock is not a desirable characteristic for a low-boom aircraft and Gulfstream would not produce a supersonic aircraft that exhibits such a strong shock in its signature. Thus, the analysis in section 11.5 for the Gulfstream cases was carried out for “academic” purposes.

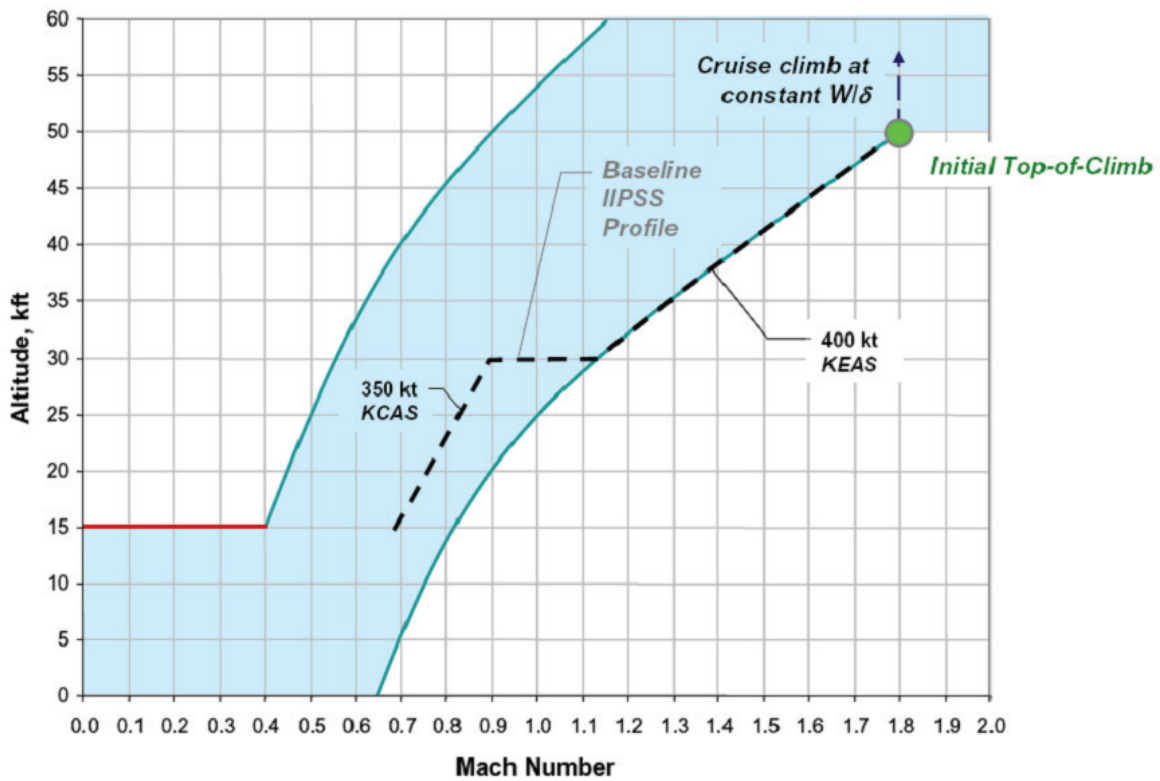


Figure 11-16. Optimal profile leveraging the NASA UEET and the IIPSS projects.

## 11.4 NASA Configuration/Profile/CFD Analysis

A NASA-designed Sonic Boom Demonstrator Class vehicle (Figure 11-17, Table 11-6) with a take-off gross weight of 36,000 pounds, an overall length of 127 feet and a maximum cruising altitude of 45,000 feet was considered in this analysis.



*Figure 11-17. NASA Sonic Boom Demonstrator Vehicle artistic rendering.*

**Table 11-6. NASA Sonic Boom Demonstrator Description**

<b>Sonic Boom Demonstrator Class Vehicle</b>
<b>36K lb. TOGW</b>
<b>Overall Length 127 ft.</b>
<b>Maximum Cruise Altitude 45K ft.</b>

### **11.4.1 NASA Demonstrator Profile Analysis**

Four profiles provided by NASA for this vehicle were examined using PCBoom and the focus conditions identified (Table 11-7). The aircraft weights for these transition points ranged from 33,000 – 33,500 pounds. For all four cases, the focus point was achieved during the level acceleration phase of the climb profile.

**Table 11-7. NASA Configuration Focus Conditions**

Climb Path	Mach	Distance
1	1.146	33,144 ft
2	1.173	35,821 ft
3	1.168	38,154 ft
4	1.157	40,524 ft

## 11.4.2 NASA Demonstrator CFD Analysis

A computational Fluid Dynamics analysis was performed using Cart3D code (Euler CFD), with 95 million cells, and a knowledge-based volume mesh refinement. The analysis used a rotated grid for Mach alignment to reduce numerical dissipation (The adjoint mesh adaption was not used). Cylinders were extracted at one body length for use in PCBoom. An under-track pressure distribution and sonic boom overpressure trace is provided in Figure 11-18. Corresponding cylinders at one body length are shown in Figure 11-19. Propagation results from the focus boom analysis are provided in Section 11.5.

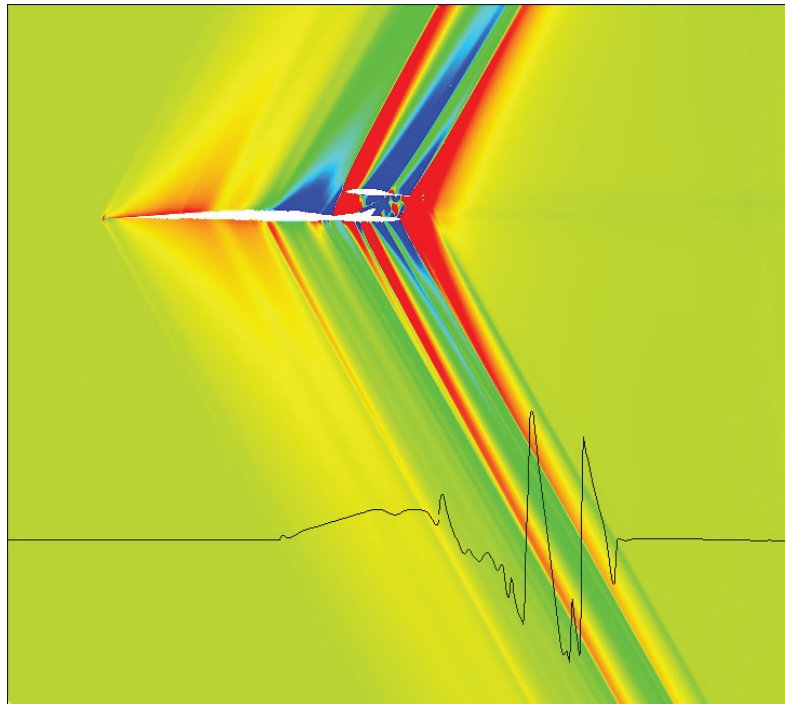
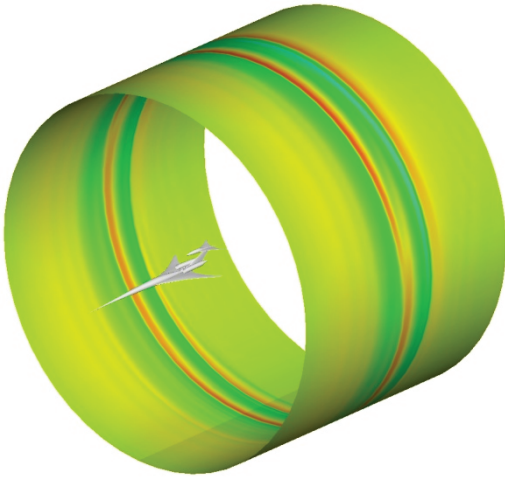


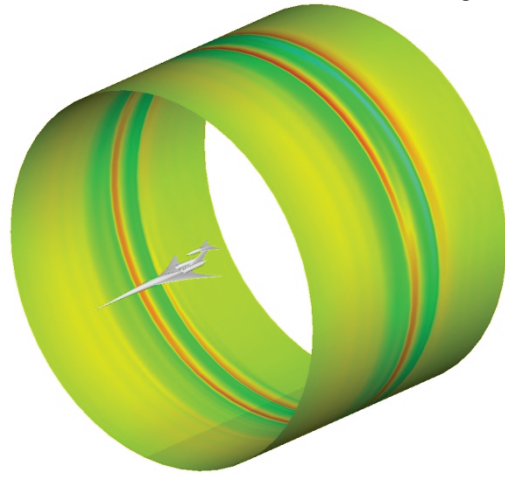
**Figure 11-18. NASA Demonstrator Vehicle CFD Analysis, under-track pressure distribution.**



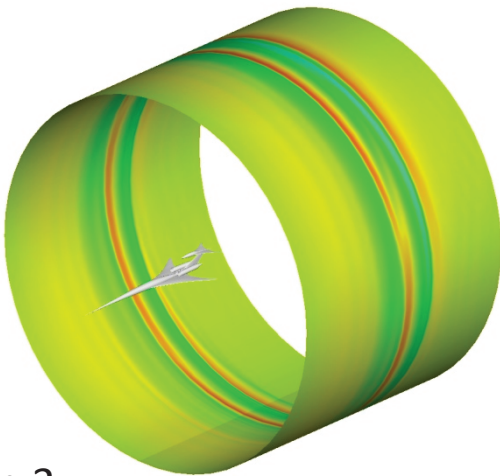
Run 1



Run 2



Run 3



Run 4

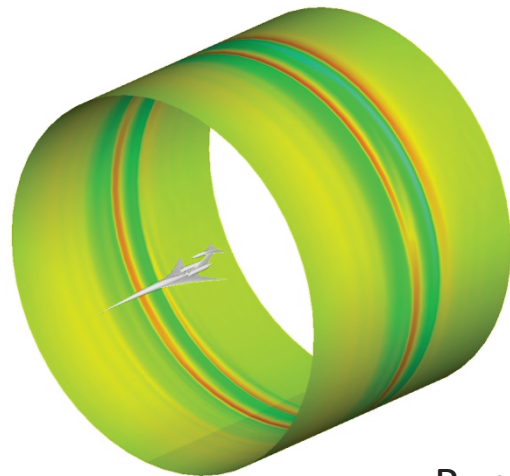


*Figure 11-19. NASA Demonstrator Vehicle CFD Analysis, cylinders at one body length.  
Note: the flow conditions for CFD runs 1-4 are indicated in Table 11-7.*

## 11.5 Lossy NTE Propagation and Low-Boom Results

### 11.5.1 Methodology

Take-off profiles were evaluated for four NASA trajectories, five Boeing trajectories, and six Gulfstream trajectories. The summary of flight conditions is listed in Table 11-8.

**Table 11-8. Summary of Flight Conditions for the Profile Exploration Study**

Case	Altitude (ft)	Mach	mdot (Mach/s)	Gamma (deg)
NASA Case 1	33479	1.166	0.00134	0.642
NASA Case 2	35821	1.175	0.00138	0.000
NASA Case 3	38154	1.169	0.00103	0.001
NASA Case 4	40525	1.161	0.00066	0.003
Boeing Case 1	40000	1.156	0.00036	0.000
Boeing Case 2	38498	1.230	0.00316	2.000
Boeing Case 3	45000	1.153	0.00010	0.000
Boeing Case 4	45000	1.170	0.00111	0.000
Boeing Case 5	45000	1.211	0.00295	0.000
Gulfstream Case 1	38000	1.182	0.00050	2.000
Gulfstream Case 2	38000	1.190	0.00100	2.000
Gulfstream Case 3	38000	1.208	0.00200	2.000
Gulfstream Case 4	40000	1.182	0.00050	2.000
Gulfstream Case 5	40000	1.190	0.00100	2.000
Gulfstream Case 6	40000	1.209	0.00200	2.000

Input signatures for the Tricomi code and the corresponding focusing conditions were obtained from PCBoom lossy propagation for each configuration and its trajectories. The low-boom signatures were evaluated using the Tricomi code from an updated version of the beta code. The “delta” version of the Tricomi code includes the following changes since the beta version:

- 1) Parallelization of most of the “for” loops;
- 2) Incorporation of the diffraction “for” loop with the absorption/dispersion “for” loop;
- 3) Modification of the timewise boundary conditions to improve the zero-pressure boundary condition;
- 4) Additional parameters to monitor iterative convergence of the solution;
  - a) solution difference associated with the maximum change in the nonlinear step,
  - b) solution difference associated with the maximum change in the diffraction step, and
  - c) including the pseudotime step-increment as an additional convergence parameter.

### 11.5.2 Low-Boom Configuration Analysis

The Tricomi code was run for a pseudotime value of 17 (10 for the linear iterations, 7 for the nonlinear iterations) for all low-boom signatures. The in-coming waveform was specified at  $\bar{z}_{\max} = 1.0$ . The computational domain was specified for a range of  $\bar{z}_{\max} = 1.0$  to  $\bar{z}_{\min} = -1.0$ . The standard atmosphere was assumed for all cases (windless atmosphere), with the temperature at 288.15 kelvin, 101.325 kPa, and a relative humidity at 59.62 percent. The focusing conditions and input parameters for the profile exploration are listed in Table 11-9.

**Table 11-9. Summary of Focusing Parameters for the Tricomi Code**

Case	$f_{ac}$ (Hz)	$R_{tot}$ (m)	Z pts	Time pts
NASA Case 1	9.20	98236	4000	32768
NASA Case 2	9.00	89950	4000	32768
NASA Case 3	9.06	89451	4000	32768
NASA Case 4	8.82	87854	4000	32768
Boeing Case 1	4.89	88793	4000	65536
Boeing Case 2	6.09	84542	4000	65536
Boeing Case 3	4.82	88809	4000	65536
Boeing Case 4	4.88	89102	4000	65536
Boeing Case 5	5.25	87281	4000	65536
Gulfstream Case 1	5.83	88575	4000	32768
Gulfstream Case 2	5.98	88275	4000	32768
Gulfstream Case 3	6.24	86445	4000	32768
Gulfstream Case 4	5.84	88606	4000	32768
Gulfstream Case 5	5.99	88325	4000	32768
Gulfstream Case 6	6.24	86881	4000	32768

Loudness metrics were also calculated by external Matlab scripts for each Tricomi code solution. Table 11-10 shows the metrics for each profile exploration case. The metrics calculated were the minimum pressure, maximum pressure, Perceived Level, A-weighted sound exposure level, C-weighted sound exposure level, and the unweighted sound exposure level. These metric levels were those observed over the entire domain for each case. Table 11-11 is the summary of the  $\bar{z}$  location associated with each value in Table 11-10.

**Table 11-10. Summary of Metric Values for Each Case in the Profile Exploration Study**

Case	Minimum Pressure (Pa)	Maximum Pressure (Pa)	Perceived Loudness (dB)	Maximum SEL <sub>A</sub> (dB)	Maximum SEL <sub>C</sub> (dB)	Maximum SEL <sub>F</sub> (dB)
NASA Case 1	-76.6	100.7	111.1	95.9	110.6	118.6
NASA Case 2	-72.7	102.0	106.7	91.5	109.5	118.3
NASA Case 3	-67.0	73.1	104.1	89.1	107.7	116.8
NASA Case 4	-65.8	68.3	103.0	88.2	107.5	116.5
Boeing Case 1	-84.4	146.5	103.8	89.0	108.4	124.1
Boeing Case 2	-113.1	129.1	109.6	94.8	109.4	124.3
Boeing Case 3	-71.9	123.1	98.9	83.6	106.7	122.8
Boeing Case 4	-78.5	119.3	99.9	84.1	107.2	123.2
Boeing Case 5	-82.4	114.3	100.3	85.1	107.0	123.2
Gulfstream Case 1	-106.6	203.8	118.3	102.9	112.8	121.4
Gulfstream Case 2	-109.2	192.4	118.0	102.6	112.7	121.4
Gulfstream Case 3	-111.4	185.7	117.9	102.4	112.5	121.4
Gulfstream Case 4	-101.5	162.9	116.5	101.2	111.6	121.0
Gulfstream Case 5	-103.3	161.7	116.5	101.2	111.4	121.0
Gulfstream Case 6	-106.0	154.3	116.3	101.2	111.3	121.0

The data presented in Tables 11-10 and 11-11 summarize the plots shown in Figures 11-20 through 11-88. There are five figures for each low-boom case that show the pressure field contour in the first figure, a metrics comparison in the second figure, the time history at maximum (or minimum) pressure in the third figure, the time history for the highest Perceived Level in the fourth figure, and time histories at  $\bar{z} = 1.0$ ,  $\bar{z} = 0.6$ ,  $\bar{z} = 0.2$ , and  $\bar{z} = -0.2$  in the fifth figure. This sequence of figures is the same for all of the low-boom cases except for the Gulfstream cases. There are only four figures for the Gulfstream cases because the  $\bar{z}$  location for the highest perceived level and the maximum pressure are the same. The ground reflection factor of 1.9 is not included in the pressure field contour plots, but is included in all other plots.

An observed trend for the NASA and Boeing cases in the metrics data from Tables 11-10 and 11-11 is that the  $\bar{z}$  location of the peak overpressure and underpressure do not correspond to the  $\bar{z}$  location of the highest perceived level. This observation should be further investigated. An additional observation for the NASA and Boeing cases is that the metric levels are increasing but the peak pressure levels are decreasing as one approaches the focus location predicted by geometric acoustics. The metrics results in the Gulfstream cases are dominated by the aft shock focusing and do not follow the same trends as the NASA and Boeing cases. For the Gulfstream cases, the peak loudness levels do coincide with the peak overpressure  $\bar{z}$  locations. An examination of the plots in figures 11-67, 11-71, 11-75, 11-79, 11-83, and 11-87 reveals that the shaping persists in the front part of the signature, but did not in the aft part of the signature. That is, when looking at only the front part of the focused signatures, if the in-coming signature is shaped, the corresponding focused signature will be shaped. One last observation that is consistent for all cases is that accelerating through Mach 1 at higher altitudes results in lower loudness levels than accelerating at lower altitudes. For the Gulfstream cases, this is still true but the decrease in loudness is not as much as that observed in the NASA and Boeing cases.

**Table 11-11. Summary of  $\bar{z}$  Locations that Correspond to Each Metric Value in Table 11-15**

Case	Zbar location for min. pressure	Zbar location for max. pressure	Zbar location for max. PL	Zbar location for max. SEL <sub>A</sub>	Zbar location for max. SEL <sub>C</sub>	Zbar location for max. SEL <sub>F</sub>
NASA Case 1	0.5294	0.1893	0.0313	0.0313	0.0773	0.2198
NASA Case 2	0.2303	0.1693	0.0293	0.0288	0.1108	0.2288
NASA Case 3	0.2453	0.1763	0.0333	0.0338	0.1123	0.2213
NASA Case 4	0.2683	0.1658	0.0363	0.0378	0.1023	0.2223
Boeing Case 1	0.3063	0.2193	0.0423	0.0448	0.0723	0.3378
Boeing Case 2	0.2703	0.2453	0.0183	0.0198	0.0683	0.3428
Boeing Case 3	0.3108	0.2128	0.0513	0.0523	0.0758	0.3373
Boeing Case 4	0.3653	0.2168	0.0588	0.0588	0.0748	0.4029
Boeing Case 5	0.5099	0.2278	0.0628	0.0613	0.0763	0.3638
Gulfstream Case 1	0.3263	0.0483	0.0483	0.0478	0.0503	0.2203
Gulfstream Case 2	0.3233	0.0473	0.0473	0.0473	0.0483	0.2183
Gulfstream Case 3	0.3178	0.0458	0.0458	0.0453	0.0478	0.2183
Gulfstream Case 4	0.3293	0.0433	0.0433	0.0428	0.0463	0.2403
Gulfstream Case 5	0.3248	0.0418	0.0418	0.0418	0.0448	0.2373
Gulfstream Case 6	0.3193	0.0418	0.0418	0.0413	0.0448	0.2383

Each low-boom focusing case has a corresponding “real-world” focusing region consisting of the projection of the Tricomi solution domain in the vicinity of the caustic intercept at the ground. The size of this region is dependent on the characteristic acoustic frequency, total radius of curvature, speed of sound at the ground, and also on the transient flight conditions for the vehicle trajectory that correspond to the focusing conditions at the ground. Table 11-12 shows a comparison of the focal region size as it intersects with the

ground for each low-boom case in terms of the PCBoom physical coordinates. The first column is the case type. The second column is the x-coordinate of the ground intercept for the ray associated with  $\bar{z} = -1.0$ . The third column is the x-coordinate of the ground intercept for the ray associated with  $\bar{z} = 1.0$ . Only the x-coordinate is considered because the vehicle is travelling along the x-direction. The ground elevation is located at z-coordinate of zero. The fourth column is then the second column minus the first column. That is, the Tricomi footprint distance is the size of the diffraction layer due to the intersection of the ground plane with the Tricomi domain plane. The data in Table 11-12 indicates that the footprint distance increases with a decrease in the acceleration rate.

**Table 11-12. Comparison of Tricomi Domain Distances in Terms of the Physical Coordinates**

Case	Ray Gnd Intercept @ $\bar{z}=-1$ (ft)	Ray Gnd Intercept @ $\bar{z}=1$ (ft)	Tricomi Footprint Distance (ft)
NASA Case 1	423672.2	436132.2	12460.0
NASA Case 2	483078.1	493327.3	10249.2
NASA Case 3	577542.3	588707.1	11164.8
NASA Case 4	755562.0	773514.4	17952.4
Boeing Case 1	133084.4	157752.0	24667.6
Boeing Case 2	104381.6	113389.2	9007.6
Boeing Case 3	164611.4	204863.2	40251.8
Boeing Case 4	125023.4	140486.6	15463.2
Boeing Case 5	106164.4	116097.2	9932.8
Gulfstream Case 1	136025.7	158108.7	22083.0
Gulfstream Case 2	122321.9	137796.9	15475.0
Gulfstream Case 3	108334.1	119841.9	11507.8
Gulfstream Case 4	139581.5	161431.1	21849.6
Gulfstream Case 5	125546.1	141286.3	15740.2
Gulfstream Case 6	111736.4	122741.6	11005.2

Spectral plots are presented in Figures 11-95 through 11-97 for the NASA Case 4, Boeing Case 3, and Gulfstream Case 4 simulations. Each plot shows Power Spectral Density spectra from  $\bar{z} = 1.0$ , the  $\bar{z}$  corresponding to the maximum (or minimum) pressure amplitude, the  $\bar{z}$  corresponding to the maximum perceived level, and at  $\bar{z} = -0.2$ . As one would expect, the levels in the evanescent region are considerably lower than for the illuminated zone, especially at the higher frequencies.

### 11.5.3 Critical Analysis of Focus Boom Modeling

The convergence of the solutions for all cases should be more closely examined. This is recommended for convergence with respect to the choice of the Tricomi domain temporal and spatial gridding and also to the iterative convergence of the solution. These can be addressed by increasing the grid density and also increasing the amount of pseudotime iterated for each additional change in grid density. That is, the solution should be closely monitored to observe how the features and trends in the solutions persist with respect to increasing grid density. This would also include convergence for each grid scenario as a function of pseudotime.

As with any numerical implementation of a physics-based model equation, there are computational aspects that have the potential to introduce numerical artifacts into the solutions. Future work for this topic should include detailed investigation of the loudness trends identified in the Tricomi solutions and examine whether these trends are indeed rooted in the physics of sonic boom focusing or are potentially due to the prediction

methodology, or some combination of the physics and numerics. Some of this recommended work may require in-depth studies that are beyond the scope of this NRA.

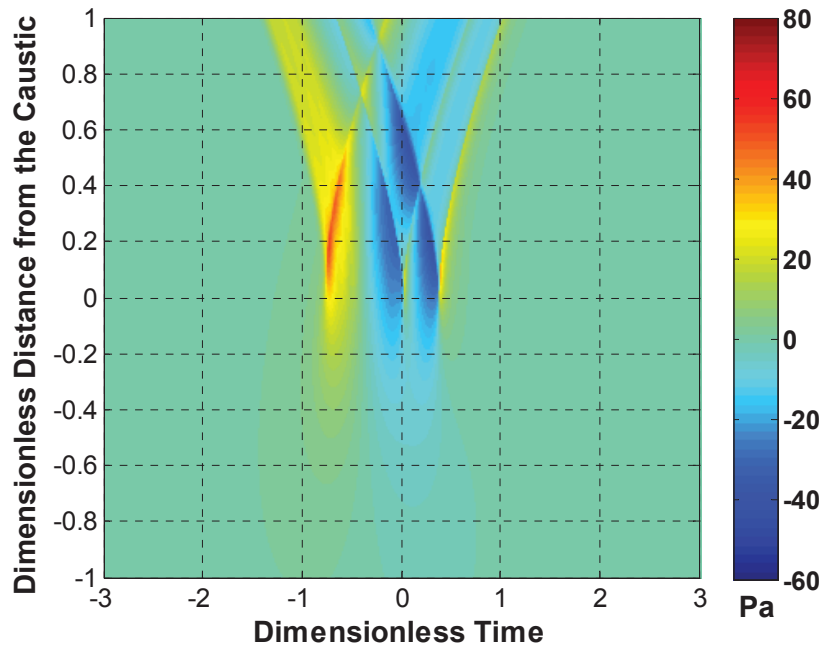


Figure 11-20. Pressure field contour for NASA Case 1, 33479 ft, Mach 1.166,  $\dot{m} = 0.00134$ .

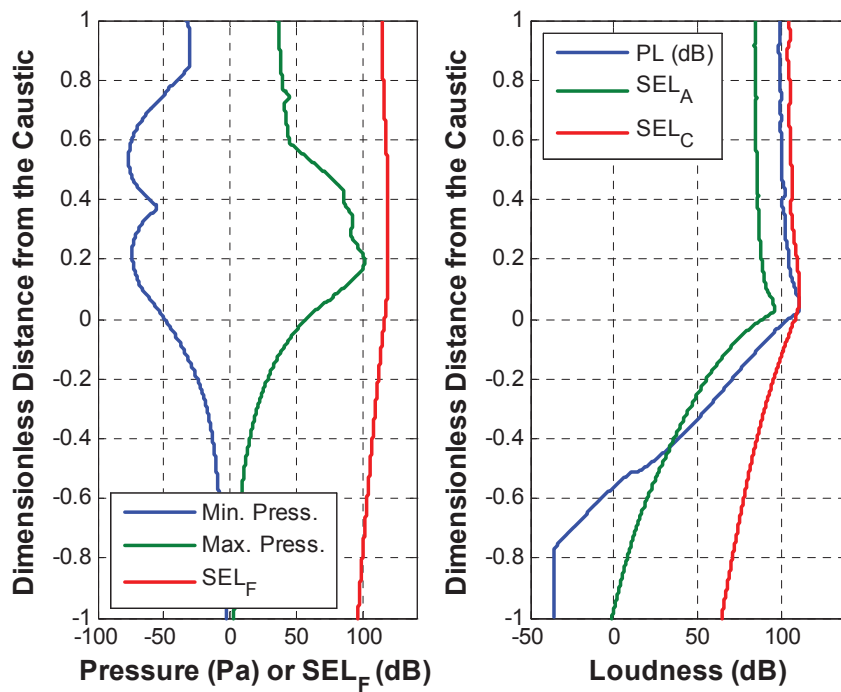


Figure 11-21. Metrics plots for NASA Case 1, 33,479 ft, Mach 1.166,  $\dot{m} = 0.00134$ .

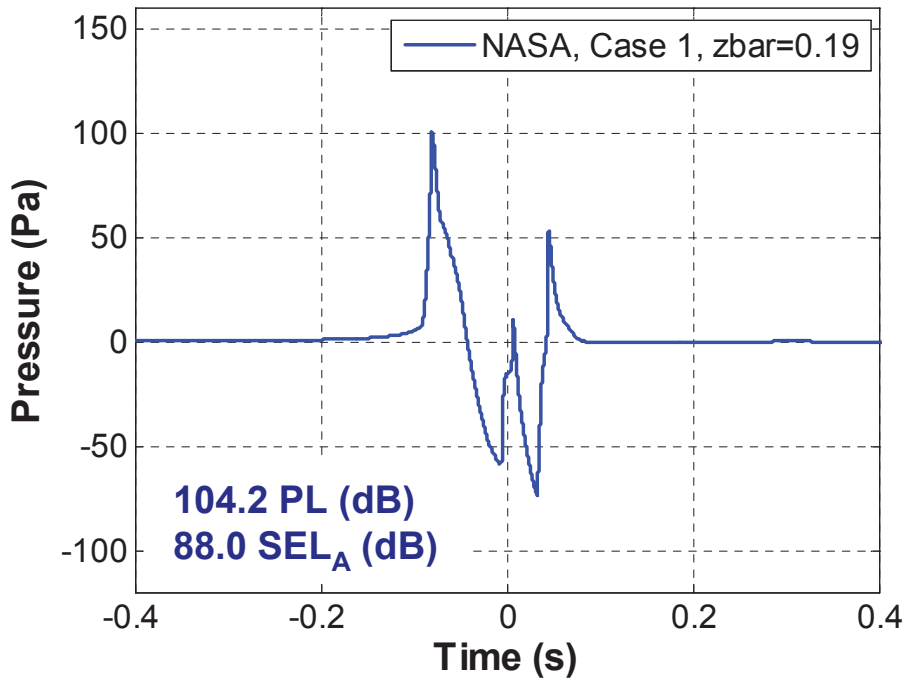


Figure 11-22. Time history corresponding to the peak overpressure ( $\bar{z}=0.19$ ) for NASA Case 1, 33,479 ft, Mach 1.166,  $\dot{m} = 0.00134$ .

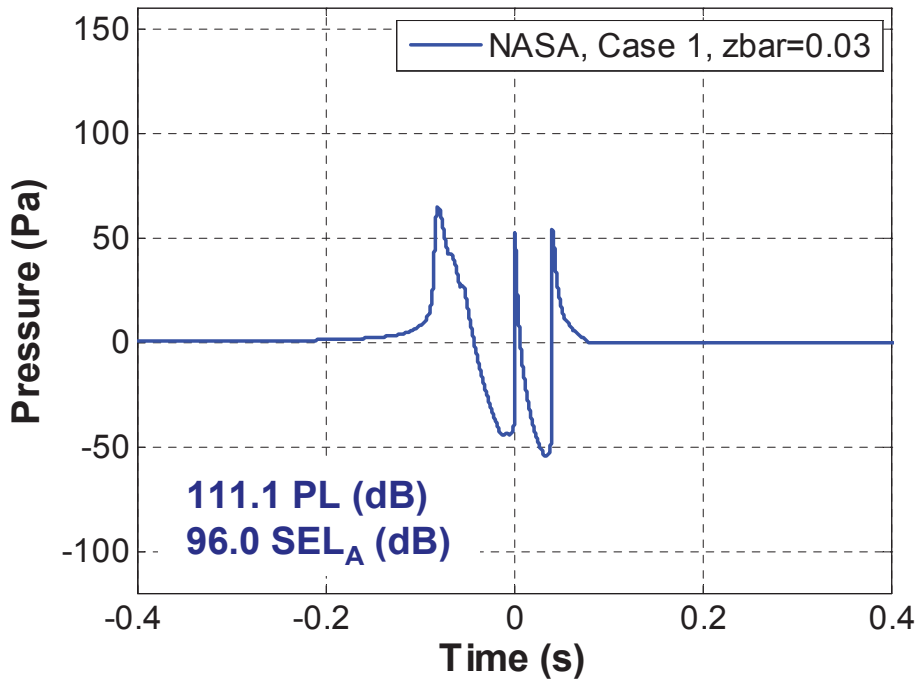


Figure 11-23. Time history corresponding to the highest PL ( $\bar{z}=0.03$ ) for NASA Case 1, 33,479 ft, Mach 1.166,  $\dot{m} = 0.00134$ .

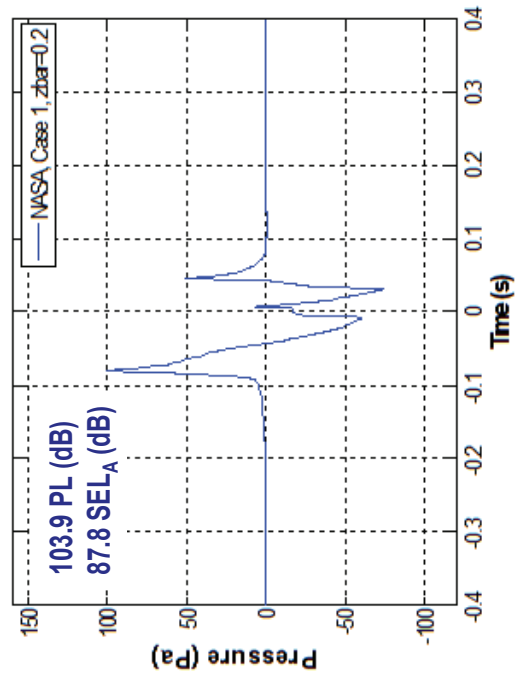
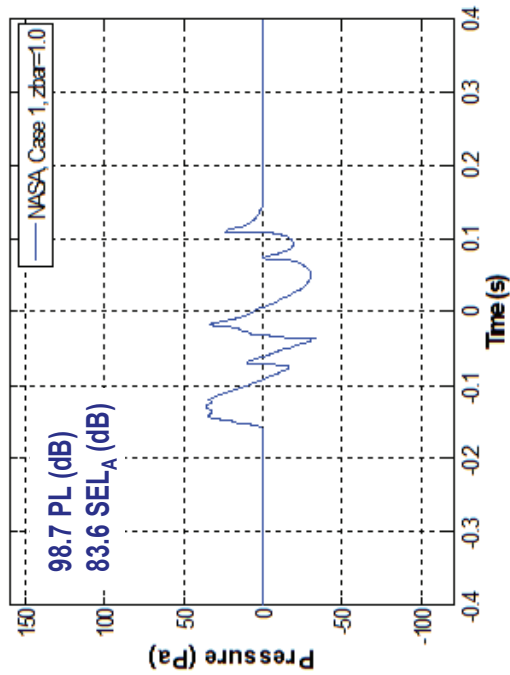
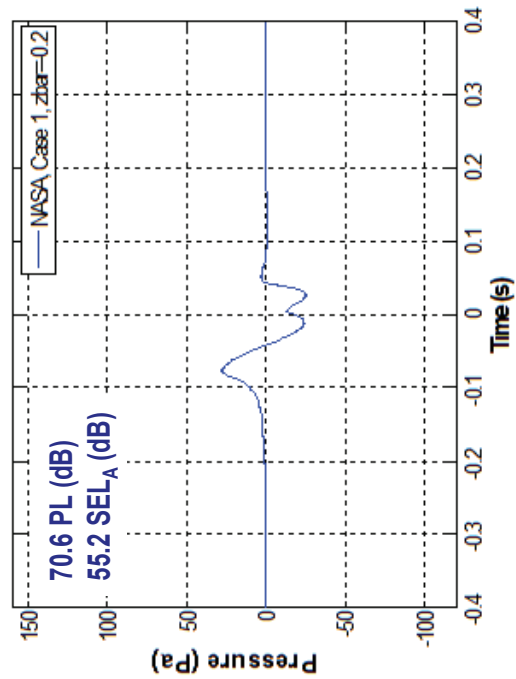
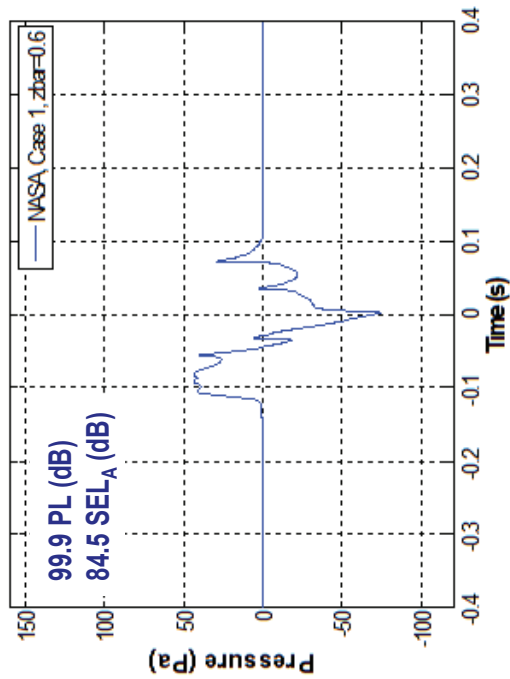


Figure 11-24. Time histories for NASA Case 1, 33,479 ft, Mach 1.166,  $\dot{m} = 0.00134$  at four different  $\bar{z}$  locations – a)  $\bar{z} = 1.0$ , b)  $\bar{z} = 0.6$ , c)  $\bar{z} = 0.2$ , and d)  $\bar{z} = -0.2$ .



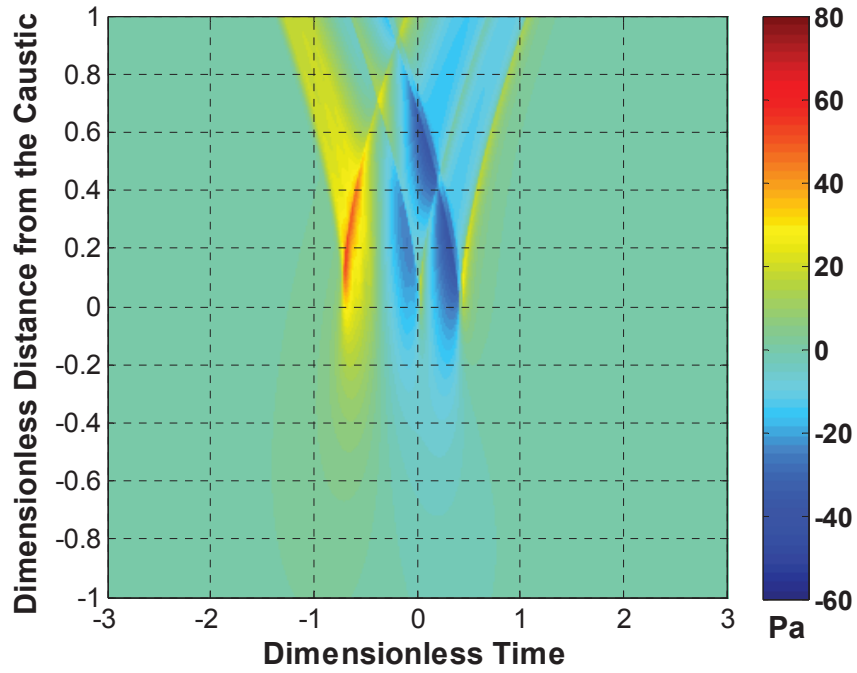


Figure 11-25. Pressure field contour for NASA Case 2, 35,821 ft, Mach 1.175,  $\dot{m} = 0.00138$ .

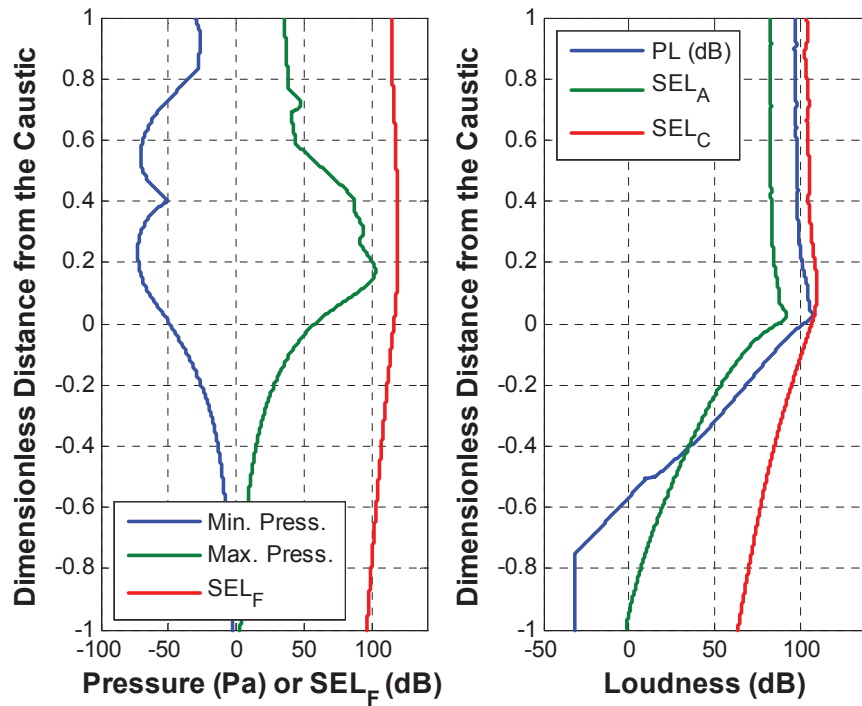


Figure 11-26. Metrics plots for NASA Case 2, 35,821 ft, Mach 1.175,  $\dot{m} = 0.00138$ .

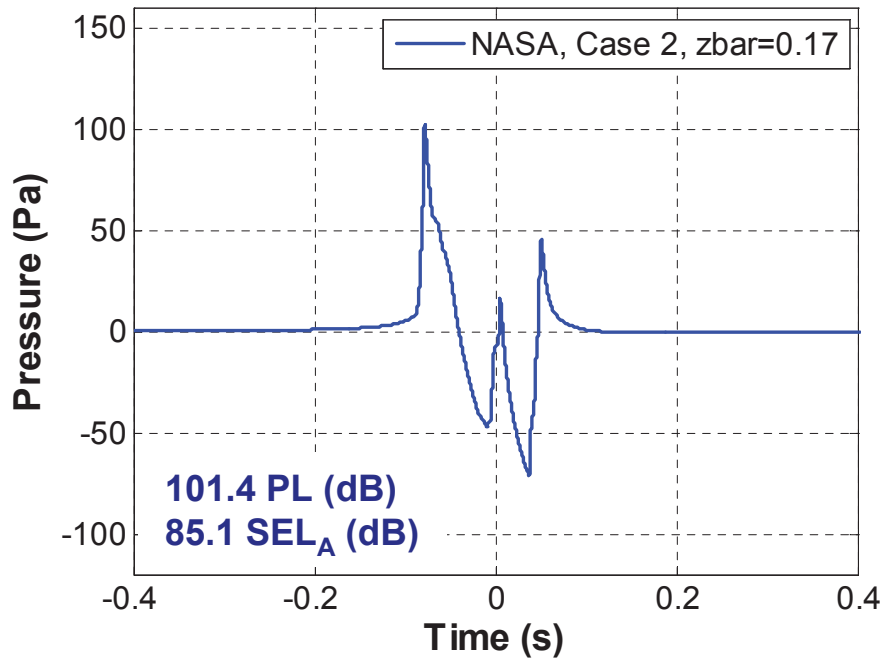


Figure 11-27. Time history corresponding to the peak overpressure ( $\bar{z} = 0.17$ ) for NASA Case 2, 35,821 ft, Mach 1.175,  $\dot{m} = 0.00138$ .

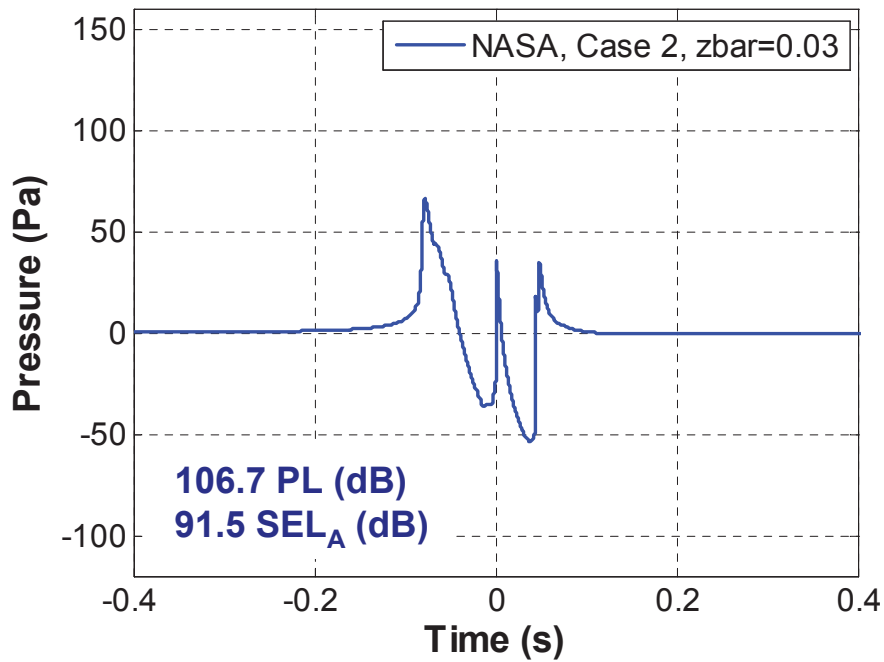


Figure 11-28. Time history corresponding to the highest perceived level (PL) ( $\bar{z} = 0.03$ ) for NASA Case 2, 35,821 ft, Mach 1.175,  $\dot{m} = 0.00138$ .

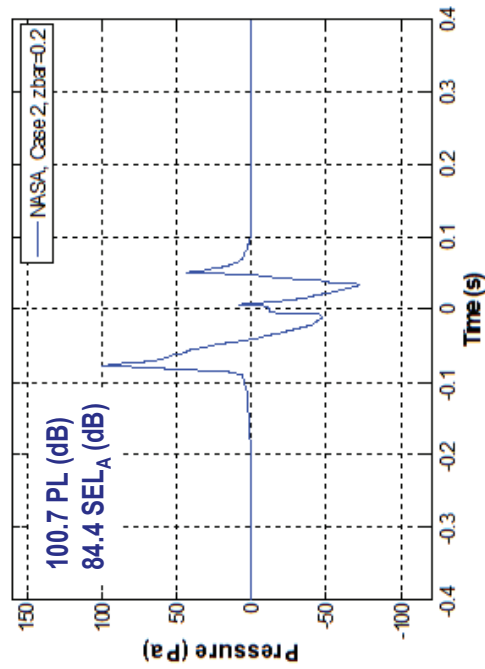
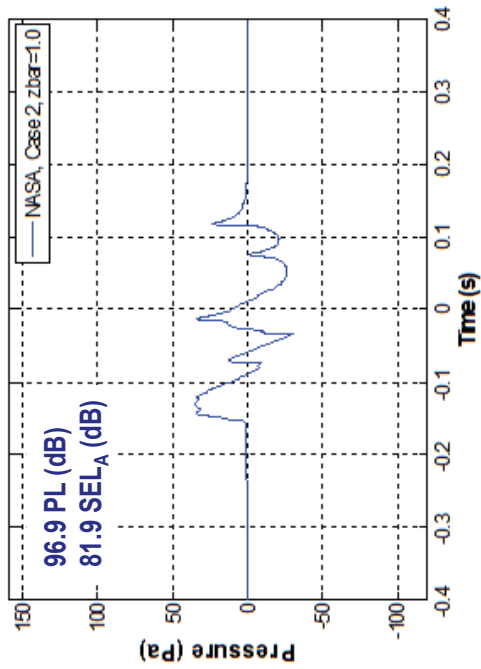
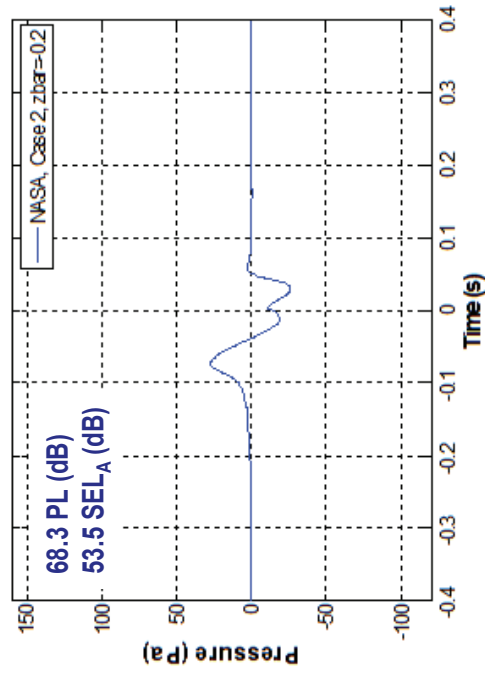
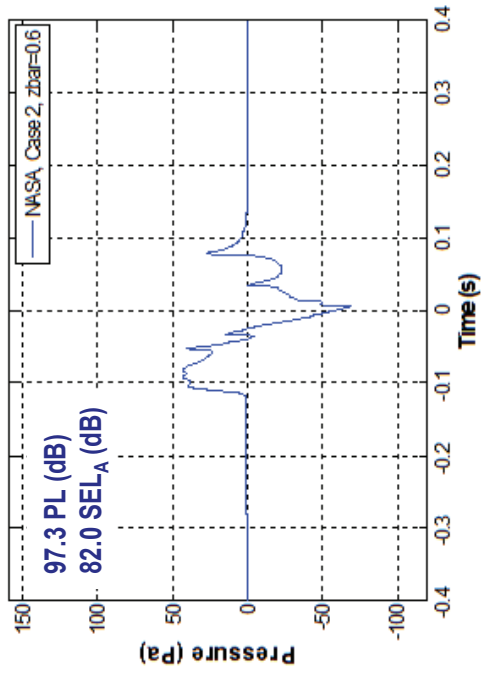


Figure 11-29. Time histories for NASA Case 2, 35,821 ft, Mach 1.175,  $\dot{m} = 0.00138$  at four different  $\bar{z}$  locations – a)  $\bar{z} = 1.0$ , b)  $\bar{z} = 0.6$ , c)  $\bar{z} = 0.2$ , and d)  $\bar{z} = -0.2$ .

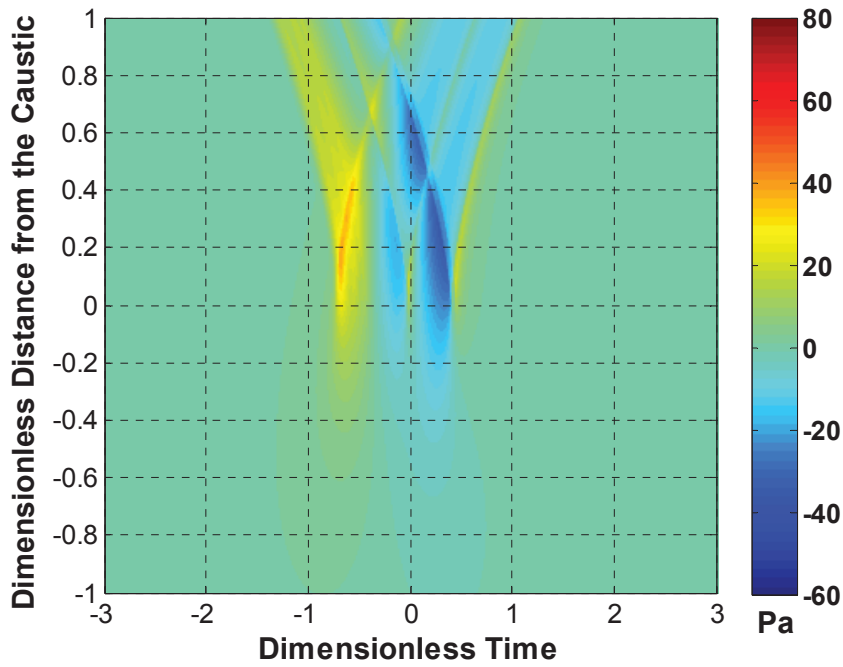


Figure 11-30. Pressure field contour for NASA Case 3, 38,154 ft, Mach 1.169,  $\dot{m} = 0.00103$ .

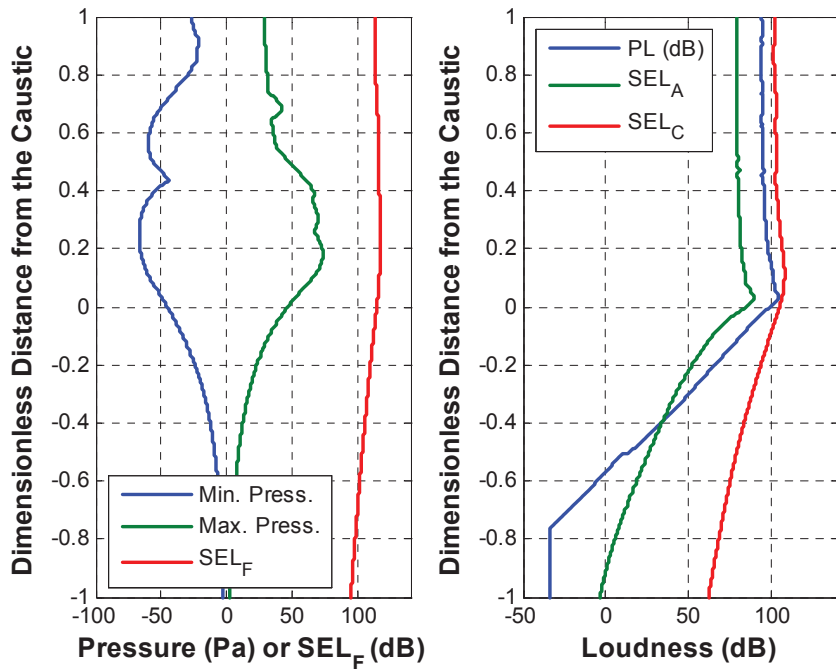


Figure 11-31. Metrics plots for NASA Case 3, 38,154 ft, Mach 1.169,  $\dot{m} = 0.00103$ .

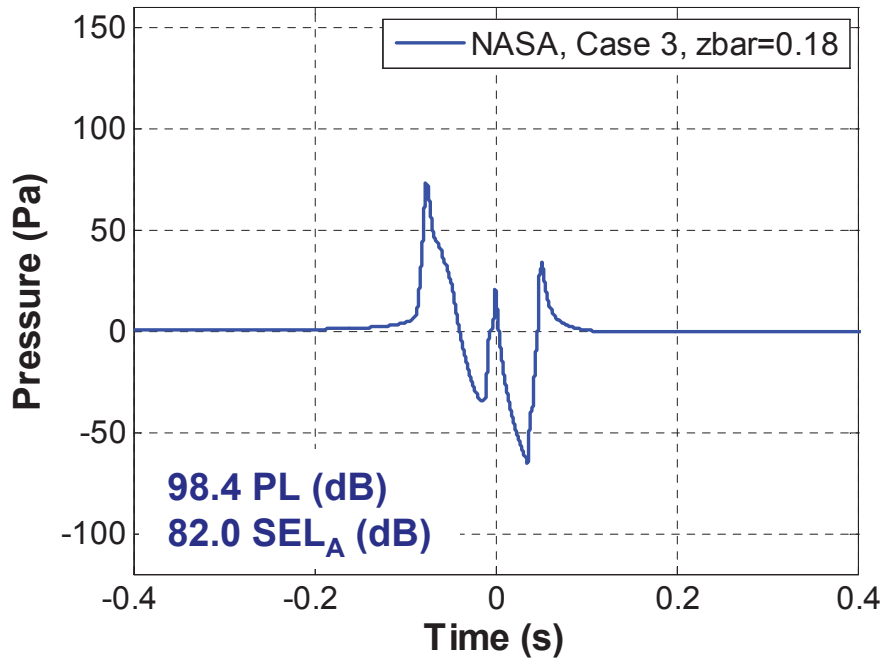


Figure 11-32. Time history corresponding to the peak overpressure ( $\bar{z}=0.18$ ) for NASA Case 3, 38,154 ft, Mach 1.169,  $\dot{m} = 0.00103$ .

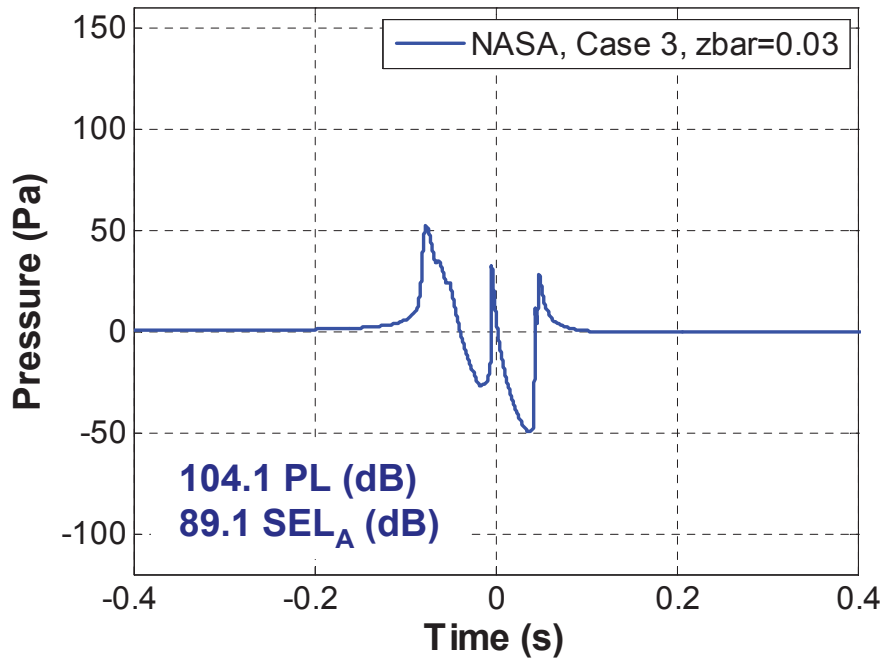


Figure 11-33. Time history corresponding to the highest PL ( $\bar{z}=0.03$ ) for NASA Case 3, 38,154 ft, Mach 1.169,  $\dot{m} = 0.00103$ .

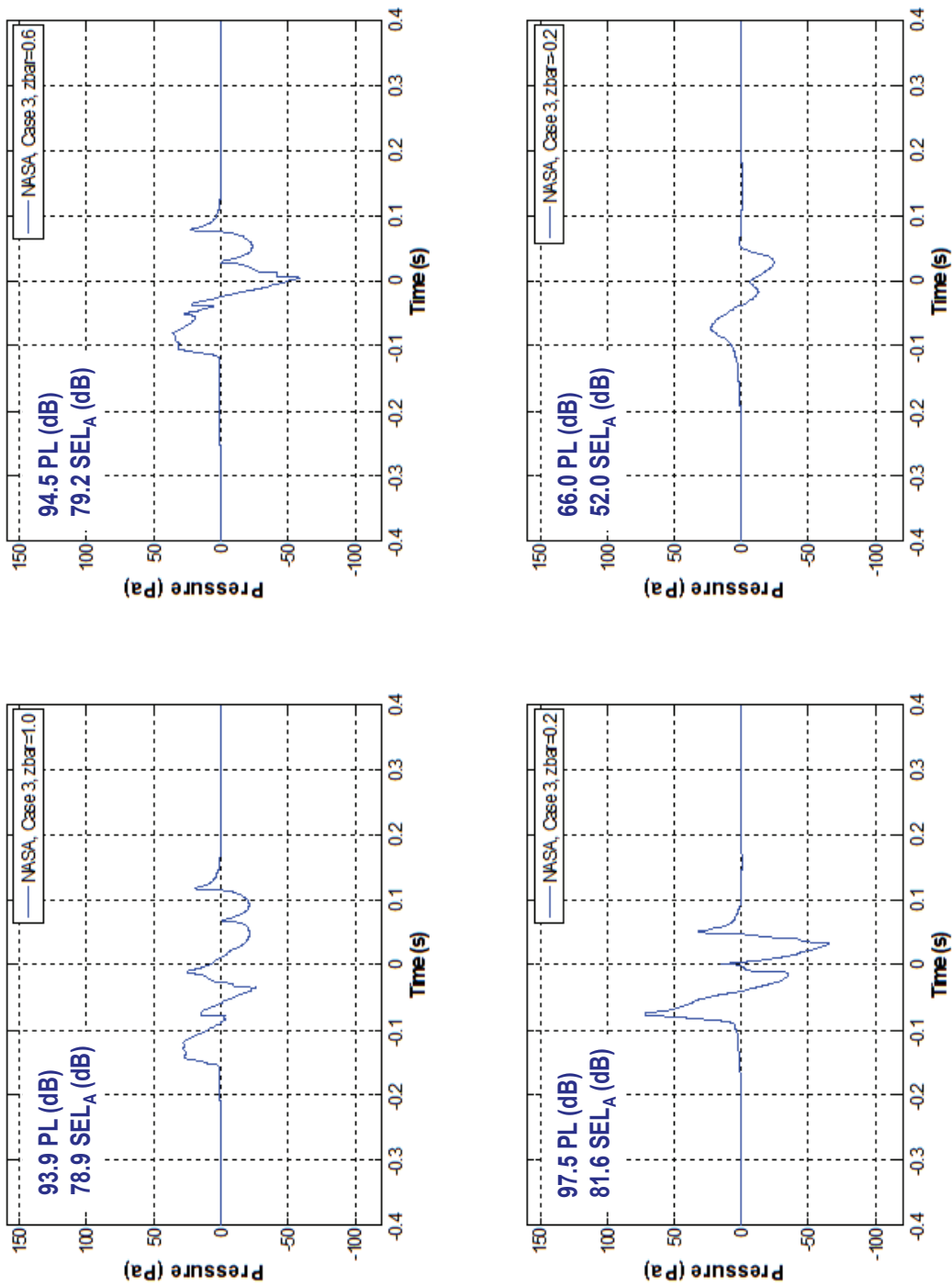


Figure 11-34. Time histories for NASA Case 3, 38,154 ft, Mach 1.169,  $\dot{m} = 0.00103$  at four different  $\bar{z}$  locations – a)  $\bar{z} = 1.0$ , b)  $\bar{z} = 0.6$ , c)  $\bar{z} = 0.2$ , and d)  $\bar{z} = -0.2$ .

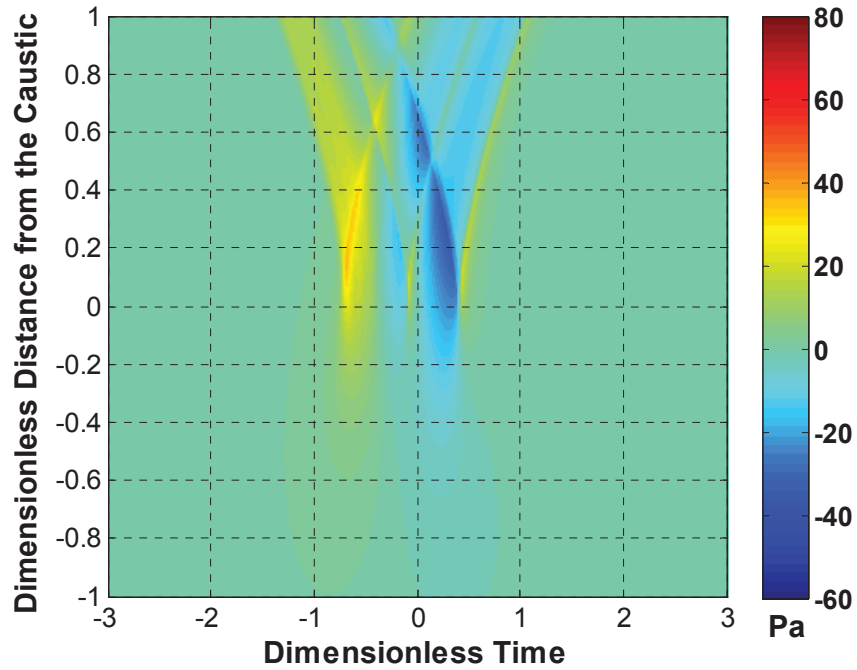


Figure 11-35. Pressure field contour for NASA Case 4, 40,525 ft, Mach 1.161,  $\dot{m} = 0.00066$ .

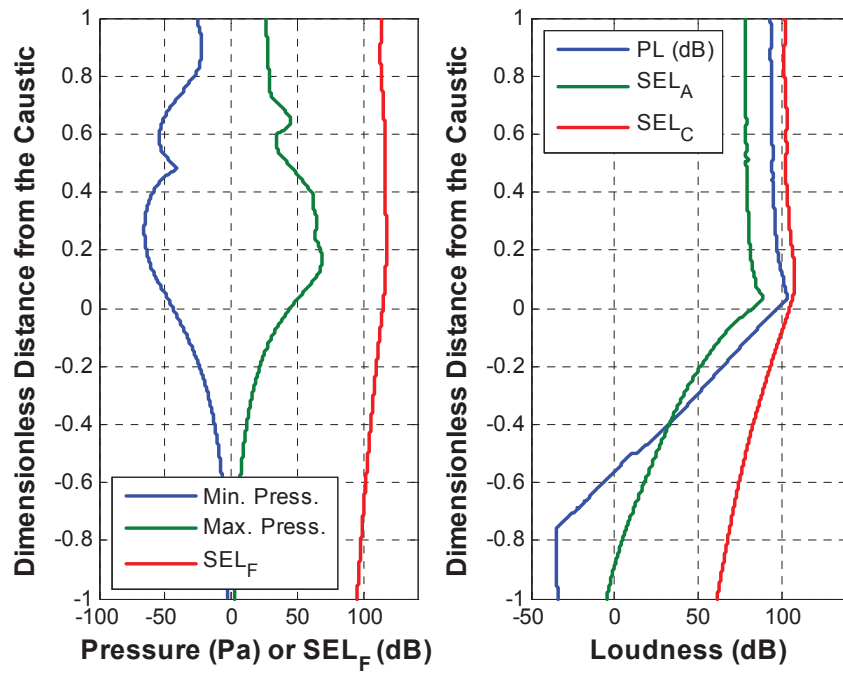


Figure 11-36. Metrics plots for NASA Case 4, 40,525 ft, Mach 1.161,  $\dot{m} = 0.00066$ .

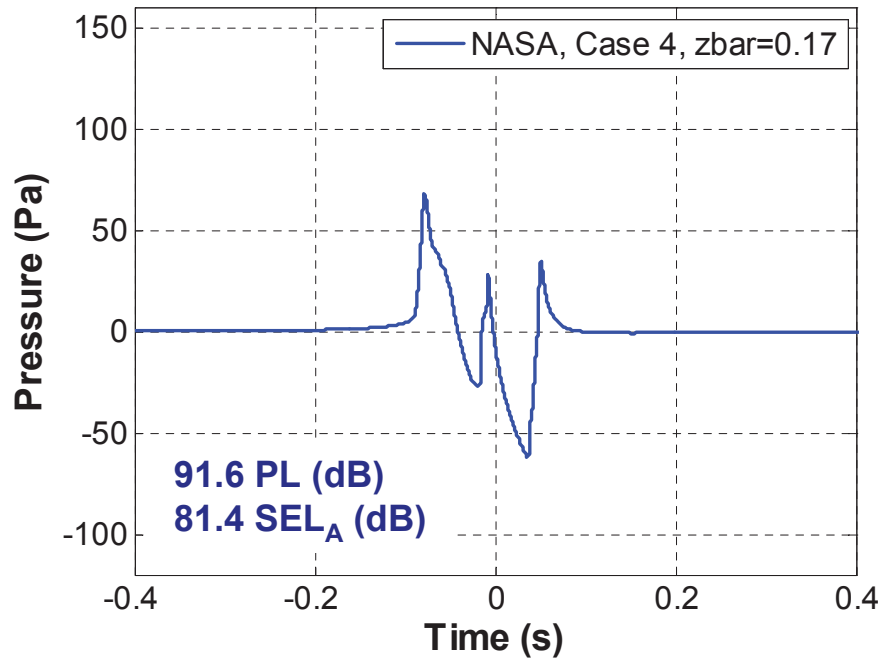


Figure 11-37. Time history corresponding to the peak overpressure ( $\bar{z}=0.17$ ) for NASA Case 4, 40,525 ft, Mach 1.161,  $\dot{m}=0.00066$ .

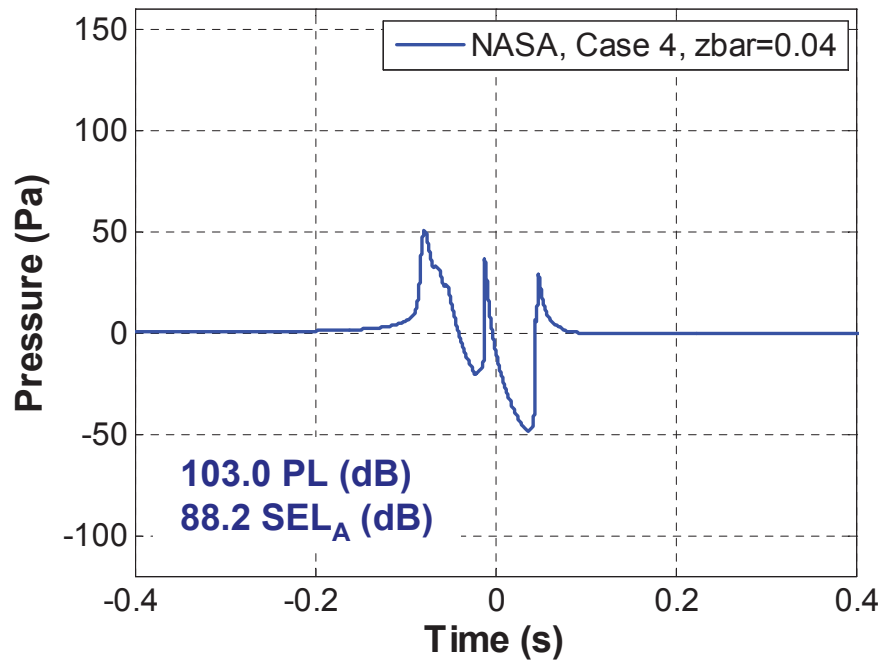


Figure 11-38. Time history corresponding to the highest PL ( $\bar{z}=0.04$ ) for NASA Case 4, 40,525 ft, Mach 1.161,  $\dot{m}=0.00066$ .



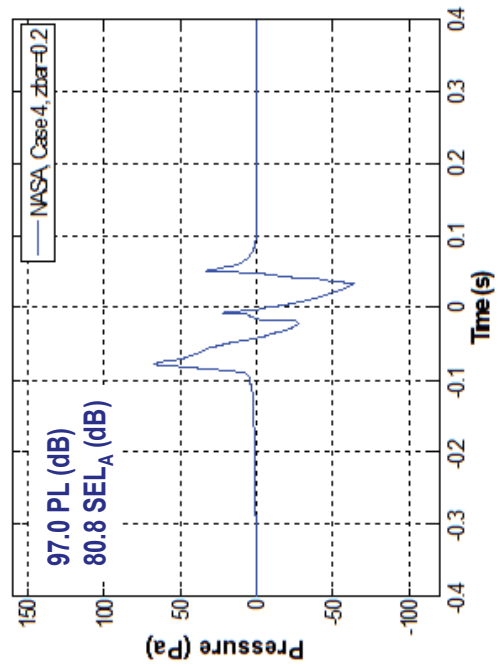
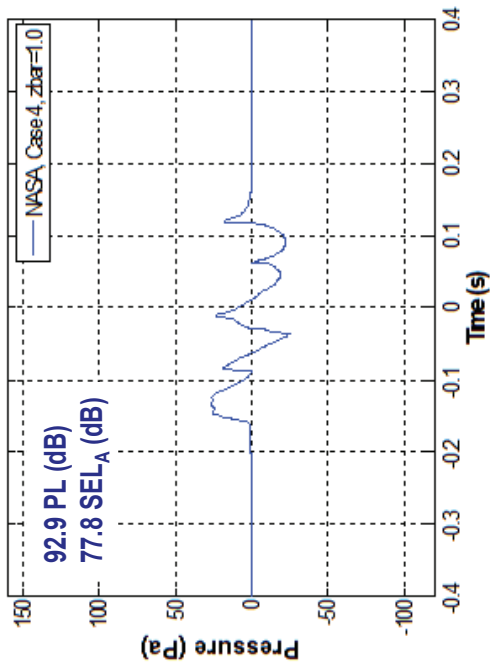
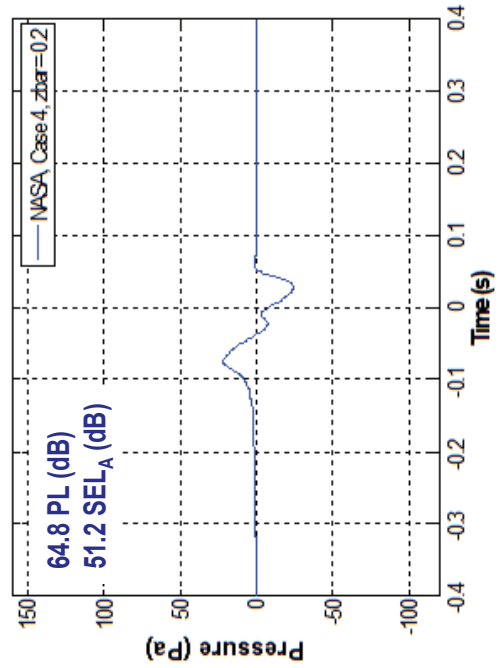
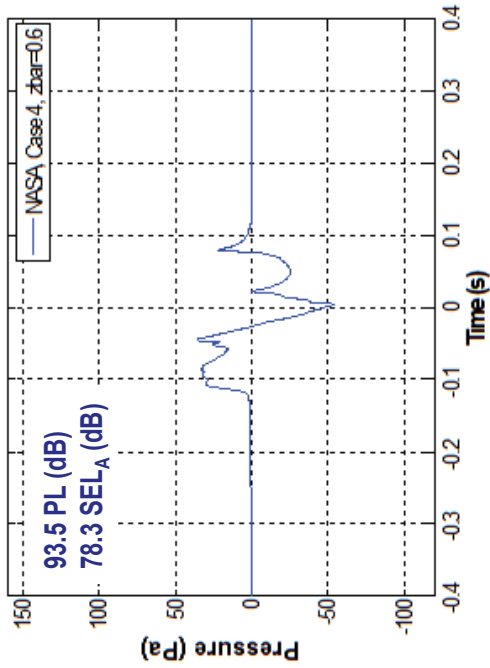


Figure 11-39. Time histories for NASA Case 4, 40,525 ft, Mach 1.161,  $\dot{m} = 0.00066$  at four different  $\bar{z}$  locations – a)  $\bar{z} = 1.0$ , b)  $\bar{z} = 0.6$ , c)  $\bar{z} = 0.2$ , and d)  $\bar{z} = -0.2$ .

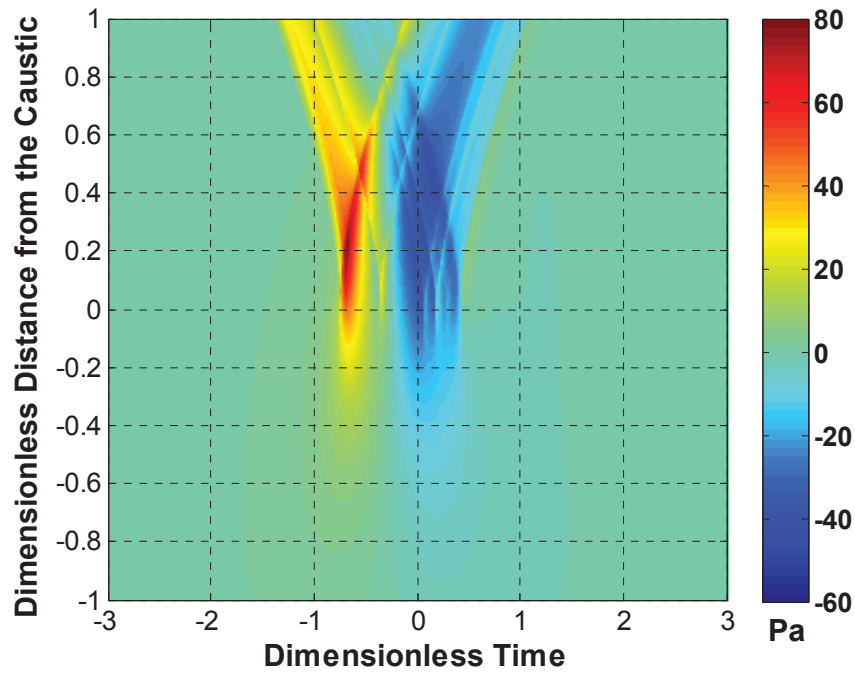


Figure 11-40. Pressure field contour for Boeing Case 1, 40,000 ft, Mach 1.156,  $\dot{m} = 0.00036$ .

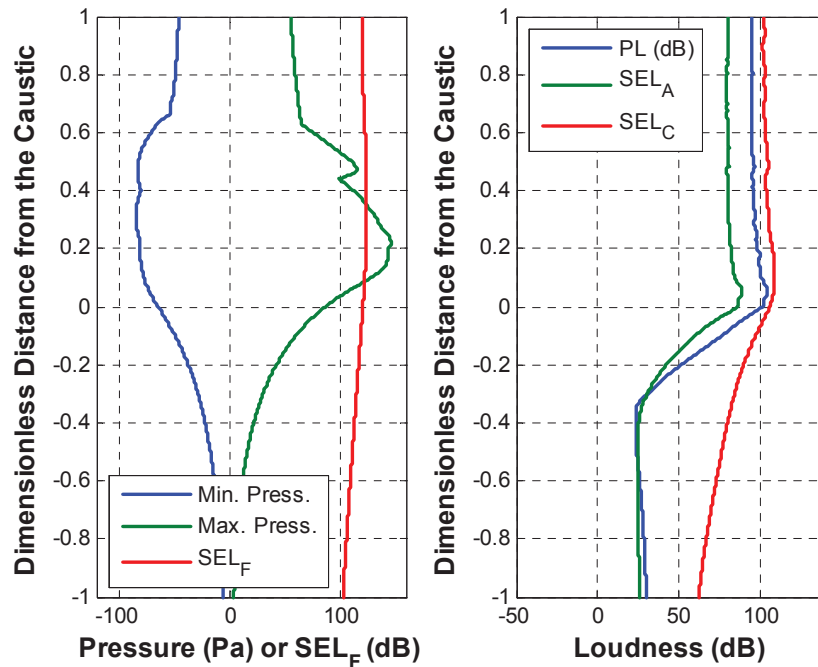


Figure 11-41. Metrics plots for Boeing Case 1, 40,000 ft, Mach 1.156,  $\dot{m} = 0.00036$ .

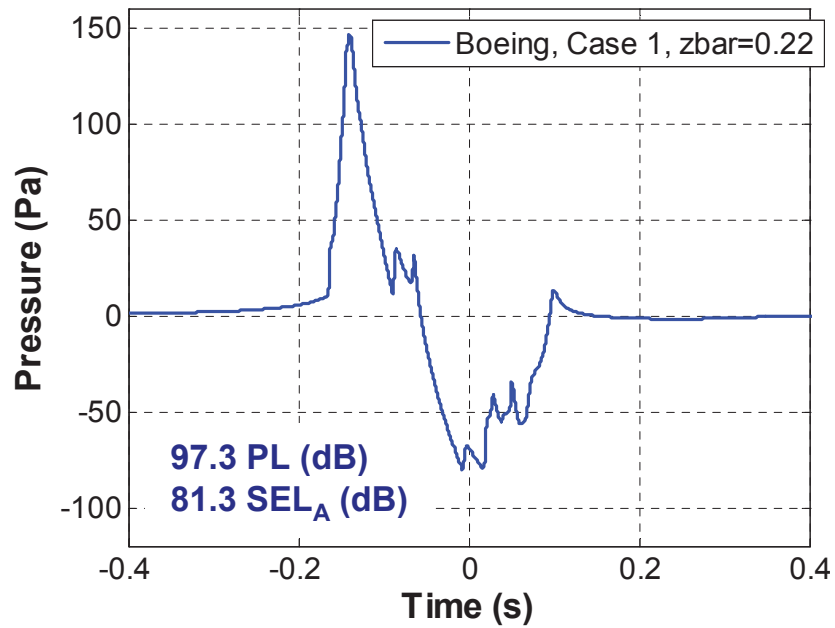


Figure 11-42. Time history corresponding to the peak overpressure ( $\bar{z}=0.22$ ) for Boeing Case 1, 40,000 ft, Mach 1.156,  $\dot{m} = 0.00036$ .

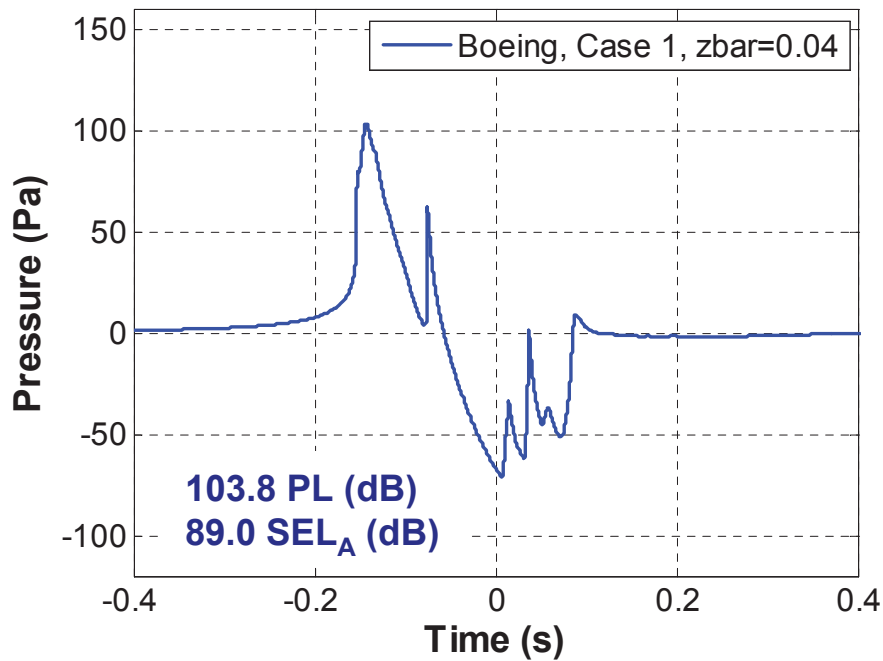


Figure 11-43. Time history corresponding to the highest PL ( $\bar{z}=0.04$ ) for Boeing Case 1, 40,000 ft, Mach 1.156,  $\dot{m} = 0.00036$ .

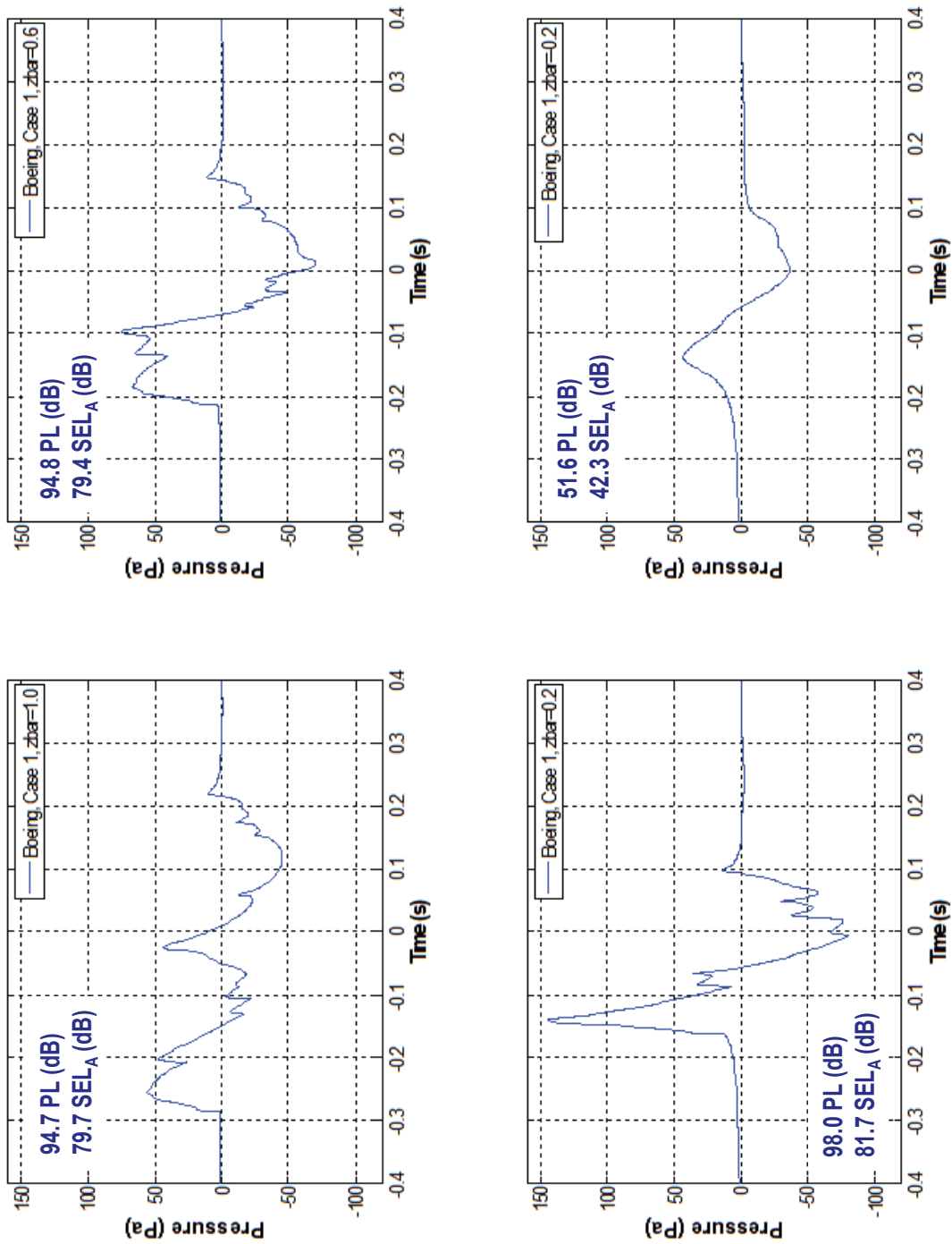


Figure 11-44. Time histories for Boeing Case 1, 40,000 ft, Mach 1.156,  $\text{mdot} = 0.00036$  at four different  $\bar{z}$  locations – a)  $\bar{z} = 1.0$ , b)  $\bar{z} = 0.6$ , c)  $\bar{z} = 0.2$ , and d)  $\bar{z} = -0.2$ .

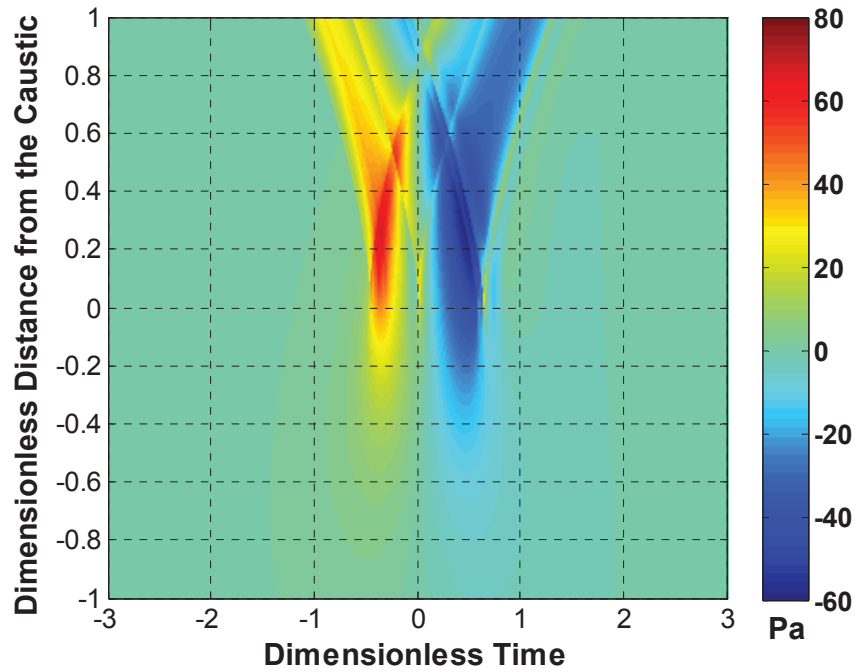


Figure 11-45. Pressure field contour for Boeing Case 2, 38,498 ft, Mach 1.23,  $\dot{m} = 0.00316$ .

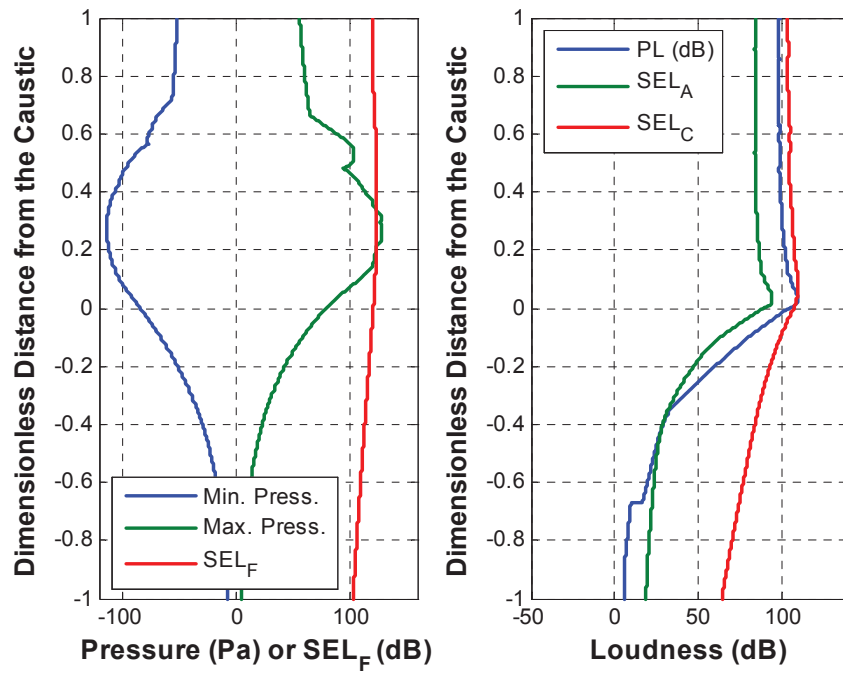


Figure 11-46. Metrics plots for Boeing Case 2, 38,498 ft, Mach 1.23,  $\dot{m} = 0.00316$ .

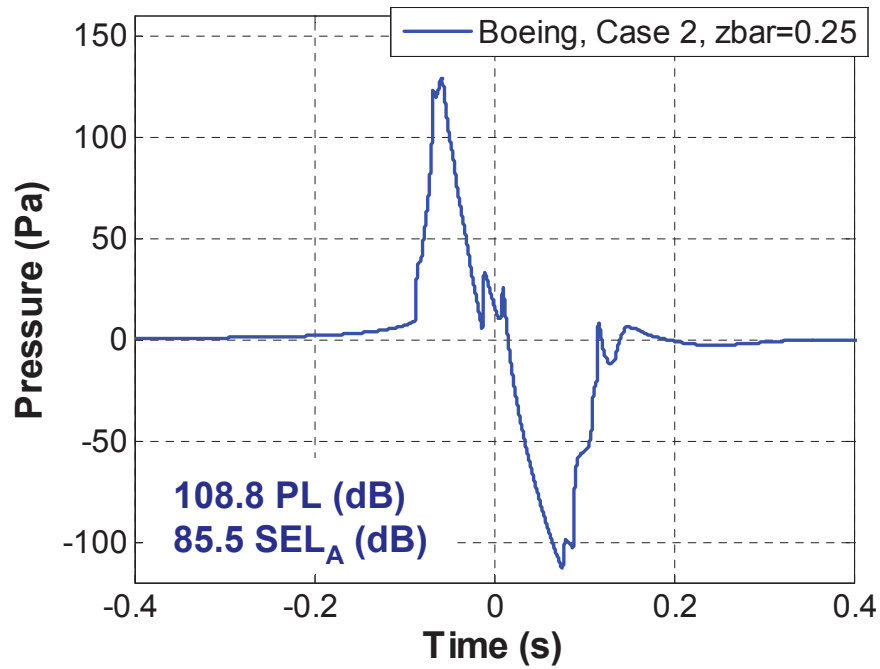


Figure 11-47. Time history corresponding to the peak overpressure ( $\bar{z}=0.25$ ) for Boeing Case 2, 38,498 ft, Mach 1.23,  $\dot{m}d_0 = 0.00316$ .

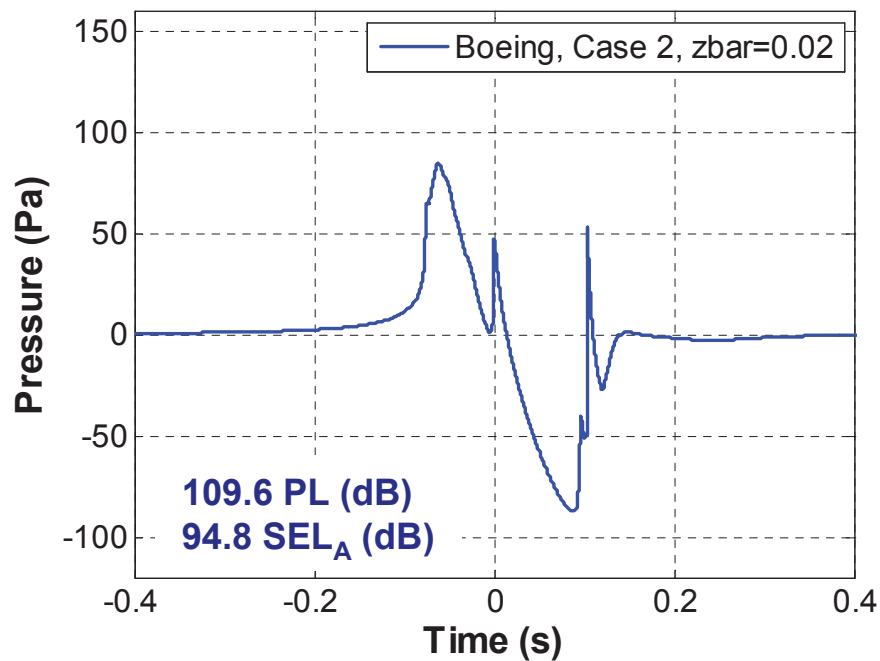


Figure 11-48. Time history corresponding to the highest PL ( $\bar{z}=0.02$ ) for Boeing Case 2, 38,498 ft, Mach 1.23,  $\dot{m}d_0 = 0.00316$ .

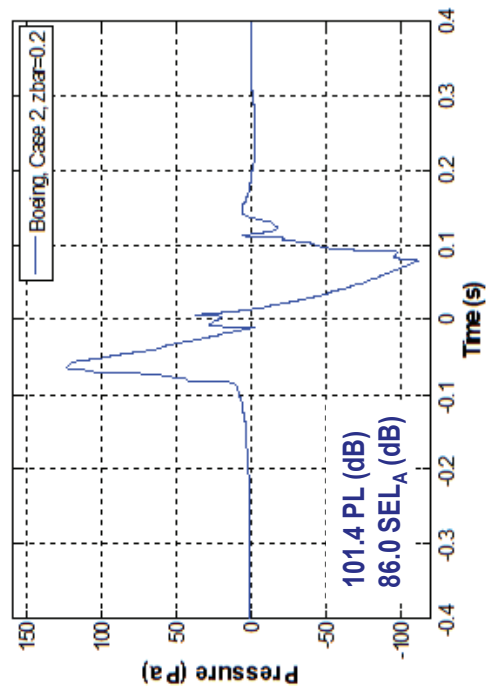
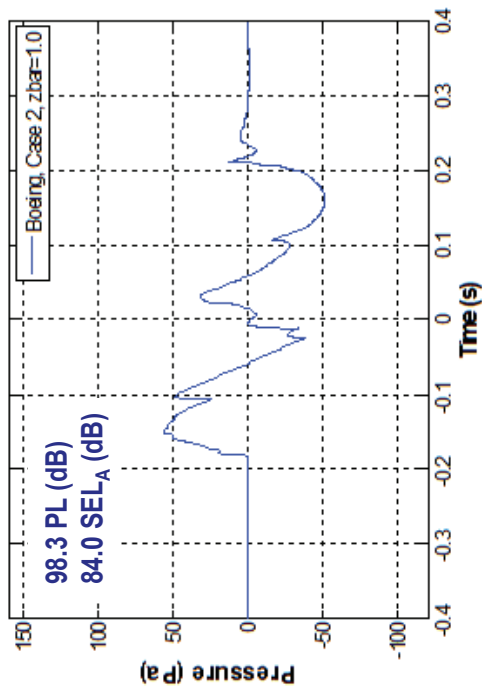
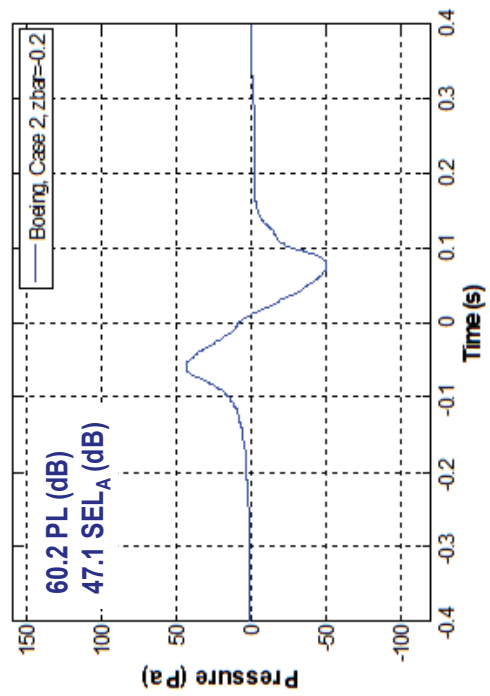
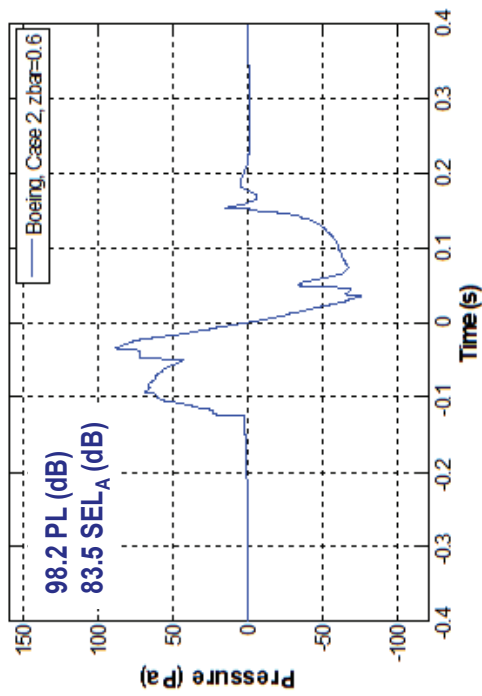


Figure 11-49. Time histories for Boeing Case 2, 38,498 ft, Mach 1.23,  $\dot{m} = 0.00316$  at four different  $\bar{z}$  locations – a)  $\bar{z} = 1.0$ , b)  $\bar{z} = 0.6$ , c)  $\bar{z} = 0.2$ , and d)  $\bar{z} = -0.2$ .

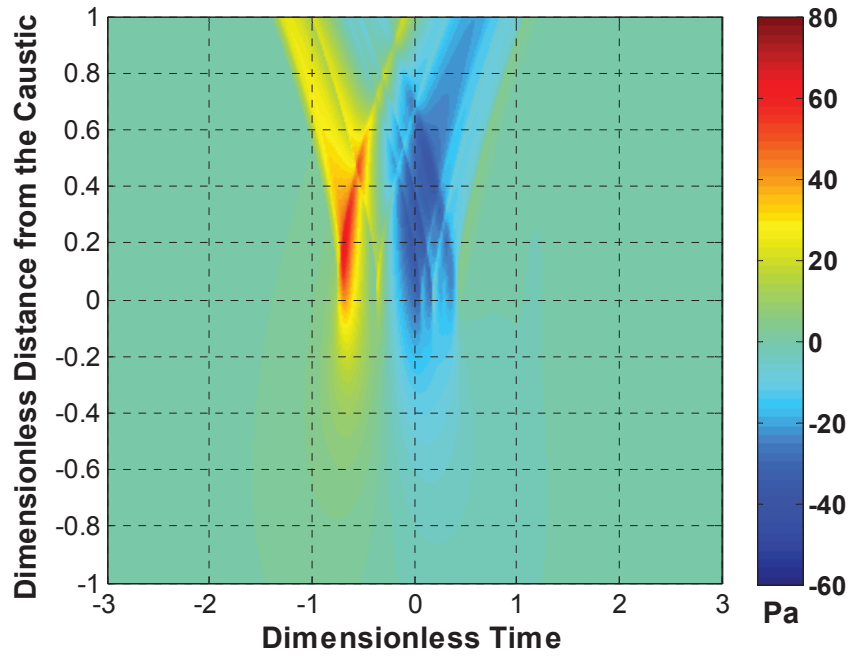


Figure 11-50. Pressure field contour for Boeing Case 3, 45,000 ft, Mach 1.153,  $\dot{m} = 0.0001$ .

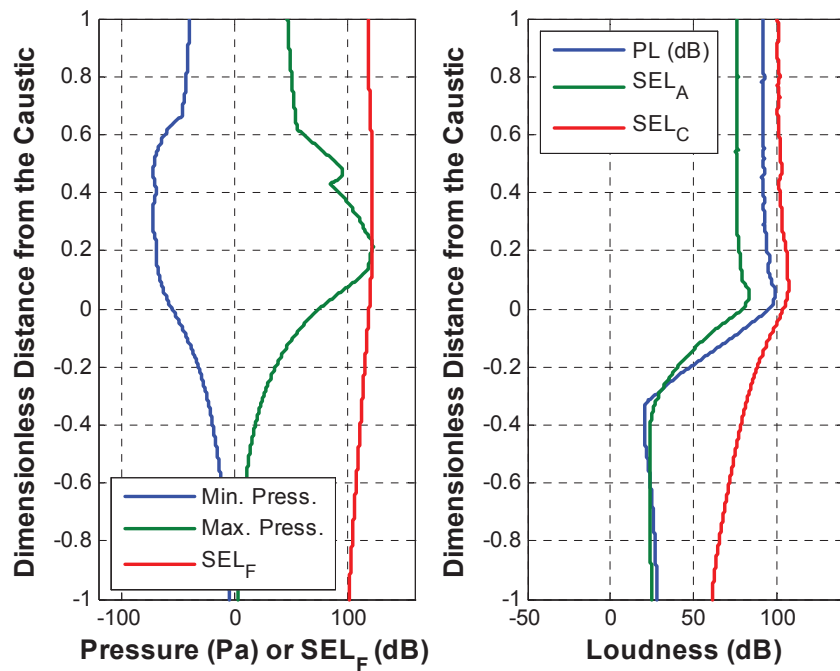


Figure 11-51. Metrics plots for Boeing Case 3, 45,000 ft, Mach 1.153,  $\dot{m} = 0.0001$ .



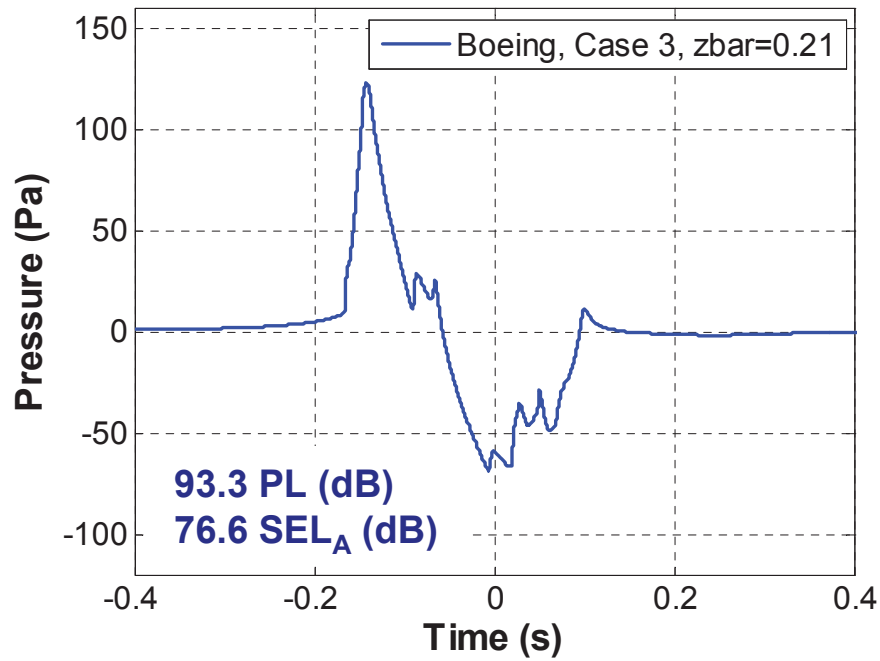


Figure 11-52. Time history corresponding to the peak overpressure ( $\bar{z}=0.21$ ) for Boeing Case 3, 45,000 ft, Mach 1.153,  $\text{mdot} = 0.0001$ .

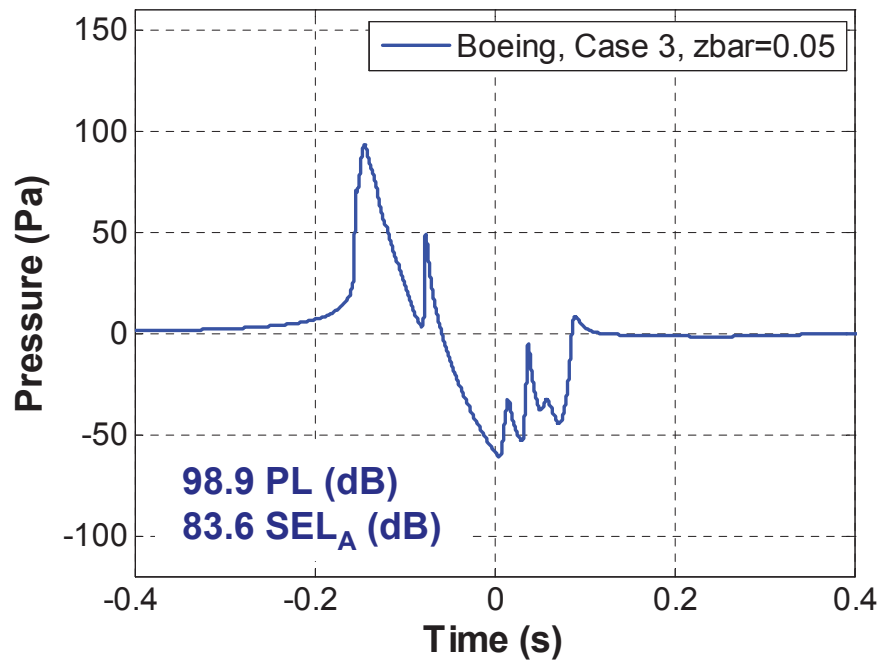


Figure 11-53. Time history corresponding to the highest PL ( $\bar{z}=0.05$ ) for Boeing Case 3, 45,000 ft, Mach 1.153,  $\text{mdot} = 0.0001$ .

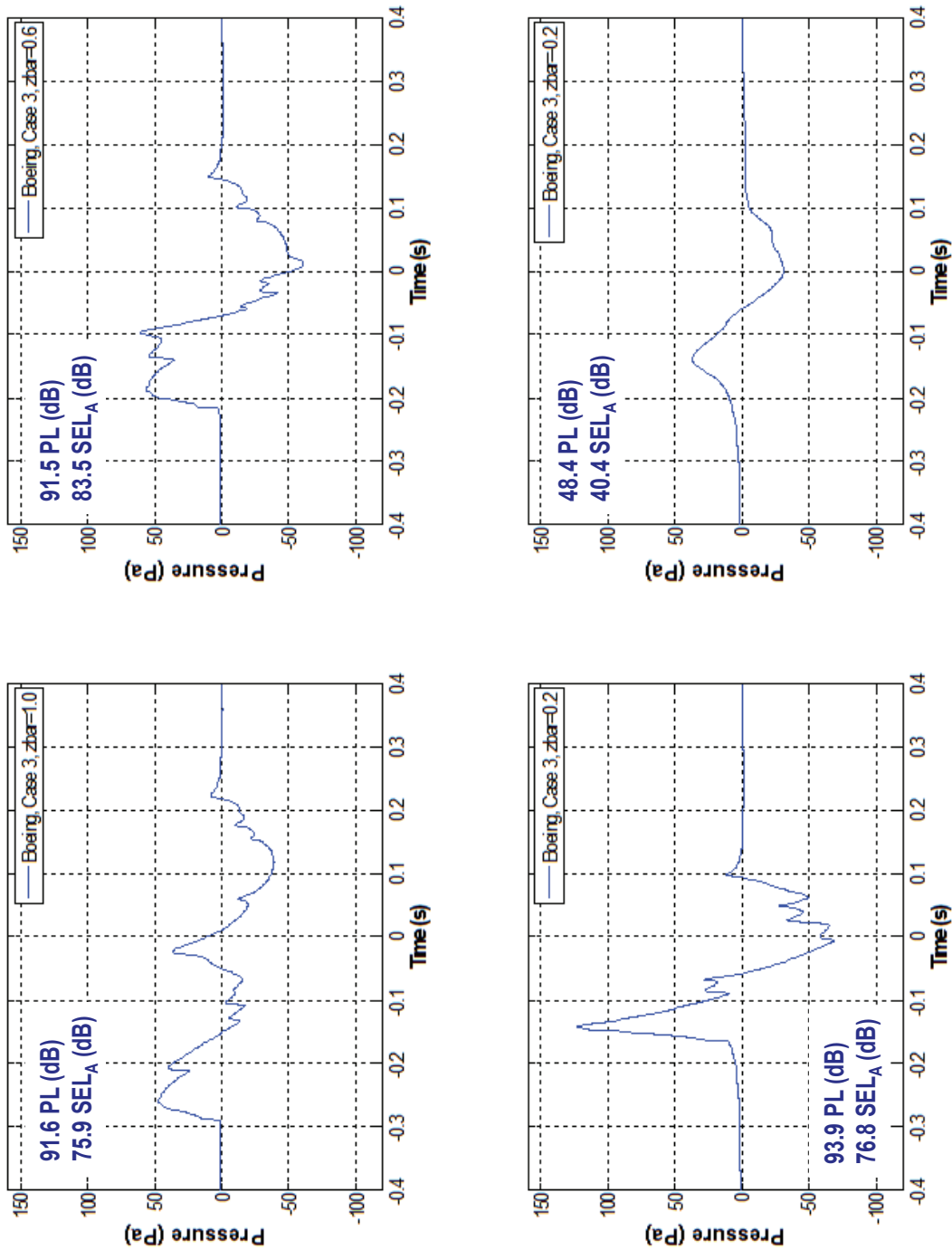


Figure 11-54. Time histories for Boeing Case 3, 45,000 ft, Mach 1.153,  $\text{mdot} = 0.0001$  at four different  $\bar{z}$  locations – a)  $\bar{z} = 1.0$ , b)  $\bar{z} = 0.6$ , c)  $\bar{z} = 0.2$ , and d)  $\bar{z} = -0.2$ .

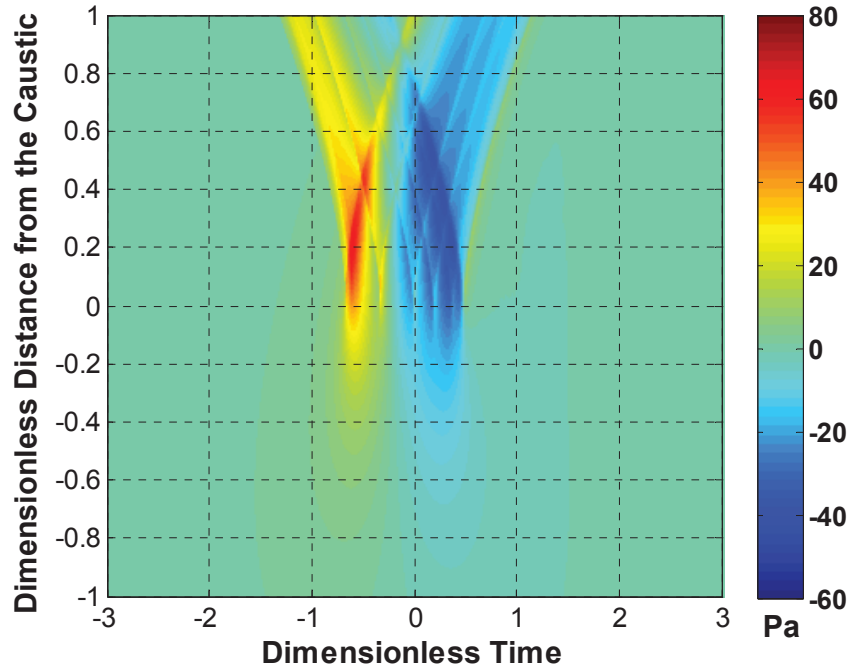


Figure 11-55. Pressure field contour for Boeing Case 4, 45,000 ft, Mach 1.17,  $m\dot{d}ot = 0.00111$ .

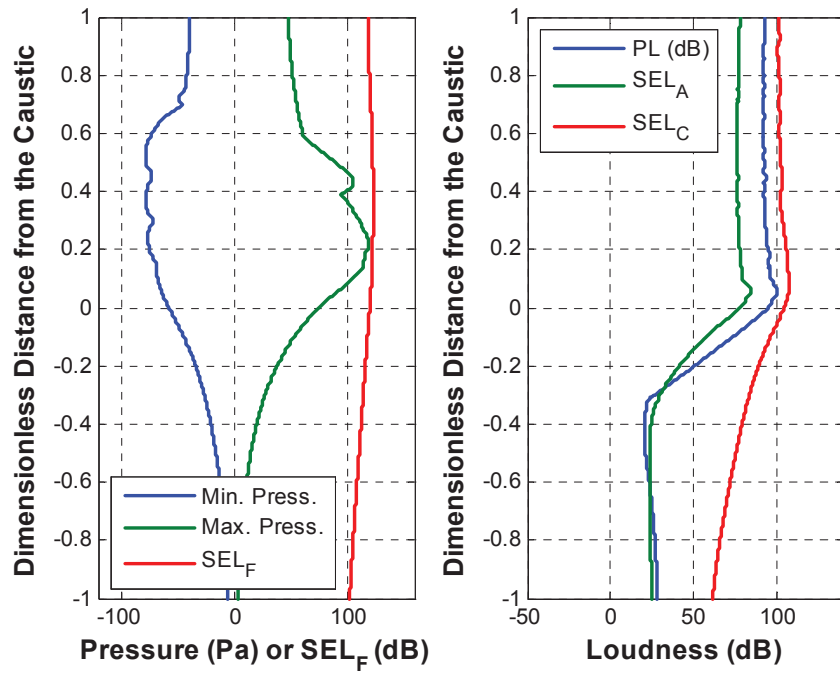


Figure 11-56. Metrics plots for Boeing Case 4, 45,000 ft, Mach 1.17,  $m\dot{d}ot = 0.00111$ .

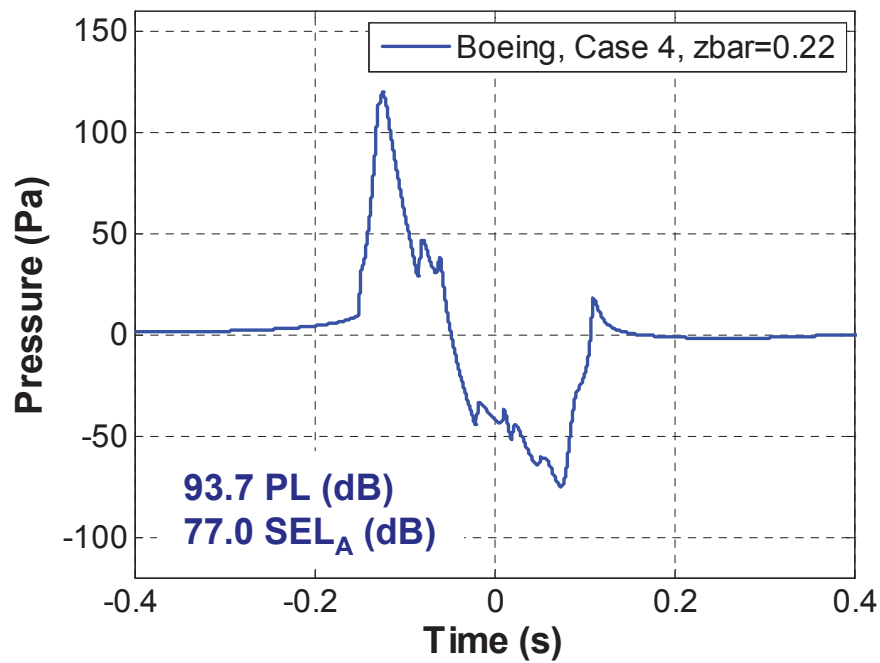


Figure 11-57. Time history corresponding to the peak overpressure ( $\bar{z} = 0.22$ ) for Boeing Case 4, 45,000 ft, Mach 1.17,  $\dot{m} = 0.00111$ .

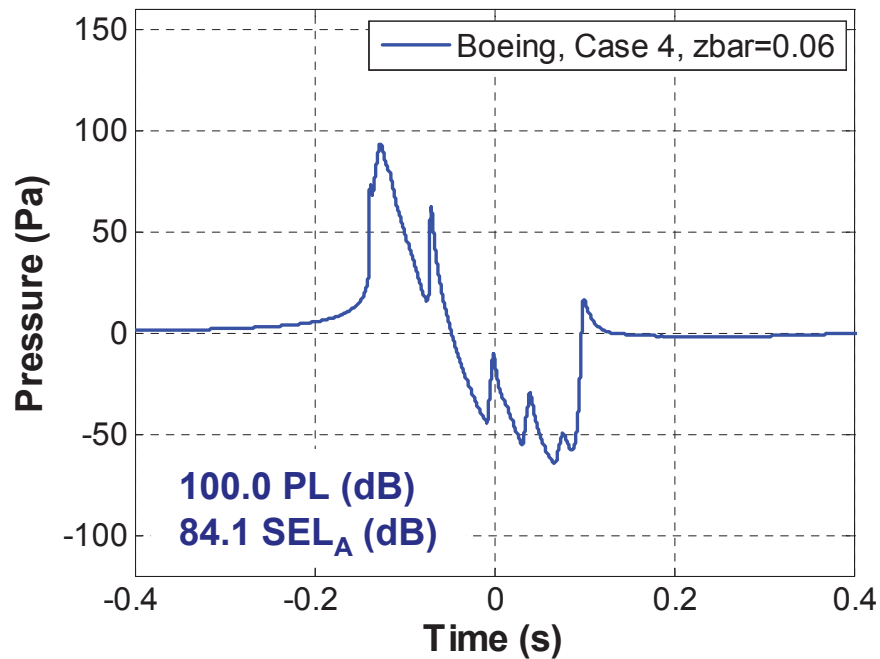


Figure 11-58. Time history corresponding to the highest PL ( $\bar{z} = 0.06$ ) for Boeing Case 4, 45,000 ft, Mach 1.17,  $\dot{m} = 0.00111$ .

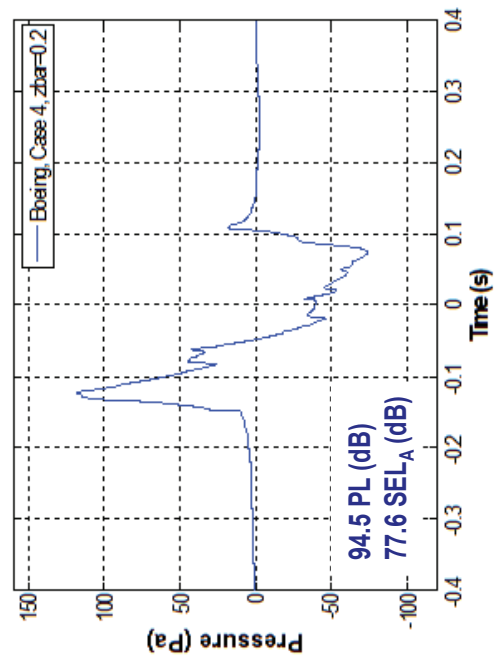
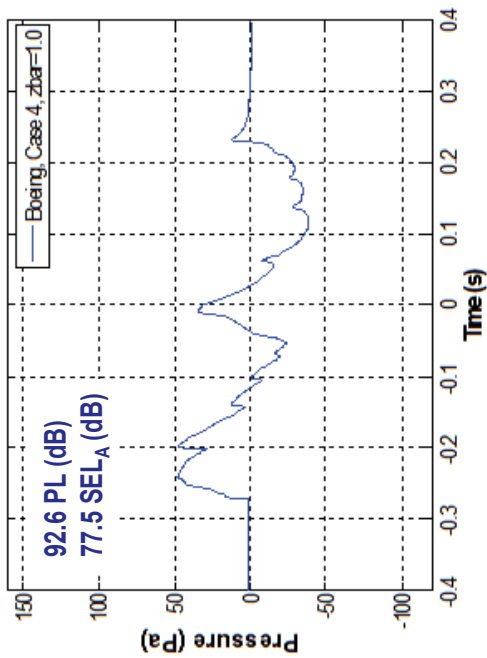
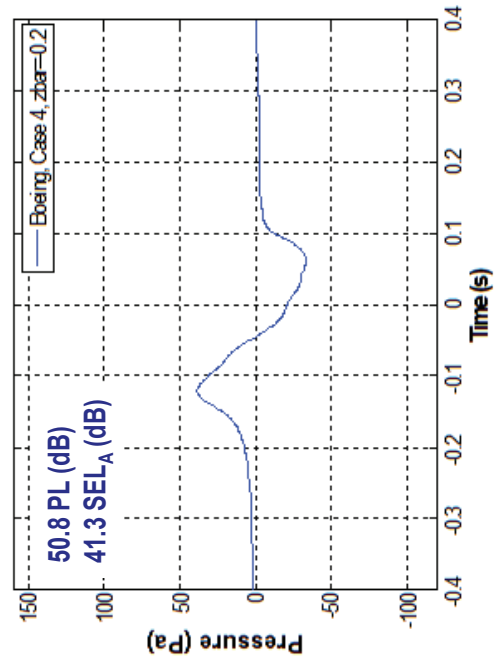
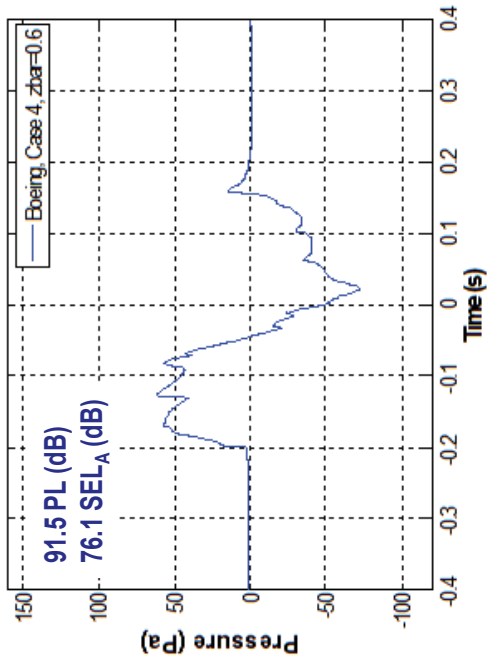


Figure 11-59. Time histories for Boeing Case 4, 45,000 ft, Mach 1.17,  $\dot{m} = 0.00111$  at four different  $\bar{z}$  locations –  
 a)  $\bar{z} = 1.0$ , b)  $\bar{z} = 0.6$ , c)  $\bar{z} = 0.2$ , and d)  $\bar{z} = -0.2$ .

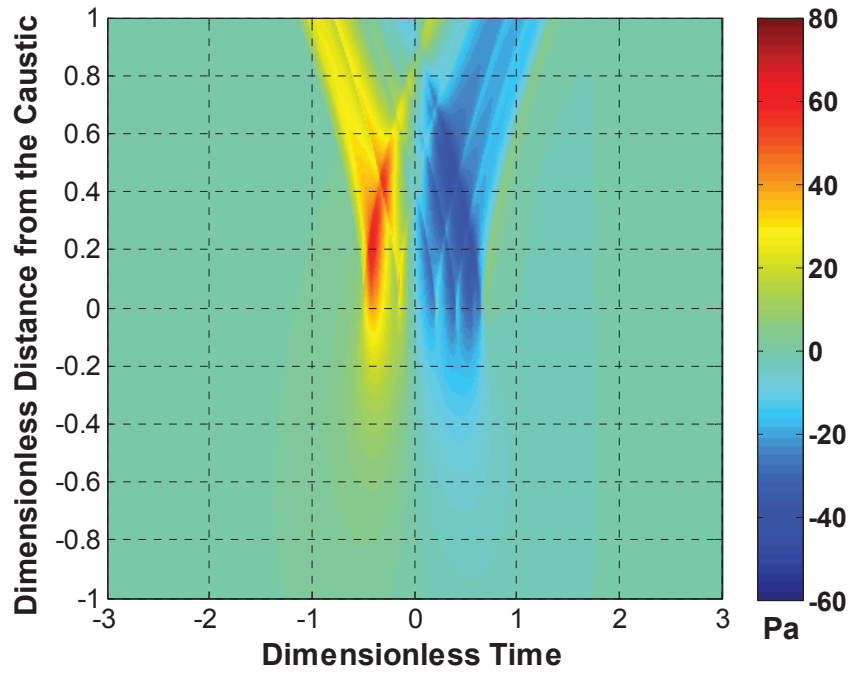


Figure 11-60. Pressure field contour for Boeing Case 5, 45,000 ft, Mach 1.211,  $\dot{m} = 0.00295$ .

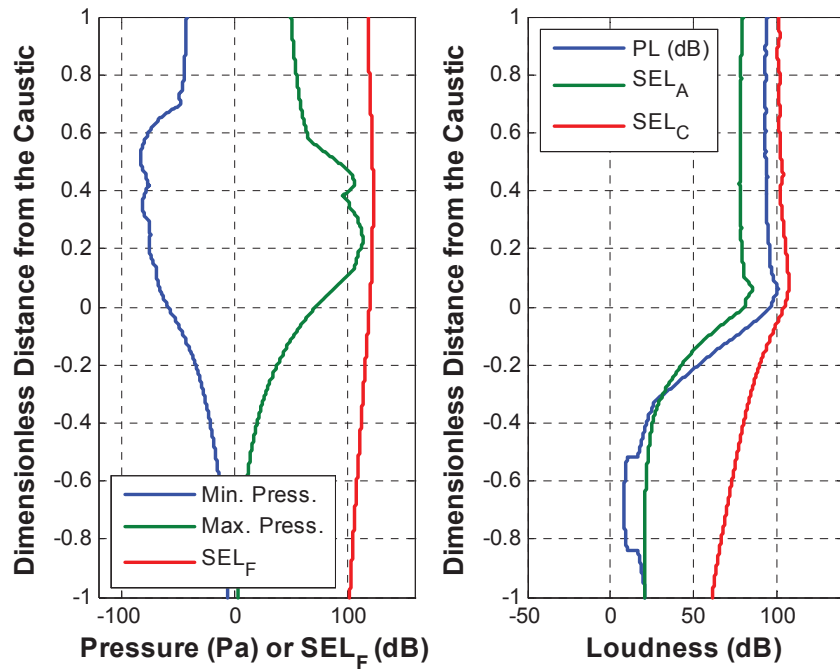


Figure 11-61. Metrics plots for Boeing Case 5, 45,000 ft, Mach 1.211,  $\dot{m} = 0.00295$ .

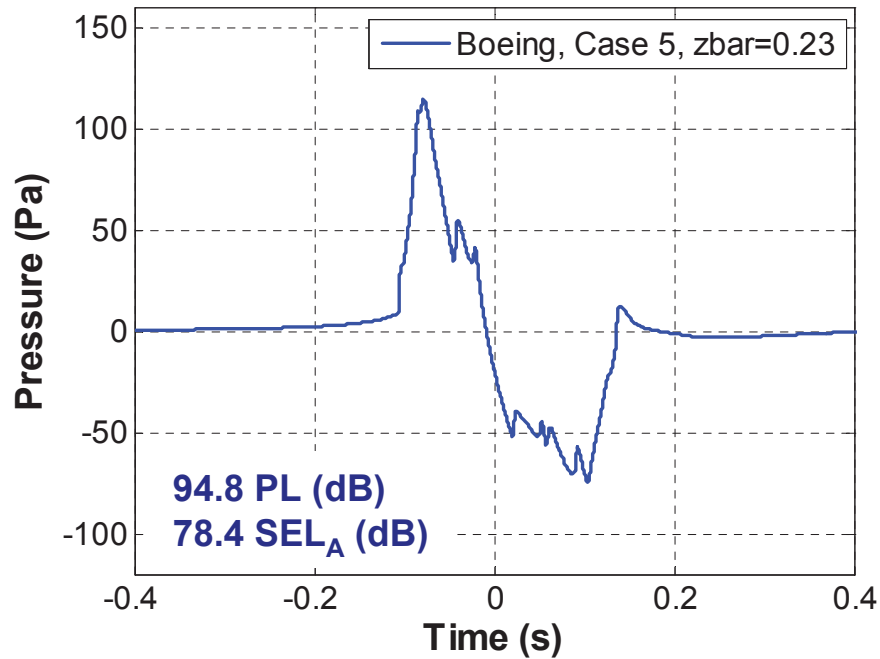


Figure 11-62. Time history corresponding to the peak overpressure ( $\bar{z}=0.23$ ) for Boeing Case 5, 45,000 ft, Mach 1.211,  $\dot{m} = 0.00295$ .

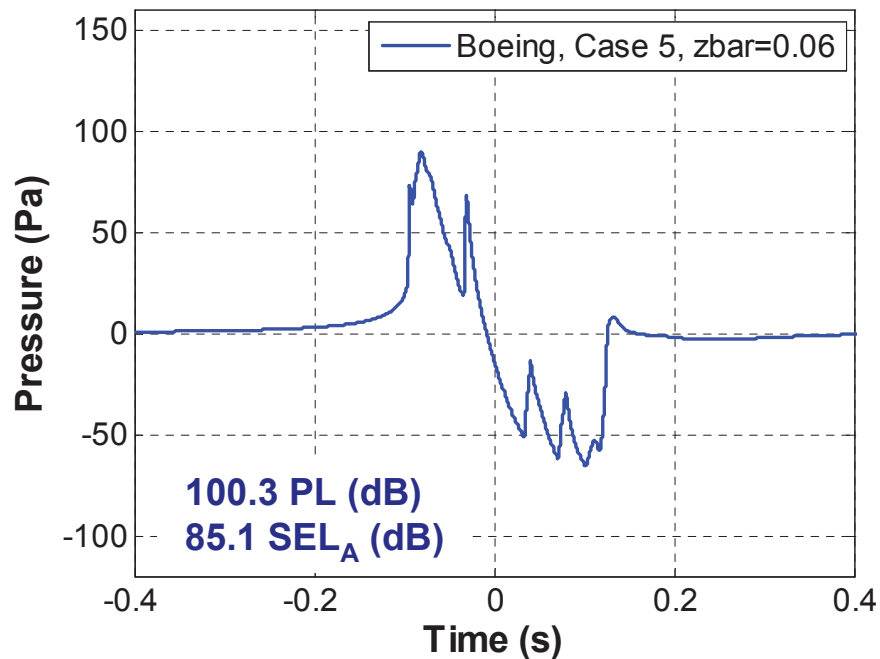


Figure 11-63. Time history corresponding to the highest PL ( $\bar{z}=0.06$ ) for Boeing Case 5, 45,000 ft, Mach 1.211,  $\dot{m} = 0.00295$ .

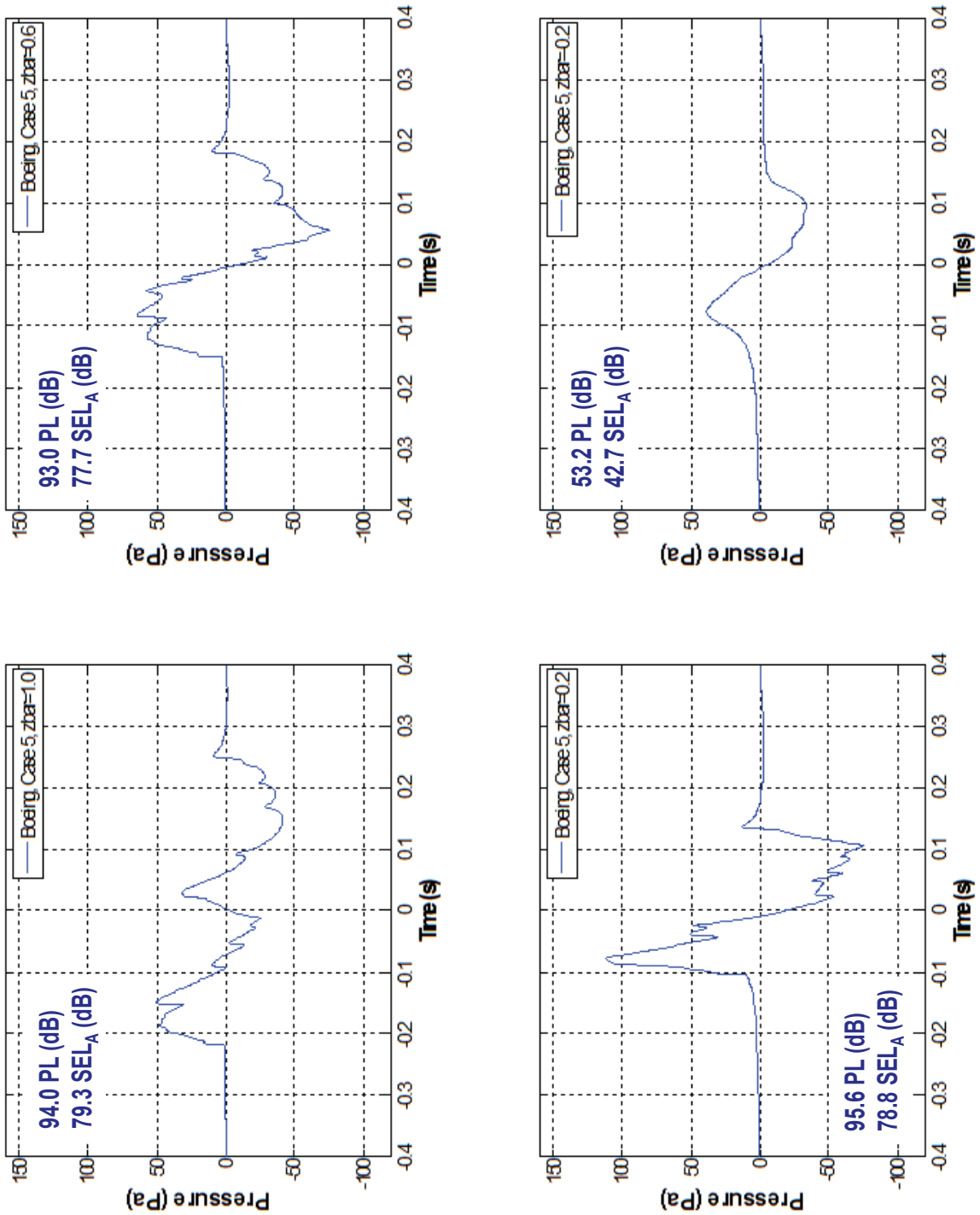


Figure 11-64. Time histories for Boeing Case 5, 45,000 ft, Mach 1.211,  $\dot{m}dt = 0.00295$  at four different  $\bar{z}$  locations – a)  $\bar{z} = 1.0$ , b)  $\bar{z} = 0.6$ , c)  $\bar{z} = 0.2$ , and d)  $\bar{z} = -0.2$ .



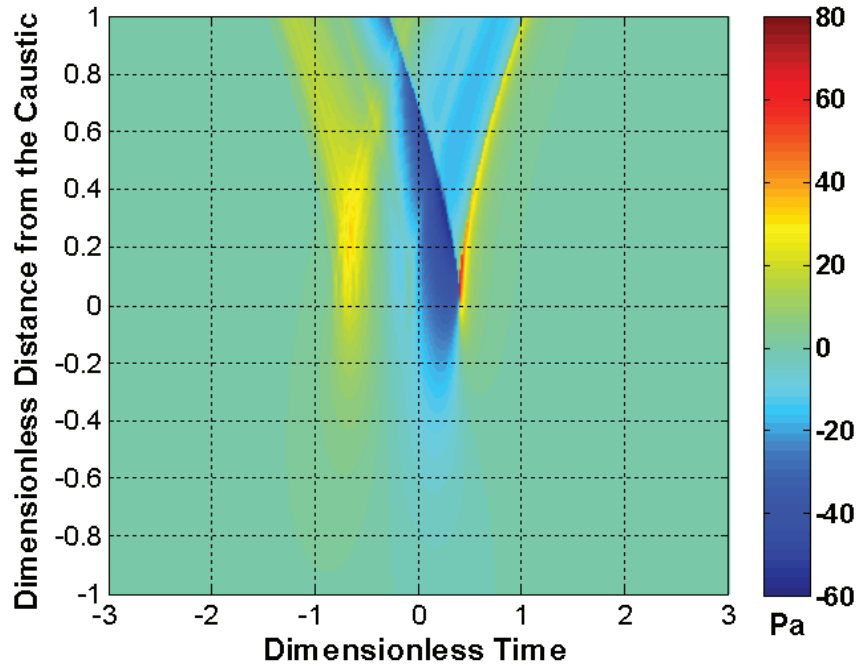


Figure 11-65. Pressure field contour for Gulfstream Case 1, 38,000 ft, Mach 1.182,  $\text{mdot} = 0.0005$ .

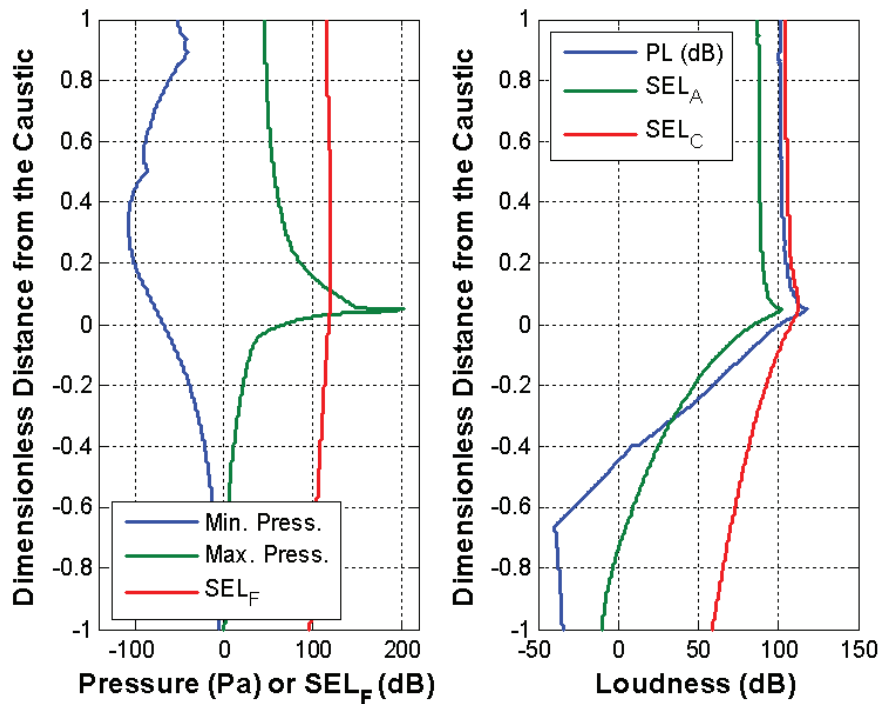


Figure 11-66. Metrics plots for Gulfstream Case 1, 38,000 ft, Mach 1.182,  $\text{mdot} = 0.0005$ .

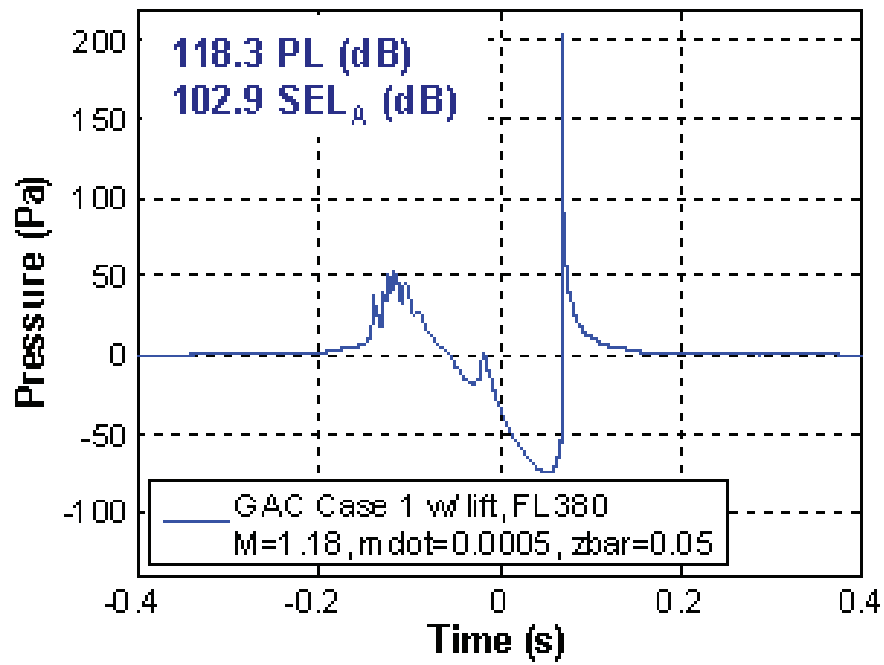


Figure 11-67. Time history corresponding to the peak overpressure ( $\bar{z}=0.05$ ) for Gulfstream Case 1, 38,000 ft, Mach 1.182,  $\dot{m}=0.0005$ .

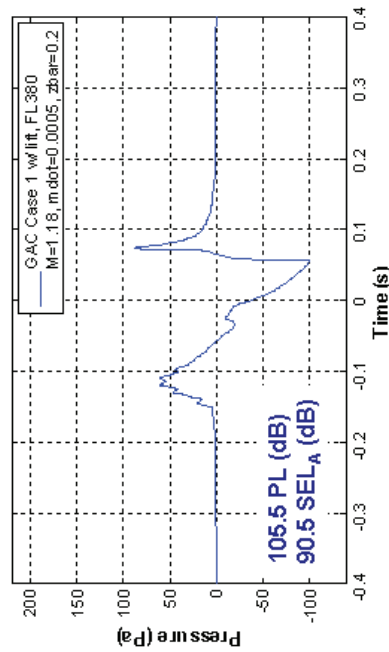
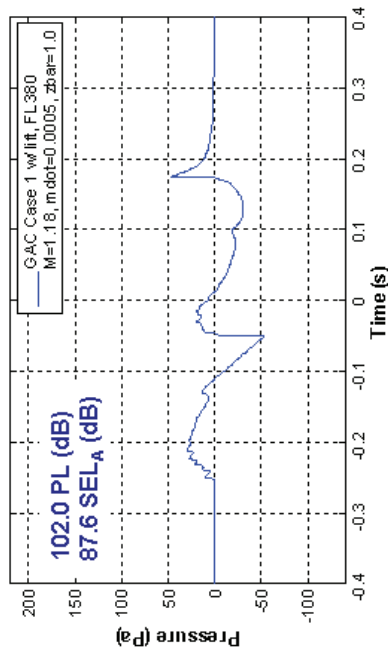
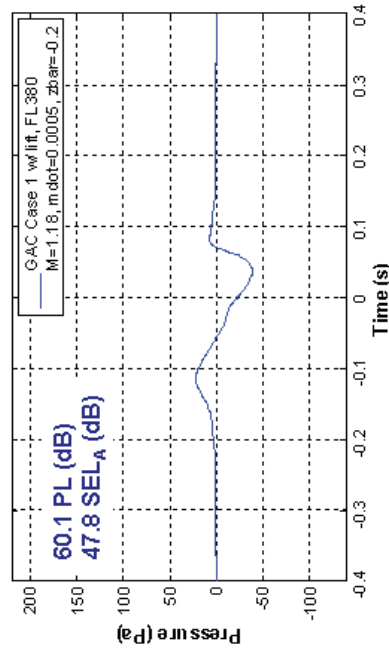
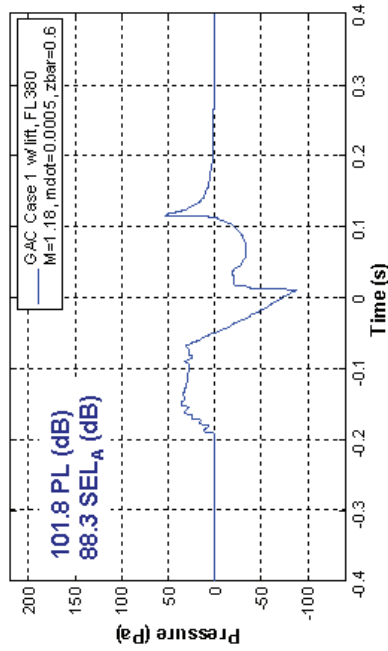


Figure 11-68. Time histories for Gulfstream Case 1, 38,000 ft, Mach 1.182,  $\dot{m} = 0.0005$  at four different  $\bar{z}$  locations – a)  $\bar{z} = 1.0$ , b)  $\bar{z} = 0.6$ , c)  $\bar{z} = 0.2$ , and d)  $\bar{z} = -0.2$ .

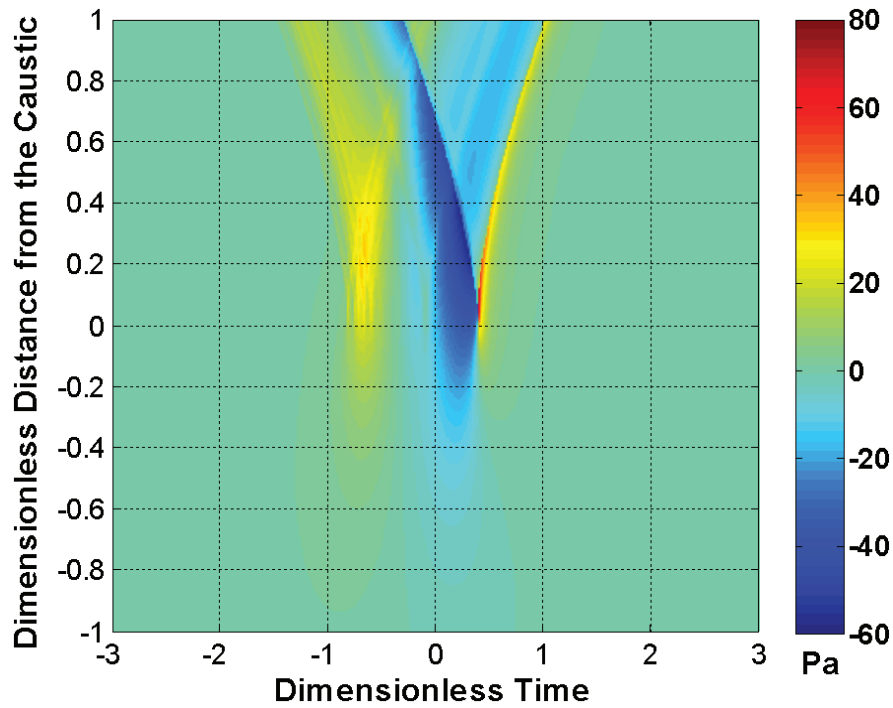


Figure 11-69. Pressure field contour for Gulfstream Case 2, 38,000 ft, Mach 1.19,  $\dot{m} = 0.001$ .

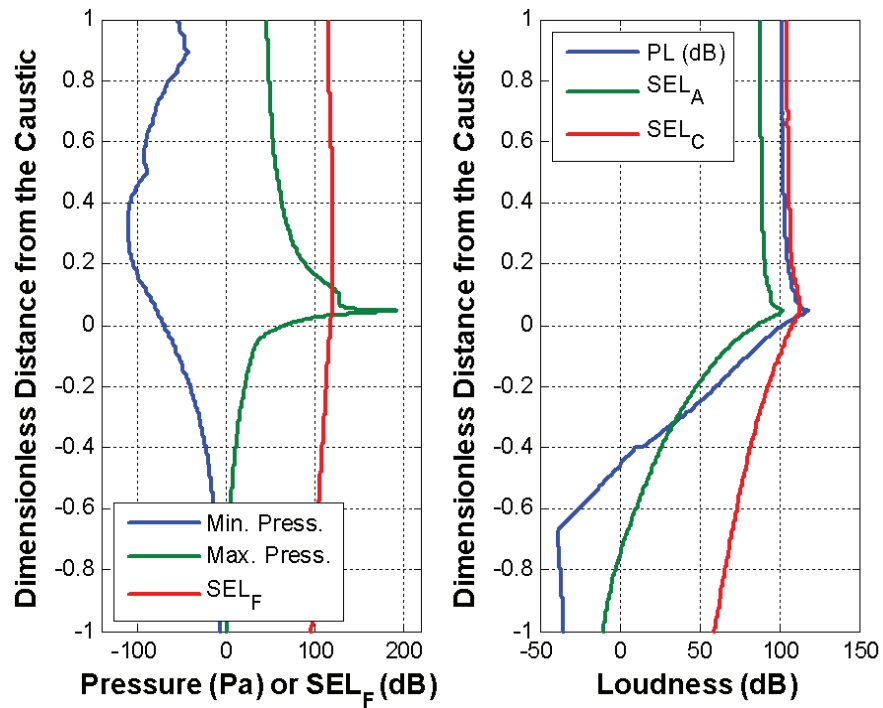


Figure 11-70. Metrics plots for Gulfstream Case 2, 38,000 ft, Mach 1.19,  $\dot{m} = 0.001$ .

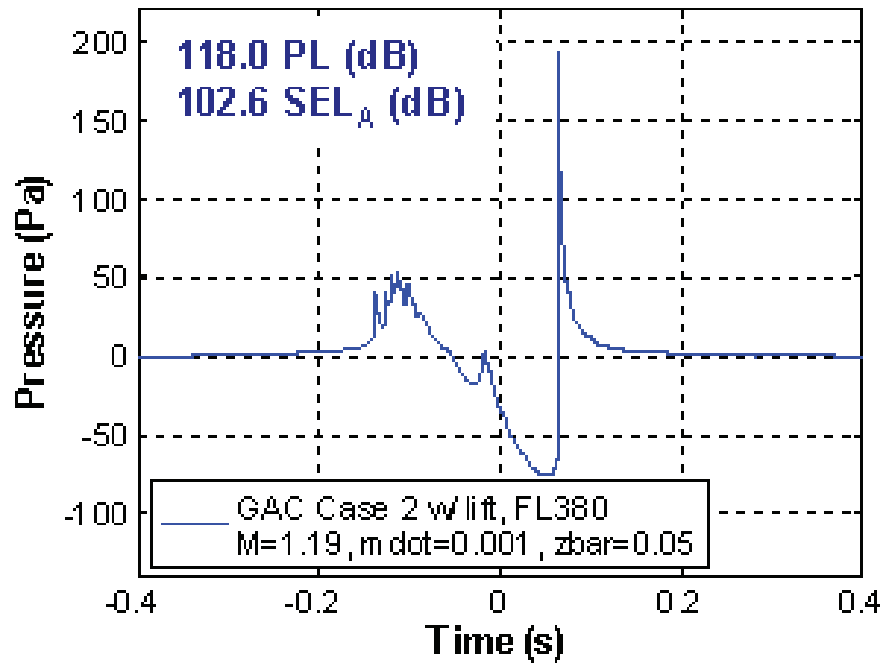


Figure 11-71. Time history corresponding to the peak overpressure ( $\bar{z} = 0.05$ ) for Gulfstream Case 2, 38,000 ft, Mach 1.19,  $\dot{m} = 0.001$ .

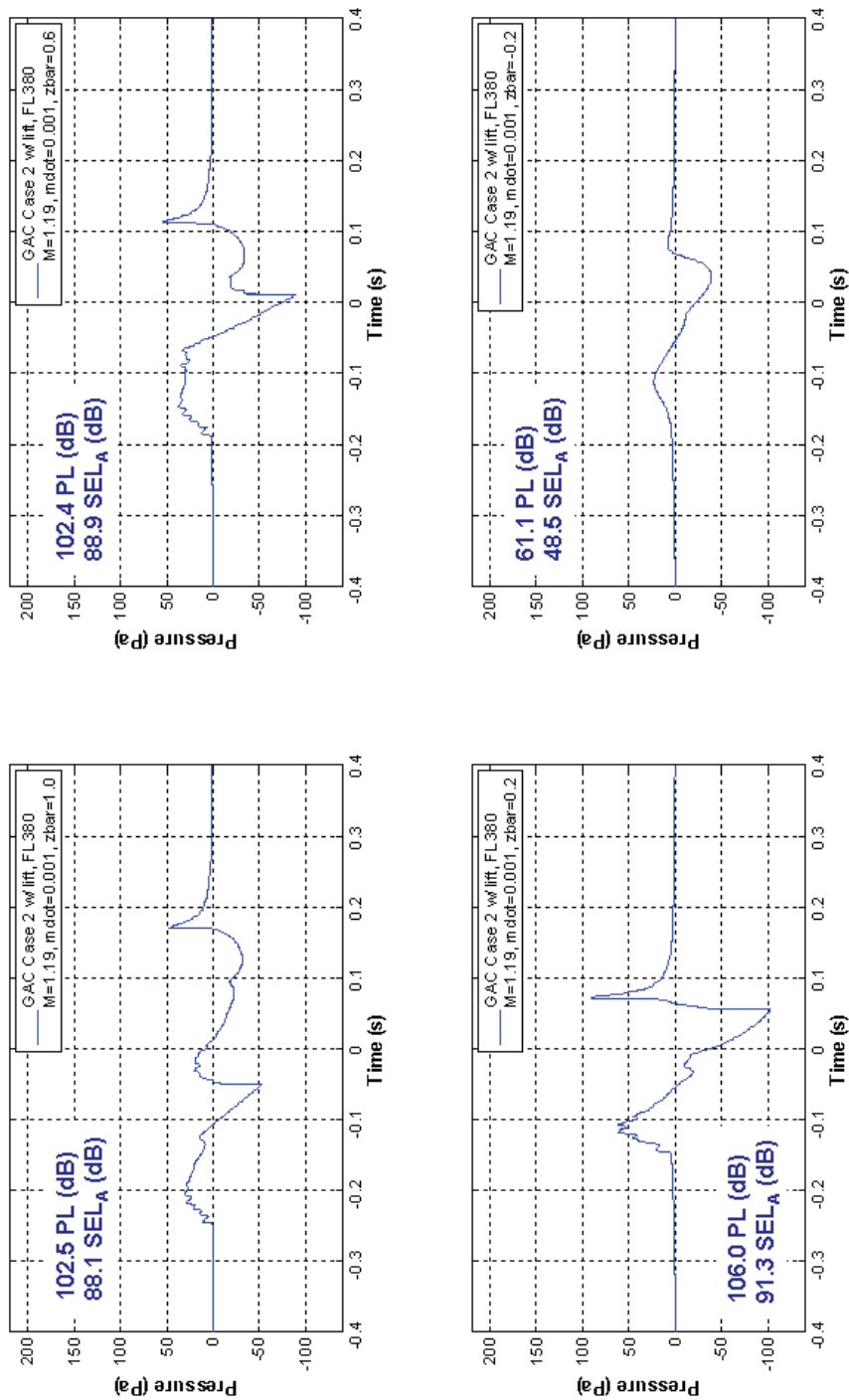


Figure 11-72. Time histories for Gulfstream Case 2, 38,000 ft, Mach 1.19, mdot = 0.001 at four different  $\bar{z}$  locations – a)  $\bar{z} = 1.0$ , b)  $\bar{z} = 0.6$ , c)  $\bar{z} = 0.2$ , and d)  $\bar{z} = -0.2$ .

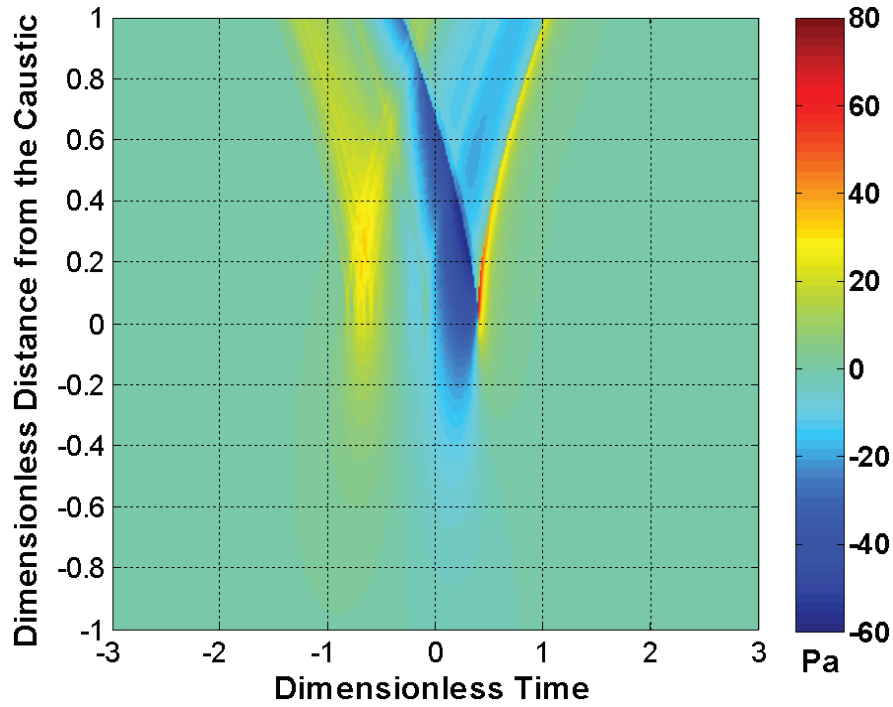


Figure 11-73. Pressure field contour for Gulfstream Case 3, 38,000 ft, Mach 1.208,  $\dot{m} = 0.002$ .

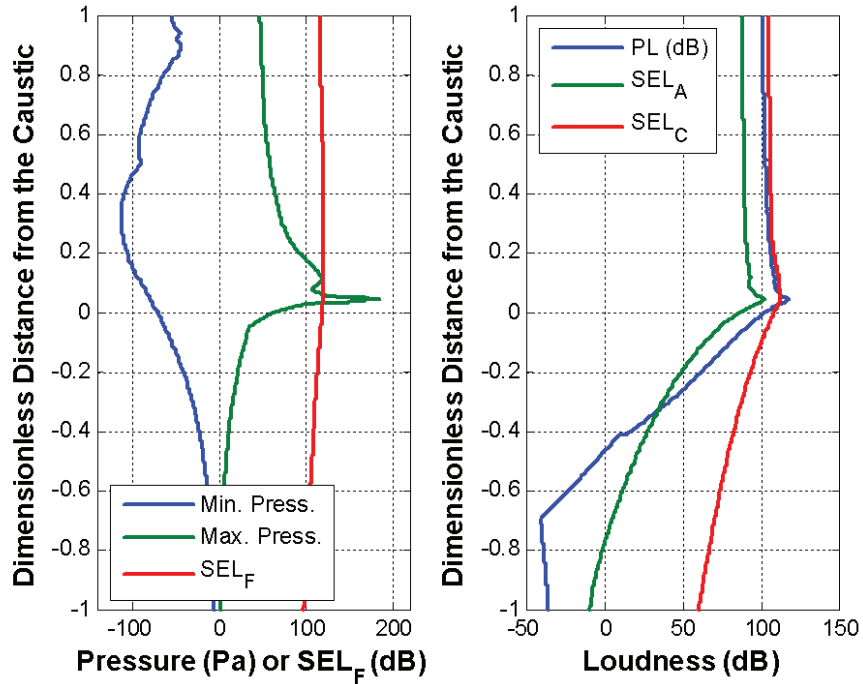


Figure 11-74. Metrics plots for Gulfstream Case 3, 38,000 ft, Mach 1.208,  $\dot{m} = 0.002$ .

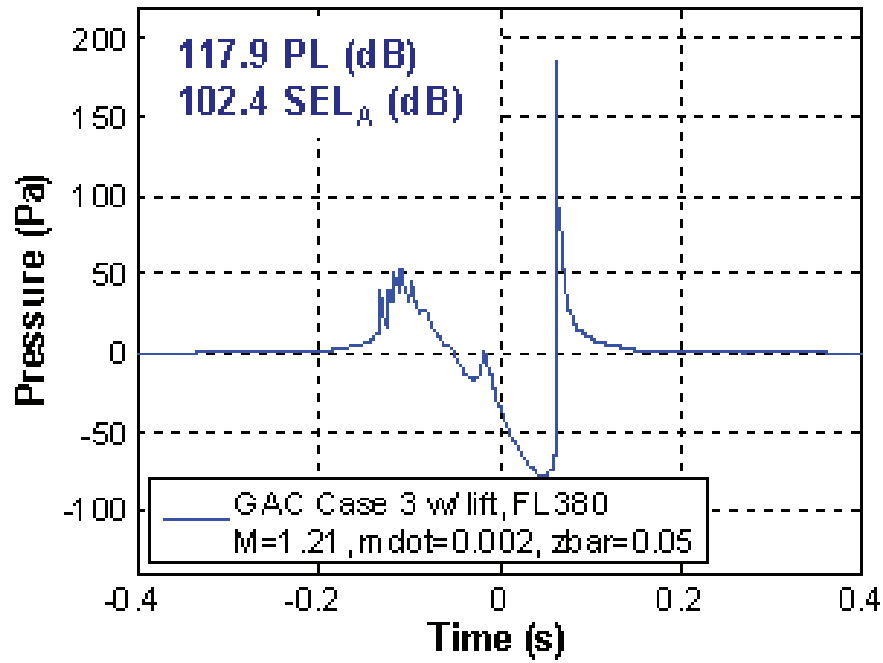


Figure 11-75. Time history corresponding to the peak overpressure ( $\bar{z} = 0.05$ ) for Gulfstream Case 3, 38,000 ft, Mach 1.208,  $\dot{m} = 0.002$ .



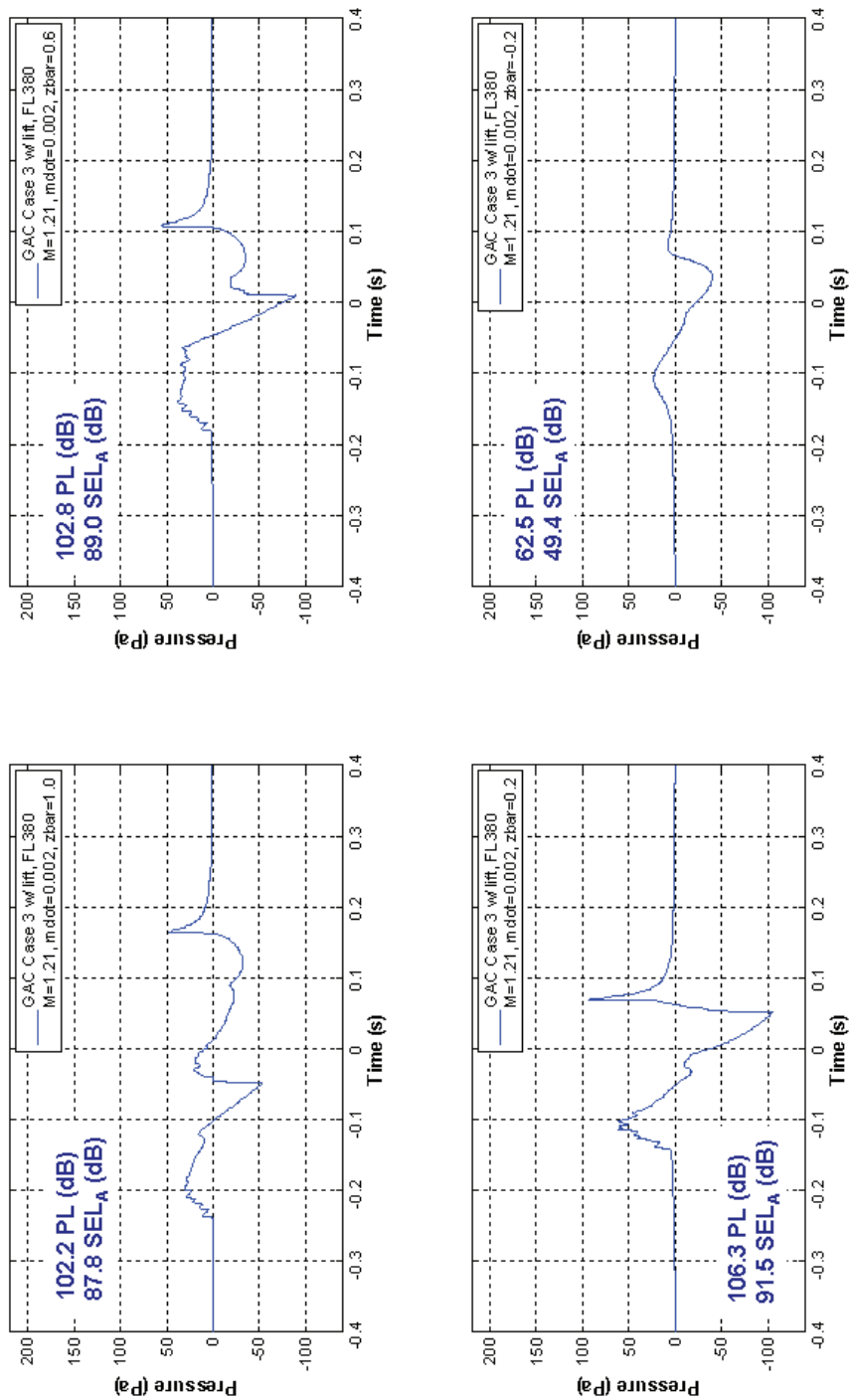


Figure 11-76. Time histories for Gulfstream Case 3, 38,000 ft, Mach 1.208,  $\dot{m} = 0.002$  at four different  $\bar{z}$  locations – a)  $\bar{z} = 1.0$ , b)  $\bar{z} = 0.6$ , c)  $\bar{z} = 0.2$ , and d)  $\bar{z} = -0.2$ .

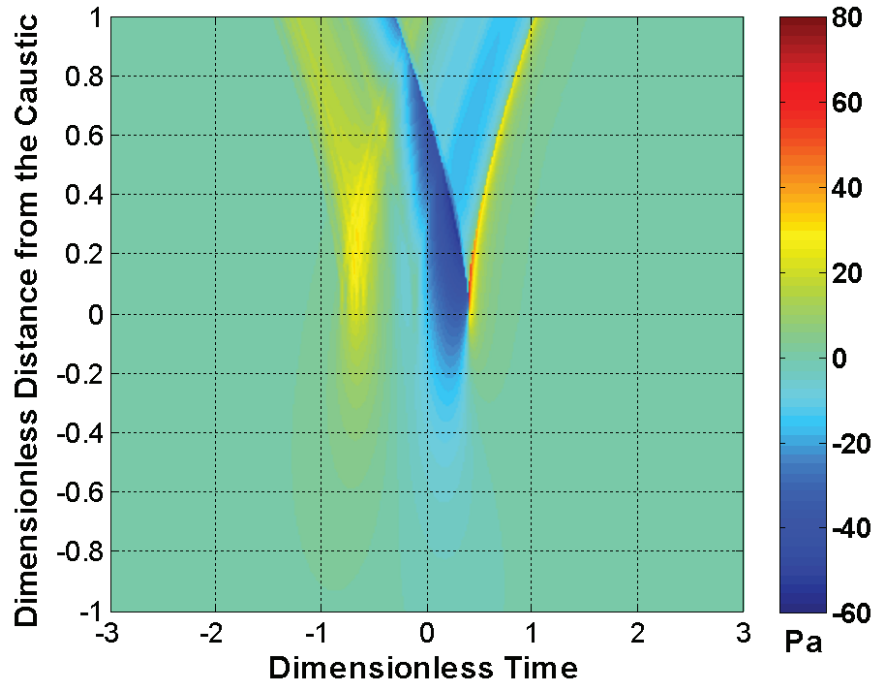


Figure 11-77. Pressure field contour for Gulfstream Case 4, 40,000 ft, Mach 1.182,  $\dot{m} = 0.0005$ .

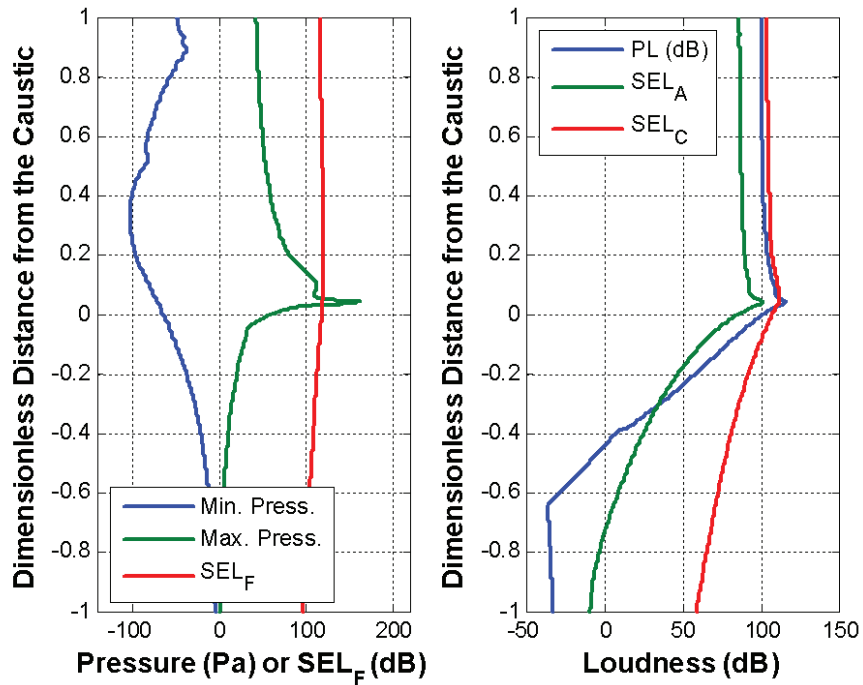


Figure 11-78. Metrics plots for Gulfstream Case 4, 40,000 ft, Mach 1.182,  $\dot{m} = 0.0005$

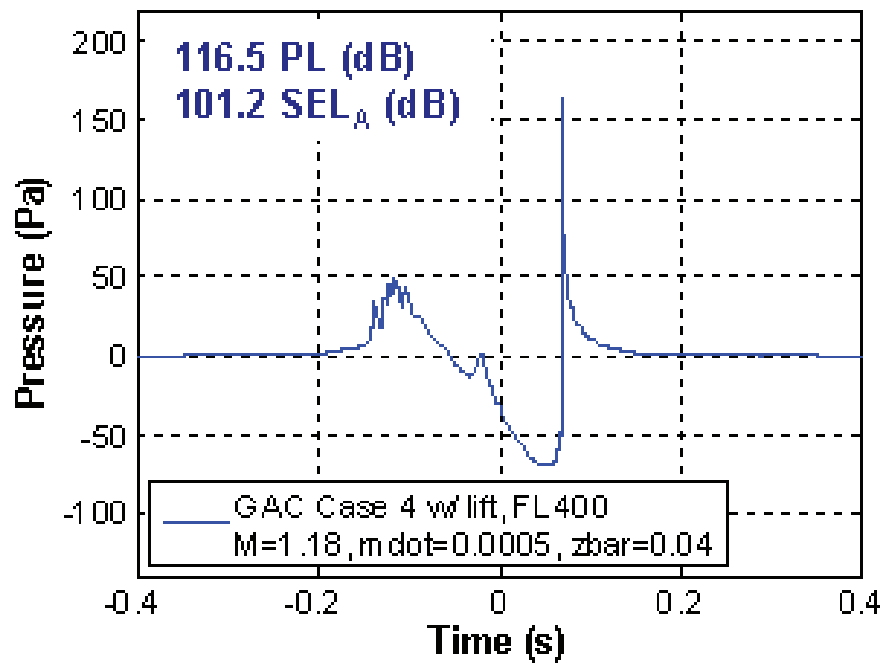


Figure 11-79. Time history corresponding to the peak overpressure ( $\bar{z} = 0.04$ ) for Gulfstream Case 4, 40,000 ft, Mach 1.182,  $\dot{m} = 0.0005$ .

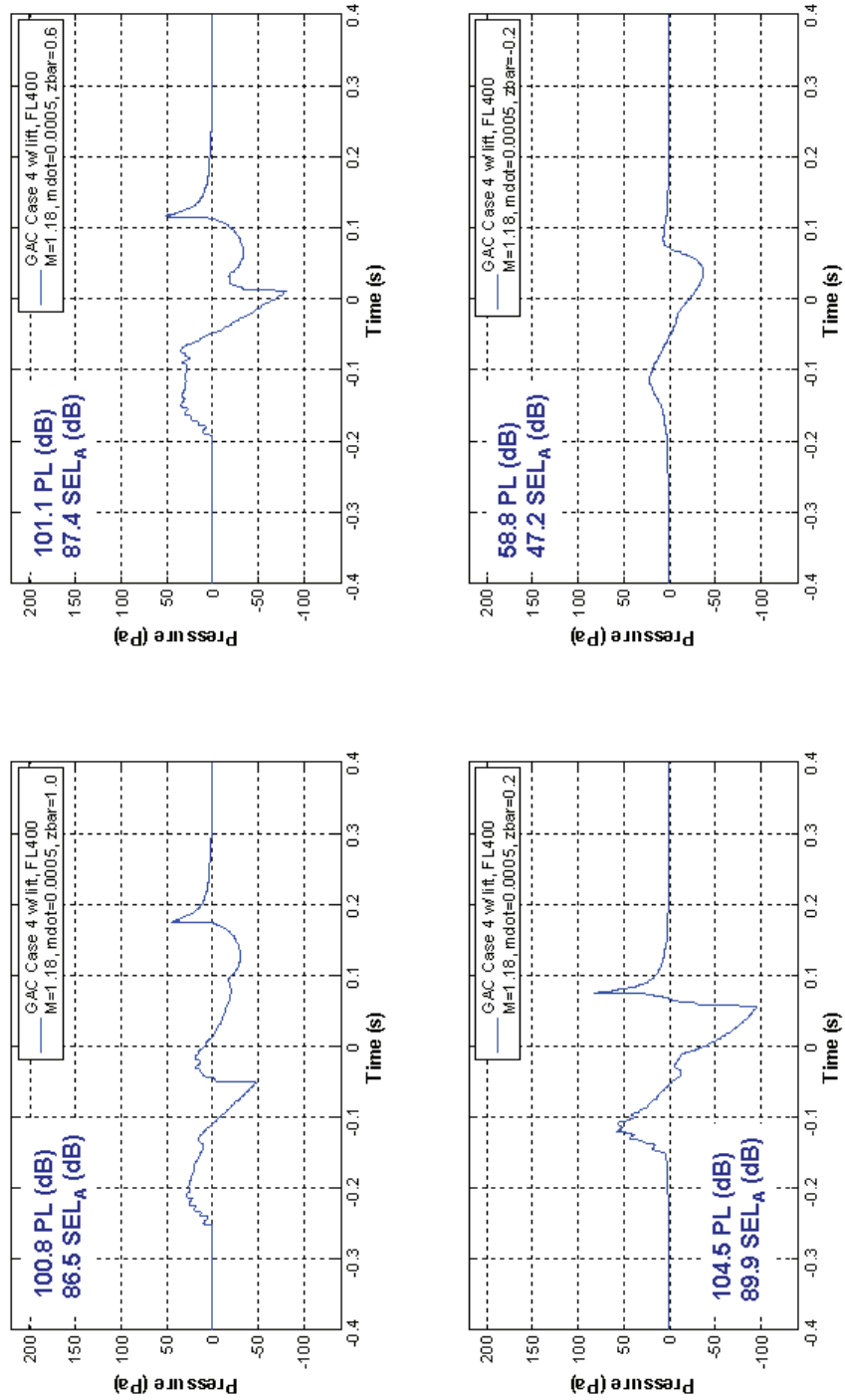


Figure 11-80. Time histories for Gulfstream Case 4, 40,000 ft, Mach 1.182,  $\dot{m} = 0.0005$  at four different  $\bar{z}$  locations – a)  $\bar{z} = 1.0$ , b)  $\bar{z} = 0.6$ , c)  $\bar{z} = 0.2$ , and d)  $\bar{z} = -0.2$ .

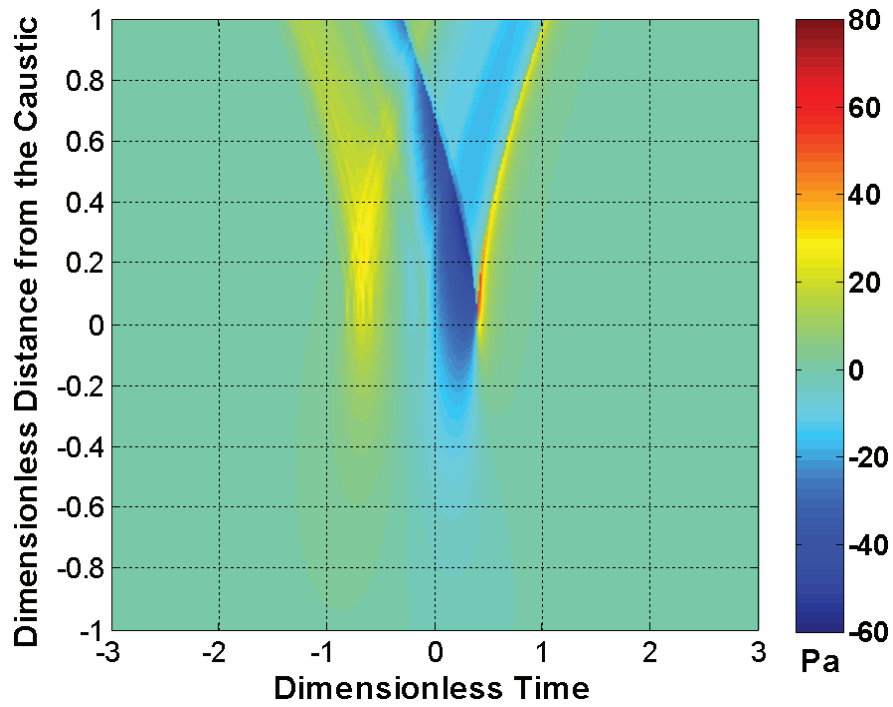


Figure 11-81. Pressure field contour for Gulfstream Case 5, 38,000 ft, Mach 1.19,  $\dot{m} = 0.001$ .

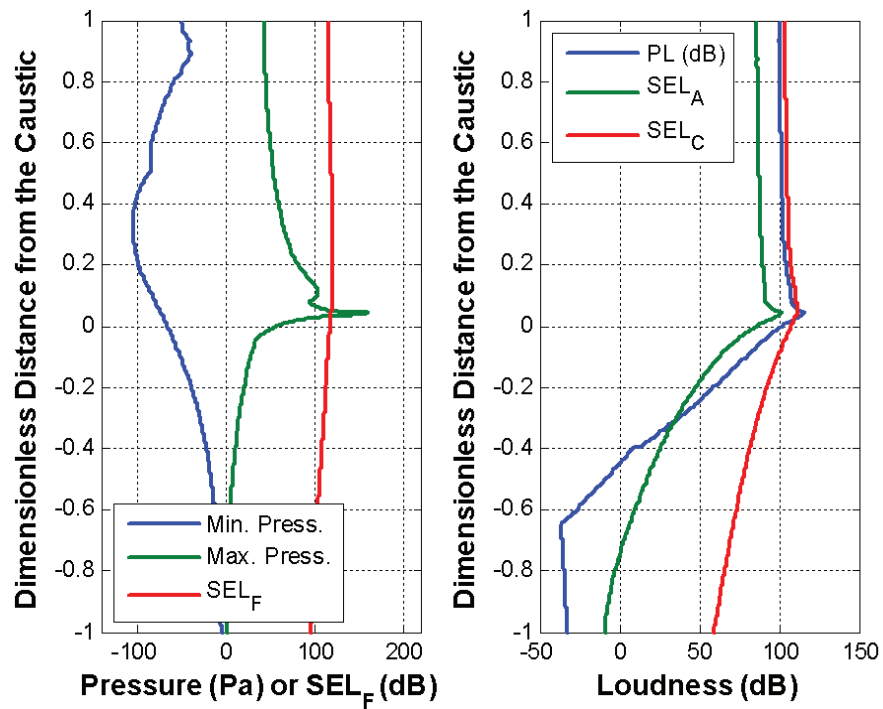


Figure 11-82. Metrics plots for Gulfstream Case 5, 40,000 ft, Mach 1.19,  $\dot{m} = 0.001$ .

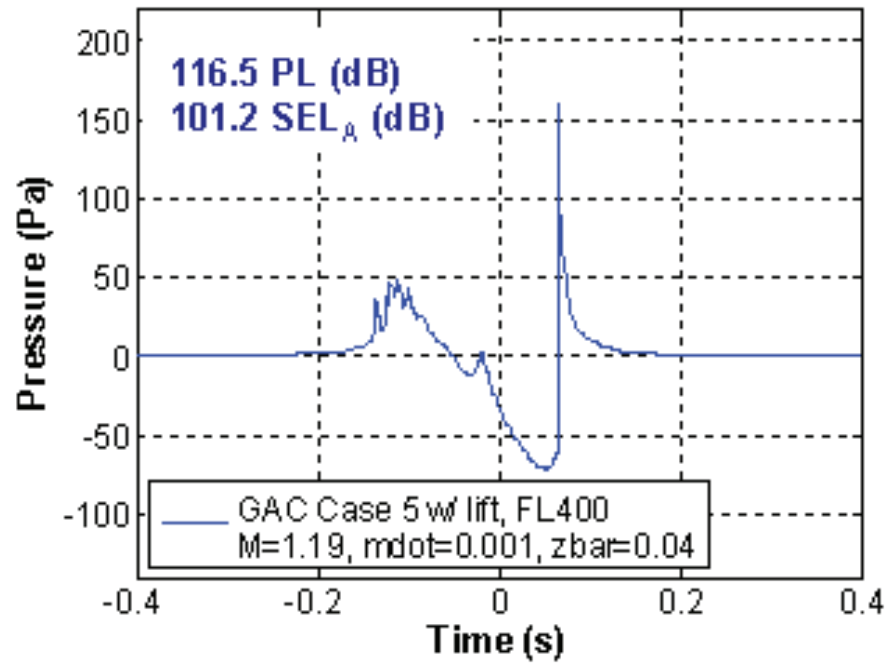


Figure 11-83. Time history corresponding to the peak overpressure ( $\bar{z} = 0.28$ ) for Gulfstream Case 5, 40,000 ft, Mach 1.19,  $\dot{m} = 0.001$ .

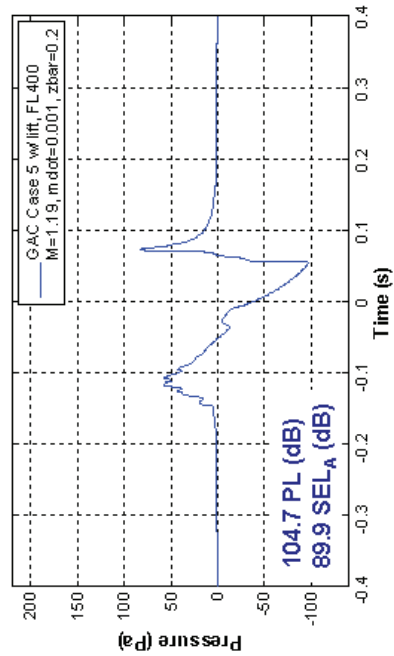
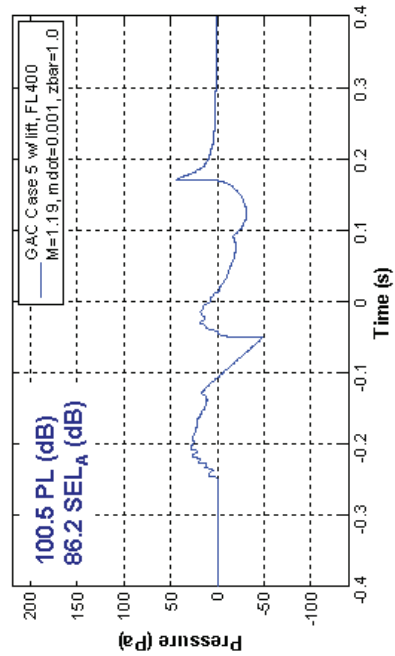
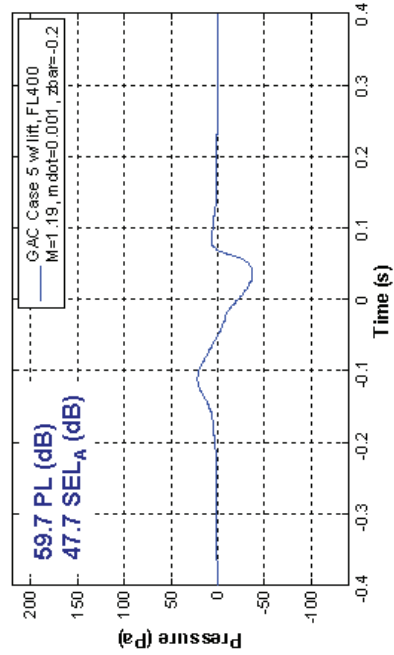
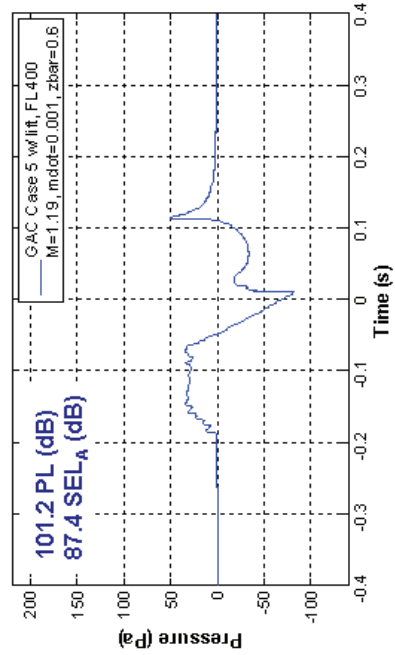


Figure 11-84. Time histories for Gulfstream Case 5, 40,000 ft, Mach 1.19,  $\dot{m} = 0.001$  at four different  $\bar{z}$  locations – a)  $\bar{z} = 1.0$ , b)  $\bar{z} = 0.6$ , c)  $\bar{z} = 0.2$ , and d)  $\bar{z} = -0.2$ .

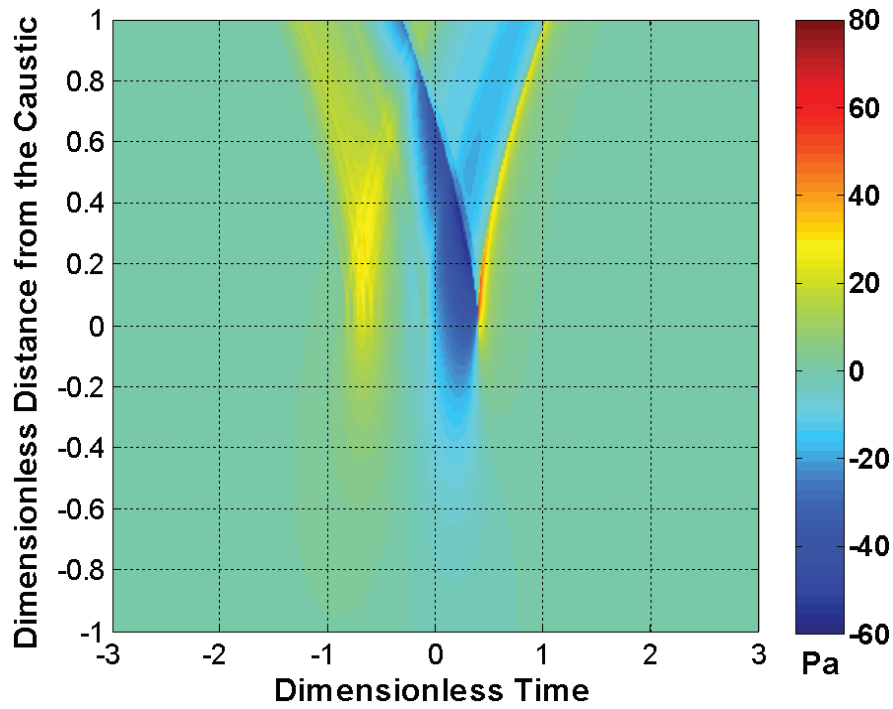


Figure 11-85 Pressure field contour for Gulfstream Case 6, 40,000 ft, Mach 1.208,  $\dot{m} = 0.002$ .

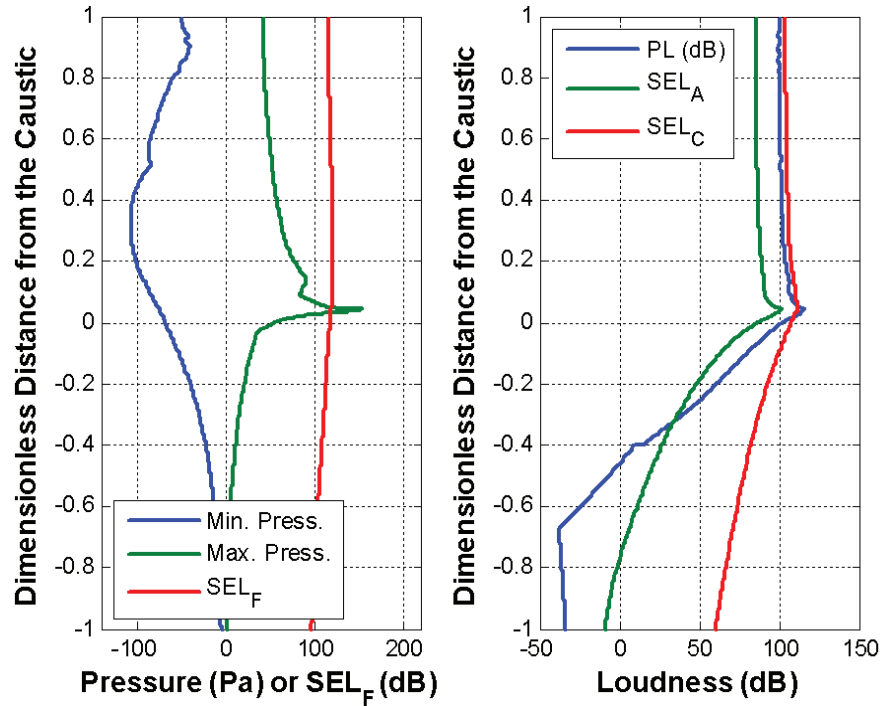


Figure 11-86. Metrics plots for Gulfstream Case 6, 40,000 ft, Mach 1.208,  $\dot{m} = 0.002$ .



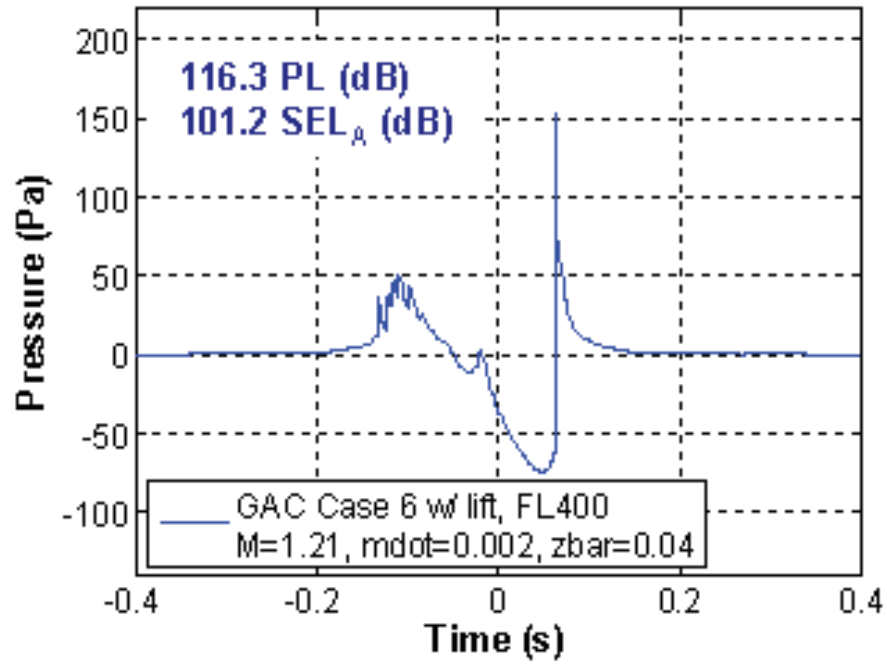


Figure 11-87. Time history corresponding to the peak overpressure ( $\bar{z}=0.27$ ) for Gulfstream Case 6, 40,000 ft, Mach 1.208,  $\dot{m}=0.002$ .

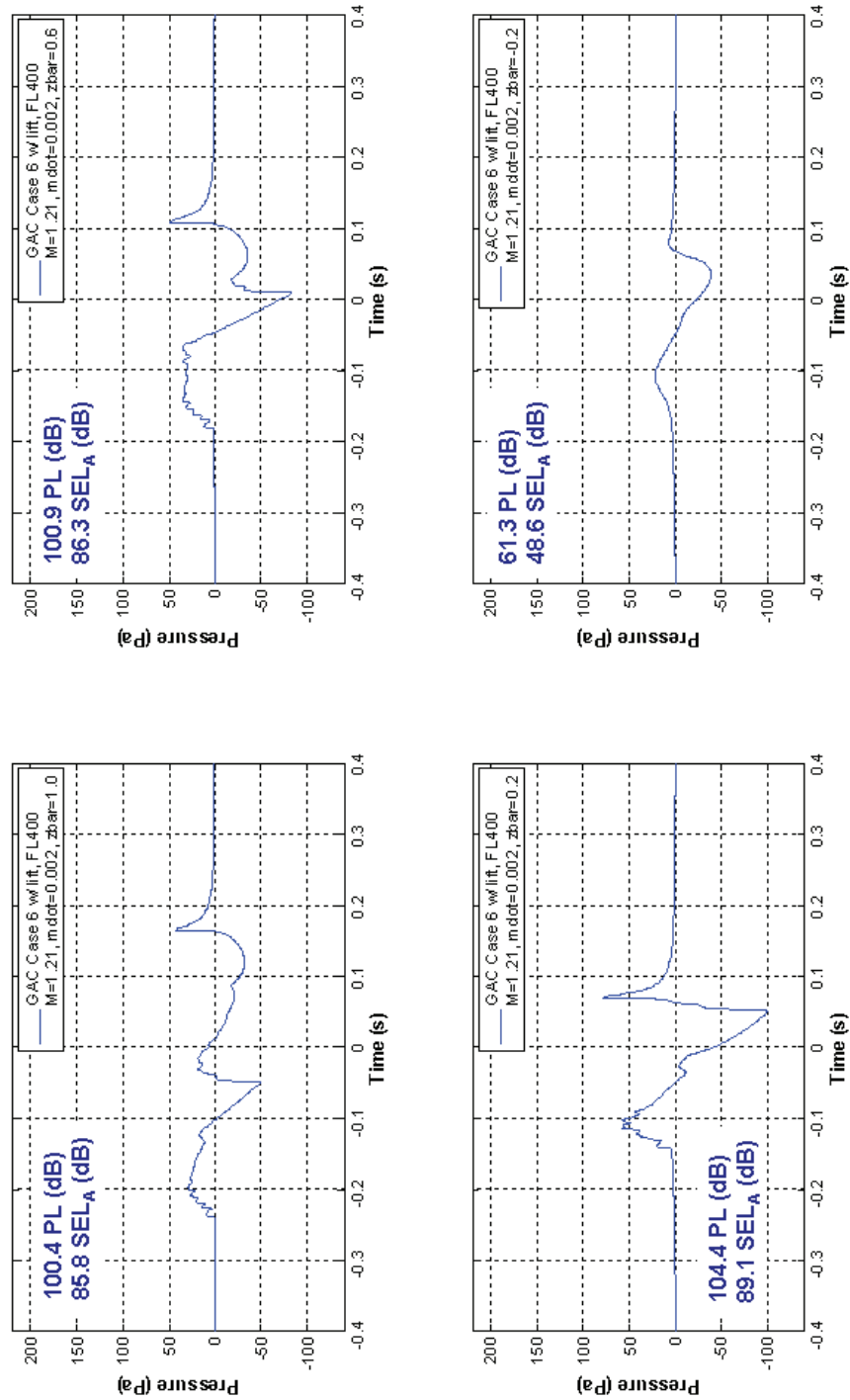


Figure 11-88. Time histories for Gulfstream Case 6, 40,000 ft, Mach 1.209, mdot = 0.002 at four different  $\bar{z}$  locations – a)  $\bar{z} = 1.0$ , b)  $\bar{z} = 0.6$ , c)  $\bar{z} = 0.2$ , and d)  $\bar{z} = -0.2$ .

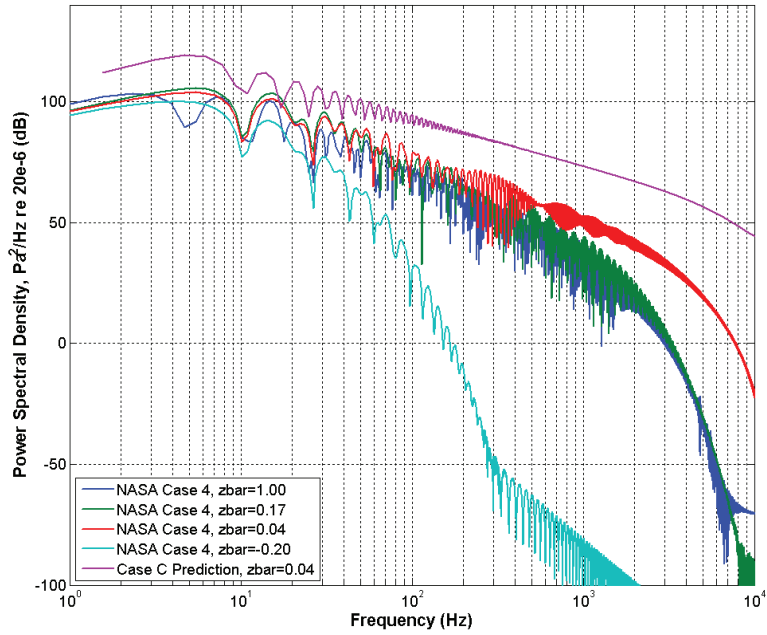


Figure 11-89. Comparison of Power Spectral Density (PSD) spectra at different  $\bar{z}$  locations for NASA Case 4.

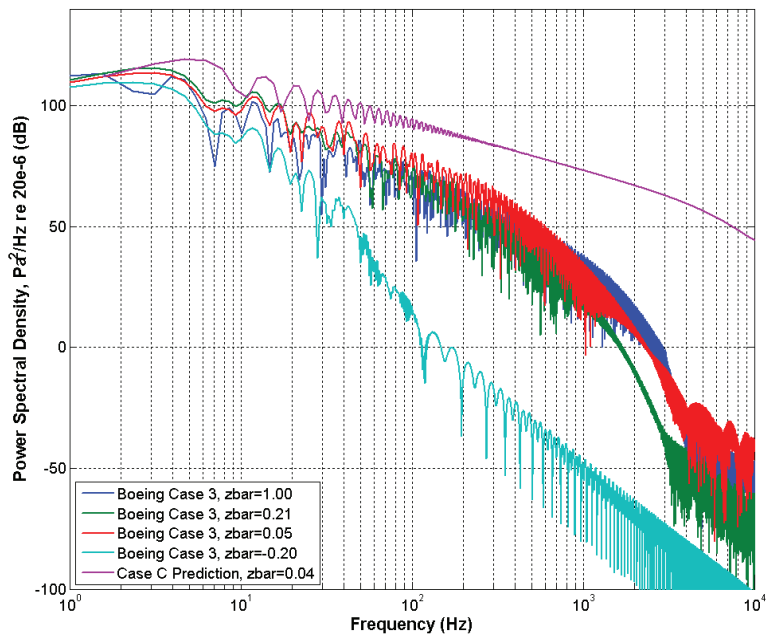
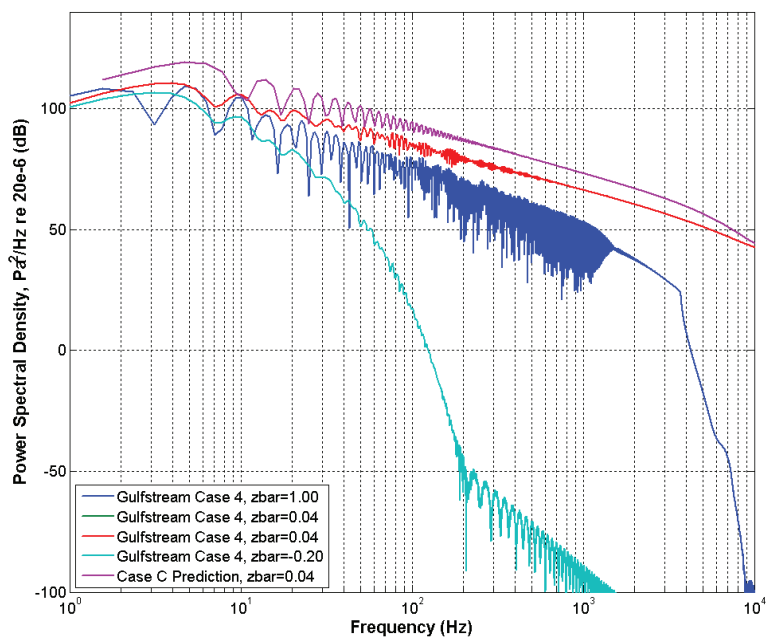


Figure 11-90. Comparison of Power Spectral Density (PSD) spectra at different  $\bar{z}$  locations for Boeing Case 3.



**Figure 11-91. Comparison of Power Spectral Density (PSD) spectra at different  $\bar{z}$  locations for Gulfstream Case 4.**

## 11.6 Analysis of Profile Exploration Results

### 11.6.1 Summary

Table 11-13 summarizes the noise metrics ( $P_{\max}$ , PL, and  $SEL_A$ ) that were computed in Section 11.5. The  $\bar{z}$  value at which each maximum occurred is also presented. Cases are identified by their file names. Table 11-14 shows maximum PL and  $SEL_A$  together with the flight conditions. Cases are identified by their working descriptive names. The order is the same in both tables, with the five Boeing cases first, the six Gulfstream cases next, then the four NASA cases. The caustic curvature (relative radius of curvature between caustic and focusing ray) for these cases is between 283,000 feet and 322,000 feet. This is comparable to the 334,000-foot radius of curvature for SCAMP's  $M_{\dot{0}} = .0035$  level acceleration Maneuver A (Page, 2011a, Page, 2011b). Curvature for constant angle acceleration is dominated by ray curvature, so the difference between the current cases and the SCAMP flight test is associated with the standard atmosphere versus the conditions at the time of the SCAMP test. SCAMP pushover Maneuvers C and D had radii of curvature of 170,000 feet and 110,000 feet, respectively, so the curvature range is bracketed.

**Table 11-13. Key Noise Metrics and Positions within Diffraction Layer**

**Metrics and zbar Locations**

Case Name	ZP <sub>max</sub>	P <sub>max</sub>	ZPL <sub>max</sub>	PL <sub>max</sub>	ZSEL <sub>A</sub>	SEL <sub>A</sub>
bcyl3_c1	0.2193	146.5	0.0423	103.8	0.0448	89.0
bcyl3_c2	0.2453	129.1	0.0183	109.6	0.0198	94.8
bcyl3_c3	0.2128	123.1	0.0513	98.9	0.0523	83.6
bcyl3_c4	0.2168	119.3	0.0588	99.9	0.0588	84.1
bcyl3_c5	0.2278	114.3	0.0628	100.3	0.0613	85.1
gac_fl380_m118	0.0483	203.8	0.0483	118.3	0.0478	102.9
gac_fl380_m119	0.0473	192.4	0.0473	118.0	0.0473	102.6
gac_fl380_m121	0.0458	185.7	0.0458	117.9	0.0453	102.4
gac_fl400_m118	0.0433	162.9	0.0433	116.5	0.0428	101.2
gac_fl400_m119	0.0418	161.7	0.0418	116.5	0.0418	101.2
gac_fl400_m121	0.0418	154.3	0.0418	116.3	0.0413	101.2
nasa_climb1	0.1893	100.7	0.0313	111.1	0.0313	95.9
nasa_climb2	0.1693	102.0	0.0293	106.7	0.0288	91.5
nasa_climb3	0.1763	73.1	0.0333	104.1	0.0338	89.1
nasa_climb4	0.1658	68.3	0.0363	103.0	0.0378	88.2

**Table 11-14. Summary of Maximum PL, SEL<sub>A</sub>, and Flight Conditions**

Description	PL	SEL	Z	M	Mdot	Gamma
M1.16 AB=1.0 level @40 kft	103.8	89.0	40000	1.156	0.00036	0.000
M1.23 AB=1.5 2 deg climb @38.5	109.6	94.8	38498	1.230	0.00316	2.000
M1.16 AB=1.0 level @45 kft	98.9	83.6	45000	1.153	0.00010	0.000
M1.17 AB=1.5 level @45 kft	99.9	84.1	45000	1.170	0.00111	0.000
M1.21 AB=2.0 level @45 kft	100.3	85.1	45000	1.211	0.00295	0.000
Mdot = 0.0005 2 deg climb 38 kft	118.3	102.9	38000	1.182	0.00050	2.000
Mdot = 0.0010 2 deg climb 38 kft	118.0	102.6	38000	1.190	0.00100	2.000
Mdot = 0.0020 2 deg climb 38 kft	117.9	102.4	38000	1.208	0.00200	2.000
Mdot = 0.0005 2 deg climb 40 kft	116.5	101.2	40000	1.182	0.00050	2.000
Mdot = 0.0010 2 deg climb 40 kft	116.5	101.2	40000	1.190	0.00100	2.000
Mdot = 0.0020 2 deg climb 40 kft	116.3	101.2	40000	1.209	0.00200	2.000
case1_m1.146_h33144_w33411	111.1	95.9	33479	1.166	0.00134	0.642
case2_m1.173_h35821_w33307	106.7	91.5	35821	1.175	0.00138	0.000
case3_m1.168_h38154_w33204	104.1	89.0	38154	1.169	0.00103	0.001
case4_m1.157_h40524_w33022	103.0	88.2	40525	1.161	0.00066	0.003

Figure 11-92 summarizes the PL results as a rank ordering, from best to worst, for the three configurations. Results should be examined for each configuration and not compared between configurations.

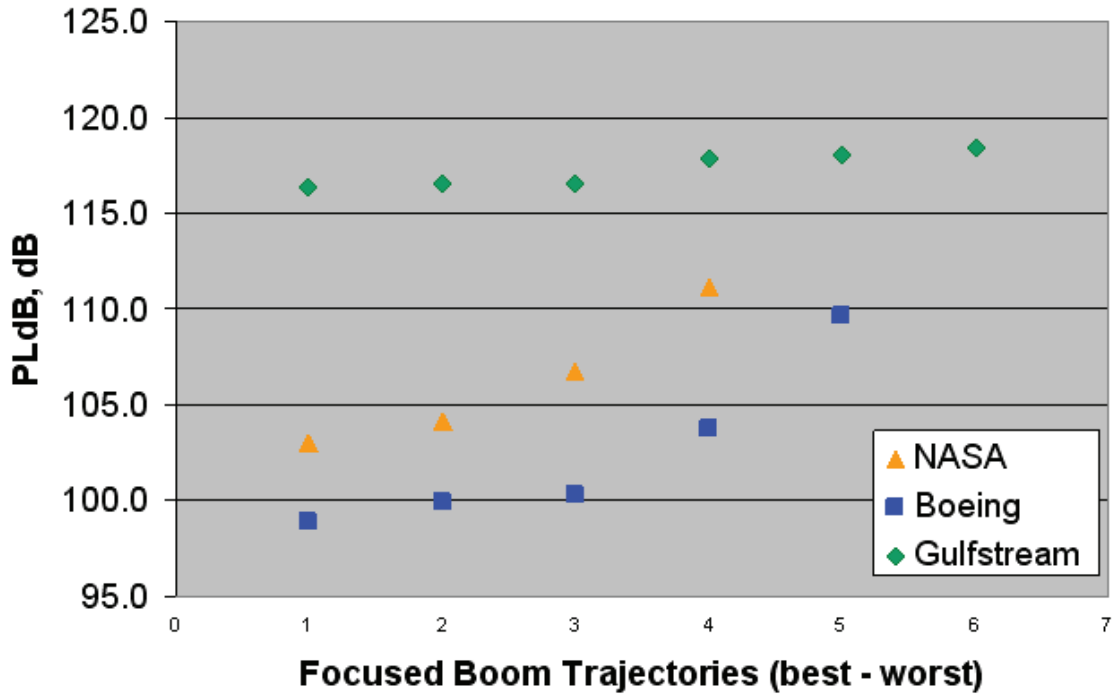


Figure 11-92. Summary of PL, rank ordered, for all configurations.

Examining Table 11-14, it is clear that for each aircraft:

- Higher altitude always results in lower loudness.
- Lower acceleration always results in lower loudness.

The sample matrix is not large, but is well chosen. Boeing and NASA had wide ranges of conditions, exploring the limits of performance for their aircraft, and obtained PL differences of up to 8 to 11 dB. Low-boom shaping characteristics, while not at the optimum design point, were retained to a degree. Gulfstream had a modest range of conditions, systematic variations near a preferred profile, but shaping at the rear was lost at this off-design condition. As noted in Section 11.3.3, the resultant strong shock is not a desirable characteristic for a low-boom aircraft and Gulfstream would not produce a supersonic aircraft that exhibits such a strong shock in its signature. The analysis was carried out for “academic” purposes, and still exhibited the same trend with altitude as the other cases.

These results are consistent with the acceleration effect estimated in (Haglund, 1974) (shown in Figure 11-1) and the altitude effect calculated in (Maglieri, 2011). There is not enough climb angle variation in the current analysis to identify a trend with climb.

The finding that high altitude and low acceleration mitigate transition focus makes physical sense. Higher altitude places the aircraft closer to its design condition, and also provides the benefit of distance. Low acceleration may have adverse effects on weight and performance, although that is configuration dependent. Low acceleration also results in low focusing Mach number, which means that the ray path will be longer, permitting the signature to age more toward its design point. There are, however, additional considerations to this result, in that the rays will be closer to grazing at the ground. The issues are:

- The focal zone itself will cover a longer distance in the trackwise direction, as sketched in Figure 11-93.

- There is greater uncertainty in predicting the focus location.
- There is a longer propagation path through the lower atmosphere, thus a greater potential for turbulent distortion.
- Grazing ground effects can affect the signature.
- Vehicles optimized for low boom at cruise have transonic acceleration boom levels higher than cruise. For the Boeing and NASA configurations considered, this was on the order of 20 PLdB.

The second and third items above have the potential to attenuate the signature, reducing the boom. The first item is a reminder that the full focal zone can matter, not just the maximum loudness within it. Currently, PCBoom can compute the full extent of a focal zone and the N-wave peak pressure within it, but calculation of loudness metrics for complex signatures via the process presented in Section 11.6 is essentially single point.

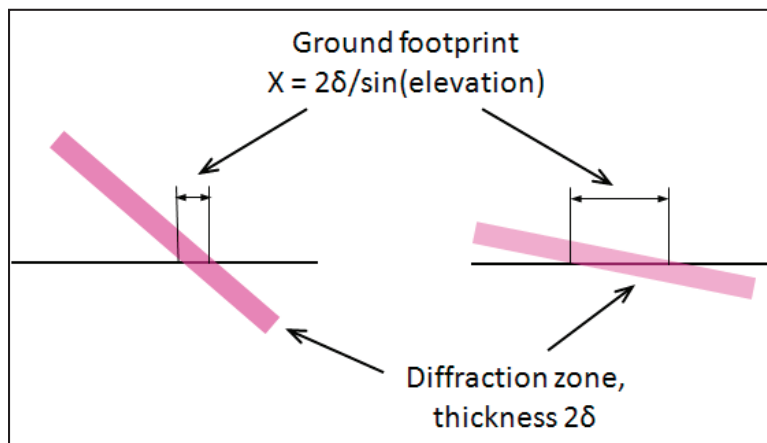


**Figure 11-93. Effect of grazing angle on focal zone ground footprint.**

## 11.6.2 Recommendations

This study has identified the appropriate trend – higher altitude and lower acceleration – to minimize transition focus boom loudness from low-boom aircraft. It has also demonstrated that further development of propagation models and tools is needed. Specific recommendations are:

1. Refinement/development is needed for the Lossy NTE program, primarily regarding convergence. A grid refinement study is needed to examine convergence of solutions. Improvement is needed for the iterative convergence criteria, with a goal of quantitative criteria that do not require manual judgment.
2. Ground impedance effects should be included in the analysis, both in the NTE solution and in non-focusing rays in the vicinity of the focal zone.
3. Turbulence should be included to account for – a) experimentally observed spoiling of foci, b) the variation of waveforms entering the diffraction zone, and c) effects within the Tricomi region.
4. Off-track focusing predictions are needed for full footprints. The Tricomi formulation has a 2-D plane assumption, ignoring diffraction in the lateral direction. Focus at the lateral edge of the caustic intercept at the ground is expected to have 3-D effects.
5. Tools are needed for complete footprint predictions. The process used in this study, which includes atmospheric absorption, is quasi-single point. Information is available that allows some interpolation

of NTE results onto the ground plane, but there is no tool like PCBoom’s “wcon” to generate footprints. Current tools (wcon) do not address signatures and loudness in the shadow zone.

6. Investigate the physics of the transonic boom using the new codes to better understand appropriate vehicle shaping techniques for minimization in this flight regime.
7. Continue to investigate an operational approach to minimizing the transonic acceleration focus boom levels.
8. Investigate aircraft shaping trades between cruise and transonic speeds using the new codes in conjunction with operational techniques to minimize transonic acceleration focus boom.
9. Ground test and flight-test verification.

Experimental verification of results is necessary. Some confirmation may be possible in small-scale experiment, but ultimately full-scale demonstration from a shaped boom flight vehicle will be needed.





The Superboom Caustic Analysis and Measurement Program was aimed at advancing the understanding of sonic boom focal zones as they are expected to occur during supersonic transition acceleration of commercial supersonic aircraft. The effort included defining the relevant flight regime, designing and conducting a flight-test experiment to measure focus booms, development and validation of analytic models for focus boom signatures, and application of those models to low-boom aircraft configurations.

## 12.1 Transition Focus Regime and Candidate Analytic/Numeric Focus Models

Transition focus occurs during the initial acceleration from subsonic flight to supersonic flight, and is the only focus condition that is unavoidable for a supersonic vehicle. Based on design studies by industry team partners Boeing and Gulfstream, and by NASA, for a supersonic transport this will occur in the altitude range of about 35,000 to 45,000 feet, at an acceleration between 0.5 and 2 kts/second (Mach rate of 0.0009 to 0.0035 per second), and in level or slightly climbing (up to 2°) flight. This does not correspond to cruise design conditions of (typically) Mach 1.8 and altitude of 50,000 to 55,000 feet. Focusing signatures are expected to be more complex than the simple N-waves that have been the subject of most past focus studies.

Guiraud wrote the nonlinear Tricomi equation (NTE) that governs the behavior of sonic boom signatures in the vicinity of a caustic, and derived a scaling law for focusing of a single weak shock wave. Key scaling parameters were shock amplitude and the relative radius of curvature between a focusing ray and the caustic. Gill and Seebass developed a numerical solution for single shock focusing that matched available flight-test and laboratory shock focusing data. PCBoom successfully applied this to N-wave boom focusing, applying that to each shock. Auger and Coulouvrat wrote a more general form of the nonlinear Tricomi equation, suitable for arbitrary signatures and including the signature length in the scaling.

Three candidate models were selected for evaluation:

- Lossy nonlinear Tricomi equation (LNTE), an extension of Auger and Coulouvrat's pseudospectral numeric solution of the NTE. The inclusion of molecular relaxation loss effects would provide physically correct shock rise times, necessary for computation of perceived level (PL) that is recognized as the best measure of outdoor sonic boom perception.
- Nonlinear Progressive-wave Equation (NPE), a numeric propagation code with prior successful application to propagation of sonic booms through turbulence. While not yet incorporating molecular loss effects, it is not restricted to NTE's local gradient and scaling assumptions and thus has the potential of including turbulence effects.
- Gill-Seebass and Guiraud similitude, as implemented in PCBoom. It was not expected that the simple single shock focus model would be appropriate for complex low-boom signatures, but PCBoom itself provides the ray tracing and caustic geometry upon which LNTE and NPE are scaled.

A fourth model, a direct replication of Auger and Coulouvrat's method, was initially included, but dropped because it was a subset of the LNTE method and offered no particular advantage.

## 12.2 Flight-Test Design and Execution

A flight-test program was designed to generate focal zones within the maneuver space expected for commercial supersonic aircraft. Because a low-boom shaped aircraft does not yet exist, the experiment was performed with an F-18B, an N-wave aircraft, but with the goal of comparing detailed signature shapes, not just peak overpressures. The test matrix was centered on a 2 kt/sec acceleration at 35,000 feet. A higher power acceleration was included to assess acceleration effects. Lower acceleration (closer to 0.5 kt/sec) was not feasible because of fuel burn and airspace considerations. Two pushovers, -0.25 deg/sec and -0.50 deg/sec, both at 2 kt/sec acceleration, were included to obtain a range of caustic curvatures.

The aircraft F-function source was based on CFD analysis conducted by Boeing for nominal conditions during test planning, and for as-flown conditions after test execution. Three steady level "calibration" conditions were included in the flight-test matrix, corresponding to the pre-test CFD analysis.

The flight-test matrix evolved through a series of numeric simulations, flight simulator sessions, and test flights. NASA developed special instrumentation, an Mdot display, so that the target acceleration could be monitored and controlled by the pilot in the rear cockpit seat. The pushover rates were converted into equivalent normal g acceleration, and monitored and controlled by the pilot in the front seat.

The basic ground array for the test was a 10,000-foot linear array of 81 microphones spaced 125 feet apart. The microphone spacing was chosen so as to be comparable to or less than the expected boom wavelength, and long enough to capture complete diffraction zones from evanescent wave through peak focus U through full N-u separation. The test location was east of Cuddeback Dry Lake. The location was chosen so as to avoid community impact and because of the presence of a two mile road that could accommodate the array. The Black Mountain supersonic airspace was extended approximately three miles north of its original boundaries so as to include this region.

In addition to the ground array, a microphone was placed on a TG-14 powered glider and up to two microphones suspended from a tethered blimp. Those provided measurement points above the influence of the ground and low-altitude turbulence. GPSsonde weather profiles were obtained at the site prior to each flight, and turbulence was measured with a SODAR.

NASA developed a software package referred to as WTF, which employed PCBoom and the pre-launch GPSsonde to determine the waypoint for each F-18B pass and waypoints for the TG-14 to cross the array at the correct time and position to capture above-ground focal zone signatures.

Thirteen F-18B flights were conducted during 5 flying days over a 2-week period. There were 70 boom events, with 61 focus passes, and 9 calibration passes. Seventeen of the focus passes and three of the calibration passes were laterally offset; the remainder were centerline.

Thirty-two of the focus passes captured complete diffraction zones, as intended, with an additional five capturing at least the maximum focus. Better than 95 percent of the pushover passes placed the focus within the array. Slightly over 65 percent of the level acceleration centerline passes placed the focus within the array. Offset level acceleration passes were least successful, since deviations in lateral position as well as longitudinal waypoint affect the accuracy of placing the focus. Success rate correlated with the elevation angle of the caustic, which was steeper for the pushover maneuvers. Grazing incidence tended to make hitting the target more difficult.

The TG-14 flew for six of the F-18B flights. For the three flights without instrumentation problems, there were 17 passes with a 59 percent success rate at capturing a boom. The successful data included one maximum focus signature, several N-u combinations, several overlapped N-u signatures, and several evanescent waves.

The quality of the data was excellent. The digitally recorded microphone data, atmospheric data, and flight parameters are all time synchronized, and form an archive that satisfied the goal of obtaining high resolution data for model validation.

## 12.3 Model Validation and Development

Model validation proceeded in several stages. PCboom was first run for all focus flights, and general comparison of focus position and peak overpressure was obtained. Focus locations, as defined by the WTF “earliest arrival” algorithm, agreed very well. The PCBoom footprint peak pressure contours were, however, irregular, with the peak signatures not necessarily coinciding with the WTF algorithm and often containing anomalous values at isolated points. Caustic curvatures were not regular through the course of a computed footprint. These issues were identified with irregularities in the as-flown trajectory and atmospheric data. The irregularities were at a scale not consistent with the smooth gradient assumption for geometrical acoustic ray tracing, and the resultant footprints were not consistent with the very regular diffraction zone footprints seen in the flight-test data. PCBoom analysis for selected passes was therefore repeated with modeled trajectory and atmospheric inputs. The trajectory was modeled via PCBoom’s “TADVANCE” mode where derivatives are based on local quadratic splines. The atmospheric profile for each flight was based on three to four linear segments. The resultant footprints were well behaved, and agreed well with the geometry of the measured focal zones.

PCBoom’s Gill-Seebass model for focus signatures agreed well with measured maximum foci, but the shape in the expansion region did not match well, and post-focus signatures were only qualitative. This was expected.

PCBoom’s ray geometry and caustic curvature, together with its “PCBurg” lossy solution for booms at the edge of the diffraction zone, served as inputs to LNTE. LNTE results were excellent, agreeing extremely well with measured booms throughout the diffraction zone. Progression of LNTE and PCBoom development from initial through alpha, beta, and final versions consisted primarily of developing the interface between the two, rather than requiring improvements to the algorithms.

Applying NPE to sonic boom focusing proved to be more interesting. The original concept was that a PCBoom wavefront at some position between the flight altitude and the ground focus would serve as input, and NPE would numerically march this wave to a focus. This was not successful, with diffraction from the edges of the initial wavefront intruding into the focus region. It was found that NPE required an initial wavefront prior to formation of the caustic. Since a transition focus caustic begins at the aircraft as it passes Mach 1, this is not possible to extract from PCBoom. An alternate approach was developed, using a “ripple” wavefront with a concave center that will form a caustic, and outer portions that transition to convex shapes that will not focus and not present edge diffraction. The solution at a position after the caustic forms can then be scaled to the flight-test caustic curvature. Scaling rules were developed for this procedure to work with a particular ripple wavefront that had been successful for turbulence studies. The resultant predicted focal zone signatures had good qualitative agreement with measured signatures through the diffraction region, but tended to be about 30 percent lower in amplitude. This difference in altitude was concluded to be an artifact of the ripple wavefront yielding a variable curvature caustic, while the actual flight-test caustics had nearly constant curvature. Future development of NPE should include alternative ripple wavefronts that yield constant curvature caustics.

As with LNTE, development of NPE involved the interface between NPE and PCBoom, and did not require any changes to its algorithms. The scaling approach was based on Tricomi scaling, but does not conflict with the capability of NPE to handle turbulence as well as focusing.

## 12.4 Focusing of Low-Boom Shaped Signatures

The three focus models were applied to focus conditions of four low-boom shaped aircraft – one each provided by Boeing and Gulfstream, and two provided by NASA. Because LNTE worked very well for the SCAMP data, its results for the shaped foci were considered to be credible. There was good consistency in its behavior across the four aircraft configurations.

The PCBoom Gill-Seebass focused signatures had a very spiky appearance, associated with application of the single step shock solution to each shock. This method is not suitable for application to complex multi-shock signatures.

NPE focus signatures were, in places, very similar to LNTE, but were lower in amplitude. That was consistent with the comparison with SCAMP data. The NPE focus signatures tended to have inconsistent differences from LNTE toward the end of the signatures. That is felt to be a consequence of the variable caustic curvature from the ripple wavefront.

Following the initial application of the focus models to individual shaped focus cases, a profile exploration analysis was performed. For each of three configurations (one Boeing, one Gulfstream, and one NASA) a set of four to six alternate transition profiles were prepared. The alternate climb-outs were obtained by changing effective engine power from a baseline. Focus signatures were computed using LNTE, which is considered to be the best of the focus methods and is the only one for which loudness can be computed.

The overall conclusion from this analysis is that lower acceleration rate results in lower loudness, and higher altitude results in lower loudness. Lower acceleration and higher altitude generally imply longer propagation distances, which means lower amplitude from being further away and that the signature evolves closer to its design point.

Higher altitude and lower acceleration can have adverse effects on performance. They also result in shallower caustic incidence angles with the ground, which makes accurate placement of the focus more difficult and also makes the overall ground focus footprint larger. These can be issues if focus signatures do not fall within acceptable levels. Further analysis of shaped aircraft focusing will require tools capable of computing loudness through the full footprint. Aircraft shaping studies should also consider focus conditions in addition to cruise conditions.

## References

- Auger, T., and Coulouvrat, F. (2002), "Numerical Simulation of Sonic Boom Focusing," *ALAA Journal*, Vol. 40, No. 9, September 2002.
- Berton, J. J. (2003), "Optimum Climb to Cruise Noise Trajectories for the High Speed Civil Transport", NASA/TM—2003-212704. November 2003.
- Blokhintzev, D. I. (1946), "The Propagation of Sound in an Inhomogeneous and Moving Medium I". *J. Acoust. Soc. Am.*, 18, 322-328; also, "Acoustics of a Nonhomogeneous Moving Medium", Gostekhiyazat, Moscow, USSR, 1946: translated as NACA TM-1399. 1946.
- Coulouvrat, F. (2011), "Acoustic shock wave propagation in a heterogeneous medium: a numerical simulation beyond the parabolic approximation", *J. Acoust. Soc. Am.*, July 2011.
- Downing, J. M.; Zamot, N.; Moss, C.; Morin, D.; Wolski, E.; Chung, S.; Plotkin, K.; and Maglieri, D. (1998), "Measurement of Controlled Focused Sonic Booms from Maneuvering Aircraft," *J. Acoust. Soc. Am.*, Vol. 104, No. 1, pp 112-121, July 1998.
- Elmer, K. R.; Welge, H. R.; Salamone, J.; and Cowart, R. (2013), "SCAMP: Supersonic Passenger Transport Transonic Acceleration Flight Profiles with Considerations of Focused Sonic Boom", AIAA 2013-1065.
- Gill, P. M. and Seebass, A. R. (1975), "Non-Linear Acoustic Behavior at a Caustic: An Approximate Solution", *ALAA Progress in Astron/Aeronautics*, Nagamatsu, HJ.T. (Ed.). MIT Press, 1975.
- Gill, P. M. (1974), "Nonlinear Acoustic Behavior at a Caustic", Ph.D. Thesis, Cornell University, June 1974.
- Guiraud, J. P. (1965), "Acoustique Geometrique, Bruit Ballistique des Avions Supersonique et Focalisation", *J. Mecanique*, 4, 215-267, 1965.
- Haglund, G. T. and Kane, E. J. (1974), "Analysis of Sonic Boom Measurements Near Shock Wave Extremities for Flight Near Mach 1.0 and for Airplane Accelerations," NASA CR-2417, July 1974.
- Hayes, W. D. (1970), "Comments on the Caustic Problem", in *Third Conference on Sonic Boom Research*, Schwartz, I.R (Ed.), NASA SP-255, October 1970.
- Hayes, W. D.; Haefeli, R. C.; and Kulsrud, H. E. (1969), "Sonic Boom Propagation in a Stratified Atmosphere, With Computer Program", NASA CR-1299, April 1969.
- Hayes, W. D. (1969), "Similarity Rules for Nonlinear Acoustic Propagation Through a Caustic," *Second Conference on Sonic Boom Research*, NASA SP-180, 1969, pp. 165-171.
- Hobbs, C.; Page, J.; and Plotkin K. (2011), "SCAMP Acoustic Measurement Data", Wyle Technical Note TN 11-02, June 2011.

- Howe, D. (2005), "Improved Sonic Boom Minimization with Extended Nose Spike," AIAA-2005-1014, January 2005.
- Kandil, O. and Zheng, X. (2005), "Computational Solution of Nonlinear Tricomi Equation for Sonic Boom Focusing and Applications," Paper Number 2005 - 43, *International Sonic Boom Forum*, Penn State University, State College, PA, July 21, 2005.
- Kandil, O. and Zheng, X. (2005), "Prediction of Superboom Problem using Computational Solution of Nonlinear Tricomi Equation," AIAA 2005-6335.
- Keller, J. B. (1954), "Geometrical acoustics I: The theory of weak shock waves," *J. Appl. Physics* **25**, 938-947 (1954).
- Ludwig, D. (1966), "Uniform Asymptotic Expansions at a Caustic", *Comm. on Pure and Appl Math.* **XIX**. 215-250, 1966.
- McDonald, B. E. (2002), "High-angle formulation for the nonlinear progressive-wave equation model," *Wave Motion* **31**, 165-171 (2002).
- McDonald, B. E., and Ambrosiano, J. (1984), "High-order upwind flux correction methods for hyperbolic conservation laws," *J. Comp. Phys.* **56**, 448-460 (1984).
- McDonald, B. E. and Kuperman, W. (1987), "Time domain formulation for pulse propagation including nonlinear behavior at a caustic," *J. Acoust. Soc. Am.*, **81** 1406-1417 (1987).
- Maglieri, D. J.; Carlson, H. W.; and Hubbard, H. H. (1980), "Status of Knowledge of Sonic Booms," *Noise Control Engineering*, Vol. 15, No. 2, Sept-Oct 1980.
- Maglieri, D. J. and Plotkin, K. J. (1991), "Sonic Boom," Chapter 10 in *Aeroacoustics of Flight Vehicles: Theory and Practice*, Volume 1: Noise Sources, H.H. Hubbard, ed., NASA Reference Publication 1258, WRDC Technical Report 90-3052, August 1991.
- Maglieri, D. J.; Bobbitt, P. J.; Massey, S. J.; Plotkin, K. J.; Kandil, O. A.; and Zheng, X. (2011), "Focused and Steady-State Characteristics of Shaped Sonic Boom Signatures: Prediction and Analysis," NASA/CR-2011-217156, June 2011.
- Maglieri, D. J.; Hilton, D. A.; and McLeod, N. J. (1966), "Experiments on the Effects of Atmospheric Refraction and Airplane Accelerations on Sonic-Boom Ground-Pressure Patterns," NASA TN D-3520, 1966.
- Marchiano, R.; Coulouvrat, F.; and Grenon, R. (2003), "Numerical simulation of shock wave focusing at fold caustics, with application to sonic boom," *J. Acoust. Soc. Am.*, **114**, 1758-1771, 2003.

## References

- Middleton, W. D. and Carlson, H. W. (1965), "A Numerical Method for Calculating Near-Field Sonic-Boom Pressure Signatures," NASA TN D-3082, November 1965.
- Norris, Guy et al. (2012), "NASA Focuses Supersonic Effort On Low-Boom Propulsion," Aviation Week Article, June, 2012, p. 50.
- Officer, C. B. (1958), Introduction to the Theory of Sound Transmission, With Application to the Ocean, McGraw-Hill, New York, 1958.
- Onyeonwu, R. O. (1973), "A Numerical Study of the Effects of Aircraft Maneuvers on the Focusing of Sonic Booms," UTIAS Report No. 192, November 1973.
- Page, J. A.; Plotkin, K. J.; and Wilmer, C. (2010), "PCBoom Version 6.6 Technical Reference and User Manual," Wyle Report WR 10-10, March 2010.
- Page, J.; Plotkin, K.; Hobbs, C.; Elmer, K.; Ladd, J.; Maglieri, D.; Piacsek, A.; Sparrow, V.; and Salamone, J. (2011a), "Superboom Caustic Analysis And Measurement Program (SCAMP) Year 1 Annual Report", Wyle Research Report 11-16, July 2011.
- Page, J.; Plotkin, K.; Piacsek, A.; Sparrow, V.; Salamone, J.; Elmer, K.; Ladd, J.; and Maglieri, D. (2011b), Superboom Caustic Analysis and Measurement Program (SCAMP) Comparison Report," Wyle Report WR 11-23, October 2011.
- Pawlowski, J. W.; Graham, D. H.; Boccadoro, C. H.; Coen, P. G.; and Maglieri, D. J. (2005), "Origins and Overview of the Shaped Sonic Boom Demonstration Program," AIAA-2005-0005, January 2005.
- Piacsek, A. (1995), "*A numerical study of weak step shocks that focus in two dimensions*," Ph. D. thesis, The Pennsylvania State University (1995).
- Piacsek, A. (2002), "Atmospheric turbulence conditions leading to focused and folded sonic boom wave fronts," *J. Acoust. Soc. Am.* **111**, 520-529 (2002).
- Plotkin, K. J. (1971), *The Effect of Atmospheric Inhomogeneities on the Sonic Boom*, Ph.D. Thesis, Cornell University, January 1971.
- Plotkin, K. J. and Cantril, J. M. (1976), "Prediction of Sonic Boom at a Focus", Wyle Laboratories Research Report WR 75-7, October 1975. Also, AIAA Paper 76-2, January 1976.
- Plotkin, K. J. (1998), "PCBoom3 Sonic Boom Prediction Model - Version 1.0e," Wyle Report WR 95-22e, October 1998.
- Plotkin, K. J.; Page, J. A.; and Hobbs, C.M. (2011), "SCAMP Program Flight Test Plan", Wyle Technical Note TN 10-07, Revision 1, Feb 2011.



- Sanai, J. Toong T. Y. and Pierce, A. D. (1976), "Ballistic Range Experiments on Superbooms Generated by Refraction". and "Ballistic Range Experiments on the Super-boom Generated at Increasing Flight Mach Numbers," *J. Acoust. Soc. Am.*, 59 (3), 513-524, 1976.
- Seebass, G. (1970), "Nolinear Behavior at a Caustic," in Third Conference on Sonic Boom Research, Schwartz, I.R (Ed.), NASA SP-255, October 1970.
- Sescu, A. and Abjeh, A. A. (2010), "On the discontinuous Galerkin computation of N-waves focusing," *Int. J. Numer. Meth. Fluids*, Wiley Online Library (wileyonlinelibrary.com). DOI: 10.1002/flid.2461
- Shepherd, K. P. and Sullivan, B. M. (1991), "A Loudness Calculation Procedure Applied to Shaped Sonic Booms," NASA Technical Paper 3134, November 1991
- Shields, E. and Li, W. (2011), "CFD-Based Redesign of a Low-Boom Supersonic Demonstrator Concept," AIAA Paper 2011-3499, June 2011.
- Stevens, S. S. (1972), "Perceived level of noise by Mark VII and decibels (E)," *J. Acoust. Soc. Am.*, 51(2):575-601, 1972.
- Thomas, C. L. (1970), "Extrapolation of Wind-Tunnel Sonic Boom Signatures Without Use of a Whitham F Function," NASA SP-255, Third Conference on Sonic Boom Research, Schwartz, I.R., (Ed.), October 1970, pp. 205-218.
- Wanner, J. C.; Vallee, J.; Vivier, C.; and They, C. (1972), "Theoretical and Experimental Studies of the Focus of Sonic Booms," *J. Acoust. Soc. Am.*, Vol 52, No. 1, Part 1, 1972.
- Welge, H. R.; Bonet, J.; Magee, T.; Chen, D.; Hollowell, S.; Kutzman, A.; Mortlock, A.; Stengle, J.; Nelson, C.; Adamson, E.; Baughcum, S.; Britt, R.; Miller, G.; and Tai, J. (2010), "N+2 Supersonic Concept Development and Systems Integration," NASA CR-2010-216842, August 2010.
- Whitham, G. B. (1952), "The Flow Pattern of a Supersonic Projectile", *Communications on Pure and Applied Mathematics*, 5, pp. 301-348, 1952.
- Whitham, G. B. (1956), "On the propagation of weak shock waves," *J. Fluid Mech.* **1**, 290-318..
- Wurman, G.; Haering Jr., E. A.; and Price, M. J. (2011), High Quality Observations of Sonic Booms, Abstract S31D-2272 presented at 2011 Fall Meeting, AGU, San Francisco, Calif., 5-9 Dec.